

PROCEEDINGS



SPIE—The International Society for Optical Engineering

ALT '94 International Conference

Laser Methods of Surface Treatment and Modification

Alexander M. Prokhorov
Chair

Vladimir I. Pustovoy
Editor

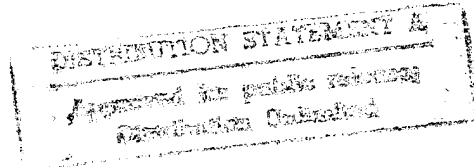
5–9 September 1994
Konstanz, Germany



Organized by
General Physics Institute, Moscow, Russia
Konstanz University, Germany

19950911 118

Cosponsored by
Russian Ministry of Science
Russian Basic Research Foundation
European Research Office of the U.S. Army
SPIE/Russia Chapter



Volume 2498

PROCEEDINGS



SPIE—The International Society for Optical Engineering

ALT '94 International Conference

Laser Methods of Surface Treatment and Modification

Alexander M. Prokhorov

Chair

Vladimir I. Pustovoy

Editor

5–9 September 1994

Konstanz, Germany

Organized by

General Physics Institute, Moscow, Russia
Konstanz University, Germany

Cosponsored by

Russian Ministry of Science
Russian Basic Research Foundation
European Research Office of the U.S. Army
SPIE/Russia Chapter

Published by

SPIE—The International Society for Optical Engineering

Accesation For	
TECH COMM	<input checked="" type="checkbox"/>
TECH EXP	<input type="checkbox"/>
Unspecified	<input type="checkbox"/>
Justification	
<i>perform 50</i>	
By... <i>MAK</i>	
Distribution	
Availability Codes	
Dist	Serial and/or Special
A-1	



Volume 2498

SPIE (The Society of Photo-Optical Instrumentation Engineers) is a nonprofit society dedicated to the advancement of optical and optoelectronic applied science and technology.



The papers appearing in this book comprise the proceedings of the meeting mentioned on the cover and title page. They reflect the authors' opinions and are published as presented and without change, in the interests of timely dissemination. Their inclusion in this publication does not necessarily constitute endorsement by the editors or by SPIE.

Please use the following format to cite material from this book:

Author(s), "Title of paper," in *Laser Methods of Surface Treatment and Modification: (ALT'94 International Conference)*, Vladimir I. Pustovoy, Editor, Proc. SPIE 2498, page numbers (1995).

Library of Congress Catalog Card No. 95-67080
ISBN 0-8194-1855-2

Published by

SPIE—The International Society for Optical Engineering
P.O. Box 10, Bellingham, Washington 98227-0010 USA
Telephone 360/676-3290 (Pacific Time) • Fax 360/647-1445

Copyright ©1995, The Society of Photo-Optical Instrumentation Engineers.

Copying of material in this book for internal or personal use, or for the internal or personal use of specific clients, beyond the fair use provisions granted by the U.S. Copyright Law is authorized by SPIE subject to payment of copying fees. The Transactional Reporting Service base fee for this volume is \$6.00 per article (or portion thereof), which should be paid directly to the Copyright Clearance Center (CCC), 222 Rosewood Drive, Danvers, MA 01923. Other copying for republication, resale, advertising or promotion, or any form of systematic or multiple reproduction of any material in this book is prohibited except with permission in writing from the publisher. The CCC fee code is 0-8194-1855-2/95/\$6.00.

Printed in the United States of America.

Contents

vii *International Program Committee*
ix *Introduction*

LASER METHODS OF SURFACE TREATMENT AND MODIFICATION

2 **Laser surface processing of thin films for microelectronics applications [2498-01]**
M. Takai, Osaka Univ. (Japan)

11 **Photophysical processes on a surface studied by laser methods [2498-02]**
A. M. Bonch-Bruevich, T. A. Vartanyan, S. G. Przhibelskii, V. V. Khromov, S.I. Vavilov State Optical Institute (Russia)

19 **Building surface nanostructures with laser near fields [2498-03]**
V. I. Balykin, Institute of Spectroscopy (Russia)

22 **Practical excimer-laser-assisted cleaning of solid surfaces [2498-04]**
H. K. Park, C. P. Grigoropoulos, Univ. of California/Berkeley (USA); A. C. Tam, IBM Almaden Research Ctr. (USA)

32 **Optical probing of the temperature and pressure transients at a liquid/solid interface due to pulsed laser-induced vaporization [2498-05]**
H. K. Park, C. P. Grigoropoulos, Univ. of California/Berkeley (USA); C. C. Poon, A. C. Tam, IBM Almaden Research Ctr. (USA); O. Yavaş, P. Leiderer, Univ. Konstanz (FRG)

41 **Memory effect on acoustic cavitation [2498-06]**
O. Yavaş, P. Leiderer, Univ. Konstanz (FRG); H. K. Park, C. P. Grigoropoulos, Univ. of California/Berkeley (USA); C. C. Poon, A. C. Tam, IBM Almaden Research Ctr. (USA)

45 **Laser-induced etching and deposition of tungsten in tungstenhexafluoride-hydrogen atmosphere [2498-07]**
K. Piglmayer, Z. Toth, Z. Kantor, Johannes-Kepler-Univ. Linz (Hungary)

51 **Pulsed-laser deposition of boron nitride films on silicon [2498-08]**
R. Schmauder, G. Dodel, G. Bilger, Univ. Stuttgart (FRG)

58 **Diamondlike film deposition by laser-initiated dissociation of benzol vapor [2498-09]**
V. A. Astapenko, Moscow Institute of Physics and Technology (Russia); O. E. Sidoryuk, E. Ushanova, Polus Research Institute (Russia)

61 **Production of diamondlike films by laser ablation in the presence of residual gas in a reaction chamber [2498-10]**
V. A. Astapenko, Moscow Institute of Physics and Technology (Russia); O. E. Sidoryuk, Polus Research Institute (Russia)

65 **Laser distillation-deposition synthesis of silica glasses with variable concentrations of oxygen-deficient centers [2498-11]**
V. F. Lebedev, V. M. Marchenko, General Physics Institute (Russia); A. O. Rybaltovski, V. A. Tikhomirov, Moscow State Univ. (Russia)

72 **Laser-deposited thin films of biocompatible ceramic [2498-12]**
M. Jelínek, V. Olšan, L. Jastrabík, Institute of Physics (Czech Republic); T. Dostálová, L. Himmlová, Institute of Dental Research (Czech Republic); J. Kadlec, M. Pospíchal, Military Academy of Brno (Czech Republic); M. Šimečková, Institute of Physics (Czech Republic); C. Fotakis, Foundation for Research and Technology—Hellas (Greece)

79 **Processing parameters influence on structural properties of PZT layers deposited by pulsed laser deposition (PLD) [2498-13]**
V. Trtík, M. Jelínek, L. Jastrabík, Institute of Physics (Czech Republic)

84 **Deposition of thin polymer films by pulsed excimer laser ablation [2498-14]**
M. Metal, V. Myslík, M. Jelínek, Institute of Chemical Technology (Czech Republic)

88 **Laser-annealed deep ohmic contacts [2498-15]**
P. Macháč, V. Myslík, M. Vrňata, Institute of Chemical Technology (Czech Republic)

95 **Laser method of preparation of high-T_c superconducting films on bulk ceramic YBa₂Cu₃O_(7-δ) [2498-16]**
Yu. V. Denisov, V. A. Madii, Moscow Institute of Physics and Technology (Russia); Yu. I. Krasilov, Institute of General and Inorganic Chemistry (Russia); A. Zubovich, Moscow Institute of Physics and Technology (Russia)

107 **Investigation of high-T_c superconducting tunnel junction after laser radiation processing [2498-17]**
U. U. Broslavetz, A. A. Fomitchev, M. A. Yakshin, Moscow Institute of Physics and Technology (Russia)

115 **Electric-current-stimulated diffusion of heavy ions and oxygen in YBCO (123) and Bi (2223) HTCS films at 4.2–300 K [2498-18]**
E. N. Lubnin, G. N. Mikhailova, A. M. Prokhorov, A. S. Seferov, A. V. Troitskii, General Physics Institute (Russia); D. G. Andrianov, S. O. Klimonskii, State Institute of Rare Metals (Russia)

126 **Backscattered heterodyne Doppler diagnostics of laser-induced near-surface transport phenomena [2498-19]**
V. M. Gordienko, Moscow State Univ. (Russia); E. M. Chastookhin, Science Research Ctr. for Technological Lasers (Russia); N. N. Kurochkin, Moscow State Univ. (Russia); V. Ya. Panchenko, Science Research Ctr. for Technological Lasers (Russia)

134 **Computer simulation of mass transfer during laser doping of materials [2498-20]**
V. V. Kartuzov, I. V. Krasikov, C. E. Rotmistrovsky, Institute for Problems of Materials Science (Ukraine)

138 **Statistical thermodynamics for the alloy under irradiation model [2498-21]**
V. V. Kamychenko, Institute for Problems of Materials Science (Ukraine); V. G. Vaks, Kurchatov Institute (Russia); V. V. Kartuzov, Institute for Problems of Materials Science (Ukraine)

143 **Resonant electromagnetic field effects on trimers and dimers [2498-22]**
V. V. Maksimov, N.S. Kurnakov Institute of General and Inorganic Chemistry (Russia); A. N. Orlov, A. M. Prokhorov, General Physics Institute (Russia)

NEW LASER SYSTEMS FOR TECHNOLOGICAL APPLICATIONS

154 **Recent developments in solid state laser materials and devices [2498-23]**
J.-M. Breteau, Thomson-TRT Défense (France)

164 **Stimulated Raman scattering in barium nitrate crystal in the external optical cavity [2498-24]**
P. G. Zverev, T. T. Basiev, I. V. Ermakov, A. M. Prokhorov, General Physics Institute (Russia)

171 **Passive Q-switching of 1.3- μ m Nd-lasers with Nd²⁺:SrF₂ and V³⁺:YAG crystalline saturable absorbers and application to Raman shifting to the eye-safe region [2498-25]**
T. T. Basiev, V. B. Sigachev, M. E. Doroshenko, A. G. Papashvili, P. G. Zverev, V. V. Osiko, General Physics Institute (Russia)

179 **Spectroscopic and laser properties of Nd³⁺ doped fluoride crystals in 1.3- μ m region [2498-26]**
T. T. Basiev, V. B. Sigachev, M. E. Doroshenko, A. G. Papashvili, V. V. Osiko, General Physics Institute (Russia)

193 **Cr⁴⁺:Y₃Al₅O₁₂ laser crystal in a tunable subpicosecond laser under strong aberration [2498-27]**
U. U. Broslavetz, A. A. Fomichov, V. D. Lokhnygin, O. O. Silichev, Moscow Institute of Physics and Technology (Russia)

202 **Up-conversion: factors in absolute efficiency [2498-28]**
W. A. Sibley, Univ. of Alabama/Birmingham (USA)

211 **Optical properties of nonstoichiometric fluorite crystals doped with Nd³⁺ and Pr³⁺ in 1.3- μ m spectral range [2498-29]**
M. Yu. Sharonov, B. K. Sevastyanov, Z. I. Zmurova, E. A. Krivandina, A. A. Bystrova, I. I. Buchinskaya, B. P. Sobolev, Institute of Crystallography (Russia)

223 **Excited-state absorption (ESA) spectroscopy measurement of charge transfer bands in doped ionic crystals [2498-30]**
B. K. Sevastyanov, Institute of Crystallography (Russia)

231 **Excited state absorption spectra of RE-doped laser glasses [2498-31]**
A. K. Przhevuskii, M. Yu. Kirshin, Research and Technological Institute of Optical Materials (Russia)

241 **Characterization of Nd:GdVO₄ crystals for high-efficiency diode-pumped lasers [2498-32]**
I. A. Shcherbakov, A. I. Zagumennyi, General Physics Institute (Russia)

250 *Author Index*

International Program Committee

Conference Chairman

Alexander Prokhorov, General Physics Institute (Russia)

Organizing Chairman

Vladimir Pustovoy, General Physics Institute (Russia)

Program Cochairs

Paul Leiderer, Konstanz University (Germany)

Anatoly Sukhorukov, Moscow State University (Russia)

Members

E.I. Akopov (Russia)

V.V. Apollonov (Russia)

T.T. Basiev (Russia)

V.I. Beklemishev (Russia)

M. Bertolotti (Italy)

A.M. Bonch-Bruevich (Russia)

J. Boneberg (Germany)

V.G. Bordo (Russia)

T.J. Chuang (Taiwan)

M. Ducloy (France)

M. Jelinek (Czech Rep.)

V.I. Konov (Russia)

D. von der Linde (Germany)

A. Maslov (Russia)

S. Metev (Germany)

I. Mihailescu (Romania)

K.A. Prokhorov (Russia)

M. Stuke (Germany)

F. Träger (Germany)

Introduction

The International Conference on Advanced Laser Technologies ALT'94 was held in Konstanz, Germany, from September 5-9, 1994. It was intended as a forum for discussing fundamental problems as well as advanced scientific developments in the field of laser treatment of solid surfaces, laser diagnostics and novel optical materials.

The rapid development of laser sources opens up new and fascinating ways for using light as a tool to characterize and modify surfaces and thin films. Quite remarkable progress is being made in improving lasers in their performance with respect to power, tunability, or generation of ultrashort light pulses. In particular, the application of laser diodes both as a direct light source and for pumping other laser materials is flourishing. Among the laser methods for surface treatment and modification a large variety of processes are under investigation, such as etching by laser induced chemical reactions, annealing and cleaning of semiconductor surfaces, or the maskless production of submicron periodic structures. Also film deposition by means of laser processing is widely being used, including high-temperature superconductors and diamond-like films. In laser diagnostics new time domains have become accessible by optical microscopy with femtosecond light pulses, and nonlinear effects are exploited e.g. to characterize adsorbates by their nonlinear optical response, or magnetic interfaces by means of the nonlinear magneto-optic Kerr effect. New materials with characteristic dimensions on nanoscopic scales - a particularly prominent example being porous silicon - are attracting tremendous attraction due to quantum size effects which give rise to novel optical phenomena not observed in the corresponding bulk materials. As a result of this wealth of developments it is difficult yet essential to obtain thorough reviews of the field, covering fundamental aspects as well as applications. For the latter, it is also very important to realize which processes are already well accepted in industry, which phenomena may not be so suitable for industrial purposes, and which are the most desirable new directions to go.

The ALT'94 conference in Konstanz provided a wide and up-to-date overview of these topics. It was the third ALT meeting, after the first interdisciplinary ALT'92 Conference in Moscow and the ALT'93 Workshop in Prague (SPIE vol. 2332), and was organized as a Satellite Meeting to the EQEC-CLEO/Europe'94 Conference (Amsterdam) jointly by the General Physics Institute, Moscow, and the Physics Department at the University of Konstanz. As a special objective, the ALT conferences are to promote the communication and strengthen the relationships between scientists and engineers from scientific centres of the former Soviet Union and from Western countries, an urgent task regarding the challenges of modern technological developments. Also in this respect ALT'94 can be considered as a very successful meeting.

**Alexander Prokhorov
Paul Leiderer**

Laser Methods of Surface Treatment and Modification

Laser surface processing of thin films for microelectronics application

Mikio Takai

Faculty of Engineering Science and Research Center for Extreme Materials,
Osaka University, Toyonaka, Osaka 560, Japan

ABSTRACT

Laser maskless patterning of magnetic thin films and transparent electrode films for microelectronics application has been performed to realize higher precision and higher rate processes than conventional techniques. Single crystalline ferrite and metallic alloy thin films such as FeAlSi, FeZrN, and CoZrNb have been etched without a mask in chemical solutions to realize magnetic head gap structures for future applications. Indium tin oxide (ITO) thin films on a glass substrate have been etched by laser ablation to provide a maskless patterning process for flat panel display (FPD) fabrication. Laser cleaning has been applied to a magnetic head slider and glass substrates as an alternative technique to conventional wet cleaning processes.

Keywords: laser processing, magnetic thin film, laser etching, ferrite, magnetic head, ITO, flat panel display, maskless patterning, laser cleaning

1. INTRODUCTION

Laser microprocessing has widely been applied to microelectronics in the last 20 years^{1,2}. Table 1 summarizes the applications of laser processing to microelectronics fields. Laser beams have mostly been used as a localized heat source and the processes applied to microelectronics in the early stage were scribing wafers such as silicon-on-sapphire (SOS) or ceramic wafers, or trimming thin film resistors and capacitors in monolithic integrated circuits (ICs). Laser annealing was studied to remove damage of ion implanted layers in the late 70's and was extended to a technique realizing silicon-on-insulator (SOI) structures or three dimensional integration in the 80's. This technique was recently studied for thin film transistor (TFT) fabrication of flat panel displays (FPDs). Laser mixing for new material synthesis, alloying for contact formation, and impurity gettering were studied at the same time.

Table 1 A summary of laser processing applications to microelectronics.

PROCESS	APPLICATIONS
ANNEALING	Damage by Ion Implantation TFT for FPD, SOI (Recrystallization)
MIXING	New Material Synthesis
ALLOY	Contact Formation
GETTERING	Impurity Gettering
HOLOGRAPHY	Grating, Alignment
SCRIBING	SOS, Ceramics
TRIMMING	Thin Film Resistor, Capacitor
REPAIR	Mask Pattern
BLOW	Redundancy Circuits of Memories
DEPOSITION	LCVD (Maskless Dry Process)
ETCHING	Localized or Maskless Process
DOPING	Dry Process with Annealing
EPINTAX	Atomic Layer Epitaxy with MOCVD
ABLATION	Via Hole Drilling in Polymer
LITHOGRAPHY	Below 0.35 μm Lithography

Laser blowing of redundancy circuits of memory IC chips and repairing of mask patterns for lithography were well accepted laser processing in semiconductor IC production procedures. Laser ablation of polymers using ultra violet (UV) laser light such as excimer lasers provided various industrial applications like via-hole drilling for multi-chip modules (MCM) or polymer drilling for ink jet printer heads.

As compared to removal processing using laser lights discussed here, additive processes such as deposition using laser chemical vapor deposition (LCVD), laser epitaxy, and laser doping have also been extensively studied. However these processes were not yet accepted as industrial processes because of the process incompatibility and inadequate quality of obtained layers.

Laser holography combined with ion beam etching was an epoch making process to provide a new technique for optical grating fabrication developed in Japan.

One of the big issues prohibiting laser processing from industrial application in the IC manufacturing is the minimum process resolution of laser processing limited by the wavelength of laser lights. The minimum feature size of the state-of-the-art CMOS (complementay metal oxide semiconductor) process used for DRAM (dynamic random access memory) fabrication ranges from 0.35 μm to 0.25 μm for 64 Mbit and 256 Mbit DRAMs, respectively. Therefore the laser wavelength applicable to these ranges is limited to a deep UV region. Excimer laser lithography is, therefore, in a waiting list for lithography in the next generation of 64 and 256 Mbit DRAM chips.

In this study, laser surface processing, still applicable to microelectronics components, such as magnetic recording head fabrications for hard disk drives (HDDs)^{3 - 7} and video tape recorders (VTRs), and transparent electrode, indium tin oxide (ITO), patterning for FPDs⁸ has been performed to develop high precision and high rate process techniques. Laser surface cleaning^{9 - 11} of such components has also been performed to provide a new cleaning process alternative to conventional wet chemical cleaning processes. Besides semiconductor devices (memories and processors), both magnetic recording and FPD components are key devices and, hence, very important for realizing multi-media oriented information societies in the 21st century.

2. MAGNETIC HEAD FABRICATION

Among various storage devices, HDDs and tape drives have huge market and capacity, though the access time is slower than that of semiconductor memory devices. The storage capacity of HDDs is still increasing and a new tape recording system with digital techniques will be realized even for a consumer video recording system in a few years. The recording bit density is determined by a recording head structure, which is mostly fabricated by a mechanical procedure. The minimum feature size of head tracks ranges about 10 μm , while that of track gaps is already below 1 μm . The precision of track fabrication by conventional mechanical processes is $9 \mu\text{m} \pm 1 \mu\text{m}$ ⁷. Therefore the head structure can still be fabricated by laser processing.

The materials for magnetic recording heads have been single or poly crystalline Mn-Zn ferrite ($\text{MnO:ZnO:Fe}_2\text{O}_3 = 31:17:52$). The ferrite has characteristics of high hardness and brittleness like other ceramics. Therefore high precision micromachining without crack formation was quite difficult. Fig. 1 shows the trend of VTR recording heads. Home VTRs use ferrite heads, while wide-band recording systems such as S-VHS employ metal-in-gap (MIG) heads with additional metal layers like sendust (FeAlSi) having a high magnetization for the use of metal tapes. Future systems with digital recording techniques will use thin film metal heads with high magnetization of sendust, FeZrN , and CoZrNb . The trend of HDDs is almost the same with that of VTRs.

Fig. 2 shows the comparison of magnetic head fabrication processes between conventional mechanical and laser processing. Multiple mechanical processes will be replaced by a single laser process. Fig. 3 shows the etched depth as a function of Ar ion laser power for single crystalline ferrite in 25 % H_3PO_4 for

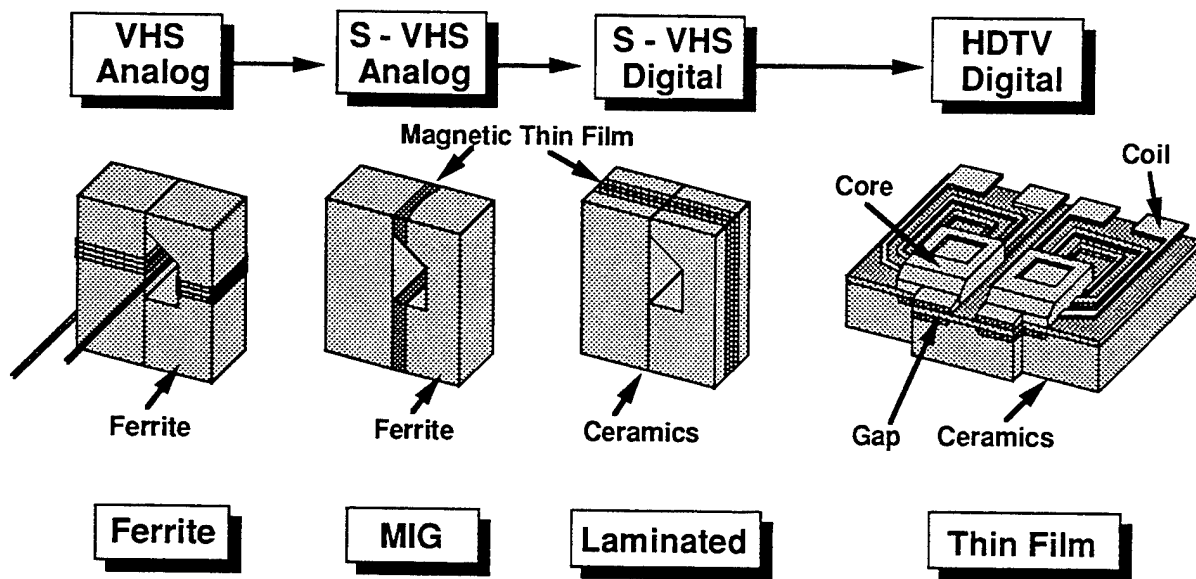


Fig. 1 A trend of video tape recorder (VTR) recording heads.

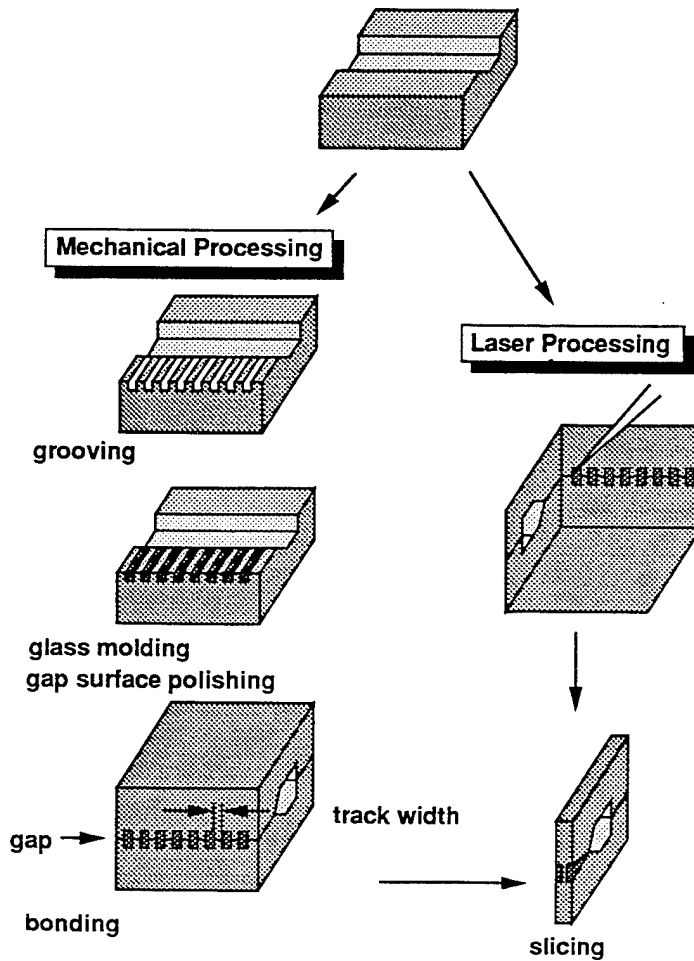


Fig. 2 A comparison of magnetic head fabrication processes between a conventional mechanical and laser processing.

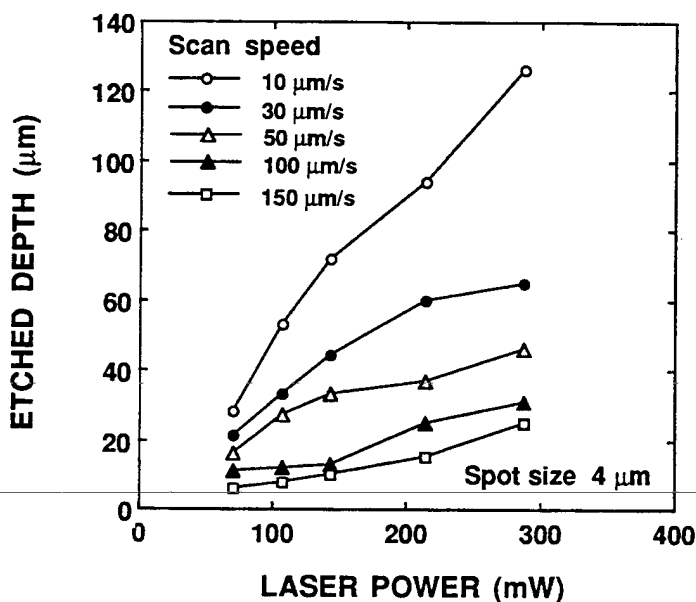


Fig. 3 Etched depth as a function of laser power for Mn-Zn ferrite in a 25 % H_3PO_4 solution.

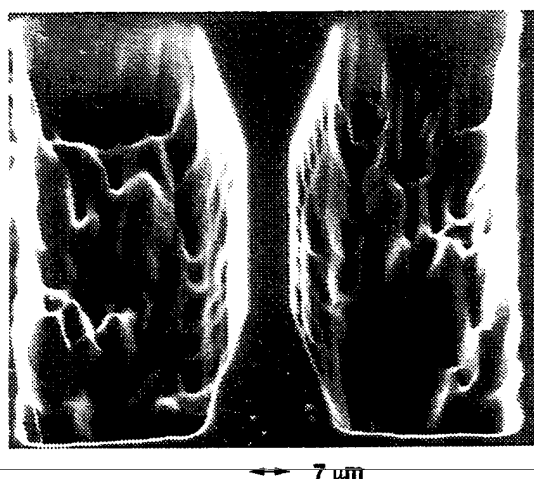


Fig. 4 A top SEM view of laser patterned Mn-Zn ferrite. Laser power, scan speed, and spot size were 100 ~ 140 mW, 10 ~ 60 $\mu m/s$, and 4.5 μm , respectively. The etchant was 25 % H_3PO_4 in a flowing mode.

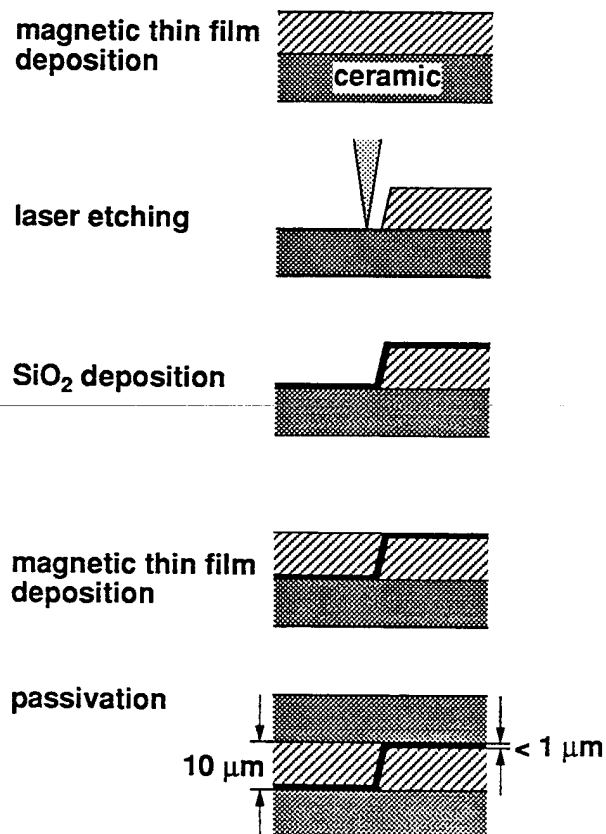


Fig. 5 Schematic of a magnetic head gap process for a thin film head.

Table 2 A summary of etching rate, minimum width, and aspect ratio for laser induced chemical etching of Mn-Zn ferrite

Thermochemical etching in CCl_4

Etching rate	4.1 ~ 68 $\mu m/s$
Minimum width	< beam spot
Aspect ratio	~ 8

Wet chemical etching in H_3PO_4

Etching rate (flow)	250 $\mu m/s$
Minimum width	> beam spot
Aspect ratio	~ 40

Wet chemical etching in KOH

Etching rate (flow)	215 $\mu m/s$
Minimum width	> beam spot
Aspect ratio	~ 3

various laser scanning speeds. The etching takes place through thermochemical reaction. The etched depth increases drastically with the increase in laser power. The maximum etched depth of 125 μm can be obtained by a single scan of laser light. Thus high rate etching rates can be obtained by the laser processing. Fig. 4 shows the top SEM view of patterned ferrite by laser processing. A sharp definition for a recording track within an accuracy of 0.9 μm is possible with the laser etching procedure. Table 2 summarizes the etching characteristics of single crystalline Mn-Zn ferrite by laser processing in ambient chemicals. The etching rates obtained by laser-induced wet chemical etching are 3 ~ 5 times higher than those by thermochemical etching in CCl_4 and about 5 ~ 6 orders of magnitude higher than those obtained by conventional wet chemical or ion beam induced processes. Thus the laser induced wet chemical etching provides higher process rates and higher precision. Crack formation during processing can also be avoided by laser processing and higher output signals can be attained by heads processed by laser irradiation than those by mechanically processed heads.

Fig. 5 shows the schematic of a cross sectional view for a thin-film magnetic-head gap-structure. A key issue for laser processing of a thin-film head gap-structure is to fabricate a vertical side wall. Magnetic metal alloy thin films with a high magnetization such as FeSiAl (sendust), FeZrN, and CoZrNb can be easily etched with a vertical side wall angle of greater than 70°. The maximum etching rates of 300, 250, and 180 $\mu\text{m}/\text{s}$ can be obtained for FeSiAl (sendust), FeZrN, and CoZrNb, respectively, by a single scan of an Ar laser beam in a KOH solution. Fig. 6 shows the top SEM view of laser patterned FeAlSi on a ceramic substrate. Only the magnetic film is patterned with a side wall angle of greater than 70°. Magnetic characteristics of such films before and after laser processing are found by Kerr effect measurement not to be deteriorated by the processing. Thus the laser chemical etching seems very promising even for head fabrications of future systems.

Laser chemical processing can further be applied to head slider fabrications. Fig. 7 shows the cross sectional SEM view of the laser etched groove in Al_2O_3 -TiC. The etched groove has smoother side walls

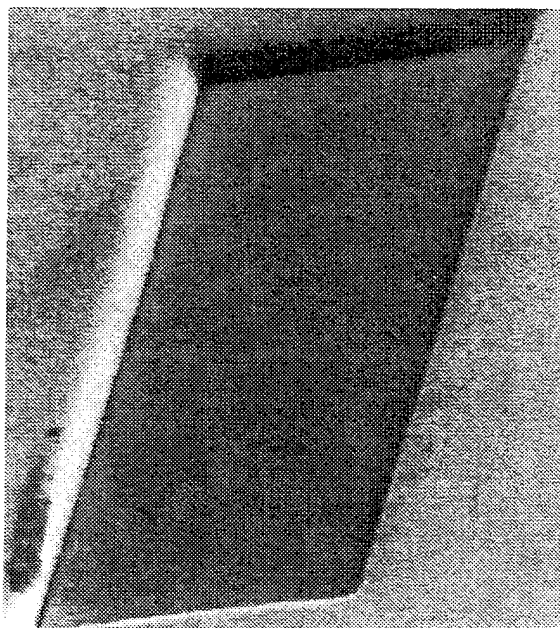


Fig. 6 A top SEM view of laser patterned FeAlSi. Ar ion laser at 100 mW was scanned at 20 $\mu\text{m}/\text{s}$ in a 30 % KOH solution.

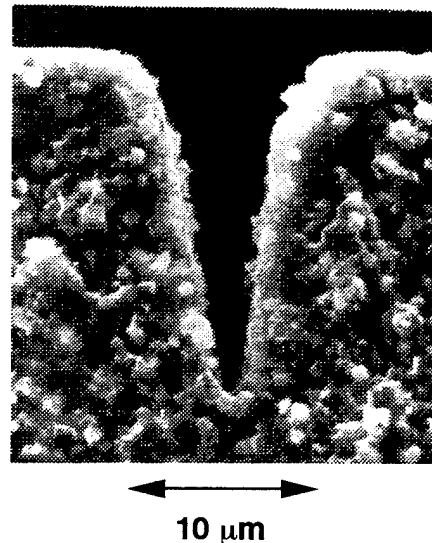


Fig. 7 A cross sectional SEM view of an Al_2O_3 -TiC film. Ar ion laser at 0.24 W with a beam spot size of 1.2 μm was scanned at 5 $\mu\text{m}/\text{s}$ in a 30 % KOH solution.

than the cleaved surface. Fig. 8 shows the top optical view of patterned Al₂O₃-TiC substrates. Automatic patterning by laser chemical reaction without a mask can be easily made and further be applied to head slider fabrication, i.e., air bearing for HDD heads.

3. TRANSPARENT ELECTRODE PATTERNING FOR FLAT PANEL DISPLAY

ITO layers have widely been used as transparent electrodes for solar cells and, recently, for FPDs. The transparent electrodes are conventionally patterned and structured using photolithography followed by wet etching. The process itself consists of 5 technological steps including resist spin-coating, optical lithography, developing, wet or dry etching, and ashing (i.e. removal of the photoresist). On the other hand, direct patterning without a mask using a scanning laser beam would reduce the conventional process steps to a single step. Laser maskless processing, however, has not been used in microelectronics production such as VLSI (very large scale integration) chips because of the feature size feasibility and the time consumption of the serial process. In contrast to VLSI microelectronic circuits, the minimum feature sizes of FPDs and solar cells reach down to about 3 μm and much fewer contours are used. Therefore, laser maskless processing seems to be applicable to these FPD and solar cell processes⁸.

The laser induced maskless etching of semiconductors, metals, and insulators has been extensively investigated to date. However, etching of transparent electrode materials such as an ITO layer has been only roughly investigated using Nd:YAG laser irradiation, in which crack formation due to substrate glass heating took place or complete removal of ITO layers was not achieved. In this study, ITO layers have been masklessly etched using scanning laser lines of a diode pumped Nd:YLF to develop a single step process of ITO structuring for FPDs. The diode pumped laser is compact and, hence, easily installed in process equipment. With nonlinear optical crystals it is also possible to generate the second and fourth harmonic wavelength of a Nd:YLF laser in the visible and UV ranges, which is an alternative to the excimer laser.

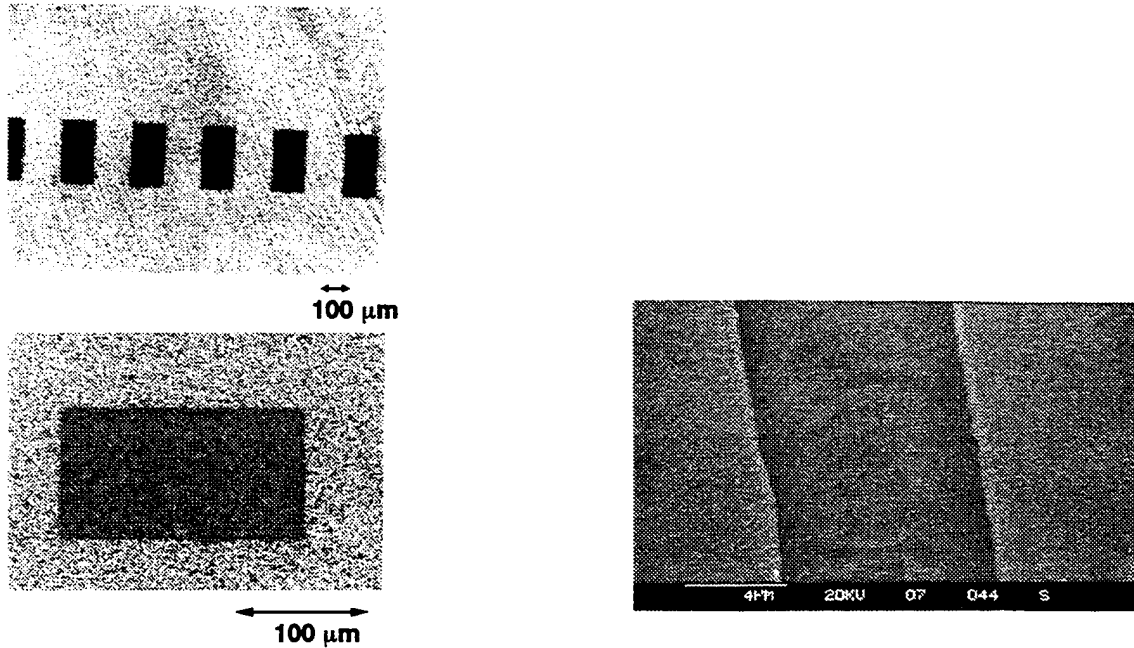


Fig. 8 Top optical microscope views of laser patterned Al₂O₃-TiC film. Ar ion laser at 0.24 W with a beam spot size of 1.2 μm was scanned at 5 μm/s in a 30 % KOH solution.

Fig. 9 A top SEM view of a laser etched groove in ITO on a glass substrate. A frequency doubled Nd:YLF laser with a pulse duration of 6 ns at an energy density of 7.7 J/cm² was scanned at 2.4 mm/s with a pulse repetition rate of 3 kHz.

The sample consisted of an ITO layer of 150 nm thickness deposited by sputtering on a lime glass substrate. The sheet resistance was about $7.5 \Omega/\square$. A Nd:YLF laser of the type TFR from Spectra-Physics with an electrooptical Q-switch produced pulses of 6 ns duration and has a maximum pulse repetition rate of 10 kHz. The infrared wavelength of 1047 nm and frequency doubled green line of 523 nm have been used. The maximum output power was 540 μJ in 1047 nm and 240 μJ in 523 nm. The light intensity was attenuated with gray filters in our experiment in order to achieve smooth profiles of the grooves, though higher repetition and scanning rates with less intensity attenuation would provide higher throughput of the patterning process. The laser beam was focused by single lenses with a focal length of 50 or 10 mm and a numerical aperture of 0.2. A working distance of at least several millimeters was necessary because the vaporized material should be prevented from condensing on the surface of the lens. The sample was located on a motor-driven stage and was scanned with a velocity of 2.4 mm/sec relative to the fixed beam for both wavelengths and all power densities. After laser processing the samples were analyzed with a stylus profilemeter (Dektak II). It had a tip curvature of 12.5 μm . When a step height of 150 nm was taken into consideration, the grooves were 2 μm broader than the measured value shown in the diagram. The shapes of the patterned edge and the bottom were evaluated by top and cross sectional SEM observation after aluminum sputtering.

Fig. 9 shows the top SEM view of a laser etched groove in an ITO layer on a glass substrate. The 523.5 nm line at a pulse energy density of 7.7 J/cm^2 with a repetition rate of 3 kHz was scanned over the sample. A groove width of about 8.5 μm was obtained. However, the underlying glass substrate was slightly etched, showing a ripple pattern at the groove bottom, and redeposited residues at the fringe of the ITO layers were observed. This over-etching of the underlying glass substrate could be avoided by reducing the pulse energy density or using the 1047 nm line. The crack formation at the etched groove bottom did not occur in this study.

Fig. 10 shows the cross sectional SEM view of a laser etched groove in an ITO layer on a glass substrate after aluminum sputter-coating. The 1047 nm line at a pulse energy density of 7.1 J/cm^2 with a repetition rate of 1 kHz was scanned over the sample. The top rough surface is due to the sputtered aluminum. The bottom of the groove was flat and showed the interface between glass and ITO layers, so only the ITO layer was selectively evaporated by laser irradiation. The edge of the ITO layer had a slope of about 30° and a residue presumably due to redeposition of evaporated ITO.

Fig. 11 shows the cross sectional profile of a laser etched groove in an ITO layer on a glass substrate. The 1047 nm line at a pulse energy density of 1.8 J/cm^2 with a repetition rate of 5 kHz was scanned over the sample. It should be noted that a flat groove bottom a roughness of $\pm 4 \text{ nm}$ was obtained. Although the ITO layer was completely removed by laser irradiation, shoulders at the fringes of the ITO layers remained with a height of $50 \sim 60 \text{ nm}$ and a width of less than 1 μm . These residues at the etched fringes should be further removed for FPD application.

Thus, the ITO layer was fully removed by laser irradiation in the air in the case of the 1047 nm line with pulse energy densities ranging from 1.8 to 7.1 J/cm^2 , corresponding to power densities of 3 to $12 \times 10^8 \text{ W/cm}^2$, at a repetition rate of 1 ~ 5 kHz, while much higher energy density was required for the 523.5 nm line. Furthermore, over-etching of glass substrates occurred for the 523.5 nm line. The groove width obtained in this study ranged from 5 to 8.5 μm for the 523.5 nm line, and from 16 to 18 μm for the 1047 nm line, respectively. Electrical measurement showed that the resistance across the several cm long etched ITO grooves was higher than $20 \text{ M}\Omega$. This result proves that the conducting layer has been totally removed.

4. LASER CLEANING

Since the protection of Ozone layer depletion was declared, the use of carbon fluorochloride for cleaning microelectronics materials was strictly prohibited. Laser cleaning using UV laser light irradiation,

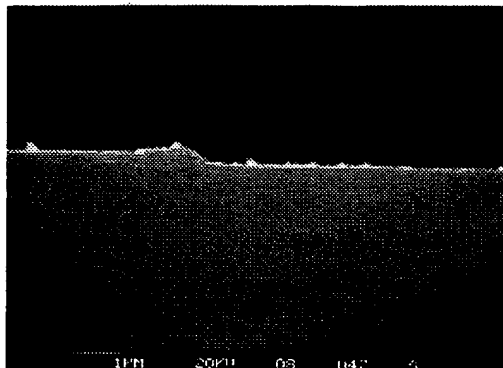


Fig. 10 A cross sectional SEM view of a laser etched groove in ITO on a glass substrate. A Nd:YLF laser at an energy density of 7.1 J/cm^2 was scanned at 2.4 mm/s with a pulse repetition rate of 3 kHz .

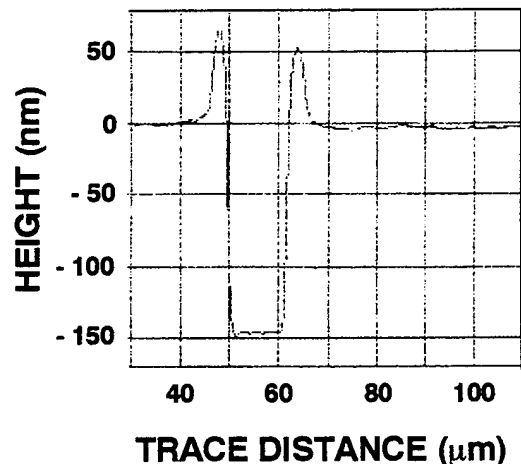
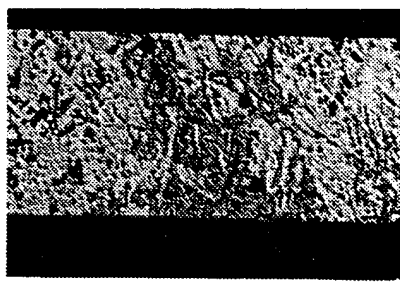


Fig. 11 A DEKTAK trace of an etched ITO groove on a glass substrate.



(a) — $100 \mu\text{m}$



(b) — $100 \mu\text{m}$

Fig. 12 Epoxy resin on magnetic head sliders (a) before and (b) after KrF excimer laser cleaning at an energy density of 60 mJ/cm^2 and 2500 pulses.



(a) — $100 \mu\text{m}$

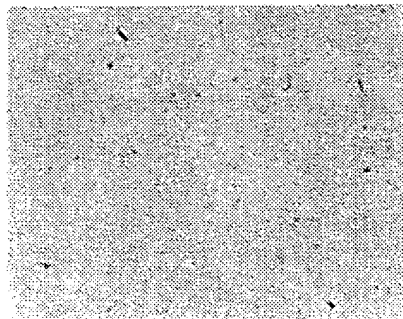


Fig. 13 Finger prints on glass substrates (a) before and (b) after KrF excimer laser cleaning at an energy density of 500 mJ/cm^2 and 1 pulse.

resulting in photodecomposition, thermal ablation, and surface vibration due to laser pulse impact, seems to be one of the alternative methods used for microelectronics application^{9 - 11}.

Fig. 12 shows the magnetic head slider surface stained with epoxy resin before and after KrF excimer laser irradiation. The epoxy resin layer can be completely removed by 2500 pulses of KrF excimer laser irradiation. This epoxy resin layer cannot be removed easily by organic cleaning solutions. Fig. 13 shows the glass substrate surface stained with finger prints before and after KrF laser irradiation of 1 pulse. The finger print can be removed by single shot of KrF excimer laser. Thus the laser cleaning can be applied to localized cleaning of electronic materials without organic solutions. Extensive works for semiconductor cleaning using excimer laser irradiation have been reported elsewhere¹².

5. SUMMARY

The trend and limitation of laser applications to microelectronics processing have been discussed. Laser patterning of magnetic materials, transparent electrodes, and laser cleaning of ceramic components and glass substrates have been studied as laser surface processing of thin films for microelectronics application. Laser processing of magnetic recording head fabrication can provide higher process rate and higher precision than conventional mechanical processes. Indium tin oxide, a transparent electrode material, can be easily patterned by laser ablation without damaging underlying glass substrates. Epoxy resin or finger prints contamination on ceramic components or glass substrates can easily be removed by excimer laser cleaning processes without organic solvents.

6. ACKNOWLEDGEMENTS

The author is indebted to S. Nagatomo, H. Kohda, and C. Yada (D.S. Scanner Co.,Ltd.) for laser processing of magnetic materials, H. Murase (Osaka University), J. Fujita, and S. Horibata (Mitsubishi Electric Corporation) for laser processing of thin film magnetic materials, D. Bollmann and K. Haberger (Fraunhofer Institut fuer Festkoerpertechnologie) for ITO patterning, and Y.F. Lu (National University of Singapore) for laser cleaning.

REFERENCES

1. D. Bäuerle, *Laser Processing and Diagnostics*, Springer-Verlag, Heidelberg, 1984.
2. D.J. Ehrlich and J.Y. Tsao, *Laser Microfabrication: Thin Film Processes and Lithography*, Academic Press, San Diego, 1989.
3. M. Takai, Y.F. Lu, S. Nagatomo, T. Koizumi, and S. Namba, "Thermochemical dry etching of single crystal ferrite by laser irradiation in CCl₄ gas atmosphere", *Appl. Phys. A46*, pp. 197 - 205, 1988.
4. Y.F. Lu, M. Takai, S. Nagatomo, and S. Namba, "Wet-chemical etching of Mn-Zn ferrite by focused Ar⁺ laser irradiation in H₃PO₄", *Appl. Phys. A47*, pp. 319 - 325, 1988.
5. Y.F. Lu, M. Takai, S. Nagatomo, T. Minamisono, and S. Namba, "Laser-induced etching of Mn-Zn ferrite and its application", *Japan. J. Appl. Phys. 28*, pp. 2151 - 2156, 1989.
6. M. Takai and S. Namba, "Laser induced chemical processing of electronic materials", *Laser Surface Microprocessing*, SPIE 1352, pp. 18 - 28, 1989.
7. M. Takai, S. Nagatomo, H. Kohda, C. Yada, H. Sandaiji, and F. Takeya, "Laser chemical processing of magnetic materials for recording head application", *Appl. Phys. A58*, pp. 359 - 363, 1994.
8. M. Takai, D. Bollmann, and K. Haberger, "Maskless patterning of indium tin oxide layer for flat panel displays by diode-pumped Nd:YLF laser irradiation", *Appl. Phys. Lett. 64*, pp. 2560 - 2562, 1994.
9. Y.F. Lu, M. Takai, T. Shiokawa, and Y. Aoyagi, "Excimer-laser removal of SiO₂ patterns from GaAs substrates", *Japan J. Appl. Phys.*, **33**, pp. L324 - L327, 1994.
10. Y.F. Lu, M. Takai, S. Komuro, T. Shiokawa, and Y. Aoyagi, "Surface cleaning of metals by pulsed laser irradiation in air", *Appl. Phys.*, **A59**, 1994 (in press).
11. Y.F. Lu, Y. Aoyagi, M. Takai, and S. Namba, "Laser surface cleaning in air -- mechanisms and applications", *Japan J. Appl. Phys.* (in press)
12. A.C. Tam, W.P. Leung, and W. Zapka, "Laser cleaning techniques for removal of surface particulates", *J. Appl. Phys.* **71**, pp. 3515 - 3523, 1992.

Photophysical processes on a surface studied by laser methods

A. M. Bonch-Bruevich, T. A. Vartanyan, S. G. Przhibelskii, and
V. V. Khromov

S. I. Vavilov All-Russian Research Center, 199034 St-Petersburg,
Russia

ABSTRACT

Principles and ultimate potentialities of laser diagnostics are expanded for absorption systems taking photodesorption of alkali metal atoms from a surface of transparent dielectrics and photoevaporation of metal surface as an example. A possibility is shown to record extra-low atomic fluxes, time-of-flight spectra of desorbed atoms, surface adatoms' concentration at a sub-monolayer coating, adsorption energies and sticking coefficients of atoms impacting the surface, as well as processes of atoms' surface diffusion and their condensation on the surface. Feasibilities of using laser diagnostics for molecular systems' studies are discussed.

1. INTRODUCTION

Laser diagnostics of atomic-molecular systems is presently well developed and characterized by extremely high sensitivity (single atom and molecule may be detected within 1 cm^3) and extremely high, of the order of $1 \mu\text{m}$, spatial resolution. The methods have been successfully employed for composition and dynamic characterization of gas mixtures, fluxes, and flames and also for detection of small atmospheric impurities.

The paper is devoted to applications of these methods to study surface phenomena. Based on our own studies, we have made an attempt to show feasibilities of laser spectroscopy for recording and measuring the most traditional surface properties.

Experimental studies of physical processes on a solid surface come, as a rule, to a need for measurement of low atomic and molecular fluxes desorbed from a surface and low surface concentrations of adsorbed species. To measure these values, fairly well developed optical laser techniques, both taken alone, and in combination with other more traditional physical methods, such as mass-spectrometry, Auger, UV and X-ray spectrosopies, are used. The paper discusses application of these methods for studying adsorption systems and physical processes in them and as an example presents studies of photodesorption of alkali metal atoms from a surface of transparent dielectrics and evaporation of metal surface.

2. PHOTODESORPTION OF SODIUM FROM A SURFACE OF SAPPHIRE

The first of the processes mentioned above has been discovered by us in 1984. Although optical spectra of sodium atoms adsorbed on monocrystalline sapphire surface have evidenced the adsorption to be accompanied by significant reconstruction of the atoms' electronic structure (broadening and shift of atoms' electronic transition frequencies are considerable), nevertheless valence electron of the adatom was found to be localized near the

ionic core. Consequently, it is an appreciable electronic-vibration interaction between adsorbed atom and own atoms of crystal surface, which is responsible for the broadening of optical atomic spectra. The above complex : atom + surface may be presented as peculiar molecule, the interaction in which has a significantly many-particle character caused by considerable difference between the wave function dimensions in the ground and the excited atomic states and lattice parameters of crystal surface. Excitation of this molecule by a photon causes the excitation energy to be redistributed between vibration degrees of freedom of interacting partners (the alkali metal atoms and atoms of crystal lattice), thus leading to its "photodissociation" and escaping of adatom a surface. The probability of this process depends, in particular, on the energy of exciting photon.

We studied this process under the condition of dynamic equilibrium between the gaseous and adsorbed atomic phases. Photodesorption was excited and recorded by traditional optical (laser) techniques using experimental scheme shown in Fig.1.

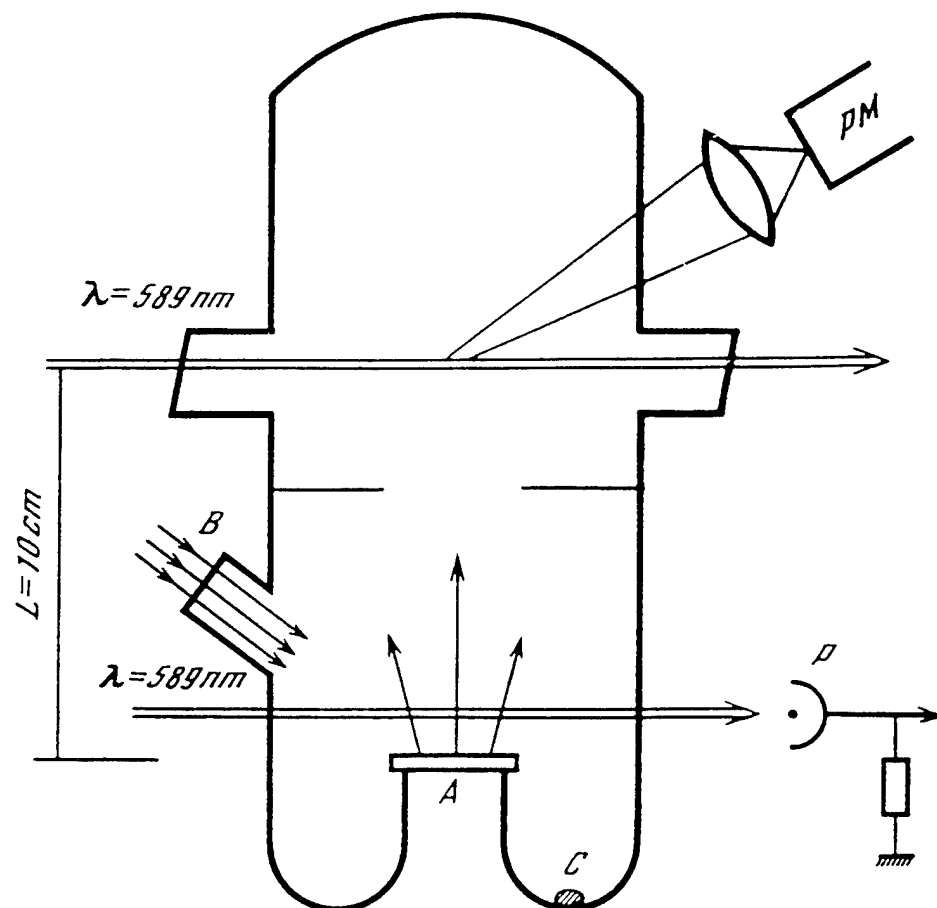


Fig.1. Arrangements for detecting the photodesorption of sodium atoms: A-sapphire plate with adsorbed atoms; B-window for introducing pulsed exciting radiation; C-drop of metallic

sodium: $\lambda=5890\text{\AA}$ -beam of continuous dye laser whose frequency is in resonance with the $3S_{1/2}-3P_{3/2}$ transition in sodium;

PM-photomultiplier detecting the luminescence of a beam of photodesorbed atoms; P-photoelectric cell for measuring the absorption of the atomic beam.

Sapphire plate placed in a closed volume filled with sodium vapors ($P = 10^{-11}$ Torr, bulk concentration is 10^6 cm^{-3}) was exposed to a fundamental, second, or third harmonic radiations of a neodymium and ruby lasers with a 10^{-8} sec pulse length at intensities of about $10^2 - 10^5 \text{ W cm}^{-2}$. This exciting pulse length (shorter compared with the escaping and recording times of the desorbed atomic flux) significantly simplified interpretation and processing of the obtained experimental data. Photodesorbed atoms were detected by their luminescence, or by resonance absorption of a continuous radiation of a dye laser, whose frequency can be tuned on the center of the atomic absorption line.

The first method reveals higher sensitivity, since in time required for an atom to cross a 1-mm laser beam with intensity 1 W cm^{-2} , every atom can irradiate 10^2-10^3 resonance photons, the amount could be readily detected by photomultiplier. The sensitivity of the recording scheme corresponding to temporal resolution of the 10^{-6} sec reached $10^3-10^4 \text{ atom cm}^{-3}$ (or fluxes $10^7-10^8 \text{ atom cm}^{-2} \text{ s}^{-1}$), and was principally limited by technical reasons, such as scattering of exciting radiation by set-up details and by laser light temporal instability.

The luminescence excitation region spatially separated from the studied sapphire surface made it possible to measure time-of-flight photodesorption spectra. The experimental scheme allowed detection of time-of-flight spectra with a single shot of photodesorbing laser at the signal-noise ratio 30-50. A clear advantage of the experimental set-up is its nearly δ -shaped spread function, simplifying spectra data processing.

Some of the spectra are shown in Fig.2. At the upper right corner of the figure are presented experimental photodesorption signals excited by radiation of second (1) and third (2) harmonics of a neodymium laser. The spectra processed to detect the effective photodesorption temperature are shown in the center of the figure in the $\ln [t^3 S(t)]$ and E_{kin} coordinate frame. Here, the points denote the obtained experimental data, and the straight lines correspond to the Maxwellian velocity distribution of atoms assuming 750 and 1000 K effective temperatures, respectively. The detected spectra have evidenced the velocity distribution of atoms escaping the surface to be close to that of Maxwellian with the effective temperature proportional to the photon energy incident on the adsorbed atoms. This circumstance allowed us to develop the photodesorption model mentioned above.

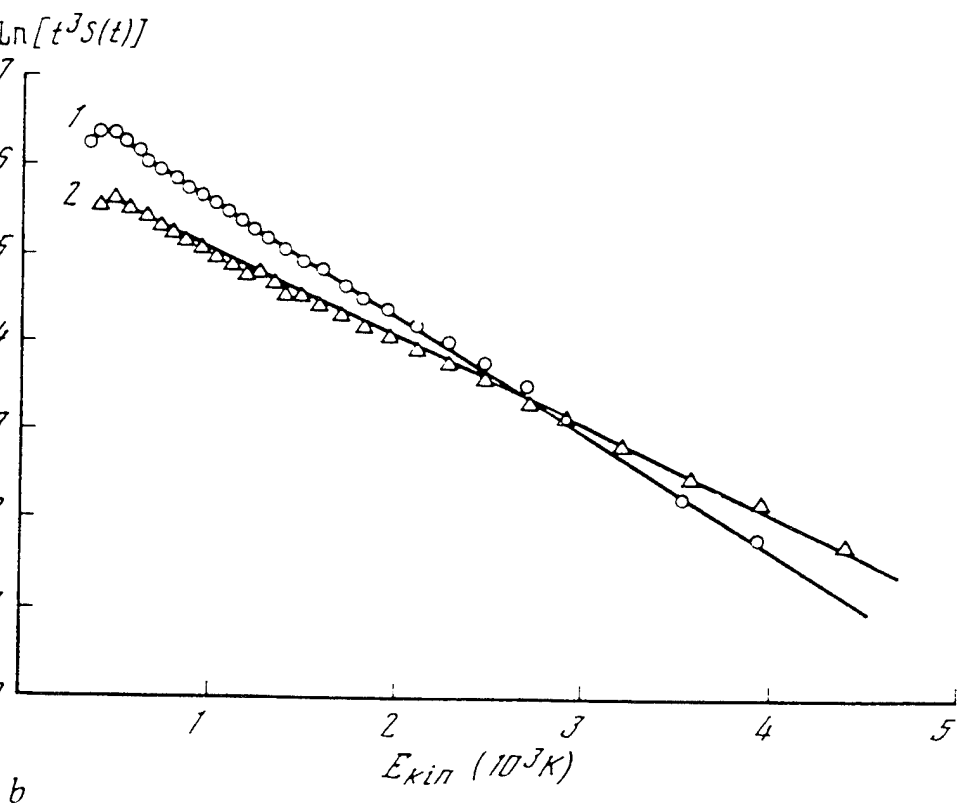
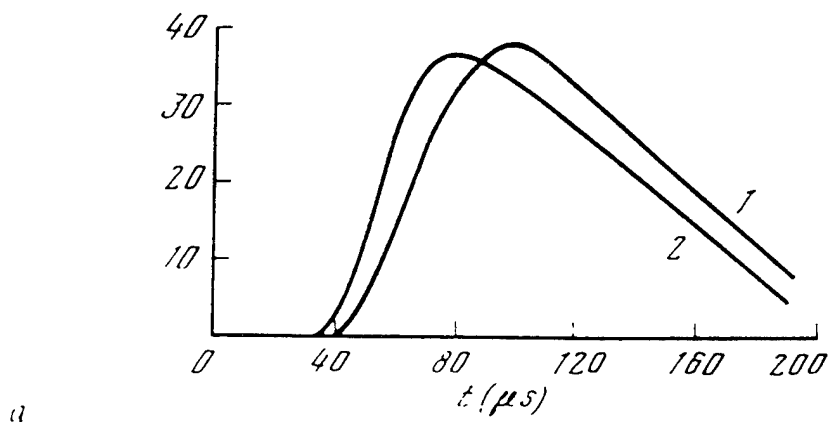


Fig. 2. Time-of-flight spectra of desorbed sodium atoms under action of radiation of the second (1) and third (2) harmonics of neodymium laser (a) and determination of effective desorption temperature (b); explanations are in the text.

3. PHOTODEVAPORATION OF ATOMS FROM A CONTINUOUS SURFACE OF A METAL
The next question is a novel effect, photodevaporation of metallic surface, i.e., one-photon detachment of an own atom from the surface of metal irradiated by visible and near-UV radiation. Though we have³ studied this novel effect only on surfaces of alkali metals, presently it is studied for almost

all metals of the first group. In a number of experiments it was found that photoevaporation process is associated with some structural defects, like single atoms adsorbed on terraces or at steps; no other atoms can be detached by optical radiation. The activation energy for these defects formation makes nearly 1/4 part of the metal sublimation energy. These defects have, in addition, an extra negative charge equal nearly 0.03 part of the electronic charge.⁴ It is therefore evident that electronic state of these defects is considerably different from that of atoms in common sites. It was also found that spectrum of photoevaporation efficiency is not similar to the bulk metal absorption spectrum. Apparently, there is a reason to assign this effect to electronic excitations of surface atoms, assuming their detachment to be caused by these excitations' relaxation.

The interesting data were obtained from measurements of time-of-flight photodesorption spectra presented in Fig.3.

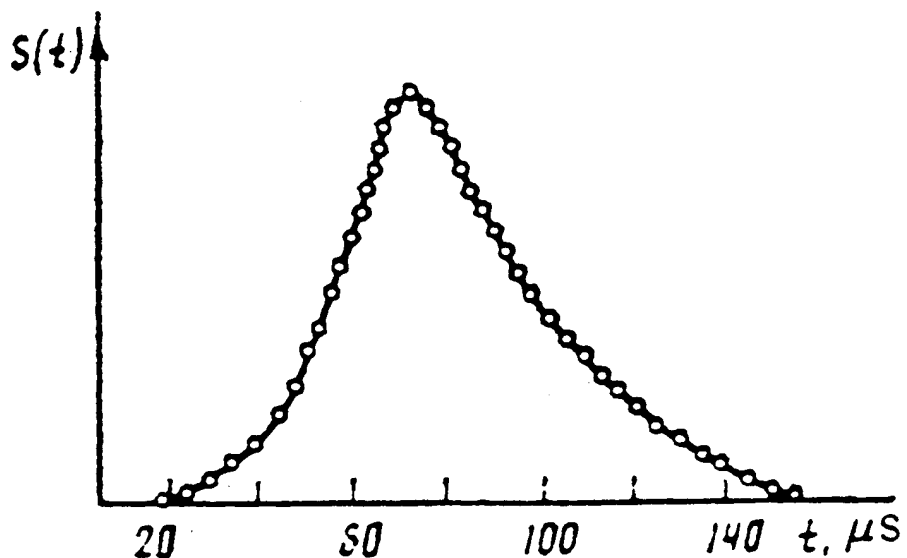


Fig.3. Time-of-flight spectrum of sodium atoms detached from the surface of a metal by a laser radiation ($\lambda=530$ nm) pulse. The circles represent the calculated time-of-flight spectrum with the parameters $T=700$ K and $\tau/a = 24 \cdot 10^{-6}$ sec (see text).

Note, the shape of this spectrum is not at all similar to the Maxwellian distribution; the most probable escaping velocities corresponding to energy 0.2 eV amounted $1.2 \cdot 10^5$ cm/sec. This spectrum shape was found to be well described on the assumption that photodetachment event is related to excitation of an electron to the state localized on the desorbing atom, whose life time, τ , being small near the surface increases exponentially when atom is escaping the surface. This assumption means the photoevaporation quantum yield to exponentially depend on time, in which excited atom exists in the surface potential region. Then, the time-of-flight spectrum acquires the form shown in Fig.3. Here, a is the characteristic scale of the atom-surface interaction region, and l is the distance between

the metal surface and the recording point. It is evident that the obtained spectrum can be presented by the Maxwellian velocity distribution with suppressed contribution of slow-velocity atoms. The explanation of this slow-velocity cut-off is evident: slowly escaping excited atoms undergo a quenching in the course of their movement within the surface potential region.

The best similarity of the calculated and experimental spectra is achieved at $a = 1\text{ \AA}$ and $\tau = 3 \cdot 10^{-14} \text{ sec}$. Circles and line in Fig. 3 denote, respectively, the calculated and experimental data. So, the measured time-of-flight spectra allowed us to estimate the life time of the excited atomic state on the metal surface. Note that this value considerably exceeds the decay times typical for the bulk excitation in a metal.

Finally, it should be noted that detection of small atomic concentrations by luminescence method enters principal difficulty in obtaining absolute values of measured parameters, since rather complex calibration of the experimental scheme, such as, for example, measurements of the excitation region geometry, are required in this case.

4. RESONANCE ABSORPTION AS A METHOD FOR RECORDING SMALL ATOMIC FLUXES AND SUB-MONOLAYER SURFACE CONCENTRATIONS

In the second method small atomic fluxes are detected by their resonance absorption. Although this method has, in principle, lower sensitivity than luminescence method, it is more technological and could be readily treated experimentally. Since absorption signal is proportional to the probing radiation spectral density, use of laser source is also more preferable in this case. Moreover, small value of laser radiation divergency makes it possible to perform detection of atomic absorption at about 1-mm distances from the studied surface, where atomic concentration desorbed by short laser pulses, and therefore, the absorption signal are at a maximum. In addition, angular diagram of escaped atoms can be also determined by this method, if desorbing beam is shifted along the surface relative to the recording beam. Under the experimental geometry, where all the desorbed atoms have passed through the probing beam one can readily calculate the total number of the desorbed atoms; hence, their surface concentration can be determined, if the dimension of laser beam is available and its power is sufficient for all adsorbed particles being detached from the surface.

The calculated sensitivity of this method is proportional to the square root of the probing intensity and its value corresponding to power of the order of 1-10 mW is enough to make possible recording of adsorbed, not desorbed, particles with surface concentration much lower than a monolayer ($10^{10} - 10^{11} \text{ cm}^{-2}$). Assuming cross sections of 10^{-16} cm^2 typical for adsorbed systems, these concentrations correspond to a $10^{-5} - 10^{-6}$ absorption of the probing light. This absorption, if excited in a pulsed periodical regime or by modulated probing radiation of higher intensity, can be readily detected. These

techniques establish less requirements on probing source, because the broaden absorption bands, of the order of 1000-3000 Å, of these systems allow to use standard gas-discharge or semiconductor lasers operating at the single frequency, which falls into the studied system absorption band.

Of course, this technique may be applied only for adsorbents transparent to probing radiation and for highly reflecting surfaces. A possibility to change surface concentration of adsorbed atoms in a short, 10^{-8} sec, period of time and to record this change by continuous laser radiation makes it also possible to determine the sticking coefficient of atoms escaping the surface simultaneously irradiated by atomic flux with known (calibrated) parameters. The value of the sticking coefficient for the sodium atoms and sapphire surface and the frequency factor in the Arrhenius formula were estimated to be 10^{-2} and 10^{11} sec⁻¹, respectively.

At dimensions of probing beam of the order of few micrometers, readily achievable with laser sources, this method warrants for the adsorbed particles to determine in a similar manner (from the reconstruction kinetics of the disturbed surface concentration) the parameters of surface diffusion and the effect of exciting optical radiation on this process. These experiments are being successfully developed in our laboratory. In first of them we have observed the diffusion process leading to condensation of 2D-atomic gas on the sapphire surface. It was found that this process effectively proceeds even at liquid nitrogen temperature and the activation energy for the diffusion of sodium atoms on a sapphire surface does not exceed 0.1 eV, though the adsorption energy equals to 0.7 eV.

Besides needed lasing frequency, the essential feature required of any laser sources applicable in this kind of experiments is its amplitude and phase-frequency noise, which in practice limits the sensitivity of the measurements. Suppressing and compensating this noise by currently developed techniques suggests operation at sensitivities close to the calculated limit determined only by photodetector's shot effect.

All the above is related to atomic systems but holds, of course, for the molecular systems. A considerably, 3-4 order of magnitude, smaller cross sections inevitably imply for these systems decreased, but still very high, recording sensitivities, which make it possible to determine also the rotation and vibration temperatures of desorbed molecules by their luminescence (or absorption) spectra.

To conclude, laser diagnostics possesses now a wide class of continuous and pulsed laser sources operating at different powers and pulse lengths in the spectral range from far UV to far IR. It is a hope that wide application of these methods to the experimental studies of surface processes will be successful.

5. ACKNOWLEDGMENTS

The research described in this publication was made possible in part by Grant N R3K000 from the International Science Foundation and also by financial support from the Russian Found for the Fundamental Researches.

6. REFERENCES

1. I. N. Abramova, E. B. Aleksandrov, A. M. Bonch-Bruevich, and V. V. Khromov, "Photostimulated desorption of metal atoms from surface of transparent insulators", JETP Lett., Vol. 39, pp. 203-205, Feb. 1984.
2. A. M. Bonch-Bruevich, T. A. Vartanyan, A. V. Gorlanov, Yu. N. Maksimov, S. G. Przhibelskii, and V. V. Khromov, "Photodesorption of sodium from the surface of sapphire", Sov. Phys. JETP, Vol. 70, pp. 604-608, March 1990.
3. A. M. Bonch-Bruevich, T. A. Vartanyan, Yu. N. Maksimov, S. G. Przhibelskii, and V. V. Khromov, "Photodesorption of atoms from a continuous surface of a metal", Sov. Phys. JETP, Vol. 70, pp. 993-996, June 1990.
4. A. M. Bonch-Bruevich, T. A. Vartanyan, S. G. Przhibelskii, and V. V. khromov, "Charge state of structural defects on a homogeneous metal surface", Sov. Phys. Dokl., Vol. 36, pp. 772-773, Nov. 1991.

Building of surface nanostructures with laser near field

V. I. Balykin

Institute of Spectroscopy, Troitzk, Russia.

ABSTRACT

We consider creation of surface nanostructures by using two different laser near-field configuration. One configuration arising in the course of diffraction of a plane laser light wave by an aperture of a small size (less than the optical wavelength) causes a normally incident atomic beam to undergo deep focusing to a size 10 Å. The second configuration is the evanescent fields of two laser beams experiencing total internal reflection at dielectric - vacuum interface. This configuration can produce a surface trap for neutral atoms permitting to deposit single atom on a surface.

1. LASER NEAR- FIELD ATOMIC LENS.

Several approaches exist in atomic optics focus of neutral atomic beams. The most familiar atomic focusing method is based on the use of static magnetic or electrical fields¹. These approaches failed to ensure a sharp focusing of atomic beams, the aberrations of the actual magnetic and electrical lenses proving incapable of providing for a resolution better than 0.1 mm.

The experiment² with the atomic Fresnel lens has demonstrated that it is possible to focus atoms into a spot about 20 μm in diameter. The large focal lens of Fresnel lenses means their large numerical apertures, hence poor resolution.

The resonance character of the atom - field interaction can make the interaction potential higher by many orders of magnitude as in the case of static fields. Such high frequency fields are produced by means of high intensive laser. The first experiments³ on the focusing of atomic beams with the dipole force exerted by a Gaussian laser beam have demonstrated that it possible to focus an atomic beam into a spot with a diameter of 26 μm. The possibility of focusing atoms into Å-size spot by means of the TEM₀₁ laser mode has been suggested and examined in⁴. Much attention has been recently attracted to the use of standing laser light waves as focusing elements for atomic beams. Metastable He atoms have been focused by a single period of a large- period (14 μm) standing light wave into a 4 μm spot⁵. The deposition of narrow strips of Cr atoms on a dielectric substrate by means of serious lenses formed by a standing light wave has been demonstrated⁶. In the experiment with chromium⁶, the strips were 65 nm wide and spaced λ = 212 nm apart. The theoretical limit of the strip width is about 30 nm.

In all the above works on the focusing of atoms by means of dipole force, use has been made of traveling (propagating) waves. This inevitably causes substantial aberration (a thick- lens aberration in the ordinary optics).

We have suggested and examined^{7,8} a different approach to the focusing of atomic beams. This approach is based on the use of spatially localized and not traveling fields. We believe that such an approach to the focusing of atoms in atomic optics holds much promise.

The atom optics focusing element⁷ is the near field arising in the diffraction of light by an aperture of small size (compare to the optical wavelength) in a thin conducting screen. Laser radiation is incident from one side on a conducting screen with a small aperture. With the aperture diameter being smaller than the incident radiation wavelength, the field on the other side of the screen consists of two components. One of them is a traveling wave (it's Poynting's vector is other than zero). The intensity of this field component is substantially lower than the laser radiation incident on the screen. The second field component is the near field. Its strength in the vicinity of aperture is of the same order of magnitude as the field strength of the incident laser radiation, and what is most important for our objective is that the near field decays away from the screen with characteristic length of the size of aperture and the field featuring an axial symmetry in a plane parallel to the screen and varying in strength almost as square of the distance from the axis of the aperture.

The trajectory of the atom moving through such an aperture is perceptibly affected in the vicinity of the aperture only by the second field component. What is remarkable is that the quasiresonant- atom - diffraction- field interaction potential is close to the potential of the ideal atomic lens.

The exact formal solution of the problem of diffraction of a plane wave by a round aperture was obtained in the fifties⁹. The near- field strength distribution in the case of diffraction by a small aperture can be expressed in terms of elementary functions¹⁰. In the paraxial approximation, the exact formulas are reduced to the form

$$\langle E \rangle^2 = (kaE_0/3\pi)^2 \{ b(z) - d(z) r^2 \} \quad (1)$$

where $b(z)$ and $d(z)$ are the constants which are determined by the parameters of the hole¹⁰. The analysis of the interaction of atoms with the field (1) shows that if the laser frequency detuning relative to the transition frequency is positive, atoms are pushed to the periphery of the aperture, i. e., the atomic beam is defocused. In the case of negative detuning, the gradient force potential is attractive and the atoms in this case are concentrated near the axis of the aperture. The focusing properties of the near field of laser radiation can be quantitatively analyzed for arbitrary field and atomic field parameters by the direct numerical modeling of the motion of the atoms in the potential using the exact expressions for the field strength distribution (1).

The results have shown^{7,8} that there takes place a deep focusing of the monochromatic atomic beam, practically no matter what the problem parameters. The position of the focal point varying over wide limits following variations of the laser radiation intensity and frequency detuning and the initial atomic velocity.

The velocity nonmonochromaticity of the atomic beam gives rise to a chromatic aberration and the corresponding enlargement of the focal sport. The exact calculation for the initial spread of atomic velocities of $\delta v/v = 0.1$ and the parameter value $v = 100$ m/s, the saturation parameter $G = 10^6$, the laser frequency detuning $\Delta = -400 \gamma$ (2γ - the natural linewidth) yields for the focal sport $\delta r \approx 5 \times 10^{-2} a \approx 10^{-2} \lambda$, i. e., the size of the focal sport falls within nanometer region. At a higher degree of monochromatization, the weaker spherical aberrations become dominant, and as a result, the radius of the focal sports will be around 40 Å.

2. ATOM TRAP ON SURFACE.

When a plane electromagnetic wave is reflected at a dielectric-vacuum interface, the field that finds its way into the vacuum is an evanescent wave. The characteristic depth of the field penetration into the vacuum is of the same order of magnitude as the radiation wavelength. Thus, the total internal reflection gives rise to gigantic light field gradient near the dielectric surface. If the frequency of the laser field is close to that of some transition of a two level atom located in the field, the atom will be acted upon by the gradient force. A characteristic feature of the gradient force is that its direction is determined by sign of the frequency detuning. With the detuning being blue, the atom is expelled from the evanescent wave, whereas in the case of red detuning, it is drawn into the wave. This feature of the gradient force was used to implement the reflection of atoms from an evanescent wave^{11,12}.

We suggest¹³ using this feature of the gradient force to create an atomic trap on a surface. The trap is formed by two evanescent waves differing by the sign of frequency detuning and the depth of penetration into the vacuum. The main idea of this trap is to produce a short-range repulsive force and a long-range of attractive force, similar to repulsive and attractive forces acting between two atoms in a molecule.

The attractive evanescent wave is formed by a red detuned laser beam incident upon the dielectric-vacuum interface at an angle only slightly greater than the critical value. The depth of field penetration into the vacuum may in this case be as great as a few wavelength of the light. The repulsive evanescent wave is produced by a blue detuned laser beam incident upon the interface at very small angle. If an atom is placed close enough to the dielectric surface, the first wave will tend to push the atom away from the surface, while the second will tend to pull it towards the surface, the equilibrium position being at about a wavelength light distant from the surface.

If the trap is formed by two laser beams with a Gaussian transverse intensity distribution, the atomic motion along the surface plane can be also restricted. To do this, it is sufficient to make the cross section of the laser beam forming the attractive wave much smaller than that of the beam forming the repulsive wave. In that case, the resultant gradient force of the two laser beams along the surface plane will be directed toward the center of the trap. This force is the same order of magnitude as the gradient force in the Gaussian beam forming the attractive evanescent wave.

We are interested in the case of weak atomic transition saturation, because such condition provides the longest possible time of atomic localization in the trap¹³. If this condition is satisfied, the resulting force on the atom in the trap may be represented as a sum of two forces acting on the atom in each of two evanescent waves. If the condition $\Delta \gg \gamma$ satisfied in addition to the condition of weak atomic transition saturation, the potential of the trap may be represented in the form

$$U = h\gamma (\gamma G_1/2\Delta_1 + \gamma G_2/2\Delta_2) \quad (2)$$

where Δ_1 and Δ_2 are the frequency detuning of the two evanescent wave and G_1 and G_2 their local saturation parameters, respectively. In the case of one dimensional trap relying on the total internal reflection of two plane waves, the saturation parameters of their respective evanescent waves have the form $G_1 = G_{01} \exp(-2\alpha_1 y)$ and $G_2 = G_{02} \exp(-2\alpha_2 y)$ where G_{01} and G_{02} stand for saturation parameters at the interface. The corresponding depth of potential well for $G_{01} = G_{02} = 4*10^7$, $\Delta_1 = 5*10^5 \gamma$, $\Delta_2 = -10^6 \gamma$, and the incident angles $\Theta_1 = 47^\circ$, and $\Theta_2 = 45.7^\circ$ equals $\Delta U = 7hy$. The spatial width of potential well is of the order the wavelength of light.

The lifetime of atoms in such trap is determined mainly by their heating as a result of momentum diffusion in the light field forming the trap. One can find¹³ the atomic lifetime in it:

$$\tau = M\Delta U/D \quad (3)$$

where M is the atomic mass, D is the atomic momentum diffusion. For the trap with $\Delta U = 7hy$ and Na atom we then have $\tau \approx 3$ s.

A characteristic feature of such trap that it is located close to the dielectric surface, around a wavelength of light distant from it. What is more, this distance can be reduced, for instance, by lowering the intensity of the repulsive evanescent wave. Such a trap may prove useful in studying the interaction between cold atoms and a surface and analysis its microstructures. When the repulsive potential is switched off, the atoms in the trap can be seated onto the surface. The seating accuracy may be less than the wavelength of light forming the trap.

3. REFERENCES.

1. N. F. Ramsey, "Molecular beams", Oxford Univ. Press, London, 1985.
2. O. Carnal, M. Sigel, T. Sleator, H. Takuma, and J. Mlynek, "Imaging and focusing of atoms by a Fresnel zone plate", Phys. Rev. Lett., Vol. 67, pp. 3231- 3234, 1991.
3. D. B. Person, R. R. Freeman, J. E. Bjorkholm, and Ashkin, "Focusing and defocusing of neutral atomic beams using resonance- radiation pressure", Appl. Phys. Lett., Vol. 36, pp. 99-101, 1980.
4. V. I. Balykin and V. S. Letokhov, "The possibility of deep laser focusing of an atomic beam in to the Å size", Opt. Commun., Vol. 64, pp. 151- 157, 1987.
5. T. Sleator, T. Pfau, V. Balykin, and J. Mlynek, "Imaging and focusing of an atomic beam with a large period standing light wave", Appl. Phys., Vol. B54, pp. 375- 379, 1992.
6. J. J. McCleland, R. E. Scholten, E. C. Palm, R. J. Celotta, "Laser-focused atomic deposition", Science, Vol. 22, pp. 877- 880, November 1993.
7. V. I. Balykin, V. S. Letokhov, and V. V. Klimov, "Sharp atomic beam focusing by the near field of laser radiation", Pis'ma ZhETF, Vol. 59, pp. 219- 223, 1994.
8. V. I. Balykin, V. S. Letokhov, and V. V. Klimov, "Laser near field lens for atoms", to be published.
9. H. A. Bethe, "Theory of diffraction by a small hole", Vol. 66, pp. 163- 182, October 1944.
10. V. S. Letokhov and V. V. Klimov, "A simple theory of the near field in diffraction by a round aperture", Vol. 106, pp. 151-154, March 1994.
11. R. J. Cook and A. K. Hill, "An electromagnetic mirror for neutral atoms", Opt. Commun., Vol. 43, pp. 258- 262, 1982
12. V. I. Balykin, V. S. Letokhov, Yu. B. Ovchinnikov, and A. I. Sidorov, "Reflection of atomic beam from gradient of an optical field" Pis'ma ZhETF., Vol. 45, pp. 282 -285, 1987.
13. Yu. B. Ovchinnikov, V. I. Balykin, and S. V. Shu'lga, "An atomic trap based on evanescent wave", J. Phys. B: At. Mol. Opt. Phys., Vol. 24, pp. 3173-3178, 1991.

Practical excimer laser-assisted cleaning of solid surfaces

Hee K. Park¹, Costas P. Grigoropoulos¹, and Andrew C. Tam²

¹Department of Mechanical Engineering, University of California
Berkeley, California 94720

²IBM Almaden Research Center, 650 Harry Road
San Jose, California 95120-6099

ABSTRACT

Pulsed-laser irradiation on a solid surface induces a highly efficient surface cleaning of submicron-sized particulates and undesirable organic overcoat films. The nanosecond-pulsed UV laser irradiation, shortly after the deposition of a thin liquid film on the surface, induces rapid vaporization of the liquid film and removal of particulates ("steam cleaning"). The laser beam also causes ablative photodecomposition of organic film contaminants on the surface ("dry cleaning"). A laser cleaning tool is constructed with an aim toward practical use based on an industrial grade KrF excimer laser. The tool includes a computer-controlled laser beam scanning system and a stable liquid film deposition unit, providing a cleaning rate of over 200 cm²/min. The cleaning strategy and the physical mechanisms of the laser cleaning techniques are also studied.

Keywords: laser cleaning, microcontamination, laser-induced particle removal, microdevice manufacturing, industrial laser application, explosive vaporization

1. INTRODUCTION

As semiconductor and microelectronic device fabrication technology advances toward higher densities and smaller circuit dimensions, contamination control becomes one of the most critical problems in industry. As current VLSI technology requires circuit dimensions as low as 0.2 micron for 256 MBit DRAMs, submicron-sized contaminants adhering to the surface can cause a substantial number of defects with a serious impact on the manufacturing yield^{1,2}. Consequently, there have been significant efforts to develop effective techniques to remove surface contaminants, such as high-pressure jet spraying, mechanical wiping and scrubbing, wet chemical cleaning, etching, plasma cleaning, ultrasonic cleaning, megasonic cleaning, UV/ozone cleaning, and CO₂ snow cleaning³⁻⁶. However, these techniques are prone to damaging delicate parts because they rely on mechanical contact forces and chemical reaction^{3,4}. In addition, these cleaning techniques are not adequate for removal of submicron-sized particulates because the forces required to overcome the adhesion force between the surface and particulates increase tremendously with decreasing particulate size^{7,8}. A study of ultrasonic cleaning shows that it is difficult to attain high cleaning efficiency as particulate sizes decrease below 0.5 μm⁴.

Wet cleaning processes, which usually refer to techniques requiring the immersion of a sample into a liquid bath such as wet chemical cleaning (RCA cleaning)⁹ and sonic cleaning⁴ have a number of serious drawbacks. First, it is widely known that wet techniques could add contaminants due to insufficient cleaning and filtering of the liquid at the submicron level⁴. Secondly, the bulk usage of hazardous chemicals and solvents such as CFC's becomes undesirable for environmental and industrial hygiene reasons. There is a strong tendency in all industry to avoid toxic and ozone-depleting chemical solvents in cleaning processes and consequently to develop environmentally sound techniques of cleaning and stripping surface contaminants and coatings. Other problems associated with wet techniques are rinsing/drying difficulties, and incompatibility with other processes.

Recently, a noncontact "dry" laser cleaning technique, using a short-pulse laser irradiation on the surface, has been demonstrated as a potentially promising means to meet cleaning needs¹⁰⁻¹⁴. Since laser cleaning does not resort to direct contact or chemical reaction, it substantially reduces the likelihood of damage to sensitive parts or surface structures. Laser cleaning also eliminates the use of toxic chemicals and the problem of waste disposal. Solvent-free cleaning by laser is of interest in a variety of fields, such as paint-stripping and graffiti removal¹⁵. A thorough cleaning of high-power optical lenses and mirrors is mandatory to provide prolonged lifetime and enhanced reli-

ability since slight contaminations on optical material surfaces are known to cause a dramatic increase of optical materials damage probability.

This paper will present the laser cleaning technique, its physical mechanisms, and methods of optimization. The implementation of laser cleaning in a practical cleaning process using an ultraviolet (UV) excimer laser will also be discussed.

2. PHYSICAL MECHANISM OF THE LASER CLEANING TECHNIQUE

The physical mechanisms responsible for laser cleaning can be classified into three categories : explosive vaporization, acoustic excitation due to rapid thermal expansion, and ablative photodecomposition.

The first mechanism utilizes flash heating by short-pulsed laser irradiation to drive subsequent explosive vaporization of either the particles themselves¹⁴ or other foreign substances¹⁰⁻¹². The foreign substance can be a thin liquid film introduced deliberately¹⁰. The explosive evaporation of liquid and creation of bubbles generate forces lifting particulates off the surface. The laser energy necessary for vaporization of the liquid film is far lower than that for melting or vaporization of the solid, so that it provides a damage-free and effective means for cleaning.

Fast laser heating of the substrate with moderate energy density ($< 1 \text{ J/cm}^2$) results in the sudden expansion and contraction of the surface and produces acoustic vibration. Although the expansion length amplitude is very small (e.g., $\sim 10^{-8} \text{ m}$), the time scale is also very short, (i.e., on the order of tens of nanoseconds), resulting in a strong acceleration (e.g., $\sim 10^{10} \text{ cm/s}^2$), which can cause particles to be ejected off the surface at high speed¹⁰.

The ablative photodecomposition relies on the selective absorption of UV radiation and the different ablation thresholds of the surface and contaminants. Organic film-type contaminants or adsorbed foreign materials absorb UV light more strongly than metal or semiconductor surfaces. It is known that UV irradiation on organic polymers leads to photochemical dissociation (photolysis), i.e., break-up of their structure with following ejection of the fragments from the surface¹⁶. A pulsed laser additionally induces photothermal desorption of moisture and adsorbates¹⁷, as demonstrated for the cleaning of optical materials¹⁸. The laser energy density required for the cleaning process is typically less than the ablation threshold of the substrate. The laser fluence for the cleaning process is about 0.1 J/cm^2 , which is one order higher than the ablation thresholds of organic materials and one order lower than the ablation thresholds of substrates. Therefore, ablative photodecomposition is highly effective for removal of film-type organic contaminants and adsorbed impurities, without resorting to chemical methods. It has been observed previously that pulsed laser irradiation produces an "atomically" clean silicon surface¹⁹.

Of the three laser cleaning mechanisms, the explosive vaporization of liquid has been reported the predominant mechanism for removal of particulates^{10,12}. Previously it was observed that a water overcoating on a solid surface significantly increases the magnitude of laser-generated pressure waves at the water-solid interface²⁰. Studies on the explosive vaporization of a liquid film using a piezoelectric transducer and the photo-deflection method show

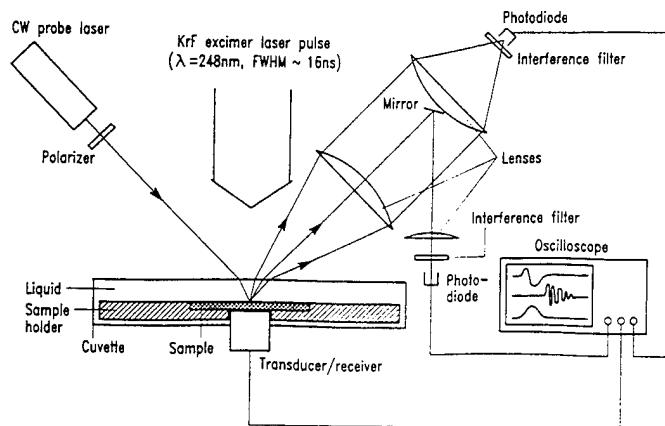


Fig. 1 Experimental setup to probe the nucleation and growth of bubbles at a liquid-solid interface.

that a strong photoacoustic signal ("ablative-piston signal") is generated due to the ejection of liquid above a certain threshold laser fluence^{21,22}. Lee et al.²³ observed the shock wave propagating in air from the CO₂ laser-irradiated silicon surface dosed with water by the probe beam reflection/scattering technique. Transient optical transmission probe measurements indicate that the thin liquid film on an amorphous silicon surface explodes in several hundreds of nanoseconds after the firing of the excimer laser pulse²⁴. Therefore, the laser cleaning technique can be divided into two general types depending on the presence of a thin liquid film coating, e.g. "dry" cleaning and "steam" cleaning¹⁰. It should be pointed out that the "steam" laser cleaning is not a wet cleaning technique. Although steam laser cleaning involves a liquid film deposition, the laser beam dries out the thin liquid film completely. Therefore, none of the drawbacks of standard wet cleaning techniques using bulk liquid baths applies to the steam laser cleaning.

3. STUDY ON THE RAPID VAPORIZATION OF LIQUID

To enhance the understanding of the steam laser cleaning process, the dynamics of the rapid vaporization of liquids on an absorbing solid surface heated by nanosecond-pulsed laser irradiation are studied. The transient development of the bubble nucleation process and the onset of phase change are monitored by simultaneous application of optical reflectance and scattering, and piezoelectric transducer probe. The schematic of the experimental setup is shown in Fig. 1. The solid sample is immersed entirely into the liquid which is filled in a cuvette made of fused quartz. The 248-nm KrF excimer laser pulse (FWHM \sim 16 ns) is directed at normal incidence on the sample. The liquids tested are pure water, methanol, and isopropanol, which are transparent to the excimer laser beam. The absorbing solid sample is 0.2 μm -thick chromium film on a 0.25 mm-thick sapphire substrate. Further details of the experimental setup have been described elsewhere²⁵. The optical properties of chromium are insensitive to temperature changes so that any change on the reflectance signal can be ascribed to nucleation and growth of bubbles at the liquid-solid interface. The reflectance and scattering signals show distinct transients for excimer laser fluences above a certain liquid-dependent threshold as shown in Fig. 2. The reflectance loss is caused by nucleation

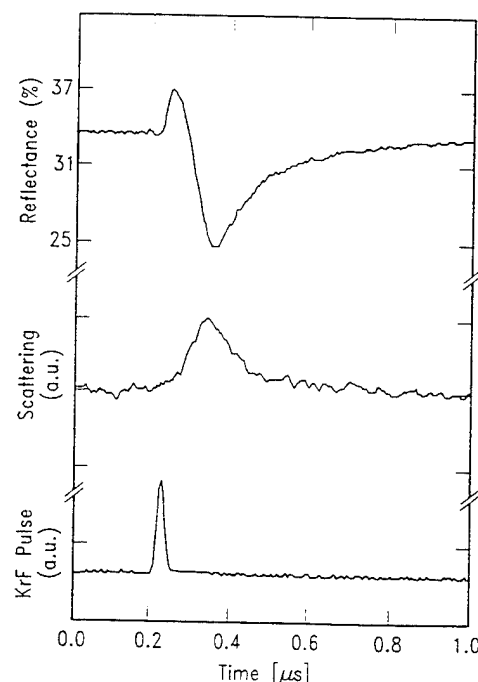


Fig. 2 Transient reflectance (top curve) and scattering (middle curve) signals for isopropanol as the liquid are shown together. The probing HeNe laser beam ($\lambda = 632.8 \text{ nm}$) is unpolarized and irradiates the liquid-solid interface at an incident angle of 20° . Lower curve represents the KrF excimer laser pulse at the fluence of 32 mJ/cm^2 .

and growth of bubbles at the liquid-solid surface. The heat conduction calculation also shows that the solid surface achieves the temperature of tens of degrees of superheat²⁶. The shape of the reflectance signal depends on the angle of incidence and the polarization of the probe beam. The transient reflectance signals are analyzed using the effective medium theory by Maxwell Garnett²⁷. Based on the experimental results, it is expected that a layer of bubbles is created at the chromium surface when it is suddenly heated above a certain level of superheat. The change in the reflectivity signal is accompanied by a sudden increase of the amplitude of the acoustic signal detected by the piezoelectric transducer simultaneously. The explosive growth and collapse of bubbles on the surface produces a strong acoustic wave, which is responsible for the cleaning of contaminants. A previous photographic study¹⁰ shows that a jet of steam is ejected from the irradiated surface due to explosive vaporization of the liquid film.

4. DESIGN OF THE LASER CLEANING SYSTEM

The choice of the laser is made primarily on the cleaning efficiency. However, in order to adapt the technique to the manufacturing environment, some other factors such as cost-effectiveness, throughput, reliability, maintenance, safety, and availability have to be important considerations. Excimer lasers have proven to be very reliable tools in manufacturing over billions of pulses^{28,29}. The UV light generated by the excimer laser has higher photon energy to induce photodecomposition, which is the major cleaning mechanism for organic films. Thus, an industrial grade KrF excimer laser (Lumonics Index 200) was selected as the operating laser. It has a maximum energy of 400 mJ and the highest pulse repetition rate of 300 Hz. The laser pulse width is 16 ns FWHM, which is one order less than the liquid explosion time. The laser gas lifetime is more than several million pulses, which is roughly equivalent to continuous operation for 24 hours at a pulse repetition rate of 100 Hz.

Surface contaminants usually consist of various kinds of materials from diverse origins. Therefore, laser cleaning should be able to remove any kind of surface contaminants. A typical cleaning operation combines both steam and dry cleaning to achieve the best use of each cleaning mechanism. It is often necessary to operate in multiple cleaning cycles to maximize the cleaning efficiency.

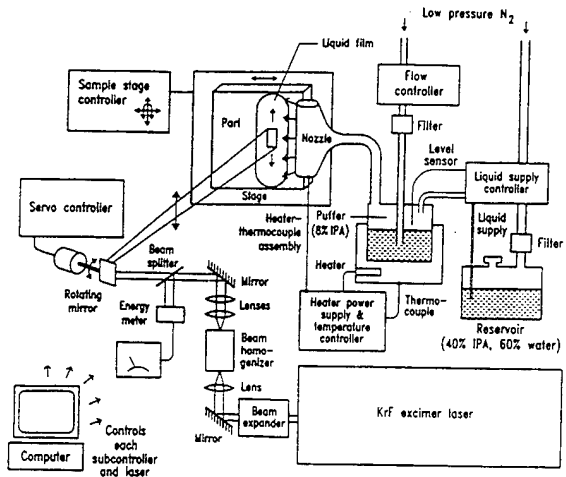


Fig. 3 Schematic diagram of the laser cleaning tool constructed for production using a KrF excimer laser.

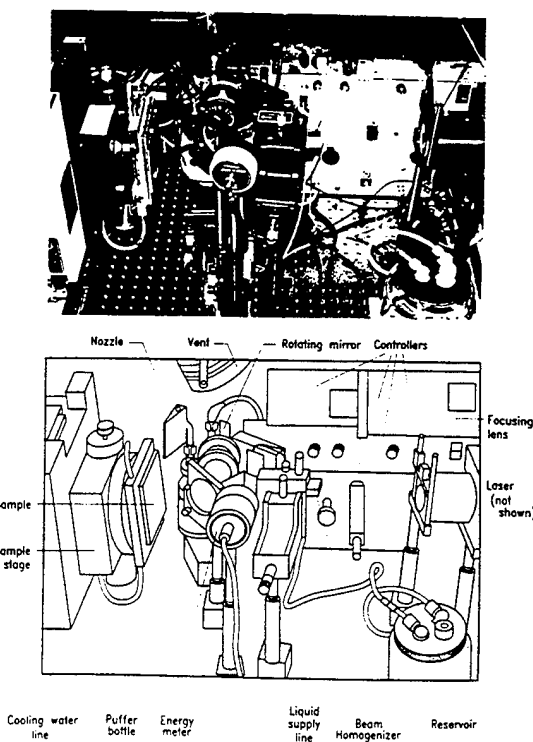


Fig. 4 Photograph of the laser cleaning tool.

Figure 3 shows the schematic of the laser cleaning system constructed. It consists of a laser, beam delivery system, a liquid deposition system, and a sample handling and motion stage. Figure 4 shows a photograph of the prototype laser cleaning tool for production.

The function of the beam delivery system is two-fold. First, it makes the laser beam profile spatially uniform and focuses the beam to the correct size at the desired position. Second, it scans and sweeps the laser beam across the sample with the help of a galvanometer scanning mirror. In the current configuration, the laser beam sweeps in the vertical direction, while the sample stage moves in the horizontal direction. The use of laser beam scanning eliminates the vertical movement of the sample stage and enhances the cleaning throughput dramatically. A tunnel-type beam homogenizer made of aluminum is used to assure the beam spatial uniformity. The rectangular tunnel with mirror-finished inner surfaces mixes the laser beam by multiple reflection. Figure 5 shows the laser beam intensity profile before and after the homogenizer, measured by the Sensor Physics Film Scan FS 100. The transmission loss due to the homogenizer is less than 10%, which is remarkably lower than that of a fly's eye type homogenizer. CaF₂ lenses and mirrors focus the laser beam to a $1 \times 1.5 \text{ cm}^2$ spot on the sample surface. A pyroelectric energy meter monitors the laser energy.

The liquid coated on the sample surface is isopropanol (IPA) and water mixture. Isopropanol is chosen to blend with water because IPA wets most of surfaces well. The IPA concentration in the mixture decreases due to evaporation as time elapses. Therefore, a working container ("puffer") is designed to be fed automatically from another replenishing reservoir containing higher concentration. Coating of the liquid film on the solid surface is achieved through condensation of saturated vapor onto the relatively cold sample surface. Therefore, it is necessary to heat the working liquid a couple of tens of degrees Celcius above room temperature. Low pressure nitrogen, which passes through a 0.3 μm particle filter, is blown into the lukewarm liquid in the puffer bottle, and becomes

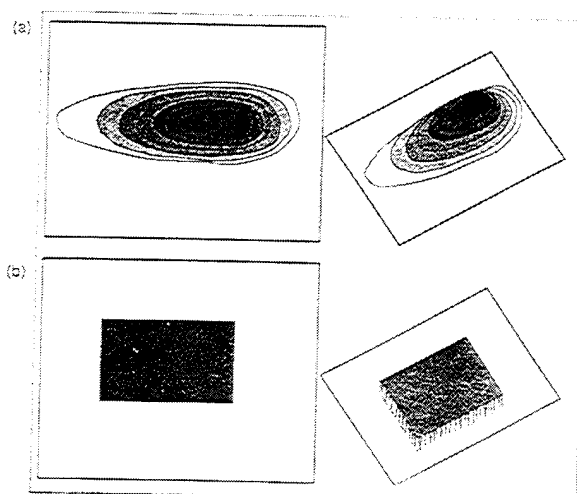


Fig. 5 Spatial laser intensity maps (a) at the laser exit aperture and (b) at the tunnel-type beam homogenizer exit.

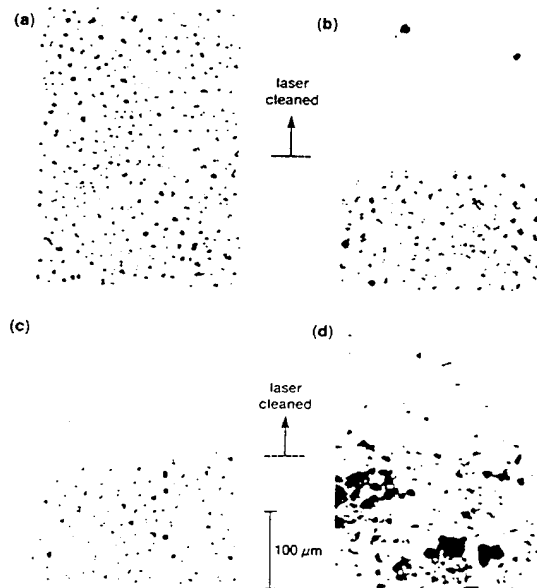


Fig. 6 Microscope photographs of KrF excimer laser cleaning of 1.0 μm alumina particles on a crystalline silicon surface. (a) after 10 dry cleaning cycles with the laser fluence of 110 mJ/cm^2 (b) after 10 dry cleaning followed by 2 steam cleaning cycles with the laser fluence of 110 mJ/cm^2 (c) after 10 dry cleaning followed by 5 steam cleaning cycles with the laser fluence of 110 mJ/cm^2 (d) after 10 dry cleaning cycles with the laser fluence of 180 mJ/cm^2

saturated with IPA/water vapor. The saturated nitrogen gas is ejected from a long and slender nozzle forming a vapor sheet jet.

The sample is mounted on a translational and rotational stage which is controlled by a CompuMotor 3000 Indexer. In one cleaning cycle, the stage moves in the horizontal direction, rotates by 180 degrees, and moves in the horizontal direction again. The rotation is to prevent any shadowing effect on the laser beam. More detailed technical information on the system can be found elsewhere³⁰.

5. IMPLEMENTATION OF LASER CLEANING

Utilizing the laser cleaning system described in previous sections, a variety of sample surfaces contaminated with various kinds of dirts have been tested. The objectives of the test operation were to test the applicability of a laser cleaning system in a simulated manufacturing environment and to determine the best strategies for the laser cleaning operation.

Since the laser is running at high power, the reliability of the laser and the beam delivery system has to be considered first. Failure of the laser is unusual if it is running under normal condition. The laser used in the present system has been running well even without maintenance for the 5 month test period. A UV grade calcium fluoride lens can withstand millions of excimer laser pulses without degradation at a fluence level of 370 mJ/cm² with transmission loss of less than 1%³¹. In comparison, a synthetic fused silica lens has poor durability under high repetition rate and fluence condition³². Use of calcium fluoride lenses enhances the durability of the beam delivery system.

The system up-time is very important in manufacturing. The laser and overall tool up-time was estimated to be 85% during the test run period. Overall, the laser cleaning tool shows good applicability and feasibility in a manufacturing environment. Another field study, compiled over 4 years of operation, indicated that an excimer laser-based machining tool was available over 80% of time with less than 1% of system faults²⁹.

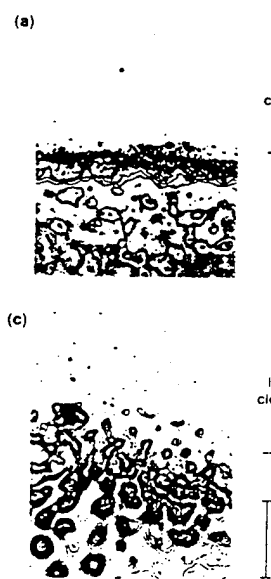


Fig. 7 Microscope photographs of KrF excimer laser cleaning of epoxy film on a crystalline silicon surface. (a) after 2 dry cleaning cycles with the laser fluence of 110 mJ/cm² (b) after 2 dry cleaning followed by 3 steam cleaning cycles with the laser fluence of 110 mJ/cm² (c) after 2 times of 2 dry cleaning followed by 3 steam cleaning cycles with the laser fluence of 110 mJ/cm²

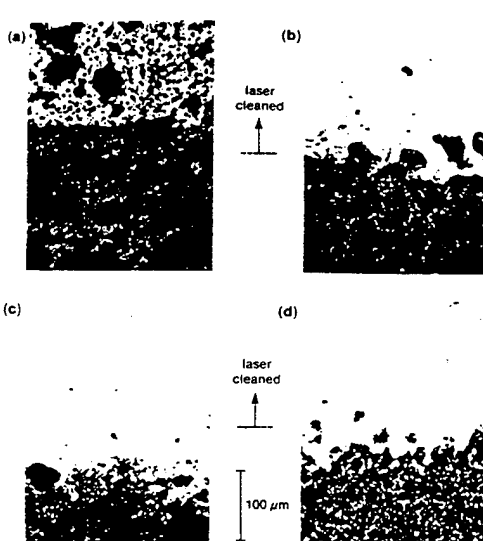


Fig. 8 Microscope photographs of KrF excimer laser cleaning of alumina particles with epoxy film on a crystalline silicon surface with the laser fluence of 110 mJ/cm² (a) after 2 dry cleaning cycles (b) after 2 dry cleaning followed by 3 steam cleaning cycles (c) after 2 times of 2 dry cleaning followed by 3 steam cleaning cycles (d) after the ultrasonic cleaning in DI water for 10 minutes of laser-cleaned surface.

In order to determine the best cleaning strategy, test samples of crystalline silicon (c-Si) wafers with two different types of contaminants have been prepared. Epoxy and 1.0 μm -sized alumina particles have been selected to represent organic and particulate surface contaminants. Alumina particles are dispersed and suspended in methanol and the epoxy is diluted by acetone. Both are applied to the substrate surface. A high-pressure air jet is blown over the surface to remove loose particles. Epoxy in acetone forms micron-thick films on the surface. For the combination of both types of contaminants, alumina particles are dispersed in the epoxy-acetone solution.

Figure 6 (a) shows the surface of c-Si contaminated with alumina after 10 dry cleaning cycles with a laser fluence of 110 mJ/cm². It is seen that the dry cleaning cycle has no effect towards cleaning of the alumina particles on the silicon surface at this laser energy. Figure 6 (b) shows the same surface after 10 dry cleaning cycles followed by 2 steam cleaning cycles at the fixed laser fluence of 110 mJ/cm². It is shown that most of the alumina particles are removed except for the large chunks. Figure 6 (c) shows complete removal of alumina after 10 dry cleaning cycles followed by 5 steam cleaning cycles. Figure 6 (d) compares the surface after 10 dry cleaning cycles with higher laser fluence of 180 mJ/cm². The dry cleaning at higher energy cleans off alumina particles only partially. This indicates that dry cleaning by vibrational excitation requires much higher energy and is less effective than steam cleaning.

However, the dry cleaning is very effective in cleaning off organic films. Figure 7 (a) shows the surface of epoxy-contaminated c-Si after 2 dry cleaning cycles with the laser fluence of 110 mJ/cm². It is seen that the 2 dry cleaning cycles remove all the epoxy film except for some small broken pieces. These tiny pieces are also removed by subsequent application of 2 steam cleaning cycles as shown in Fig. 7 (b). Figure 7 (c) shows the same surface cleaned only by 2 steam cleaning cycles. Steam cleaning produces similar results as dry cleaning, in removing organic films.

The steam cleaning is shown more efficient but the dry cleaning is advantageous in removal of organic films since it is a simpler process compared to the steam cleaning. When the surface is contaminated by both particulates and organic films, the combination of the two cleaning techniques is desirable. Figure 8 (a) shows a c-Si surface contaminated by alumina particles and epoxy films after 2 dry cleaning cycles. A sharp discontinuity separating the dry laser-cleaned area where the epoxy film has been removed from the uncleaned dirty surface is observed. It is noted, however, that alumina particles remain unaffected on the surface. Figure 8 (b) shows the surface subjected to 3 steam cleaning cycles following the dry cleaning. Alumina particles are now removed by the steam cleaning process. A complete cleaning of the surface after additional cycles is seen in Fig. 8 (c). In order to compare the laser cleaning technique with other traditional techniques, the laser-cleaned sample is subjected to ultrasonic cleaning in deionized water for 10 minutes. It is seen that ultrasonics removes only the large particles of alumina in Fig. 8 (d).

It is noted that the laser fluence used in the cleaning operation, 110 mJ/cm², is so low that it does not induce any surface damage. As a proof, a silicon wafer is subjected to continuous steam laser cleaning with the laser fluence of 150 mJ/cm² and the pulse repetition rate of 100 Hz for 4 hours and inspected. No visual damage was observed.

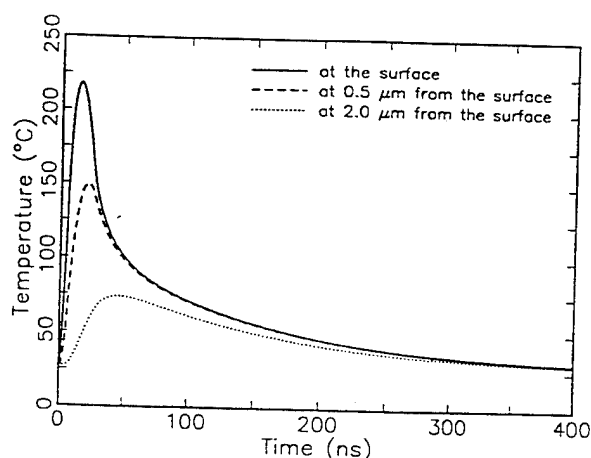


Fig. 9 Temperature transients at the different locations inside a crystalline silicon irradiated with a KrF excimer laser ($\lambda = 248 \text{ nm}$) at laser fluence of 110 mJ/cm².

In the test operation results, it is worth to note that the total operation time required for the 4-inch diameter silicon wafer by applying two sequences of 2 dry cleaning followed by 3 steam cleaning cycles is less than 4 minutes, including loading and unloading of the sample. Hence, the laser cleaning would be a faster process compared to other cleaning techniques. For moderately-contaminated samples usually found in production line, the number of cleaning cycles can be reduced, yielding even faster operation.

6. ANALYSIS OF LASER-INDUCED DAMAGE

Heat transfer analysis based on the one-dimensional heat conduction equation has been performed to estimate the maximum surface temperature of the sample. Higher laser energy does not only result in higher cleaning efficiency but also in higher damage probability. It is therefore essential to predict the damage threshold. The laser-induced damage occurs via a thermally driven mechanism. Hence, it is vital to correctly estimate the maximum temperatures induced by the laser.

The one-dimensional transient conductive heat transfer equation with temperature dependent properties and bulk heat absorption of the laser light is solved numerically²⁶. It is noted that the convective heat transfer is negligible for the nanosecond time scales considered in this work. The computed peak surface temperature induced in the cleaning operation (laser fluence of 110 mJ/cm²) is 219°C. This temperature level is too low to induce thermomechanical damage or to affect any permanent change on the substrate. The temporal temperature history at the laser fluence of 110 mJ/cm² shown in Fig. 9 indicates that the surface stays over 100 °C only for a few tens of nanoseconds. In addition, heat penetration is very shallow as shown in Fig. 9. The heat-affected region, where the peak temperature is over 100°C, is confined to about 2 microns. It is noted that the temperature cools down quickly in a microsecond. Since the laser is running at the pulse repetition rate of less than 150 Hz, the time interval between consecutive pulses is several milliseconds. Therefore, heat accumulation does not take place. It can be thus stated that the KrF excimer laser cleaning with laser fluence up to 200 mJ/cm² is safe from damaging a silicon surface.

7. SUMMARY

An implementation of the laser cleaning technique in practical use has been presented. It has been shown that the KrF excimer laser-based cleaning tool is capable of cleaning submicron-sized particulates and organic films and is tested in a simulated manufacturing environment. It is demonstrated that the laser cleaning technique can be adapted to a stable, reliable, and robust tool, withstanding 24 hour operation with high system availability. Cleaning strategies using the dry and steam laser cleaning modes have been discussed. Test cleaning results with sample contaminant-substrate systems have shown that the cleaning efficiency can be maximized by the combination of dry and steam laser cleaning cycles. It has also been shown that the laser cleaning energy is insufficient to induce substrate damage because of relatively low temperature increase and shallow thermal loading.

8. ACKNOWLEDGEMENTS

The authors thank C. C. Poon, I. K. Pour, D. Krajnovich of IBM Almaden Research Center, O. Yavas of University of Konstanz, Germany, and W. Zapka of IBM GMTC, Germany, for their valuable contributions to this work. Support to this work by the National Science Foundation under Grant CTS-9317708 and in part by the Computer Mechanics Laboratory of the University of the California at Berkeley is gratefully acknowledged.

9. REFERENCES

1. M. Duffalo and J. R. Monkowski, "Particle contamination and device performance," *Solid State Tech.*, pp.109-114, 1984.
2. S. A. Hoenig, "Fine particles on semiconductor surfaces : sources, removal, and impact on the semiconductor industry," in *Particles on Surfaces I*, K. L. Mittal, Ed., Plenum, New York, 1988.

3. J. Bardina, "Methods for surface particle removal : a comparative study," in *Particles on Surfaces 1*, K. L. Mittal, Ed., Plenum, New York, 1988.
4. V. B. Menon, L. D. Michaels, R. P. Donovan, and D. S. Ensor, "Effects of particulate size, composition, and medium on silicon wafer cleaning," *Solid State Tech.*, pp. s7-s12, 1989.
5. J. R. Vig and J. W. Le Bus, "UV/ozone cleaning of surfaces," *IEEE Trans. Parts, Hybrids, Packg.*, Vol. PHP-12, pp. 365-370, 1976.
6. R. Sherman, J. Grob, and W. Whitlock, "Dry surface cleaning using CO₂ snow," *J. Vac. Sci. Technol.*, Vol. B9, pp. 1970-1977, 1991.
7. S. Kim and C. J. Lawrence, 1988, "Suspension mechanics for particle contamination control," *Chem. Eng. Sci.*, Vol. 43, pp. 991-1016, 1988.
8. R. A. Bowling, "An analysis of particle adhesion on semiconductor surfaces," *J. Electrochem. Soc.*, Vol. 132, pp. 2208-2214, 1985.
9. W. Kern and D. A. Puotinen, "Cleaning solutions based on hydrogen peroxide for use in silicon semiconductor technology," *RCA Review*, Vol. 31, pp. 187-206, 1970.
10. A. C. Tam, W. P. Leung, W. Zapka, and W. Ziemlich, "Laser-cleaning techniques for removal of surface particulates," *J. Appl. Phys.*, Vol. 71, pp. 3515-3523, 1992.
11. W. Zapka, W. Ziemlich, and A. C. Tam, "Efficient pulsed laser removal of 0.2 μm sized particles from a solid surface," *Appl. Phys. Lett.*, Vol. 58, pp. 2217-2219, 1991.
12. K. Imen, S. J. Lee, and S. D. Allen, "Laser-assisted micron scale particle removal," *Appl. Phys. Lett.*, Vol. 58, pp. 203-205, 1991.
13. S. J. Lee, K. Imen, and S. D. Allen, "CO₂ laser assisted particle removal threshold measurements," *Appl. Phys. Lett.*, Vol. 61, pp. 2314-2316, 1992.
14. T. J. Magee and C. S. Leung, "Scanning UV laser removal of contaminants from semiconductor and optical surfaces," in *Particles on Surfaces 3*, Mittal, K. L., Ed., Plenum, New York, 1991.
15. A. M. Frank and P. A. Lovoi, "Method of and apparatus for the removal of paint and the like from a substrate," U.S. Patent No. 4588885, 1986.
16. R. Srinivasan, "Ablation of polymers and biological tissue by ultraviolet lasers," *Science*, Vol. 234, pp. 559-565, 1986.
17. A. C. Tam and H. Schroeder, "Laser-induced thermal desorption of moisture from a surface in atmospheric conditions," *J. Appl. Phys.*, Vol. 64, pp. 3667-3671, 1988.
18. S. D. Allen, J. O. Porteus, W. N. Faith, and J. B. Franck, "Contaminant and defect analysis of optical surfaces by infrared laser induced desorption," *Appl. Phys. Lett.*, Vol. 45, pp. 997-999, 1984.
19. D. M. Zehner, C. W. White, and G. W. Ownby, "Preparation of atomically clean silicon surfaces by pulsed laser irradiation," *Appl. Phys. Lett.*, Vol. 36, pp. 56-59, 1980.
20. B. P. Fairand and A. H. Clauer, "Effect of water and paint coatings on the magnitude of laser-generated shocks," *Opt. Commun.*, Vol. 18, pp. 588-591, 1976.
21. W. P. Leung and A. C. Tam, "Noncontact monitoring of laser ablation using a miniature piezoelectric probe to detect photoacoustic pulse in air," *Appl. Phys. Lett.*, Vol. 60, pp. 23-25, 1992.
22. N. Do, L. Klees, A. C. Tam, P. T. Leung, and W. P. Leung, "Photodeflection probing of the explosion of a liquid film in contact with a solid heated by pulsed excimer laser irradiation," *J. Appl. Phys.*, Vol. 74, pp. 1534-1538, 1993.
23. S. J. Lee, K. Imen, and S. D. Allen, "Shock wave analysis of laser assisted particle removal," *J. Appl. Phys.*, Vol. 74, pp. 7044-7047, 1993.
24. P. T. Leung, N. Do, L. Klees, W. P. Leung, F. Tong, L. Lam, W. Zapka, and A. C. Tam, "Transmission studies of explosive vaporization of a transparent liquid film on an opaque solid surface induced by excimer-laser-pulsed irradiation," *J. Appl. Phys.*, Vol. 72, pp. 2256-2263, 1992.

25. O. Yavas, P. Leiderer, H. K. Park, C. P. Grigoropoulos, C. C. Poon, W. P. Leung, N. Do, and A. C. Tam, "Optical and acoustic study of nucleation and growth of bubbles at a liquid-solid interface induced by nanosecond-pulsed laser heating," *Appl. Phys. A*, Vol. 58, pp. 407-415, 1994.
26. H. K. Park, X. Xu, C. P. Grigoropoulos, N. Do, L. Klees, P. T. Leung, and A. C. Tam, "Transient optical transmission measurement in excimer-laser irradiation of amorphous silicon films," *ASME Trans. J. Heat Transfer*, Vol. 115, pp. 178-183, 1993.
27. O. Yavas, P. Leiderer, H. K. Park, C. P. Grigoropoulos, C. C. Poon, W. P. Leung, N. Do, and A. C. Tam, "Optical reflectance and scattering studies of nucleation and growth of bubbles at a liquid-solid interface induced by pulsed laser heating," *Phys. Rev. Lett.*, Vol. 70, pp. 1830-1833, 1993.
28. F. G. Bachmann, "Industrial laser applications," *Appl. Surf. Sci.*, Vol. 46, pp. 254-263, 1990.
29. J. R. Lankard and G. Wolbold, "Excimer laser ablation of polyimide in a manufacturing facility," *Appl. Phys. A*, Vol. A54, pp. 355-359, 1992.
30. H. K. Park, C. P. Grigoropoulos, W. P. Leung, and A. C. Tam, "A practical excimer laser-based cleaning tool for removal of surface contaminants," *IEEE Trans. Comp., Hybrids, Manufac. Technol.*, in press.
31. D. J. Krajnovich, M. Kulkarni, W. Leung, A. C. Tam, A. Spool, and B. York, "Testing of the durability of single-crystal calcium fluoride with and without antireflection coatings for use with high-power KrF excimer lasers," *Appl. Opt.*, Vol. 31, pp. 6062-6075, 1992.
32. W. P. Leung, M. Kulkarni, D. Krajnovich, and A. C. Tam, "Effect of intense and prolonged 248 nm pulsed-laser irradiation on the properties of ultraviolet-grade fused silica," *Appl. Phys. Lett.*, Vol. 58, pp. 551-553, 1991.
33. The use of trade names or manufacturers in this paper does not constitute an endorsement of their products or equipments.

Optical probing of the temperature and pressure transients at a liquid/solid interface due to pulsed laser-induced vaporization

Hee K. Park¹, Costas P. Grigoropoulos¹, Chie C. Poon², Andrew C. Tam², Oguz Yavas³, and Paul Leiderer³

¹Department of Mechanical Engineering, University of California
Berkeley, California 94720

²IBM Almaden Research Center, 650 Harry Road
San Jose, California 95120-6099

³Department of Physics, University of Konstanz
D-78434 Konstanz, Germany

ABSTRACT

The transient temperature and pressure field development in the excimer laser-induced vaporization of liquids in contact with a solid surface is studied. A thin silicon film, which has temperature-dependent optical properties, is embedded between an absorbing chromium film and a transparent fused quartz substrate. Static reflectivity measurement is performed to determine the thin film optical properties at elevated temperatures. The transient backward reflectance responses from the silicon layer are compared with heat transfer modeling results. The backward reflectance probe is not affected by the creation of bubbles and is successfully employed for the first time to measure non-intrusively the temperature development during the rapid vaporization process. The optical reflectance probes are applied from the front-side and back-side of the sample simultaneously to monitor the dynamic bubble nucleation behavior and transient temperature development, respectively, at various ambient pressures using a high-pressure cell. The investigation on the effect of ambient pressure on the bubble nucleation threshold combined with the surface temperature measurement determines the thermodynamic state of the superheated metastable liquid at the interface and subsequently the explosion pressure.

Keywords: laser-induced vaporization, heterogeneous nucleation, explosive vaporization, photothermal diagnostic method

1. INTRODUCTION

Laser beam interaction with materials in liquid provides a very unique laser processing environment¹⁻³. The explosive vaporization of liquid films on the opaque solid surfaces heated by short-pulsed laser irradiation is utilized in laser-assisted cleaning of microcontaminants⁴ and the liquid-film-enhanced laser-hardening of materials⁵. Short-pulsed laser-induced nucleation and cavitation in a tissue or an organ produces a sharp incision with minimal injury which enables the surgical operation in great accuracy. The therapeutic use of a laser instead of a surgical knife is already practiced clinically to a large extent, from the intraocular surgery in ophthalmology⁶ to laser lithotripsy for the fragmentation of bilinary and urinary calculi^{7,8} and laser angioplasty for the treatment of in cardiovascular disease⁹.

The physical understanding of superheated pure or mixed liquids, such as limit of superheat and critical phenomena, has been sought for a better control of such technical applications. The science of metastability of liquid has been established in the near-steady-state regime. There have been efforts to understand the thermodynamics of the rapid vaporization of liquids on an absorbing solid surface heated by nanosecond-pulsed laser irradiation. The transient development of the bubble nucleation process and the onset of phase change are monitored by simultaneous application of optical reflectance and scattering probes¹⁰. The reflectance and scattering signals show the distinct transients of nucleation and growth of bubbles at the liquid-solid interface when the excimer laser fluence exceeds a certain liquid-dependent threshold¹⁰. The numerical heat conduction calculation also shows that the solid surface achieves temperatures of tens of degrees of superheat¹¹. However, no real-time measurement of the surface temperature development in the course of the laser-induced vaporization process has been

made, although the surface temperature (i.e., the wall superheat) is the most important parameter in the heterogeneous nucleation phenomenon^{12,13}. The thermodynamic considerations on the problem including the degree of superheat required for a liquid-vapor transition in nanosecond time scale have never been addressed. Disturbances by bubbles near the liquid-solid interface, the relatively low temperature change, and the insensitivity of electric and optical properties of metals on temperature have prohibited the precise detection of surface temperature during the laser-induced vaporization. Recently, it has been proven that the transient optical transmission or reflectivity probe is a fast, reliable method with nanosecond resolution to monitor the temperature field development during the processing of semiconductor films by short-pulsed laser¹⁴⁻¹⁸. In this work, the optical reflectance probe is applied from the backside to the embedded thin semiconductor film. The backward reflectance probe is not affected by the creation of bubbles in the liquid and is successfully employed to measure the temperature field development during the rapid vaporization process.

The precise assessment of the value of pressure produced by the growing and collapsing bubbles is a critical step in designing the technical applications. The generation of strong pressure waves in liquid pools under intense short pulsed-laser irradiation has been investigated by various methods, for example, using hydrophone or piezoelectric transducers¹⁹⁻²¹, high-speed photography²², interferometry²³, and optical probing^{24,25}. However, most of optical (photographic) methods rely on the shock wave velocity measurements and the shock wave velocity-pressure relations for the quantification of pressure²⁶. In a lower energy regime where velocity is not supersonic, such a calibration is not applicable. The hydrophone or piezoelectric transducer probe also has a limit in general usage due to the transducer ringing and the lack of bandwidth. In this work, a systematic study is performed on the pressure generation by monitoring the bubble growth kinetics combined with the photothermal temperature measurement at several ambient pressures in a pressure cell. Hence, the thermodynamics state is determined for the rapid vaporization of liquids. Consequently, the precise evaluation on the pressure level and the metastability behavior of liquid is obtained.

2. EXPERIMENTAL ARRANGEMENT AND PROCEDURE

The experimental setup is shown in Fig. 1. A liquid is filled in a massive high pressure cell (maximum pressure ~ 100 atm) made of stainless steel and quartz windows. The pressure cell is designed to minimize the en-

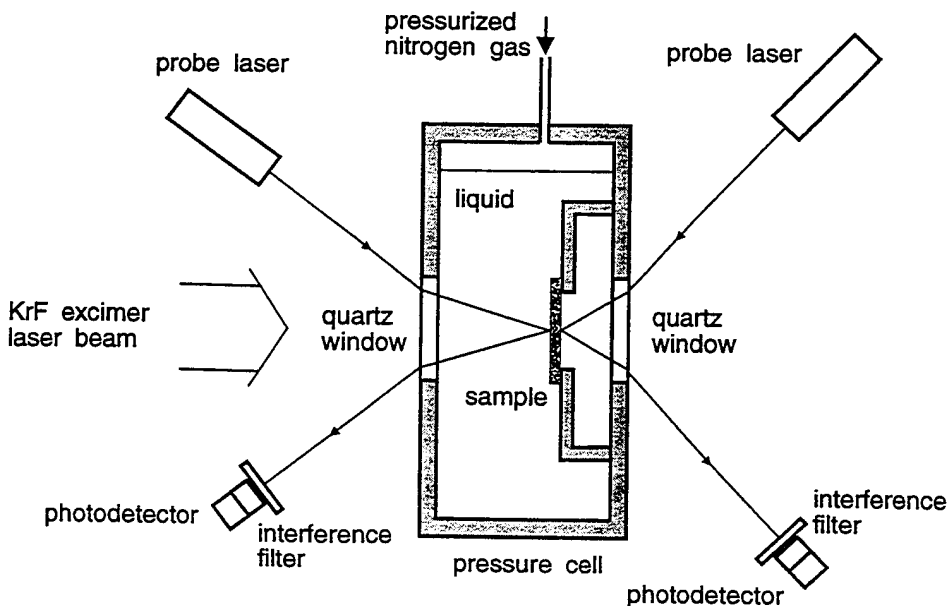


Fig. 1 Schematic of experimental setup.

vironmental vibrations. The pressure of liquid is varied by applying compressed nitrogen into the pressure cell. The solid sample has 3 layers as shown in Fig. 2. The top layer is an absorbing film, the intermediate layer is an optical temperature sensor whose optical properties vary with temperature, and the bottom layer is a transparent substrate. In the temperature monitoring scheme of this work, the change of optical properties, i.e., the change of the temperature, is probed by the photothermal reflectance of the intermediate layer irradiated from the backside (substrate side). The advantage of the probe from the backside is the ability of avoiding the occurrence of events near or on the laser irradiated surface such as bubble nucleation. In this study, chromium is selected as a top layer material, polycrystalline silicon (p-Si) as an optical sensor, and fused quartz as a substrate. The thickness of the chromium layer is determined to be larger than the optical penetration depth at the excimer laser light wavelength, which is 9.8 nm for the bulk chromium. Therefore, the direct heating of the temperature sensor layer by the excimer laser will not occur. On the other hand, the thickness of the chromium layer is sufficiently smaller than the thermal penetration depth. The thermal penetration depth of chromium is $0.17 \mu\text{m}$ at 1 ns. The optimum thickness of the temperature sensor layer has to be well designed for better temperature sensitivity. In order to maximize the temperature sensitivity, the thickness of the sensor film has to maximize dR/dT , where R is the reflectivity of the sensor film. It is known that the change of reflectivity due to the change of refractive index is maximum when the optical thickness nd is similar to the wavelength. In this work, the sample with the $0.15 \mu\text{m}$ -thick Cr film and $0.35 \mu\text{m}$ -thick p-Si film deposited on a $500 \mu\text{m}$ -thick fused quartz substrate is fabricated. Both sides of the surface are probed by two CW lasers. Since the Cr film has no intrinsic thermoreflectance effect, any change of the optical reflectance is ascribed to the formation of bubbles on the surface. On the other hand, due to the absence of bubbles in the backside, any change on the reflectance from the p-Si layer is only caused by the temperature change. Hence, the temperature and the bubble nucleation behavior can be obtained separately at the same time. The KrF excimer laser beam ($\lambda = 248 \text{ nm}$, pulse width = 16 ns FWHM) is irradiated over a large area ($1 \times 1 \text{ cm}^2$) and absorbed by the Cr layer. The probe CW lasers are an Ar⁺ ($\lambda = 488 \text{ nm}$) for the forward reflectance, and a HeNe laser ($\lambda = 632.8 \text{ nm}$) for the backward reflectance. It is noted that the incident angle for the forward reflectance is so small ($< 10^\circ$) that the photoacoustic deflection of the beam can be neglected.

3. STATIC TEMPERATURE CALIBRATION

First the photothermal reflectivity from the back-side of the sample is calibrated by the static experiment. The sample is mounted on an aluminum block of which temperature is controlled within $\pm 0.1^\circ\text{C}$. The measured static reflectivity are fitted to obtain the optical properties of quartz substrate and p-Si film:

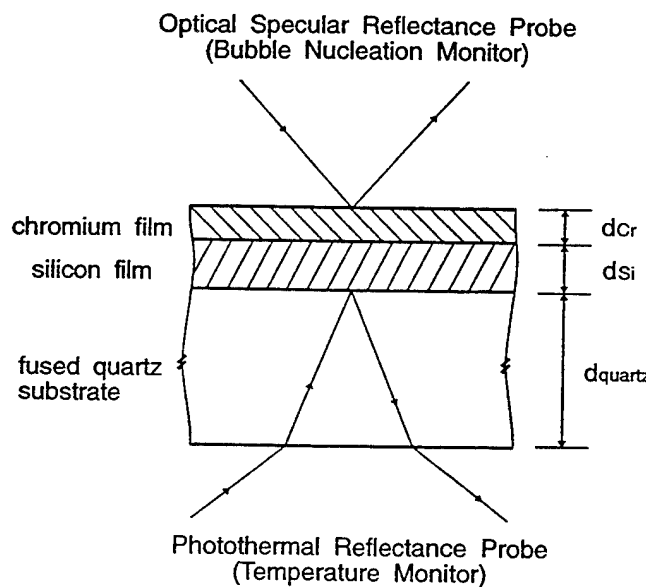


Fig. 2 Schematic of sample structure and optical detection scheme.

$$n_{\text{quartz}} = 1.457 + 9.64 \times 10^{-6} \times (T - 20) + 6.1 \times 10^{-9} \times (T - 20)^2 \quad (1)$$

$$n_{p-Si} = 4.01 + 3.31 \times 10^{-4} \times (T - 20) \quad (2)$$

$$k_{p-Si} = 0.0355 \times \exp\left(\frac{T}{590}\right) \quad (3)$$

where the temperature T is in degree Celcius. It is noted that the obtained optical properties are close to the literature values²⁷. The accuracy of the fitting is better than 1%. The optical property change of the fused quartz does not affect the transient temperature measurement in nanosecond time scale because of the poor thermal conductivity of quartz. The temperature profile in the sample is modelled by the one-dimensional heat diffusion equation. Detailed procedure on the temperature modeling appear elsewhere¹⁷. In the calculation of the theoretical reflectivity response, a stratified-layer approach is utilized to take an account of the steep temperature gradient across the sample in the nanosecond time scale¹⁷. In this approach, the sample is assumed to be comprised of multiple layers with the calculated temperature and corresponding optical properties determined by the static calibration. The reflectivity is calculated by the thin-film matrix method²⁸.

4. TRANSIENT TEMPERATURE MEASUREMENT

Figure 3 shows the results of the transient temperature measurement. The excimer laser irradiates the water/chromium interface of the sample at the fluence of 42.2 mJ/cm^2 at atmospheric pressure. The top panel shows a slight change in the forward reflectance, indicating the water-chromium interface is right at the threshold for nucleation. The signal shown in the figure is an average of 5 shots of laser pulses so as to minimize the noise level. The middle panel shows the experimental photothermal reflectance curve (solid line) and the theoretical

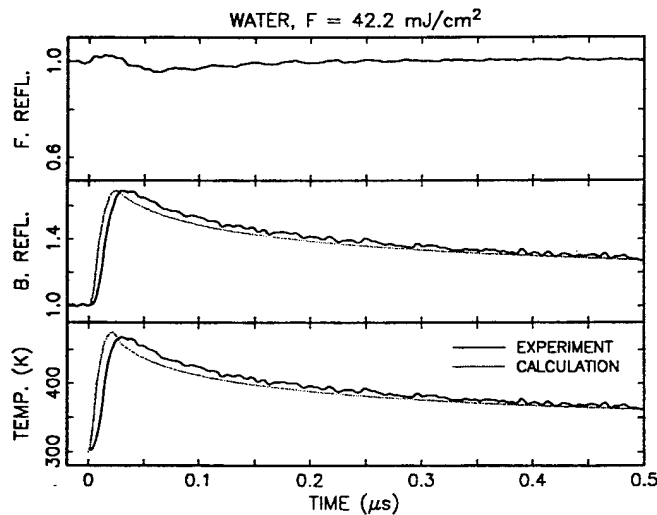


Fig. 3 The experimentally obtained reflectance curves (solid lines) are shown in the top panel (forward reflectance) and middle panel (backward photothermal reflectance) for water. The dotted lines are calculated transient reflectivity response (middle panel) and surface temperature (bottom panel). The converted surface temperature from the measured reflectance is shown for comparison. The excimer laser fluence is 42.2 mJ/cm^2 .

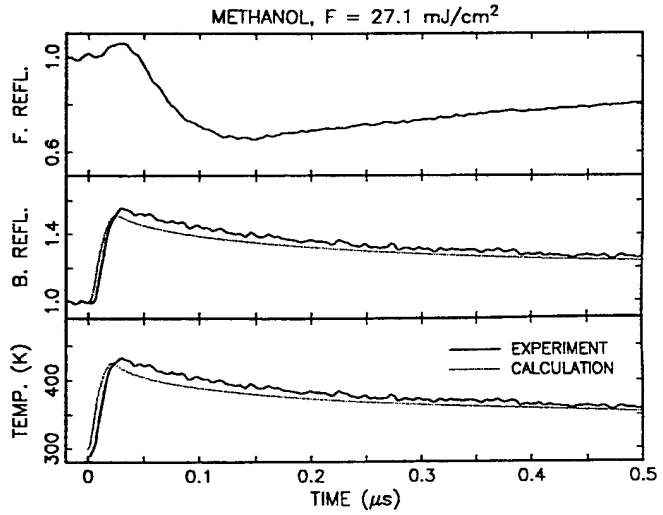


Fig. 4 The experimentally obtained reflectance curves (solid lines) are shown in the top panel (forward reflectance) and middle panel (backward photothermal reflectance) for methanol. The dotted lines are calculated transient reflectivity response (middle panel) and surface temperature (bottom panel). The converted surface temperature from the measured reflectance is shown for comparison. The excimer laser fluence is 27.1 mJ/cm^2 .

photothermal reflectance response (dotted line). The measured (solid line) and calculated (dotted line) evolutions of surface temperature are compared in the bottom panel. The measured surface temperature trace is converted from the obtained reflectance signal. The measured maximum surface temperature value is the same as the calculated, 476 K, which is 103 K above the boiling temperature.

The transient temperature measurement for the methanol/chromium interface of the sample at the fluence of 27.1 mJ/cm² at atmospheric pressure is shown in Fig. 4. A drop in the forward reflectance is seen in the top panel of the figure. Hence bubble nucleation takes place at this fluence level. By repeated measurements, the threshold for nucleation is determined to be 23.5 mJ/cm². The temperature measurement on methanol results in the maximum surface temperature of 422 K and the calculation yields 409 K. Consequently the degree of superheat required for the nucleation in the nanosecond heating is approximately 80 K (boiling point = 337.9 K).

The measured peak surface temperature at atmospheric pressure is plotted as a function of the excimer laser fluence in Fig. 5 for water. The temperature is approximately linear with the fluence. The discrepancy between the measurement and calculation arises from the possible departure of thermal properties of thin films from bulk values and the existence of contact resistance between layers. Nevertheless, it can be stated that the technique used in this work can measure the surface temperature with accuracy of 30°C. The different slope of the temperature rise versus fluence between experiment and calculation is due to the increasing departure of properties from bulk values at higher temperatures. It is also in part due to the assumption in the computation that no phase change is taken into account. This is a fair assumption, however, because a large fraction of heat is transferred to solid and only a small fraction of the absorbed heat is transferred to the liquid. Therefore, the temperature field is not strongly affected by the occurrence of vaporization and the interface temperature can be well estimated by the simple conduction equation. It is however noted that the trend of lower measured temperature compared with the calculated values at higher laser fluence suggests the increasing amount of vaporization at higher temperatures. It is also observed in methanol as illustrated in Fig. 6. The trend of lower measured temperature than calculated temperature is more pronounced in methanol. Generally, experimental data of methanol are not as good as those of water. This is attributed to the lower temperature rise of methanol, i.e., worse signal-to-noise ratio, and higher volatility. Error bars are indicated in Fig. 6. The limit of superheat of methanol is 477 K²⁹. Surface temperature exceeding the limit of superheat is also measured (see Fig. 6). At this condition, it is expected that the liquid adjacent to the surface would completely evaporate, forming a vapor film. This hypothesis is indeed confirmed experimentally. Figure 7 shows the forward reflectance transients for increasing laser fluences. When the surface temperature is below the limit of superheat at 30.3 mJ/cm², the forward reflectance curve shows typical bubble growth and collapse signatures (see Fig. 4). At higher fluences, the experimental reflectance curve shows the characteristics of a vapor film. First, the

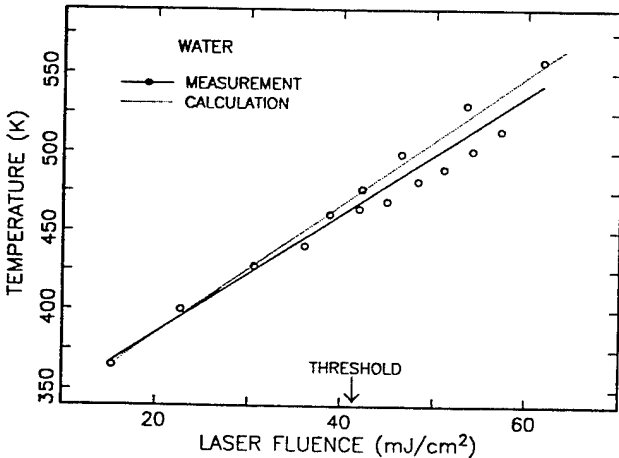


Fig. 5 The measured surface temperature is compared with the calculated surface temperature as a function of laser fluence for water. The nucleation threshold is indicated by arrow. Solid line is a linear fitting of experimental data.

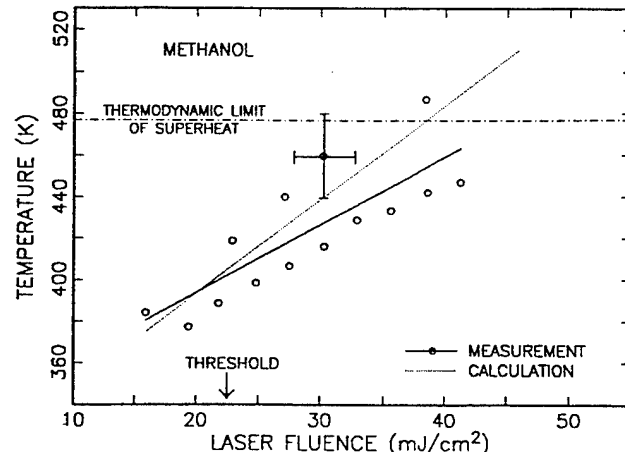


Fig. 6 The measured surface temperature is compared with the calculated surface temperature as a function of laser fluence for methanol. The nucleation threshold is indicated by arrow. Solid line is a linear fitting of experimental data.

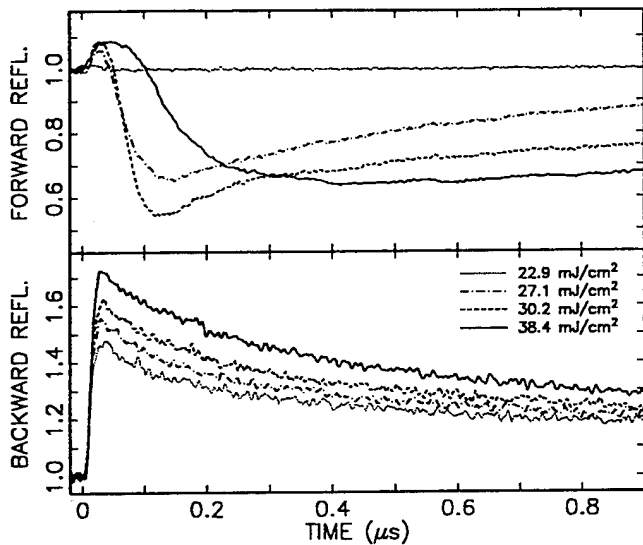


Fig. 7 The comparison of transient reflectance traces at various laser fluences for methanol.

amount of the reflectance drop is smaller, i.e., the scattering loss is smaller. It is known that a smooth vapor film will scatter less light than a cloud of bubbles. Secondly, the evolution of signal is much slower. Once a vapor film forms, the creation of bubbles (drop of the reflectance signal) is delayed until the vapor film collapses and breaks up due to cooling. Since the limit of superheat of water is very high (596 K)²⁹, such an effect has not been observed for water.

5. BUBBLE GROWTH DYNAMICS IN HIGH PRESSURE

The change of the specular reflectance in a high-pressure cell is monitored for the measurement of pressure. The transient signatures of the forward specular reflectance at various pressure levels at the fixed excimer laser

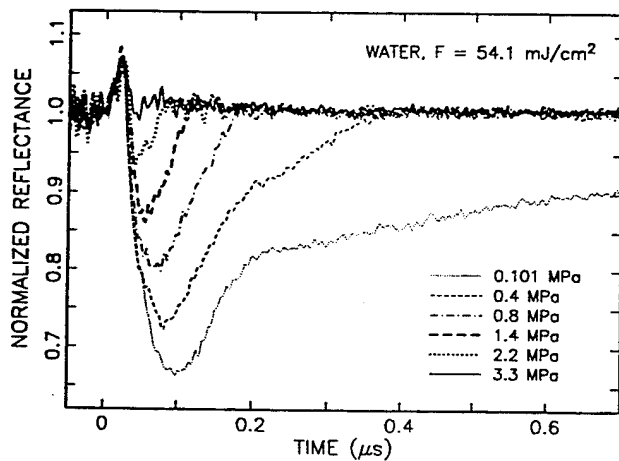


Fig. 8 The set of specular reflectance signals at various liquid pressures for water. The excimer laser fluence is 54.1 mJ/cm^2 . The probe beam is s-polarized Ar^+ laser ($\lambda = 488 \text{ nm}$) at an incident angle of 10.5° .

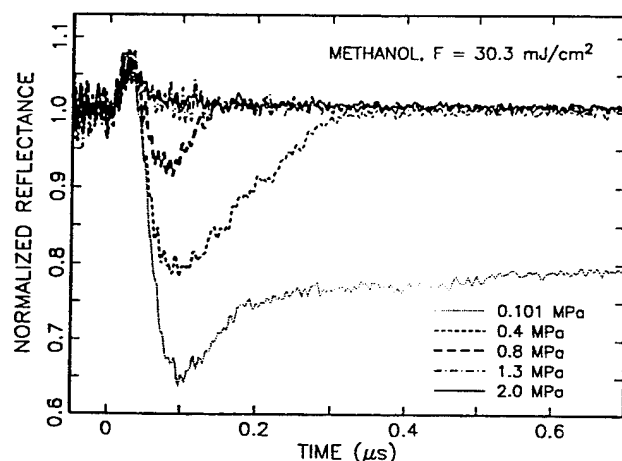


Fig. 9 The set of specular reflectance signals at various liquid pressures for methanol. The excimer laser fluence is 30.3 mJ/cm^2 . The probe beam is s-polarized Ar^+ laser ($\lambda = 488 \text{ nm}$) at an incident angle of 10.5° .

Table 1 The measured peak surface temperature and cut-off pressure of the chromium sample. The saturation vapor pressure values at the measured peak temperature are provided for reference.

Liquid	Laser fluence (mJ/cm ²)	Peak surface temperature (K)	Cut-off pressure (MPa)	Vapor pressure (MPa)
Water	44.9	468.8	1.7	1.42
	48.2	481.4	2.9	1.84
	54.1	500.8	3.5	2.68
Methanol	24.8	398.5	0.8	0.75
	30.3	416.0	1.6	1.17

fluence are shown in Fig. 8 for water and Fig. 9 for methanol. The initial increase of the reflectance is due to the interference of the thin layer of small bubbles¹⁰. The nucleation of bubbles at the stage of initial rise of signal where the bubble size is $\ll \lambda/2\pi n$ (Rayleigh scattering regime)¹⁰ is nearly insensitive to the increase of ambient pressure. This finding indicates that the transition temperature of liquid to vapor is not sensitive to the pressure. It agrees with the fact that the limit of superheat, i.e., the liquid spinodal, is only a very weak function of pressure. It is, however, clearly seen that the negative amplitude of the reflectance, i.e., the growth of large bubbles ($\gg \lambda/2\pi n$: Mie scattering regime), decreases with the ambient pressure. At $p_l = 3.3$ MPa for water and at $p_l = 1.3$ MPa, the bubble growth is completely suppressed so that the negative phase of the specular reflectance is not observed. The negative drop of the reflectance is an indicator of the number and the size of bubbles causing Mie scattering ($r \gg \lambda/2\pi n$)^{10,11}. Figures 10 and 11 display the magnitude of the negative drop of the specular reflectance as a function of liquid pressure for water and methanol, respectively. The zero reflectance drop indicates that no bubble much bigger than $\lambda/2\pi n$ is detectable. Therefore the "cut-off pressure" is defined as the minimum liquid pressure at which no bubble with size much bigger than $\lambda/2\pi n$ is generated, i.e., as the intercept of the reflectance drop curve on the abscissa. The measured cut-off pressure is summarized in Table 1 for water and methanol at various laser fluences. The measured surface temperature and corresponding saturation pressure are also listed. It is noted that the cut-off pressure is higher than the saturation pressure. Under thermal equilibrium, the condition for bubble formation is that the vapor pressure must be larger than the ambient liquid pressure. Therefore the difference between the cut-off

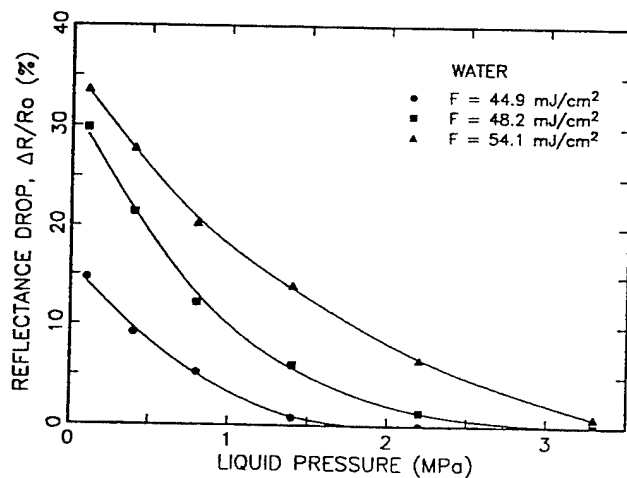


Fig. 10 The amplitude of the negative reflectance is plotted versus the liquid pressure for water at various excimer laser fluences. Curves are spline fits of experimental data (symbols).

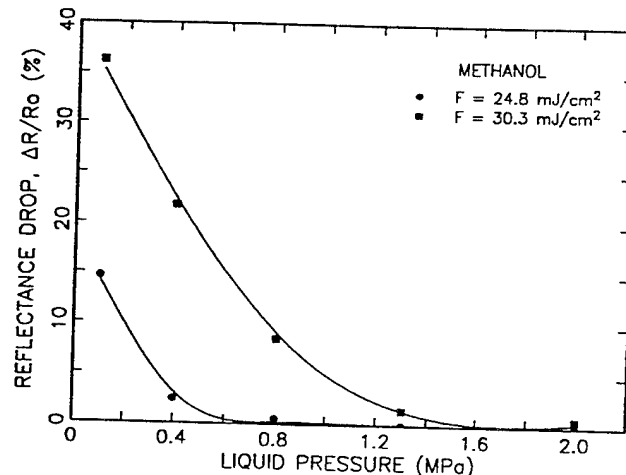


Fig. 11 The amplitude of the negative reflectance is plotted versus the liquid pressure for methanol at various excimer laser fluences. Curves are spline fits of experimental data (symbols).

pressure and the saturation vapor pressure $p_{sat}(T)$ is an amount to be accounted for nonequilibrium vaporization. This can be understood as an excessive pressure force preventing further bubble growth or as a dynamic pressure generated by the exploding bubbles. The excessive pressure p_{ex} is defined as the difference between the cut-off pressure and the saturation vapor pressure, i.e., $p_{ex} = p_{cut-off} - p_{sat}(T)$. Hence p_{ex} is a measure of the transient component of pressure generated upon vaporization and is of the order of 1 MPa in Table 1. It is noted in Table 1 that p_{ex} increases with laser fluences. Therefore, the transient force is greater when the laser fluence is higher, i.e., the surface is hotter.

6. CONCLUSION

Transient optical techniques including photothermal reflectance and specular reflectance probes have been utilized together with a high-pressure cell to obtain quantitative temperature and pressure values during the laser-induced vaporization of liquids on a solid surface. Two time-resolved optical probes for bubble growth kinetics and temperature measurements are applied simultaneously in a high-pressure cell at elevated ambient pressures. The transient temperature measurement revealed that liquids can sustain about a hundred of degrees of superheat before the vaporization occurs. It has been found that bubble growth can be suppressed under tens of atmospheric pressure. It has been also estimated that pressure level generated by the explosive bubble growth is of the order of a few atmospheric pressure.

7. ACKNOWLEDGEMENTS

The authors thank D. Krajnovich and I. K. Pour of IBM Almaden Research Center for their valuable contributions to this work. Support to this work by the National Science Foundation under Grant CTS-9317708 is gratefully acknowledged.

8. REFERENCES

1. N. Morita, S. Ishida, Y. Fujimori, and K. Ishikawa, "Pulsed laser processing of ceramics in water," *Appl. Phys. Lett.*, Vol. 52, pp. 1965-1966, 1986.
2. A. Polman, W. C. Sinke, F. W. Saris, M. J. Uttermark, and M. O. Thomson, "Quench rate enhancement in pulsed laser melting of Si by processing under water," *Appl. Phys. Lett.*, Vol. 52, pp. 535-537, 1988.
3. R. J. von Gutfeld and R. T. Hodgson, R.T., "Laser enhanced etching in KOH," *Appl. Phys. Lett.*, Vol. 40, pp. 352-354, 1982.
4. A. C. Tam, W. P. Leung, W. Zapka, and W. Ziemlich, "Laser-cleaning techniques for removal of surface particulates," *J. Appl. Phys.*, Vol. 71, pp. 3515-3523, 1992.
5. B. P. Fairand and A. H. Clauer, "Effect of water and paint coatings on the magnitude of laser-generated shocks," *Opt. Comm.*, Vol. 18, pp. 588-591, 1979.
6. A. Vogel, P. Schweiger, A. Frieser, M. N. Asiyo, and R. Birnberg, "Intraocular Nd:YAG laser surgery: Light-tissue interaction, damage range, and reduction of collateral effects," *IEEE J. Quant. Elect.*, Vol. 26, pp. 2240-2260, 1990.
7. P. Teng, N. S. Nishioka, R. R. Anderson, and T. F. Deutsch, "Optical studies of pulsed-laser fragmentation of biliary calculi," *Appl. Phys. B*, Vol. 42, pp. 73-78, 1987.
8. K. Kink, G. Delacrétaz, and R. P. Salathé, "Fragmentation process induced by nanosecond laser pulse," *Appl. Phys. Lett.*, Vol. 22, pp. 2644-2646, 1992.
9. J. M. Isner and R. H. Clarke, "The current status of lasers in the treatment of cardiovascular disease," *IEEE J. Quant. Elect.*, Vol. 20, pp. 1406-1420, 1984.

10. O. Yavas, P. Leiderer, H. K. Park, C. P. Grigoropoulos, C. C. Poon, W. P. Leung, N. Do, and A. C. Tam, "Optical reflectance and scattering studies of nucleation and growth of bubbles at a liquid-solid interface induced by pulsed laser heating," *Phys. Rev. Lett.*, Vol. 70, No. 12, pp. 1830-1833, 1993.
11. O. Yavas, P. Leiderer, H. K. Park, C. P. Grigoropoulos, C. C. Poon, W. P. Leung, N. Do, and A. C. Tam, "Optical and acoustic study of nucleation and growth of bubbles at a liquid-solid interface induced by nanosecond-pulsed laser heating," *Appl. Phys. A*, Vol. 58, pp. 407-415, 1994.
12. V. P. Carey, *Liquid-Vapor Phase-Change Phenomena*, Hemisphere, Washington, 1992.
13. V. P. Skripov, *Metastable Liquids*, John Wiley & Sons, New York, 1974.
14. G. E. Jellison Jr., D. H. Lowndes, D. N. Mashburn, and R. F. Wood, "Time-resolved reflectivity measurements of silicon and germanium using a pulsed excimer KrF laser heating beam," *Phys. Rev. B*, Vol. 34, No. 4, pp. 2407-2415, 1986.
15. L. A. Lompré, J. M. Liu, H. Kurz, and N. Bloembergen, N., "Time-resolved temperature measurement of picosecond laser irradiated silicon," *Appl. Phys. Lett.* Vol. 43, pp. 168-170, 1983.
16. D. H. Lowndes, "Time-resolved optical transmission and reflectivity of pulsed-ruby-laser irradiated crystalline silicon," *Phys. Rev. Lett.*, Vol. 48, pp. 267-271, 1982.
17. H. K. Park, X. Xu, C. P. Grigoropoulos, N. Do, L. Klees, P. T. Leung, and A. C. Tam, "Transient optical transmission measurement in excimer-laser irradiation of amorphous silicon films," *Trans. ASME J. Heat Transfer*, Vol. 115, pp. 178-183, 1993.
18. X. Xu, C. P. Grigoropoulos, and R. E. Russo, "Transient temperature measurement during pulsed excimer laser heating of thin semiconductor films," *Trans. ASME J. Heat Transfer*, in press, 1994.
19. H. Schoeffman, H. Schmidt-Kloiber, and E. Reichel, E., "Time-resolved investigations of laser-induced shock waves in water by use of polyvinylidenefluoride hydrophones," *J. Appl. Phys.*, Vol. 63, pp. 46-51, 1988.
20. W. P. Leung and A. C. Tam, "Noncontact monitoring of laser ablation using a miniature piezoelectric probe to detect photoacoustic pulses in air," *Appl. Phys. Lett.*, Vol. 60, pp. 23-25, 1992.
21. A. A. Oraevsky, S. L. Jacques, and F. K. Tittel, "Determination of tissue optical properties by piezoelectric detection of laser-induced stress waves," *Laser-Tissue Interaction IV*, S. L. Jacques and A. Katzir Ed., Vol. 1882, pp. 86-101, SPIE, Bellingham, 1993.
22. A. Vogel, W. Lauterborn, and R. Timm, "Optical and acoustic investigations of the dynamics of laser-produced cavitation bubbles near a solid boundary," *J. Fluid Mech.*, Vol. 206, pp. 299-338, 1989.
23. B. Ward and D. C. Emmony, "Direct observation of the pressure developed in a liquid during cavitation-bubble collapse," *Appl. Phys. Lett.*, Vol. 59, pp. 2228-2230, 1991.
24. A. G. Doukas, A. D. Zweig, J. K. Frisoli, R. Birngruber, and T. F. Deutsch, "Non-invasive determination of shock wave pressures generated by optical breakdown," *Appl. Phys. B*, Vol. 53, pp. 237-245, 1991.
25. N. Do, K. Klees, A. C. Tam, P. T. Leung, and W. P. Leung, "Photodeflection probing of the explosion of a liquid film in contact with a solid heated by pulsed excimer laser irradiation," *J. Appl. Phys.*, Vol. 74, pp. 1534-1538, 1993.
26. M. A. Harith, V. Palleschi, A. Salvetti, D. P. Singh, M. Vaselli, G. V. Dreiden, Y. I. Ostrovsky, and I. V. Semenova, "Dynamics of laser-driven shock waves in water," *J. Appl. Phys.*, Vol. 66, pp. 5194-5197, 1989.
27. X. Xu and C. P. Grigoropoulos, "High temperature radiative properties of thin silicon films at the $\lambda = 0.6328 \mu\text{m}$ wavelength," *Int. J. Heat Mass Transfer*, Vol. 36, pp. 4163-4172, 1994.
28. M. Born and E. Wolf, *Principles of Optics*, 6th Ed., Pergamon, Exeter, United Kingdom, pp. 51-70, pp. 611-633, 1986.
29. C. T. Avedisian, "The homogeneous nucleation limits of liquids," *J. Phys. Chem. Ref. Data*, Vol. 14, pp. 695-729, 1985.

Memory-Effect on Acoustic Cavitation

Oğuz Yavaş, Paul Leiderer,

Department of Physics, University of Konstanz, D-78434 Konstanz, Germany

Hee K. Park, Costas P. Grigoropoulos,

Department of Mechanical Engineering, University of California Berkeley, CA 94720

Chie C. Poon, and Andrew C. Tam

IBM Almaden Research Center, 650 Harry Road, San Jose, CA 95120-6099

ABSTRACT

The formation of bubbles at a liquid-solid interface due to acoustic cavitation depends particularly on the pre-conditions of the interface. Here, it will be shown that following laser-induced bubble formation at the interface the acoustic cavitation efficiency is strongly enhanced. Optical reflectance measurements reveal that this observed enhancement of acoustic cavitation due to preceding laser-induced bubble formation, which could be termed as a memory effect, decays in a few hundred microseconds. By performing a double-pulse experiment using two excimer lasers the influence of process parameters, such as liquid temperature and salt concentration, on the temporal decay of the memory effect has been studied. An analysis of the experimental results by a diffusion model is presented.

1. INTRODUCTION

Acoustic cavitation, i.e., the formation of bubbles or cavities in a liquid induced by the tensile pressure of an acoustic field, is of importance in many technical applications, such as sonochemistry, ultrasonic cleaning, laser surgery in medicine, and lithotripsy.¹⁻⁴ Theoretically, it has been predicted that a tensile pressure of about 500 MPa is needed to generate cavitation in water. However, cavitation can experimentally be achieved at acoustic amplitudes of the order 0.1 MPa. In order to account for this discrepancy it has been assumed that long-lived cavitation nuclei, such as ultramicroscopic bubbles or other inhomogeneities, are usually present in liquids.⁵ However, small bubbles are thermodynamically unstable and may either dissolve and vanish quickly or grow and rise to the liquid surface.⁶ Therefore, several models have been suggested to account for the generation and stabilization of microbubbles, including cosmic radiation,^{5,7,8} clusters of organic or ionic molecules,⁹⁻¹¹ van der Waals stabilization,¹² and gas inclusion in crevices on container wall or solid impurities in the liquid.^{13,14} In addition, for highly purified and degassed water a significant decrease of the cavitation threshold due to neutron irradiation has been observed. This decrease is reversible, i.e., the threshold returns to the initial level in about half an hour when the source of radiation is removed,⁵ and can be termed as a memory effect.

The physical mechanism underlying this effect has not been understood yet, and, to our knowledge, there has not been any study on a possible memory effect for acoustic cavitation at a liquid-solid interface. Here, we demonstrate the generation of acoustic cavitation by nanosecond pulses and show for the first time the existence of a bubble memory effect at a liquid-solid interface. The temporal decay of this memory effect has been determined and can be explained by a diffusion process.

2. EXPERIMENTAL PROCEDURE AND RESULTS

A detailed description of the experimental approach can be found in Refs. 15 and 16, and shall be discussed in the following only briefly: A solid film (0.2 – 0.3 μm thick chromium films on a sapphire substrate) is immersed in a test liquid contained in a quartz cuvette. A short pulsed laser irradiation heats the surface of the solid film above the boiling temperature of the liquid in about 20 ns. As a result, bubbles are formed at the liquid-solid interface, which can be monitored by the transient change of an optical reflectance signal. The laser irradiation also leads to the generation of an acoustic pulse of high intensity via the thermoelastic effect¹⁷ and bubble collapse.¹⁶ Previously, it has been observed that this high intensity acoustic pulse causes cavitation at the liquid-solid interface after being reflected at the quartz window of the cuvette, giving rise to repetitive “echoes” in the optical reflectance signal when the surfaces of the solid sample and the quartz window are parallel.^{16,18}

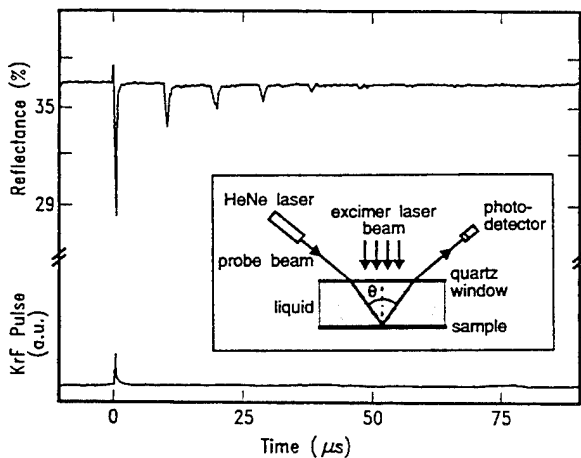


Fig. 1. Optical reflectance signal due to bubble formation at a methanol-chromium interface. $\lambda_{\text{probe}} = 632.8 \text{ nm}$, unpolarized, $\Theta = 15^\circ$. The solid sample and the quartz window are parallel as shown in the inset. The initial reflectance drop is due to thermally induced bubbles and the following echoes are due to acoustic cavitation caused by the travelling acoustic pulse. (The distance between the solid sample and the quartz window is $\sim 7 \text{ mm}$.)

An example for a methanol-chromium interface is shown in Fig. 1. While the initial reflectance drop is due to bubble formation induced by the excimer laser heating, the succeeding echoes are solely due to acoustic cavitation induced by the travelling pressure pulse. The decrease of the amplitude of these successive echo signals had been ascribed to the attenuation of the acoustic pulse.¹⁶ However, as shall be seen, this decrease is also due to the slow decay of the cavitation efficiency, i.e., the memory effect.

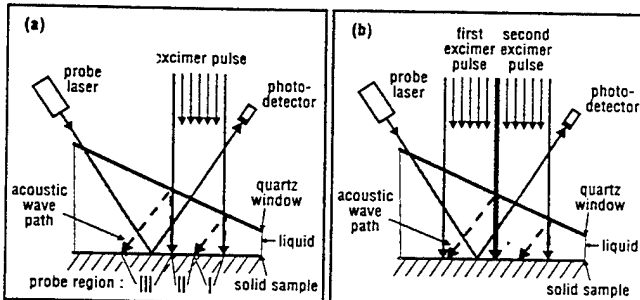


Fig. 2. (a) Experimental setup used to proof the existence of the memory effect. Solid line represents the path of the laser beam, dashed line the path of the acoustic pulse in the liquid. (b) Experimental setup for the measurement of the temporal decay of the memory effect. The first laser pulse initiates the memory effect and the second generates the acoustic pulse.

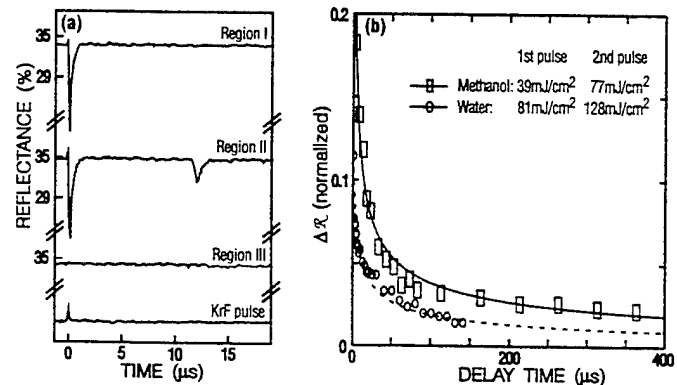


Fig. 3. (a) The optical reflectance signal for the three regions shown in Fig. 2(a) confirming the existence of a memory effect at the laser-irradiated area. (b) The echo signal peak amplitude as a function of delay time between the laser pulse and the acoustic pulse (temporal decay of the memory effect) for liquid-chromium interface. The lines represent the fit of the experimental data with the diffusion model.

The memory effect is demonstrated using the experimental configuration shown in Fig. 2(a). The quartz window is tilted with respect to the solid sample so that after a round-trip travel in the cuvette the acoustic pulse is displaced and partly overlaps with the laser-irradiated area. Consequently, there are three distinct regions on the solid surface. Region I is irradiated by the excimer laser pulse only. Region II is irradiated by the excimer laser and additionally subjected to the acoustic pulse with a delay time corresponding to its round-trip period in the cuvette. Region III is free from laser irradiation and is subjected to the acoustic pulse only. The HeNe laser beam is positioned to probe each of the three different regions. Representative results for a water-chromium interface are shown in Fig. 3(a). For Region I, only one reflectance signal is observed, which is due to initial bubble formation induced by the excimer laser heating. For Region II, two separate reflectance signals are observed. The first is due to the initial bubble formation and the second due to acoustic cavitation. For Region III, no reflectance signal is observed, i.e., the acoustic pulse cannot cause any cavitation at a previously unirradiated surface. Thus, the laser-induced bubble

formation at the solid surface results in a long-term enhancement of acoustic cavitation. Any thermal effect can be excluded as a possible explanation for this effect since our heat diffusion computations reveal that the temperature at the water-chromium interface decreases to room temperature in about 1 μs following the laser pulse.¹⁶ Therefore, it is hypothesized that the laser-induced bubbles collapse into metastable ultramicroscopic bubbles, i.e., long-lived cavitation nuclei. These nuclei, which are deemed absent on the unirradiated surface, subsequently enhance acoustic cavitation.

In order to determine the temporal decay of the memory effect, we have performed a series of double laser-pulse experiments. The setup of this experiment is shown in Fig. 2(b). The beams from two separate 248-nm KrF excimer laser units are directed to the solid sample without any spatial overlap. The HeNe laser beam probes the location which corresponds to Region I for the first pulse and to Region III for the second pulse. The first laser pulse initiates the memory effect and the second pulse generates the high-intensity acoustic pulse of short duration. While the time delay between the first and the second laser pulses is varied, the fluences are kept constant to assure that at each time both the amount of microbubbles formed and the intensity of the acoustic pulse are about the same. When the two lasers are fired simultaneously, the same signal as in Fig. 3(a) is observed (signal for Region II). With increasing delay time the amplitude of the second reflectance signal decreases, i.e., the memory effect decays. Eventually, the acoustic cavitation returns to normal efficiency. Representative results for water-chromium and methanol-chromium interfaces are shown in Fig. 3(b). The temporal decay in the reflectance signal can be well fitted with the following formula:

$$\Delta R(t) = C/\sqrt{t + t_0},$$

where $\Delta R(t)$ is the peak reflectance drop normalized with respect to the initial reflectance value, C the proportionality constant, t the delay time between the laser pulse and the acoustic pulse $t \geq 0$, and t_0 a constant to account for the time required for the laser-induced stabilized nuclei formation. Typical values for C are ranged as $0.1 - 0.2 \mu\text{s}^{1/2}$ for water and $0.2 - 0.4 \mu\text{s}^{1/2}$ for methanol. The values for t_0 are found to be $0.3 - 3.2 \mu\text{s}$ for water and $0.9 - 9.7 \mu\text{s}$ for methanol. These constants are dependent upon the first and the second laser fluences. The values of t_0 are consistent with the expected higher bubble collapse speed for water because of its higher surface tension compared to methanol. The fitting equation resembles the well-known equation for the surface history for a one-dimensional diffusion process.¹⁹ The change on the reflectance signal due to scattering losses caused by small non-absorbing particles in a host medium, such as micron-sized bubbles in a liquid, can be approximated by:^{20,21}

$$\Delta R(t) \approx \sum_r N(t, r) r^2(t),$$

where $N(t, r)$ is the bubble number density of radius r . Thus, the reflectance signal is only a function of the distributed bubble radius and number density. Since the intensity of the acoustic pulse is kept constant, the changes on these properties of grown-up bubbles (post-cavitation bubbles) are directly related only to the changes on the properties of laser-induced metastable ultramicroscopic bubbles (cavitation nuclei). Therefore, the observed temporal decay of the peak reflectance drop, i.e., the diffusive decay of the quantity $\sum_r N(t, r) r^2(t)$, is attributed to a net diffusive change on the properties of laser-induced ultramicroscopic bubbles.

The observed diffusive decay of the memory effect could be ascribed to three different mechanisms. First, the bubble radius can decrease by diffusion of entrapped gases into the liquid. Second, stable microbubbles may diffuse away from the sample surface to yield a smaller bubble number density. However, this effect is expected to be small since the diffusion velocity for bubbles is small^{6,11} and the time scale considered is less than hundreds of microseconds. The third mechanism is the coalescence of microbubbles to form bigger bubbles. From the present data it is not possible to rank the first and the third mechanisms because the bubble size and the number density have not been independently determined.

The interpretation of the temporal decay in the reflectance signal by a diffusion process of microbubble properties could be verified by varying the laser fluences in the double-pulse experiments. When the fluence of the first laser is increased more microbubbles will be formed on the solid surface. Similarly, when the fluence of the second laser is increased an acoustic pulse of higher intensity will be generated. Both mechanisms will lead to an increase of cavitation yield. This has indeed been observed as shown in Fig. 4(a) for water-chromium interface, where the decay of the memory effect is compared for two different fluence values of the first laser pulse. The amplitude of the reflectance drop increases as the laser fluence is increased. The same trend is observed when the fluence for the second laser is varied. An interesting result is obtained when the ion concentration of water is increased by introducing NaCl. Figure

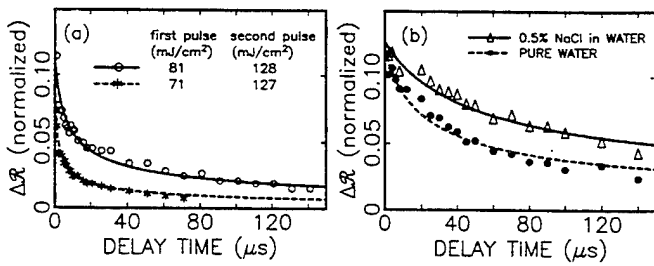


Fig. 4. (a) Effect of fluence variation for the first laser pulse on the memory effect. (b) Stabilizing effect of ion concentration on the temporal decay of the memory effect for water-chromium interface. $F_1 = 82 \text{ mJ/cm}^2$ (first pulse) and $F_2 = 120 \text{ mJ/cm}^2$ (second pulse). The lines represent the fit of the experimental data with the diffusion model.

4(b) shows the results for pure (spectroscopic grade) water and for water with NaCl (0.5%). As can be seen, the introduction of ions has a stabilizing effect on the microbubbles and consequently the memory effect is prolonged. This result could be explained by the hypothesis of the ionic cluster formation^{10,11} as a possible stabilization mechanism for ultramicroscopic bubbles.

3. CONCLUSION

We have demonstrated the existence of a long-term memory effect, i.e., the enhancement of acoustic cavitation at a liquid-solid interface following laser-induced bubble formation. The temporal decay of the memory effect for two different liquids on a chromium surface has been determined and could be explained by a diffusion process.

4. ACKNOWLEDGMENTS

This work has been performed at the facilities of IBM Almaden Research Center, San Jose, California. The authors thank I. K. Pour, D. Krajnovich, and W. P. Leung of IBM Almaden Research Center, and J. Boneberg of the University of Konstanz, Germany, for their valuable support, assistance, and contributions to this work. Support by the Computer Mechanics Laboratory of the University of California at Berkeley is gratefully acknowledged. O. Yavas gratefully acknowledges the fellowship from the Friedrich-Ebert-Stiftung, Bonn, Germany.

REFERENCES

1. F. R. Young, *Cavitation* (McGraw-Hill, London, 1989), and references therein.
2. R. E. Apfel, in *Methods of Experimental Physics*, ed. by P. T. Edmonds (Academic, New York, 1981), Vol. 19 (Ultrasonics), p. 355.
3. T. J. Mason, *Practical Sonochemistry* (Ellis Horwood, New York, 1991).
4. J. Bardina, in *Particles on Surfaces*, ed. by K. L. Mittal (Plenum, New York, 1988), Vol. 1, p. 327.
5. R. D. Finch, *J. Acoust. Soc. Am.* **36**, 2287 (1964).
6. P. S. Epstein and M. S. Plesset, *J. Chem. Phys.* **18**, 1505 (1950).
7. D. Lieberman, *Phys. Fluids* **2**, 466 (1959).
8. D. Sette and F. Wanderlingh, *Phys. Rev.* **125**, 409 (1962).
9. F. E. Fox and K. F. Herzfeld, *J. Acoust. Soc. Am.* **26**, 984 (1954).
10. V. A. Akulichev, *Sov. Phys. Acoust.* **12**, 144 (1966).
11. N. F. Bunkin and F. V. Bunkin, *Sov. Phys. JETP* **74**, 271 (1992).
12. R. A. Wentzell, *Phys. Rev. Lett.* **56**, 732 (1986).
13. M. Strasberg, *J. Acoust. Soc. Am.* **31**, 163 (1959).
14. A. A. Atchley and A. Prosperetti, *J. Acoust. Soc. Am.* **86**, 1065 (1989).
15. O. Yavas, P. Leiderer, H. K. Park, C. P. Grigoropoulos, C. C. Poon, W. P. Leung, N. Do, and A. C. Tam, *Phys. Rev. Lett.* **70**, 1830 (1993).
16. O. Yavas, P. Leiderer, H. K. Park, C. P. Grigoropoulos, C. C. Poon, W. P. Leung, N. Do, and A. C. Tam, *Appl. Phys. A* **58**, 407 (1994).
17. A. C. Tam, *Rev. Mod. Phys.* **58**, 381 (1986).
18. A. Polman, W. C. Sinke, M. J. Uttermark, and M. O. Thompson, *J. Mater. Res.* **4**, 843 (1989).
19. J. Crank, *The Mathematics of Diffusion* (Clarendon, Oxford, 1975).
20. H. C. van de Hulst, *Light Scattering by Small Particles* (Dover, New York, 1981).
21. O. Yavas, P. Leiderer, H. K. Park, C. P. Grigoropoulos, C. C. Poon, and A. C. Tam, *Phys. Rev. Lett.* **72**, 2021 (1994).

Laser-induced etching and deposition of Tungsten in
Tungstenhexafluoride-Hydrogen-atmosphere

K. Piglmayer, Z. Toth⁺, and Z. Kantor⁺
Angewandte Physik, Johannes-Kepler-Universität Linz, A-4040
Linz, Austria

⁺ on leave from Research Group on Laserphysics of the
Hungarian Academy of Sciences, H-6720 Szeged, Dóm tér 9,
Hungary.

ABSTRACT

Combined thermally induced etching and deposition of W in a mixture of WF_6 and H_2 is investigated by local laser-induced patterning of thin tungsten layers on quartz. The process divides into areas of pure etching and deposition, depending on the partial pressures of the gases.

1. INTRODUCTION

With application of lasers in materials processing the broad field of standard chemical vapor deposition (CVD) has found a new and promising extension. A large effort on theoretical and experimental investigations of localized patterning of substrates has led to a highly developed scientific level, and offered a lot of promising applications¹⁻⁵.

Laser processing also revealed new phenomena in various heterogeneous chemical systems⁶⁻⁹. This is mainly due to the fact that laser heating of surfaces provides high temperatures and strong localization, conditions which cannot be achieved in conventional CVD systems. Let us consider one example, the deposition of W. Creighton¹⁰⁻¹¹ has shown that in CVD of tungsten from a mixture of WF_6 and H_2 a loss in selectivity of deposits is observed, i.e. tungsten is deposited in small amounts also far from the processing area. This effect is explained by the formation of tungsten pentafluoride via the reaction

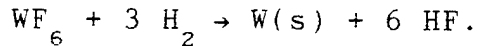


WF_5 diffuses out of the reaction zone and is reduced to tungsten at colder parts of the reaction chamber.

McCarty et al¹² investigated the etching of tungsten coils with WF_6 at high temperatures, and included reaction (1) as a main part in the analysis.

Therefore, thermal laser-chemical processing (LCP) with mixtures of WF_6 and H_2 can proceed along two pathways:

- a) etching of tungsten via reaction (1)
- b) deposition of tungsten due to the overall reaction



In this paper, phenomena arising in laser-induced localized patterning of a thin tungsten layer on a quartz substrate, using different relative concentrations of WF_6 and H_2 , or a pure WF_6 -atmosphere, are discussed.

2. EXPERIMENTAL

Tungsten hexafluoride is strongly reactive and attacks many materials, thereby leading to unstable experimental conditions. To avoid these difficulties, experiments have been performed in a flow chamber.

Fig. 1.
Experimental setup used in the experiments.

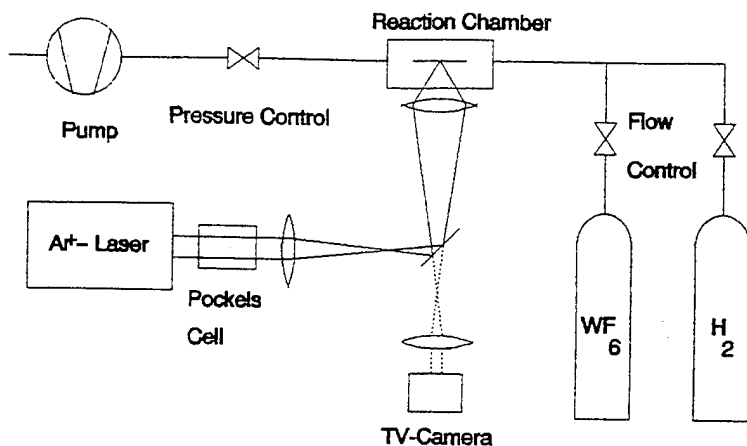


Fig. 1 shows a schematic picture of the experimental setup. The vacuum system has exclusively been fabricated out of stainless steel. The substrates used were quartz, covered with a 700 Å thick layer of sputtered tungsten. The 514.5nm line of an Ar+ laser was focused onto the substrate to a diameter of 3 μm ($1/e^2$ -intensity). The focusing procedure and the process itself were observed via a TV-camera in combination with a high magnification lens system. The flow reactor was mounted onto a translation stage. Laser pulses with variable duration were obtained with the help of a Pockels-cell. The flow rate of the gases was controlled by finely adjustable needle valves and by flow meters and kept constant during the experiments on a value of 15 sccm. Deposited and etched patterns have been investigated by means of a light microscope and a scanning electron microscope (SEM).

3. RESULTS AND DISCUSSION

3.1 WF_6-H_2 mixture

Let us define the ratio of partial pressures by $\gamma = p(H_2)/p(WF_6)$. First, we keep the partial pressure of WF_6 fixed at $p(WF_6) = 2$ mbar, and change the amount of hydrogen. Then, with both the substrate and the laser beam fixed, circular deposits (dots) of tungsten are produced. The use of a tungsten layer on the quartz substrate permits clear visualization of the process.

Fig. 2a shows a SEM picture of a dot deposited at $\gamma = 5$. Here, only deposition is observed, and diameters of dots are much larger than the focal width. For $\gamma \gg 1$ the morphology of the deposits is fine grained⁸. This regime is typical for standard CVD. No contamination of the substrate surrounding the reaction zone is observed, as can be seen from the photomicrograph in Fig. 2b, for $\gamma = 2$.

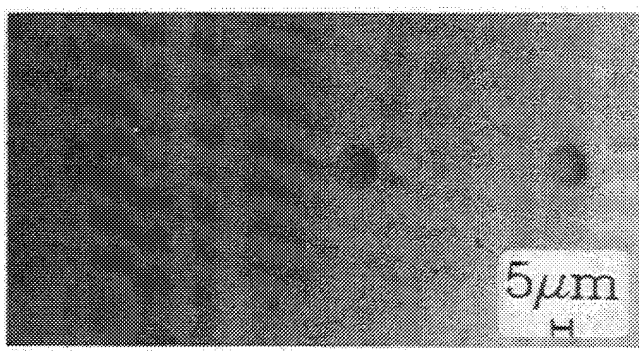
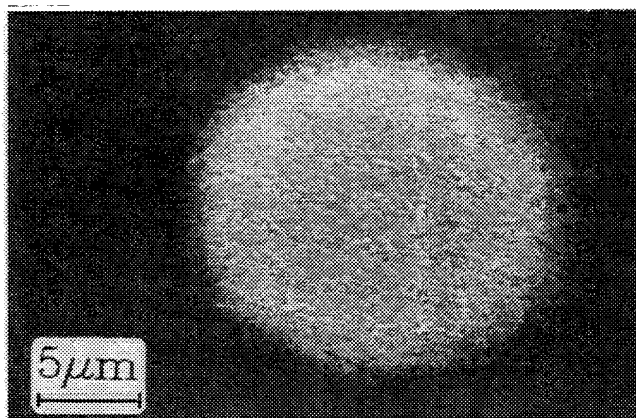


Fig. 2.

a. SEM picture of a tungsten dot deposited from 5 mbar H₂ and 1 mbar WF₆. The incident laser power was 160 mW and the illumination time 0.8 s.

b. Photomicrograph of dots deposited from 2 mbar H₂ and 1 mbar WF₆, at a laser power of 160 mW.

With $\gamma = 0.5$ an etch through ring appears at the border of the deposit. With further decrease in γ , the diameter of the etched ring decreases, but much less than that of the deposit. With $\gamma = 0.25$ the size of the etched area is comparable to that of deposition, which is restricted to the center of the laser beam. The morphology of the deposit is single-crystal like. A SEM picture of this type of structure is shown in Fig. 3a. The corresponding photomicrograph, Fig. 3b, reveals a halo. A SEM microprobe analysis shows no fluorine contamination within the halo, but it indicates a slight increase of thickness of the tungsten layer compared to that of the unchanged substrate, which is in agreement with the model of tungsten deposition from tungsten pentafluoride^{11,12}. Fig. 3c is a photomicrograph of structures formed at $\gamma = 0.25$. It clearly shows the separation of areas where deposition and etching take place.

Finally, with $\gamma \rightarrow 0$ there is no deposition but only formation of a hole with a diameter smaller than the focal width.

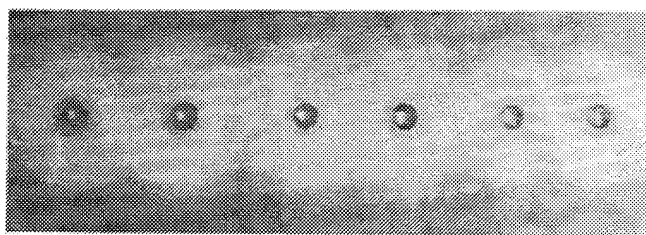
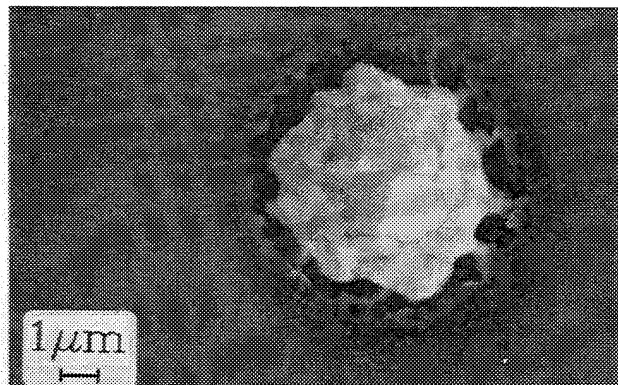
Fig. 4 shows schematically the experimental observations with decreasing γ .

The appearance of holes with diameters smaller than the laser-beam spot size indicates an Arrhenius-type behaviour of the process. On the basis of these observations a simple analysis of the etching kinetics is possible, yielding the relation $\Delta E_e < \Delta E_d$, ΔE_e and ΔE_d being the activation energies of etching and of deposition, respectively. Comparison with investigations on deposition kinetics¹³⁻¹⁵ yields ΔE_e

< 14-16 kcal/mole. A more detailed analysis of the process will be presented later.¹⁶

Fig. 3.

a. SEM picture of a tungsten dot with etched ring. Deposition was performed at a power of 160 mW and an illumination time of 0.6 s, using a gas mixture of 0.5 mbar H₂ and 2 mbar WF₆.

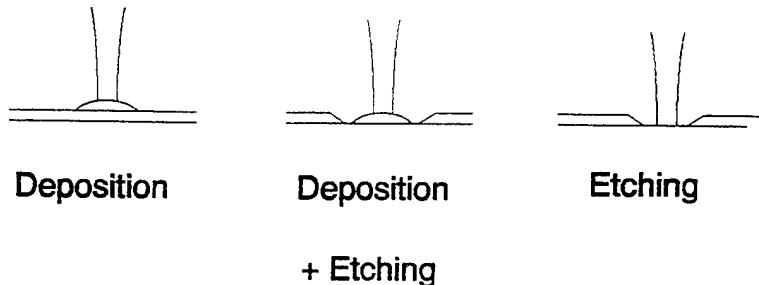


b. Photomicrograph of tungsten dots, surrounded by etched rings. Note the halo.

c. Photomicrograph which shows conditions where both deposition and etching occurs

Fig. 4.

Schematic picture showing the 'transition' from deposition to etching, observed with decreasing partial pressure of H₂.

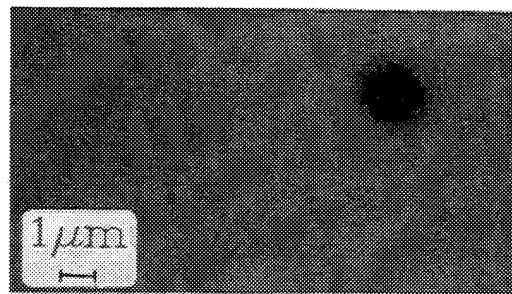


3.2 Pure WF₆

In the absence of hydrogen and below a certain temperature only etching occurs, and the tungsten layer can be etched through with well defined edges. Fig. 5 shows a SEM picture of a typical hole etched in the tungsten layer.

Fig. 5.

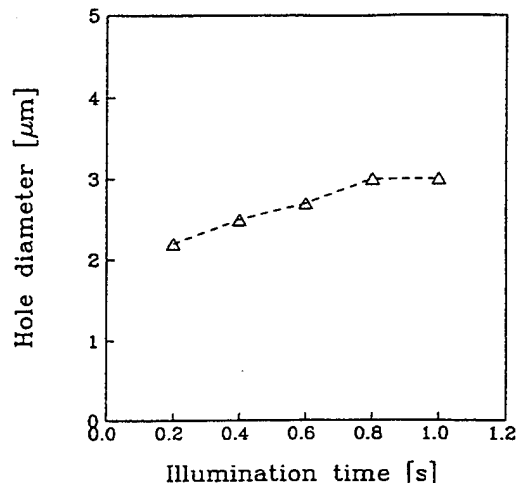
Hole etched with 2 mbar WF₆, an incident laser power of 96 mW, and an illumination time of 0.4 s.



In Fig. 6 the dependence of the hole diameter on illumination time is plotted for a fixed laser power. It shows that even when a hole is already etched through, etching is still maintained. Thus, even when the layer is already etched through, the material around still absorbs enough laser light to sustain the temperature at a level that permits further etching.

Fig. 6.

Diameter of holes etched in a 700 Å thick tungsten layer on quartz, for a WF_6 -pressure of 2 mbar, and a laser power of 128 mW.



This effect permits tungsten layers to be patterned by direct writing. An example is shown in Figs. 7a,b. A more detailed investigation of the process will be presented elsewhere¹⁷.

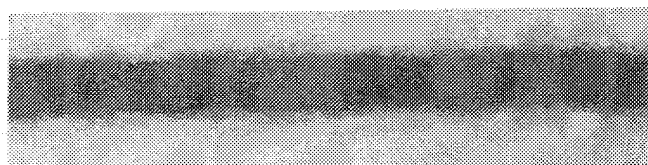
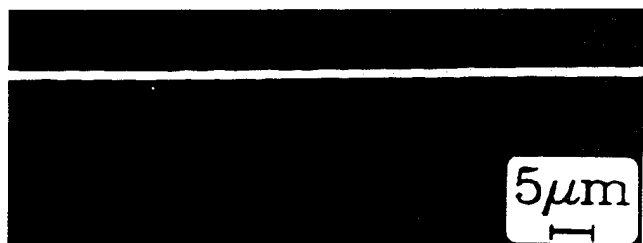


Fig. 7.

a. Scanning electron micrograph of a stripe etched in 700 Å tungsten at a pressure of 5 mbar, with an incident laser power of 96 mW and a scanning velocity of 4.2 $\mu\text{m}/\text{s}$.

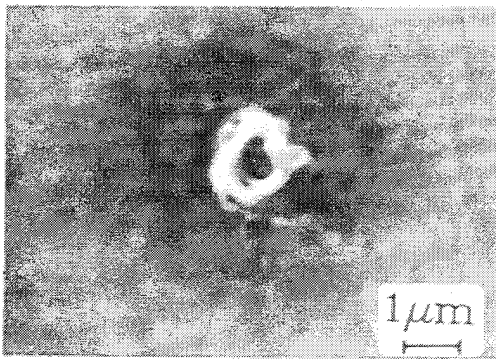


b. Photomicrograph showing an etched line. The conditions were the same as in a..

Illumination of the substrates at higher laser powers results, for short illumination times, in the formation of holes with ring structures of tungsten deposited inside. Fig. 8 shows a SEM picture of this phenomenon. With increasing illumination time the ring structure vanishes. A thermodynamic analysis shows^{12,16,18}, that above a certain temperature reaction (1) proceeds in the reverse direction, i.e. deposition of tungsten occurs. Numerical simulations of the etching/deposition process on the basis of such a thermodynamic approach explain the appearance of these ring structures¹⁶.

Fig. 8.

SEM of a ring structure appearing at $p(WF_6) = 2$ mbar, an incident laser power of 160 mW, and an illumination time of 0.2 s.



4. ACKNOWLEDGEMENTS

We wish to thank Prof. D. Bäuerle for valuable discussions and the Jubiläumsfonds of the Österreichische Nationalbank for financial support.

5. REFERENCES

1. A.W. Johnson, D.J. Ehrlich, H.R. Schlossberg, Eds., *Laser Controlled Chemical Processing of Surfaces* (North-Holland, Amsterdam, 1984)
2. D. Bäuerle, *Chemical Processing with Lasers* (Springer, Berlin 1986)
3. I.W. Boyd, *Laser Processing of Thin Films and Microstructures* (Springer, Berlin 1987)
4. D.J. Ehrlich, J.Y. Tsao, Eds., *Laser Microfabrication - Thin Film Processes and Lithography* (Academic, San Diego, CA, 1989)
5. A.W. Johnson, G.L. Loper, T.W. Sigmon, Eds., *Laser and Particle Beam Chemical Processes on Surfaces* (Mat. Res. Soc., Pittsburgh, PA, 1989)
6. Y.C. Du, U. Kempfer, K. Piglmayer, D. Bäuerle: *Appl. Phys. A* 39, 167 (1986)
7. C.R. Moylan, T.H. Baum, C.R. Jones: *Appl. Phys. A* 40, 1 (1986)
8. Z. Toth, P. Kargl, C. Grivas, K. Piglmayer, T. Szörenyi, D. Bäuerle: *Appl. Phys. B* 54, 189 (1992)
9. S. Johansson, J.A. Schweitz, H. Westberg, M. Boman: *J. Appl. Phys.* 72 (12), 5956 (1992)
10. J.R. Creighton, *J. Vac. Sci. Technol. A* 7 (3), 621 (1989)
11. J.R. Creighton, *J. Electrochem. Soc.* 136 (1), 271 (1989)
12. L.V. McCarty, W.E. Reith, M.T. Simon: *J. Electrochem. Soc.* 121 (10), 1372 (1974)
13. W.A. Bryant, *J. Electrochem. Soc.* 125 (9), 1534 (1978)
14. E.K. Broadbent, C.L. Ramiller, *J. Electrochem. Soc.* 131 (6), 1427 (1984)
15. G. Auvert, Y. Pauleau, D. Tonneau: *J. Appl. Phys.* 71 (9), 4533 (1992)
16. K. Piglmayer, to be published
17. K. Piglmayer, Z. Toth, Z. Kantor, to be published
18. G. Dittmer, U. Niemann, *Philips J. Res.* 36, 89 (1981)

Pulsed laser deposition of boron nitride films on silicon

R. Schmauder, G. Dodel, and G. Bilger*

Institut für Plasmaforschung, Universität Stuttgart
Pfaffenwaldring 31, D-70569 Stuttgart, Germany

* Institut für Physikalische Elektronik, Universität Stuttgart
Pfaffenwaldring 47, D-70569 Stuttgart, Germany

ABSTRACT

Boron nitride (BN) films were deposited on (001) faces of silicon (Si) using pulsed excimer laser ablation at 308 nm and 248 nm. The films were analyzed by Fourier-transform-infrared (FTIR) transmission spectroscopy, X-ray photoelectron-spectroscopy (XPS) and by X-ray diffractometry (XRD). The films are boron rich and contain hexagonal BN (h-BN). They are X-ray amorphous. So far we found no evidence for the formation of cubic BN (c-BN) crystallites in the films.

Keywords: pulsed laser deposition, boron nitride films, XPS plasmon loss features of cubic and hexagonal boron nitride.

1. INTRODUCTION

BN is a III-V molecule, being isosteric to a pair of carbon atoms, i.e. having the same number of atoms, electrons and nuclear charges. Therefore, a number of physical properties of BN are strikingly similar (though not identical) to those of carbon. This is particularly true for the crystalline modification ($\text{h-BN} \leftrightarrow \text{graphite}$ and $\text{c-BN} \leftrightarrow \text{diamond}$) and many properties associated therewith. On the other hand there are obvious differences which are explicable in terms of the unlike electron configurations: graphite, e.g., is black and electrically conducting while h-BN is white and insulating.

Cubic BN films offer unique prospects for

- (i) *passive electronics* due to the high thermal conductivity (of the order of that of silver) combined with the electrically insulating properties (energy gap > 6 eV),
- (ii) *active electronics* due to the fact that c-BN can be doped both, p- and n-type, while diamond can be doped only p-type,
- (iii) *mechanical applications* due to its hardness (second best after diamond) combined with its oxygen resistance and low solubility in iron up to temperatures of ~ 1500 K.

Various plasma assisted techniques to produce c-BN films have been tried and published¹. In a different approach using pulsed 248 nm excimer laser deposition Doll, G.L. et al.² claimed successful heteroepitaxial growth of c-BN films on (001) faces of Si. In subsequent papers^{3,4} which we came to know only recently, these results were partly relativized by the statement that "these films were later found to exhibit an epitaxial crystalline-to-amorphous phase transition when the thickness exceeded a critical value of ~ 200 Å"³.

In an attempt to reproduce the findings reported in Ref. 2 we deposited BN films on Si by pulsed excimer laser ablation of BN from a pyrolytic h-BN target (p-BN). We present here first results of our investigations. Until now, we found no evidence for the formation of the cubic phase in the BN films. In our experiments, however, we did not yet "cover" the whole parameter space. In so far, this communication has to be considered as preliminary.

2. EXPERIMENT

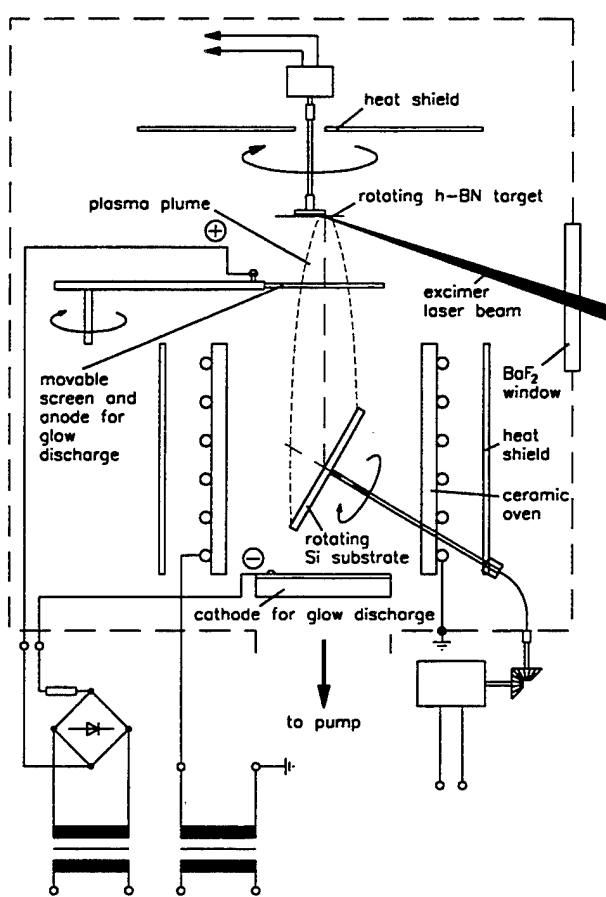


Fig. 1. Schematic of the deposition chamber.

Substrate: The (001) faced Si wafers were chemically cleaned ex situ in a standard procedure using HNO_3 and HF. Before deposition they were exposed for ~ 20 minutes to the plasma of a H_2 glow discharge to remove the SiO_2 layer formed unavoidably on Si surfaces in the atmosphere. Until now, however, we were not able to measure whether this procedure was sufficient for a complete removal of the SiO_2 layer. The Si substrates could be heated in the radiation field of the ceramic oven to temperatures up to ~ 700 °C.

Vacuum chamber: The oil diffusion pumped system allowed to achieve a base pressure of ~ 10^{-3} Pa. The deposition was done in a N_2 atmosphere (purity 99.9995 %) with background pressures ranging up to ~ 1 Pa.

Characterization of the films: Ex situ FTIR transmission spectroscopy was done to search for the characteristic marks of the crystalline modifications of BN: the infrared active vibrational phonon mode at 1067 cm^{-1} of c-BN and the modes of h-BN at 780 cm^{-1} and 1380 cm^{-1} . XPS was used to investigate the stoichiometry, the chemical bonding and the crystallinity. XRD was applied to investigate the structure of the films. The layer thickness was measured interferometrically and mechanically.

Deposition chamber: The setup of the deposition chamber is shown in Fig.1. A disc shaped p-BN target is positioned in or near the focus of an excimer laser beam. It can be rotated to reduce cratering. The Si substrate is placed inside an ohmically heated cylindrical ceramic oven. It can be rotated as well to achieve homogeneous coating. A movable screen allows shielding of the substrate during cleaning laser shots on the target. A glow discharge in hydrogen can be ignited between electrodes Θ and $\bar{\Theta}$ for in situ cleaning of the Si substrates.

Laser: The commercial excimer laser (pulse duration ~10 ns) was operated at 10 Hz repetition rate. The laser fluence on the target was between 1 and 2 J/cm^2 . Experiments were done at 308 nm (XeCl) and 248 nm (KrF). The angle of incidence on the target was ~ 70°.

Target: The disc shaped p-BN target (0.8 mm thick) was provided by SGL Carbon, Ringsdorff-Werke, Bonn. The purity of the material is specified to be better than 10 ppm as far as metallic impurities are concerned while it is worse (~ 100 ppm) with regard to carbon and oxygen contaminations. The rotating target was exposed to the laser radiation a couple of minutes for cleaning. To avoid coating during this procedure the substrate was blocked by the screen.

3. RESULTS

As mentioned above, until now we looked only in a relatively small window of the parameter space. We present in the following results of films deposited using the 308 nm and the 248 nm wavelength of the excimer laser. The nitrogen background pressure was chosen ~ 1 Pa, the substrate temperature ~ 500 °C, i.e. conditions close to those reported in Refs. 2,3.

The distance between target and substrate was ~ 7 cm. Films ~ 300 nm thick were grown in 20 minutes, corresponding to 12,000 laser pulses and a deposition rate of 0.025 nm/pulse, i.e. less than one monolayer/pulse.

FTIR Transmission Spectra

Figures 2a and 2b show transmission spectra of films (labelled 1, 1', 2, and 2') which were deposited operating the excimer laser at 308 nm and 248 nm, respectively. The spectra represent the transmissivity T of the BN coated wafer divided by the transmissivity T_0 of the uncoated substrate. The vertical scale is arbitrary, but the same for all spectra. The base lines of the spectra are offset and do not coincide for the sake of clarity. The positions of the phonon absorption dips characteristic for the crystalline modifications of BN are indicated by arrows.

While the vibrational modes of h-BN centered at 780 cm $^{-1}$ and 1380 cm $^{-1}$ can be identified unambiguously, there is no significant indication for a dip at 1067 cm $^{-1}$, the characteristic mark for c-BN.

At both wavelengths films were deposited on Si substrates without any pretreatment (1', 2') and on substrates (1, 2) which had undergone the pretreatment described in Section 2. As can be seen the FTIR spectra of the films do not significantly depend on the pretreatment. On the other hand the spectral dips of the films deposited at 248 nm appear to be more peaked suggesting that the shorter wavelength favours crystallinity of the deposited films.

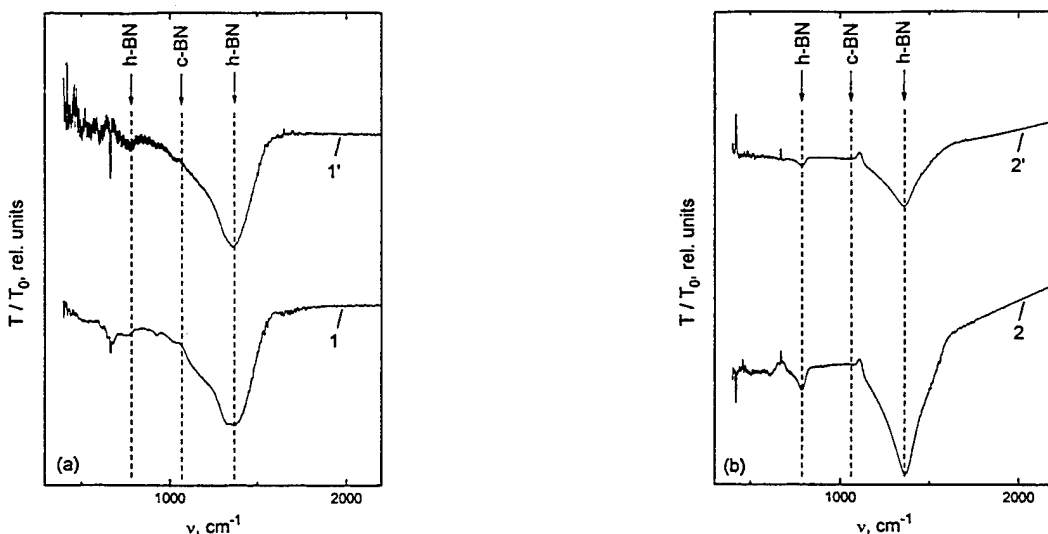


Fig. 2. FTIR spectra of BN films with (1, 2) and without (1', 2') substrate pretreatment.

(a) ablation/deposition at $\lambda = 308$ nm,

(b) ablation/deposition at $\lambda = 248$ nm.

Film characterization by XPS

XPS allows to determine the stoichiometry of the outer layers of the films. The mean escape depth of 1s photoelectrons from B, N, O, and C which have kinetic energies in the range 700 eV - 1000 eV is about three atomic layers. In addition, owing to chemical shift, the method permits at least a guess concerning the chemical compounds in which the elements identified are present in the film. The plasmon loss peaks in the vicinity of the main core level peaks allow to distinguish between sp^3 bonded (cubic-like) and sp^2 bonded (hexagonal-like) BN as was pointed out in Ref. 5. We used bulk samples of h-BN and c-BN (the latter manufactured by Somitomo, Japan) as reference materials for the XPS spectra of the films.

Stoichiometry: All films investigated were found to be more or less boron rich with large oxygen and carbon contaminations. For film 1 (deposited at $\lambda = 308$ nm), e.g., the atom-percent ratios are B:N:O:C = 33 : 18.7 : 28.7 : 19.4 . The corresponding numbers for film 2 (deposited at $\lambda = 248$ nm) are B:N:O:C = 40 : 20.1 : 30.8 : 8.9 .

Sputtering off a few atomic layers from the film by means of an Ar⁺ beam in the XPS surface analysis system did not notably change the impurity content. We ascribe the oxygen-carbon contamination of the films predominantly to the relatively poor base pressure ($\sim 10^{-3}$ Pa) and/or the use of an oil diffusion pump. At present it cannot be ruled out, however, that a further reason lies in the target material itself. Although the purity of the p-BN disc is specified to be better than 10 ppm with regard to metallic impurities⁶, its purity with regard to carbon and oxygen contamination is less since it undergoes deposition on and ablation from a graphite mandrel during the production process. Using ultra high vacuum equipment should eliminate the former possible impurity source. Pyrolytic BN targets heated to ~ 1600 °C in ultra high vacuum (10^{-7} Pa - 10^{-8} Pa) should eliminate the latter possibility⁷.

Core level spectra: In Fig. 3 the core level peaks of the B 1s and N 1s lines, respectively, are depicted for films 1 and 2. The positions of the peaks are calibrated using the C 1s line present in all spectra and setting the C 1s binding energy equal to 284.6 eV, which is the binding energy representative for C-C and C-H bonding of carbon.

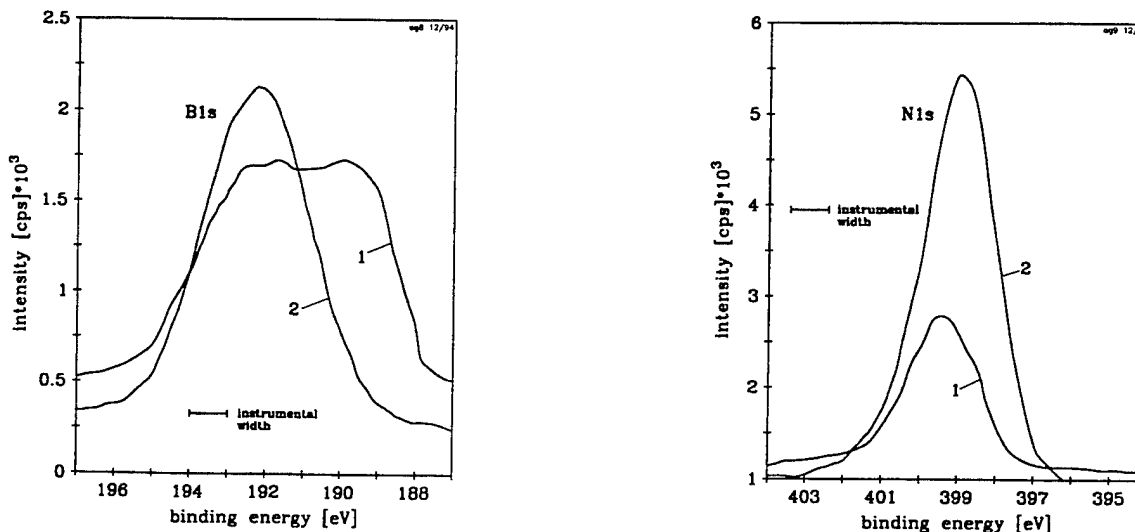


Fig. 3. Core level peaks of B 1s and N 1s in films 1 and 2.

While it is very delicate to interpret the absolute values of the binding energies, the widths of the core level lines allow a guess concerning the chemical binding of the elements identified in the films. The full width half maximum (FWHM) values of the N 1s lines in Fig. 3 agree well with the widths measured for the reference materials (~ 2.1 eV for h-BN and ~ 2.3 eV for c-BN). This indicates that there is only one binding state of N in the films. In contrast, the widths of the B 1s lines in Fig. 3 are significantly broader than those of the reference materials (~ 2 eV for h-BN and c-BN). The B 1s FWHM of film 2 is ~ 3 eV while the B 1s feature of film 1 may be a superposition of at least two lines, each also ~ 3 eV wide. The broadening of the B 1s line in the boron rich films can be associated with two binding states of boron, one to nitrogen and one to oxygen. This is consistent with the relatively high oxygen concentration and the fact that O and N have an electronegativity of 3.5 and 3.0, respectively. The "doublet" feature of the B 1s line of film 1 can possibly be ascribed to amorphous boron being incorporated in the film.

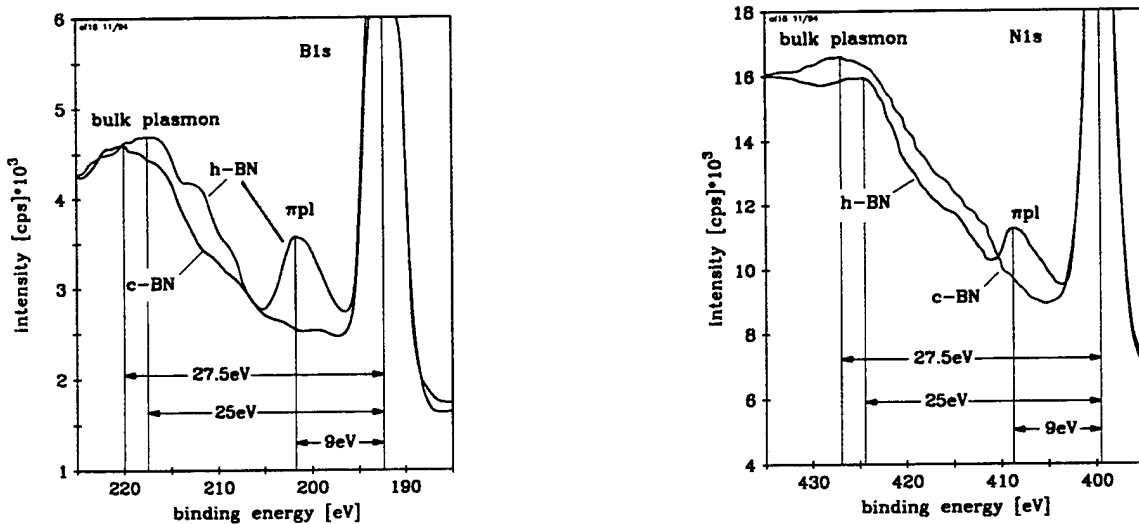


Fig. 4. Plasmon loss features of bulk h-BN and c-BN material in the vicinity of the B 1s and N 1s core level peaks.

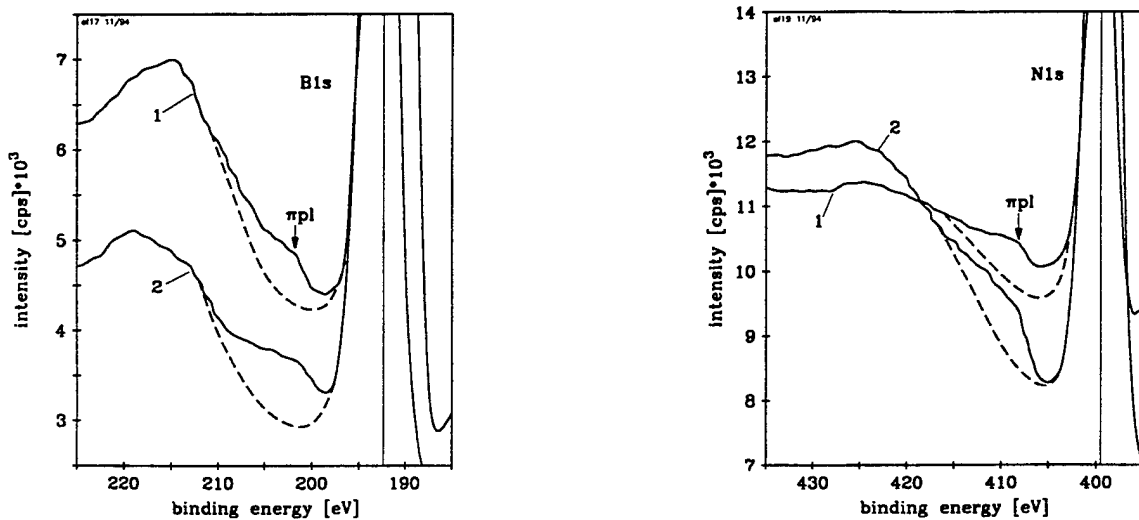


Fig. 5. Plasmon loss features of films 1 and 2 in the vicinity of the B 1s and N 1s core level peaks. (The dashed lines are inserted somewhat arbitrarily to guide the eye along a shape which might be expected in the case of c-BN films.)

Plasmon loss features of the XPS spectra: As mentioned, the plasmon loss features in the vicinity of the main core level peaks represent a valuable signature to distinguish between h-BN and c-BN. We verified these "fingerprints" for bulk h-BN and c-BN material (Fig. 4). In the case of h-BN there are a π plasmon peak and a bulk plasmon peak indicating ~ 9 eV and ~ 25 eV energy loss of the 1s photoelectrons, respectively. In contrast, the π plasmon peak is missing in the spectrum of the c-BN sample. Only a bulk plasmon peak with ~ 27.5 eV energy difference to the core level is present.

The plasmon loss features of the XPS spectra of films 1 and 2 are depicted in Fig. 5. The bulk plasmon features can be identified unambiguously. The π plasmon features are believed to be present in the spectra as indicated although they are less pronounced than in the spectra of the bulk material. The blurring of the π plasmon peaks may be due to the pronounced boron richness of the films.

XRD INVESTIGATIONS

The films were investigated in a high resolution Bragg-Brentano X-ray diffractometer. Except film 2 all other films investigated so far were X-ray amorphous. Film 2 exhibited a diffraction maximum at $2\theta = 18.6^\circ$ (primary wavelength of the diffractometer: 1.54056 Å) which may be associated with the (011) plane of orthorhombic BN (JCPDS Datahandbook Nr. 18-251).

4. CONCLUSIONS

Boron nitride films ~ 300 nm thick were deposited on Si(001) substrates using pulsed laser ablation/deposition at 308 nm and 248 nm. The films were analyzed by Fourier-transform-infrared transmission spectroscopy, X-ray photoelectron spectroscopy and X-ray diffractometry. Hexagonal boron nitride in the films was unambiguously identified while no indication for the presence of the cubic phase was found. The films were essentially X-ray amorphous. They were found to be boron rich with large oxygen and carbon contaminations at least in the outer atomic layers investigated. There is some evidence that the shorter deposition wavelength (248 nm) favours crystallinity of the films.

The preliminary character of these investigations must be emphasized. Neither could the parameter space be thoroughly "covered" until now, nor was it possible to achieve clean ultra high vacuum base pressure conditions. At this stage it can not be ruled out that the p-BN target material, though of high purity with respect to metallic contaminations, may be responsible for at least part of the O and C contaminations of the films.

5. ACKNOWLEDGEMENTS

We are grateful to Dr. L. Fischer from SGL Carbon, Ringsdorff-Werke, Bonn for providing the target material and for his suggestions concerning purity. Further, we acknowledge the kind help of Dr. H. Wulff, Universität Greifswald, and Dipl.-Phys. V. Härtle, Universität Stuttgart, regarding the XRD measurements.

6. REFERENCES

1. S. Reinke, M. Kuhr, and W. Kulisch, "Mechanisms in ion induced c-BN growth", Diamond and Related Materials 3 (1994) 341-345
2. G.L. Doll, J.A. Sell, C.A. Taylor II, and R. Clarke, "Growth and characterization of epitaxial cubic boron nitride films on silicon", Phys. Rev. B 43 (1991) 6816-6819

3. R. Clarke, C.A. Taylor II, G.L. Doll, and T.A. Perry, "New developments in the growth of epitaxial cubic boron nitride and diamond films on silicon", Diamond and Related Materials 1 (1992) 93-97
4. A.K. Ballal, L. Salamanca-Riba, G.L. Doll, C.A. Taylor II, and R. Clarke, "Ion-assisted pulsed laser deposition of cubic BN films on Si(001) substrates", J. Mater. Res. 7 (1992) 1618-1620
5. R. Trehan, Y. Lifshitz, and J.W. Rabalais, "Auger and x-ray electron spectroscopy studies of *h*BN, *c*BN, and N₂⁺ion irradiation of boron and boron nitride", J. Vac. Sci. Technol. A 8 (1990) 4026-4032
6. J. Kubis and L. Fischer, "Pyrolytic Boron Nitride and Pyrolytic Graphite Deposition and Determination of Purity", Carbon '92, 5th Int. Carbon Conference, Essen, Germany, 22-26 June 1992, Proc. 973-975
7. F.A. Chambers, G.W. Zajac, and T.H. Fleisch, "Auger electron spectroscopy, X-ray photoelectron spectroscopy, secondary ion mass spectroscopy and bulk analysis of boron nitride crucibles after vacuum baking", J. Vac. Sci. Technol. B 4 (1986) 1310-1315.

Diamond-like films deposition by laser-initiated dissociation of benzol vapour.

Valerie Astapenko

Moscow Institute of Physics & Technology, Laser Center,
141700 Russia, Dolgoprudnyi

Oleg Sidoryuk

"Polus" Research Institute, 117342 Russia, Moscow

Elena Ushanova

"Polus" Research Institute, 117342 Russia, Moscow

ABSTRACT

New method of diamond-like film deposition using laser-initiated discharge of benzol vapor is described. The investigation of the discharge parameters was carried out. Dependence of these parameters on characteristics of laser radiation, electric field, vapor pressure was obtained. It has been shown that this method allows to produce the coatings with low optical absorption.

1. INTRODUCTION

Among many ways of production of the carbon diamond-like films a particular place is held by the method of their formation from the products of decomposition of gaseous hydrocarbons in electrical discharge. In this case the optimal mode of the coating growth process is gained as a result of a combination of many parameters, among which a particular role is played by characteristics of electrical discharge, composition and pressure of the gas, substrate temperature ¹⁻³.

The potentialities of technology for production of films with given parameters may be extended using non-stationary discharge. Pulsed discharge makes it possible to stop the process of hydrocarbon decomposition at a certain stage, influencing the end composition of hydrocarbon decomposition products and their concentration. In this work for excitation of electrical breakdown of gaseous hydrocarbons in the reaction chamber laser emission was used which was focused on the solid-state target.

2. EXPERIMENTAL

The scheme of deposition of the diamond-like films from the hydrocarbon mixture is shown in Fig. 1. Pulsed laser emission (1) of the neodymium laser at 1.06 μm is focused on the solid-state cylindrical target (2) which in the process of laser ablation rotates around its axis to provide uniform conditions of the plume (3) formation from the target erosion products. Between the substrate (4) for coating deposition and the target (2) the electrode (7) is situated, to which dc voltage U_1 , positive relative to the lobe (8), is applied for excitation of

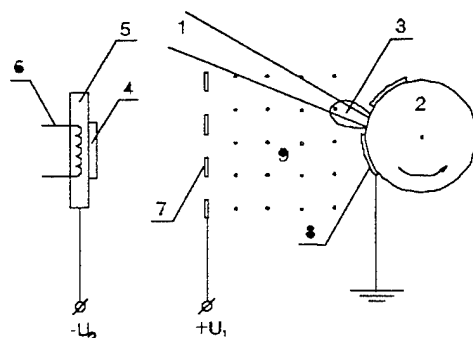


Fig. 1 Experimental setup.

discharge in the area (9) of the reaction chamber. Since the electrode (7) is a high-transparent grid, positive ions from the discharge area (9) can freely enter the accelerating gap (10) and reach the substrate (4).

It is essential that voltage U_1 is inadequate to excite discharge in the absence of laser emission. The breakdown of the reaction chamber gas is of a threshold nature from the point of view both of voltage and laser power density.

In this work for the carbon film deposition the benzol vapours were used at the p_1 value of $1 \dots 15 \times 10^{-2}$ Torr.cm (p - pressure, 1 - distance between target and electrode (7)). In this case the threshold breakdown voltage $U_{1\text{th}}$ was 270 V, and the threshold laser intensities at the graphite target were $I_{\text{th}} = 10^8 \text{ W} \cdot \text{cm}^{-2}$ for pulse width of 10 ns and $I_{\text{th}'} = 10^7 \text{ W} \cdot \text{cm}^{-2}$ for pulse width of 100 ns, the threshold intensity strongly depending on gas pressure (Fig. 2). The electrical discharge of benzol vapours in the area (9) was developing in fractions of microseconds after action of laser pulse on the target and within $t = 5 \mu\text{s}$ experienced breaking as a result of voltage drop at the electrode (7). The oscillogram of the pulse of voltage U_1 during discharge is shown in Fig. 3.

The temporal functions of positive ion current on the substrate at $U_2 = 0$ in case of action of laser pulses with the width of 10 ns on the target are shown in Fig. 4 (d - target - substrate distance). The comparison of curves 1-4 in Fig. 4 obtained at different laser intensities in the range of $0.1 \dots 2.0 \times 10^7 \text{ W} \cdot \text{cm}^{-2}$ allows one to conclude that ions of two sources are acting on the substrate:

- 1) laser erosion plume on solid-state target;
- 2) electrical discharge in benzol.

Mass-spectrometric research has shown that under the low value of the laser intensity the set of ions produced in discharge is practically fully limited by C_6H_6^+ , C_6H_5^+ , H^+ ions. At the same time at stationary rf discharge there are also the singly charged ions of products of destruction of benzol molecules with three, two and four carbon atoms³. It is obvious that in the area of accelerating voltage all singly charged ions receive the same energy. However, from the point of view of growth of coatings on the substrate it is necessary to optimize the specific energy which falls at one carbon atom. Monoenergization of atoms may not be achieved at formation of different types of ions in stationary discharge. To the contrary, it takes place in case of non-stationary pulsed discharge at laser excitation.

Let us notice that concentration of ions of products of laser ablation of the solid-state target may be minimized at decrease of laser intensity. In case of pulse widths of 100 ns it is possible to produce initiation of electrical discharge at accessory emission of the target material at the level of 10^{-3} and less from integral flux of the electrical discharge products. On the other hand, since laser power density and characteristics of electrical discharge are independent parameters in the above-threshold area, it is possible to produce separately the optimization of laser intensity to obtain the necessary energies (50...150 eV) of ions and recombination carbon atoms in case of laser ablation of the target of graphite or glass-carbon. The carbon ion energies as functions of laser power density calculated at recording of their direct-flight spectra are shown in Fig. 5. However, the use of an additional source of

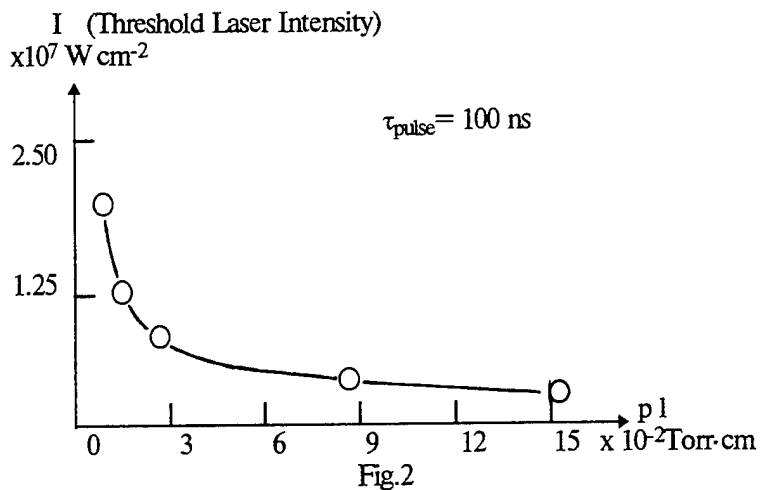


Fig.2

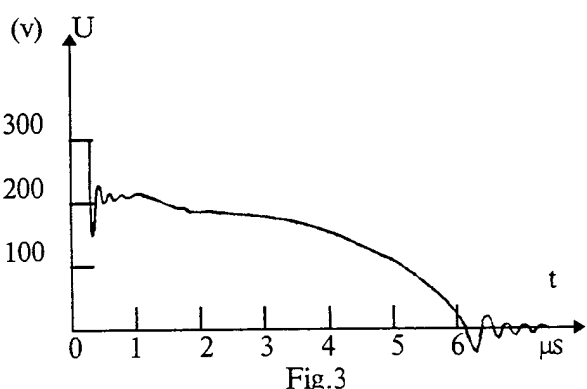


Fig.3

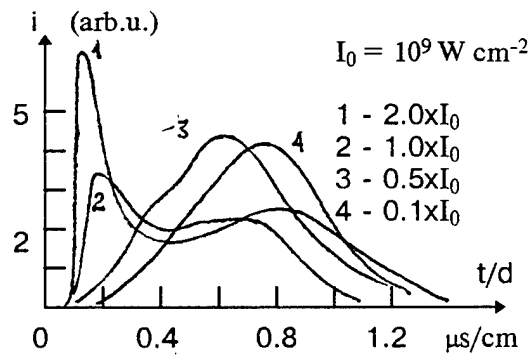


Fig.4

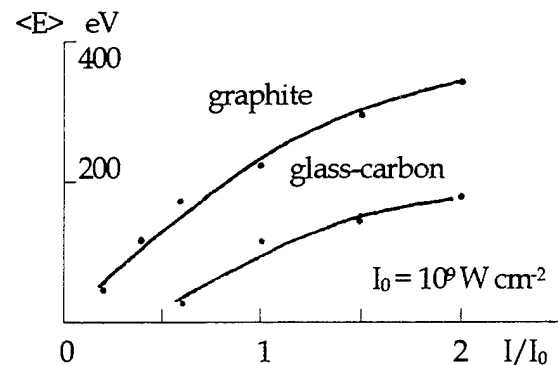


Fig.5

carbon has no any appreciable advantages. At the same time doping of the diamond-like coatings being deposited at sputtering of a suitable target in the process of electrical discharge initiation may be of practical importance.

In this work the diamond-like coatings were deposited on substrates of silicon and fused silica. Optimal films from the point of view of their hardness, density and absorption were produced at accelerating voltage of 200 V for ions obtained in the benzol vapour discharge initiated by laser pulses ($\lambda = 1.06 \mu\text{m}$, $\tau_p = 100 \text{ ns}$, $I = 1.0 \times 10^7 \text{ W cm}^{-2}$) with pulse repetition rate of 4 kHz.

Hydrogenated films (with IR absorption band within $3.4 \mu\text{m}$) have been produced. The band gap was $E = 2.0 \text{ eV}$, extinction coefficient at $1.06 \mu\text{m}$ was less than 0.01.

3. CONCLUSION

So in this work the possibilities of production of the diamond-like carbon coatings from benzol vapour discharge at its initiation by pulsed laser emission are shown. The method allows one to produce high-quality coatings, moreover, it may prove to be promising in production of doped carbon films.

4. REFERENCES

1. L.Payasova, J.Zemek, J.Jauca, K.Navratal. "Optical, electrical, mechanical and photoelectronic properties of hard amorphous carbon films", J.of Non.-Cryst. Solids, v.97-98, Pt.1, p.451-454, 1987.
2. A.Bubenzer, B.Dischles, G.Brandt, and P.Koidl. "Rf-plasma deposited amorphous hydrogenated hard carbon thin films: preparation, properties, and application", J.Appl.Phys., v.54, p.4590-4595, 1983.
3. C.Weissmantel, K.Bewilogua, D.Dietrich, H.-J.Erder, H.-J.Hinneberg, S.Klose, W.Nowick and G.Reisse. "Structure and properties of quasi-amorphous films prepared by ion beam techniques", Thin Solids Films, v.72, p.19-31, 1980.

Production of diamond-like films by laser ablation in presence of residual
gas in reaction chamber

Valerie Astapenko

Moscow Institute of Physics and Technology, Laser Center
Russia, 141700 Dolgoprudnyi, Institutskii per.9

Oleg Sidoryuk

"Polus" research Institute
Russia, 117342 Moscow, Vvedenskogo 3

ABSTRACT

Diamond-like films were produced by laser ablation of glass-carbon target in presence of residual gas (Ar) in reaction chamber. It was appeared that the band gap value of the films deposited in this case is more than by 20 % greater than that of the films deposited at high vacuum. This influence of a gas on optical properties of the produced coatings was explained in the framework of simple mechanical model.

1. INTRODUCTION

Considerable recent attention has been focused on production of the diamond-like films.

Whereas under ordinary conditions a stable form of carbon in the constitutional diagram is graphite, the technologies under development are based on metastability of the crystalline diamond which is a consequence of the fact that at the crystal nucleation the dominant factors are not thermodynamical ones, but physical kinetics processes.

By efforts of many researchers a new class of materials has been formed: the hydrogenous diamond-like films and the amorphous diamond-like films. Correspondingly the main methods of the carbon film production are arbitrarily divided into two large classes:

1) deposition of coatings on a substrate by activation of mixture of gases, one of them being a hydrocarbon, say, methane or acetylene, and the other being a buffer, more commonly pure hydrogen;

2) deposition of films from atomic beams and carbon ions with certain energies.

Among many ways of formation of molecular and ion beams one of the promising methods is the method of the particle flux production in a vacuum chamber by pulsed action of intensive laser radiation on a solid-state target. In this case the main parameter of the particles in the laser plume is the value of their energy. In the literature the various data regarding the range of optimal energies for deposition of the diamond-like coatings from the carbon particle flux are given. However, the most plausible values are likely to be 100 eV^{1,2}.

The flux of particles with such energies may be formed from the laser plume at laser ablation of graphite in case of the action of pulses with power density over 10⁸ W cm⁻² on the target in vacuum. The solution of this problem in general terms is known and described in the literature. The problem is complicated under conditions of the technological process which is carried out at gas input to the reaction chamber for the purpose of additional doping of the coatings being deposited.

In this work the influence of the gas in the reaction chamber on the process of deposition of the diamond-like coatings and ways of attainment of a compromise between technological parameters are discussed from the point of view of the provision of necessary energies in the carbon particle beam.

2. ENERGY REDISTRIBUTION OF DEPOSITED PARTICLES

2.1 High vacuum case

Fig. 1 shows the oscillograms of currents of positive carbon ions at different laser intensities ($\lambda = 1.06 \mu\text{m}$, $\tau_{\text{pulse}} = 10 \text{ ns}$) under conditions of high vacuum (d is target-substrate distance). Consideration of only ion fluxes proves to be correct in view of the known fact of the correlation of ion energy distributions and corresponding recombination-produced atoms³.

From the temporal form of the ion current pulse the carbon particle energy distribution functions have been calculated presuming the uniformity of their movement at the most of the path from the carbon target to the coating deposition surface. Fig. 2 presents the average energies of carbon ions as functions of laser intensity ($\lambda = 1.06 \mu\text{m}$, $\tau_{\text{pulse}} = 10 \text{ ns}$) for different target types: graphite and glass-carbon.

One can see from obtained results that the optimal energies from the point of view of deposition of the diamond-like coatings may be achieved at $I = 0.3 \dots 0.6 \times 10^9 \text{ W cm}^{-2}$ in case of graphite and at $I = 1.0 \dots 1.5 \times 10^9 \text{ W cm}^{-2}$ in case of glass-carbon. It is significant that the consequence of a higher value of optimal laser intensity in case of glass-carbon is obviously a higher density of the carbon particle flux. So long as this factor is of vital importance for technological problems, preference in this work was given to the glass-carbon target.

The degree of purity of the glass-carbon (total amount of impurities is less than 0.02%) suffices to solve some technological problems concerning the deposition of the diamond-like coatings. More easy degassing of the material surface in comparison with graphite may be noted. More successful combination of thermal and optical properties is also an advantage for laser sputtering.

2.2 Gas influence

The presence of gaseous medium in technology processes for deposition of the doped coatings produces additional difficulties at consideration of problem of formation of the particle flux with optimal energy distributions.

Gas doping during the growth of the films is usually produced at the value of parameter $p d$ (gas pressure \times target-substrate distance) from 5×10^{-3} to 10^{-1} Torr cm. At these values the analysis of influence of the reaction chamber gas on energy parameters of the carbon particle beam from laser plume is carried out in this work.

For this purpose the function of energy loss per unit path by carbon particles was calculated when they were scattered on atoms in case of the simplest model of interaction with inert gases. The expression for this function is given by following formula⁴:

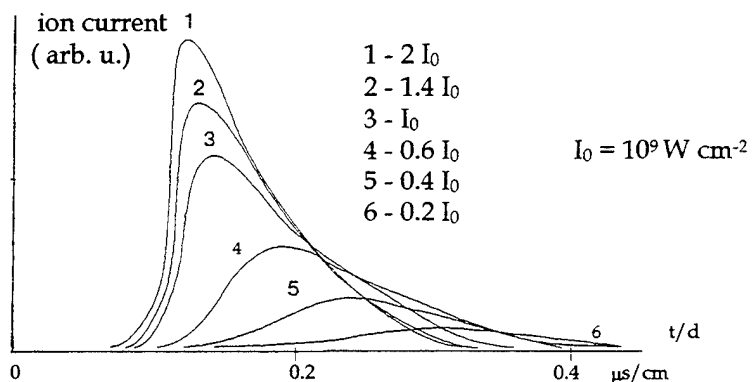


Fig.1

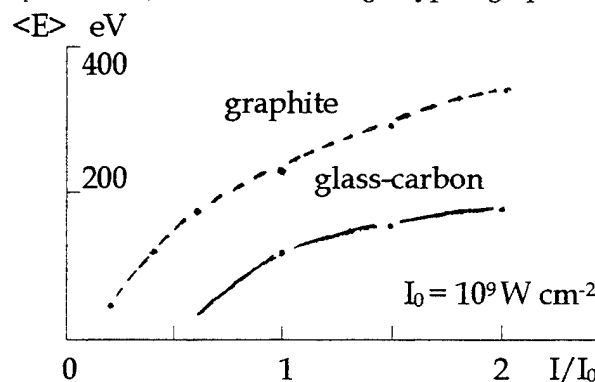


Fig.2

$$-\frac{dE}{dr} = S_x(\varepsilon) \frac{4\pi N_x Z_c Z_x e^2 a_{TF} M_c}{(M_c + M_x)} / (M_c + M_x)$$

here: $\varepsilon = E/E_0$ - normalized energy; $E_0 = Z_c Z_x (e^2 / a_{TF}) M_c / (M_c + M_x)$; $Z_{c,x}$ - nuclear charge numbers of C, X atoms; $M_{c,x}$ - masses of C, X atoms, N_x - concentration of X atoms; a_{TF} - Tomas-Fermi radius for "C+X" interaction, $S_x(\varepsilon)$ - normalized function of energy loss for "C+X" scattering.

The latter function is connected with the transport scattering cross-section $\sigma_{tr}(\varepsilon)$ in the following way:

$$S(\varepsilon) = \varepsilon \sigma_{tr}(\varepsilon) / 2\pi$$

here

$$\sigma_{tr}(\varepsilon) = 2\pi \int (1 - \cos\varphi) \rho d\rho$$

ρ - impact parameter, φ - scattering angle which is defined as follows:

$$\varphi = \pi - 2 \int \rho r^2 (1 - \rho^2/r^2 - U(r)/(\varepsilon E_0))^{-1/2} dr$$

where integration is produced from the minimum distance between colliding particles to infinity.

In energy range necessary for technology for coating deposition the scattering angle is well fitted by Born-Mayer potential. Energy loss for some gases ($pd=0.06$ Torr cm) calculated with this potential are shown in Fig.3.

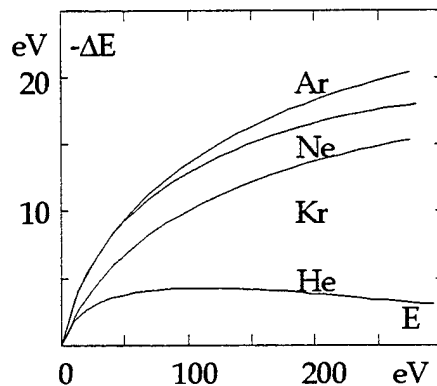


Fig.3

3. EXPERIMENTAL

In general terms the check of theoretical result was carried out by registration of ion current from the target using a small blocking screen in the path of direct-flight ions. In this case scattered particles were recorded for which the noted first approximation change of energy is in agreement with calculated one. For example, the energy redistribution of carbon particles due to their scattering on argon atoms for $pd = 6 \cdot 10^{-2}$ Torr cm is shown in Fig.4.

In this case scattering leads to relative increase of content of particles of the coating being deposited up to 20% in optimal energy interval.

For experimental verification of this result the deposition process of the diamond-like coatings was produced in argon atmosphere at $pd = 6 \cdot 10^{-2}$ Torr cm. The films with the band gap more than 1.6 eV were manufactured using the target of glass-carbon in argon at the laser power density of 2×10^9 W cm⁻² whereas in high vacuum an analogous value is 1.3 eV.

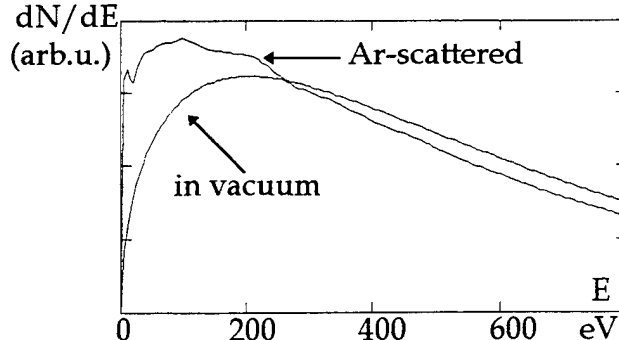


Fig.4

4. CONCLUSIONS

Thus using optimal gas pressure during doping of the diamond-like films produced by laser sputtering one may maintain the necessary energy parameters of the carbon particle flux. Besides that, opportunity of its additional optimization is also apparent

Let us call attention to the fact that presented knowledge about the process of gas interaction with the particle flux of the laser plume may be used successfully in another essential case when deposition of the diamond-like coatings is produced from the hydrocarbon discharge plasma, and doping of film during its growth is produced by atoms from the laser plume at ablation of the solid-state target.

Thus the questions of the particle flux interaction with gas of the reaction chamber discussed in the work may be used in some perspective technological processes of the diamond-like film deposition.

5. ACKNOWLEDGMENT

The authors wish to thank Alexander Mayer for the computer assistance.

6. REFERENCES

1. T. Miyazawa, S. Misawa, S. Yoshida, S. Gonda. "Preparation and structure of carbon film deposited by a mass separated C⁺ ion beam", J. Appl. Phys., Vol.55, pp. 188-193, January 1984.
2. J. Ishikawa, Y. Takeiri, K. Ogawa, T. Takagi. "Transparent carbon film prepared by mass-separated negative-carbon-ion beam deposition", J. Appl. Phys., Vol.61, pp. 2509-2515, April 1987.
3. Yu. Bykovskii, S. Silnov, E. Sotnichenko, B. Shestakov. "Mass-spectrometric investigation of the laser plasma neutral particles", Zh.Exp.&Teor Fiz., Vol.93, pp.500-508, 1987 (in Russian).
4. Yu. Gott. *Interaction between particles and matter in plasma investigations*, Atomizdat, Moscow, 1978 (in Russian).

Laser distillation-deposition synthesis of silica glasses with variable concentrations of oxygen deficient centers

V.F.Lebedev, V.M.Marchenko, A.O.Rybaltovski*, V.A.Tikhomirov*

General Physics Institute of Russian Academy of Science,
38 Vavilov St., Moscow 117333

*Moscow University, Leninskije Gory, Moscow 119899

ABSTRACT

Samples of silica glasses of $\sim 1 \text{ cm}^3$ scale were synthesized with 100 W cw CO_2 laser torch on the target surface of silica materials in oxide, neutral and reductive atmospheres. Fused quartz glass, silica glasses synthesized by $\text{SiCl}_4 + \text{H}_2 + \text{O}_2$ flame hydrolysis and in $\text{SiCl}_4 + \text{O}_2$ plasma and Ge-doped glass were used as starting materials. Oxygen deficient center concentrations of $\sim 10^{16} \text{ cm}^{-3}$ were registered in samples synthesized in neutral and reductive conditions by optical absorption and luminescence spectroscopy. Transformations of spectra in dependence on Ge concentration confirm that the spectra are characteristic of oxygen deficient =Si: and =Ge: point defects.

1. INTRODUCTION

Steady state laser torch distillation-deposition synthesis of the refractory oxide materials was founded by investigations of interaction of 100 W cw CO_2 laser radiation with silica glass surface in atmosphere. The technique was first called LAD (laser aerosol deposition). Steady flow of submicron white soot powder was produced by laser dissociative evaporation of silica heated up to boiling point and formation of aerosol reactive jet in atmosphere because of condensation of products of silica decomposition. Energy efficiency of such a process was shown by theoretical and experimental examination of balance of energy- and mass transfer to be of $\sim 1 \text{ kW/g/min}$ that was of 2-3 orders higher of known pulse laser deposition (PLD) and was comparable with efficiency of silica glass synthesis by flame hydrolysis of SiCl_4 .

Conditions of laser erosion torch stabilization where investigated and the steady and spatially controlled form of the torch was realized. Layers and bulk silica glass samples were prepared by deposition of flow particles on a substrate introduced into the laser torch with efficiency of $\sim 50\%$. Structure of samples of $\sim 1 \text{ cm}^3$ scale depended on temperature of the torch being porous or vitreous and controlled by substrate position.

It was discovered that concentrations of contaminants in synthesized samples depended on distillation-deposition purification of starting materials from volatile and refractory oxides and doping by ambient atmosphere gas^{5,6}. Silica glass of optical grade may be fabricated directly from common river sand. Silica glass for optical fibers may be obtained by means of additional chemical purification of LAD porous preforms. Doping of synthesized silica glasses with Er and F_2 was realized via formation of laser target and modification of ambient gas composition. Synthesis of double

silica systems $\text{SiO}_2 - \text{Me}_x\text{O}_y$, $\text{Me} = \text{Fe}, \text{Ni}, \text{Ti}, \text{Cu}$, was carried out with composite metal-silica glass laser targets⁷.

First results of investigations of an influence of initial materials and ambient gas composition on oxygen deficient center (ODC) concentration in silica glasses synthesized by LAD technique are presented in the article. ODC doped silica glasses are photosensitive materials for advanced optical fiber devices based on photoinduced phenomena but nature of corresponding transitions is still debated⁸.

2.EXPERIMENTAL RESULTS AND DISCUSSION

Experimental setup is shown in Fig. 1. Focused laser beam was directed on silica rod end surface and heated material in laser spot up to boiling temperature ~ 3 kK. Silica decomposition products formed laser erosion jet. The vapour products condensed in to submicron particles because cooling during expansion. The jet was deviated by a screening gas flow for protection from ambient atmosphere. Vitreous samples were grown on rotating silica rod substrate at deposition temperature of ~ 2 kK. Samples of silica glasses of ~ 1 cm long and of ~ 5 mm in diameter were synthesized in oxide (air), neutral (Ar, N₂) and reductive (vapour of SiO, Si) conditions using 100 W cw CO₂ laser.

Fused quartz glass, grade I, silica glasses synthesized in SiCl₄ + H₂ + O₂ flame, grade III, and in SiCl₄ + O₂ plasma, grade IV, and Ge-doped glass were used as initial materials (Table 1). Gas composition was varied as by Ar or N₂ jet screening of the target, the laser torch and the substrate at atmospheric pressure as by additional laser evaporation of SiO and Si.

Concentration of Ge in samples was measured by X-ray microanalysis with scanning electron microscope JSM-840. ODC were registered by UV optical absorption spectroscopy in samples synthesized at neutral (Table 1) and reductive conditions. Optical density in last a case did not exceed 0.3 cm⁻¹. Dilution of screening gas flow by air was followed by decrease of optical density. Saturation effect, concentration of silicon ODC $N_{\text{ODC}}(\text{Si}) \leq 10^{16} \text{ cm}^{-3}$, may be explained by small adhesion of SiO ($T_{\text{boil}} = 2075$ K) on the surface of the substrate ($T_s \geq 2000$ K). $N_{\text{ODC}}(\text{Si})$ is hoped to be increased by both reductive deposition at lower temperature and sintering of porous preform. Coloration of porous layers at reductive conditions was observed in experiments.

Laser distillation of Ge doped silica glasses was accompanied by purification of grown samples from doping component of ≥ 100 times. It was tested by X-ray microanalysis and UV absorption measurements of Ge concentrations in SiO₂ - GeO₂ glasses (Table 1.) and by change of absorption and luminescence spectra of ODC after LAD of KI (I-grade) silica glass.

Laser distillation purification was accompanied by transformation of absorption spectrum. Optical density of absorption band at 242 nm decreased of ≥ 100 times after laser distillation of SiO₂ - GeO₂ glass (Table 1). Absorption band at 245 nm arose after distillation of SiO₂ - GeO₂ glass in N₂ and was explained as superposition of absorption bands of ODC(Si) and ODC(Ge) with comparable optical densities.

Absorption band 242 nm disappeared after laser distillation of KI, I-grade, glass in air (Fig.2) but absorption band 248 nm arose after distillation in N_2 . One can see (Fig.3) that after distillation in air intensity of luminescence bands at 4.2 eV (290 nm) and 3.1 eV (400 nm) fell down for ≥ 100 times and after distillation in N_2 new bands at 4.4 eV (280 nm) and 2.7 eV (460 nm) arose instead. This fact was explained by simultaneous influence of purification from Ge and oxygen deficient atmosphere so that $N_{ODC}(Si) \gg N_{ODC}(Ge)$.

Transformation of absorption and luminescence spectra of LAD synthesized silica glasses by modification of atmosphere composition in agreement with the change of Ge concentration confirms the hypothesis that ODC spectra are characteristic of two-coordinated =Si: and =Ge: accordingly.

3.CONCLUSION

LAD is evidently the new technique for fabrication of advanced high purity and doped refractory oxide submicron powders, porous and vitreous layers and bulk samples. High purity fabrication of the materials is based on laser evaporation of starting materials, formation of vapor and aerosol reactive jets in atmosphere with controlled gas composition and deposition of chemically modified distillation products on substrate.

Silica glasses doped by ODC, $N_{ODC}(Si) \leq 10^{16} cm^{-3}$, may be synthesized by one stage LAD process in neutral and reductive conditions. $N_{ODC}(Si)$ is waited to be increased by two stage process: reductive LAD and sintering of porous preform.

$N_{ODC}(Ge)$ is decreased during one stage LAD process of ≥ 100 times in accordance with laser distillation purification. The process may be used for purification of raw materials.

Dependence of transformations of absorption and luminescence spectra of LAD synthesized samples on concentration of Ge confirms the interpretation of investigated point defects as two-coordinated ODC =Si: and =Ge:.

4.REFERENCES

1. Dianov E.M., Koryakovskiy A.S., Lebedev V.F., Marchenko V.M., Prokhorov A.M., "Steady state laser torch on silica glass", Zhurnal tehnicheskoi fiziki, Vol.61, No.5, pp.90-96, 1991.
2. Dianov E.M., Koryakovskiy A.S., Lebedev V.F., Marchenko V.M., Prokhorov A.M., "Laser aerosol deposition of fibre preform", Sov. Lightwave Communications, Vol.1, pp.223-226, August 1991.
3. Dianov E.M., Koryakovskiy A.S., Lebedev V.F., Marchenko V.M., Prokhorov A.M., "Preparation of transparent silica glass by laser aerosol deposition", Sov. Lightwave Communications, Vol.2, pp.79-82, February 1992.
4. Dianov E.M., Koryakovskiy A.S., Lebedev V.F., Marchenko V.M., Prokhorov A.M., "Laser aerosol deposition of porous and transparent silica glasses", XVIth Intern.Congr. on Glass, Proc of the Congr., Vol.5, pp.207-210, Madrid, 1992.
5. Dianov E.M., Koryakovskiy A.S., Lebedev V.F., Marchenko V.M., Prokhorov A.M., "Chemical composition of silica glasses prepared by laser aerosol deposition", ESG 2nd Intern. Conf. Fundamentals of Glass Science and Technology. Proc.of the Conf., pp.551-554, Venice, 1993.

6. Dianov E.M., Koryakovskiy A.S., Lebedev V.F., Marchenko V.M., Pimenov V.G., Prokhorov A.M., "Purification and doping of silica glass by laser aerosol distillation", Zhurnal tehnicheskoi fiziki, Vol.63, No. 11, pp.196-200, 1993.

7. Koryakovskiy A.S., Lebedev V.F., Marchenko V.M., Myzina V.A., Prokhorov A.M., "Steady state laser torch for synthesis of double silicate systems", Kvantovaja electronica, Vol.21, No.2, pp.194-196, 1994.

8. D.L Griscom, "Optical properties and structure of defects in silica glass", J.Ceram.Sci.Japan, Vol.99, pp.899-916, 1991.

9. L.Skuja, "Isoelectronic series of twofold coordinated Si, Ge, and Sn atoms in glassy SiO_2 : a luminescence study", J.Non-Cryst.Solids, Vol.149, Nos.1,2, pp.77-95, 1992.

Table 1.
Dependence of optical density (cm^{-1}) at 248 nm
(5.04 eV) on initial material and ambient gas

Glass grade	Air	Ar	N_2
I, KI	< 0.01	0.3	0.7
III, KU-1	< 0.01	0.3	0.5
IV, KUVI	< 0.01		0.4 - 0.5
0.89 SiO_2 + 0.11 GeO_2	1.2 (242 nm)		0.5 (245 nm)

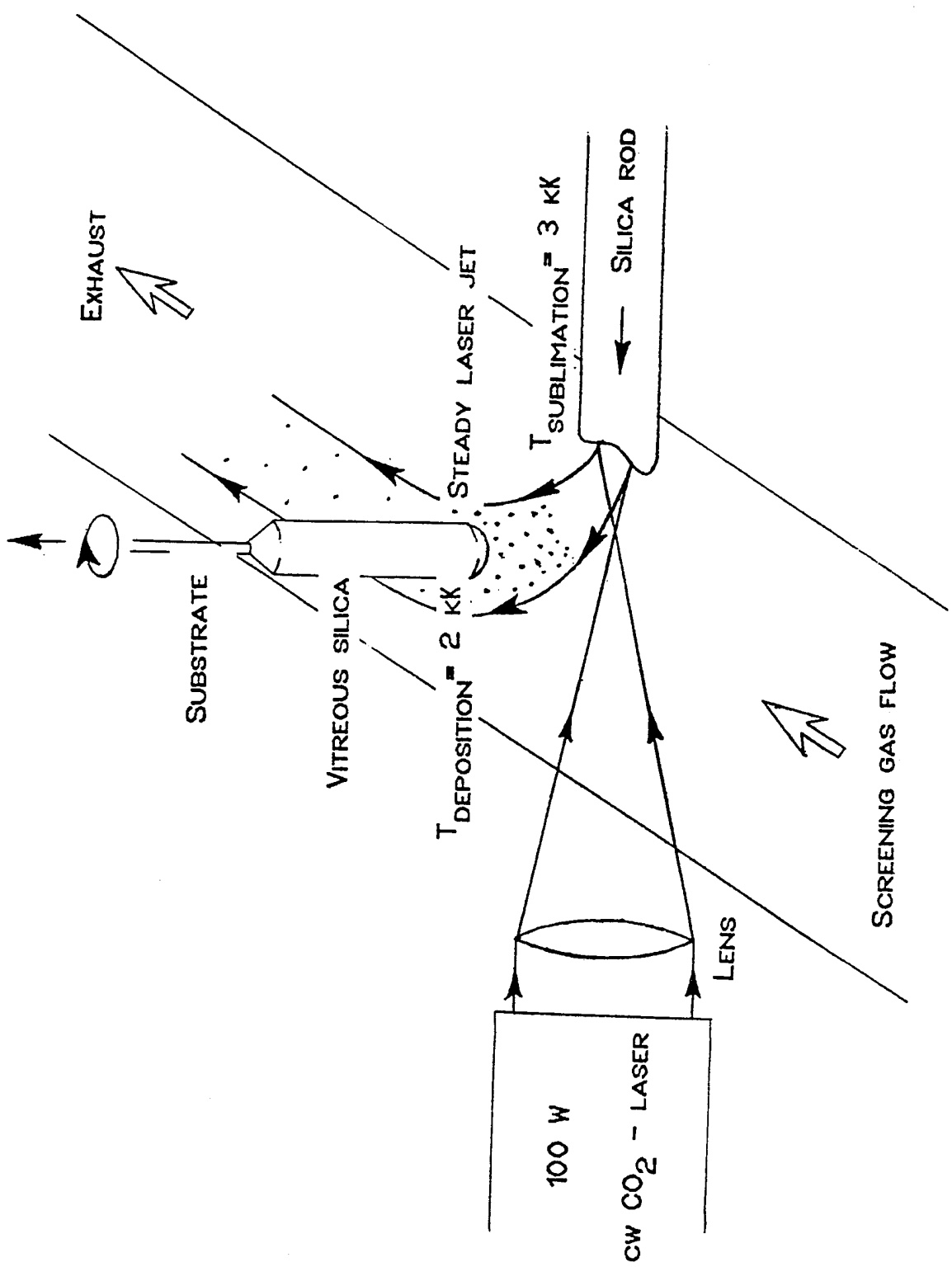


Fig. 1. Experimental setup.

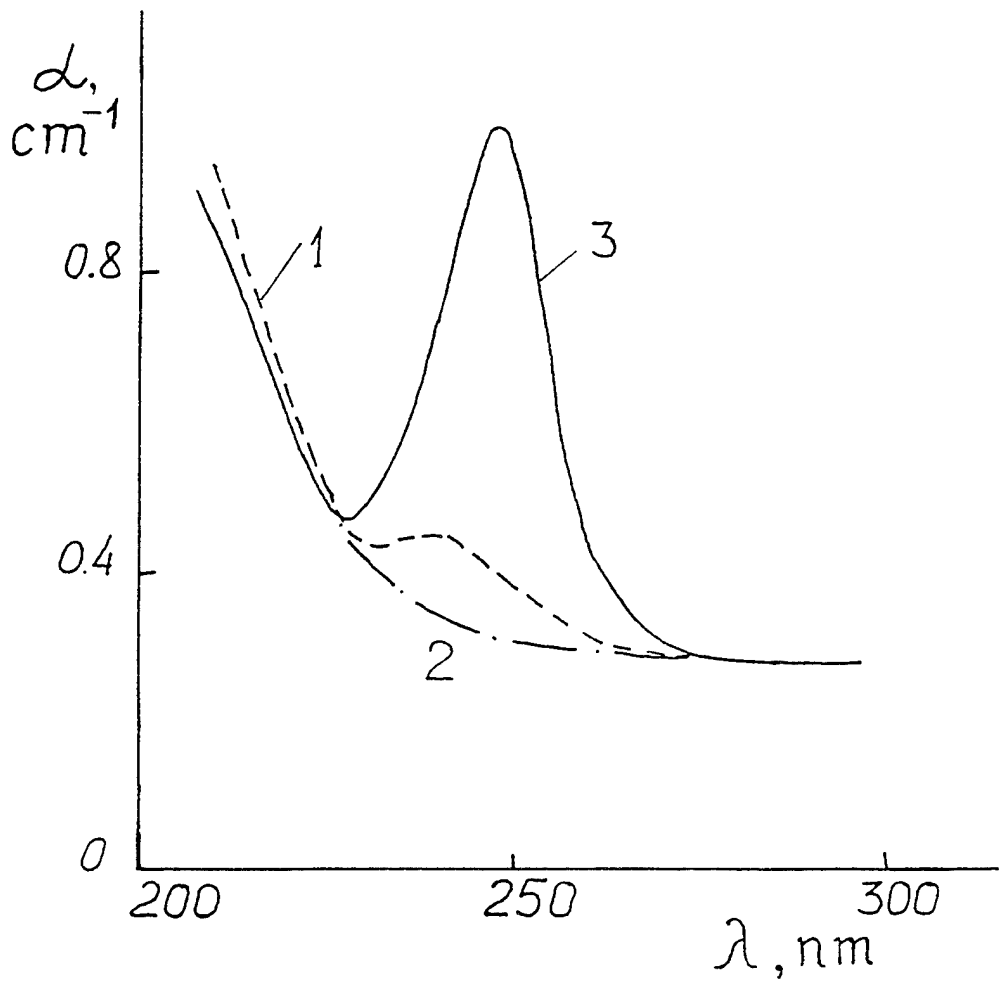


Fig. 2. Absorption spectra of initial electrofused silica glass KI (1) and of samples synthesized by LAD in air (2) and in N_2 (3).

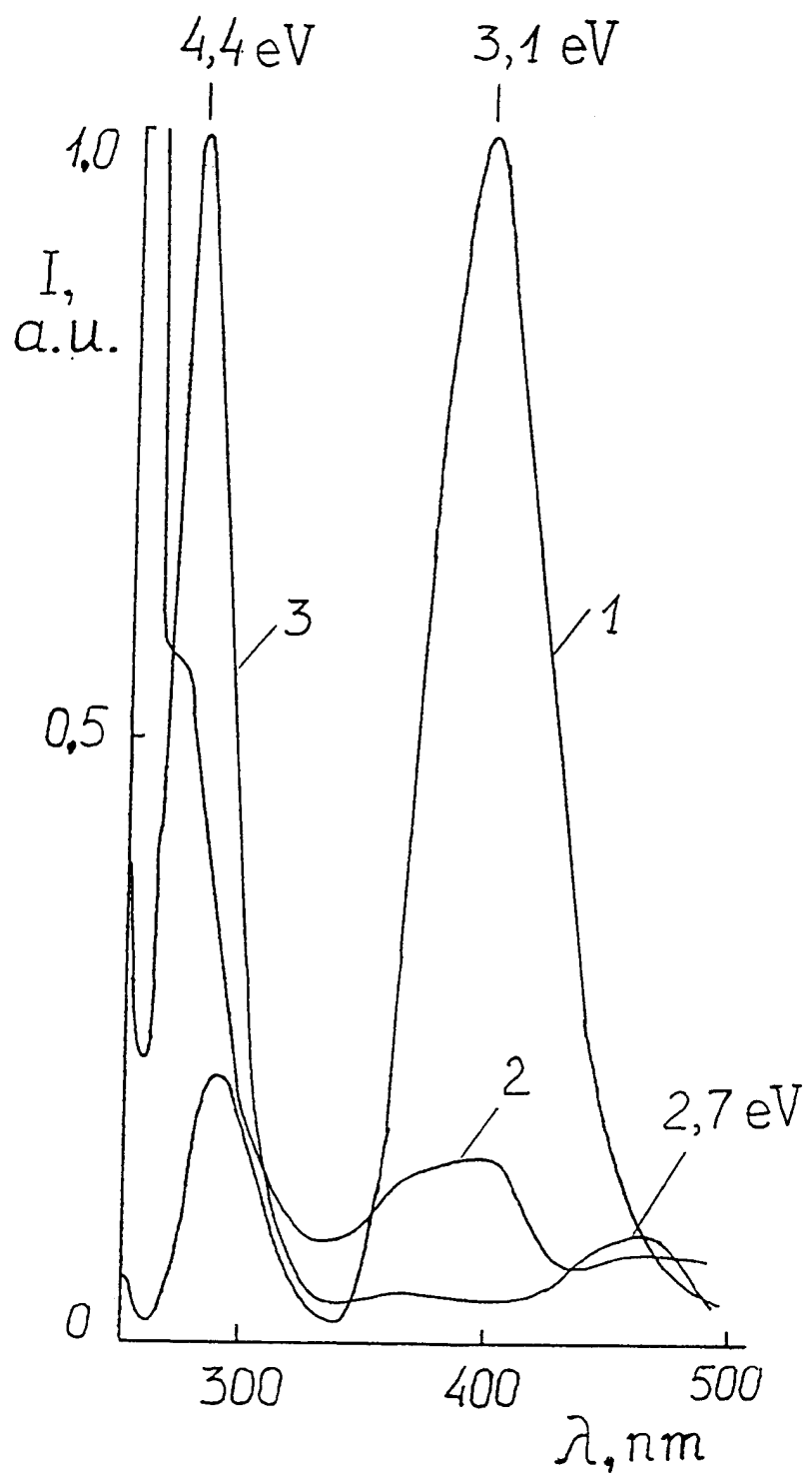


Fig. 3. Luminescence spectra of initial electrofused silica glass KI (1) and of samples synthesized by LAD in air (2) and in N_2 (3). Approximate relation of intensities: 1 (1) : 0.1 (2) : 0.4 (3).

Laser deposited thin films of biocompatible ceramic

M.Jelínek¹, V.Olšan¹, L.Jastrabík¹, T.Dostálová², L.Himmlová², J.Kadlec³, M.Pospíchal³, M.Šimečková¹, C.Fotakis⁴

1) Institute of Physics, Czech Academy of Sciences, Na Slovance 2, 18040 Prague 8, Czech Republic

2) Institute of Dental Research, Vinohradská 48, 12060 Prague 2, Czech Republic

3) Military Academy, Brno, Czech Republic

4) Foundation for Research and Technology- Hellas, P.O.Box 1527, Heraklion 71110, Crete, Greece

ABSTRACT

Thin films of biocompatible materials as hydroxylapatite (HA) - $\text{Ca}_{10}(\text{PO}_4)_6(\text{OH})_2$ were deposited by laser ablation technique. The films of HA were created on Ti substrates by KrF laser. The layers were deposited in vacuum, in pure H_2O vapors (pressure 2×10^{-3} mbar - 2×10^{-1} mbar), and in $\text{Ar}/\text{H}_2\text{O}$ vapor mixture. Influence of laser energy density E_T (3 Jcm^{-2} , 13 Jcm^{-2}) and substrate temperature T_s (500°C - 760°C) on the film parameters were studied. Two different technological processes were used for HA target preparation. Films and targets were characterized by Rutherford backscattering analysis (RBS), Particle Induced X-ray Emission (PIXE), X-ray diffraction (XRD), Scanning Electron Microscopy (SEM) and by Knoop microhardness and scratch test. The best crystalline HA films were reached in the mixture of $\text{Ar}/\text{H}_2\text{O}$. Higher T_s had to be used for such deposition. Higher T_s was also preferable from the point of film microhardness. Adhesion of films to the substrates in the range of tens of Newtons was measured. The preliminary results of *in vitro* experiments of films biotolerance and resorbability are also presented.

1. INTRODUCTION

Bioactive materials received great attention over the last decades because they are biocompatible and capable of forming tight bonds with surrounding bone. Calcium phosphate ceramics are particularly interesting for implant purposes because of the close chemical and crystallographic similarities of these materials with the mineral constituents of the bones and teeth of vertebrates. Implant materials containing calcium phosphate are frequently used in surgery for jaw augmentation, tooth replacement, bone substitution and middle ear reconstruction. Different phases of calcium phosphate ceramics are used depending upon whether a resorbable or bioactive material is desired. Attention is focused mainly on calcium hydroxylapatite, $\text{Ca}_{10}(\text{PO}_4)_6(\text{OH})_2$, abbreviated apatite or HA, and its phases. They have the ability to bond to osseous and epithelial tissue and are accepted by muscle tissue. The reason for this acceptability lies in a composition similar to the mineral phase of bone - bone consists of collagen and HA¹. However, hydroxylapatite has a low tensile strength, is quite brittle, have low impact resistance and suffers from a fatigue². Consequently, most orthopedic implants comprise metals. While the mechanical integrity of metal devices exceeds that of the ceramics, corrosion products give rise to tissue irritation and inflammation. Metal implants can suffer from corrosion and loss of metal ions into tissues³. These potential problems can be diminished by using a biocompatible calcium phosphate based ceramic material as a coating of high strength metal implants. It is well known that HA-coatings have the ability to induce new bone ingrowth and subsequently increase fixation stability. The satisfactory HA coating must be dense, adherent, and with structures not altered irreversibly by the coating techniques, 95% crystalline HA phase is required⁴. The HA-coatings are used in human surgery in order to enhance the biocompatibility and the osteointegration of metallic alloys⁵.

Pulsed laser deposition (PLD) by laser ablation is promising method for deposition of such complex ceramic, as HA. The PLD method makes possible to create relatively smooth films having the similar stoichiometry as that of the HA target. Another advantage is the possibility to vary, by deposition conditions, the Ca/P ratio or calcium phosphate phases. It is significant for various implantology applications. The quality and properties of the films are influenced by many factors as laser parameters, laser power density, target-substrate distance d_{ts} , environment in the interaction chamber (gas composition, pressure), film growth rate, film thickness, substrate material, the T_s deposition regime, deposition geometry, etc.

In this paper, our experiences with the PLD deposition of HA layers using KrF excimer laser, films properties and preliminary results of biological tests are presented and discussed.

2. EXPERIMENTAL

2.1. Film deposition

Targets were made of dry HA powder supplied by the MERCK Company in the form of three different particle sizes : 2- $20\mu\text{m}$ (75%), $<2\mu\text{m}$ (~20%) and $>20\mu\text{m}$ (~5%). The first group of targets was produced by ram pressing (50 MPa) of HA powder suspension in ethylacohol and pellet annealing in oxygen at 550 - 1150 °C. The second group was produced by isostatic pressing (150 MPa) of powder and pellet annealing at 550- 650 °C. The Ca/P ratio of all fabricated targets, measured by RBS (α -particles, 1.3 MeV), was in the range from 1.6 to 1.8 (optimum value - 1.67). The best mechanical properties of the targets from the first group were reached by annealing at 1150°C (target T1 - diameter of 25 mm and thickness of 5 mm). The T1 target was relatively hard (Knoop microhardness $\text{HK}_{25\text{g}} \sim 40$), the Ca/P was 1.69. From the second group, the best target semi- product was fabricated for oxygen annealing at 550 °C (T2 - diameter of 35 mm and thickness of 35mm). The Knoop microhardness $\text{HK}_{25\text{g}} \sim 40$, and Ca/P was 1.58. The measured XRD spectra of both targets were comparable with those of the standard pattern for hydroxylapatite (JCPDS File Number 9- 432).

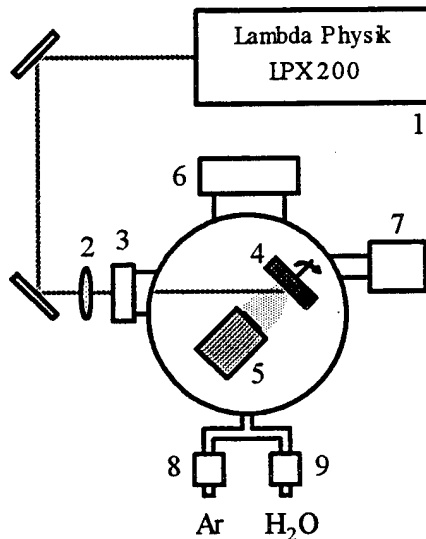


Fig.1. Experimental setup for HA film deposition : 1- KrF excimer laser ($\lambda = 248\text{ nm}$, $\tau = 30\text{ ns}$, $f = 10\text{ Hz}$); 2- focusing optics; 3- quartz windows; 4- target; 5- heated substrate holder; 6- turbomolecular pump; 7- Barratron; 8- mass flow meter for argon; 9- mass flow meter for pure H_2O vapors

The experimental setup consists of a KrF excimer laser (Lambda Physik LPX200) and a stainless steel vacuum chamber, where the target and substrate were placed - see Fig.1. The laser beam was focused down onto the target through high quality quartz optics (20 cm focal length) at 45° angle. The target was rotated during the deposition. The substrate was placed directly onto the resistively heated stainless steel holder and was thermally connected to the holder using paste. The d_{sub} was 7.5 cm. The vacuum chamber was pumped out to a pressure of 10^{-4} mbar by a turbomolecular pump. The pure water vapor was supplied into the chamber from a tank, containing liquid water at room temperature. Under a low pressure the water vapor flow into the chamber. The vapor flow rate was controlled by a valve. Argon was supplied from a pressure gas vessel.

The films were ablated from T1 and T2 HA targets in vacuum ambient (3×10^{-4} mbar), in pure water vapors (in the range from 2×10^{-3} to 2×10^{-1} mbar), and in the mix of Ar/H₂O vapors (total pressure 4×10^{-1} mbar, H₂O vapor pressure 10^{-3} mbar, Ar vapor flow rate ~ 6 sccm). Laser energy densities on the target of 3 Jcm^{-2} or 13 Jcm^{-2} were used. Different E_T were obtained by changing the irradiated spot size. The deposition rate was in the range of 0.01 - 0.1 nm per laser shot. The value of T_s was gradually adjusted from 500 °C to 760°C (in some cases from 200°C)⁶.

The Ca/P films and targets ratio was characterized by RBS and PIXE techniques. The standard RBS measurements were performed using 1.3 MeV ⁴He ions and the particles scattered under the angle of 120° were registered with a Si(Au) surface barrier detector (FWHM=15 keV). The PIXE analyses were performed with 2.5 MeV protons and the characteristic X-rays were registered using a Si(Li) detector (FWHM=180 eV/5.9 keV). The results from RBS and PIXE measurements agree within 5%.

The Bragg-Brentano goniometer type (CuK_α radiation, 200 mA, 50kV) was used for XRD measurements. The film topography was observed by SEM using a 10kV electron beam and 2000x magnification. The Knoop microhardness of the films was determined using the Matsuzawa MXT70 Digital Microhardness Tester. The measurement was made at the dwell time of 10s, with the constant force of 25g. The film thickness was measured with a stylus profilometer (Perthometer S5P) and checked by RBS or PIXE measurements. The adhesion of the layer to the substrate was measured by a scratch test. The tested layer was scratched by a slowly moving diamond tip, which was pressed with a continuously raising force against the tested layer. The scratch tip was a standard Rockwell diamond cone (radius 0.2mm and angle 120°). The value of adhesion was determined by the force F needed for the tip to penetrate through the tested layer to the substrate. The best way how to find the critical point of the scratch is to record the force acting on scratch tip. At the point, where the tip penetrates through the layer to the substrate, the tangential component of this force begins to rise sharply.

2.2. Biological analysis

Study of specimens biotolerance - the T-lymphocyte activity was evaluated by a test of proliferation based on proliferative activity of stimulated and non-stimulated cells. This proportion is described as index of stimulation (SI). Specimens were cultivated in RPMI 1640 medium⁷. Mononuclear cells were isolated from heparinised blood of healthy donor. The cells were stimulated by phytohemagglutinin (Difco) in a concentration of 1µg/ml in medium RPMI 1640. The proliferation was evaluated by the method of radioactively labeled 3H thymidin incorporation.

Study of resorbability - bioceramic specimens have changed their characteristics by cultivation in RPMI 1640 medium. Surface resorbability was evaluated by morphological changes of bioceramic film surface in course of cultivation.

3. RESULTS AND DISCUSSION

a) Film properties

As calcium hydroxylapatite is the most stable calcium phosphate in contact with the body, the research in laser deposition is directed toward the creation of crystalline HA films⁸. In our experiments a wide scale of deposition conditions was investigated. The XRD spectra of crystalline HA films were observed mainly when the mixture of Ar/H₂O vapors and higher T_s (600°C - 760°C) were used, independently of the target. The XRD spectra of such a HA film and those of the responsible target are in Fig.2a,b.

Preference orientation of the x-ray HA layer was found to be changed according to deposition conditions from (300) to (002) and (112). Beside HA peaks usually also peaks of Ca₄O(PO₄)₂, or occasionally other calcium phosphate phases were identified. Some small HA peaks were also found in the layers deposited in pure water vapors (2×10^{-1} mbar of H₂O). We did not find crystalline HA spectra for vacuum deposition. Deposition on a wider scale of T_s (200°C - 760°C) was used for the study of film parameters only in pure H₂O vapors (2×10^{-3} mbar). For lower temperatures (200°C - 400°C) an amorphous phase was usually found.

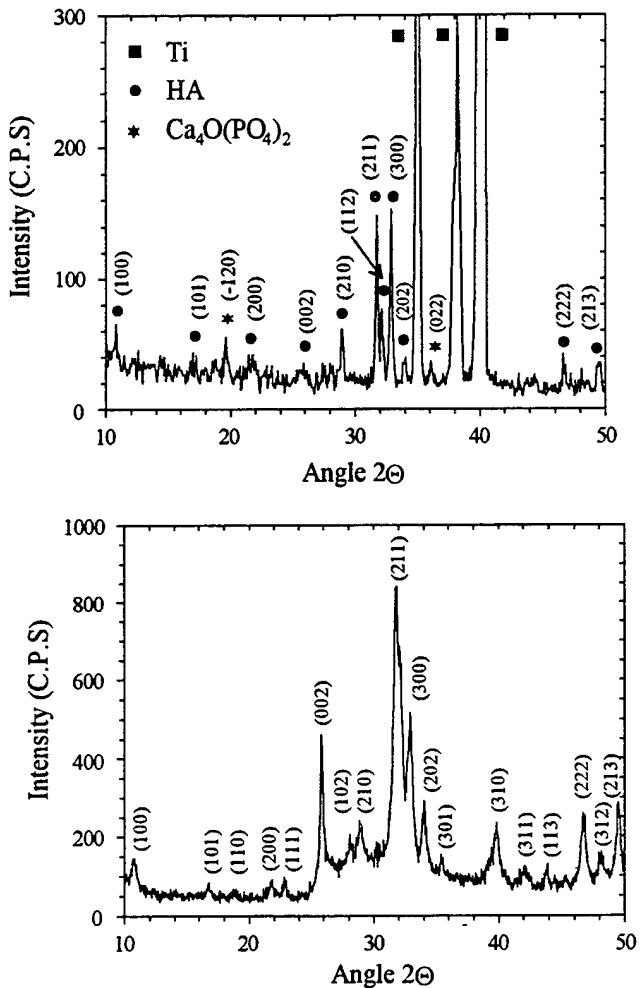


Fig.2. XRD spectra of : a) HA film deposited on Ti substrate (in mix of Ar/H₂O vapors, $T_s = 600^\circ\text{C}$, $E_T = 3 \text{ Jcm}^{-2}$, film thickness 240 nm) , b) target

The RBS and PIXE measurements of Ca and P contents in the films show that a better Ca/P ratio, closer to the optimum value (1.67), was reached for higher energy density E_T . The change of Ca/P ratio with T_s was observed⁶

Morphology of the deposited films was generally better for deposition with lower T_s . For higher T_s the film smoothness has worsened and in some cases the unhomogenities and film buckling were observed. For higher E_T the smooth film surface with very small droplets density was created. Usually, the droplets density was higher for the films deposited in vacuum than for the films deposited in pure water or in Ar/H₂O vapor. The influence of target preparation is seen from Fig.3.

The Knoop microhardness of HA films has increased with increasing T_s . For Ar/H₂O mixture and $T_s = 760^\circ\text{C}$ the microhardness of $\text{HK}_{25g} \sim 400$ -500 was measured. For lower T_s the microhardness was a little higher than that for Ti substrate (microhardness of Ti substrate $\text{HK}_{25g} \sim 180$). In vacuum deposition the $\text{HK}_{25g} \sim 850$ -900 was reached.

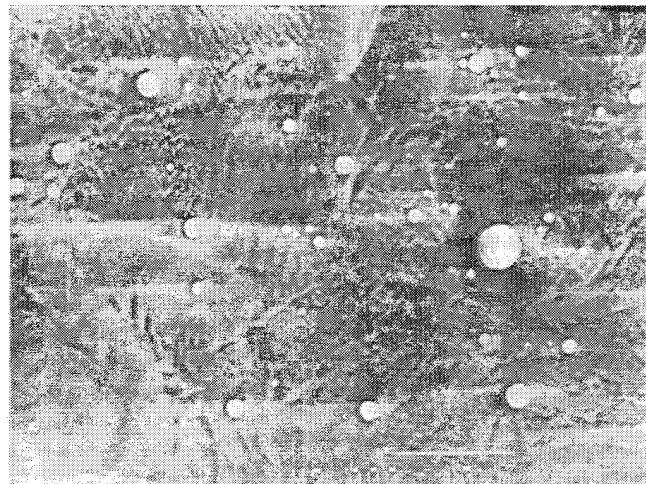
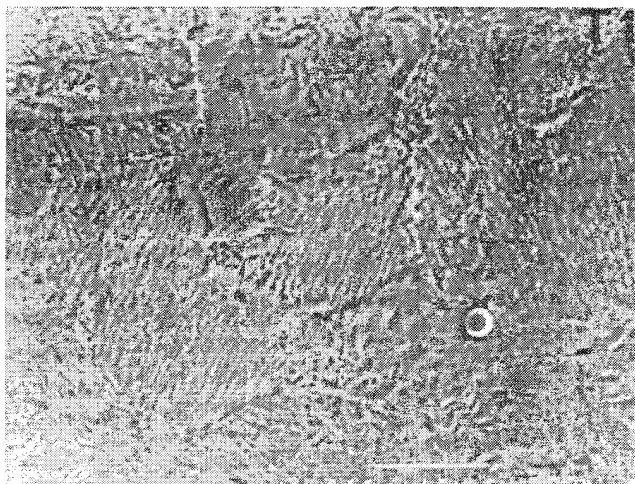


Fig.3. Morphology of HA films deposited from T1 (left picture) and T2 (right picture) targets (2000 x magnification, $E_T = 13 \text{ Jcm}^2$, $d_{ts} = 7.5 \text{ cm}$, $T_s = 300^\circ\text{C}$, pure water vapor - $2 \times 10^{-3} \text{ mbar}$, samples No. 27 (T1) and No.30 (T2).

The values F_N of adhesion were usually in the range of tens of newtons. The maximum reached F_N was 47N. This value approaches to the F_N measured for TiN layers, but created on harder substrates. Examples of adhesion measurements are in Fig.4.

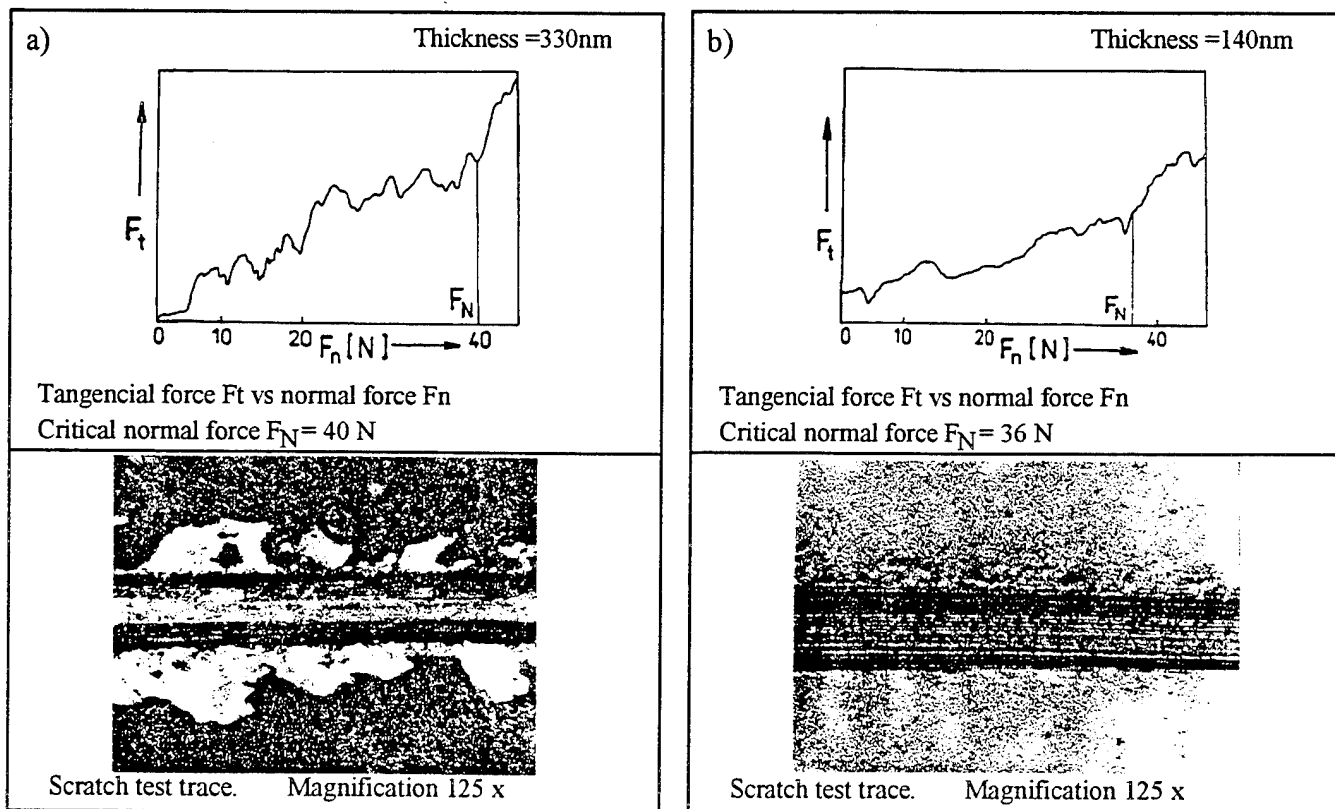


Fig.4. Results of scratch tests: a) Sample 9 (pure H_2O vapor, pressure $2 \times 10^{-3} \text{ mbar}$, $T_s = 760^\circ\text{C}$, $E_T = 3 \text{ Jcm}^2$, T1 target, $F_N = 40 \text{ N}$); b) Sample 22 (pure H_2O vapor, pressure $2 \times 10^{-3} \text{ mbar}$, $T_s = 500^\circ\text{C}$, $E_T = 13 \text{ Jcm}^2$, T1 target, $F_N = 36 \text{ N}$)

b) Biological properties

The basic value for evaluation the proliferative activity of bioceramic specimens is the activity of titanium substrate, SI, which was found to be 1.45. The highest index of stimulation $SI = 3.12$ exhibited the specimen No. 11 (created at $T_s = 600^\circ\text{C}$, in pure H_2O , pressure 2×10^{-1} mbar). Specimens having higher proliferative activity than that of titanium substrate were those having crystalline HA, tricalciumprophosphate and tetracalciumphosphate phases, and were deposited in H_2O or in the mixture of $\text{Ar}/\text{H}_2\text{O}$ vapors at higher T_s . No one sample deposited in vacuum or at lower T_s exhibited SI higher than that of titanium.

Bioresorbability was studied only for samples having SI higher than 1.45. No dependence between the value of SI and the specimens resorbability (comparison of surface morphology of films before and after treatment in cultivation medium) was observed. In some cases the blisters and resorbed areas of films or cracked films were found. It seems that the smallest changes of morphology exhibited mainly the layers created in $\text{Ar}/\text{H}_2\text{O}$ mixture at higher T_s . Example of change of surface morphology with film cultivation is in Fig. 5.

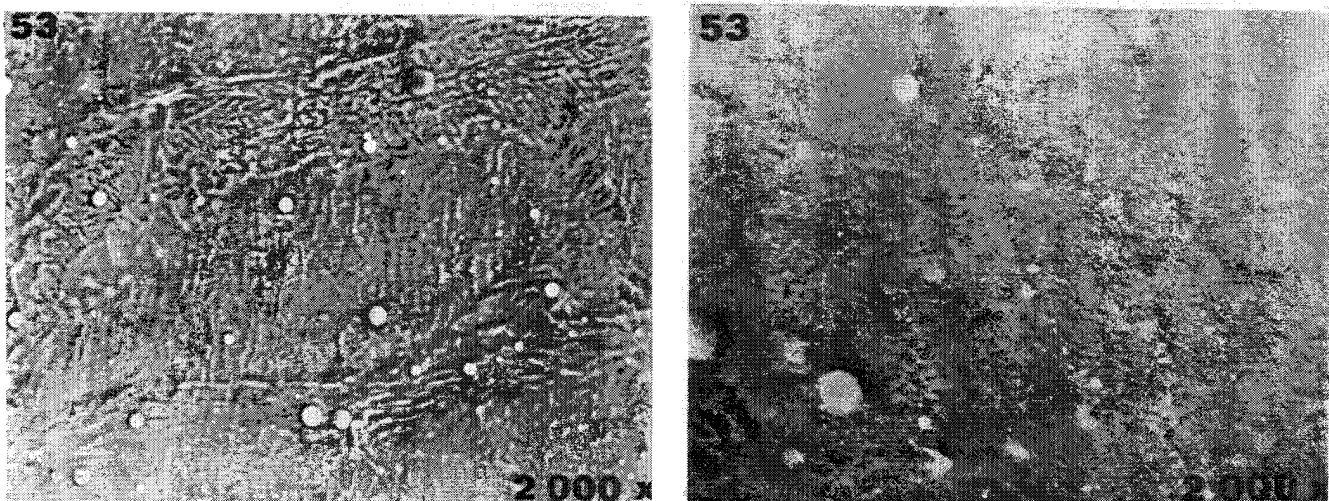


Fig.5. Surface morphology of film before - left picture, and after treatment in cultivation medium - right picture (sample No. 53, deposited in $\text{Ar}/\text{H}_2\text{O}$, $T_s = 600^\circ\text{C}$, T2 target).

4. CONCLUSION

Deposition of thin films of calcium phosphate based bioceramics was studied in vacuum, pure H_2O vapors and in the mixture of $\text{Ar}/\text{H}_2\text{O}$ vapors. From the results of analysis follow that the best crystalline HA films were reached in the mixture of $\text{Ar}/\text{H}_2\text{O}$, but usually also another crystalline calcium phases were observed, mainly in films deposited in pure water atmosphere. Higher T_s is preferable for incresion of percentage of crystalline HA phase and also from the point of film microhardness. The film surface was smoother for lower T_s , but generally the film morphology can be acceptable for all used T_s . The preliminary results of biological analysis (biotolerance and resorbability) were more favorable for films deposited in $\text{Ar}/\text{H}_2\text{O}$ or in pure water vapor, and at higher T_s . No distinct influence of target preparation and laser energy density on the results of biological treatment of samples were observed.

5. ACKNOWLEDGMENT

The authors wish to thank V. Studnička his technical assistance in XRD measurement. This work was supported by the Grant Agency of Czech Republic under grant No. 202/93/0464.

6. REFERENCES

1. K.A.Gross, C.C. Berndt, "In vitro testing of plasma-sprayed hydroxyapatite coatings," Journal of Materials Science: Materials in Medicine 5, pp.219-224, 1994.
2. M.Jarcho, "Calcium phosphate ceramics as hard tissue prosthetic", Clinical Orthopaedics and Related Research", 157, pp. 259-278, June 1981.
3. L.L.Hench, J.Wilson, "Bioceramics", MRS Bulletin, pp.62-73, September 1991.
4. D.M.Liu, H.M.Chou, J.D.Wu, "Plasma-sprayed hydroxyapatite coating: effect of different calcium phosphate ceramics", Journal of Materials Science: Materials in Medicine,5, pp. 147-153, 1994.
5. P.Frayssinet, F.Tourenne, N.Rouquet, P.Conte, C.Delga, G.Bonel, "Comparative biological properties of HA plasma-sprayed coatings having different crystallinities", Journal of Materials Science : Materials in Medicine 5, pp. 11-19, 1994.
6. M.Jelínek, V.Olšan, L.Jastrabík, V.Studnička, V.Hnatowicz, J.Kvítek, V.Havránek, T.Dostálková, Y.Zergioti, A.Petrakis, E.Hontzopoulos, C.Fotakis, "Effect of Processing Parameters on the Properties of HA Films Grown by PLD", Thin Solid Films, 1994 - in print
7. H.Tlaskalová, " Isolace MB z periferní krve", Vybrané diagnostické metody kěkařské imunologie, Avicenum 1986 -in Czech.
8. C.M.Cotell, " Pulsed laser deposition and processing of biocompatible hydroxylapatite thin films", Applied Surface Science 69, pp. 140-148, 1993.

The study of processing parameters influence on structural properties of PZT layers deposited by PLD

V. Trtik, M. Jelinek, L. Jastrabik

Institute of Physics, Czech Academy of Sciences, Na Slovance 2, 180 40 Prague 8, Czech Republic

ABSTRACT

Ferroelectric thin film of $\text{Pb}(\text{Zr}_{0.48}\text{Ti}_{0.52})\text{O}_3$ (PZT) was deposited on lattice mismatched (0001)sapphire for substrate temperatures T_s in the region from 470 to 590 °C and oxygen pressure of 200 and 900 mTorr. Structural properties were characterized by XRD. Improvement of XRD patterns of deposited films with post-annealing temperature of the furnace was studied. The development of the plasma plume shape from PZT target under changing deposition conditions was investigated by CCD camera. Results show strong dependence of plume shape with oxygen pressure and laser beam spot size.

1. INTRODUCTION

In the past several years, the interest in the use of ferroelectric films has greatly increased due to their potential applications. Recent research interest has been focused on the development of a radiation hard nonvolatile memory with the most investigated material $\text{Pb}(\text{Zr}_x\text{Ti}_{1-x})\text{O}_3$ (PZT). Beside direct industrial applications the PZT films are interesting for fundamental research in theoretical and applied physics.

Thin ferroelectric films have been deposited using different methods such as sol-gel, ion-beam sputtering, electron-cyclotron resonance plasma assisted-deposition, photoenhanced metalorganic chemical-vapor deposition and pulsed laser deposition (PLD)¹. The PLD, with its considerable success in the growth of high-quality, epitaxial thin films of high temperature superconductors, has been recently used in our laboratory to produce high-quality thin ferroelectric films (PZT, PLZT, PMN)^{2,3} and multilayer heterostructures with high temperature superconductors $\text{YBa}_2\text{Cu}_3\text{O}_{7-\delta}$, serving as bottom electrode. Laser ablation has a number of advantages such as the production of stoichiometric films because of congruent evaporation of many components from single target, lower processing temperature and highly oriented epitaxially grown films due to intrinsic bombardment by the high energy atomic and molecular species, direct and clean deposition of multilayers, a high deposition rate, and wide applicability - materials having a high melting temperature can be also easily deposited.

For the purpose of measurement of lattice dynamics of thin PZT layers it is needed to create PZT layers on (0001)sapphire. Sapphire has isotropic optical properties in perpendicular direction to surface of the substrate. Earlier we have successfully created epitaxial, pure perovskite PZT thin films on lattice matched substrate (SrTiO_3) at temperature of about 550 °C and oxygen pressure of 200 mTorr^{2,3}. It is problem to create high-quality PZT films of sapphire substrate⁴ because of PZT and sapphire have large mismatch and difference in the thermal expansion coefficients. We have tried to deposited PZT layers at lower T_s and post-annealed the deposited films at higher temperatures to promote crystallization⁵.

Another goal was to contribute to understanding the PLD process from the PZT target. For deposition of homogenous ferroelectric films by PLD it is very important to get to know and control the distribution of ablated flux. One of the methods to roughly estimate changes of ablated species distribution is observing the plasma plume shape and measuring of thickness profile of deposited films⁶. In our case we have studied the plasma plume shape using CCD camera.

2. EXPERIMENTAL

The growth and CCD camera analyzing system used in our experiment is shown in Figure 1. A PZT sintered ceramic target was ablated by an KrF excimer laser in an ambient oxygen gas at a pressure of 200 and 900 mTorr. The laser beam was focused onto the target in the vacuum chamber through a quartz lens and quartz window. Substrates of (0001)sapphire was mounted parallel to the target on a stainless steel resistively heated holder and was thermally connected to the holder by

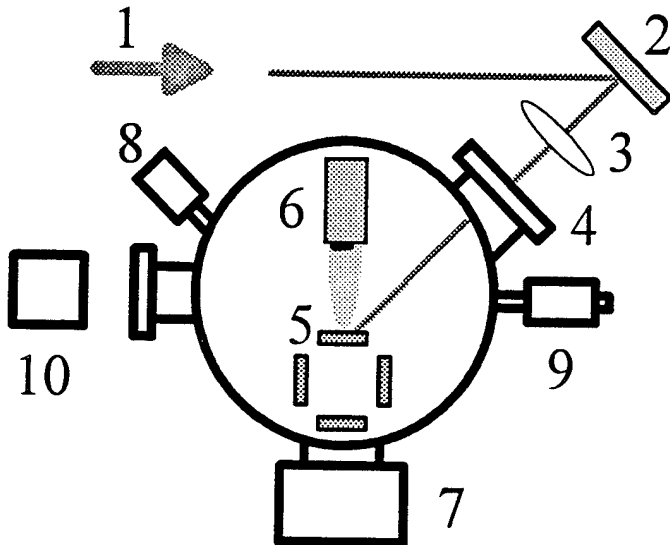


Figure 1. Experimental setup. 1. KrF laser beam ($\lambda=248$ nm, $\tau=25$ ns, $E_{out}=200$ mJ), 2. dielectric mirror, 3. focusing lens, 4. fused silica window, 5. targets, 6. heated substrate holder, 7. vacuum pump, 8. vacuum gauge, 9. oxygen filling, CCD camera.

InGa paste. Substrate temperatures was adjusted in the region from 470 to 590 °C. The distance between the target and the center of the substrate was 5cm. The substrate temperature was measured by a Ni-NiCr thermocouple fixed on the surface of the heater. The deposition rate 0.05 nm per laser pulse was obtained at the laser energy density 2 Jcm^{-2} . After deposition the layers was slowly cooled down in 1 atm of oxygen. Conventional furnace annealing of deposited layer was performed at a temperature in the range from 600 to 700°C in the air. The experimental conditions are summarized in Tab.1.

Laser	KrF excimer laser
Wavelength	248 nm
Repetition rate	5 Hz
Pulse duration	25 ns
Laser fluence	2 Jcm^{-2}
Deposition rate per pulse	0.05 nm
Target-substrate distance	5 cm
O ₂ gas pressure	200, 900 mTorr
Substrate temperature: ferroelectrics	470-590 °C
Annealing temperature	600-700 °C

Table 1. Summary of experimental conditions

The phase purity and grain-orientation of the films were characterized by X-ray diffraction (XRD) technique. XRD measurements were carried out using a 18 kW Cu target rotating anode operated at 50 kV and 200 mA. Step scan data sets were collected using a standard Bragg-Brentano goniometer with a diffracted beam plane LiF (200) monochromator. The goniometer had a 250 mm radius and a receiving slit 0.4 mm wide. The scanning step was 0.02 deg in θ . One step exposition time was 4 sec. A rotating sample holder was used (one rotation per 4 sec). For observation of plasma plume shape was used CCD camera SBIG ST-4 with an array of 192 by 165 detector elements. Imaging camera was connected to a personal computer. On this computer was carried out image processing and analysis. Automatic dark frame subtraction was turned on, anti-blooming gate was turned off. For all images was used the same "background" and "range" parameters. The plume is that of one laser pulse, exposure time was much longer than the plume lifetime.

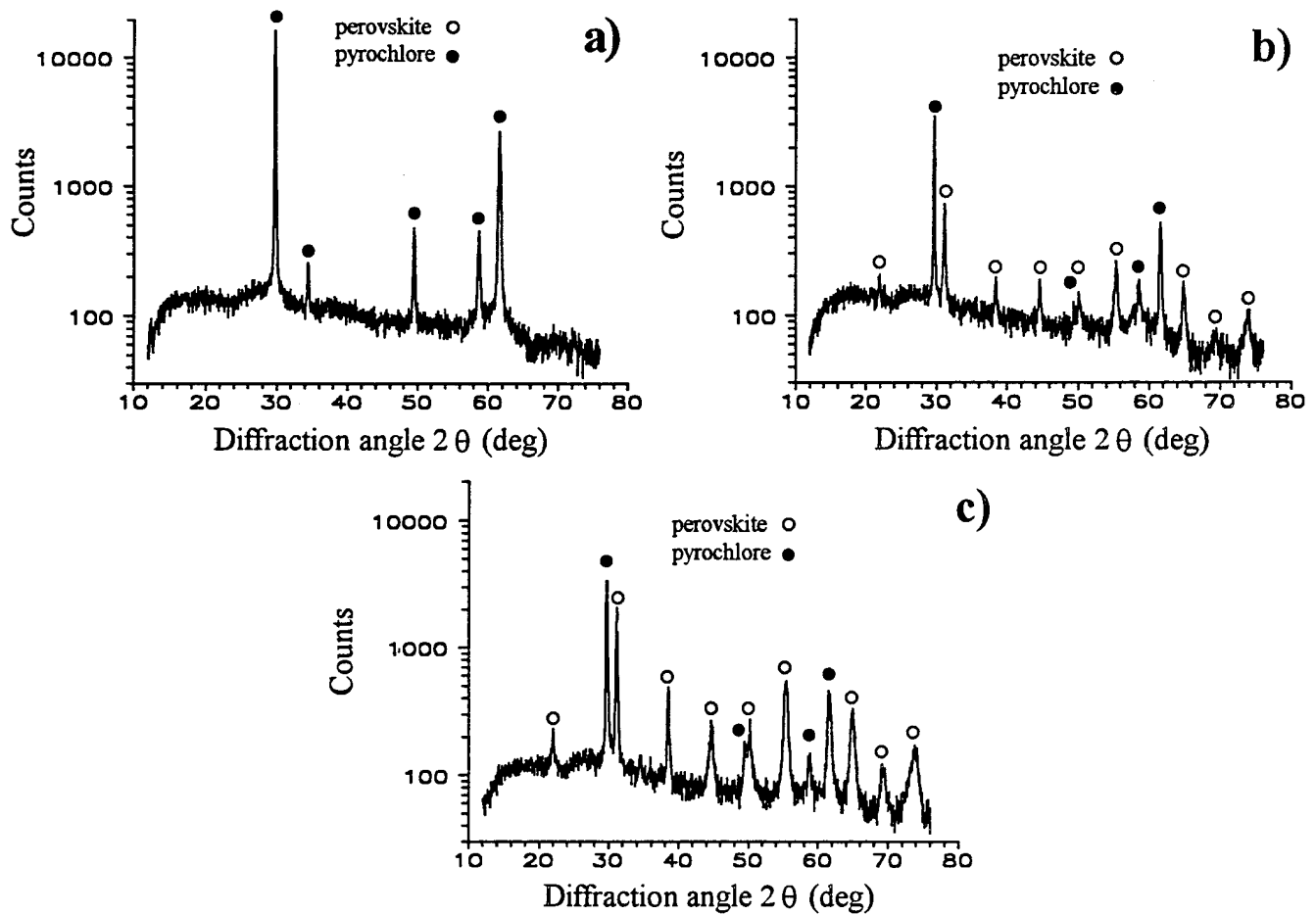
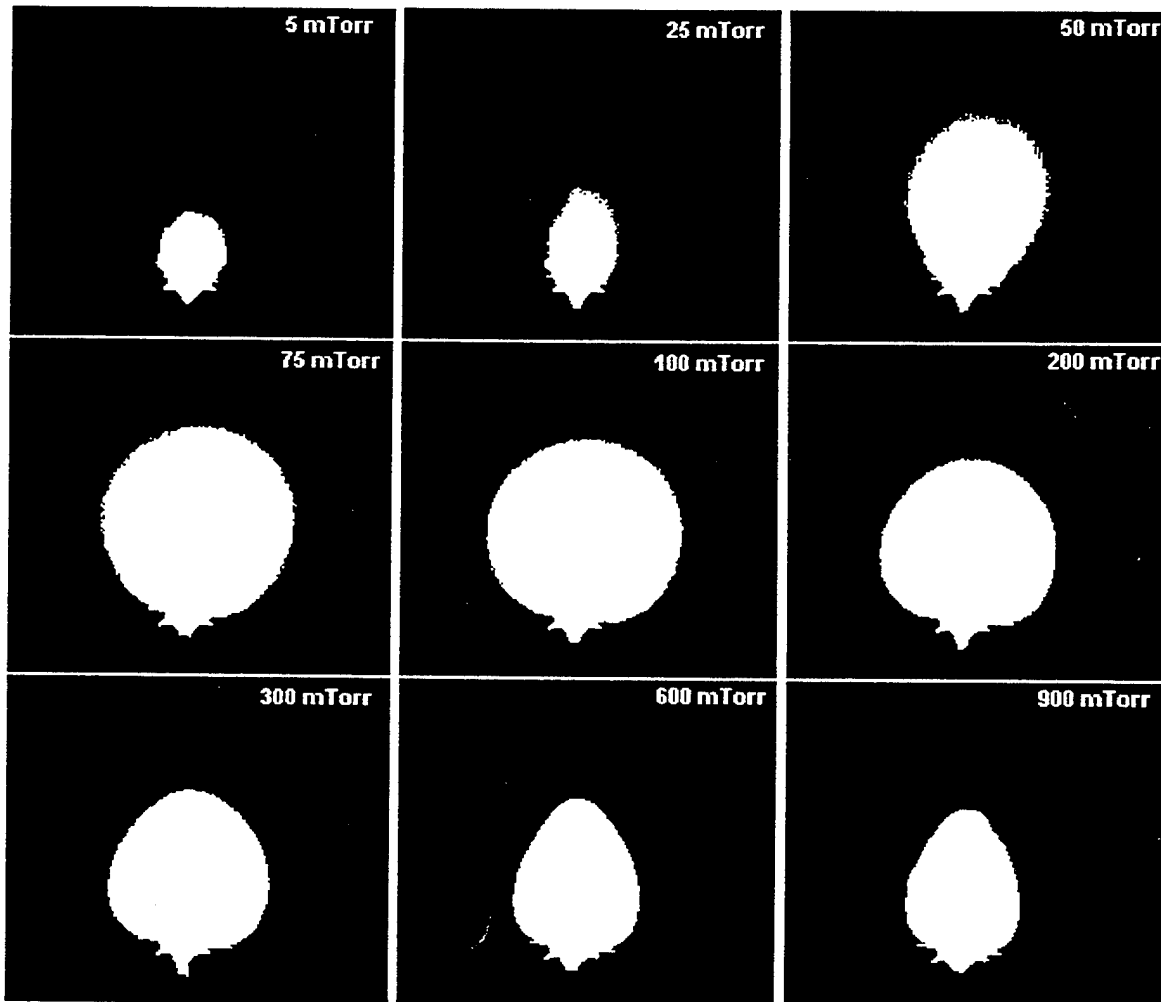


Fig.2. The XRD patterns of $\text{PbZr}_{0.52}\text{Ti}_{0.48}\text{O}_3$ thin film deposited on (0001)sapphire at 500°C and oxygen pressure of 200 mTorr. a) as-grown, b) annealed at 600°C , c) annealed at 700°C .

3. RESULTS AND DISCUSSION

From results of our experiments of PLD deposition follows that only pure perovskite structure in the films were not reached. The mixture of the perovskite and pyrochlore phases were observed. We can say that the percentage of perovskite structure has increased with increasing T_a . We didn't found the distinct influence of oxygen pressure on the film properties. Improvement of the properties of as-grown layers was observed after post-annealing of films in furnace. Example of the XRD patterns of the PZT films deposited on (0001)sapphire at temperature 500°C in oxygen ambient of 200 mTorr containing only non-ferroelectric pyrochlore phase is shown in Figure 1 (a). Open and close circle indicate the peaks for perovskite and pyrochlore phases of PZT, respectively. No one peak of the substrate has occurred in the round measuring angle. Only the peaks of pyrochlore phase was obtained for layer deposited at whole deposition temperature range. Figure 1 (b) and (c) shows the XRD patterns for PZT layer annealed at temperature 600°C and 700°C , respectively. After annealing peaks for the perovskite phase appears besides the peak for pyrochlore phase. Ratio of perovskite phase is increasing with increasing of annealing temperature.

The effect of change of plasma plume during PLD with oxygen pressure (5 - 900 mTorr) in the range of oxygen pressure is seen from Fig.2. With increasing of oxygen pressure the plasma plume has narrowed due to background gas scattering. The shape of plasma plume depends also on the spot size of laser beam on the PZT target. We have observed that with the increasing spot size the plasma plume has also tendency to be narrower.



The development of a plasma plume shape from $\text{PbZr}_{0.52}\text{Ti}_{0.48}\text{O}_3$ target with oxygen pressure (mTorr). Target was irradiated by KrF laser, laser fluence 2 Jcm^{-2} . Colors of pictures correspond to intensity of light.

4. CONCLUSION

We have presented our preliminary results of the growth of oriented PZT films on mismatched (0001)sapphire substrate using the PLD technique. In the region of the used T_a ($470\text{-}590^\circ\text{C}$) and oxygen pressures (200 and 900 mTorr) we didn't find pure perovskite structure. The amount of perovskite structure was improved by annealing of the layer in the furnace. For higher annealing temperature (700°C) the results were better.

Study of development of the plasma plume with the oxygen pressure and spot size show the great influence of these parameters and will open the way for creation of large-area, homogeneous ferroelectrics films.

5. ACKNOWLEDGMENT

The authors wish to thank V. Studnička his technical assistance in XRD measurement. This work was supported by the Grant Agency of Czech Republic under grant No. 202/93/0464.

6. REFERENCES

1. S.L. Swartz and V.E. Wood, "Ferroelectric thin films", *Cond. Matter News*, Vol. 1. Iss. 5, pp. 4 -13, 1992
2. M. Jelínek, J. Brádler, V. Trtík, L. Soukup, S.V. Gaponov, L.A. Suslov, E.B. Kluenkov, Yu.N. Drozdov, T.A. Shaplygina, V.A Trepakov., "Preparation and Investigation of Laser Ablated PZT, PLZT and $PbMg_{1/3}Nb_{2/3}O_3$ (PMN) Ferroelectric Films", *Ferroelectrics* Vol. 152/II, pp. 163 - 168, 1994.
3. V. Trtík, M. Jelínek, E.B. Kluenkov, "Study of Laser Deposited PZT, PLZT, PMN and YBCO Thin Films", *Journal of Physics D : Applied Physics*, Vol. 27, pp. 1544 - 1547, 1994.
4. S. Otsubo, T. Maeda, T. Minikawa, Y. Yonezava, A. Morimoto, T. Shimizu, "Preparation of $Pb(Zr_{0.52}Ti_{0.48})O_3$ films by laser ablation", *Jpn. J. Appl. Phys.*, Vol. 29, No. 1, pp. L133 - L136, 1990.
5. H. Hu, C.J. Peng, S.B. Krupanidhi, "Effect of heating rate on the crystallization behavior of amorphous PZT thin films", *Thin Solid Films*, Vol. 223, pp. 327-333, 1993.
6. D.J. Lichtenwalner, O. Auciello, R. Dat, R. Barnes, A.F. Schreiner, O.E. Hankins, and A.I. Kingon, "Effect of process parameters on the ablated flux characteristics during pulsed-laser ablation of lead zirconate titanate (PZT)", *Ferroelectric Thin Films III*, ed's: E.R. Myers, B.A. Tuttle, S.B. Desu, P.K. Larsen, Vol. 310, pp. 481 - 486, MRS, Pittsburgh, Pennsylvania, 1993.

Deposition of thin polymer films by pulsed excimer laser ablation

Martin Metal, Vladimír Myslík, Miroslav Jelínek

Institute of Chemical Technology, Dept.of Solid State Engineering
Prague 6, Czech Republic

ABSTRACT

Deposition of thin Polytetrafluoroethylene (PTFE) film by laser ablation deposition (LAD) technique is described in brief. The method utilization, transport conditions and optimal setup are presented. The paper also deals with the methods of prepared thin films characterization (Scanning Electron Microscopy, X-ray diffraction and Fourier Transform Infrared Spectroscopy) and comments all data achieved from all characterization measurements.

Keywords: polymer, thin film, laser ablation deposition

1. Introduction.

The deposition of thin inorganic films by laser ablation deposition (LAD) has undergone explosive growth and development in the past 5 years. The technique can provide compositional control for the growth of oriented thin films with distinctive morphologies and properties. The successful application of LAD has been reported for the deposition of high quality metallic layers, magnetic, piezoelectric, non-linear optical layers. In the past few years the reports appeared describing the harnessing the LAD for the thin polymer films preparation. The potential of technique in the production of polymer films is mostly illustrated by polytetrafluoroethylene (PTFE) and its copolymers. Although PTFE is inert, has excellent material properties, its application to the electronic industry has been limited due to its poor adhesion and difficulties related to the thin layer preparation. Therefore the PTFE is the most interesting polymer in LAD experiments.

In this paper we report on the deposition and characterization of the thin film of PTFE GoodFellow FP306010/2 by pulsed excimer laser ablation. The Fourier transform infrared (FTIR), X-ray diffraction (XRD) spectroscopy and scanning electron microscopy (SEM) have been used for thin film characterization.

2. Experimental

The depositions have been carried out in a small vacuum glass chamber with a background pressure of 10^{-6} Torr. The chamber has been equipped with quartz window allowing the laser beam to be incident on the sample at 45 °angle. The targets have been prepared by melt pressing PTFE GoodFellow powder at 140 000 PSI into 2.1 diam pellets at 195 °C. Chosen temperature has been at 65 °C above the corresponding glass transition temperature. The targets have been ablated using the KrF excimer laboratory laser ($\lambda=248$ nm, $E=220$ mJ). The beam

has been modified by a pair of apertures and weaken using the quartz attenuator. The beam has been directed into the chamber by optic prism and focused onto the target by a 370 mm focal length lens. Uniform coverage of the substrate, placed 3.5 cm away, has been assured by target rotating. The photon fluency has varied from 0.5 to 3.2 J/cm² in 15 ns pulses (5 Hz repetition rate) by changing the spot size at the target. PTFE films have been deposited in Ar atmospheres of 75-300 mTorr. The temperature has ranged from 25 to 270 °C.

3. Results

Following deposition the film have been characterized by scanning electron microscopy (SEM), Cu K α 2θ x-ray diffraction (XRD) and Fourier transform infrared (FTIR).

Fig.1 shows the infrared spectra of the ablated film (c) and that of fine PTFE powder (b) which has been used for target preparation. Both of spectra could be compared to the PTFE bulk spectra (a) published by Hummel/Scholl in spectra atlas. It is evident that ablated spectrum shows the asymmetrical and symmetrical CF₂ stretching of PTFE at 1207 and 1155 cm⁻¹. The PTFE rocking and bending modes at about 500-520 cm⁻¹ and 553 cm⁻¹ and the CF₂ wagging and chain stretching modes at 630 and 650 cm⁻¹ are also clearly observable. On the contrary the absence of bands at 1342, 913, and 407 cm⁻¹ and at 960 cm⁻¹ reflect very low concentration of monomers and C₄F₈ species respectively.

The influence of the distance target-substrate (a,c) and influence of the atmosphere pressure (b,c) can be observed in the fig.2. All depositions have been carried out in the atmosphere pressure at 75 mTorr and the spectra (b) shows the situation when the pressure has been changed to 300 mTorr. The only difference can be observed in the area of 677 cm⁻¹. The narrow band has arrived due to the higher concentration of C=O groups. The spectra (a) shows the change of film thickness when the distance target-substrate has been reduced at 30 %.

The last IR fig.3 represents the optimization study. The photon fluency has been changed from 1.0 to 3.2 J/cm² while the other experimental conditions remained constant. The maximum of intensity in IR signal appeared at photon fluency at about 2.0 J/cm². (spectrum b in fig.3)

Micrographs A,B show scanning electron micrographs of PTFE film deposited on sapphire (1-102) substrate at room temperature. The charging of the film by incoming electrons was reduced by applying a thin aluminum layer. Micrograph A shows an edge of deposited film. The large pieces of PTFE could be clearly visible. That is a characteristic effect for laser ablation deposition. Micrograph B shows the typical morphology of deposited film at room temperature. The debris are not so clearly visible and its dimension is much smaller. The film thickness fluctuations are in order of 10 per cent.

The x-ray spectra of the deposited films have only one striking peak. The bulk spectrum of used target shows the same peak in the same position. Therefore we suppose that the deposited layer has the same crystallographic orientation as the initial bulk material.

4. Conclusion

In this paper we have contrived the plausibility of thin PTFE film preparation using the LAD technique. The prepared films have been characterized by three different techniques and

all achieved data are in good agreement with theoretically supposed values.

An optimization study has been performed and all obtained outcomes have been published. The optimal value 2.0 J/cm^2 has been found for given experimental setup (Ar atmosphere pressure 10 Pa, distance target-substrate 3.5 cm, deposition time 4 min). We have prepared the thin PTFE films with quite smooth relief using the deposition temperatures 60°C above the glass transition temperature.

It is our present belief that LAD can be suitable for the deposition of most polymers that thermally decompose into the monomer or other low molecular weight fragments.

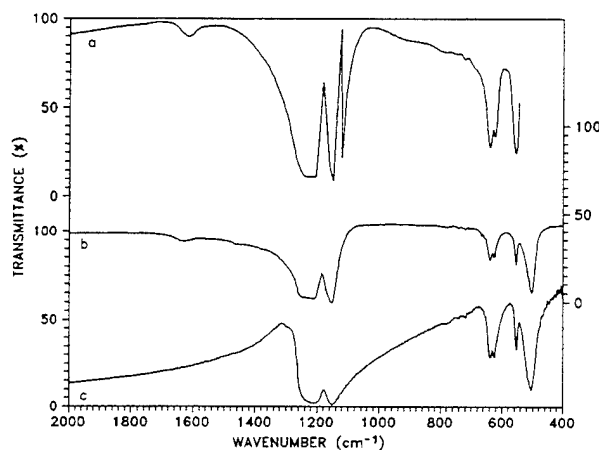


Figure 1 IR Spectrum of deposited thin layer (c), of that initial fine PTFE powder (b) and the atlas spectrum published by Hummel/Scholl.

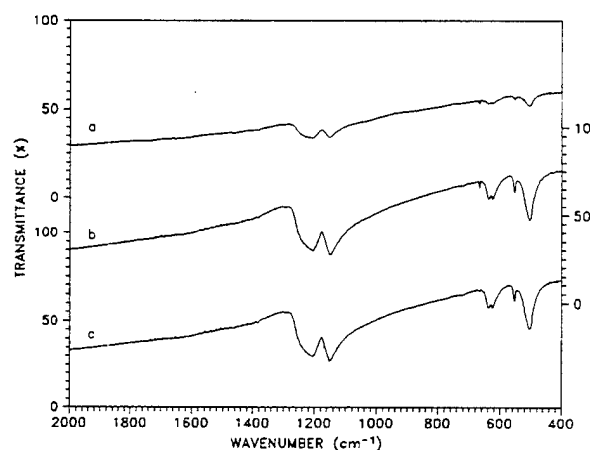


Figure 2 IR spectra of deposited thin films. The influence of distance (a-c) and influence of pressure (b-c)

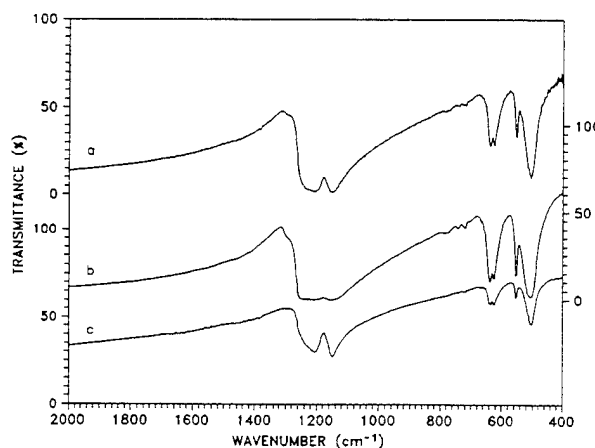
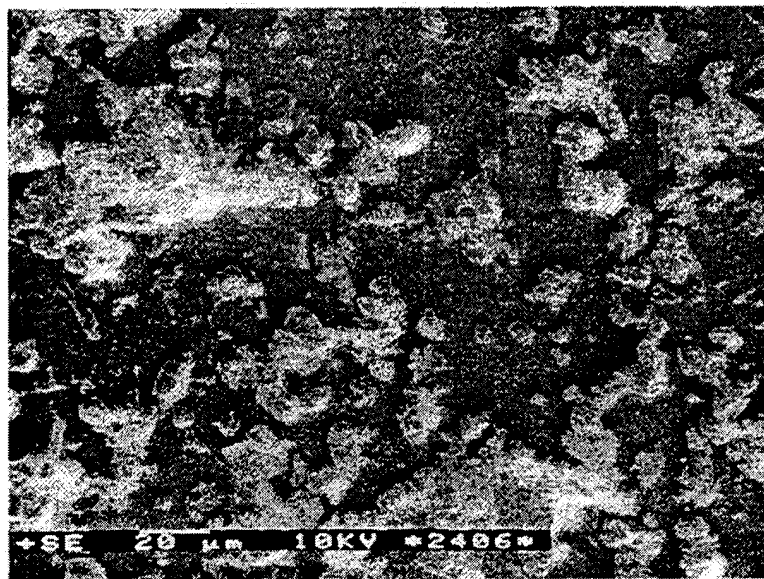
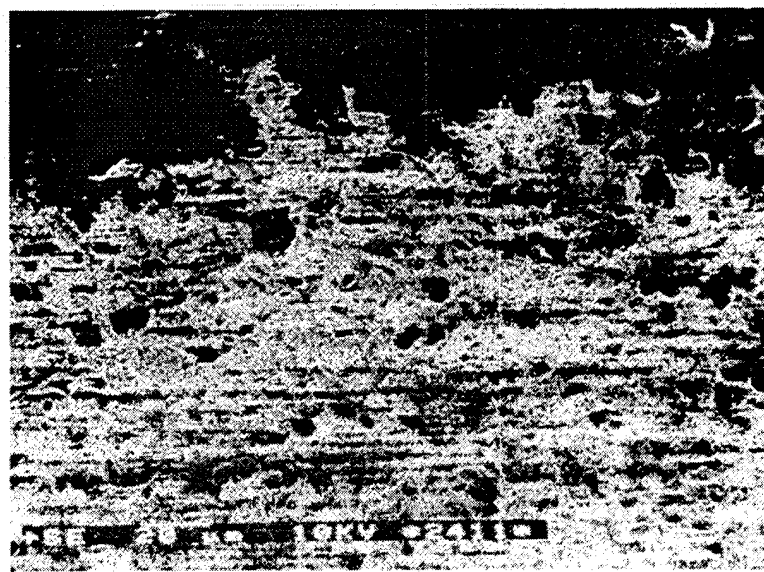


Figure 3 IR spectra of deposited PTFE films. The figure shows the results of optimization study. Photon fluence ranged from $1.0 \text{ to } 3.2 \text{ J/cm}^2$. Spectrum (c) belongs to the density 1.0 J/cm^2 .



Micrograph A: An edge of LAD technique deposited thin PTFE film. The large debis, characteristic feature of LAD, are clearly visible.



Micrograph B: The middle area of prepared thin film by LAD technique. The picture shows the typical morphology of layer deposited by room temperature. The smoother surface could be reached with increasing temperature.

Laser Annealed Deep Ohmic Contacts

Macháč P., Myslík V., Vrňata M.,

Institute of Chemical Technology

Department of Solid State Engineering

Technická 5, 166 28 Prague 6, Czech Republic

ABSTRACT

The contribution deals with the results of our work on ohmic contact formation, the process optimization. The contacts should be optimized with respect to chemical composition of metallization, energy density of laser radiation and repetition rate of laser pulses. These contacts also enable to interconnect surface of the samples with a very thin layer under the surface (δ -doped layer).

KEYWORDS: laser annealing, n-GaAs, ohmic contact, contact resistance

1. INTRODUCTION

Laser annealing is an attractive technology used in microelectronics. Perfection of technological systems (precise exposure, stability, radiation homogeneity, etc.) permits work with micron- and even submicron- structures in both the lateral and transverse directions. The ability to change the wavelength of the laser radiation is also a great advantage. Thus, a specific type of substance can be affected, work can be carried out on only a super-thin surface layer, etc. These factors provide completely new technological capabilities. As for the optimal chemical composition of metallization, there are two possibilities used in the practise for ohmic contacts production :

1) Reducing the energy barrier width of the contact by the help of a strong doping of semiconductor within the metal-semiconductor junction region preferring thus the tunnel-transition of a junction current. Sn and Ge are n-type dopants in GaAs in our samples.

2) Decreasing the energy barrier using the graded heterojunction, i.e. reducing the width of semiconductor forbidden-band in a subcontact region. In our experiments addition of In to metallization causes formation of $\text{Ga}_x\text{In}_{1-x}\text{As}$ phase with gradually variable composition and forbidden-band width.

2.EXPERIMENTAL

Laser Nd:YAG pulsed Q-switched has been used for our purpose. The laser has operated at fundamental harmonic frequency of radiation (wavelength 1064 nm) and has produced about 250 ns pulses at the repetition rate ranging from 50 Hz to 5000 Hz with the peak power 10 kW. The laser radiation was focused to a diameter of 40 micro-meters. The laser scanning was realized by P.C. controlled XY slide. In the work-chamber there can be used vacuum or inert atmosphere. (Fig.1) The contacts were formed in n-type GaAs using an N_d concentration of $(1.5-2) \times 10^{18} \text{ cm}^{-3}$. The surfaces of the plates were washed with distilled water and degreased with acetone. Then the surfaces of the plates were etched with a mixture of 5 H₂SO₄:1 H₂O₂:1 H₂O for a period of 30 s and again washed with water and dried. Standard optical lithography was employed to form a resist mask on the surface of the plates with a pattern designed for measuring contact resistances. The metal contacts were deposited by the sputtering method using an MRC 903 apparatus from the TTS Co.Ltd.(CR). The combinations of metals, thicknesses of their layers and energy density ranges are shown in Fig.2. The plates are heated on the side to which the metallization is applied.

3.RESULTS

Fig.3 depicts contact resistances vs laser radiation energy density for AuGeNi and GeAuNiW+Ti contacts on n-GaAs. W+Ti surface layer was used in order to attain lower reflectance and to reduce radiation energy density necessary for annealing. Fig.4 and Fig.5 show contact resistances vs laser energy density for PdSnW, SnW and GeAuW, PdInW, GeInW respectively. So as to optimalize repetition rate of laser pulses, we have applied several frequencies for every radiation energy density. It is seen from Fig.6 that the best results were achieved for 500 Hz. The rate of sample motion was 0.36 mm s⁻¹ in all cases. The AuGeNi and InW metallization was then used for preparing contacts to 2D-structure, which is shown in Fig.7. The results presented in Fig.8 were evaluated by TLM-method measurement. Sheet resistances of δ -layer are also presented here. Fig.9 is a table, which summarises the best results achieved and also the parameters of experiments.

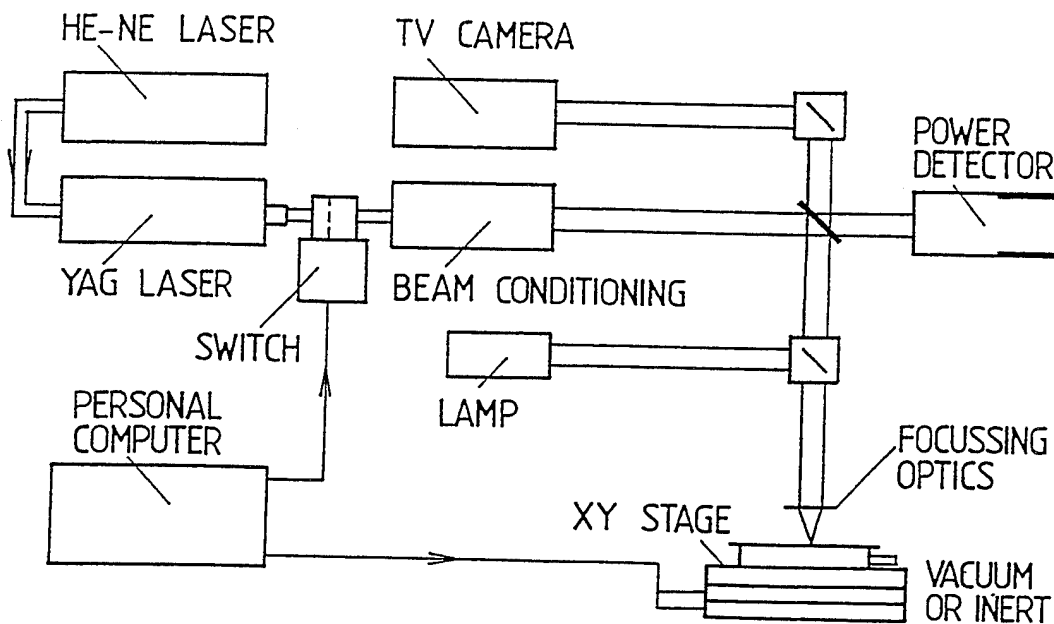


Fig.1 The technological set-up for laser annealing

Structure of contacts	Interval of radiation energy density during alloying [J/cm ²]	Repetition rate [Hz]
N-GaAs/Au(77.2%)Ge(10.5%)Ni(12.3%) - 200 nm	0.18 - 0.375	500
N-GaAs/Pd-40nm/Sn-40nm/W-100nm	0.03 - 0.12	50 - 5000
N-GaAs/Sn-40nm/W-100nm	0.04 - 0.12	150
N-GaAs/Ge-40nm/Au-80nm/W-100nm	0.03 - 0.39	150
N-GaAs/Pd-10nm/In-10nm/W-100nm	0.045 - 0.375	150
N-GaAs/Ge-10nm/In-10nm/W-100nm	0.05 - 0.36	150
N-GaAs/Ge-40nm/Au-80nm/Ni-40nm/W(90%)Ti(10%)-100nm	0.015 - 0.15	500
δ -GaAs/Au(77.2%)Ge(10.5%)Ni(12.3%) - 200 nm	0.045 - 0.1125	150
δ -GaAs/In-40nm/W-100nm	0.09 - 0.15	150

Fig.2 Summary of realized contacts

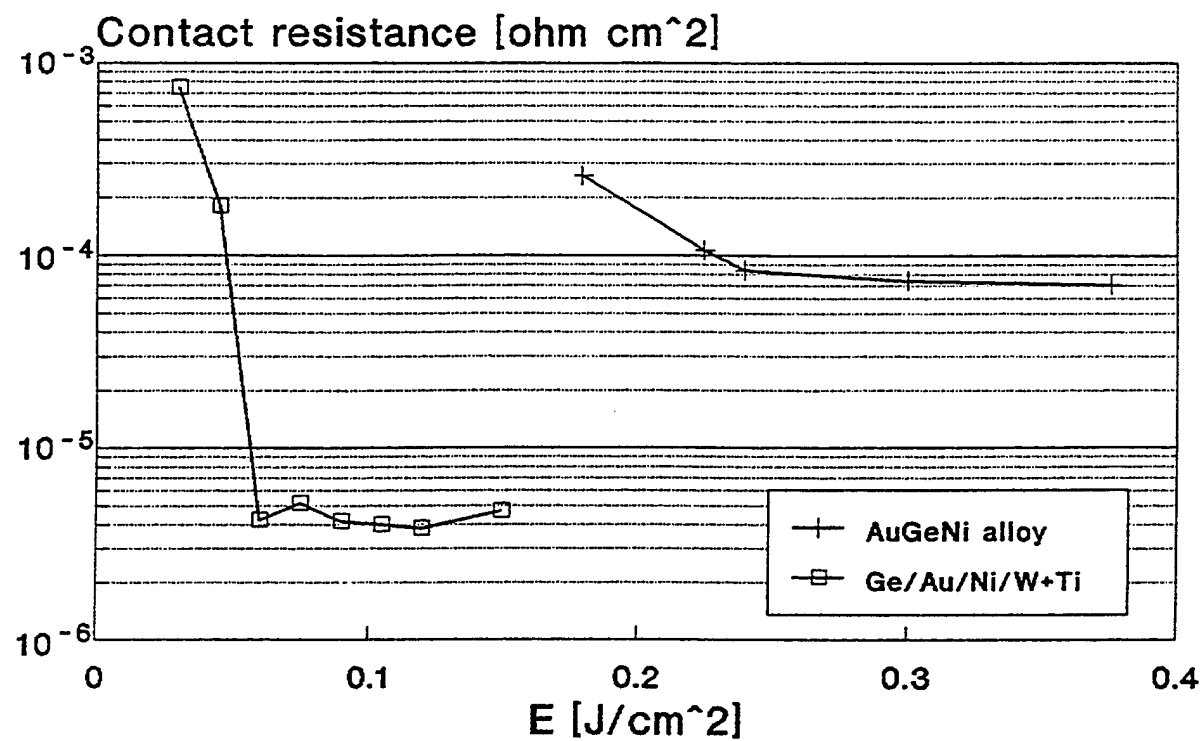


Fig.3 Contact resistance of AuGeNi contacts on N-GaAs

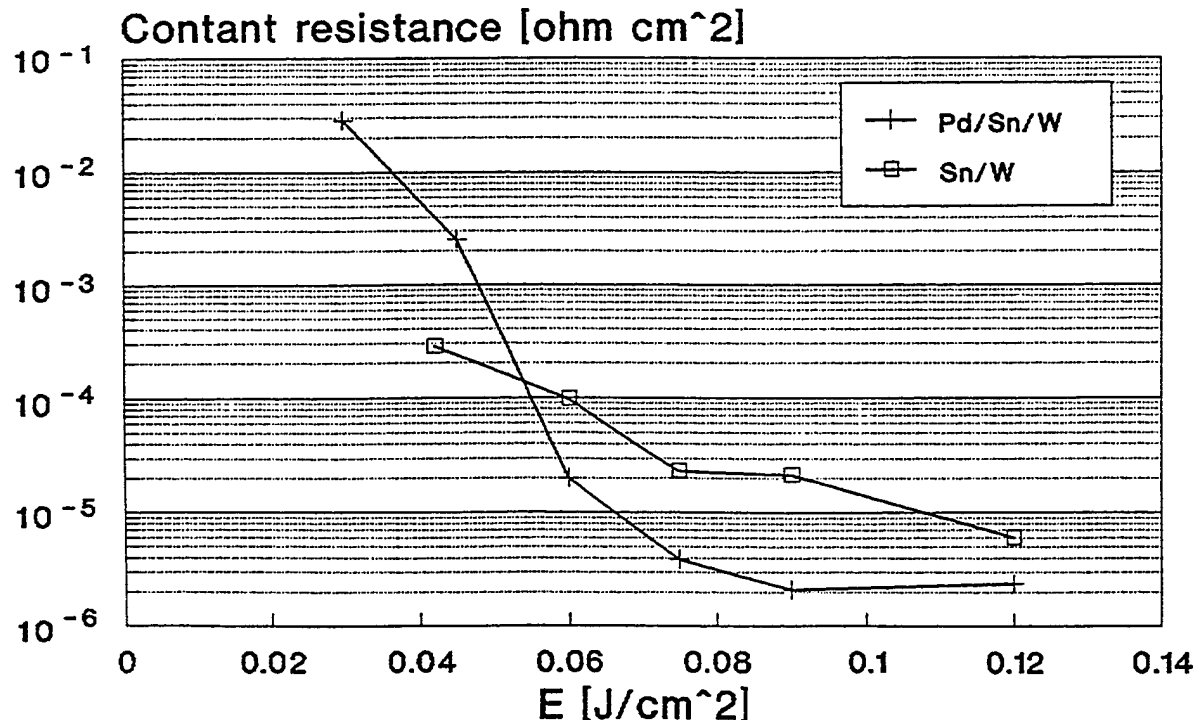


Fig.4 Contact resistance of Sn/W and Pd/Sn/W contacts on N-GaAs

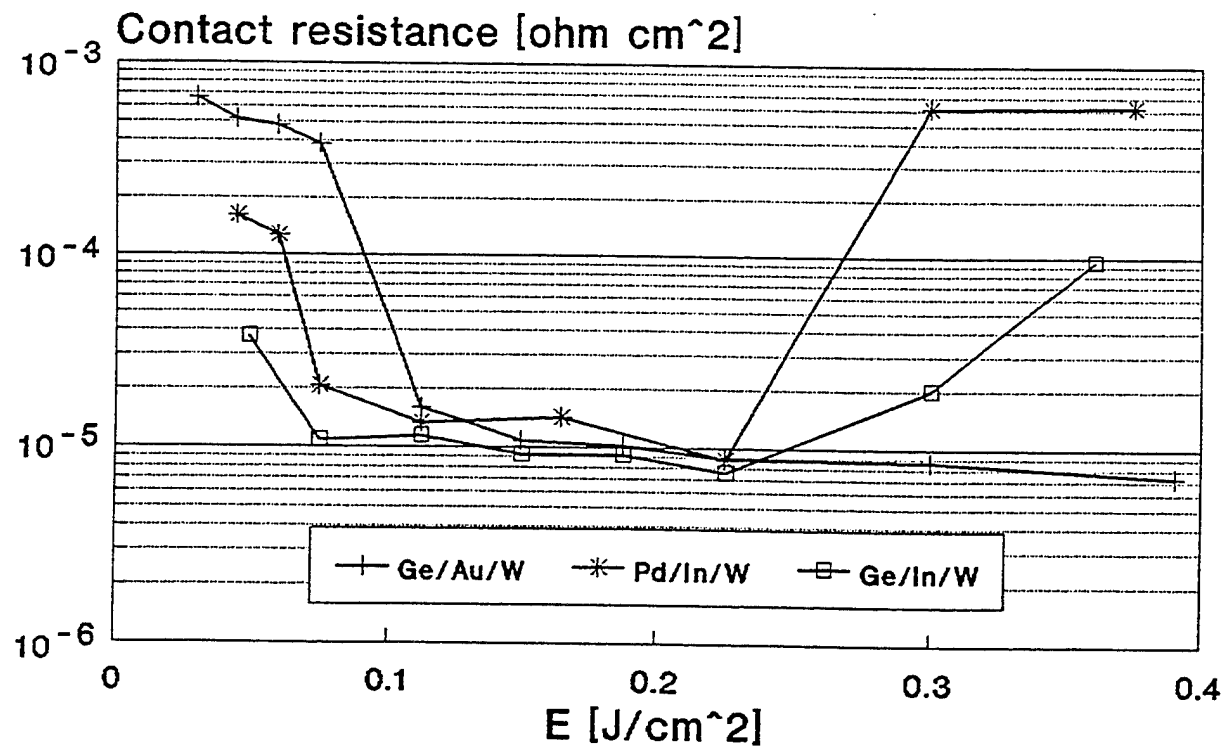


Fig.5 Contact resistance versus density of radiation energy

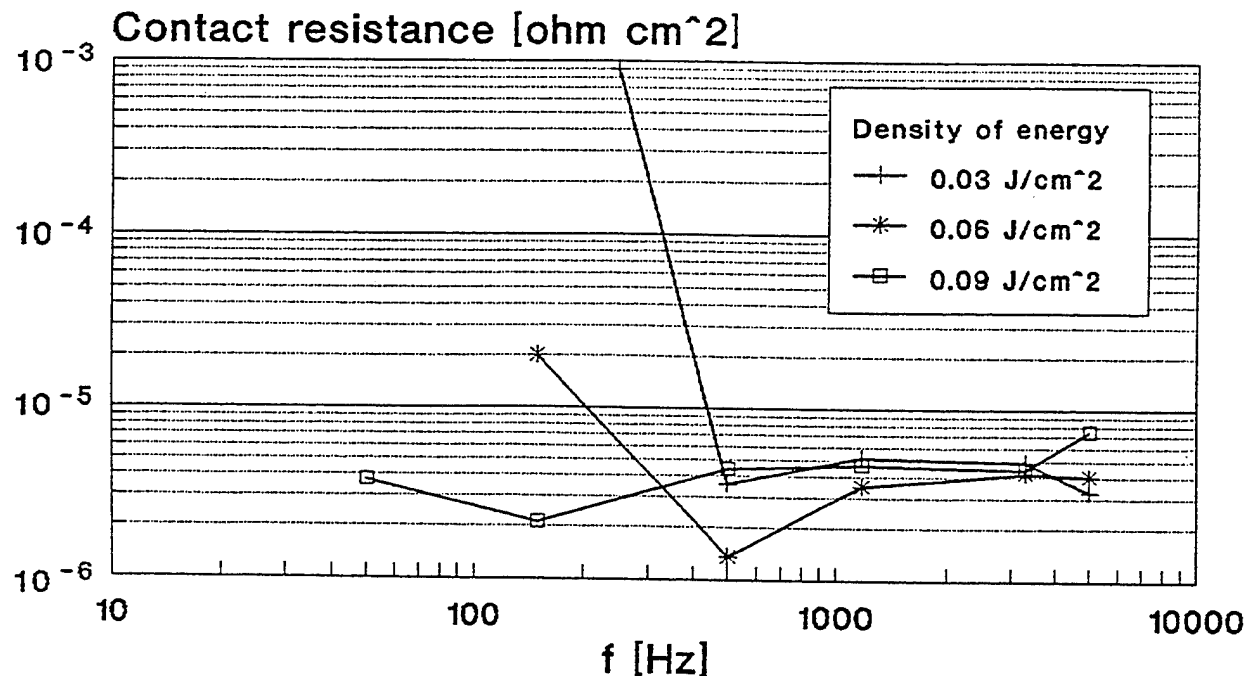


Fig.6 Contact resistance of Pd/Sn/W contact versus repetition rate and density of radiation energy

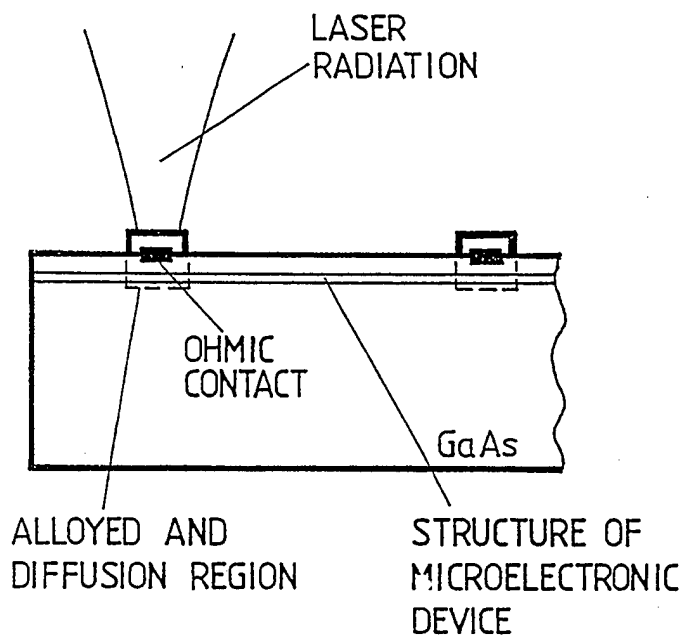


Fig.7 Laser preparing of ohmic contacts to 2-D structures

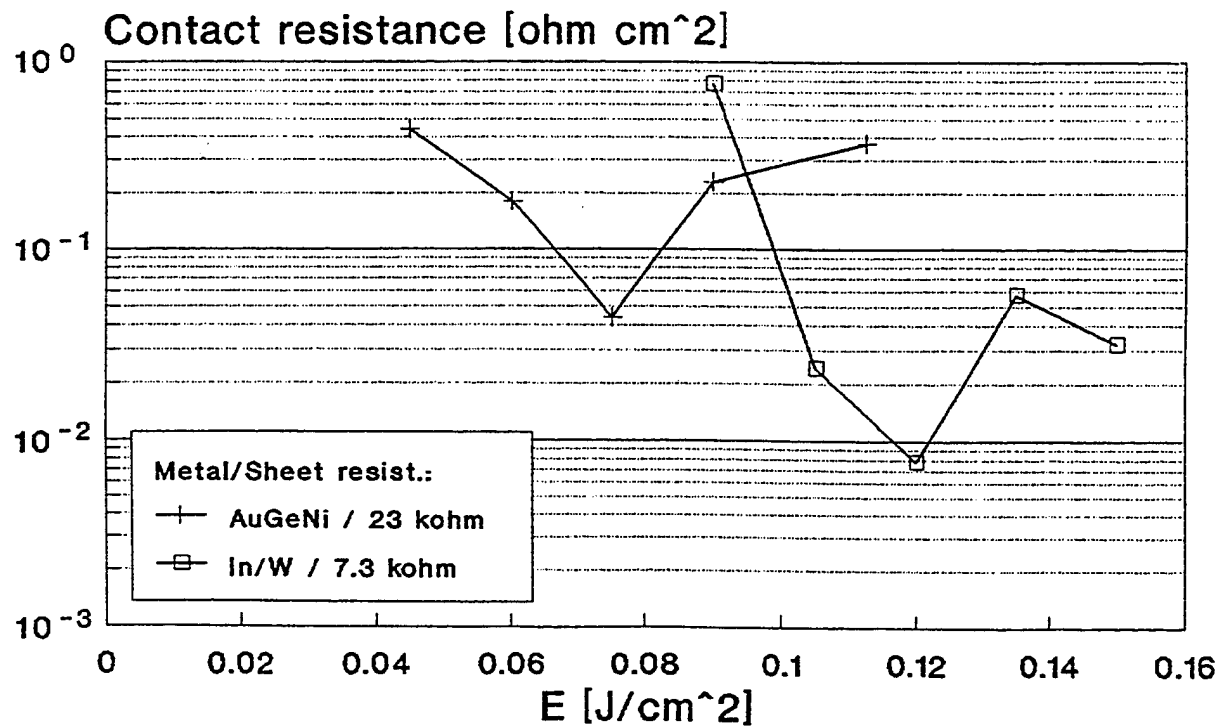


Fig.8 Contact resistance of contacts on GaAs wafers with 2D structures

Contacts	E / f [J/cm ² ; Hz]	$r_C \text{ min}$ [Ω cm ²]
N-GaAs/AuGeNi	0.375 / 500	7.10×10^{-5}
N-GaAs/Pd/Sn/W	0.06 / 500	1.36×10^{-6}
N-GaAs/Sn/W	0.12 / 150	6.00×10^{-6}
N-GaAs/Ge/Au/W	0.26 / 150	7.28×10^{-6}
N-GaAs/Pd/In/W	0.225 / 150	8.75×10^{-6}
N-GaAs/Ge/In/W	0.225 / 150	7.53×10^{-6}
N-GaAs/Ge/Au/Ni/WTi	0.12 / 500	3.80×10^{-6}
δ-GaAs/AuGeNi	0.075 / 150	4.40×10^{-2}
δ-GaAs/In/W	0.12 / 150	7.77×10^{-3}

Fig.9 Summary of the best values

Laser method of preparation of the high $T_{(c)}$ superconducting films on the bulk ceramic $\text{YBa}_2\text{Cu}_3\text{O}_{(7-\delta)}$

Yu. V. Denisov*, V. A. Madii*, Yu. I. Krasilov**, A. Zubovich***

* - Department of General and Applied Physics,
Moscow Institute of Physics and Technology

** - Institute of General and Inorganic Chemistry,
Russian Academy of Science, Moscow, 117 907 Russia

*** - Laser Center, Moscow Institute of Physics and
Technology, Dolgoprudny, Moscow Region
141 700 Russia

ABSTRACT

The authors of the report developed the method of the modifying the surface of ceramic Y-Ba-Cu by laser irradiation. This method permits to obtain ceramic superconducting structures on the surface with $T_c = 88 \pm 1$ K, $\Delta T = 1.4 \pm 0.1$ K, $I_c \geq 10^4$ A/cm². Such structures are the films 5 - 10 μm thick on the ceramic Y-Ba-Cu which are in the non-superconducted state.

1. INTRODUCTION

The change of the properties of high - T_c superconductors by laser irradiation have been studied by many authors. In most works investigations was been fulfilled on the thin films on the monocrystal substrate¹⁻⁹. Only two works were devoted to the change of the surerconducting properties of the surface of the bulk ceramic Y-Ba-Cu after it was irradiated by the laser beam^{10,11}. In this works have been demonstrated the possibility of the modification of the superconducting ceramic surface, but the detail investigation was not done.

In the present paper we discuss the results obtained after processing the surface of bulk ceramic samples by the laser radiation. The choice of bulk samples was caused by two reasons. First, a decrease of porosity of the surface layer will doubtlessly make HTSC sample more stable. Second, there is the possibility of the creation of the superconducting phase on the surface of the ceramic Y-Ba-Cu in nonsuperconducting state. In such a way we will be the method permitting to obtain two-dimensional superconductive film structures with designated configuration on non-superconductive ceramic 1-2-3, as a substrate, without using film technology.

2. MATERIALS AND METHODS

The essence of the proposing method consists in the thermal processing of the surface by the laser beam. The investigations were carried out onto ceramic $\text{YBa}_2\text{Cu}_3\text{O}_{(7-\delta)}$, obtained by different technology.

The characteristics of initial samples were in the range $T_c = 81-89.5 \text{ K}$, $\Delta T = 3.1-5.4 \text{ K}$, $I_c = I - 10 \text{ A/cm}^2$. The correlation between T_c , ΔT and of the critical current value were not observed.

Experimental set up is shown schematically in Fig. 1. The laser worked in CW regime on the wavelength 1.06μ . The size of heated and luminous spot caused by laser beam on the sample's surface was from 0.2 to 1.0 mm. It depended on the mode structure, focusing and power of the laser beam. The beam scanning was realized by the motion of the sample and was controlled by the computer. The sample's velocity was in the range from 0.1 mm/min to 10 mm/min.

The measurement of the sample temperature was made with using electro-optical set up (elements 12-18 in Fig.1) of the energy type. The diameter of the region, in which the temperature was averaged, was in the range from 0.1 to 1.5 mm. The measuring channel was been

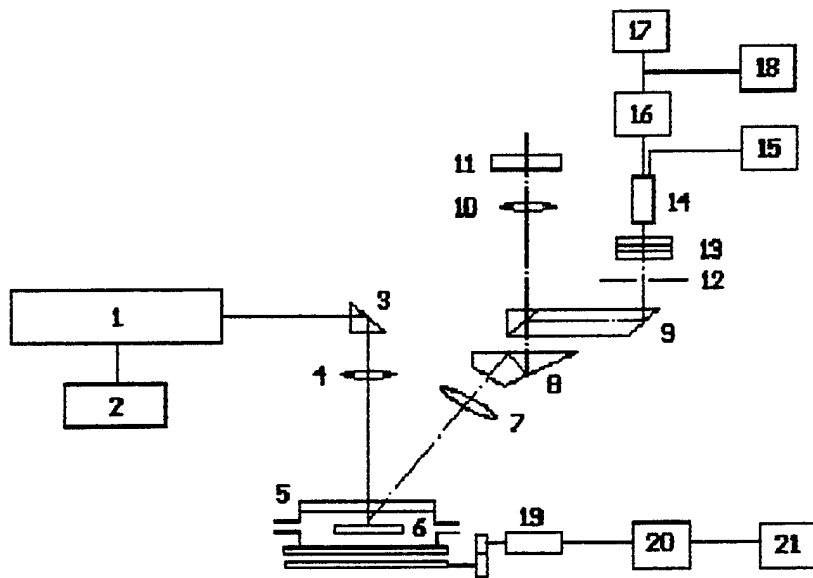


Fig.1. Experimental set up for processing the HTSC samples by the laser irradiation:

- 1. - LTI-501 laser; 2. - laser's power supply;
- 3.-turning prism; 4.- objective; 5.-sample's box;
- 6. - HTSC sample; 7. - objective; 8, 9. - prisms;
- 10. - ocular; 11. - protection light filter;
- 12. - diaphragm; 13. - interference filter;
- 14.- photo-electron multiplier; 15.- high voltage rectifier; 16.- amplifier; 17.-digital voltmeter;
- 18. - fountain potentiometer, 19. - motor;
- 20.- power amplifier; 21. - computer.

calibrated using irradiation from the ceramic in the temperature region $800^{\circ} - 1150^{\circ}$ C. The change in the surface temperature of the motionless sample during laser irradiation is shown in Fig. 2.

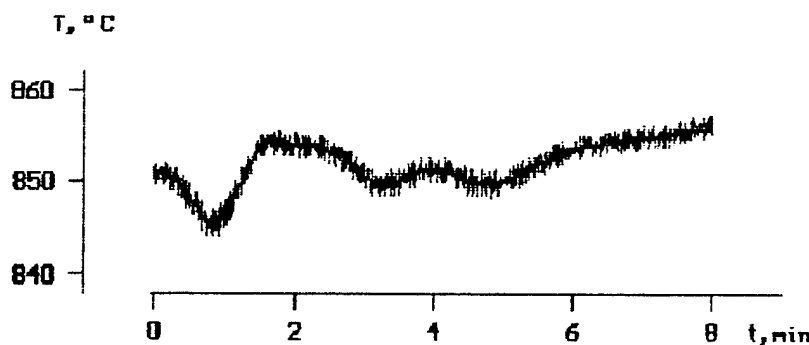


Fig. 2. Time (t) dependence of the temperature (T) on motionless sample surface.

Efficiency of the laser radiation influence on the surface of HTSC ceramic has been defined by the polycrystallinity of the sample and phase composition. Crystals in the ceramic are of different size and differently oriented to the direction of the laser beam. Because the anisotropy absorption and the distinction of the polarization characteristics on their edges the crystals absorb the laser radiation differently. As a result the surface of the ceramic sample will be heated irregularly even if the distribution of the power in laser beam is the regular. The change of the temperature during the CW laser beam scanning on ceramic surface is shown in Fig. 3A. It is seen from Fig. 3A that the temperature changing reaches 100° C and more. Multiply repeated scanning on the given route gives the same result. Such temperature fluctuations are not permissible in the process of the surface modification for carrying out regular superconductive film. The temperature stabilization is necessary.

The temperature stabilization in the laser spot was realized by laser power operating. The set up allows to carry out the process of

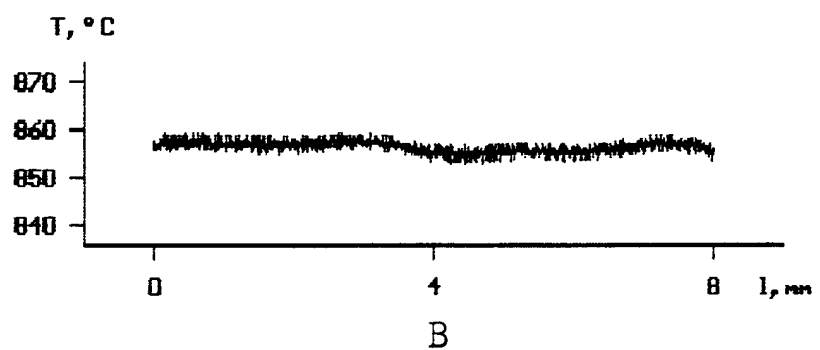
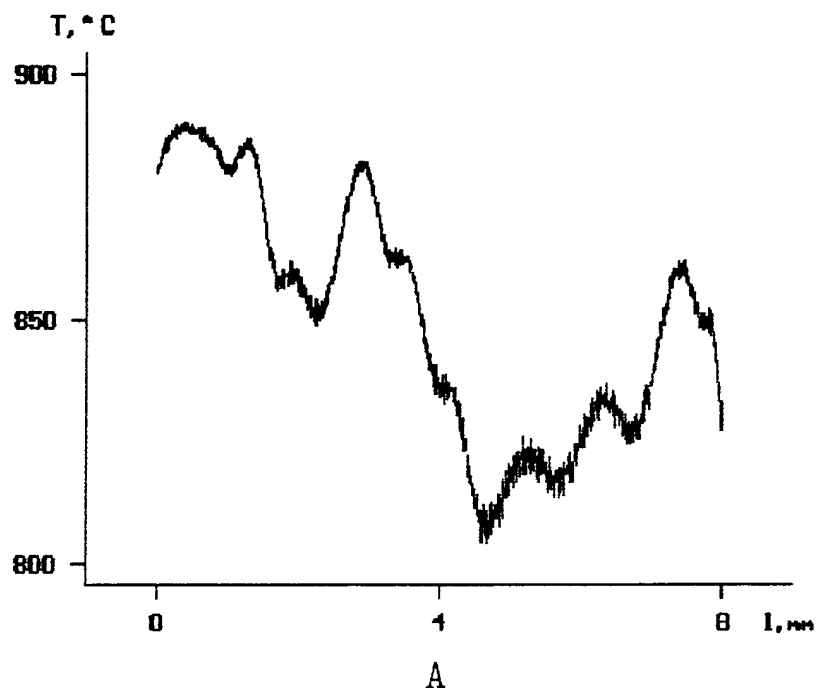


Fig. 3. Dependence of the temperature change (T) in a process of CW laser beam scanning without (A) and with (B) temperature stabilization.

the laser heating with the temperature accuracy $\pm 2.5^\circ \text{C}$ (Fig. 3B) with the space separation of the temperature sensing elements about 0.1-0.3 mm.

Measuring of the resistance was carried out using four point scheme with the current 1-10 μA . The electro-optical connections were used for increasing of the sensitivity.

3. RESULTS AND DISCUSSION

The superconductive phase was created when the average temperature in the center of the spot was in the range from 920°C to 1150°C . It was depended on the ceramic technology and the laser irradiation conditions. The concentration ratio of the superconductive and non-superconductive phases in ceramic 1-2-3 essentially depends on the cooling velocity ¹², ¹³. That is why we used the different scanning velocity.

The general characteristics of superconductive film elements which were obtained by laser processing of initial materials are the following. Their resistance monotonous reduced during the cooling process. It was equal $(5-50)*10^{-3} \text{ Ohm}$ at the temperature beside the temperature of transition in superconductive state. The width of the transition at the superconductive state was changed from 1.4 K to 5 K. The temperature at which the resistance was equal to zero lied in the range from 77 K to 88 K in different samples. The superconductivity in high quality films we received on the surface of the ceramic which have be transferred to non-superconductivity state.

The best characteristics were be reached by selecting the regime of the laser irradiation and scanning velocity.

We obtained the elements with $T_c = 88 \pm 1$ K and $\Delta T = 1.4 \pm 0.1$ K selecting the temperature and scanning velocity. These values do not depend on the characteristics of the initial ceramics. Temperature dependence of the resistance of superconductive structure after different regime of processing are shown in the Fig. 4A,B.

The temperature regime changes the structure of the ceramic surface largely. Obtained in the region of small temperature ($950^\circ\text{--}970^\circ\text{C}$) and high scanning velocity superconductive films have polycrystal structure. Them structure differ a little from it of the initial materials. Long processing regime at higher temperature gives the amorphousation of a surface. The surface became more density and had smaller distance between the grains after laser processing. The characteristics became more stable. Multiplied cooling of the obtained samples on air by dropping in liquid nitrogen during a year. We did not led any change in their superconductive features. The surface amorphysation was observed also after laser irradiation of thin films 1-2-3¹⁵.

In bulk samples obtained by the standard ceramic technology¹⁵ the density of the critical current I_c at temperature $T = 77$ K isn't in excess of 10^3 A/cm².

After the laser processing we obtained lager increasing of the density critical current. The Volt-Ampere characteristics of initial HTSC ceramic sample and the initial sample which first was transferred in non - superconductive material with following laser processing are shown in Fig.5. It is obvious that the value of the density of the critical current is larger in processed sample than in bulk one, which cross section area is much more than the film's one.

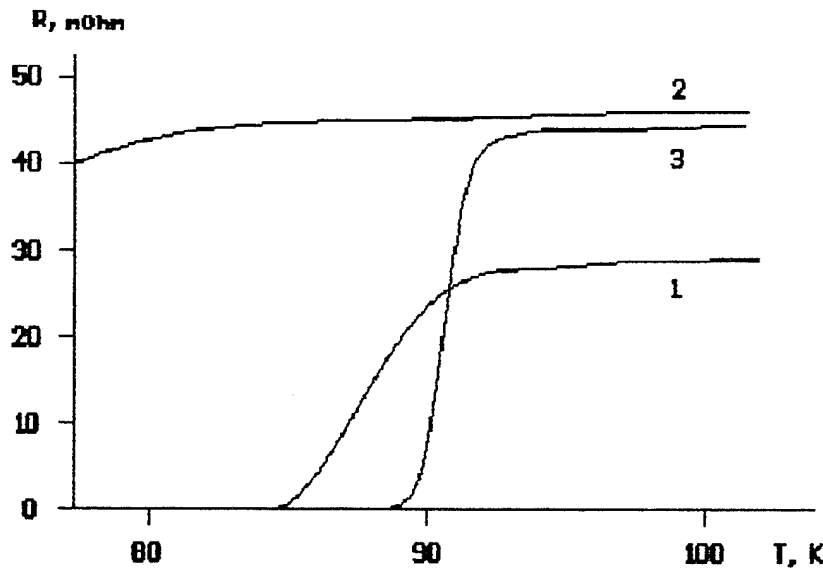


Fig. 4A. Temperature dependence of resistance of:
 1. - initial HTSC ceramic sample;
 2. - initial fritting HTSC ceramic sample;
 3. - stripe which was obtained in fritting HTSC ceramic sample

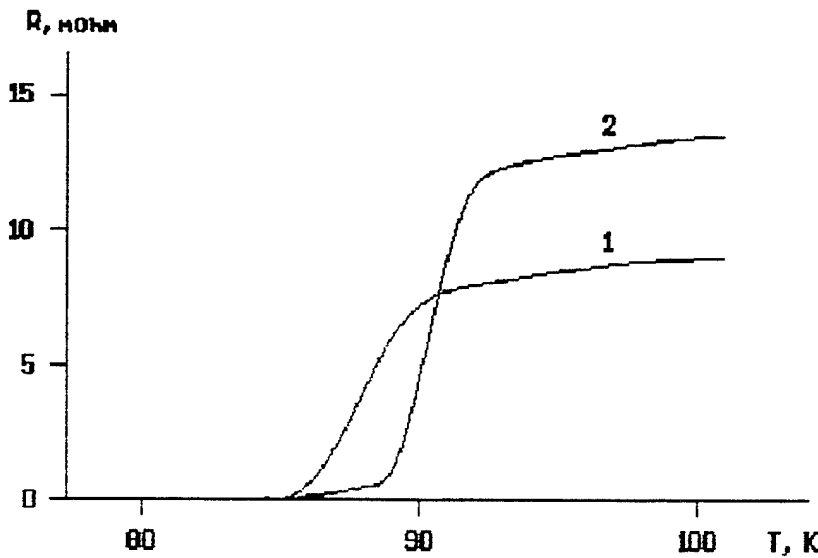


Fig. 4B. Temperature dependence of resistance of:
 1. - initial HTSC ceramic sample; 2. - the same HTSC ceramic sample with stripe in fritting HTSC ceramic sample;

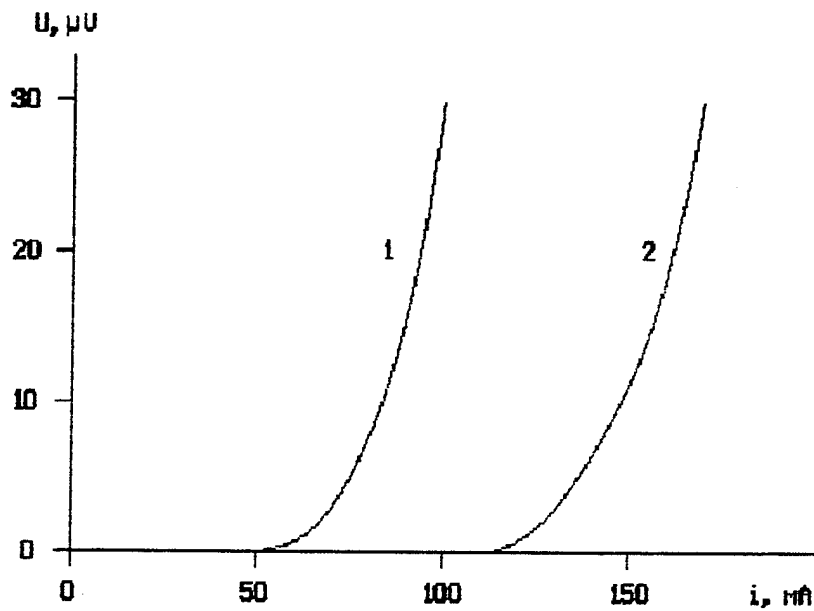


Fig. 5. Volt-Ampere characteristic of:
 1. - initial HTSC ceramic sample;
 2. - the same HTSC ceramic sample with stripe
 in fritting HTSC ceramic sample

In order to determine the density of critical current it is necessary to know the cross section area of the conductive element. It is impossible to measure exactly the thickness of forming film now. The estimation of the thinness of thin film structure were obtained when it was ground away⁸. This method is unfit for the bulk sample.

The authors have made the theoretical estimation of the depth of superconductive layer.

The temperature distribution is putted out in stationary regime of the irradiation. This distribution depends on the mode structure of the beam and its focusing. The temperature distribution inside ceramic $T(r,z)$ is possible to find from the solution of

the thermal conductivity equation ¹⁶ at given boundary conditions on the surface - $T(r, 0)$. It is found expression in a form of Bessel function $J_0(x)$:

$$T(r, z) = \int_{-\infty}^{\infty} \exp(-\lambda/z) J_0(\lambda r) \lambda d\lambda \int_0^{\infty} T(\rho, 0) J_0(\lambda\rho) \rho d\rho.$$

The results of the calculation for the Gauss distribution $T_G(r, 0) = T_0 \exp[-(r/r_0)^2]$ are given in Fig. 6 (where T_0 is the

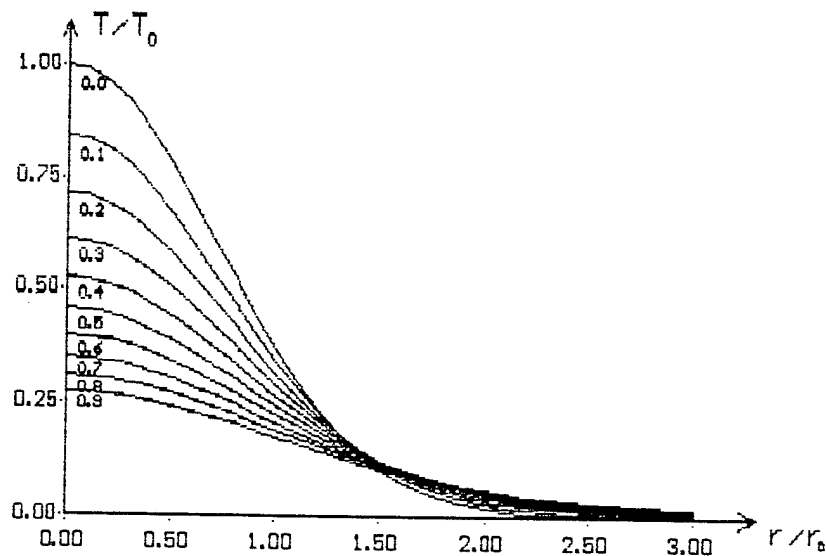


Fig. 6. Temperature distribution in YBaCuO ceramic at laser irradiation and Gauss temperature distribution on its surface, z is depth in units of r .

temperature in the center of the spot and r_0 is the parameter which depends on the beam configuration and was measured in experiment). It is possible to estimate the thickness of the film and the largest cross section area of the superconductive structure in the sample

from the curves shown in Fig. 6. They are defined by the temperature region of creation of superconductive phase $950^\circ\text{C} < T < 1150^\circ\text{C}$. The average film thickness was $5 \mu\text{m}$. The lower limit of the density of critical current makes up $2 \times 10^4 \text{ A/cm}^2$ for samples with Volt-Ampere curves from Fig. 5. I_c depends on processing regime like T_c and ΔT . We received that the value of the density of critical current lie in the range $2 \times 10^2 < I_c < 2.5 \times 10^4 \text{ A/cm}^2$ for different regimes.

4. CONCLUSION

The method of the laser processing of the bulk $\text{YBa}_2\text{Cu}_3\text{O}_{(7-\delta)}$ give us the possibility to receive the two-dimensional film superconductivity structure on its surface with $T_c = 88 \pm 1 \text{ K}$, $\Delta T = 1.4 \pm 0.1 \text{ K}$, $I_c \geq 10^4 \text{ A/cm}^2$ independently of the phase state of initial material. The surface amorphousation after the laser irradiation largely increases the stability of the superconductor's characteristics as regards to an influence of the external medium.

5. REFERENCES

1. G.Liberts, M.Eyett, D.Bauerle. "Laser-Inducted Surface Reduction of the High - T_c Superconduction $\text{YBa}_2\text{Cu}_3\text{O}_{(7-x)}$ ", Appl.Phys.A, Vol. A45, p.p. 313-316, 1988.
2. V.Orlov, J.Peregudova, V.Potapov. "Desorbtija kisloroda s poverhnosti ceramiki $\text{YBa}_2\text{Cu}_3\text{O}_{(7-x)}$, pod deistviem lasernogo izluchenija", Journal of physics and chemistry (rus), Vol. 64, p.p. 3378-3380, 1990.
3. M.Rothschild et al. Reversible laser chemically induced phase transformation in thin-film $\text{Ba}_2\text{YCu}_3\text{O}_x$ superconductors. Appl.Phys. Lett. 1988, v.52, No.5, p.p. 404-406.
4. V.Nikishkin, A.Sukhov, A.Sviridov. "Modifikatsija pljonok Y-Ba-Cu-O nanosecundnym impulsom neodimovogo lasera", Superconductivity: physics chemistry engineering (rus), Vol. 4,

p.p. 750-753, 1991.

- 5. T. Minamikava et al. "Prearation of $Ba_2 YCu_3 O_x$ superconducting films by laser evaporation and rapid laser annealing", Jap. Journ. Appl. Phys., Vol. 27, p.p. L619-L621, 1988.
- 6. Y. Umakoshi et al. "Radiation effect of $Bi_{0.7} Pb_{0.3} SrCaCu_{1-x} O_x$ irradiated by high-power short-pulsed laser", Less-Common Metals, Vol. 155, p.p. L25-L29, 1989.
- 7. M. Vjukov, A. Comarnitskij, A. Frolov. "Impulsnaja lasernaja obrabotka sverhprovodjastchih plenok Y-Ba-Cu-O", Superconductivity: physics chemistry engineering (rus), Vol. 2, p.p. 108-110, 1989.
- 8. V. Esetkin et al. "Impulsnaja lasernaja obrabotka ob'emnyh VTSP - materialov sostava $Bi_{1.6} Pb_{0.4} Ca_2 Sr_2 Cu_3 O_x$ ", Superconductivity: physics chemistry engineering (rus), Vol. 4, p.p. 1344-1346, 1991.
- 9. A. Sviridov et al. "Modifikatsija sverhprovodjastchih plenok $YBa_2 Cu_3 O_{7-x}$ impulsnym CO_2 laserom", Superconductivity: physics chemistry engineering (rus), Vol. 2, p.p. 142-148, 1989.
- 10. G. Liberts, M. Eyett, D. Bauerle. "Direct laser writing of superconducting patterns into semiconducting ceramic Y-Ba-Cu-O", Appl. Phys. A, Vol. 46, p.p. 331-334, 1988.
- 11. N. Grachjova, Yu. Denisov, Yu. Krasilov et all. "Ceramicheskie HTSC poluchennye metodami sverhplasticheskoi deformatsii i lasernoi obrabotki", Journal of low temperature physics (rus), Vol. 17, p.p. 1542-1545, 1991.
- 12. H.K. Ng et al. "High temperature phase transition in $YBa_2 Cu_3 O_x$: a thermodynamic key to the high temperature superconductivity", Solid State Commun, Vol. 65, p.p. 63-66, 1988.
- 13. R.J. Cava et al. "Single-phase 60K bulk superconductor in annealed $Ba_2 YCu_3 O_{7-\delta}$ ($0.3 < \delta < 0.4$) with correlated oxygen vacancies in the Cu-O chains", Phis. Rev., Vol. B36, p.p. 5719-5722, 1987.
- 14. H. Koinuma et al. "Reversible resisting control of $Ba_2 YCu_3 O_x$ thin films by laser annealing", Jap. Journ. Appl. Phys., Vol. 27, p.p. L652-654, 1988.
- 15. Yu. Bashkirov, L. Fleishman. "Massivnye vysokotemperurnye sverh provodjastchie materialy dlja silnotochnyh primenenii", Superconductivity: physics chemistry engineering (rus), Vol. 5, p. 1351-1382, 1992.
- 16. G. Karlsow, D. Eger. The solid state's thermal conductivity, Science Press, Moscow, 1964.

Investigation of high - T_c superconducting tunnel junction after laser radiation processing

U.U.Broslavez, A.A.Fomitchev, M.A.Yakshin

Moscow Institute of Physics and Technology, Laser Center,
Institutsky per., 9, Moscow reg., Dolgoprudny, 141700,
Russia

ABSTRACT

We investigate dynamic resistance (dV/dI) of high-T_c superconducting thin films and tunnel junction after laser radiation processing. The films of YBaCuO was prepared by laser and magnetron ablation on Al₂O₃ substrates. The tunnel junctions were made by fine silver wires attached to the processing surfaces. The resistance (dV/dI) was determined by a four-probe measurement. The YAG laser operating in Q-switched mode was used to interact with superconductors. The anomaly is observed in the current-voltage curve of the junction after radiation interaction. We observe hysteresis in shape of V(I) curve. These effects are not observed without laser radiation interaction and in this case the behavior of tunnel junction are described of the standard BCS theory.

1. INTRODUCTION

In this paper there are presented the results of the experiments on the influence of the surface condition of HTS film on the critical current of the Josephson junction after the laser impact and also the influence on the I-V characteristics of HTS film of the radiation laser with Q-switch and the pulse frequency to 50 Hz. In the experimental apparatus there is used a pumped cryostat in which the HTS film is placed in vacuum Fig.8. The I-V characteristics measurement was conducted using four-probe method at quasi-direct current.

2. THEORETICAL MODEL

In this paper there is made an attempt to explain the experimental results obtained during the investigation of the problem of improving the properties of HTS films surface deposited on laser radiation. For the achievement of this goal the influence of the laser radiation with various parameters (wavelength, power density, pulse duration) on HTS films characteristics was investigated. The film properties were studied by measuring the temperature dependence of resistance, I-V characteristics and investigating tunneling and Josephson effect on specially made structure with weak interaction and also on contacts formed by HTS surface and contacting conductor after laser radiation. The measurement of the tunnel current for superconducting contacts makes it possible to find the value of energy gap, the electron-phonon interaction constant. The probability for the particle to pass through the barrier if the barrier is higher than the energy of the particle¹:

$$\omega \approx \exp\left\{-(2 / \hbar) \cdot \int_{x_1}^{x_2} \text{Im}(p_x) dx\right\} = \exp\left\{-2\sqrt{2m} / \hbar \cdot \int_{x_1}^{x_2} [U(x) - E]^{1/2} dx\right\}$$

where the integral is taken over the area with $U(x) > E$. The probability of tunneling decreases with increasing the barrier height ($U_{\max} - E$) and width ($x_2 - x_1$). For a tunnel contact of two normal metals in the state of equilibrium there chemical potentials are equal. If the voltage is applied than all the potential drop will fall on the tunnel dielectric layer due to its high resistance and the chemical potentials will have different height. Assuming the barrier height much bigger than eV we find that the number of electrons which can jump to the free energy levels of the other metal is proportional to eV and they all pass the barrier with equal possibility. The current will then be proportional to voltage in accordance with the Ohm law². In the other case one of the metals is normal and the other is superconducting. Supposing T=0 in equilibrium if the voltage drop is zero the chemical potentials must be equal, but the electrons in the superconductor are coupled and are in bose-condensate, so the energy level of the pair will be equal to the chemical potential. In normal metal the pair corresponds to a pair of gas model quasi-particles at the Fermi level. If the electron is tunneled from the normal metal to the superconductor its energy will be Δ greater than the energy of an electron in the pair if the joint energy of the pair is 2Δ . So, to transit the electron from

normal metal to superconductor it must be given energy Δ . The possibility of the transition of the pair through the barrier is much smaller because it has a double mass and charge. If $eV \gg \Delta$ the difference between normal metal and superconductor must disappear and the current must be the same as in the tunnel contact of two normal metals:

$$J / J_n = [(eV)^2 - \Delta^2]^{1/2} / (eV) \quad (1)$$

For the tunnel contact of two superconductors the current is different from zero if $eV > 2\Delta$. The results in the following¹:

$$J / J_n = E\{[(eV)^2 - (2\Delta)^2]^{1/2} / (eV)\} - 2(\Delta / eV)^2 K\{[(eV)^2 - (2\Delta)^2]^{1/2} / eV\}$$

where K and E - full elliptical integrals:

$$K(k) = \int_0^{\pi/2} (1 - k^2 \sin^2(\phi))^{-1/2} d\phi$$

$$E(k) = \int_0^{\pi/2} (1 - k^2 \sin^2(\phi))^{1/2} d\phi$$

In this equations if $eV \rightarrow \infty$, $J/J_n \rightarrow 1$ but in difference to the case of the contact of normal metal with superconductor the subcritical current is at $eV=2\Delta$ and the subcritical current has a finite jump at $V=0$. The equations above were derived under the condition of $T=0K$ and in case of finite temperature there must be substituted the dependence $\Delta(T)$ and the distribution at finite temperatures². In the contact of metal and superconductor at finite temperature there are some uncoupled electrons and so part of the electrons may pass through the contact without energy loss Δ . On the other hand there is a possibility for the electron to make a pair. Thus at finite temperature and any little voltage drop V there is a current in the contact. At T different than T_c the current significantly grows at the moment $eV=\Delta(T)$ which corresponds to the moment of mass discoupling. Thus it is convenient to measure $\Delta(T)$ at maximum of dJ/dV derivative. It is worth to mention that besides the current related with the transition of the quasi-particles trough the contact there is also superconducting current at $V=0$ which is due to the formation of the coherent state in the system of the contact superconductor-superconductor. It is possible for the two electrons from different metals to form a Cooper pairs in the contact of two superconductors. It leads to the possibility of tunneling with the probability comparative with the probability of one electron tunneling and formation of condensate. The current through the contact may be found as^{1,2}:

$$J = J_c \sin(\phi_1 - \phi_2)$$

where the critical current through the contact for two superconductors at finite temperatures is given by the equation¹:

$$J_c = [\pi\Delta(T) / 2eR] \text{th}[\Delta(T) / 2T]$$

$$T = 0 \Rightarrow J_c = \pi\Delta / 2eR$$

$$T \rightarrow T_c \Rightarrow J_c \cong \pi\Delta^2(T) / (4eRT_c)$$

where R - the resistance of 1 cm² of the contact square and has a dimension of Ohm cm², $\phi_1 - \phi_2$ - phase difference of the wave functions of the superconductors on the both sides of the weak tunnel junction, for the dependence $\Delta(T)$ there are the equations corresponding to the BCS theory³ in the limits:

$$\text{if } T \rightarrow 0 \text{ then } \Delta(T) = \Delta_o \left\{ 1 - \sqrt{2\pi T / \Delta_o} \exp(-\Delta_o / T) \right\}$$

$$\text{if } T \rightarrow T_c \text{ then } \Delta(T) = T_c \sqrt{8\pi^2 / [7\xi(3)](T_c - T) / T_c}$$

where $\xi(x) = \sum_1^{\infty} (1/n)^x$ -the Riman function;

$$\Delta_0 = 2hW_D \exp\{-1/(N_0 V)\}$$
 - gap at T=0;

N_0 -state density on the Fermi surface;

V - the electron-phonon interaction potential ².

For the BCS theory there is valid the equation:

$$2\Delta_0 = 3.52kT_c$$

-corresponding the condition $\Delta(T_c)=0$

3. EXPERIMENTAL PROCEDURE.

In this paper we present the results of the experiments on the influence of the high-temperature superconductivity (HTS) film surface state on the Josephson-junction critical current after the laser deposition and also the influence of the laser radiation on the I-V characteristics of the HTS film at boiling N₂ temperature. We have found some interesting dependencies V(J), for example there were obtained the characteristics in which at some temperature T=80 K the linear dependence V(J) j Fig. 1 dumped into the curve shown in Fig. 2-4 that is in accordance with the classical theory and corresponds to the superconducting and non-superconducting currents balance. The measurements were taken at the boiling N₂ temperature but the contacts were oxygenated in air for two days. When the same experiment was taken with well cleaned contact surfaces there measured the following characteristics Fig. 1. In the first experiment the silver contacts surface was covered with Ag₂S layer, and so the isolating layer functioning as a barrier was formed, and in the second experiment the Ag₂S layer could not be formed as the experiment was taken in vacuum. In accordance with the above mentioned theory the existence of the barrier should lead to tunnel current between the superconductor and the metal contact in accordance with the formula (1) Fig. 0. As zero resistance was not achieved in the experiments without the Ag₂S film, it means that together with the superconducting condensate, the current is conducted also by usual electrons. That's why on our experimental dependence there is no such current jump as in Fig. 0. The dV estimation is in accordance with the experimental data ⁶. The described experiment gives one more way for investigation of the surface of HTS film allowing more accurate determination of the superconducting phase occurrence than the magnetic method or determining the superconducting transition from the R(T) dependence. At some film after the laser radiation deposition there where obtained the dependencies Fig. 5-7 in which after every radiation pulse train with the total energy in train of 0.5 J/cm² the slope and form of the curves changed. The anomaly is observed in the current-voltage curve of the junction after radiation interaction. We observe hysteresis in shape of V(I) curve. These effects are not observed without laser radiation interaction and in this case the behavior of tunnel junction are described of the standard BCS theory. The observed hysteresis may be explained by partial HTS film destruction and S-N-S contacts formation which at some measurement regimes may give such dependencies.

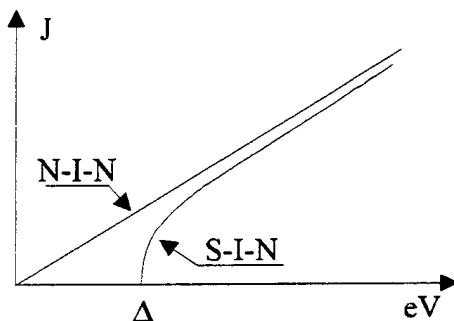


Fig.0.

4. CONCLUSION

We have investigated dynamic resistance (dV/dI) of high-Tc superconducting thin films and tunnel junction after laser radiation processing. We have observed the anomaly in the current-voltage curve of the junction after radiation interaction. We observe hysteresis in shape of V(I) curve. These effects are not observed without laser radiation interaction and in this case the behavior of tunnel junction are described of the standard BCS theory.

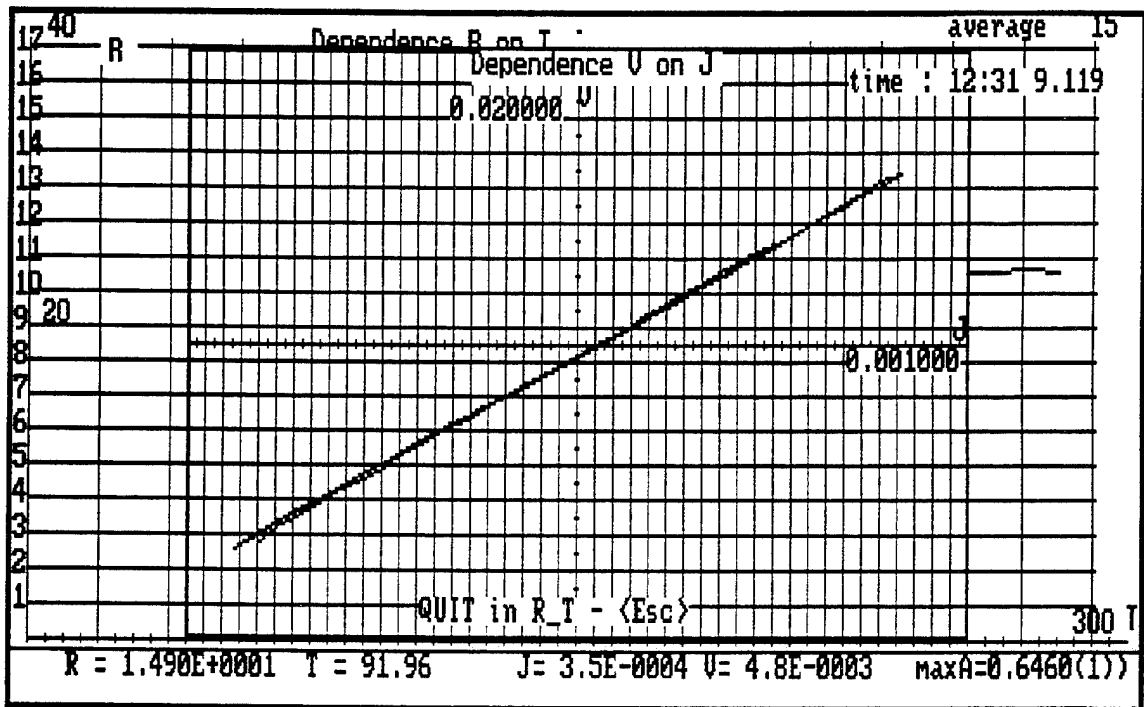


Fig.1.

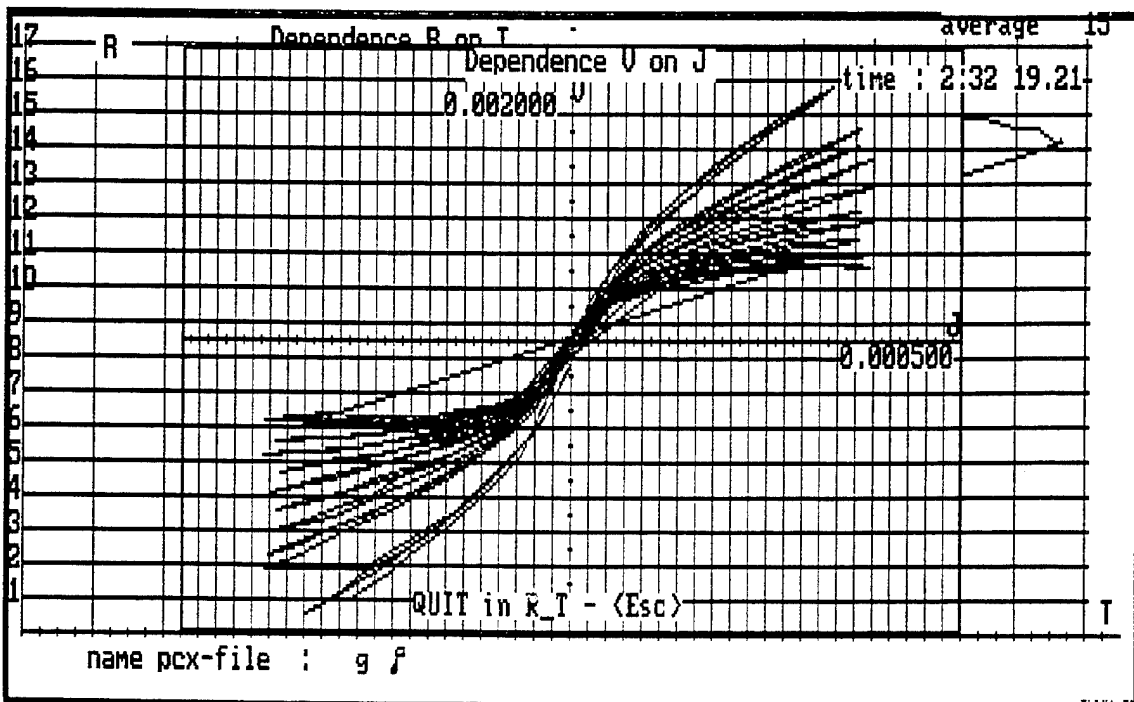


Fig.2.

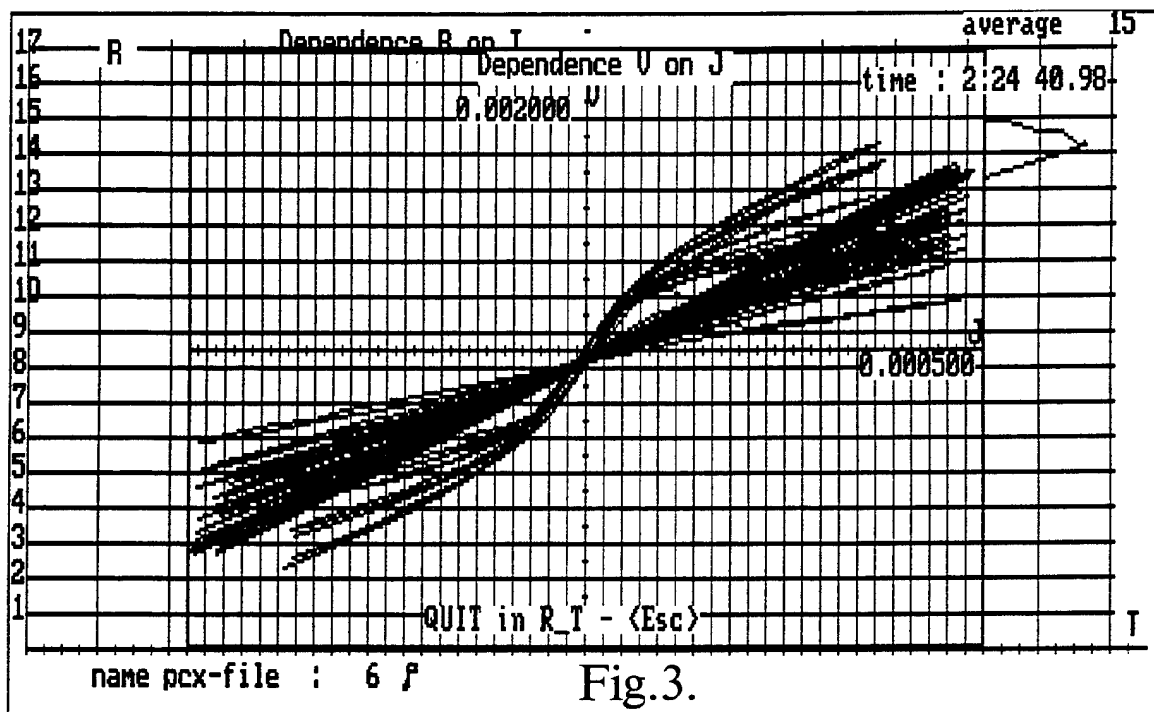


Fig.3.

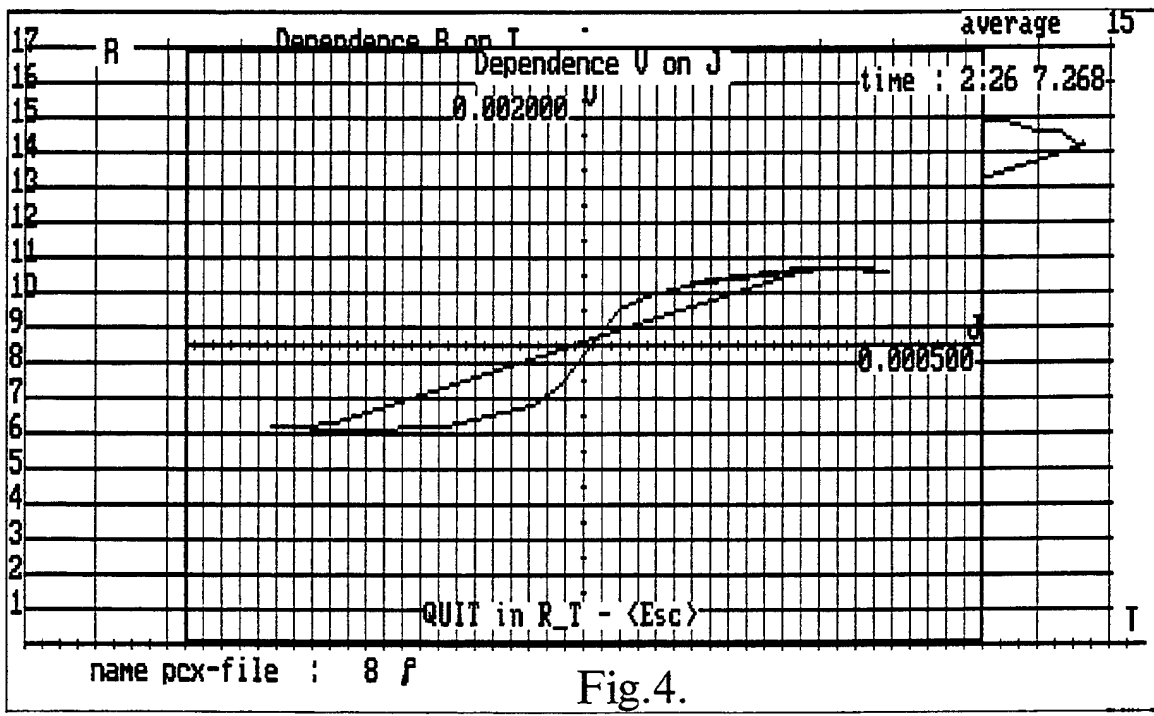


Fig.4.

Fig. 2-4. The characteristics in which at temperature $T=80$ K the linear dependence $V(J)$ jumped into the curve that is in accordance with the classical theory BCS and corresponds to the superconducting and non-superconducting currents balance.

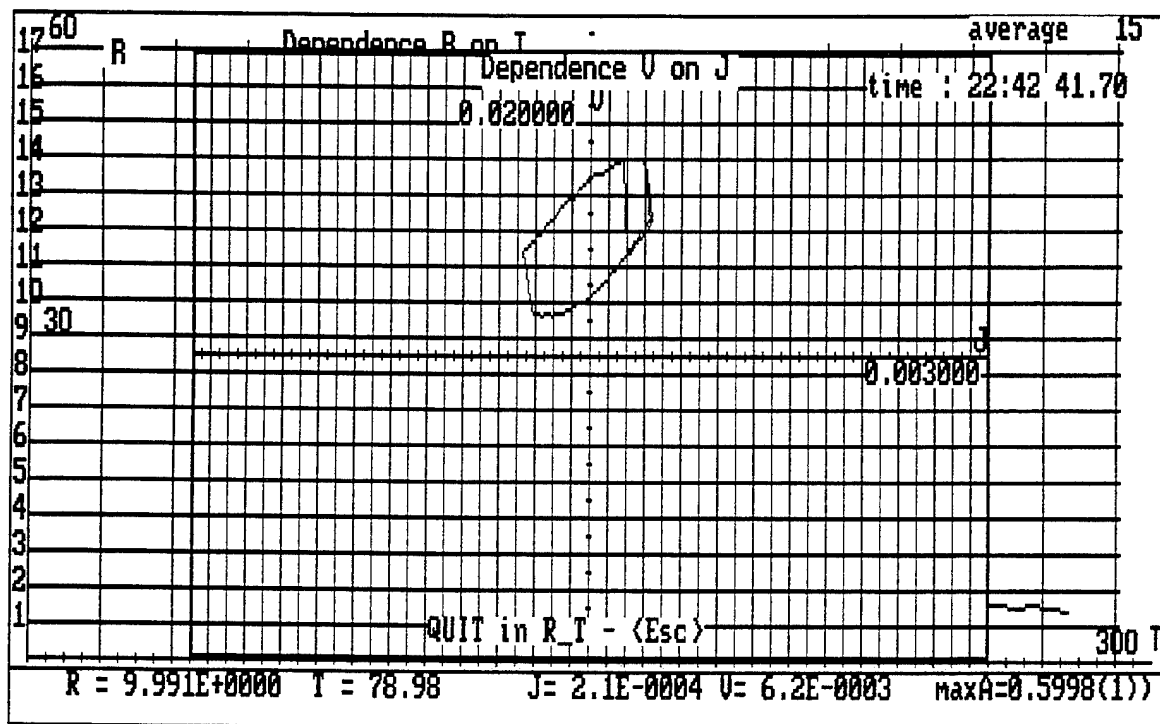


Fig.5.

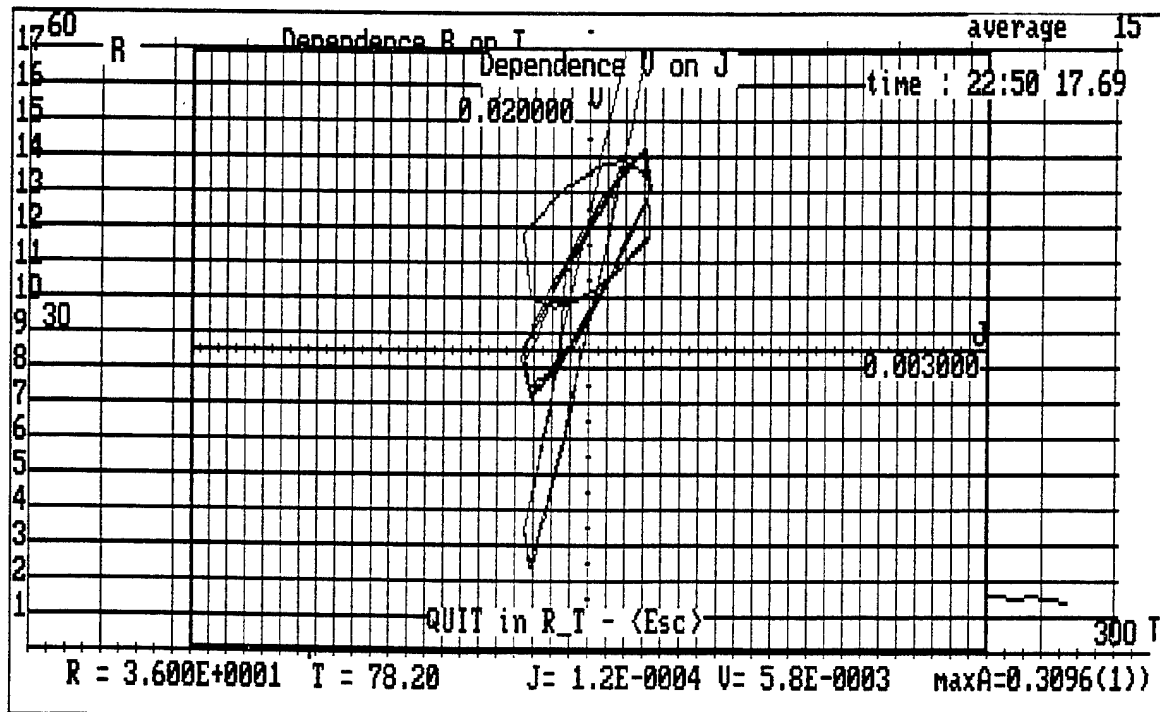


Fig.6.

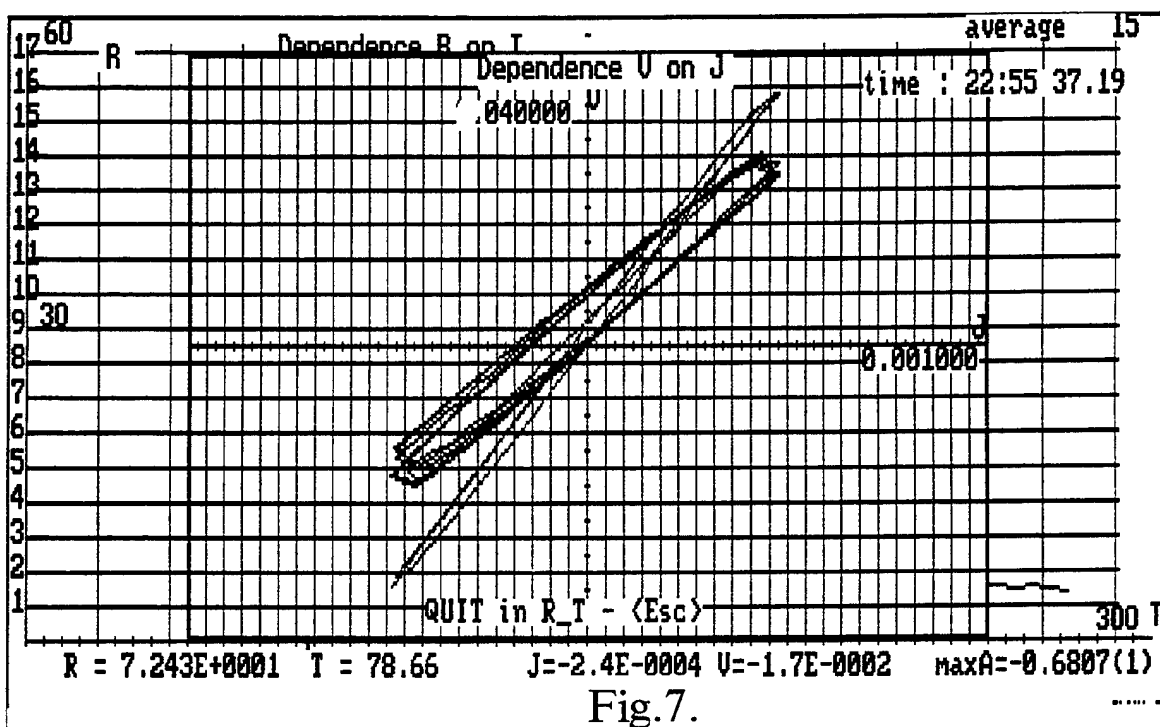


Fig.7.

Fig.5-7. There where obtained the dependences in which after every radiation pulse train with the total energy in train of 0.5 J/cm^2 the slope and form of the curves changed. The anomaly was observed in the current-voltage curve of the junction after radiation interaction. We observed hysteresis in shape of $V(T)$ curve.

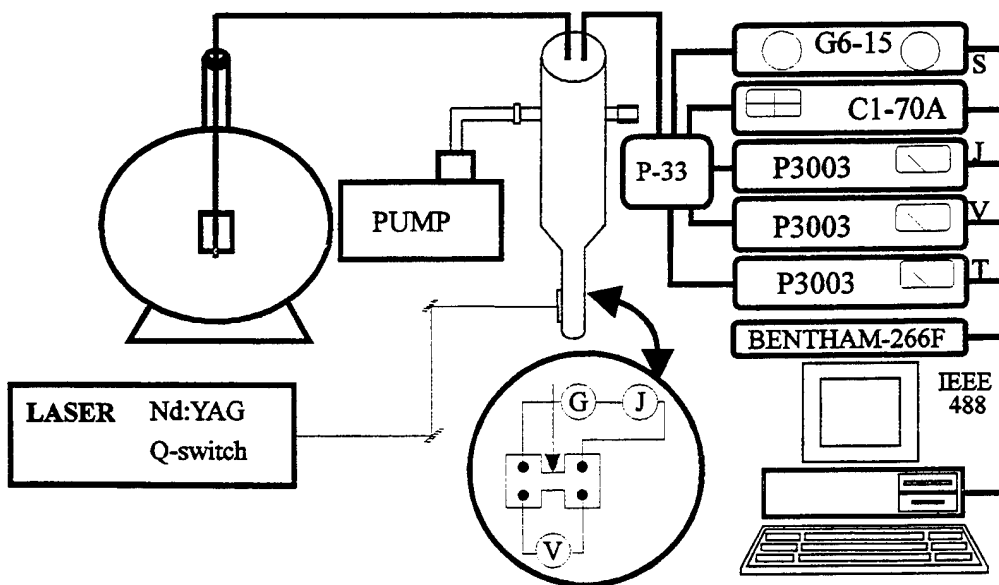


Fig.8.

5. REFERENCES

1. A.A. Abrikosov, "The foundations of the metals theory" Nauka, Moscow 1987
2. N.V. Zavaritsky, "Superconductivity". MPTI, Moscow 1985.
3. S.T. Belyaev, U.A. Bychkov, S.A. Gordunin, A.V. Iljin, V.P. Kuznetsov, L.A. Maksimov, V.P. Mineev, V.P. Smilga, "The theory of condensed state" MPTI, Moscow 1990.
4. A.S. Davydov, "High temperature superconductivity" Naukova Dumka, Kiev 1990.
5. V.S. Edelman, "The development of scanning tunneling and power microscopy" // Pribory i technika experimenta. 1991. N1 pp. 24-42.
6. Wiener-Avnear E., E. Cooper. et al., "Laser patterning of YBaCuO weak link bridges" // IEEE transactions on magnetics. V.25. No. 2. pp. 935-938, 1989.
7. D. Nelson, M. Wittingham, T. George, "High temperature superconductors" Mir, Moscow 1988.

Electric-current-stimulated diffusion of heavy ions and oxygen in YBCO (123) and Bi (2223)
HTCS films at 4.2 - 300 K

E.N. Lubnin, G.N. Mikhailova, A.M. Prokhorov, A.S. Seferov, A.V. Troitskii,
D.G. Andrianov*, S.O. Klimonskii*

General Physics Institute RAS, Vavilov str. 38, Moscow 117942, Russia

* State Institute of Rare Metals, Moscow, Russia

ABSTRACT

The results of the study of electrostimulated diffusion in polycrystalline and epitaxial YBCO (123) and ceramic Bi (2223) HTCS films give evidence of the motion of heavy ions and oxygen under the transport superconducting current flow.

Long-duration d.c. flowing in films in the superconducting state at 4.2 and 77 K leads to new morphological forms with modified chemical composition, formation of nonsuperconducting phases. The effect in the high-quality epitaxial films exists, but it is weaker.

Long-duration flowing of high-power 36 GHz current leads to formation of periodic strip structures enriched with copper and oxygen. The experiments with thick (25 μm) Bi (2223) films reveal modified stoichiometry practically over the entire film. At 300 K the YBCO (123) system is shown to have the ionic conduction component. Possible mechanisms of the observed experimental effects are discussed.

1. INTRODUCTION

Experimental study of the samples of oxide HTCS showed that their initial characteristics are unstable and modified under the action of different chemical and thermal factors¹⁻³, deformations⁴, long-duration current flowing at high temperatures⁵. The causes of these phenomena are different, but they seem to be connected not only with imperfect technologies of manufacturing the samples, but also with specific features of crystallochemical structure of these substances^{6,7}.

We payed attention that owing to its crystallochemical properties, the YBaCuO system reminds superionic conductors much more than stable stoichiometric oxides. The transport of ions caused by the current flow in such a structure may lead to the formation of crystallochemically stable compounds. We presumed that these properties may hold also in the superconducting state. Experiments confirmed this supposition and for the first time the electrochemical reaction in the superconducting film was observed at 4.2 K^{8,9}.

In there experiments^{8,9} we used polycrystalline films (with weak links between superconducting granules) and the effects were easily observed, but later the same effects were discovered at higher-quality samples of Y¹⁰⁻, Bi¹¹⁻ and Tl-based systems¹², Y-ceramics¹³ with specific features dependent on temperature (at lower temperatures the effect is smaller), structural

perfection (the strongest modification occurs in granular ceramic samples and polycrystalline nonoriented films), current frequency.

The phenomenon of electrostimulated diffusion seems to be inherent in HTCS systems and its study is important from the fundamental and practical point of view.

2. SAMPLES AND METHODS OF INVESTIGATION

We studied polycrystalline YBCO (123) films 2–3 μm thick on (YSZ) substrates obtained by the condensate-diffusion method, textured epitaxial films on MgO and LaAlO₃ substrates obtained by magnetron sputtering and laser deposition, and Bi (2223) ceramic films on Ag substrates.

The samples had 4 indium contacts. The inner ones were used for potential measurements, and through the outer contacts the transport superconducting current was passing for many hours (days). The samples were placed in an ampule filled with gaseous helium at the atmospheric pressure plunged into liquid helium or nitrogen.

Scanning electron microscopy, energy-dispersive X-ray microanalysis (Camscan-4, EDX Link), diffractometry, Auger-spectrometry, statistical analysis were applied to the film characterization and comparison with the reference samples. Dependences $R(T)$ were measured by the 4-probe resistive method.

3. FIRST RESULTS ON THE ELECTROSTIMULATED MODIFICATION OF SUPERCONDUCTING FILMS AT 4.2 K

Here we briefly describe the experimental results^{8,9}, where for the first time the modified chemical composition and film morphology were observed under the influence of long-duration superconducting transport current flowing.

The experiments were carried out at polycrystalline Y₁Ba₂Cu₃O_{7-x} films about 3 μm thick. The analysis showed them to be homogeneous and single-phased, with the grain structure (3–5 μm in size) and nonoriented c-axis.

The superconducting current lower than the critical one ($I = 0.3I_c$) was passing through the sample with the 2 dimensions of 12 × 5 mm² for 166 hours, and the charge transferred through the film was 2.7×10^4 C. After that the parameters of the superconducting transition remained practically unchanged.

To characterize the film morphology and composition before and after the experiment, SEM Camscan-4 with the energy dispersive X-ray analysis (EDX Link) was used.

The phase contrast in the reference sample is uniform, the surface is smooth. After the current flowing a “road” with an irregular surface was formed between the electrodes. The phase contrast of the experimental sample is nonuniform, scaled formations with sizes of 1–20 μm are observed mainly near electrodes.

The total composition was determined on the areas of 300 × 300 μm near the electrodes and in the center. The content of Cu was higher by 4–6 wt.% in the initial film than after

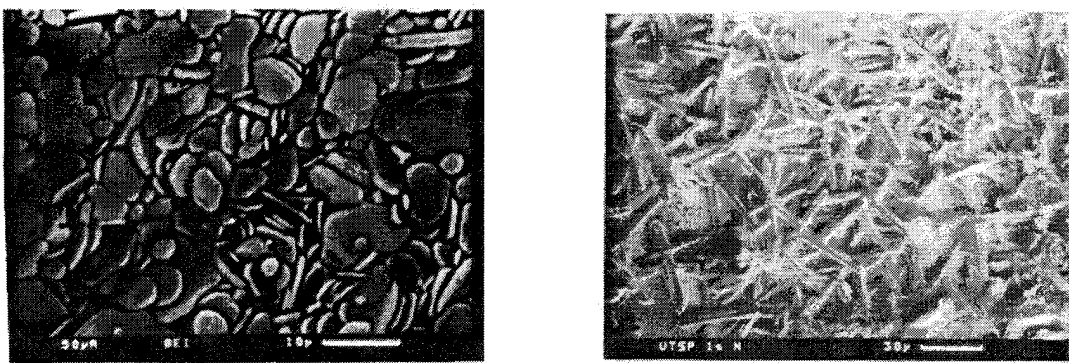


Fig. 1. Microphotograph (BEI) of the initial YBaCuO (123) film. The mean grain size is 3–5 μm .

Fig. 2. Microphotograph (BEI) of the modified area of (123) at 77 K.

the experiment (the relative error was 2%) and by 2–3 wt.% for Ba. The local composition was studied with the a spatial resolution of 1 μm . In the initial sample a high homogeneity was found, and after the current flowing point formations with CuBaO₂ composition were revealed. In addition, statistical processing of the results showed that the region near the negative electrode is enriched with Cu by 4 wt.% in comparison with the positive one. In some areas the Cu concentration was up to 38 wt.%. That was the first evidence of the mass transfer accompanying the superconducting current.

4. ELECTRODIFFUSION OF HEAVY IONS IN YBaCuO AT 77 K COMPARISON OF POLYCRYSTALLINE AND EPITAXIAL FILMS¹⁰

It was important to investigate the stability of HTCS films at 77 K, because this is the working temperature for the HTCS devices. From the technological point of view the stability of HTCS is the key problem. The experiment was carried out in the same scheme. The samples similar to those studied at 4.2 K were studied at 77 K (see Fig. 1). The studied and reference polycrystalline samples were mounted at $T = 77$ K at helium atmosphere close to each other. The d.c. of 1 mA ($0.3 j_c$) was passing during 575 hours. Before and after the experiment the characteristic of the superconducting transition $R(T)$ was measured, and the composition and morphology studies were performed. The effect at 77 K for polycrystalline films is shown in Fig. 2. The formation of needle-like crystals is rather homogeneous over the whole sample. The superconducting transition curve remained practically unchanged indicating that nonsuperconducting phases do not entirely block the film cross section.

Similar experiment was carried out for epitaxial textured films 0.5 μm thick on MgO substrates obtained by magnetron sputtering in oxygen. The disorientation in c-plane was within 1°, in ab-plane — 2.5°, j_c (77 K) = 10^6 A/cm^2 . The resistance of aluminum electrodes with vanadium sublayer was $\sim 10^{-2}$ Ohm. The current density $j < j_c$ was passing for 70 hours through the film, which was controlled to stay in the superconducting state. The charge of 10^5 C was transferred. As a result, the migration of Cu and O ions to opposite electrodes was found (see Fig. 3).

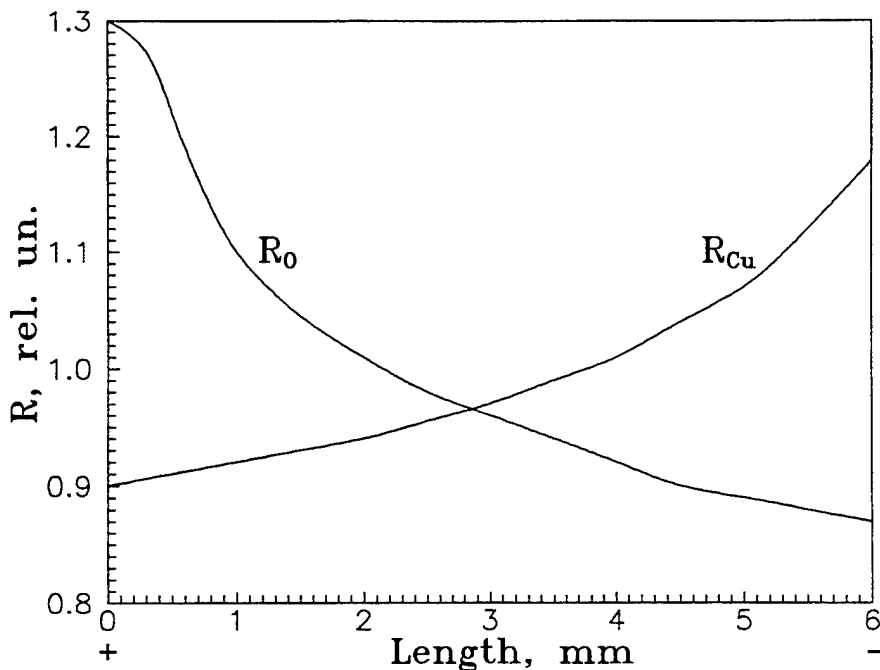


Fig. 3. Spatial distribution of Cu and O in the epitaxial (123) film after d.c. flowing. $R = 1$ corresponds to the stoichiometric concentration.

In contrast to the case of polycrystalline films, the surface modification of epitaxial ones are not so dramatic. The migration process leads to the change of specific volume of grains. Their boundaries become deeper, and the film – more porous (from 100 nm to 150 nm) (see Fig. 4 and 5).

The study of high-quality thin and narrow (bridge-type) epitaxial films (laser deposition, $100 \mu\text{m} \times 0.24 \mu\text{m}$, $j_c = 3 \times 10^6 \text{ A/cm}^2$) revealed a modification of the superconducting transition curve. After the charge $Q \approx 10^5 \text{ C}$ passed through the film, a step appeared in the transition curve (Fig. 6).

Thus the diffusion and decomposition effects exist also in quasi-monocrystalline films, but they have specific features. This study shows that the problem under consideration is complex, and we must distinguish the fundamental crystallochemical factors and the causes connected with the structural perfection, intergrain boundaries and other mechanisms.

5. DECOMPOSITION PROCESSES IN A HIGH-POWER MICROWAVE FIELD

Analyzing the probable causes of ion diffusion in the superconducting state, we may suspect the electrodes to be sources of heating and gradual destruction of superconductivity of separate grains and development of superionic processes. Therefore, it was important to study these effects by contactless methods at the microwave frequencies. In addition, the application of HTCS elements as microwave devices demands detailed investigation of electrostimulated diffusion of ions in this field.

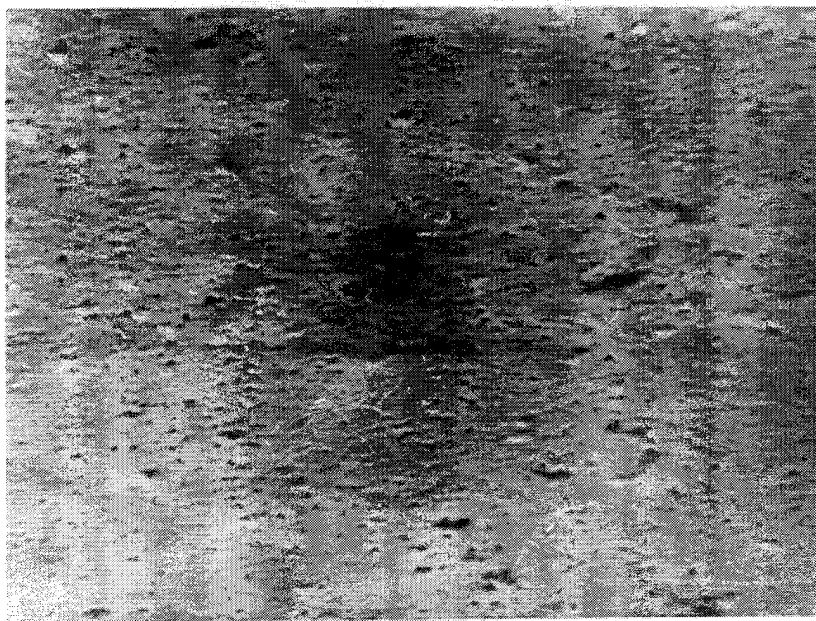


Fig. 4. Surface microphotographs of the epitaxial film before current flowing at 77 K. The area is $8 \times 11 \mu\text{m}^2$.

In the microwave field the absorption always exists even in usual superconductors (LTCS), because the alternative motion of carriers is always connected with the internal electric field. For instance, estimates show that at $f = 50 \text{ Hz}$ and $I = 1 \text{ A}$ the internal electric field is $E_i = 10^{-12} \text{ V/cm}$. With the diminishing T the microwave absorption decreases, because the number of absorbing normal carriers reduces.

The film (123) YBCO under study on a single-crystal LaAlO_3 substrate was $0.3 \mu\text{m}$ thick with the size of $8 \times 10 \text{ mm}^2$, $T_c = 84 \text{ K}$, $j_c = 10^4 \text{ A/cm}^2$ (this film was obtain by method of magnetron deposition). It replaced a part of the wide wall of the microwave resonator, and the microwave current much lower than the I_c was flowing through the film for 30 hours at $T = 77 \text{ K}$. The generated microwave power was 5 W at the frequency of 36 GHz.

As a result, convex formations $\sim 2 \mu\text{m}$ sized with prevailing light elements (Cu, O) and new strip periodical structures (Fig. 7) with a period of $\sim 10 \mu\text{m}$ were formed¹⁴. Superconducting properties were not lost, although j_c became lower — 10^3 A/cm^2 . These results can be treated within the framework of a new spatial-time model of a dissipationless current flow¹⁵ that leads to an anomalous ion diffusion from the current-carrying regions, formation of Cu- and O-enriched phases and their “freezing”, which are experimentally observed. The spatial parameter deduced from this theory is close to the period of the experimentally observed structures.

6. RECRYSTALLIZATION AND IN-SITU EXPERIMENTS IN YBaCuO FILMS AT 300 K UNDER D.C. FLOWING

In order to study the current-carrying properties of the YBCO (123) system in nonsuper-

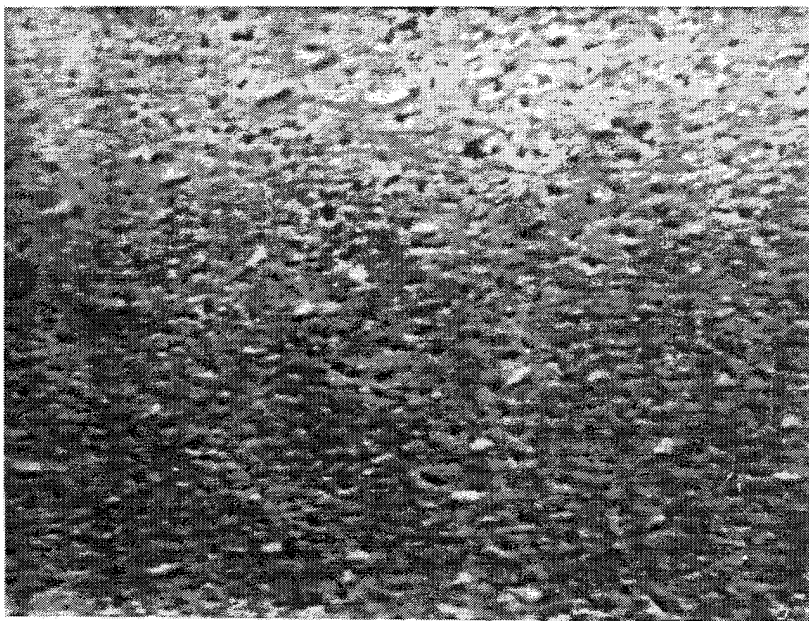


Fig. 5. Surface microphotographs of the epitaxial film after current flowing at 77 K. The area is $8 \times 11 \mu\text{m}^2$.

conducting state we performed the experiments at 300 K. As was already mentioned, chrystallochemical properties of new oxide superconductors are close to solid electrolites, and this determines a mixed character of their conductivity and its ion component. It was expected that during the superionic current flow the forming crystallochemically stable compounds may block the current channels, and this should result in an inhomogeneous distribution of new phases between the electrodes. In addition it was necessary to measure the diffusion characteristics of this material.

The samples of YBaCuO similar to those studied at 4.2 K were studied at 300 K (see Fig. 1). The resistance of the film and the summary resistance of two contacts were 43 and 3 Ohm, respectively. The direct current of 28 mA ($j = 600 \text{ A/cm}^2$) was passing through the film during 336 hours.

In contrast to the reference sample that remained unchanged, in the experimental one a boundary dividing the regions of the positive and negative electrodes appeared approximately in the center. Near the positive electrode there appeared needle-like, prismatic and triangular crystals resembling those at 77 K (see Fig. 2). New phases – Y_2BaCuO_x , $\text{YBa}_2\text{Cu}_3\text{O}_y$, BaCuO_z , CuO_5 – were revealed by X-ray spectral measurements in the modified film areas. Near the negative electrode the film morphology and chemical composition remained unchanged.

In the second experiment with the similar sample (transport current density was $3 \times 10^3 \text{ A/cm}^2$) the total charge transfer was $2.9 \times 10^3 \text{ C}$. Periodically the current was switched off and the sample was measured by the four-probe method. It was found that the film resistance was

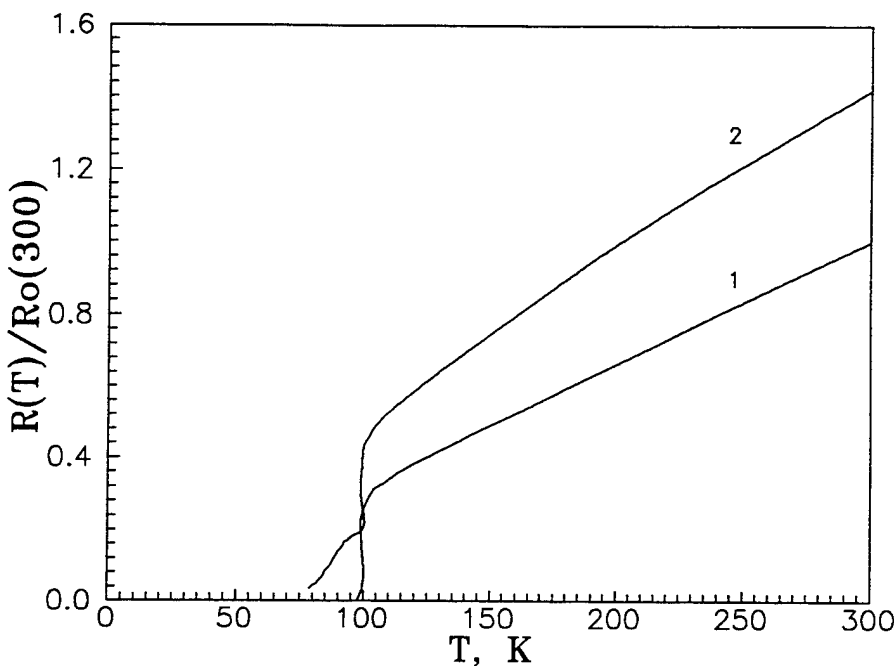


Fig. 6. Temperature dependences $R(T)$ for a high-quality epitaxial film $0.3 \mu\text{m}$ thick before (1) and after (2) current passing at 77 K .

growing as a function of the transferred charge from 24 up to 35Ω

In-situ SEM experiments showed that at a short-duration current flowing (0.5 s , 300 mA) through two needle electrodes applied to the film with the distance of 0.5 mm between them the region of the positive electrode is enriched with Cu.

Using local heating of various parts of the film up to 600 K with the help of electron beam we estimated the thermodiffusion coefficient D for Cu ions, which varied within a large range from 10^{-3} to $10^{-8}\text{ cm}^2 \cdot \text{s}^{-1}$ in different probed areas. Such a spread of D , in our opinion, is due to the film inhomogeneity and presence of carbon impurities on its surface.

The obtained results show a high ion mobility in (123) film at room temperature. Essential morphological modifications of the film surface and large distance of the ion transfer may indicate that this process in YBaCuO film is realized not by the usual thermodiffusion mechanism. The results of this study confirmed a mixed character of the conductivity and an essential contribution of the ionic component.

7. ELECTROSTIMULATED DIFFUSION IN $(\text{Bi},\text{Pb})_2\text{Sr}_2\text{Ca}_2\text{Cu}_3\text{O}_8$ HTCS FILMS AT 4.2 K ¹⁷

Bi-based HTCS are of special interest being chemically more stable than YBCO material. They have high critical parameters and are promising for high-power current application, such as creation of superconducting cables and wires. The films under study were prepared by depositing the superconducting powder on silver substrates with subsequent cyclic pressing, rolling

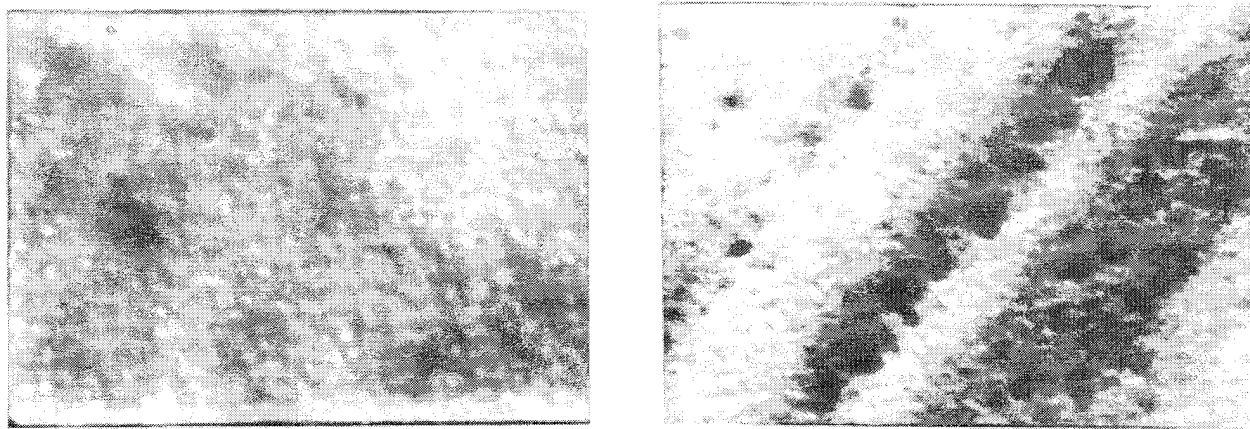


Fig. 7. SEM microphotographs of HTCS (123) film before (*a*) and after (*b*) the microwave current flowing at 77 K. The area is $30 \times 40 \mu\text{m}^2$.

and annealing¹⁶. Their characteristics and size are: $T_c = 105 \text{ K}$, $j_c \sim 900 \text{ A/cm}^2$ (77 K, 20 Oe) and 3300 A/cm^2 (12 K, 20 Oe), $10 \times 5 \text{ mm}^2$, $\sim 25 \mu\text{m}$ thick. The ampule containing two similar samples was filled with heat-exchange helium and plunged into liquid helium. After the d.c. flowing in the superconducting state for 400 hours at 4.2 K remarkable changes in the initial film composition and surface morphology were found. X-ray spectral microanalysis reveals small areas of chemical inhomogeneities including Ca_2CuO_3 . Quantitative statistical characteristics of inhomogeneities accumulated on the film surface in the course of current flowing are obtained.

Fig. 8 shows the resultant morphology of Bi (2223) film¹⁷ (SEM, secondary electrons, charge transferred $Q = 31500 \text{ C}$). Needle-like particles present a new phase Ca_2CuO_3 . Dark regions are depleted of heavy elements.

The phase composition before and after current flowing was determined by diffractometry with the subsequent identification of phases with standard diffractograms for HTCS phases.

Chemical inhomogeneities, volume fractions of phases were determined using the statistical method of X-ray microanalysis (Camebax-Micro).

The initial films are smooth. The prevailing phase is the tetragonal modification of (2223) phase. The identified phases are: CuO , SrO , Bi_2O_3 and (2223) — 85%. As a result, a more precise composition of the initial film is determined: $\text{Bi}_{1.7}\text{Pb}_{0.2}\text{Sr}_{1.7}\text{Ca}_{1.8}\text{Cu}_{2.5}\text{O}_{8.5}$. To obtain more detailed data on chemical inhomogeneities that appeared after the superconducting current flowing we used statistical processing of the results of X-ray spectral microanalysis and showed that the modifications of the initial chemical composition are accumulated over the entire film. To construct the correlation matrix, we calculated the coefficients of linear correlation for pairs

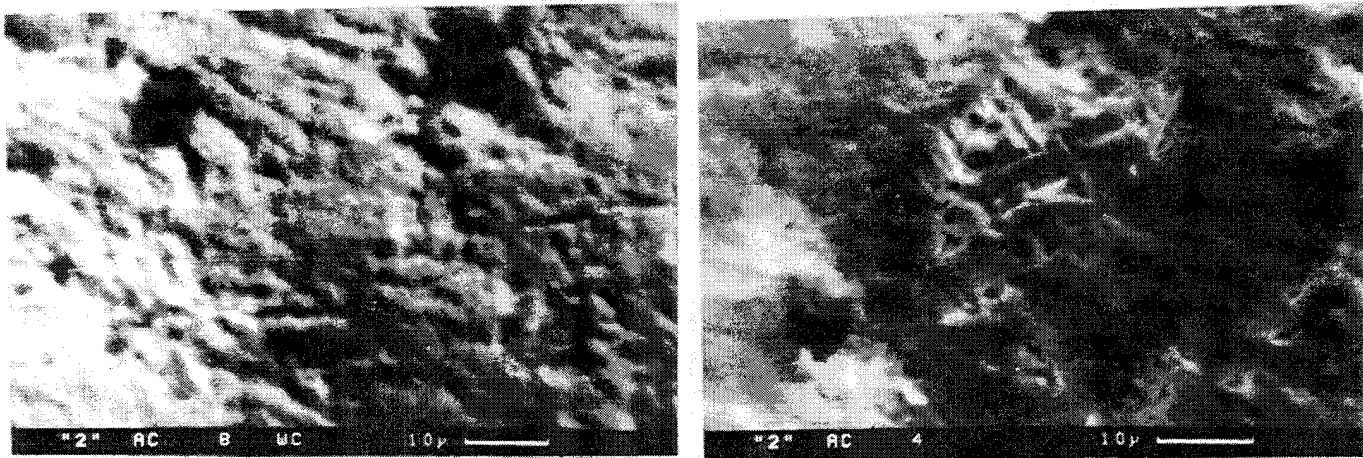


Fig. 8. SEM microphotograph (secondary electrons) of a section of Bi (2223) ceramic film surface before (a) and after (b) 440 hours of transport superconducting current flowing at 4.2 K. Needle-like particles belong to a new Ca_2CuO_3 phase. Dark regions are depleted of heavy elements.

of elements:

$$r_{i=1}^N(A, B) = \sum (I_i^A - I_m^A) \cdot (I_i^B - I_m^B) / (N - 1) \cdot S^A \cdot S^B$$

where I_i^A , and I_m^A are the intensity at i -th point and the mean intensity, S^A is the r.m.s. deviation for the element A , $N = 400$.

Correlation matrix for Bi (2223) film after current flowing at 4.2 K

	Bi*	Sr	Ca	Cu
Bi	-	-0.428	0.631	0.528
Sr	-0.428	-	-0.419	-0.714
Ca	0.631	-0.419	-	0.374
Cu	0.528	-0.714	0.374	-
<i>N</i> = 400; Significance level 0.1 %				

The negative signs of the correlation coefficients indicate mutually inverse variations of concentrations for pairs of elements with respect to the initial film, for which $0 < r < 1$. This means that the initial film is homogeneous in most of its microvolumes in contrast to the structure modified during the experiment, when the film stoichiometry becomes strongly violated.

The obtained results show that the electrostimulated diffusion of heavy ions discovered in YBCO (123) films exists also in Bi (2223) films.

8. THEORETICAL ASPECTS OF THE PROBLEM

For the present there is no consistent theories explaining the observed effects of the electrostimulated ion motion in HTCS at superconductive state. Additional difficulties are connected

with the fact that as a rule theories developed for ideal models are compared with the experiment performed at quasi-single-crystals or polycrystalline samples with weak links between granules. Theoretical studies^{6,7} of crystallochemical stability of oxide HTCS predicted the possibility of the displacement of oxygen and heavy ions during the current flowing at low temperatures. The structure of YBaCuO (123) has a sublattice of Cu²⁺ ions with a low energy barrier for the ion motion between partially occupied positions. Crystallochemical calculations show that such a system is unstable relative to the displacements of Cu²⁺ and O²⁻ ions to the distances comparable with the elementary cell, and the problem of motive forces is important for understanding the nature of the phenomena under consideration.

The problem of motive forces is not yet clear, especially at 4.2 K when the film is not overheated and remains superconducting. It is almost obvious that the forces have electric origin, because the experimental pictures near positive and negative electrodes are different, and we come to a hypothesis that an electric field exists in the bulk of oxide material in the superconducting state. This is possible if there is no unpaired carriers in the superconductor, which always compensate for the inhomogeneous charge distribution of Cooper pairs in metallic superconductors in the course of superconducting current flow. Calculations performed by Gufan et al.¹⁸ showed that at $I = 0.1 \text{ A}$ at 4.2 K in the surface layer of $\sim 10^{-7} \text{ cm}$ an electric field of $\sim 1 \text{ kV/cm}$ may appear at the film thickness below 10^{-4} cm and Cooper pair density less than 10^{17} cm^{-3} . Such a field can destabilize a loose structure of (123) and explain the observed effects.

From paper¹⁹ it follows that in general the growing temperature of the superconducting transition leads to smaller structural stability.

9. CONCLUSION

The experimental results recently obtained while studying the YBCO, Bi (2223) structural instability at the current flowing at helium, nitrogen, and room temperatures show that there exists a phenomenon that, in case it is not overcome, may cause principle limitations for the possible applications of this class of substances in practice. If our first results obtained at polycrystalline samples were regarded with criticism, now the analogous effects are observed at quasi-single-crystal films with the c-axis perpendicular to the film surface and a high critical current.

Despite the fact that the crystalline structure of the cuprate HTCS, as it was noted in one of the previous papers, is favorable for the transfer of certain ions, the problem of the direct connection of the superconductivity phenomenon with the crystalline instability is still unsolved.

REFERENCES

1. N.N. Oleinikov et al. "Vliyanie parov vody na processy degradacii ceramiki sostava YBa₂Cu₃O_{7-x}" In: Proc. All-Russia Conf. "Physico-Chemistry and Technology of HTCS Materials", Moscow: Nauka, p. 439, 1989.
2. V.I. Nefedov et al. "Vliyanie vneshnikh vozdeistvii na sostav poverkhnostnogo sloya VTSP-ceramiki i plenok po rentgenoelectronnym dannym" In: Proc. All-Russia Conf. "Physico-Chemistry and Technology of HTCS Materials", Moscow: Nauka, 445, 1989.

3. A.V. Stepanenko et al. "Issledovanie degradacii i rezhimov vosstanovleniya svoistv VTSP-materialov" In: Proc. All-Russia Conf. "Physico-Chemistry and Technology of HTCS Materials", MoscoF: Nauka, 447, 1989.
4. Murr L.E. et at. "Shock Fave induced changes in superconductivity in $\text{YBa}_2\text{Cu}_3\text{O}_{7-\delta}$ " *Appl. Phys. Lett.*, 55, 1575, 1989.
5. Govinda, ParamesFaran et. al. "Electromigration of oxygen in Y-Ba-Cu-O" *J. Phys. D.: Appl. Phys.*, 23, p. 694-697, 1990.
6. A.M. Prokhorov et al. "Termodinamicheskaya teoriya fazovykh diagram vysokotemperaturnykh sverkhprovodnikov" *Dokl. Akad. Nauk*, Vol. 310, No. 3, pp. 596-599, 1989.
7. A.M. Prokhorov et al. "Fenomenologicheskaya teoriya fazovykh perekhodov v neodnorodnuyu nesorazmernuyu fazu so sverkhprovodyashchim tokom" *Dokl. Akad. Nauk*, Vol. 310, No. 3, pp. 599-603, 1989.
8. A.M. Prokhorov et al. "Predskazanie, obnaruzhenie i issledovanie massoperenosu pri prokhozhdenii elektricheskogo toka v sverkhprovodyashikh plenkakh Y-Ba-Cu-O pri 4.2 K" *Dokl. Akad. Nauk*, Vol. 311, No. 1, pp. 75-78, 1990.
9. A.M. Prokhorov et al. "Peremeshchenie tyazhelykh ionov v VTSP-systemakh tipa Y-Ba-Cu-O pri 4.2 K i sverkhprovodyashchii tok" *Pis'ma v ZhETF*, Vol. 51, No. 3, pp. 132-134, 1990.
10. G.N. Mikhailova et al. "Lokalnoe izmenenie khimicheskogo sostava plenok Y-Ba-Cu-O pri propuskanii electricheskogo toka pri 78 K" *Superconductivity; Physics, Chemistry, Technology*, Vol. 5, No 12, pp. 2304-2309, 1992.
11. E.N. Lubnin et al. "Elektrostimulirovannoe izmenenie khimicheskogo sostava VTSP-plenok $(\text{Bi},\text{Pb})_2\text{Sr}_2\text{Ca}_2\text{Cu}_3\text{O}_8$ pri $T = 4.2 \text{ K}$ " *Dokl. Akad. Nauk*, Vol. 332, No 3, pp. 303-305, 1993.
12. N.E. Alekseevskii et al. "Vliyanie propuskaniya electricheskogo toka na perenos anionov i kationov v vysokotemperaturnykh sverkhprovodnikakh" *Superconductivity: Physics, Chemistry, Technology*, Vol. 5, No. 10, pp. 1861-1863, 1992.
13. V.I. Nefedov et al. "Izmenenie parametrov struktury VTSP-keramiki Y-Ba-Cu-O posle propuskaniya postoyannogo toka" *Superconductivity: Physics, Chemistry, Technology*, Vol. 5, No. 6, pp. 1081-1083, 1992.
14. D.M. Karfidov et al. "Modifikatsiya VTSP-plenok $\text{YBa}_2\text{Cu}_3\text{O}_{7-\delta}$ pod deistviem SVCh toka pri 77 K" *Superconductivity: Physics, Chemistry, Technology*, Vol. 6, No. 9, pp. 1852-1855, 1994.
15. A.E. Trenin and G.V. Sholin, "Microscopic model of in demping current in superconductor" Preprint IAE-5145/9 (Kurchatov Scientific Center) MoscoF: 1990.
16. T.E. Os'kina and Yu.D. Tretyakov, "The synthesis of Bi(Pb)-Sr-Ca-Cu-O superconductors with the use of separately precalcined precursors" *Physica C*, Vol. 190, pp. 183-184, 1991.
17. E.N. Lubnin et al. "Elektrostimulirovannoe izmenenie khimicheskogo sostava VTSP-plenok $(\text{Bi},\text{Pb})_2\text{Sr}_2\text{Ca}_2\text{Cu}_3\text{O}_8$ pri $T = 4.2 \text{ K}$ " *Dokl. Akad. Nauk*, Vol. 332, No. 3, pp. 303-305, 1993.
18. Yu.M. Gufan et al. (to be published).
19. A.A. Gorbatshevich and Yu.V. Kopaev, "Localno neustoichivye kristallicheskie konfiguratsii i elektronnyi mekhanizm sverkhprovodimosti" *Pis'ma v ZhETF*, Vol. 51, No. 6, p. 327, 1990.

Backscattered Heterodyne Doppler Diagnostics of Laser Induced Near-Surface Transport Phenomena

V.M Gordienko, E.M.Chastookhin*, N.N.Kurochkin, V.Ya Panchenko*

Physics Dept., International Laser Center, Moscow State University, Moscow, Russia.

*Science Research Center for Technological Lasers RAS, Shatura, Moscow Region, Russia.

1. INTRODUCTION.

Laser processing has become a powerful tool for surface or bulk modifications and is applied successfully in many areas^{1,2}.

The use of laser in technology depends on the knowledge of the physics of the processes that occur on interaction between laser radiation and matter. Transport phenomena accompanies of laser technology depending on the incident intensity or energy density of the laser radiation. The hydrodynamic behaviour of melt layers or melt pool determines the main features of such processes as deep penetration laser welding, keyhole formation, laser cutting and alloying^{3,4}. To optimize laser material processing an effective diagnostic methods should be developed.

Interaction of CW intense laser radiation with condensed matter under energy contribution comparable with internal energy of molecular bond (or atoms in crystal lattice) is specific in nature. The principle role in dynamics of process plays phase transitions in matter (melting and vaporization) and corresponding transport phenomena. The occurrence of phase transitions under interaction of intensive laser radiation with condensed matter is connected with essential contribution in energy transfer such transport phenomena as convection and vaporization, in the last named is attended with injection of liquid component in droplet form. The velocity field of hydrodynamic flows from in interaction zone and depends on heating regime.

Strong light scattering is very typical for laser processing, so measured parameters of scattered light bring information of the process, including velocity field. That opens the way to developing laser physic methods for non-destructive diagnostics and on-line control.

The main idea our measurements are by irradiating the surface of strongly absorbing condensed matter with the intense coherent radiation on the one hand to induce such phase transitions as thermocapillary convection and evaporation and on the other hand to form and to observe the Doppler shift in the frequency of radiation backscattered from scatterers within the irradiated volume and consequently to measure the velocity of laser induced near-surface hydrodynamic processes.

2. EXPERIMENTAL.

There are many different schemes of laser Doppler flowmetry⁵. We used that one utilizing backscattered radiation similar to coherent wind velocity Doppler lidar. The scheme can be adapted to real technological processes. The monostatic flow velocity remote sensing scheme with reference beam is one of most promising from viewpoint of the performance.

In the frame of the scheme the radiation backscattered by particles moving at a velocity of v follows in an opposite direction the same optical track as probing beam an is mixed in the photoreceiver with the preattenuated reference beam. The mixing results of optical heterodyning in the quadratic photoreceiver with isolation of a difference (Doppler) signal with a frequency of $f_D = 2v_z / \lambda$, where v_z is the projection of the velocity of the scattering particles on the probing direction. A velocity of $v = 1\text{m/s}$ corresponds to $f = 0.2\text{ MHz}$ for $\lambda = 10\mu\text{m}$.

Several factors can degrade the system e.g. dissimilar intensity distribution of the two beams, different phase front curvature and different polarization. The sensitivity of the scheme is lowered dramatically if the propagation direction of the two beams does not agree.

The useful current i_u on the output from the photoreceiver with coherent reception is described by the expression:

$$i_u = \frac{ce\eta}{4\pi v} \operatorname{Re} \int_s E_h E_s^* ds, \quad (1)$$

where c is the speed of the light, e is the electron charge, hv is the photon energy of laser radiation, η is the quantum effectivity, E_h is the heterodyne field, E_s is the signal field, and S is the area of the receiving aperture.

The output current of the heterodyne photoreceiver is proportional to the magnitude of the signal field. The phase of backscattered from one particle field depends on the particle position. Aerosol particles are positioned independently hence the power spectrum of the photocurrent is a superposition of the partial power spectra, generated by individual scattering particles.

The power spectrum of such a signal will be a sum of the power spectra of the signal of the scattering particles which backscatter the laser radiation.

The power spectrum of the photodetector current with an accuracy to instrumental broadening gives an information about the distribution of scatterers in term of velocity in the measurement volume.

In approximation of the absence absorption and distortion of probing and scattered radiation one can obtain the expression for the spectrum power of photocurrent generated by individual scattering i -th particle⁶:

$$P_i = \sigma_i P(L, r) = \sigma_i \frac{8B\eta P_p P_s (\Delta L)^2}{(L - L_{max})^2 + (\Delta L)^2} \exp \left\{ -\frac{4L_p \Delta L}{(L - L_{max})^2 + (\Delta L)^2} \left(\frac{r}{R} \right)^2 \right\} \quad (2)$$

where σ_i is backscattering cross-section, B is the sensitivity of photoreceiver, η is the system optical efficiency, P_p , P_s is the power of the probing and backscattered radiation consequently, L is the distance along the probing direction, r is the radius-vector in the plane perpendicular to the probing direction, R is the radius of the probing beam,

$L_D = \pi R^2 / \lambda$ is the diffractional length, $L_{max} = \frac{F}{1 + (F/L_D)^2}$, F is the distance at which the probing radiation

is focused, $\Delta L = \frac{L_{max} F}{L_D}$.

Formula of this form was obtained to fit wind Doppler lidar⁷. Also the absence of the absorption in optical part of the system is assumed.

Thus the power of Doppler photocurrent caused by backscattering from one particle and depends on cross-section and the location. The function $P(L, \bar{r})$ describes the dependence on the location of particle. The function $P(L, \bar{r})$ has maximum at the distance L_{max} along the probing axis.

In the case $F \ll L_D$ magnitudes L_{max} , ΔL are $L_{max} = F$, $\Delta L = \lambda F^2 / \pi R^2$.

The characteristic transverse dimension of measurement volume is $\lambda F / R$. As it is shown in Ref.⁶ the power spectrum of photocurrent for monostatic Doppler measurer is a histogram of velocity field projection weighted by $\beta(L, \bar{r})P(L, \bar{r})$, where $\beta(L, \bar{r})$ is the backscattering coefficient. If the backscattering process realized with low number of scatterers, so the power spectrum of photocurrent is a velocity projection histogram weighted by $\sigma_i P(x, p)$.

Since the radiation at different section of the probing track has different curvatures of the wave front only a portion of it is mixed coherently with the reference beam having plane wave front and makes a significant contribution to the Doppler signal. Most of this signal arises from the section of the track of length ΔL , which determines the longitudinal dimension of the probing volume or the spatial resolution. This depends on the diffractional and the focal length of the system.

It should be noted that the heterodyne receiver field of view is $\Omega = \lambda^2 / D^2$, where D is the diameter of collecting lens in the optical receiver. Because of this heterodyne receiver protected effectively against background.

Light scattering occurs during laser processing can bring information about the surface roughness and of the micromovements of hydrodynamic flows that opens the way to developing of high sensitive methods of diagnostics.

Fig.1 shows the optical layout of the system. It is based on CW CO₂ laser and has been built according to the monostatic heterodyne scheme⁸. All basic optical components are mounted on the optical table. The radiation of a single-frequency CW CO₂ laser with wavelength 10.6 μm is divided into two beams by an acousto-optic modulator with a relative frequency shift 26 MHz. The more intensive beam with the nonshifted frequency is used as a probing one. It is expanded by a 1:2 telescope up to 6 mm in diameter and acquires a circular polarization after crossing a quarter-wave plate. Then it is brought to an output lens focusing the beam at a target. The focal length F is 10 cm.

The light backscattered by a target is collected by the same lens. It crosses again the quarter-wave plate, gaining linear polarization orthogonal relative to that of the original beam. To select the scattered light a Brewster's plate is used. The reference beam expanded by a similar telescope gains similar polarization after crossing a half-wave plate. The two beams are mixed with the help of a plate and a lens at the surface of a cooled HgCdTe photodiode.

The output photocurrent after preliminary amplification is brought to the spectrum analyzer type S4-74. The spectra of the signal carry information on the magnitude and the sign of the projection of the flow velocity vector to the direction of the probing. We can obtain either the subsequently measured spectra with the frequency 20 Hz or a spectral component at desired frequency. These spectra are introduced into a computer. After digital processing (averaging, subtraction of background noise, etc.) the data are put to the information bank.

3. EXPERIMENTAL RESULTS.

In deciding on a target for experimental investigations of laser induced near-surface hydrodynamic flows an effort was made to model of experimental conditions similar to real technological processes. The hydrodynamic behaviour of melt bath determines the main feature of the processes keyhole formation, laser beam deep penetration into matter. Inhomogeneous heating of thin liquid layer sets the liquid in convective motion mainly because of the surface tension forces⁹. The main feature of deep penetration laser welding are strong evaporation and two phase flows from laser interaction zone. The criterium in deciding on targets was incipience of mass transport in form thermocapillary convection or strong evaporation at interaction of the intense laser radiation with the target. During interaction process there are three characteristic mechanisms of heat and mass transport, i.e. mechanism of heat conductivity playing main role in energy transfer under heating of matter up to melting temperature, thermocapillary convection setting at interaction laser radiation with melt layer; when the radiation flux density on surface reached threshold value at which the surface temperature rose to a value of the order of the boiling point strong evaporation dominates. We use water, solid paraffin and plexyglass as a target.

Calibrating measurement of the velocity and power of backscattered signal of a rotating plexyglass disk were initially performed (see Fig.2). The signal/noise ratio was about 10⁴ in our experiment. Doppler signal spectra generated with frequency 20 Hz. The spectra from the output of the analyzer are fed, after conversion to digital form, to a personal computer. The spectra are obtained from 1000 averagings, i.e. the averaging time about 50 s. The number of averaging was preferred from operational consideration.

Thermocapillary convection.

We observed laser induced convection at focusing laser radiation on the water plane as well as the surface of the paraffin, machine oil and naphthalene target. In the case of paraffin and naphthalene there was noticeable molten bath of diameter about 1 cm. Doppler spectra is shown in Fig.3a-d.

Sign of Doppler shift corresponds the circulation of the liquid from the center of heated region to the periphery (see Fig.4). Power of backscattered radiation in the experiment is comparable with that one for rotating plexyglass disk, that is the signal is the result of backscattering by the surface of the liquid. We measured the projection of the velocity in the probing direction that is the surface of the liquid is not plate and the surface sagging occurs^{1,10}. Since for the majority of materials the surface tension α decreases on increase in the temperature of the material, it follows that during melting by laser radiation the surface experienced a force directed away from the center of the bath toward periphery and setting the melt in motion. The motion becomes viscous thermocapillary flow¹¹, characterized by the velocity:

$$v_c^2 = \frac{I_0}{\rho \kappa \sqrt{\text{Pr}}} \left| \frac{d\alpha}{dT} \right| \quad (3)$$

where I is the intensity of the radiation absorbed on the surface of the material, $d\alpha / dT$ is the temperature coefficient of the surface tension, κ is the thermal conductivity, Pr is Prandtl number, v_c is velocity estimation for the surface of the melt.

The surface tension tends to reduce the curvature of the melt surface, but inhomogeneous heating weakens the surface tension force.

In the case of paraffin ($\rho = 0.9 \cdot 10^3 \text{ kg/m}^3$, $\kappa = 0.12 \text{ W/m K}$, $Pr = 7$, $d\alpha / dT = 10^{-4} \text{ N/m K}$) under intensity $I = 10^3 \text{ W/cm}^2$ we find that $v = 1.8 \text{ m/s}$.

To estimate the vertical projection of the thermocapillary convection we must evaluate characteristic angle of the surface sagging using the expression for the depth of the surface sagging Δh^1 :

$$\Phi = \frac{\Delta h}{d} = \frac{3}{2d} \frac{1}{\rho gh + \pi^2 \alpha h / d^2} \frac{d\alpha}{dT} \Delta T, \quad (4)$$

where d is the diameter of the molten bath, h is the depth of the molten bath, ΔT is the difference between the temperature of the surface of the melt at the center of the beam and the temperature of the melt at the boundary of the molten region. In the case of paraffin $\Delta T \sim 10^2 \text{ K}$, $h \sim 0.2 \text{ cm}$, $d \sim 1 \text{ cm}$, and $\Phi = 0.05 \text{ rad}$. Thus, the estimation for the vertical projection of the convection velocity for paraffin is 0.07 cm/s and close to experimental value 0.1 m/s .

The half-bandwidth of the Doppler spectrum characteristic maximum is proportional to the sensitivity of microcirculation in the convection flow.

Strong evaporation and keyhole formation regime.

To model the regime of strong evaporation we used water and plexyglass plate as a target. We had not observed that one during the interaction process of intense laser radiation up to 10^3 W/cm^2 with paraffin.

The Doppler spectra is shown in Fig.5. From this figure we notice that characteristic magnitude of velocity projections is localised within the interval $1-10 \text{ m/s}$.

The interaction of laser radiation with the water plane also was accompanied with the formation vapor-gaseous stream and strong issuing of burst vapor in combination with liquid droplets fracion from interaction zone. We have observed the thermal cavitation a bubble formed in an overheated part of the liquid which collapsed because of cooling in a region with a lower temperature. The collapse increased the local temperature and created a hydraulic shock.

During of evaporation process the vapor burst and liquid droplets are main scattering centers giving information about velocity field in the interaction zone. Under gravitational force these droplets later on have a good chance to return to interaction zone and consequently can contribute in forming as positive as negative projection of velocity.

The spectrum of the Doppler signal clearly defines peaks in strong evaporation regime. On the one hand this demonstrated backscattering by particles during which number of peaks on the spectral analyzer cycle (50 ms) is an average of 5 for plexyglass target. On the other hand the characteristic time duration of the peaks was 0.1 ms and supposedly corresponds the time it takes for a scatteres to cross through measurement volume. From our rough estimates the Doppler signal spectra was obtained in one particle backscattering regime.

The properties of Doppler spectra in vicinity low velocity magnitude shows Fig.6. As in the case with thermocapillary convection the power of Doppler signal is comparable with that one from the rotating disk. Consequently the signal is a result of back scattering from moving surface.

From our point of view the measured Doppler spectra for water demonstrate two-phase regime of hydrodynamic processes: on the one hand there is moving surface (characteristic velocity is about 10 cm/s) and on the other hand is steam and gas jet (characteristic velocity is about 10 m/s). It should be noted that distinct maximum in lower side Doppler spectra and corresponding of moving surface defines velocity field pointed downward as contrasted to the results for the thermocapillary convection.

The evaporation of plexyglass one can conceived in the frame of next in order of complexity process: plexyglass in common with polymer is softened at the temperature about 130°C and is discomposed with forming liquid and gaseous fractions at the temperature about 220°C.

The availability liquid and gaseous fractions simulates this process similar to strong evaporation at least from the point of view release matter from interaction zone. It should be note that interaction of intense laser radiation with plexyglass occurs in deep penetration regime. The resultant keyhole parameter $l/d = 50$, where l is the depth of the keyhole. It follows from our experiments that the measurement volume is shifted to melting zone in deep penetration regime. Doppler spectra for plexyglass target is shown on Fig. 7,8.

The liquid formation resulting in decomposition process of plexyglass is an evaporating hydrocarbon compounds that quickly evaporates or undergoing destructive combustion. This account for insignificant of lower side-band Doppler backscattered spectra for plexyglass.

The distinctions in spectra can indicate probability the peculiarities of setting mechanism and chemical composition of vapor-gaseous mixture.

5.CONCLUSION.

The results of our model experiment indicate that backscattered heterodyne Doppler spectroscopy is efficient method for diagnostics of laser induced near-surface transport phenomena. The method make it possible to obtain information about the flow velocity in the volume immediately adjacent to the interaction zone. The proposed method can be perspective in advanced laser technology to study transport phenomena and to develope a theoretical model describing laser deep melting and alloying of metals.

As mentioned above the spatial resolution Δl for continious monostatic system is determined by the diffraction length and the focal length of the probing radiation. The use of lasers with mode locking has considerable opportunity to increase essentually the spatial resolution by a factor two or more since in this case it will be determined by the duration of ultrashort pulses.

A coherent aerosol flow remote system utilizing a solid-state picosecond CW Nd:YAG laser operation at $\lambda = 1.06 \mu\text{m}$ has been developed⁸. The principle scheme of the system is similar to that one of the CW CO₂ system.

It should be noted that solid state ps systems offer some technological advantages and new possibilities. In the mode-locked regime both the local oscillator and transmitter beams represent trains of phase correlated ultrashort pulses. Coherent mixing of backscattered radiationwith local oscillator pulses providesthe Doppler signal from the measurement volume which is composed as a set of thin slices of width $\Delta l = c\tau_p$ localized around the waist of focused probe beam.

Finally the backscattered heterodyne Doppler diagnostics can be used for optimization of laser-tissue interaction in laser surgery applications.

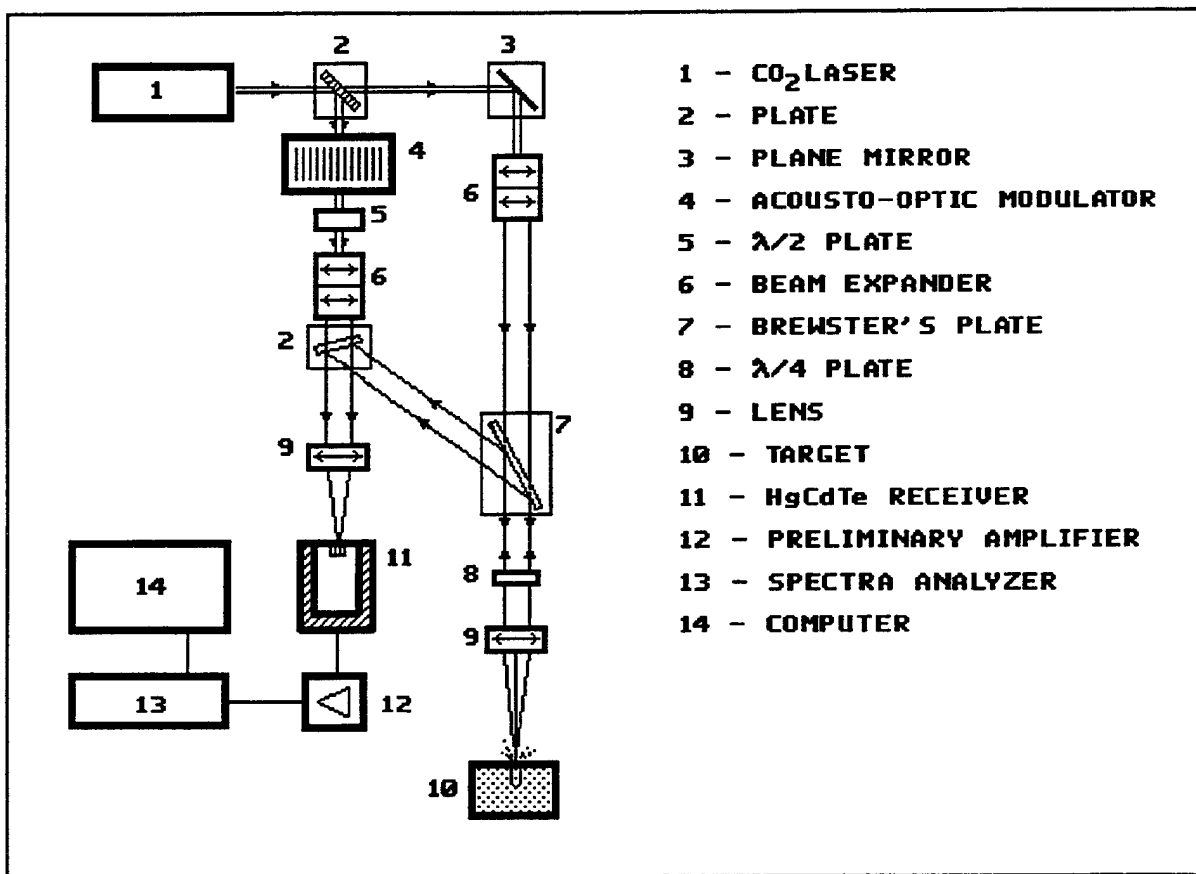


FIG.1. EXPERIMENTAL SETUP.

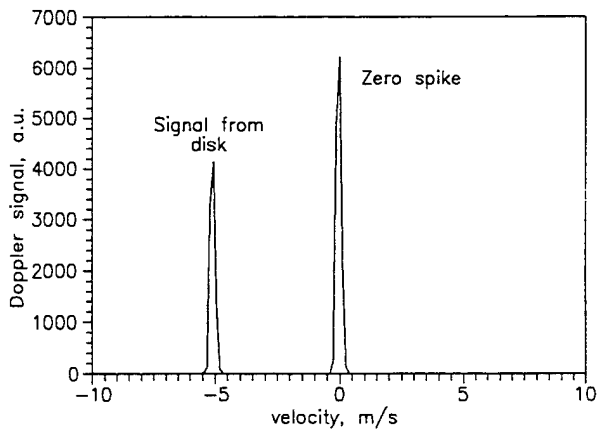


Fig 2. Doppler spectrum for rotating disk.

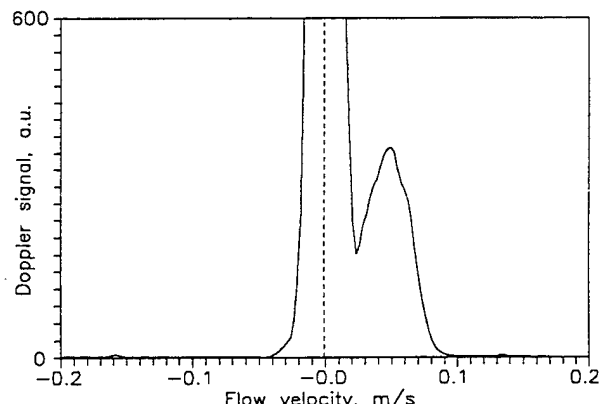


Fig 3a. Doppler spectrum for water target.
Thermocapillary convection.

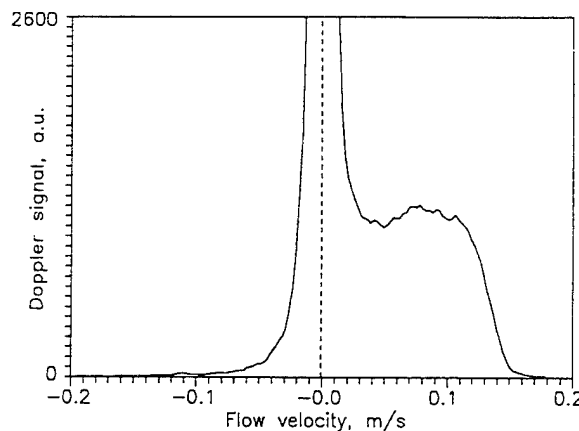


Fig 3b. Doppler spectrum for paraffin target.
Thermocapillary convection.

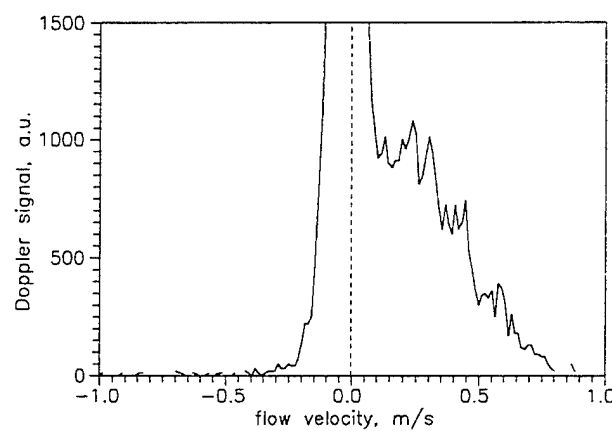


Fig 3c. Doppler spectrum for naphthalene target.
Thermocapillary convection.

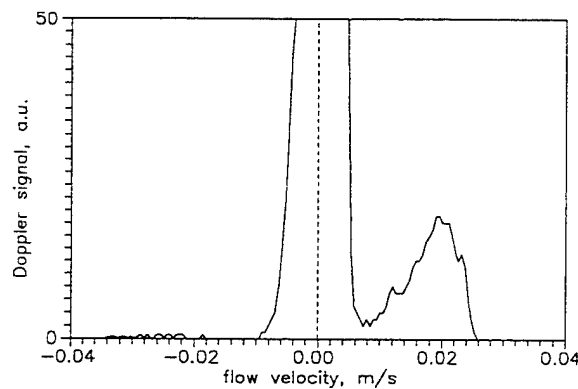


Fig 3d. Doppler spectrum for machine oil target.
Thermocapillary convection.

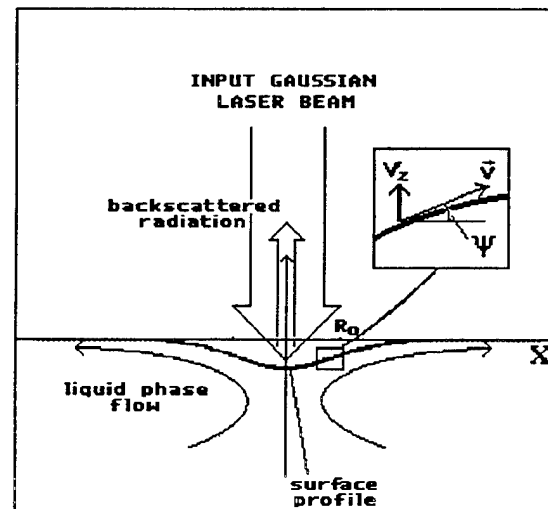


Fig.4. Surface backscattering

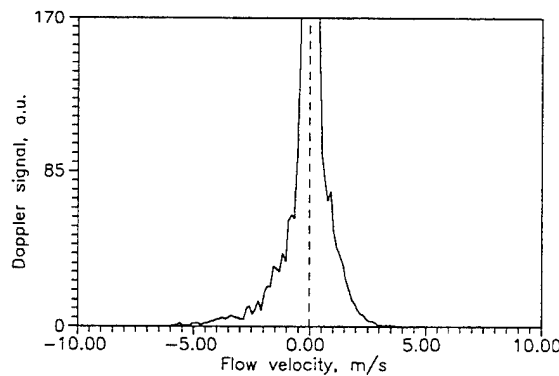


Fig 5. Doppler spectrum for water target.
Strong vaporization.

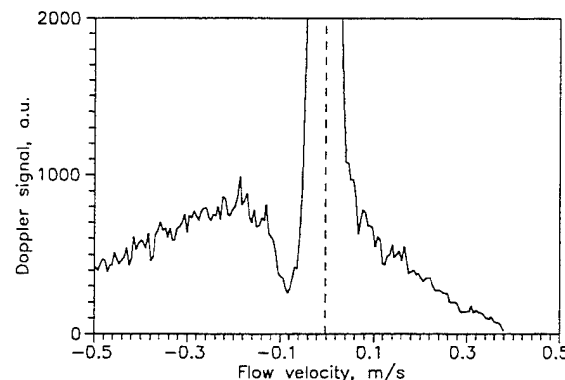


Fig 6. Doppler spectrum for water target.
Strong vaporization. Low velocity range.

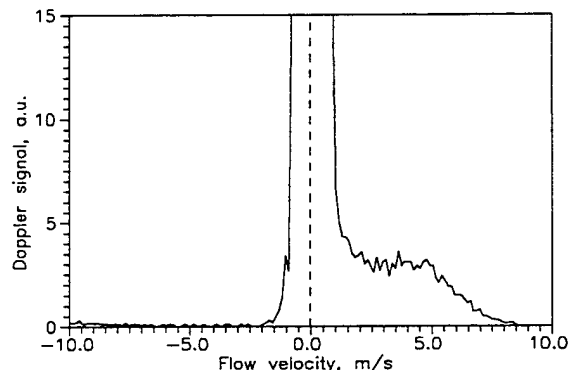


Fig 7. Doppler spectrum for plexyglass target.
Keyhole formation.

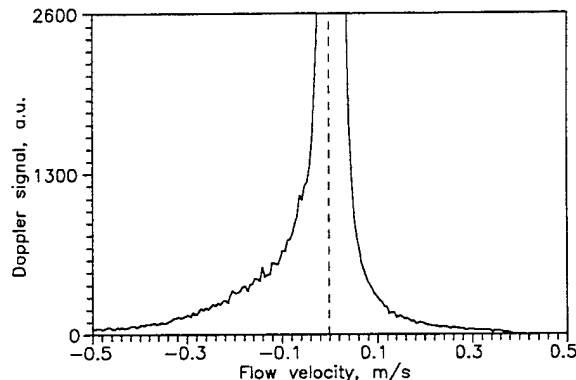


Fig 8. Doppler spectrum for plexyglass target.
Keyhole formation. Low velocity range.

REFERENCES.

1. Handbook for Technological Lasers, ed. G.A. Abil'siitov, *Mashinostroenie*, Moscow, 1991.
2. S.Jacques "Laser-tissue Interactions" in *Laser in General Surgery*, v.72, No.3, pp.531-557, 1992.
3. A.A.Vedenov and G.G.Gladush "Physical Processes by Laser Treatment of Material", *Energoizdat*, Moscow, 1985 (in Russian).
4. J.Mazumder, *Opt. Engineering*, v.30, No.8, pp.1208-1219, 1991.
5. B.S.Rinkevichius "Laser Diagnostics in Fluid Mechanics", *Moscow Power Institute Pub.*, Moscow, 1990 (in Russian).
6. N.N.Kurochkin, V.M.Gordienko and A.V.Priesszhev, *Proceedings SPIE*, v.1714, pp.176-184, 1992.
7. S.M.Sonnershine and T.A.Horrigan, *Appl. Opt.*, v.10, No.7, pp.1600-1604, 1970.
8. V.M.Gordienko, S.A.Akhmanov, V.I.Bersenev, L.A.Kosovskii, N.N.Kurochkin, A.V.Priesszhev, S.A.Pogosov, Yu.Ya.Putivskii, *Proceedings SPIE*, v.1416, pp.102-114, 1991.
9. J.R.Pearson, *J. Fluid Mech.*, v.4, p.489, 1958.
10. R.D.Seidgazov and Yu.M.Senatorov, *Sov. J. Quant. Electr.*, v.18, p.408, 1988.
11. G.G.Glagush, L.A.Krasitskaya, E.R.Levchenko, A.L.Chernyakov, *Sov. J. Quant. Electr.*, v12. p.408, 1982.

Computer simulation of mass transfer during laser doping of materials.

Valery V.Kartuzov, Igor V.Krasikov, Cyril E.Rotmistrovsky.

Institute for Problems of Materials Science, Department of
Applied Math. and Computer Experiment, Kiev, Ukraine

Studying of picularities of laser beam interaction with different materials remains an actual problem in spite of large amount of investigations being carried out during more than thirty-year period since first industrial lasers have appeared. It is connected with number of reasons, such as insufficiency of detailed information about physical and physico-chemical processes occurring in the zone of laser influence, as well as about mechanisms, which are responsible for forming of definite structure and chemical composition of surface layers under laser processing of materials. The most developed is computer simulation of thermal processes. In spite of essential non-linearity (thermoconductivity and heat capacity depend on temperature) of mathematical models of laser heating, there are examples of successful application of computer simulation.

More modest results are achieved in computer simulation of hydrodynamical processes, which can't be neglected, because streams of liquid, transporting energy, modify temperature distribution in melting pool and influence character of physico-chemical processes. Thermocapillary convection is responsible for transportation of doping material into melting pool, but one ought to remember, that the same hydromechanical processes can throw out melted material. This can sharply modify character of the process, for example, under laser welding. On melting of material via laser beam the motion of phase transformation front effects considerably on mixing and mass-transition of doping material. Analysis of the motion of melted material shows that in shallow pool approximation it has spiral structure. The velocity all over the pool is same in order as that of front of melting, except thin boundary layer near bottom of the pool and in the centre of the spiral. Region Z, where the velocity of melted material is greater enough than zero, is in size of $Z \approx \sqrt{\nu(t - t_m)}$, where: ν is viscosity, t - the time, t_m is time when melting started. For material processing it is necessary to analyse possibility of transportation of doping material from surface into melted pool via thermocapillary mixing. Here modes, which lead to even doping distribution, as well as to sharp nonhomogeneity, are possible.

To determine fields of doping concentration, with account of motion of melting pool borders, joint solution of hydrodynamical and non-stationary thermoconductivity problems is required. As this takes place it is necessary to calculate positions of both melting and evaporation fronts, because simulation of melting without evaporation (as well as evaporation without melting) works only in narrow intervals of density of laser power absorbed and its influence time.

Let's consider laser beam action on metal in following terms. In cylindrical coordinate system r, z, φ (z -axis is directed from surface into metal) the fronts of phase transitions can be defined by equations $z = S_1(r, t)$; $z = S_2(r, t)$. Assume heat conductivity, temperature conductivity of solid and liquid phases, density, dynamical and kynematical viscosities of the melt are constant and that power density absorbed at surface is distributed by Gauss law: $q(r) = q_0 \exp(-\beta r^2)$. I.e. the problem has cylindrical symmetry.

At time moment $t = t_m$ (melting start) projections of velocities of melt motion v_r and v_z equal zero; and for

$t \geq t_m$ we obtain following set of equations:

$$\begin{aligned} \frac{\partial \vec{v}}{\partial t} + (\vec{v} \nabla) \vec{v} &= -\frac{1}{p} \nabla p + \vec{v} \Delta \vec{v}, \\ \operatorname{div} \vec{v} &= 0, \end{aligned} \quad (1)$$

$$\begin{aligned} \frac{\partial T_1}{\partial t} + \nu \nabla T_1 &= a_1 \Delta T_1, \\ \frac{\partial T_2}{\partial t} &= a_2 \Delta T_2. \end{aligned} \quad (2)$$

with appropriate initial and border conditions:

$$\begin{aligned} \left. \frac{\partial v_r}{\partial z} \right|_{z=0} &= \frac{\alpha}{\eta} \left. \frac{\partial T_1}{\partial r} \right|_{z=0}, \\ v_z|_{z=S_1} = v_r|_{z=S_1} &= v_z|_{z=S_2} = v_r|_{z=S_2} = 0, \\ -\lambda_1 \left. \frac{\partial T_1}{\partial z} \right|_{z=S_1} &= q(r) - \rho L_v v_* (\exp(-T_*/T(S_1, t)) - \exp(-T_*/T_k)), \\ T_1(r, z = S_2, t) &= T_2(r, z = S_2, t) = T_m; \end{aligned} \quad (3)$$

$$\begin{aligned} -\lambda_1 \left. \frac{\partial T_1}{\partial z} \right|_{z=S_2} &= -\lambda_2 \left. \frac{\partial T_2}{\partial z} \right|_{z=S_2} + \rho L_m \frac{\partial S_2}{\partial t}, \\ T_2(r, \infty, t) &= T_2(\infty, z, t) = T_2(r, z, 0) = T_0 < T_m; \end{aligned} \quad (4)$$

where Δ is Laplacian, ∇ is nabla operator, v is melt motion velocity, v_r and v_z are projections of the velocity to directions given, $p(r, z, t)$ is pressure, η, ν are dynamical and kynematical viscosities of the melt correspondently, $\alpha = \frac{d\sigma}{dT}$, $\sigma(T)$ is surface tension, ρ is density, T_i – temperature of the liquid ($i = 1$) and solid ($i = 2$) phases, T_0 is initial temperature, T_k is boiling temperature at normal pressure, T_m is melting temperature, L_v, L_m are specific heats of evaporation and melting of the material, $S_1(t), S_2(t)$ are coordinates of evaporation and melting fronts, $v_* = \bar{c} \left(\frac{3}{4\pi} \right)^{1/3} \approx 0.62\bar{c}$, \bar{c} is mean sound velocity in material, $T_* = L_v A/R$, A is atomic weight, R – universal gas constant. λ_i, a_i are heat conductivities and temperature conductivities.

If we assume that free surface of the melt is flat, and melting pool is shallow (i.e. maximum depth of the pool $S(0, t)$ is small in comparison with its radius $R(t)$, which can be found from equation $S(R, t) = 0$), and hydrodynamical processes are neglectable for thermal transfer in liquid phase, and $t < t_k$, ($t_k : T_1(0, 0, t_k) = T_k$), so problem (1) – (4) can be split to thermal and hydrodynamical, and solution of the latter (according to assumptions accepted) would not influence the former.

From the model assumptions and on following variable substitution

$$x = \frac{zq}{q_0}, \quad \tau = t \left(\frac{q}{q_0} \right)^2 \quad (5)$$

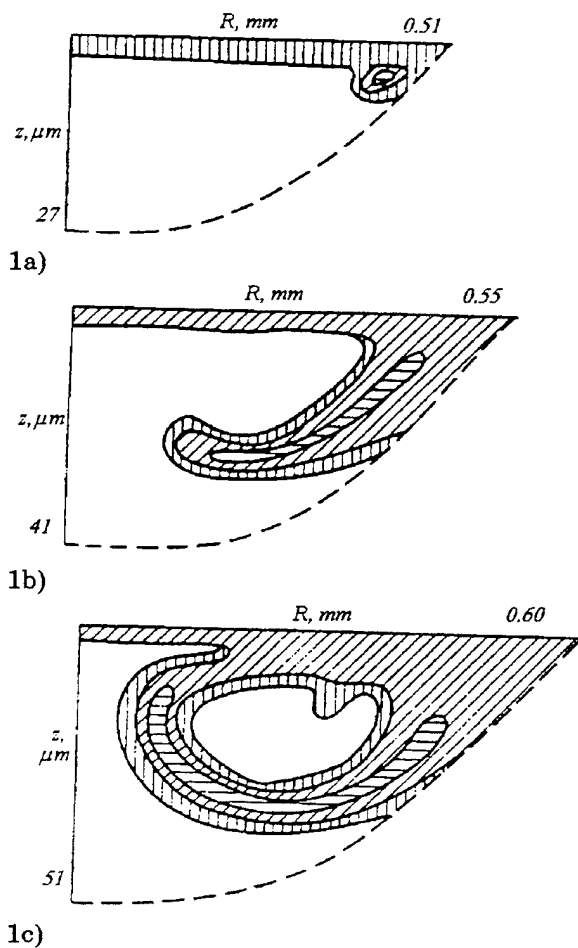


Fig. 1 a-c. Doping material concentration field for time $t=2.8, 3.6, 4.4$ ms correspondently. Doping from gas phase. Power density absorbed $q_0=2.5 \cdot 10^4 \text{ W/cm}^2$, with $\beta=150 \text{ cm}^{-2}$.

Here:

- $0 < c < 0.1$
- $0.1 < c < 0.5$
- $0.5 < c < 1$

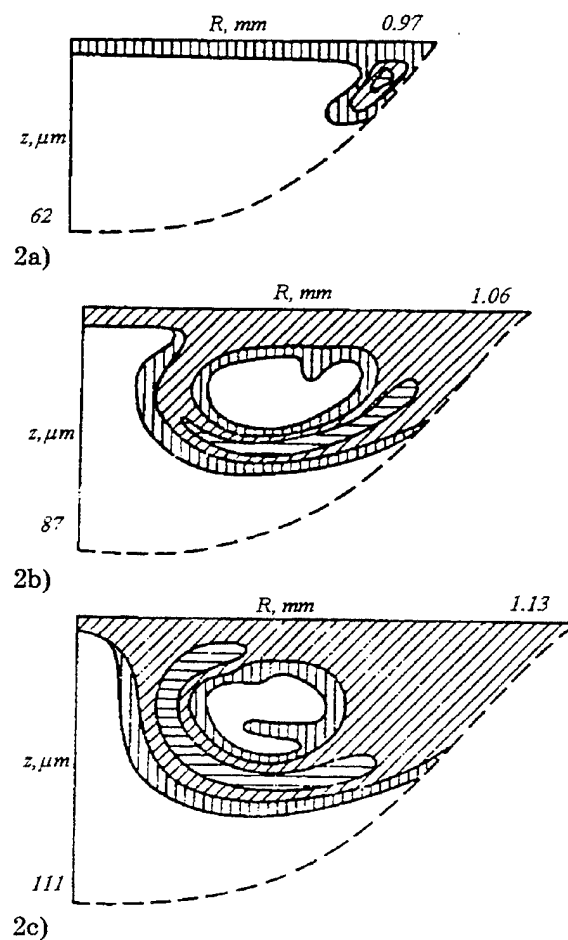


Fig. 2 a-c. Doping material concentration field for time $t=2.1, 3.1, 4.1$ ms correspondently. Doping from gas phase. Power density absorbed $q_0=5 \cdot 10^4 \text{ W/cm}^2$, with $\beta=100 \text{ cm}^{-2}$.

Here:

- $0 < c < 0.1$
- $0.1 < c < 0.5$
- $0.5 < c < 1$

we come to unidimensional (with x variable) non-stationary problem:

$$\begin{aligned} \frac{\partial G}{\partial t} &= v \frac{\partial^2 G}{\partial x^2}, \\ G(s_1, \tau) &= g(\tau), \\ \int_{s_1(\tau)}^{s_2(\tau)} dx \int_{s_2(\tau)}^x G(x_1, \tau) dx_1 &= 0; \end{aligned} \quad (6)$$

$$\begin{aligned} \frac{1}{a_1} \frac{\partial U_1}{\partial \tau} &= \frac{\partial^2 U_1}{\partial x^2}, \quad s_1(\tau) < U_1 < s_2(\tau), \\ \frac{1}{a_2} \frac{\partial U_2}{\partial \tau} &= \frac{\partial^2 U_2}{\partial x^2}, \quad s_2(\tau) < U_1 < s_3; \end{aligned} \quad (7)$$

$$\begin{aligned} -\lambda_1 \frac{\partial U_1}{\partial x} \Big|_{x=s_1} &= q_0(\tau) - \rho L_v v_* (\exp(-T_*/U_1(s_1(\tau), \tau)) - \exp(-T_*/T_k)), \\ -\lambda_1 \frac{\partial U_1}{\partial x} \Big|_{x=s_2} &= -\lambda_2 \frac{\partial U_2}{\partial x} \Big|_{x=s_2} + \rho L_m \frac{ds_2}{d\tau}; \end{aligned} \quad (8)$$

$$\begin{aligned} U_1(s_2, \tau) &= U_2(s_2, \tau) = T_m, \\ U_2(s_3, \tau) &= U_2(x, 0) = T_0; \end{aligned} \quad (9)$$

where

$$\begin{aligned} G(x, \tau) &= \left(\frac{\partial v_r}{\partial z} - \frac{\partial v_z}{\partial r} \right) / \omega r \approx \frac{\partial v_r}{\partial z} / \omega r, \\ \omega &= -2\beta\alpha/\eta, \quad g(\tau) = \tau \frac{\partial U(0, \tau)}{\partial \tau}, \\ s(\tau) &= s_r(t) \exp(-\beta r^2), \quad U_i(x, \tau) = T_i(r, z, \tau). \end{aligned} \quad (10)$$

Solution of the problem (6) - (8) can be obtained as sequential solution of the thermodynamical problem (7), (8) and hydrodynamical (6).

Below characteristic pictures of doping concentration fields for model problems are presented.

On investigation of melting of the granular media (for example, ceramics) by laser beam, one can assume that $\lambda_1 \gg \lambda_2$ in consequence of bad thermal contact between grains of solid phase, and all characteristics of the solid phase one must consider in some "homogenised" sense. Realisation of such homogenisation can be done as, for example, in¹. But the main complication of the task lies in the fact that under laser action on surface of dielectrical liquid flat evaporation front is always unstable, and the problem becomes sufficiently three-dimensional. This will be the subject of the future investigations.

REFERENCES.

1. V.V. Kartuzov, C.E. Rotmistrovsky "Computer Experiment on Investigation of Mechanical and Physico-chemical Properties of Ceramic Composites with Regular Structure." Proc. of Inter. Conf. MatTech-93. October 17-21, St.Peterburg, 1993.

Statistical thermodynamics for the alloy under irradiation model

V.V.Kamychenko*, V.G.Vaks**, V.V.Kartuzov*

*Institute for Problems of Materials Science, Kiev, Ukraine.

**Kurchatov Institute, Moscow, Russia.

Kinetic Ising model with competing dynamics is expected to reflect main qualitative features of the phase equilibria in the presence of irradiation. This model was extensively investigated by Martin, Bellon and others¹ with the use of the Kubo anzatz as well as by direct computer simulation. Nevertheless, some fundamental questions concerned with the nature of the steady state in this model seem to be not resolved yet. That is why the general formulation of the statistical thermodynamics for the model, based on the microscopic approach, seems to be interesting and promising.

In the conventional statistical mechanics the probability distribution for the different microscopic configurations of the alloy is given by the Gibbs formula:

$$P(\{n\}) = \exp \beta(\Omega - H(\{n\})) \quad (1)$$

where $\{n\}$ is a set of the variables (occupation numbers) uniquely describing the configuration with the energy $H(\{n\})$. $\beta = 1/T$ is the inverse temperature and Ω is the thermodynamic potential to be determined from the normalization condition

$$\sum_{\text{configurations}} P(\{n\}) = 1$$

The derivation of (1) is based on the energy conservation and the macroscopic multiplicativity of the probability distribution: for two macroscopic systems A and B we have (neglecting the small interface corrections)

$$P_{AB} \approx P_A P_B \quad (2)$$

In the presence of irradiation energy does not conserve, but (2) still takes place. One can write the time-independent probability distribution for the steady-state in the form similar to (1)

$$P(\{n\}) = \exp(A - Q(\{n\})) \quad (3)$$

where now the "quasienergy" $Q(\{n\})$ has to be found from the solution of the Master equation for the kinetic Ising model. In this formulation the problem becomes similar to the usual Ising problem and knowing the "Hamiltonian" Q one can use a conventional methods of equilibrium statistical mechanics to calculate thermodynamic functions and correlations in the system.

Unfortunately, the evaluation of the "quasinteractions" in (3) for the kinetic Ising model with competing dynamics is a non-trivial task, because in this case the so-called "detailed balance condition" (which makes trivial finding of the steady-state solution of the Master equation in the usual situations) does not fulfil. This circumstance has led some authors to the doubts about the existence of the solution (3) on the microscopic level².

2. EXISTENCE OF THE MICROSCOPIC DISTRIBUTION (3).

We have considered a kinetic model for the interstitial alloy, where the atoms and vacancies may interchange their positions due to two concurrent processes: thermally activated jumps with the probability $W_{i \rightarrow j}^{th} = \gamma_{ij} \exp \beta \sum V_{is} n_s$ and the "ballistic" (radiation induced) jumps $W_{i \rightarrow j}^b = \Gamma_{ij}$. Here $\gamma = \nu_{ij}^{th} \exp(-\beta E_s)$, where E_s is the "saddle-point energy" and ν is the "attempts frequency". V_{is} are the usual Ising potentials. n_s equals 1 or 0 depending on the atom or the vacancy is at the site s . Assuming the most general form for the quasi-Hamiltonian Q :

$$Q = \sum_i a_i n_i n_j + \sum_{i < j} a_{ij} n_i n_j + \sum_{i < j < k} a_{ijk} n_i n_j n_k + \dots \quad (4)$$

we have derived from the Master equation the "equation of motion" for quasiinteractions $a_{ij...k}$. The steady-state conditions in the form $da_{ij...k}/dt = 0$ appear to be in this formulation the system of non-linear equations with respect to $a_{ij...k}$. The structure of the system, however, is that the equations $da_i/dt = 0$ include only one-site potentials a_s ; $da_{ij}/dt = 0$ - only two-site interactions a_{ss} and so on. Thus, it can be solved (in principle) successively to any desired order. When the interactions V_{ij} in the "initial" Hamiltonian are long-ranged and of the same order of magnitude one can obtain also the explicit solution. For example for the pair interactions we have

$$a_{\mathbf{k}} = \frac{\beta V_{\mathbf{k}}}{1 + \frac{\Gamma_0 - \Gamma_{\mathbf{k}}}{\gamma_0 - \gamma_{\mathbf{k}}}} \quad (5)$$

while for the three-site interactions:

$$\sum_{s=0}^3 [(\Gamma_0 - \Gamma_{\mathbf{k}_s}) + (\gamma_0 - \gamma_{\mathbf{k}_s})] a(\mathbf{k}_1, \mathbf{k}_2, \mathbf{k}_3) = \\ (\gamma_0 - \gamma_{\mathbf{k}_1}) a_{\mathbf{k}_2} a_{\mathbf{k}_3} + (\gamma_0 - \gamma_{\mathbf{k}_2}) a_{\mathbf{k}_1} a_{\mathbf{k}_3} + (\gamma_0 - \gamma_{\mathbf{k}_3}) a_{\mathbf{k}_1} a_{\mathbf{k}_2} \quad (6)$$

and so on. In these formulas Fourier transform of the quantities γ_{ij} , Γ_{ij} , V_{ij} and a_{ij} is defined as

$$\phi_{\mathbf{k}} = \sum_j \phi_{ij} \exp i(\mathbf{r}_j - \mathbf{r}_i).$$

In the formula (6) $a(\mathbf{k}_1, \mathbf{k}_2, \mathbf{k}_3)$ is the Fourier transform of a_{ijk} :

$$a(\mathbf{k}_1, \mathbf{k}_2, \mathbf{k}_3) \Delta(\mathbf{k}_1 + \mathbf{k}_2 + \mathbf{k}_3) = 1/N \sum a_{ijk} \exp i(\mathbf{k}_1 \mathbf{r}_i + \mathbf{k}_2 \mathbf{r}_j + \mathbf{k}_3 \mathbf{r}_k),$$

where $\Delta(\mathbf{k}) = 1$ if and only if its argument equals zero and N is the total number of the lattice sites.

Thus, starting with the Hamiltonian with the pair interactions one arrives to the equilibrium distribution with the many-sites (and infinite-ranged) interactions. Note also, that in the effective Hamiltonian all the pair interactions are smaller than the initial ones, especially for the Fourier-component with $\mathbf{k} = 0$, which corresponds to the damping of the correlations in the system due to the random nature of the irradiation jumps. With lowering temperature all the effective interactions exponentially go to zero. Thus, the phase diagram for the model will be sharply cutted in the low-temperature region.

If we consider the model with the long-ranged interactions V_{ij} , the effective interactions are also long-ranged. In this situation the mean-field approximation (MFA) becomes exact and for the practical calculation of the phase equilibria we have used this approximation.

Self-consistent solution for the long-ranged potentials. From the Master equation the exact equation of motion for the correlation functions $\langle n_i n_j \dots n_k \rangle$ can be derived. For the long-ranged potentials (that is, having sharp maxima in the \mathbf{k} -space) we have developed the self-consistent perturbation expansion for correlators, in the close analogy with the expansion in the usual thermodynamics³. The small parameter in this expansion is $1/\zeta$, where ζ is the radius of the interactions.

In the usual ("thermodynamic") situation in the first non-vanishing order the correlator for the disordered phase in \mathbf{k} -space is given by the well-known Krivoglaz - Klapp - Moss formula:

$$K_{\mathbf{k}} = \frac{1}{\frac{1}{c(1-c)} + \beta V_{\mathbf{k}}} \quad (7)$$

where $K_{ij} = \langle (n_i - c)(n_j - c) \rangle$, $c = \langle n_i \rangle = \text{const}$ and the brackets mean the statistical averaging.

In the presence of irradiation we have obtained^{4,5} for this quantity the analogous expression

$$K_{\mathbf{k}} = \frac{1}{\frac{1}{c(1-c)} + \frac{\beta V_{\mathbf{k}}}{1 + \frac{\Gamma_0 - \Gamma_{\mathbf{k}}}{\tilde{\gamma}_0 - \tilde{\gamma}_{\mathbf{k}}}}} \quad (8)$$

where $\tilde{\gamma}_{\mathbf{k}} = \gamma_{\mathbf{k}} \exp \beta V_0 c$. Although this expression is in a close correspondence with the formula (5) for effective pair interactions, the change $\gamma \rightarrow \tilde{\gamma}$ shows that in fact the many-site interactions play a crucial role in the problem under consideration. It's evident also, that the "exponential" character of these interactions leads to the necessity to take into account all of them to calculate thermodynamic functions with the sufficient accuracy.

Fortunately, the existence of the exact relations ("sum rules") between the correlators and the thermodynamics allowed us to calculate free energy and the chemical potential for the disordered phase without the calculation of the high-order effective interactions. These relations are based on the Krivoglaz expression for the correlators

$$(K^{-1})_{ij} = \frac{\partial^2 F}{\partial c_i \partial c_j} \quad (9)$$

where F is the free energy for the arbitrary concentration distribution $\{c_i\}$. It follows from (9) that for the disordered phase

$$\frac{\partial^2 F}{\partial c^2} = \frac{\partial \mu}{\partial c} = K_0^{-1}$$

and thus the thermodynamic functions may be obtained from (8) by simple integration. In this way we had found

$$\mu = \beta V_0 c + \log \frac{1+D}{1+D_n} + \log \frac{c}{1-c}$$

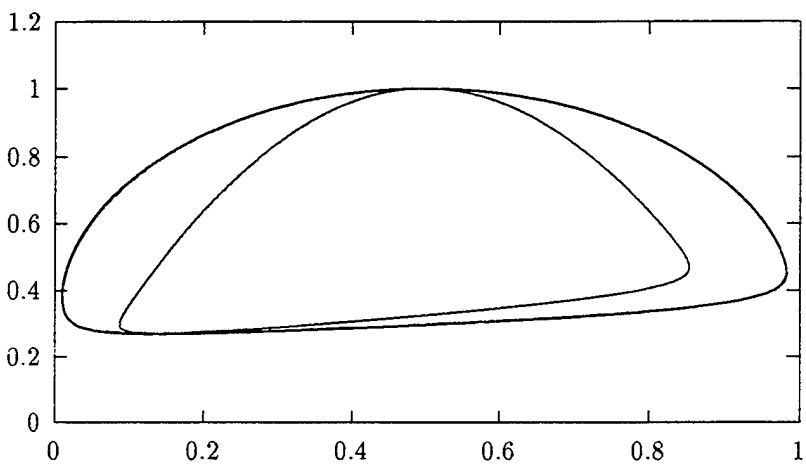
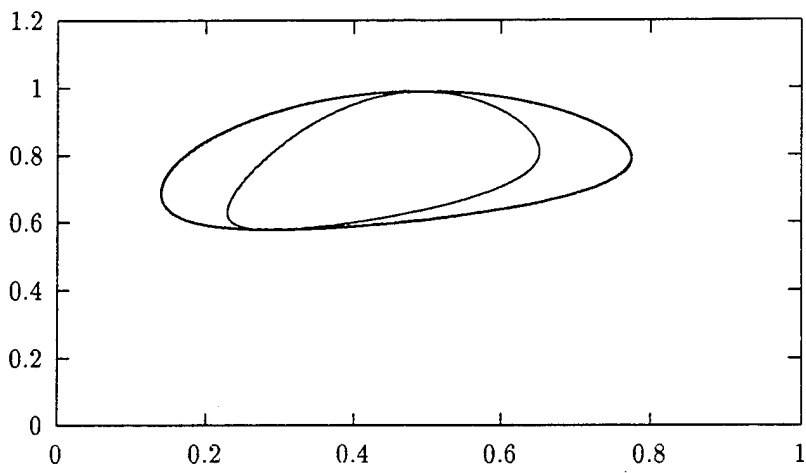


Figure 1: The miscibility gaps calculated for $V_0 = -4$ and different D_0 ; $D_0 = d \exp \beta E_s$. (a) $E_s = 5$; $d = 10^{-5}$; (b) $E_s = 5$; $d = 10^{-9}$. Thin lines represent the instability temperatures.

$$F = \frac{1}{2} \beta V_0 c^2 - c \log(1 + D_0) - \frac{1}{\beta V_0} (\text{DiLog}(D) - \text{DiLog}(D_0)) + c \log(c) + (1 - c) \log(1 - c)$$

where $D = D(c) = \lim_{\mathbf{k} \rightarrow 0} (\Gamma_0 - \Gamma_{\mathbf{k}})/(\tilde{\gamma}_0 - \tilde{\gamma}_{\mathbf{k}})$, $D_0 = D(c = 0)$ and $\text{DiLog}(x) = \int_0^x \log(1 + y)/y$

3. CONCLUSION.

In the present work we have considered both exact and mean-field solution for the alloy under irradiation model. Was found that the effective interactions which determine the thermodynamic properties of the system have essentially many-site character with compatible input in observables in all orders. The generating functional approach for the model with long-ranged interactions was formulated. Equations for correlators were found and solved in concrete models. The procedure of calculation the thermodynamic quantities was illustrated by the miscibility gap calculations for disordered phases.

4. ACKNOWLEDGMENTS.

Two of the authors (V. Vaks and V. Kamyshenko) are much indebted to Drs. G. Martin and P. Bellon for their hospitality in Saclay (France) during the work on this problem and for the illuminating discussions.

5. REFERENCES.

1. G Martin, Phys. Rev. B, **30**, 1424, (1984); P Bellon and G Martin, Phys. Rev. B, **39**, 2403, (1989); E Salomons, P Bellon and G Martin, Phys. Rev. B, **46**, 11332, (1992).
2. P L Garrido and J Marro, Phys. Rev. Lett., **62**, 1929, (1989)
3. V G Vaks, A I Larkin and S A Pikin, ZhETF, **51**, 361, (1966)
4. V G Vaks and V V Kamyshenko, "On the theory of open systems: statistical thermodynamics for the alloy under irradiation model", in Proc. of the International workshop "Statics & Dynamics of Alloy Phase Transformations", Eds. P E A Turchi and A Gonis.
5. V G Vaks and V V Kamyshenko, Phys.Lett. A, **177**, 269, (1993).

Resonant electromagnetic fields effects on trimers and dimers

Maksimov V.V. *, Orlov A.N. **, and Prokhorov A.M. **

* N.S. Kurnakov Institute of General and Inorganic Chemistry,
RAS, 117907, Moscow, Leninskii Prospekt, 31, Russia

** General Physics Institute, RAS, 117942 Moscow,
Vavilov St., 38, Russia

ABSTRACT

The interaction changes between three molecules in trimers due to excitation presence are calculated. The consideration did not take into account the resonant quanta degradation processes (heating). In the frame of two-level approximation the strengthenings of dimers and trimers were found. In case of gas this effect can lead to balance shift. If resonant molecules are on a surface, the clusters strengthening because of quantum exchange may be regarded as the adsorption potential deepening.

The clusters of several individual molecules exist both on a condensed body surface and in gaseous and condensed phases. Some molecules, e.g. chloride copper can evaporate from surfaces in gaseous phase in the form of trimers¹. For some substance molecules the most effective clusters and particularly trimers creating takes place during cooling in a gasdynamic jet.

As in previous work², where dimers were regarded, only the case when molecules unite in trimers due to London's forces and because of interaction between constant multipoles moments is under consideration.

Electromagnetic fields effects on associates consisting of several particles to decompose them or to initiate their growth in gaseous phases were investigated in works^{3,4}.

In this work the question about the additional interaction between he trimer molecules due to excitation one of them is considered. If the dipole active transition is possible, then the quantum exchange is defined by the dipole-dipole interaction at least, in the opposite case the first interaction member is quadrupole-quadrupole one. In our approach the dimer molecules are regarded as two level systems. The consideration implies the times less than the time of the complete energy of excitation transfer in the rotational, translation movements energy or in photons one. Only

for simplicity molecular constant multipoles are supposed not to be changed by the excitation. Here the simplest case is regarded - the position of any molecule in trimer is equivalent. Resonant approach is used. Further we shall consider prolong photon exchange only.

For three identical molecules, which are excited at a time

$t = 0$ with probabilities α^2, β^2 and $\gamma^2 (\alpha^2 + \beta^2 + \gamma^2 = 1)$, one can write

$$\left. \begin{array}{l} i\dot{\psi}_1 = V(\psi_2 + \psi_3) + i\alpha\delta(t) \\ i\dot{\psi}_2 = V(\psi_3 + \psi_1) + i\beta\delta(t) \\ i\dot{\psi}_3 = V(\psi_1 + \psi_2) + i\gamma\delta(t) \end{array} \right\} \quad (1)$$

where ψ_1, ψ_2 and ψ_3 are the wave functions characterizing the excitation of the first, the second and the third particles respectively, V is the matrix element of the interaction between two molecules, V is assumed not to be time-dependent, $\delta(t)$ is Dirac's delta function. The main difference of our approach here from the consideration⁵ is in that the trimer has just existed, and at an initial time the quantum excitation presence probability on any molecule is arbitrary

(but $\alpha^2 + \beta^2 + \gamma^2 = 1$). During trimer interaction with the other particles in gas phase or on a surface (with phonons) the change

of ratio between α^2, β^2 and γ^2 effectively occurs in cases, when the interaction energy is comparable with V , as if the getting out of the phase of the quantum circulating took place for the excitation quantum. The getting out of the excitation quantum circulating⁵ phase due to interaction with phonons was considered previously.

The system of the equations (1) can be deduced of Schrodinger's equation for three 2-level interacting systems under two additional predictions: 1. the excitation quantum energy should be larger than the matrix element of the interaction between two molecules V , in this case the use of Dirac's delta function is possible; 2. the matrix element of the interaction between two molecules V should be larger than the molecules interaction with the laser field $V \gg \mu_0 E$,

where μ_0^I is the matrix element of dipole moments of the molecule transition for the resonant mode, E is the electric intensity amplitude of the laser field. After perform a Fourier transformation with the system of equation (1) we obtain

$$\left. \begin{aligned} -\varepsilon\psi_I &= v(\psi_2 + \psi_3) + i\alpha \\ -\varepsilon\psi_2 &= v(\psi_I + \psi_3) + i\beta \\ -\varepsilon\psi_3 &= v(\psi_I + \psi_2) + i\gamma \end{aligned} \right\} \quad (2)$$

where $\psi_j = \int_{-\infty}^{+\infty} \psi_j e^{-i\varepsilon t} dt, \quad j = 1, 2, 3.$

To derive the functions ψ_j it is necessary to perform the inverse Fourier transformation:

$$+ \infty - i\eta$$

$$\psi_j = \frac{1}{2\pi} \int_{-\infty - i\eta}^{+\infty - i\eta} \psi_j e^{i\varepsilon t} d\varepsilon, \quad (3)$$

$$- \infty - i\eta$$

where $i\eta$ is a small imaginary component, ($\eta > 0$) shifts the contour of integration slightly.

From (2) we obtain, $\psi_I = i \frac{v(\beta + \gamma) - \alpha(\varepsilon + v)}{\varepsilon^2 + \varepsilon v - 2v^2}$

$$\left. \begin{aligned} \psi_2 &= i \frac{v(\alpha + \gamma) - \beta(\varepsilon + v)}{\varepsilon^2 + \varepsilon v - 2v^2} \\ \psi_3 &= i \frac{v(\alpha + \beta) - \gamma(\varepsilon + v)}{\varepsilon^2 + \varepsilon v - 2v^2} \end{aligned} \right\} \quad (4)$$

The functions have two poles $\xi_1 = V$ and $\xi_2 = -2V$.

Performing the inverse Fourier transformation according the formulas indicated above, for $\langle v_{ij} \rangle$ we get

$$\langle v_{ij} \rangle = \frac{1}{4\pi^2} \int \int (\psi_I^*(\xi) \hat{v}_{ij} \psi_2(\xi)) e^{i(\xi-\xi)t} d\xi d\xi + \text{c.c.} \quad (5)$$

where the contour of integration over ξ is a mirror image relative to the real axis of the contour integration over ξ . $i \neq j$, i and j are the numbers of molecules. Performing the corresponding integration, we obtain

$$\left. \begin{aligned} \langle v_{I2} \rangle &= \frac{2}{9}V \left[(\alpha + \beta + \gamma)^2 + (2\alpha - \beta - \gamma)(2\beta - \alpha - \gamma) + \right. \\ &\quad \left. + (\alpha + \beta + \gamma)(\alpha + \beta - 2\gamma) \cos(3Vt) \right] \\ \langle v_{I3} \rangle &= \frac{2}{9}V \left[(\alpha + \beta + \gamma)^2 + (2\alpha - \beta - \gamma)(2\gamma - \alpha - \beta) + \right. \\ &\quad \left. + (\alpha + \beta + \gamma)(\alpha + \gamma - 2\beta) \cos(3Vt) \right] \\ \langle v_{23} \rangle &= \frac{2}{9}V \left[(\alpha + \beta + \gamma)^2 + (2\gamma - \alpha - \beta)(2\beta - \alpha - \gamma) + \right. \\ &\quad \left. + (\alpha + \beta + \gamma)(\beta + \gamma - 2\alpha) \cos(3Vt) \right] \end{aligned} \right\} \quad (6)$$

From (6) it is easy to obtain

$$v_{\Sigma} = \langle v_{I2} \rangle + \langle v_{I3} \rangle + \langle v_{23} \rangle = 2V(\alpha\beta + \alpha\gamma + \beta\gamma) \quad (7)$$

As it was predicted in the work⁵, if only one of three value α , β , or γ would be equal to 1, the sum in (7) would be equal to 0.

If $\alpha = \beta = \gamma = \frac{1}{\sqrt{3}}$, we get $V_{\Sigma} = 2V$.

If $\beta = -\alpha = -\frac{1}{\sqrt{2}}$, $\gamma=0$ we get $V_{\Sigma} = -V$

I.e. trimer excitation can lead both to the deepening and vice-versa to the becoming more shallow of the pear potentials and V_{Σ} .

As a rule the other authors⁶ considered only dimers in two cases

$$\beta = \alpha = \frac{1}{\sqrt{2}} \quad \text{and} \quad \beta = -\alpha = -\frac{1}{\sqrt{2}} .$$

Our hypothesis is in that only the conservation laws define the limits imposed on α , β and γ . I.e. α , β and γ can be permanent.

In our case the figures $\alpha^2 + \beta^2$ and γ^2 ($\alpha^2 + \beta^2 + \gamma^2 = 1$)

characterize the casual excitation probability distribution between three molecules of trimer at an initial time. These figures define the additional potentials that vary dimer and trimer structures. It is possible to estimate the additions to a pear potential. V is the matrix element of the operator of the dipole-dipole interaction between molecules (quadrupole-quadrupole interaction is not taken into account)

$$V_{ij} = \langle \psi_i^0 \psi_j^0 | \frac{\stackrel{\rightarrow}{(\mu_i, \mu_j)} - 3(\hat{n}, \stackrel{\rightarrow}{\mu_i})(\hat{n}, \stackrel{\rightarrow}{\mu_j})}{r^3} | \psi_i^0 \psi_j^0 \rangle, \quad (8)$$

where ψ_i^0, ψ_j^0 , ψ_i^I and ψ_j^I are wave functions of nonexcited and excited molecules. The consideration uses the wave functions the unperturbed

$\stackrel{\rightarrow}{\mu_i}, \stackrel{\rightarrow}{\mu_j}$ Hamiltonian; $\stackrel{\rightarrow}{\mu_i}, \stackrel{\rightarrow}{\mu_j}$ are the operators of the dipole moments for the molecules, \hat{n} is a unit vector along the direction between the molecules centers, r is the distance between the molecules centers.

V_{ij} was analyzed in details in the work⁵.

If, e.g. $i=1$, $j=2$ and \vec{n} is perpendicular the direction $\vec{\mu}_1$ and $\vec{\mu}_2$,
the two last being

$$\text{parallel, we have } V_{12} = \frac{|\vec{\mu}_1|_0^I |\vec{\mu}_2|_0^I}{r^3} \cong \frac{(\mu_0^I)^2}{r^3}.$$

Supposing $\alpha = \beta = \gamma = \frac{1}{\sqrt{3}}$, $\mu_0^I = 0.5D$, $r \cong 3A$, we obtain $V_{12} = 32.2^{\circ}\text{K}$.

Supposing $\alpha = \beta = \gamma = \frac{1}{\sqrt{3}}$ $\mu_0^I = 1D$ (typical matrix element of

dipole moments of transition for molecules in visible range) $r = 3A$
we obtain $V_{12} = 133^{\circ}\text{K}$.

In previous work² the authors supposed, that if the two molecules were modeled by two undivided particles, than the dimers energetic states could be drawn in such way as the energetic states of two atoms molecules. Analogous energetic terms (but only in volume) must take place for trimers. In case of dimer excitation, e.g. due to previous excitation on one of the molecule before the clinging in dimer, the pear potential may be deepened by the amount V . For dimers in gaseous phases it means the time life increase, if the collisions are weak. For dimers on a surface^{7,8} it means the adsorption potential² increase of every molecules^{7,8}. As in previous work² let us consider resonant to laser radiation molecules, which built trimers, e.g. during cooling in a gasdynamic jet. The cooling gas is irradiated in the spot just after critical

part of the jet. The results in works^{9,10}, where benzonitrile molecules in the limit of several percents in the mixture with a noble gas were cooled (rotational temperature was about 4 K) and excited by the light ($\lambda=2738.8 \text{ \AA}$), should explain not only the dimers buildings², but the trimers creations too.

The excited and non excited molecules unites in dimers and in trimers. If the molecules clinging in cluster was adiabatic enough

(smooth) that the migration of a quantum of excitation phase has not been changed at the unite time point (i.e. $\alpha = 1$, $\beta = 0$, $\gamma = 0$.), the excitation quantum presence does not vary the pear potential. Further the dimer and trimer collisions with the other particles vary the phase of the quantum excitation migration, the multiplication $\alpha \cdot \beta$ and the sum $\alpha \cdot \beta + \alpha \cdot \gamma + \beta \cdot \gamma$ become not equal zero, i.e. the weakening or the deepening of the pear potential will take place.

In the dimer case the probability change of dimer decomposition after excitation was possible to find analytically for any ratio between V and kT , if the quantum time life is much more larger than the mean time between collisions and α and β can change because of the collision². The excited dimer decomposition was supposed to take place after the gaining the additional energy due to collision with another particle. The energy distribution of the new terms defined by the α and β was implied to be Boltzmann's one. The expression for the probabilities ratio in the excitation presence P_1 and in the

excitation absence P_0 was found

$$\frac{P_1}{P_0} = I_0^{-1} \left(\frac{V}{kT} \right) \quad (9)$$

where $I_0^{-1}(V/kT)$ is the modified Bessel function of zeroth order, E_a is

the dissociation energy of unexcited dimer. So the dimer excitation may lead to the dimer strengthening in common case after several collisions.

As in the work² the possibility of any molecule (i) in trimer being on the term defined by α , β and γ is equal

$$P_{\alpha\beta\gamma} = \left[\exp(-(\nu_{ij} + \nu_{ik})/kT) \right] / \left[\frac{1}{4\pi} \int_S dS \exp(-\nu_{\Sigma}/kT) \right] \quad (10)$$

The integration is made over the sphere surface with a unit radius. The expressions for ν_{ij} , ν_{ik} and ν_{Σ} are taken from (6)and (7).

The expression for the decompositions probabilities ratio in the excitation presence P_1 and in the excitation absence P_0 is

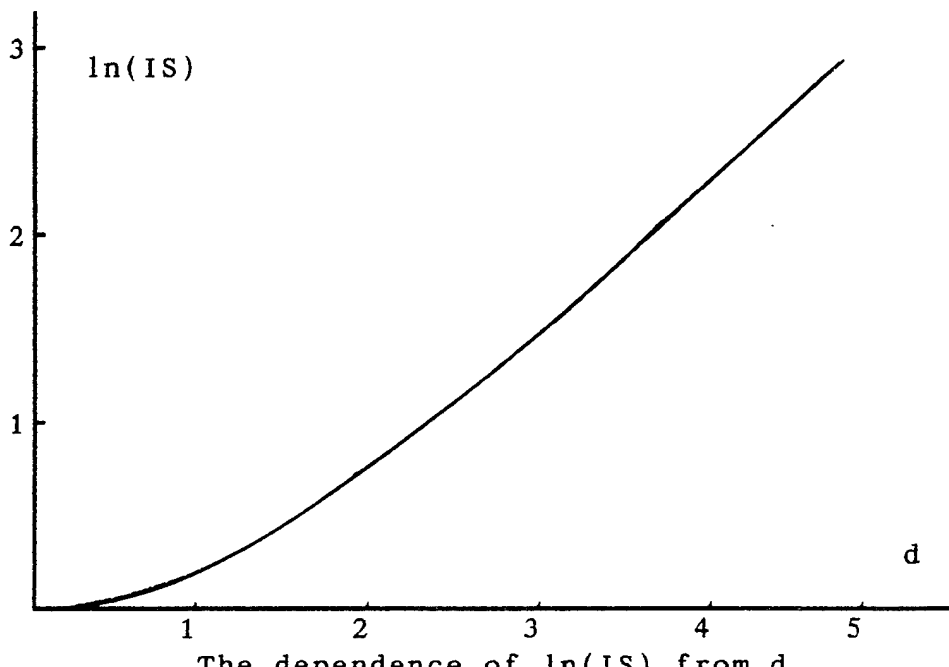
$$\frac{P_1}{P_0} = \frac{1}{4\pi} \int_S dS \sum_{i \neq k} \sum_{i \neq j} P_{\alpha\beta\gamma} \frac{\exp[-(E_a - (V_{ij} + V_{ik}))/kT]}{3\exp(-E_a/kT)} = \left[\frac{1}{4\pi} \int_S dS \exp(-V_{\Sigma}/kT) \right]^{-1} \quad (11)$$

i=1, 2, 3.

$$\text{Let denote } IS(d) = \frac{1}{4\pi} \int_S dS \exp(-V_{\Sigma}/kT),$$

S

$d = V/kT$. The numerically calculated dependence of $\ln(IS)$ from d is shown on the picture.



The dependence of $\ln(IS)$ from d .

The increase of IS from d is not so abrupt as $I(d)$ in case of dimer.

It is possible to come to conclusion that both trimer and dimer excitation may lead to the strengthening of these clusters in common case after several collisions.

In case of a surface the excitation of trimers and dimer may temporary lead to the adsorption potential deepening for the molecules united in dimers and trimers. For practical applications the strengthening dimers and trimers in gas or on a surface because of excitation one of the particles is undoubtedly interesting for gasdynamic separation methods or for surface thin films building.

ACKNOWLEDGMENT

We thank dr. Maslov A.P. for help in calculation.

REFERENCES

1. El'tsov K.N., Zueva G.Ya., Klimov A.N., Martynov V.V. and Prokhorov A.M. Reversible coverage-dependent Cu + Cl_{ads} - CuCl transition on Cu(111)/Cl₂ surface, Surface Science, 1991, v.251/252, pp.753-758.
2. Maksimov V.V., Orlov A.N., and Prokhorov A.M. Resonant electromagnetic fields effects on trimers, Proceedings of ALT'93 (to be published).
3. Alexandrov M.L., Kusner Yu.S. Gasdynamical Molecular, ions and clusters beams. (in Russian), 1989, Leningrad, 271p..
4. Kim K.C., Filip H., Person W.B., Inhibition of Homogeneous Condensation of SF₆ by Vibrational Excitation Chem. Phys. Lett. 1978, v.54, No2, pp.253-257.
5. Kravchenko V.A., Orlov A.N., Petrov Yu.N., Prokhorov A.M. Resonant Heterogeneous Processes in a Laser Field (monograph), Proceedings of General Physics Institute, Acad. of Scien. USSR, 1989, v.11, 253. Nova Science Publishers, Inc.
6. Shahparronov M.I., Philippov L.P. Study of Building, Heat Moving and Properties of Liquids.(in Russian), 1986, Moscow State Univ. 358p.
7. Karlov N.V., Orlov A.N., Petrov Yu.N., Prokhorov A.M. "Interaction between molecules in the resonant electromagnetic field", Pisma v zhurnal tehnicheskoi fiziki, 1982, v.8, No 7, pp 426-428.
8. Orlov A.N. "Resonant molecules behavior change on surface in the laser field", Pisma v zhurnal tehnicheskoi fiziki, 1988, v.14, No 6, pp 532-537.
9. Kobayashi Tohry, Honma Kenji, Kajimoto Okitsugu and Tsuchiya Soji, "Benzonitrile and its van der Waals complexes studied in a free jet. I. The LIF spectra and the structure" J. Chem. Phys. (1987), v.86, pp.1111-1118.
10. Kobayashi Tohry and Kajimoto Okitsugu "Benzonitrile and its van der Waals complexes studied in a free jet. II. Dynamics in the excited state: The effect of changing the degrees of freedom of partner molecules." J. Chem. Phys. (1987), v.86, pp.1118-1124.

New Laser Systems for Technological Applications

Recent developments in solid-state lasers materials and devices

Jean-Marc Breteau

Thomson-TRT Défense, Optronics Division
Rue Guynemer, BP 55, 78283 Guyancourt Cedex, France

ABSTRACT

The interest to solid-state lasers has been renewed in the last decade. Diode-laser pumping, tunable lasers and nonlinear optics are the main developing technologies to have revitalized the field of solid-state lasers. An overview of the more recent results in rare-earth and transition-metal doped systems is made in addition with the advances in frequency conversion by mean of optical parametric oscillators.

Keywords : rare-earth ions, transition-metal ions, nonlinear optics, diode-pumping, OPO, lasers

1. INTRODUCTION

In the last decade, solid-state lasers have become the center of an increasingly activity in research and development. Solid-state lasers come in a wide variety of applications emerging from laboratory curiosities to being key components in variety of electro-optics systems. Current applications of solid-state lasers include basic scientific investigations in spectroscopy, laboratory studies of new semiconductor and fiber-optics devices, generation of ultrashort pulses and amplification of these pulses to high peak powers. Future applications now under development include aircraft and space based laser sources for remote sensing lidars, range finding and communications, laser medicine and industrial processes.

To meet all the specific technical objectives, solid-state sources have to operate over the whole spectrum from U.V. to IR. It needs to develop laser materials emitting new wavelengths and operating with high efficiencies. Among the technical advances contributing to renew interest in solid-state lasers, laser diode pumping and nonlinear conversion have played a key role in the past ten years. This paper will review the field by providing a short presentation of recent results obtained with diode pumped rare earth and transition-metal doped solid-state lasers in addition to the frequency conversion by mean of parametric oscillators.

2. RARE-EARTH DOPED SOLID-STATE LASERS

Since the first demonstration of a diode pumped (DP) Nd : YAG laser at room temperature¹, the pumping of solid-state lasers with diodes lasers has matured into commercial units within the last few years in parallel to many studies aiming to improve the output energy or the peak power as well as the overall efficiency with still more compact systems.

2.1 Nd³⁺ lasers

Presently, the most common DP lasers involve the use of AlGaAs diode lasers to pump the Nd³⁺ absorption band near 810 nm in various hosts^{2,3,4,5}. Diode pumping allows for more efficient solid-state lasers since the diodes lasers efficiently convert electrical power to radiated power which is matched to a specific absorption line of the active medium. Typical performances of DP Nd³⁺ lasers under development in different laboratories are gathered in table I.

Parameter	Value	Laboratory
Average power	$\geq 1\text{KW}$	LLNL ³
CW power at $1.06 \mu\text{m}$	92W MM 60W TEM $_{\infty}$	STI ⁵
CW power at $0.532 \mu\text{m}$	4W	ADLAS ⁶
Q-switched Energy ($1.06 \mu\text{m}$)	$\geq 1\text{J}$	Fibertek ⁴
Peak power	$\geq 100\text{MW}$	Fibertek ⁴
Spectral width	$\leq 10^{-3} \text{ Hz}$	Stanford ⁷

Table I
Output performances of current diode-pumped Nd³⁺ lasers

If the diode pumping limits the heat deposited inside the active medium and represents the most efficient pump sources for solid-state lasers, the amount of energy that a single quasi CW laser diode bar can deliver is limited. An alternative method developed by THOMSON-CSF is based on a Monolithic Surface-Emitting Laser (MOSEL) whereby broad-area laser diode structures were grown on an engraved GaAs substrate⁸. The groove edges are etched at a 45° angle to form an integrated mirror that reflects the output beam normally to the epitaxial plane (Fig.1).

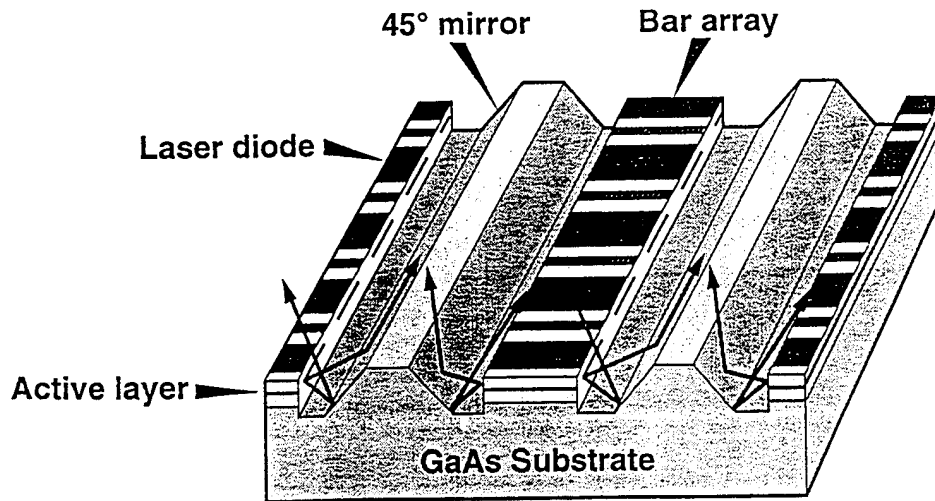


Fig.1 : Schematic diagram of a MOSEL developed by THOMSON-CSF Composants Speciaux (TCS)

Peak intensity as high as $100\text{W}/0.1\text{cm}^2$ was demonstrated and an assembly of ten MOSEL's on the same substrate delivered $1\text{KW}/1.3 \text{ cm}^2$ peak intensity in $100 \mu\text{s}$ pulse was realized⁸. An interesting particularity of MOSEL is the reduced optical

divergence of the beam (< 15 deg. (FWHM) in each direction) compared to the usually observed large divergence (\approx 60 deg.) in the direction perpendicular to the junction plane of linear arrays. A small concavity in the reflecting mirrors induces this reduction and allows to pump microchips lasers longitudinally. In order to keep the pump intensity in a volume as small as possible, laser materials with high absorption coefficients would be preferred. Furthermore, materials with a broad absorption band around 810 nm allow to release temperature requirements for the pump modules. At present, Nd : YVO₄ is a material of choice because of its high emission cross-section and high absorption cross-section (Table II).

Host	$\Delta\lambda_{\text{abs}}$ (nm)	k_{abs} (cm ⁻¹)	λ_{em} (μm)	σ_{em} (10 ⁻¹⁹ cm ²)	τ_{em} (μs)	$\sigma_{\text{em}} \cdot \tau_{\text{em}}$ (10 ⁻¹⁷ cm ² ·μs)	Ref.
YVO ₄	2 (π) 10 (σ)	40 (π) 10 (σ)	1.0641	10.7	98	10.5	⁹
GdVO ₄	1.5 (π)	73.5(π)	1.063	6.0	87	5.2	⁹
Sr(VO ₄) ₃ F (SVAP)	1.6	18	1.065	5.0	209	10.45	⁹
YPO ₄		4 (π) 8 (σ)	1.0624 1.068	10.5	140	14.7	¹⁰
YAG	1.5	3.5	1.064	2.52	230	5.17	
YLF	2 (π) 3(σ)	2.5	1.047 1.053	3.5 2.5	500	17.5 12.5	

Table II
Spectroscopic properties of Nd³⁺ doped material for microchips lasers

According ⁹, the lasing performances of the three vanadates are similar. However YVO₄ has the highest slope efficiency (66 %) and SVAP has the lowest threshold compared to GdVO₄. A 3 mm long 1% Nd : YVO₄ was longitudinally pumped by a MOSEL ¹¹. An output energy of 0.74 mJ was obtained with a 2.3 mJ incident pump energy (100 μs pulses). The slope and optical efficiencies were 35 % and 32 % respectively.

When applied to optical waveguide configuration, diode pumping offers some interesting miniatures devices possibilities ¹². Among the potential hosts of Nd³⁺ ions, LiNbO₃ is of particular interest because of its nonlinear and electrooptic properties. Effects such as self frequency doubling and self Q-switched laser action can be observed. With 1cm long proton exchanged waveguides on 0.1%Nd : LiNbO₃ substrate, Q-switched operation up to 10 KHz Pulse Repetition Frequency (PRF) was obtained with peak powers of a few hundred watts in 300 ps pulse width for 15 mW pump power at 814 nm ¹³.

2.2 Yb³⁺ lasers

Since the advent of InGaAs laser diodes, other interesting developments have occurred with Yb³⁺ doped lasers. Yb³⁺ ion is the simplest example of a RE laser ion. With only two electronic states : the ² F_{7/2} ground state and the ² F_{5/2} excited state, Yb³⁺ ion presented extremely poor pumping efficiency when flash lamp was used ¹⁴. Resonant pumping in a narrow spectral region near 950 nm provides high pumping efficiency ¹⁵. While the absence of higher-lying excited states eliminates the need to consider effects such as excited state absorption (ESA) and up conversion, ytterbium-doped crystal lasers are still quasi-three levels systems owing to thermal population of the lower laser level. To produce efficient Yb³⁺ laser emission at room-temperature, the crystal field splitting of the lower ²F_{7/2} level is a crucial issue and must be greater than 400 cm⁻¹ in a short pulse operation mode. On the other hand, the laser emission cross-section σ_e has to be greater than 10⁻²⁰ cm² to avoid optical damage of the crystal hosts when the saturation intensity ($I_{\text{sat}} = h\nu / \sigma_e \cdot \tau$) is too high. Compared to usual Nd³⁺ solid-state lasers, Yb³⁺

lasers present a longer storage lifetime ($\tau=1\text{ms}$) for a laser wavelength centered at $1.03 \mu\text{m}$. YAG¹⁶ and fluoroapatite¹⁵ FAP have been shown to be more suitable hosts for Yb^{3+} ions. Their main spectroscopic properties are given in table III. According¹⁵ with an optical efficiency $\geq 50\%$, Yb^{3+} : FAP is believed to be the most efficient crystal.

	ΔE (cm ⁻¹)	σ_{em} (10 ⁻²⁰ cm ²)	τ_{em} (ms)	λ_{em} (nm)	I_{sat} (KW/cm ²)
YAG	628	2.03	1.08	1031	8.8
FAP $\text{Ca}_5(\text{PO}_4)_3\text{F}$	603	5.9	1.08	1043	3.0

Table III
Spectroscopic properties of Yb^{3+} doped materials

2.3 Er³⁺, Tm³⁺, Ho³⁺ lasers

Lasers operating in the 2-3 μm region are of interest for a number of applications as remote sensing of windshear, optical pumping of IR Optical Parametric Oscillators (OPO) or laser surgery. On the other hand, development of the optical telecommunications based on erbium-doped fibre amplifiers (EDFA)¹⁷ has also reinforced spectroscopic studies of 1.5-1.6 μm transition of this ion. The performances of these laser centers are often enhanced by energy transfers between the active centers or with additional impurity ions as Yb^{3+} . The Tm³⁺, Ho³⁺ system is a striking example of the usefulness of such transfers. The relevant energy levels are shown in Fig.2. The 5I_7 upper laser level of Ho³⁺ is populated in two steps. A GaAlAs diode laser at 785 nm pumps the Tm³⁺ ions by mean of a self-quenching process ($^3H_4, ^3H_6 \rightarrow ^3F_4, ^3F_4$). The effectiveness of this quenching process increases with higher Tm³⁺ concentration with an optimum around 5 % in garnets crystals¹⁸. Following the quenching process, a non radiative phonon-assisted energy transfer occurs between Tm³⁺ and Ho³⁺ to populate the 5I_7 upper laser level. As a matter of fact, the theoretical maximum slope efficiency for laser output at 2 μm is 78 % if the quantum efficiency of 785 nm pumping is assumed to be two. Similar consideration can be made for Tm³⁺ lasers which emit at a shorter wavelength (2.0 μm) than Ho³⁺ laser (2.1 μm).

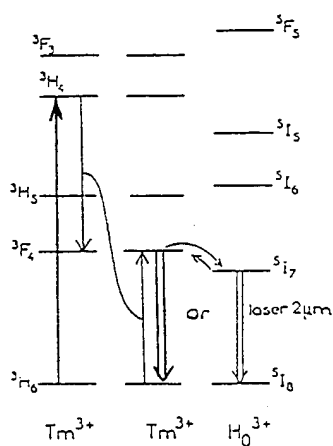


Fig.2 : Resonant pumping scheme for Tm³⁺ and Ho³⁺ laser transitions

Despite of the Tm³⁺ 2.0 μm $^3F_4 \rightarrow ^3H_6$ and the Ho³⁺ 2.1 μm $^5I_7 \rightarrow ^5I_8$ laser transitions operate as a quasi-three-level scheme, highly efficient diode pumped laser emission is obtained as with 6 % Tm³⁺ : YAG delivering up to 350 mJ in a 70 ns pulse with a 10 % optical efficiency and 3.6 % electrical to optical efficiency ¹⁹. Recent demonstration of the first diode-pumped mode-locking of Tm, Ho : YLF at 77 K was reported with 370 ps pulsedwidth and 300 mW average power at 2.0 μm ²⁰.

The possible application in surgery of Er³⁺ 3 μm lasers has induced many developments aiming to increase the power and efficiency ^{21,22}. The main limitations of laser operation at 3 μm ($^4I_{11/2} \rightarrow ^4I_{13/2}$) are attributed to bottlenecking in the lower laser level $^4I_{13/2}$ due to the longer lifetime ($\tau = 10\text{ms}$) compared to the upper laser level $^4I_{11/2}$ ($\tau = 4.8\text{ ms}$). According ²³ such a limitation can be overcome in Er³⁺ : LiYF₄ (YLF) owing to normal and inverse upconversion processes leading to the quenching of the $^4I_{13/2}$ level without reducing the output power of the laser.

2.4 Pr³⁺ lasers

The renewal of interest in studying praseodymium doped materials is firstly due to its potential application in fibre amplifiers (PDFA's) operating in the 1.3 μm low-dispersion spectral window ¹⁷ and secondly to its possible laser transitions in the visible at 491 nm, 520 nm, 635 nm and 715 nm ^{24,25,26}. The energy levels of Pr³⁺ are qualitatively sketched in Fig.3.

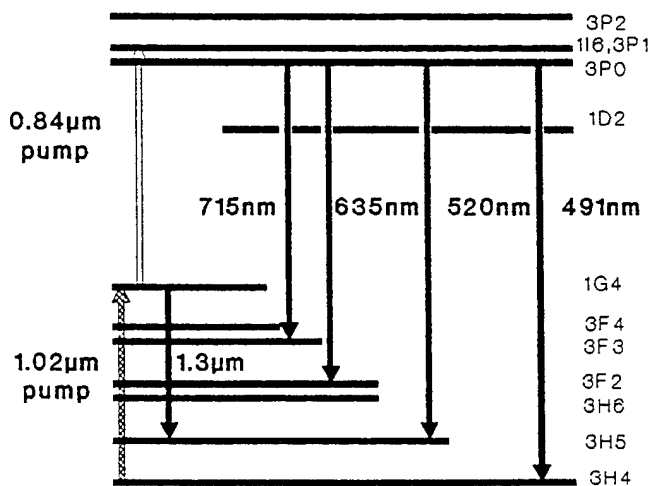


Fig. 3 : Simplified energy level diagram for Pr³⁺ ion in ZBLAN optical fibre

Compared to Nd³⁺ doped glasses, Pr³⁺ doped materials have no noticeable excited state absorption (ESA) at 1.3 μm. Nevertheless multiphonon relaxation considerably quench the 1G_4 upper level state ($\tau \approx 100\mu\text{s}$). That is the reason why successful laser and amplifier operation at 1.3 μm have been obtained in ZBLAN fibre where the confinement for the pump beam compensates the 1G_4 quenching. Unsensitized Pr³⁺ doped materials are only excitable with a pump radiation centered at 1.02 μm corresponding to the maximum absorption in the 1G_4 level. The first successful DP operation of Pr³⁺ fibre amplifiers is reported in ²⁷ where strained layer InGaAs diodes laser emitting at 1.02 μm were used.

Sensitization with Yb³⁺ ions is another way to pump Pr³⁺ ions. This solution was implemented in ²⁶ in a derived configuration. The collimated output of an Yb³⁺ doped silica fibre laser pumped in the absorption wing at 840 nm was launched into a Pr³⁺ doped ZBLAN fibre. Lasing at visible wavelengths was possible since the simultaneously need pump wavelengths 1.02 μm and 0.84 μm were co-launched into the Pr³⁺ doped fibre for upconversion-pumping of laser material. Laser action was demonstrated at 635, 520 and 491 nm with performances summarised in table IV for 1W pump at 840 nm.

λ_{em} (nm)	$P_{\text{threshold}}$ (mW)	η_{Slope} (%)	P_{out} (mW)
635	120	23	54
520	180	8.5	18
493	260	5.7	6.5

Table IV
Laser performance of Pr³⁺ ZBLAN fibre laser (from ²⁶)

Recently, new IR lasers channels at 1.6 μm ($^3\text{F}_3 \rightarrow ^3\text{H}_4$) and 5.2 μm ($^3\text{F}_3 \rightarrow ^3\text{H}_6$) were reported with Pr³⁺ : LaCl₃ at low temperature (T=123K) ²⁸. At 5.2 μm , free running pulses of 5 mJ output energy were observed with a 20 % optical efficiency and 29 % slope efficiency.

3. TRANSITION-METAL DOPED LASERS

Although tunable lasers based on solid-state active media were demonstrated as far back as 1963 ²⁹, it was not until in the 80's that they were considered for any systems applications. Transition-metal-doped lasers were the center of a great interest of research and development in the past ten years because of their advantages over dyes lasers in terms of reliability, ease of use, stability and longer storage lifetime. In terms of development the alexandrite, (BeAl₂O₄ : Cr³⁺) and Ti³⁺ : Al₂O₃ lasers are in the most mature state and widely commercialized with also the Co²⁺ : MgF₂ laser. Fig.4 shows the tuning ranges covered by each of these lasers besides other potential materials now emerging from the laboratory as Cr³⁺ : LICAF and LISAF or Cr⁴⁺- doped crystals.

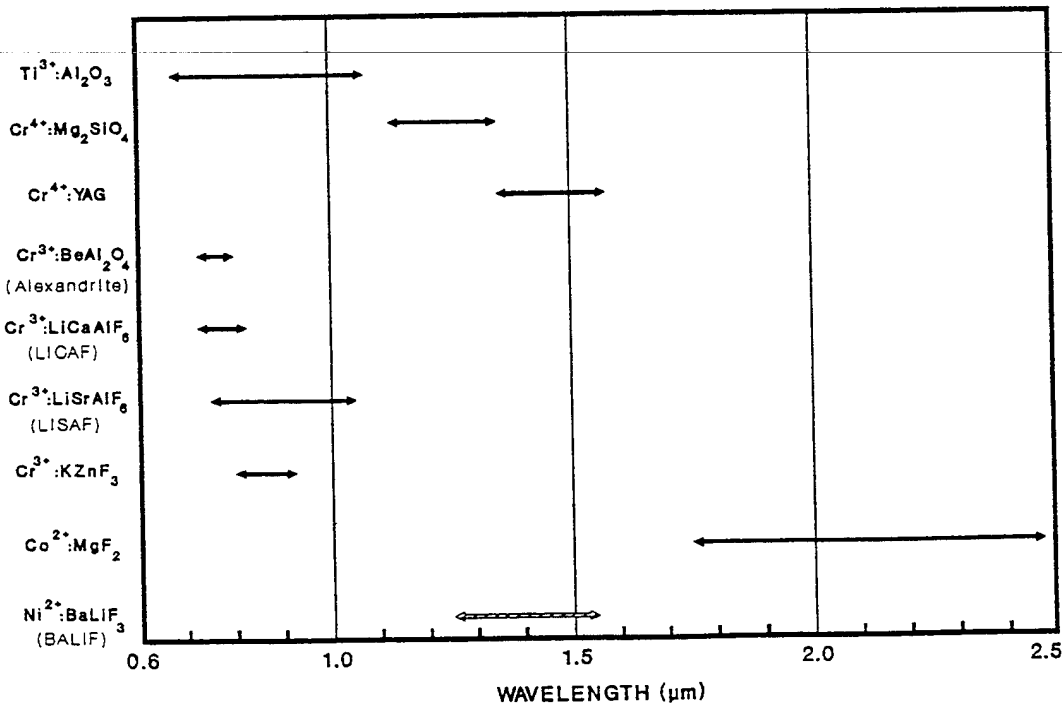


FIG. 4 : Tuning ranges for transition-metal doped lasers.

3.1 Cr³⁺ lasers

After the alexandrite system was discovered, worldwide activity took place to develop other host crystals that would allow vibronic laser action from the Cr³⁺ ion. All along the 80's researchers at Lawrence Livermore National Laboratory identified several fluoride crystals hosts as LiCaAlF₆ (LICAF)³¹, LiSrAlF₆ (LISAF)³² and LiSrGaF₆ (LISGAF)³³ exhibiting a combination of efficient laser operation and relative ease of large-size crystal growth.

In particular Cr³⁺ : LISAF was found to be an excellent candidate for an all solid-state laser tunable in the near IR range (750-1000 nm) and pumpable by GaAlInP red diodes laser around 670 nm³². The development of new high power GaAlInP diodes laser (500 mW and now 3W by Spectra Diode Laboratories) opens up new areas in the study of DP Cr : LISAF lasers. Quasi-CW operation producing 140 mW at 850 nm and tunability from 810 to 900 nm when pumped by two 500 mW single strip diodes laser (SDL 7432) at 668 nm, was recently reported³⁴. By adding an intracavity acousto-optic modulator, pulses as short as 100 ps have been obtained at 860 nm with 30 mW average power in active mode-locking.

3.2 Cr⁴⁺ lasers

The tetrahedral coordinated Cr⁴⁺ ion is a promising laser ion in the near IR spectral range between 1.1. μm and 1.7 μm . Laser operation of Cr⁴⁺ : YAG was observed³⁵ in the former Russia at about the same time as that for the forsterite laser (Cr⁴⁺ : Mg₂SiO₄)³⁶. Tuning ranges in the near IR (1.15 - 1.6 μm) covers the region of interest for fibre communication as OTDR (Optical Time Domain Reflectometers) or WDM (Wavelength Division Multiplexers) and the eye-safe region above 1.45 μm . Besides of intense efforts in research and development of new crystals hosts as Y₂SiO₅ (YOS)³⁷, Y₃Sc_xAl_{5-x}O₁₂ (YSAG)³⁸, or aluminates and gallates with melilite structure (CaYAl₃O₇ and SrGdGa₃O₇)³⁹, first commercial systems become available with laser crystals grown in Russia^{40 41}.

3.3 Co²⁺ and Ni²⁺ lasers

The Co²⁺:MgF₂ laser was first demonstrated in 1964⁴². Up to 1988, this laser was not considered for a number of applications because of the system requirement for flowing-liquid-nitrogen cooling. However, the use of short (100 μs) pump pulses ($\lambda_p = 1318 \text{ nm}$, Nd³⁺ : YAG) with fast rise times allowed to overcome the short upper-state lifetime at room temperature ($\tau \sim 36 \mu\text{s}$)⁴³. Recent results indicate room temperature normal-mode operation with pulsed energies up to 900 mJ in the 2050 nm wavelength region, at a 2 Hz pulse rate⁴⁴. With three sets of cavity mirrors, the range 1730-2450 nm was covered and at least 100 mJ of output energy was obtained over the range 1800-2450 nm, for 1.4 J of pump energy.

Analysis of laser operation in various Ni²⁺ doped crystals showed that excited state absorption (ESA) of the laser wavelengths and possibly the pump wavelengths was significant and limited laser efficiency. Furthermore, as the crystal temperature increased, reduction in quantum efficiency owing to the fluorescence quenching by multiphonon non radiative transitions, needed to operate Ni²⁺ lasers at cryogenic temperatures⁴⁵. Recently, a new IR laser material Ni²⁺ : BaLiF₃ (BALIF) has been grown⁴⁶. the 4.75 ms IR fluorescence lifetime at room temperature and $1.53 \times 10^{-20} \text{ cm}^2$ maximum emission cross-section with a 1.25-1.55 μm potential tuning range are very promising for a future tunable IR laser.

4. PARAMETRIC CONVERSION

Optical parametric oscillators (OPO's) provide an efficient and relatively simple means of frequency shifting the outputs of solid-state lasers. Typically, the output of a high-power pulsed laser is focused into a nonlinear crystal, and if the intensity of this pump laser is sufficiently high, the optical parametric process is initiated, which generates signal an idler outputs whose optical frequencies sum to equal that of the pump. In order to lower the threshold of parametric conversion, the crystal is enclosed in a resonant cavity that provides feedback at the signal and/or the idler frequency.

Since the first successful operation of an OPO in 1965⁴⁷, considerable efforts have been expended in understanding and improving the device performance. Among the difficulties encountered in realizing practical systems, the most serious have been optical damage to the nonlinear crystals and the efficiency and beam quality of the pump sources.

Now these two drawbacks have been overcome. First, because new or improved nonlinear crystals with high damage thresholds have been developed (see table V) and second, because diode pumping has provided efficient high-power pump lasers with TEM₀₀ outputs and a high shot-to-shot stability. These advances in lasers and materials technology have allowed the development of efficient tunable all solid state sources using OPO's.

Crystal	LBO	BBO	KTP	KTA	LiNbO ₃	KNbO ₃	AgGaS ₂	AgGaSe ₂	ZnGeP ₂
Transparency (μm)	0.16-3.3	0.196-3.3	0.35-3.6	0.35-5.5	0.33-5.0	0.4-5.4	0.5-13	0.78-18	0.74-12
Type	Biaxial	Uniaxial	Biaxial	Biaxial	Uniaxial	Biaxial	Uniaxial	Uniaxial	Uniaxial
Refractive Index	1.6	1.6	1.7-1.8	1.8-1.9	2.2	2.1	2.4	2.6	3.2
Nonlinear Coefficient (pm/V)	= 1	= 2	2-3	3-4	= 4	= 10	= 20	= 30	= 75
Damage Threshold (MW/cm ²)	20000	4000	>500	>350	100	1000	25	25	60-1000

Table V
Materials for visible and IR OPO

When pumped at the tripled or quadrupled output from a Nd³⁺ laser, LiB₃O₅ (LBO) and β - BaB₂O₄ (BBO) are very efficient nonlinear materials for visible and near IR ($\lambda < 3 \mu\text{m}$) OPO's. Conversion efficiencies up to 50 % between the pump energy ($\lambda = 355 \text{ nm}$) and the output signal energy ($\lambda_s = 485 \text{ nm}$) were reported ⁴⁸.

Over the last four years KTiOPO₄ (KTP) has become the material of choice for the generation of eye-safe radiation around 1.55 μm ⁴⁹ and low attenuation atmospheric radiation at 2 μm ⁵⁰. Fig. 5 plots the KTP OPO output energy at 1.58 μm versus 1.06 μm pump energy incident at the OPO cavity input mirror. For Q-switch pump pulses of 30 mJ, more than 10 mJ were obtained at the signal wavelength corresponding to a 35 % optical efficiency ⁵¹.

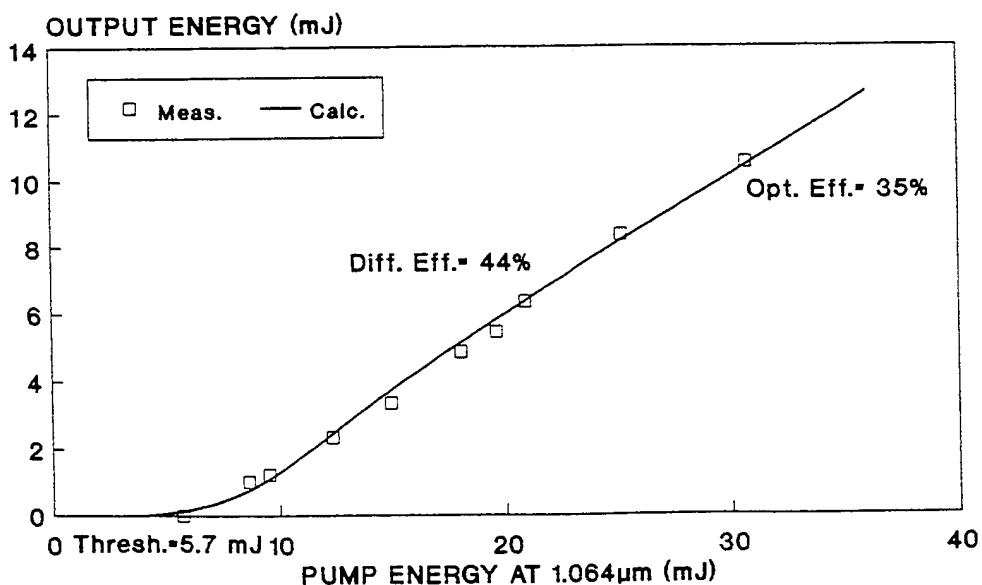


Fig. 5 : KTP OPO output energy at 1.58 μm versus 1.06 μm pump energy (from ⁵¹)

Currently KNbO_3 and KTiOAsO_4 (KTA) are promising materials for mid-IR applications, with their transparencies up to $5 \mu\text{m}$. Although AgGaS_2 and AgGaSe_2 have low damage thresholds, they are of interest for the design of low to medium powers OPO's emitting far into the infrared transmission band of the atmosphere. OPO's using AgGaSe_2 have been pumped by Tm, Ho lasers ⁵² and LiNbO_3 OPO at $2 \mu\text{m}$ ⁵³. Zinc germanium phosphide (ZnGeP_2) is a promising material for relatively high-power far IR OPO's with damage threshold a factor of three greater than AgGaSe_2 .

5. CONCLUSION

The field of solid-state lasers have now reached a high degree of technological maturity. However, the field has never been so in flux as today. The eighties have seen the revitalization of the field by at least three developing technologies :

- Diode-laser pumping, which has allowed to realize low to medium power, compact, efficient and frequency-stable Nd^{3+} and other RE³⁺ doped lasers well fitted to aircraft and space based systems.
- Tunable lasers such as alexandrite, $\text{Ti}^{3+} : \text{Al}_2\text{O}_3$, $\text{Cr}^{3+} : \text{LICAF}$ and LISAF, $\text{Co}^{2+} : \text{MgF}_2$ whose the greatest interest results in the potential combination of these sources with diode-laser pumping or diode pumped sources.
- Nonlinear optics which have permitted to efficiently frequency shifting the outputs of solid-state lasers from UV to far IR.

Development of new solid-state lasers can be considered in a modular approach and requires a marriage of the fields of crystal growth, spectroscopy, laser, heat transfer and flow physics. The resulting laser devices will have to generate new wavelengths, operate more efficiently, be produced at lower cost and have optical properties meeting specific technical objectives.

6. ACKNOWLEDGEMENTS

The author wants to acknowledge G. Feugnet, C. Larat, M. Schwartz of the Central Research Laboratory of Thomson-CSF and P. Georges of IOTA, Orsay, France for information and data on diode-pumped Nd : YVO_4 and Cr : LISAF respectively.

7. REFERENCES

1. D.L. Sipes ; Appl. Phys. Lett 47, 2 (15 July 1985)
2. J.St.P. Randall et Al. ; OSA proceedings on Advanced Solid-State Lasers, 15, pp 2-8 (Feb.1993)
- 3.B.J. Comaskey et Al ; IEEE Journal of Quant. El., 28, pp 992-996 (1192) .
4. W. Koechner et Al., SPIE 1522 , pp 169-179 (1991)
- 5.S.C. Tidwell, J.F.Seamans and D.D. Lowenthal ; OSA proceedings on Advnaced Solid-State Lasers, 15, pp 150-153 (Feb.1993)
- 6.H.P. Kortz, J. Reingruber, W.Skrilac, Adlas; LASER 93-Munich session on Lasers in Research (June 21-25,1993).
- 7.P. Fritschel, A.Jeffries and T.J.Kane; Opt.Lett., 14, 18, pp 993-995 (Sept.15,1989).
- 8.B.Groussin, F.Pitard, A.Parent and C. Carriere; Elect. Lett.29, 370 (1993)
- 9.B. Chai, G.Loutts, X.X. Zhang, P.Hong, M. Bass, I.A. Shcherbakov and A.I. Zagumennyi; OSA proceedings on Advanced Solid-State Lasers, paper AWC1, pp 230-232 (Feb.1994).
- 10.L.G. DeShazer et Al.; Conference on Lasers and Electro-Optics, CLEO 92 (May 1992).
- 11.G. Feugnet, M. Schwartz, C. Larat and J.P. Pocholle ; Opt.Lett., 18,24, pp2114-2116 (Dec.15,1993).
- 12.E.Lallier, J.M. Breteau, M. Papuchon and J.P. Pocholle; SPIE vol.1131, pp 247-251, Optical space communication (1989).
- 13.E. Lallier, phD dissertation, Université Paris-Sud (Dec.16,1992).
- 14.P.F. Moulton ; Handbook of Laser Science and Technology, vol.I, Lasers and Masers, ed. by M.J. Weber (CRC Press, Florida, 1982).
- 15.R.Scheps, J.F. Myers and S.E. Payne; IEEE Phot. Techn. Lett, vol.5, 11 (Nov. 1993).
- 16.P. Lacovara, H.K. Choi, C.A. Wang, R.L. Aggarval and T.Y. Fan; Opt. Lett. Vol. 16, pp 1089-1091 (1991).
- 17.L.J. Sweeney and R. Johson ; Lasers & Optronics, pp. 15-16 (May 1994).
- 18.A. Brenier, C. Madej, C.Pedrini and G. Boulon ; J.Phys. : Cond. Matt.3 pp 7887-7894 (1991).
- 19.S.R. Bowman, G.J. Quarles, J.G. Jynn, S.K. Searles and B.J. Feldman OSA annual meeting, paper TuMM2 (Sept.1192).

20.K.L. Schepler, B.D. Smith, F. Heine and P.A. Budni ; OSA proceedings on Advanced Slid State Lasers, paper AWF1 (Feb.1994).

21.K.S. Badgasarov, V.I. Zhekow, V.A. Lobachev, T.M. Murina and A.M. Prokhorov; *Kvant. Elektr* 10, 452 (1983).

22.R.C. Stoneman, J.G. Lynn and L. Esterowitz; *IEEE J. Quant. Elect.* 28, 4, 1041 (1992).

23.M. Pollnau, W. Lüthy and H.P. Weber ; OSA proceedings on Advanced Solid-State Lasers, paper Ath B7 (Feb. 1994).

24.D.Piehler and D. Craven; Conference on Lasers and Electro-Optics, CLEO technical digest, 11, pp406-407 (1993).

25.J.Y. Allain, M. Monerie, H. Poingnant ; *Elect. Lett.*, 27, 1157 (1991).

26.H.M. Pask, A.C. Tropper, D.C. Hanna, B.N. Samson, R.D.T. Lauder, P.R. Barber, L. Reekie, J.L. Archambault, S.T. Davey and D. Szebesta ; OSA proceedings on Advanced Solid-State Lasers, paper ATuD1 (Feb. 1994).

27.Y. Ohishi et Al.; *Elect. Lett.*, 27, pp 1995-1996 (1991).

28.S.R. Bowman, J. Ganem, B.J. Feldman and A.W. Kueny; OSA proceedings on Advanced Solid-State Lasers, paper PD1 (Feb. 1994).

29.L.F. JohNson, R.E. Dietz and H.J. Guggenheim ; *Phys. Rev. Lett.* 11, 318 (1963).

30.J.C. Walling, H.P. Jenssen, R.C. Morris, E.W.O'Dell and O.G. Petersen ; *Opt. Lett.* 4, pp 182-183 (1979).

31.S.A. Payne, L.L. Chase, H.W. Newkirk, L.K. Smith and W.K. Krupke ; *IEEE J. Quant. Elect.* 24, pp 2243-2252 (1988).

32.S.A. Payne, L.L. Chase, L.K. Smith, W.L. Kway and H.W. Newkirk ; *J. Appl. Phys.* 66, PP. 1051-1056 (1989).

33.L.K.Smith, S.A. Payne, L.L. Chase, W.L. Kway and B.H.T. Chai ; Conference on Lasers and Electro-Optics, CLEO 91, pp 388-390 (1991).

34.F. Balembois, P. Georges and A. Brun ; OSA proceedings on Advanced Solid-State Lasers, paper AMD2 (Feb. 1994).

35.N.B. Angert, N.I. Borodin, V.M. Garmash, V.A. Zhitnyuk, A.G. Okrimchuk, O.G. Siyuchenko and A.V. Shestakov; *Sov. J. Quant. Elec.*, 18, pp73-74 (1988).

36.V. Petricevic, S.K. Gayen, R.R. Alfano, K. Yamagishi, H.Anzai and Y. Yamaguchi; *Appl. Phys. Lett.* 52, pp1040-1042 (1988).

37.A.G. Avanesov, B.I. Denker, B.I. Galagan, V.V. Osiko, A.V. Shestakov and S.E. Sverchkov ; OSA proceedings on Advanced Solid-State Lasers, paper AMC5 (Feb. 1994).

38.S. Kück, K. Petermann and G. Huber; OSA proceedings on Advanced Solid-State Lasers, paper AMB2 (Feb.1994).

39.N.N. Bakhurova, A.L. Denisov, E.V. Zharikov, V.A. Smirnov and I.A. Scherbakov ; OSA proceedings on Advanced-Solide-State-Lasers, paper PD8 (Feb.1994).

40.Bestec, commercial data sheet (1993).

41.Maxima, commercial data sheet (1993).

42.L.F. Johnson, R.E. Dietz and H.J. Guggenheim; *Appl. Phys. Lett* 5, 21 (1964).

43.D. Welford and P.F. Moulton ; *Opt. Lett.* 13, 11, pp975-977 (Nov. 1988).

44.D.M. Rines, P.F. Moulton, D. Welford and G.A. Rines ; *Opt. Lett.* 19, 9, pp. 628-630 (May 1, 1994).

45.J.M.Breteau, D. Meichenin and F. Auzel; *Revue Phys. Appl.* 22, pp 1419-1429 (1987).

46.M. Mortier, J.Y. Gesland, M. Rousseau, F.Auzl and D. Meichemin ; proceedings of EURODIM conference, Lyon (July 1994).

47.J.A. Giordmaine and R.C. Miller ; *Phys. Rev. Lett.* 14, 973 (1965)

48.A. Fix, T. Schroder and R. Wallenstein ; *Laser und Optoelektronik*, 23,3, pp 106-110 (1991)

49.L.R. Marshall, J. Kasinski, A.D. Hays and R. Burnham ; *Opt. Lett.* 16, 9, pp 681-683 (May 1, 1991).

50.S. Chandra, M.J. Ferry and G. Daunt ; OSA proceedings on Advanced Solid-State Lasers, 13, pp 353 (1992).

51.J.M.Breteau, C.Jourdain, T.Lepine and F.Simon ; OSA proceedings on Advanced Solid-State lasers, vol. 15, pp 137-140 (1993)

52.N.P. Barnes, K.E. Murray, M. Jani and S.R. Harrel ; OSA proceedings on Advanced Solid-State Lasers, paper AWD5 (Feb.1994).

53.J. Raffy, T. Debuisschert, J.P. Pocholle and M. Papuchon ; OSA proceedings on Advanced Solid-State Lasers, 15, pp 127-130 (1993).

Stimulated Raman Scattering in Barium Nitrate Crystal in the external optical cavity

Petr G. Zverev, Tasoltan T. Basiev, Igor V. Ermakov, Alexander M. Prokhorov

General Physics Institute

Vavilov str., 38, Moscow 117333 Russia

Phone: (095) 135-03-18, Fax: (095) 135-02-70

ABSTRACT

Barium nitrate Raman laser pumped with nanosecond YAG:Nd laser is investigated. High energy conversion efficiencies to the first, second and third Stokes components up to 60%, 35% and 25%, respectively, are obtained. Results on development of Raman laser for eye safe spectral region are presented.

1. INTRODUCTION

Raman lasers can be used to shift laser radiation frequencies to different spectral regions. Barium nitrate crystal is one of the promising Raman materials that possess strong symmetrical vibration with 1047 cm^{-1} frequency that have been successfully used for stimulated Raman scattering (SRS). Barium nitrate Raman gain was measured to be 47 cm/GW at 532 nm^{-1} and about 11 cm/GW at $1.06\mu\text{m}^2$. Maximum SRS conversion efficiency in $\text{Ba}(\text{NO}_3)_2$ crystal single-pass cell was obtained using tunable $\text{LiF}:F_2^-$ color center laser as a pump source². Efficient SRS in $\text{Ba}(\text{NO}_3)_2$ crystals was observed with picosecond pump laser pulses³.

SRS can be observed in various configurations: single-pass and multi-pass cells, in the external cavity, inside pump laser cavity (see, for example⁴). Variety of nonlinear processes that occur in a single-pass cell limit Raman conversion efficiency at high pump intensity. Second Stokes and Antistokes components, as well as stimulated Brillouin scattering and self-focusing can be observed. The single-pass cell does not provide discrimination against these nonlinear processes at high energy inputs. It is practically impossible to obtain 100% quantum conversion efficiency of the pump only to the first Stokes component. That's why single-pass cell doesn't have many practical applications.

Raman shifter with external cavity can give a significant increase of conversion efficiency and intensity of Raman scattering with respect to single pass cell.⁵ It is possible to prepare dichroic mirrors with optimal reflectivity for the first Stokes wavelength and low for the second Stokes component. This can increase the intensity in the first Stokes component and practically delete the second Stokes oscillation. By varying the reflectivity of the cavity mirrors it is possible to prepare laser cavity working only at the first or second, or third components, independently, or at the combination of wavelengths simultaneously.

Another qualitative difference of the Raman shifter with external cavity is the possibility to concentrate Raman scattering in the narrow spatial angle close to the diffraction limited one. It is important to note that such effect can work also with a multimode pump laser that has high divergency. That's why such Raman shifter can sufficiently increase the brightness of the laser beam. SRS in $\text{Ba}(\text{NO}_3)_2$ crystal in the external optical cavity with various reflectivity mirrors is described in this paper. Development of the solid state laser source based on SRS for eye safe spectral region is presented.

2. EXPERIMENTAL SETUP.

Our investigation of SRS were based on well developed Nd laser sources. They are YAG:Nd and YAP:Nd laser working at 1.064, 1.079, 1.318 and $1.338\mu\text{m}$. The wavelengths of Stokes components that can be obtained in barium nitrate crystal under pumping with these laser sources are shown in Table 1.

Experimental setup for investigation of SRS in $\text{Ba}(\text{NO}_3)_2$ crystals in the external cavity pumped with $1.064 \mu\text{m}$ radiation is shown on Fig.1. YAG:Nd³⁺ laser working at $1.064 \mu\text{m}$ included the following components. YAG:Nd³⁺ laser rod $3 \times 60 \text{ mm}$ was placed in the laser cavity 45 cm long including electro optical Q-switch, 2.5 mm aperture, HR and 37% reflectivity mirrors. The oscillator was aligned to work in the TEM₀₀ mode regime with the pulse duration 12 ns and output energy 15 mJ . This pulse was amplified in YAG:Nd³⁺ amplifier up to 60 mJ . Half wavelength plate ($\lambda/2$) and polarizer were used as a variable attenuator for smooth decreasing the energy of the pump laser pulses. Pulse amplitude was controlled by a calibrated photodiode.

Table 1

Laser	Pump	First Stokes	Second Stokes	Third Stokes
YAG:Nd ³⁺	$1.064 \mu\text{m}$	$1.197 \mu\text{m}$	$1.369 \mu\text{m}$	$1.598 \mu\text{m}$
YAlO ₃ :Nd ³⁺	$1.079 \mu\text{m}$	$1.216 \mu\text{m}$	$1.394 \mu\text{m}$	$1.632 \mu\text{m}$
YAG:Nd ³⁺	$1.338 \mu\text{m}$	$1.556 \mu\text{m}$		
YAlO ₃ :Nd ³⁺	$1.341 \mu\text{m}$	$1.56 \mu\text{m}$		

Glass lens with 50 cm focal length was used to increase the pump laser intensity inside the Raman crystal to observe first, second and third Stokes component oscillations. The transversal dimension of the pump beam was measured at the front surface of the crystal in order to calculate the pump intensity inside the media. Raman crystals $20, 32, 40$ and 51 mm long with AR coatings were placed in the compact 70 mm long cavity made by flat mirrors with different spectral parameters.

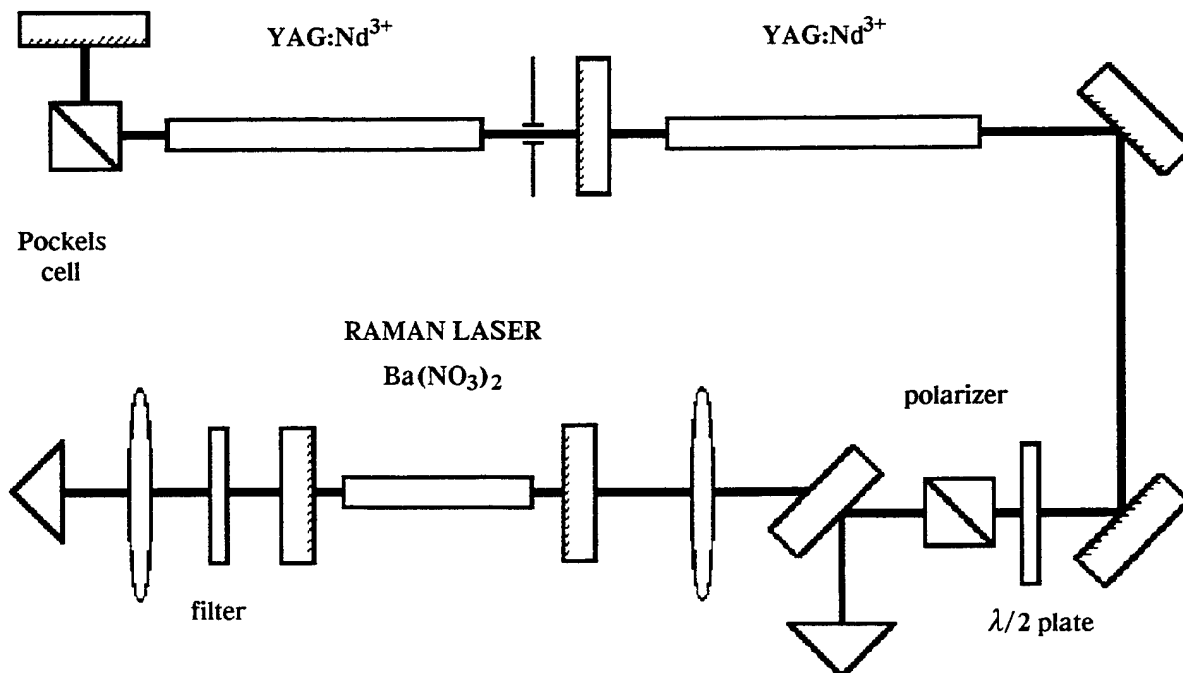


Fig.1. Experimental setup for investigation SRS in the external cavity

The Raman laser output was separated from the pumping radiation by a special dichroic mirrors and registered with the calibrated Molelectron J3-05 joulemeter. To analyze temporal behavior of the scattered light the fast avalanche photodiode LFD-2A with transient time less than 0.7 ns was used. Oscilloscope S1-70 and wide band storage oscilloscope Tektronix 7623A provide enough facilities to measure energy, stability and pulse duration in these experiments. Calorimeter IMO-2H was used for direct measurements of laser energy.

To obtain the IR radiation near $1.5\mu\text{m}$ by the first Stokes oscillation in the Raman shifter we used Q-switched neodium lasers working at $1.3\mu\text{m}$ wavelength. $\text{YAlO}_3:\text{Nd}^{3+}$ and $\text{YAG}:\text{Nd}^{3+}$ lasers with electro optic Q-switch were used as a pump sources. $\text{YAlO}_3:\text{Nd}^{3+}$ laser was working at $1.341\mu\text{m}$ wavelength with the laser bandwidth 0.34 nm . The laser pulse energy, pulse duration and divergency was 17 mJ , 64 ns and 0.5 mrad , respectively.

$\text{YAG}:\text{Nd}^{3+}$ laser for $1.3\mu\text{m}$ wavelength with the electro optical Q-switching provided a 32 ns duration pulses with 0.8 mrad beam divergency. The oscillation was observed simultaneously at two wavelengths: $1.338\mu\text{m}$ and $1.318\mu\text{m}$, while the intensity at $1.318\mu\text{m}$ wavelength was at least an order of magnitude less than that at $1.338\mu\text{m}$. It is worth to mention that the pulse duration can be increased to 60 ns by enlarging the cavity length up to 640 mm . The energy of pulses in both cases were as high as 10 mJ per pulse.

3. RESULTS AND DISCUSSIONS

3.1. SRS of YAG:Nd laser working at $1.06\mu\text{m}$ wavelength

To obtain high energy conversion efficiency in the Raman cell it is necessary to optimize pump laser intensity, pump pulse duration, input beam diameter, focusing and interaction lengths, Raman cavity parameters. By careful optimization of these parameters it is possible to achieve conversion efficiency about the theoretical limit that is ν_{st}/ν_p . In case of barium nitrate crystal ($\Delta\nu=1047\text{ cm}^{-1}$) pumped by $\text{YAG}:\text{Nd}^{3+}$ laser this limit for the first Stokes component is 0.89 and 0.85 for $1.064\mu\text{m}$ and $1.338\mu\text{m}$ pump wavelengths, respectively, and for the third Stokes component is 0.66 for $1.064\mu\text{m}$ pumping.

To obtain oscillation of the first Stokes component in external cavity we used Raman laser composed with an input mirror (HT at $1.064\mu\text{m}$ and HR at $1.17\text{-}1.6\mu\text{m}$) and an output coupler. The last one was either 12%, or 18%, or

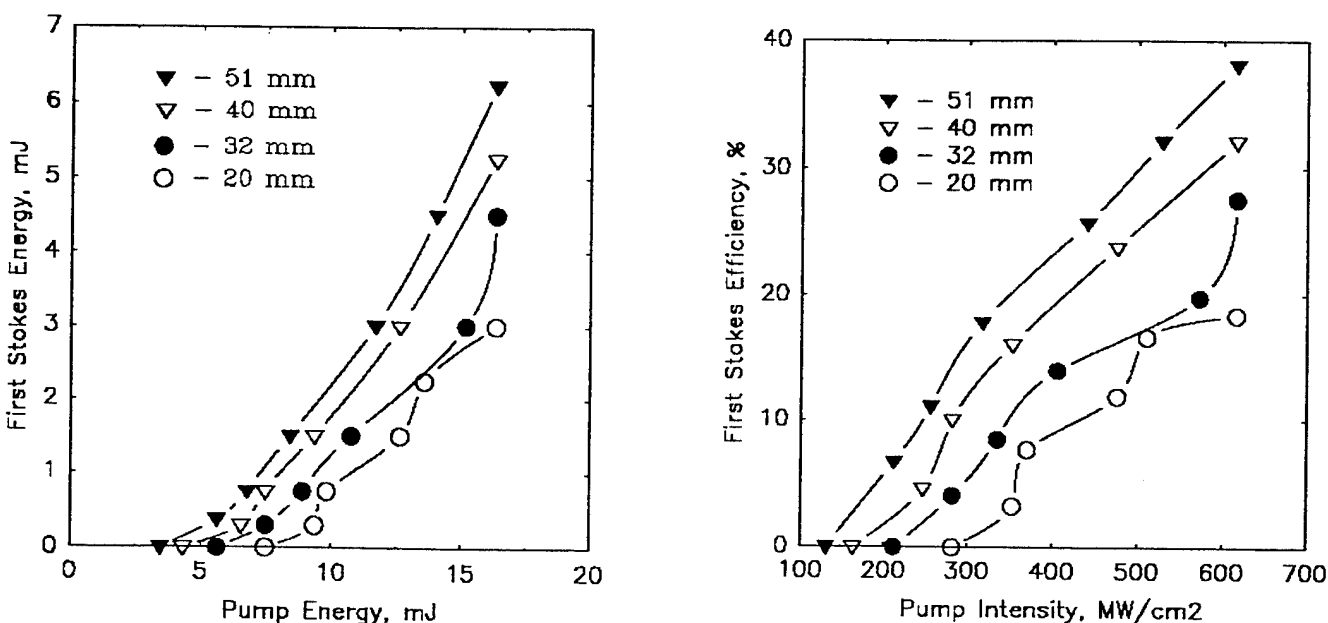


Fig.2. First Stokes energy (left) and conversion efficiency (right) versus the pump energy for Raman crystals with different length with 18% reflectivity output coupler.

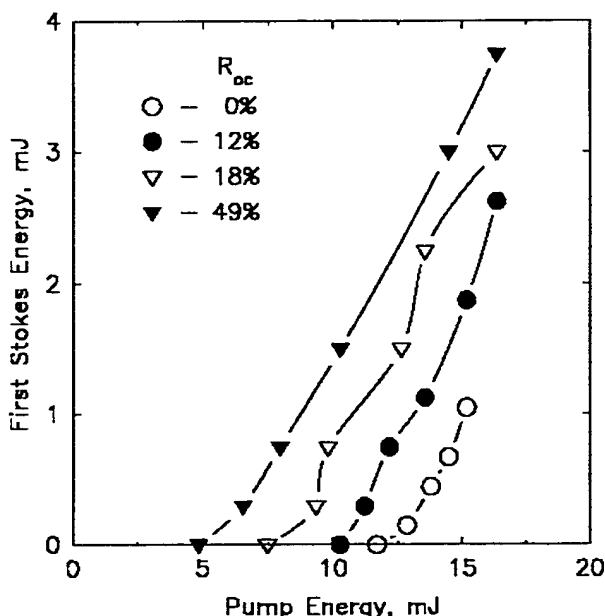


Fig. 3. First Stokes energy with respect to the pump energy for different output couplers.
Raman crystal 20 mm long.

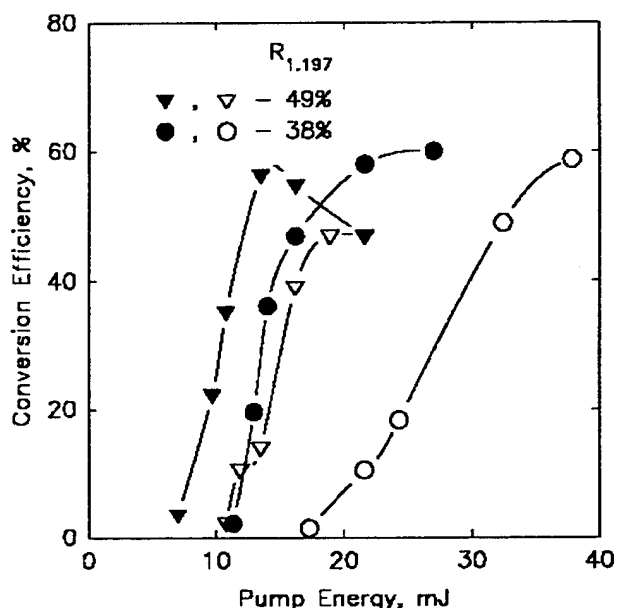


Fig. 4. First Stokes conversion efficiency of the optimized Raman laser for 32 (hollow) and 51 (filled) mm long nonlinear crystals.

49% reflectivity at $1.197 \mu\text{m}$. Fig. 2-3 show first Stokes energy and conversion efficiency dependences for Raman crystals with different length and for different output couplers. One can see that the use of the external cavity with high reflectivity output coupler reduce the threshold pump intensity and increase overall efficiency. One can measure the slope conversion efficiency from Fig.2 that was as high as 70% and 40% for 51 mm and 20 mm long nonlinear crystals, respectively. The increase of the pump intensity inside Raman media by optimizing the focusing conditions allows to obtain the energy of 7 mJ and conversion efficiency of 60% using 51 mm long Raman crystal (Fig.4). The quantum conversion efficiency was calculated to be 68%.

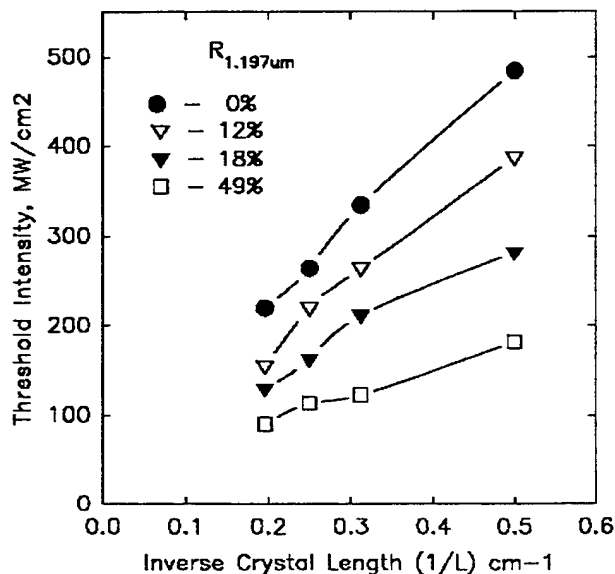


Fig.5. Dependences of the first Stokes threshold with respect to $\text{Ba}(\text{NO}_3)_2$ crystal length for different output couplers.

Fig.5 shows the first Stokes threshold pump intensity dependence on inverse crystal length $1/L$. From SRS theory is known that the first Stokes intensity I_{St} about the threshold conditions can be described by exponential law:

$$I_{\text{Stokes}} = I_{\text{sp}} \exp \{ G L I \},$$

where I_{sp} is the intensity of spontaneous Raman scattering, G is the Raman gain, L is the length of the interaction or the length of the nonlinear media, I is the pump intensity. The threshold pump intensity is usually defined as an intensity when the exponent power equals 30.

$$G L I^{\text{thresh}} = 30$$

From this equation we can see that the threshold pump intensity is inversely proportional to the length of the Raman media. This is in a good agreement with our experimental data (Fig.5). The installation of the output coupler reduce the value of threshold intensity. This can be explained by substitution L_{eff} instead of L , where $L_{eff} = N_{eff} L$, (N_{eff} is the effective number of first Stokes passes through Raman crystal). The following values N_{eff} can be obtained from Fig.5 for different output coupler reflectivities:

Roc, %	0	12	18	49
N_{eff}	1	1.25	2.1	4.5

The threshold and intensity for the second Stokes component that was accompanying first Stokes oscillation were also measured in our experiments. It was found that these values depend on the reflectivity of the cavity mirrors at $1.36 \mu m$. The use of HR at $1.36 \mu m$ cavity mirrors reduces the threshold intensity of the second Stokes oscillation. Thus to obtain only the first Stokes oscillation from the Raman laser it is necessary to prepare external cavity with an input mirror with HR at the first Stokes wavelength and HT at the pump and second Stokes wavelengths. The output coupler must have HT at the second Stokes wavelength and 10-30% reflectivity at the first Stokes wavelength depending on the length of the Raman media. The time duration of the first Stokes component in our experiments was measured to be a little bit less than that of the pump laser and was 10 ns.

The second Stokes oscillation was investigated in the Raman cavity with mirrors HR at the first Stokes wavelength. Fig. 6 shows our results on the second Stokes oscillation in the Raman laser for different Raman crystal lengths. The threshold intensity of the second Stokes oscillation was found to be independent on the reflectivity of the output coupler. It is determined by the Raman crystal length and the threshold of the first Stokes oscillation. Once the first Stokes starts it initiates the second Stokes oscillation. This proves that under single line pumping the second Stokes SRS starts not from spontaneous level of Raman scattering but it is amplified in the intense field of Raman oscillations stimulated by the biharmonic pump and first Stokes radiations with the resonant frequencies ν , that are defined as:

$$\nu_{pump} - \nu_{1st\ St.} = \nu_R = \nu_{1st\ St.} - \nu_{2nd\ St.}$$

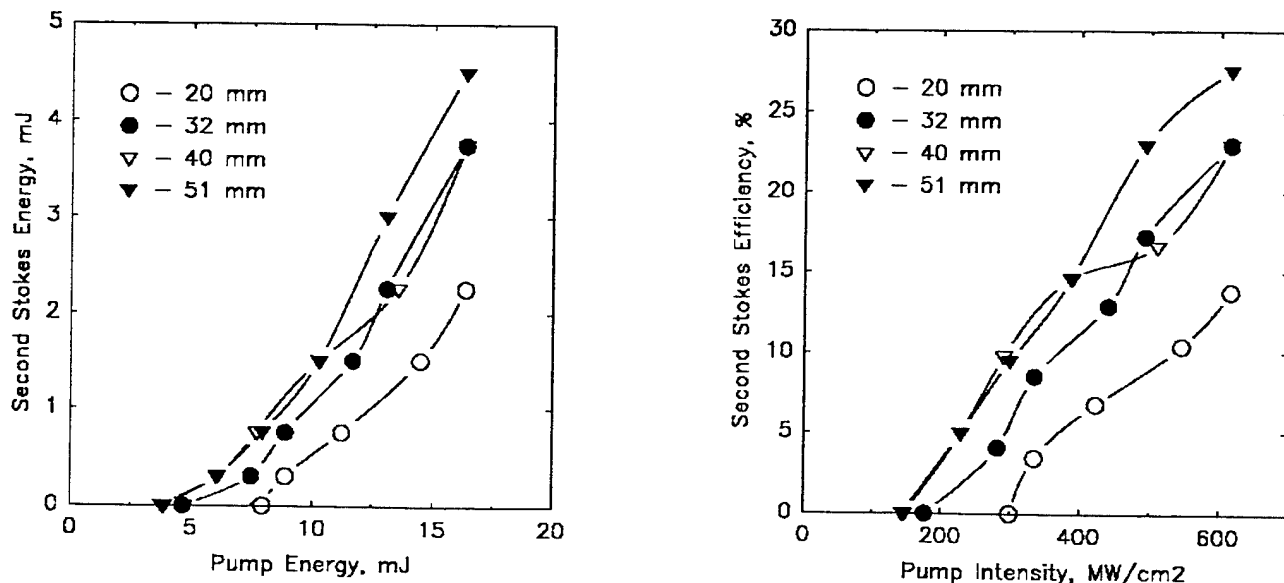


Fig. 6. Second Stokes energy (left) and conversion efficiency (right) dependences versus the pump intensity for Raman crystals with different length with the output coupler 26% reflectivity at $1.369 \mu m$

The maximum second Stokes energy and conversion efficiency were obtained by optimizing the focusing conditions of the pump and were measured to be 5.5 mJ and 35%, respectively. This is about 45% quantum conversion efficiency. The slope efficiency was estimated to be 45% for 51 mm long Raman crystal.

The best results for the third Stokes oscillation were observed in the Raman cavity with mirrors HR at the first and second Stokes wavelengths. The cascade oscillation of the first, second and finally third Stokes components needs high quality of the Raman cavity at the first and second Stokes wavelengths. Fig. 7 shows our results on the third Stokes oscillation in the Raman cavity. The energy and conversion efficiency with respect to 1.064 μm pumping were measured to be up to 3.5 mJ and 22%, respectively (quantum conversion efficiency - 33%). The slope efficiency was measured to be 36%. It is important to note that the conversion efficiency depends on the length of the Raman crystal. The increase of the output coupler reflectivity at 1.59 μm leads to subsequent conversion of the third Stokes component to the fourth one (1.92 μm) and the following absorption of the last one in Ba(NO₃)₂ crystal.

The divergency of the first, second and third Stokes components were measured in our experiments to be 2-4 mRad and was close to diffraction limited one. The beam profile reproduce the spatial distribution of the pump beam and has nearly gaussian shape when pumped with TEM₀₀ mode. The pulse duration of the Stokes components doesn't depend on the cavity parameters. It was determined by the pump pulse duration and was 10 ns for all Stokes components.

3.2. SRS of neodimium laser working at 1.3 μm wavelength

The wavelength of the first Stokes SRS in Ba(NO₃)₂ of Nd lasers working at 1.3 μm wavelength gets to the eye safe spectral region around 1.5 μm . That's why it was interesting for us to investigate this possibility to obtain eye safe laser radiation with the help of first Stokes oscillation. We observed efficient SRS in Ba(NO₃)₂ crystal under pumping with YAlO₃:Nd³⁺ laser (up to 17 mJ, 64 ns). Dichroic mirror with 55% reflectivity at 1.56 μm was found to be optimal output coupler. The dependences of the first Stokes energy and conversion efficiency vs pump intensity are shown at Fig. 8. The threshold of Raman laser oscillation was observed at the pump pulse energy about 1.5 mJ and conversion efficiency was saturated at the pulse energy 4-6 mJ for 40 mm long crystal.

For YAG:Nd³⁺ pump laser with pulse duration 64 ns the maximum energy conversion efficiency of Raman laser was up to 40% with barium nitrate crystal 51 mm long, the output coupler R_{1.56} = 35% and pump energy 11.5 mJ.

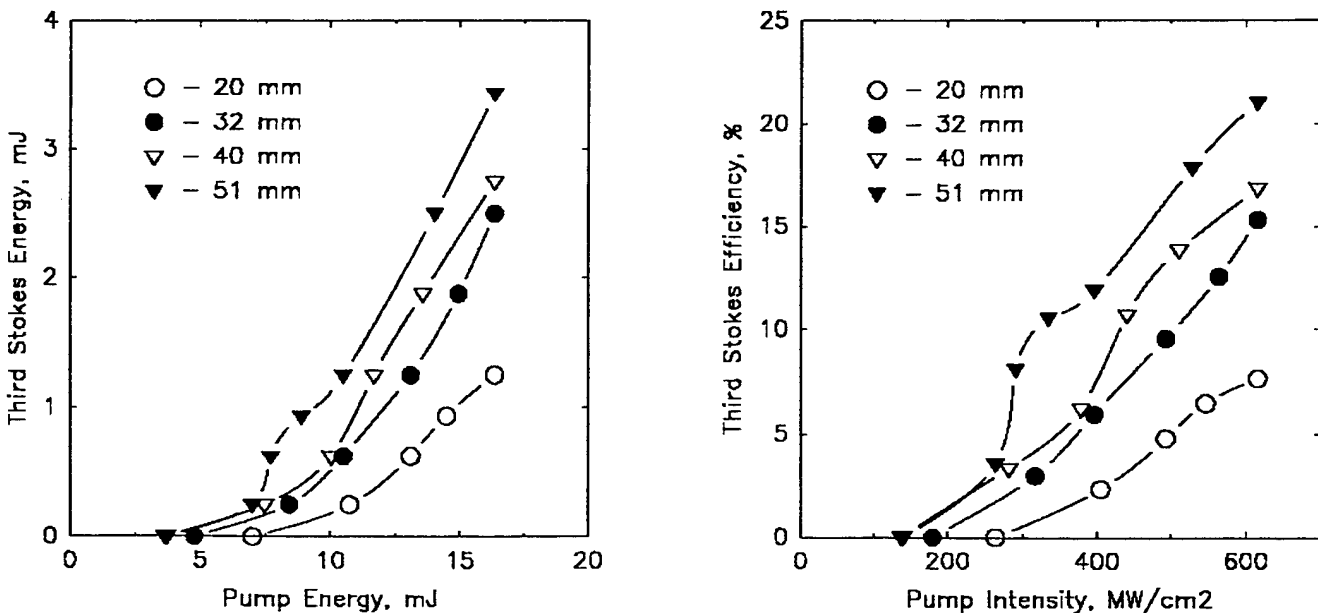


Fig.7. Third Stokes energy (left) and conversion efficiency (right) with respect to pump energy for Raman crystals with different length. Output coupler reflectivity at 1.59 μm was 25%.

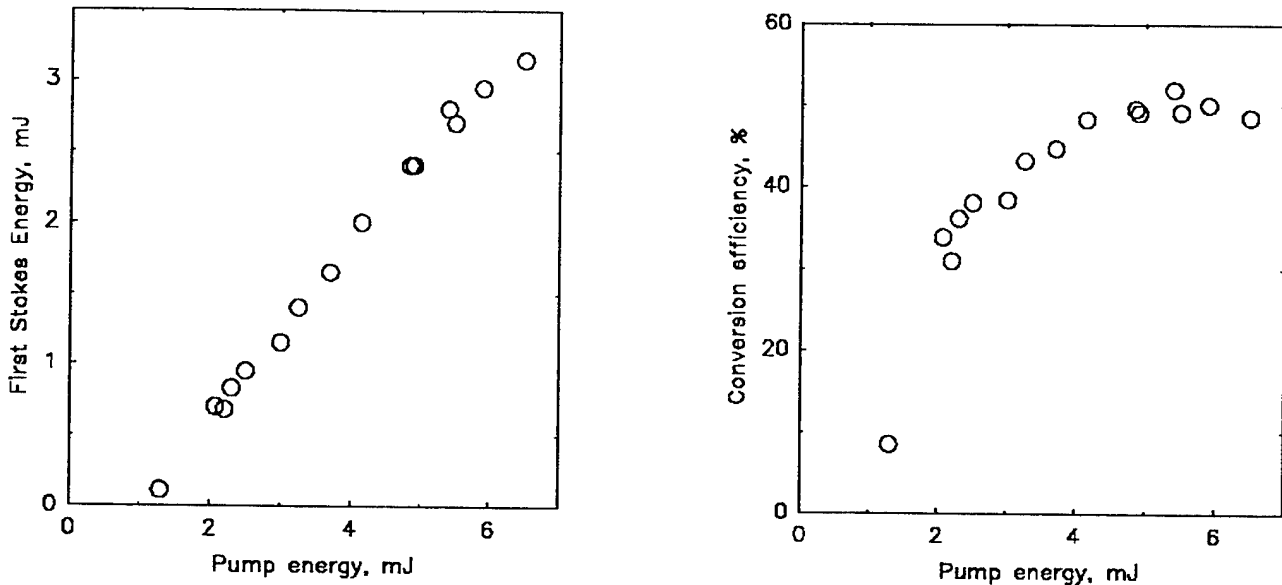


Fig.8. First Stokes energy (left) and conversion efficiency (right) versus the pump intensity at $1.34 \mu\text{m}$ for 40 mm long barium nitrate crystal.

By decreasing the pump pulse duration to 32 ns it was possible to increase the energy conversion efficiency up to 52%. The pulse duration of $1.556 \mu\text{m}$ and $1.56 \mu\text{m}$ Raman laser radiation in both cases equal to the duration of pump laser pulses and was about 32 or 64 ns respectively.

4. SUMMARY

Thus, in this report we have shown that by using mirrors at both sides of the barium nitrate Raman crystal it is possible to prepare Raman laser. Optimization of selective mirrors, length of Raman crystal and focusing conditions allow us to obtain laser oscillation either at the first, or the second, or the third Stokes components with efficiency up to 60, 35 and 25%, respectively. The laser oscillation with the wavelength above $1.5 \mu\text{m}$ shows that $\text{Ba}(\text{NO}_3)_2$ Raman laser pumped with YAG:Nd^{3+} or $\text{YAlO}_3:\text{Nd}^{3+}$ lasers can produce oscillation with the wavelength above $1.5 \mu\text{m}$ and is perspective for developing solid state lasers based on SRS for eye safe spectral region.

5. ACKNOWLEDGMENT

This work was partially supported by DRET and THOMSON-TRT DEFENSE.

6. REFERENCES

1. A.S.Eremenko, S.N.Karpukhin and A.I.Stepanov, "SRS of the second harmonic of neodimium laser in nitrate crystals," Sov. J. Quantum Electron. vol. 10, p. 113, 1980.
2. T.T.Basiev, V.N.Voitsekhovskii, P.G.Zverev, F.V.Karpushko, A.V.Lubimov, S.B.Mirov, V.P.Morozov, I.V.Mochalov, A.A.Pavlyuk, G.V.Sinitsyn and V.E.Yakobson, "Conversion of tunable radiation from a laser utilizing an LiF crystal containing F_2^- color centers by stimulated Raman scattering in $\text{Ba}(\text{NO}_3)_2$ and $\text{KGd}(\text{WO}_4)_2$ crystals," Sov. J. Quantum Electron. 17(12), pp.1560-1561, Dec. 1987.
3. P.G.Zverev, J.T.Murray, R.C.Powell, R.J.Reeves, and T.T.Basiev, "Stimulated Raman scattering of picosecond pulses in barium nitrate crystals," Optics Communications, vol. 97, pp. 59-64, 1993.
4. W.Koecner, "Solid-State Laser Engineering," Springer Series in Optical Sciences, pp. 556-565, 1990.
5. A.J.Glass, "Design considerations for Raman lasers," IEEE J. of Quantum Electr., vol. QE-3, pp. 516-520, 1967

Passive Q-switching of $1.3\text{ }\mu\text{m}$ Nd-lasers with $\text{Nd}^{2+}:\text{SrF}_2$ and $\text{V}^{3+}:\text{YAG}$ crystalline saturable absorbers and application to Raman shifting to eye-safe region

T.T.Basiev, V.B.Sigachev, M.E.Doroshenko, A.G.Papashvili, P.G.Zverev, V.V. Osiko

General Physics Institute, Russian Academy of Sciences, Vavilov Street 38, Moscow, 117942,
Russian Federation. Telephone: (095) 135-02-67, Fax: (095) 135-02-70

ABSTRACT

Passive Q-switching of $1.3\text{ }\mu\text{m}$ neodymium lasers with $\text{Nd}^{2+}:\text{SrF}_2$ and $\text{V}^{3+}:\text{YAG}$ crystalline saturable absorbers are studied. Giant pulses up to 5 mJ energy and 40 ns duration were obtained. Efficient Raman shifting of the $1.3\text{ }\mu\text{m}$ pulses of passively Q-switched lasers to $1.55\text{ }\mu\text{m}$ wavelength are realized in $\text{Ba}(\text{NO}_3)_2$ crystal.

1. INTRODUCTION

Variety of possible applications of Q-switched $1.3\text{ }\mu\text{m}$ neodymium lasers and simplicity of passive Q-switching scheme stimulates search of solid-state saturable absorbers (SA) for $1.3\text{ }\mu\text{m}$ wavelength. The $\text{Nd}^{2+}:\text{SrF}_2$ and $\text{V}^{3+}:\text{YAG}$ crystalline saturable absorbers seems to be most perspective ones^{1,2}. The $1.3\text{ }\mu\text{m}$ Nd-lasers passively Q-switched with the $\text{Nd}^{2+}:\text{SrF}_2$ and $\text{V}^{3+}:\text{YAG}$ saturable absorbers can be used as pump sources in different frequency conversion schemes, for instance harmonics generation, stimulated Raman scattering and so on. In this paper we report results on study of Q-switching mode of operation of $1.3\text{ }\mu\text{m}$ Nd-lasers with the $\text{Nd}^{2+}:\text{SrF}_2$ and $\text{V}^{3+}:\text{YAG}$ crystalline saturable absorbers, and Raman shifting of this laser wavelength in $\text{Ba}(\text{NO}_3)_2$ crystal to eye-safe spectral region.

2. RESULTS

2.2. Properties of $\text{Nd}^{2+}:\text{SrF}_2$ and $\text{V}^{3+}:\text{YAG}$ crystals as saturable absorbers

Room temperature absorption spectrum of $\text{Nd}^{2+}:\text{SrF}_2$ crystal is shown in Fig.1. The feature of Nd^{2+} ions in SrF_2 crystal is the broad absorption band, that lies in $0.9\text{-}1.8\text{ }\mu\text{m}$ region and has maximum at $1.35\text{ }\mu\text{m}$. The absorption of Nd^{2+} ions in SrF_2 crystal is due to interconfigurational $4f^n-4f^{n-1}5d^1$ transitions and possesses nonlinear properties (saturable absorption). The typical curve of energy transmittance of nanosecond light pulses at $1.34\text{ }\mu\text{m}$ wavelength for the $\text{Nd}^{2+}:\text{SrF}_2$ crystal is shown in Fig.2.

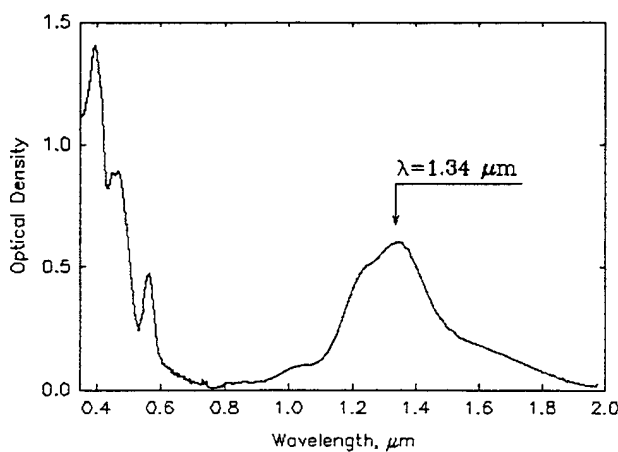


Fig. 1. Room temperature absorption spectrum of $\text{Nd}^{2+}:\text{SrF}_2$ crystal

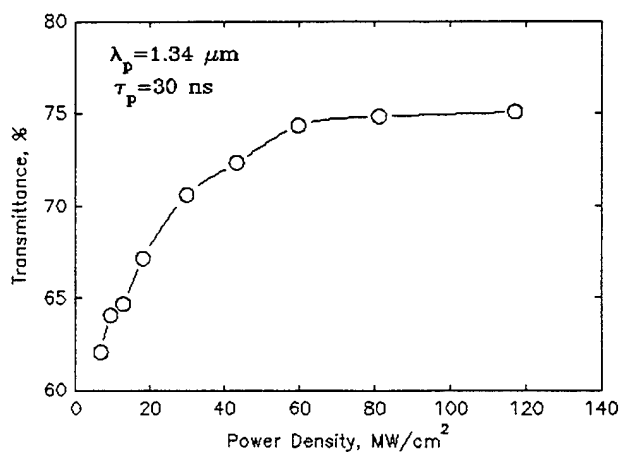


Fig. 2. Transmittance of $\text{Nd}^{2+}:\text{SrF}_2$ crystal as function of $1.34\text{ }\mu\text{m}$ radiation power density¹

Tetrahedrally coordinated V^{3+} ions in YAG crystal also possess nonlinear absorption properties at $1.34\text{ }\mu\text{m}$ wavelength. Room-temperature absorption spectrum of $\text{V}^{3+}:\text{YAG}$ crystal is shown in Fig.3. The feature of the spectrum

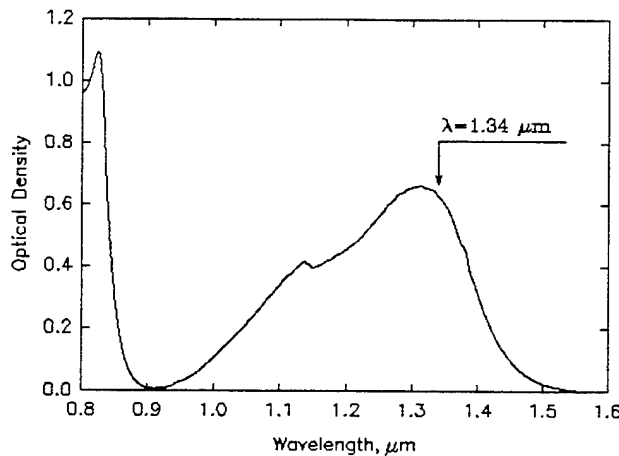


Fig. 3. Room temperature absorption spectrum of V^{3+} :YAG crystal.

is two broad absorption bands with peaks near $1.3\mu m$ and $0.83\mu m$ which are due to transitions from 3A_2 ground state of tetrahedrally coordinated V^{3+} ion to 3T_2 and 3T_1 excited states.

Major spectroscopic parameters of Nd^{2+} :SrF₂ and V^{3+} :YAG crystals in comparison with well known F₂⁻:LiF saturable absorber are summarized in Table 1, where absorption cross-section σ_a at Nd-laser wavelengths λ , relaxation time τ_r and saturation intensity $I_s=hc/(\lambda\sigma_a\tau_r)$ are listed. It should be noted, that Nd^{2+} :SrF₂ crystalline saturable absorber has about 5 times higher saturation intensity than V^{3+} :YAG and 500 times higher than F₂⁻:LiF. Application of Nd^{2+} :SrF₂ crystal as passive Q-switch requires strong focusing of intracavity radiation.

A number of Nd^{2+} :SrF₂ crystals with the 47-83% initial transmittance and V^{3+} :YAG crystal having the 55% initial transmittance were studied in laser experiments.

2.3. The $1.3\mu m$ neodymium crystalline lasers with Nd^{2+} :SrF₂ passive Q-switch

The hemispherical optical cavity possessing the focusing properties was selected. The scheme of the laser cavity is shown in Fig.4. Flash lamp pumped Nd:YAG, Nd:YAP, and Cr:Nd:GGG crystal rods (6mm x 60 mm) were used as laser active media. To optimize the energy and duration of output pulse the position of SA along the resonator axis (distance L from SA to output mirror) and the output mirror reflectivity R were varied.

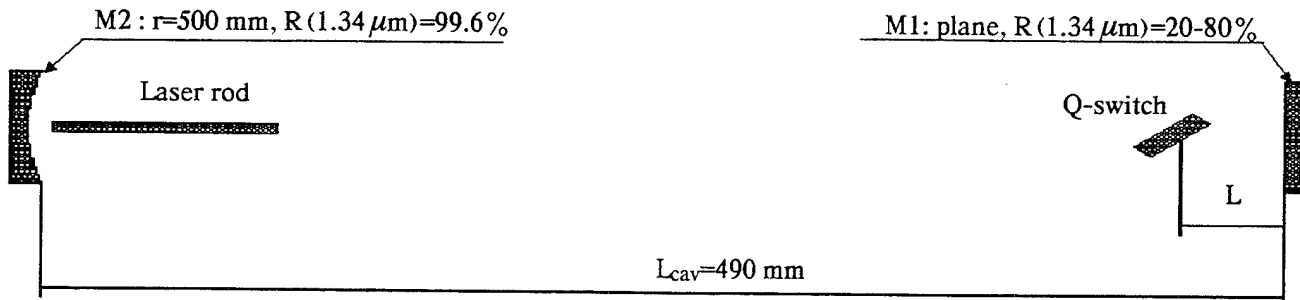


Fig. 4. Experimental laser cavity for passive Q-switching by means of Nd^{2+} :SrF₂ and V^{3+} :YAG crystals

The typical input-output characteristics of Nd:YAG, Nd:YAP, and Cr:Nd:GGG lasers with Nd^{2+} :SrF₂ crystalline SA are shown in Fig.5. These step-like dependences are the ordinary one for passively Q-switched lasers. At the first step only single laser pulse is generated, at the second step there are two pulses and so on. The feature of these $E_{out}(E_{in})$ dependences is considerable energy variation within the step, where fixed number of pulses is generated. From these

Table 1. Characteristics of Nd^{2+} :SrF₂ and V^{3+} :YAG saturable absorbers at $1.34\mu m$ wavelength and F₂⁻:LiF crystal at $1.064\mu m$.

	Nd^{2+} :SrF ₂	V^{3+} :YAG	F ₂ ⁻ :LiF
Absorption cross section, $10^{-18} cm^2$	2 ^[1]	1.7 ^[2]	17 ^[4]
Relaxation time, ns	<1 ^[1]	5 ^[2]	70-90 ^[5]
Saturation intensity, MW/cm ²	80	17	0.12-0.16

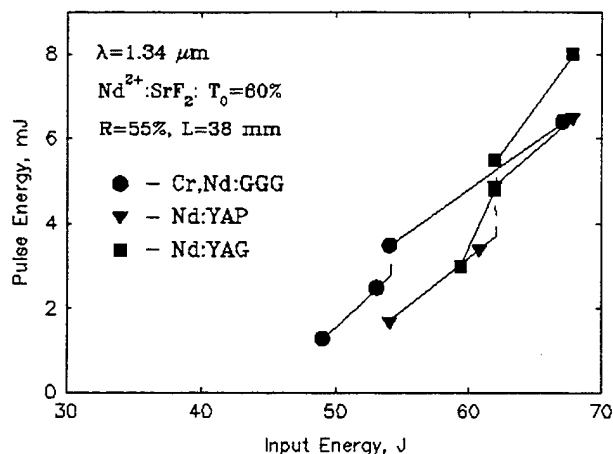


Fig. 5. Input-output characteristics of Nd:YAG, Nd:YAP and Cr,Nd:GGG lasers with $\text{Nd}^{2+}:\text{SrF}_2$ passive Q-switcher.

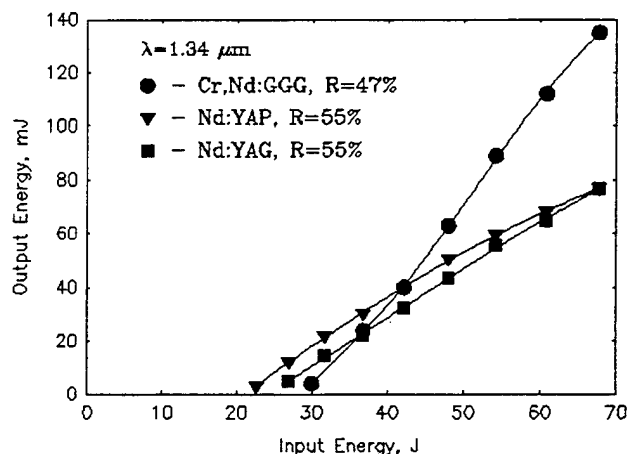


Fig. 6. Free-running input-output characteristics of Nd:YAG, Nd:YAP and Cr,Nd:GGG lasers at $1.34 \mu\text{m}$ wavelength.

dependences the slope efficiency of the laser can be determined. For Cr,Nd:GGG laser the maximum value of slope efficiency of 0.09% was achieved for the 47% reflectivity of output mirror and the $\text{Nd}^{2+}:\text{SrF}_2$ crystal having 60% initial transmittance. For Nd:YAP and Nd:YAG lasers with 55% output mirror reflectivity and the same SA the slope efficiency was 0.06%, and 0.08% respectively. It should be noted, that these passively Q-switched lasers generated single transverse mode radiation.

Input-output characteristics of free running Nd:YAG, Nd:YAP and Cr:Nd:GGG lasers with reflectivities of output mirrors corresponding to maximum slope efficiency in Q-switched mode are shown in Fig.6. The free running slope efficiency was equal to 0.36% for Cr,Nd:GGG and 0.18% for both Nd:YAP and Nd:YAG crystals. So the slope efficiency in passively Q-switched mode of operation relatively to that for free running mode is only 4; 3 and 2.25 times less for Cr,Nd:GGG, Nd:YAP and Nd:YAG lasers respectively. It's necessary to outline, that considerable difference in normal and Q-switched slope efficiencies may be caused not only by the additional losses from the passive Q-switch but also by differences in laser mode size in laser crystal for these different modes of operation.

The dependences of maximum energy of single pulse E_{out} and pulse duration τ as a function of reflectivity R of output mirror for the fixed distance L from output mirror are shown in Fig.7. Also dependences of intracavity radiation power $P_{\text{cav}} = E_{\text{out}} / [\tau(1-R)]$ as function of output mirror reflectivity are shown in Fig.7. From these data the optimal mirror reflectivity R_{opt} can be found. For Nd:YAP and Nd:YAG lasers with $\text{Nd}^{2+}:\text{SrF}_2$ passive Q-switches the optimal mirror reflectivities for both cases were the same and equal to 55%. It is seen that unlike Nd:YAP and Nd:YAG lasers in case of Cr,Nd:GGG the output mirror reflectivity, which maximize intracavity radiation power, can differ from the optimal reflectivity that maximize output energy of the laser pulse. So the optimization of laser scheme with nonlinear conversion of $1.3 \mu\text{m}$ radiation to the infrared or visible region by Raman conversion or second harmonic generation can be different for intracavity or out of cavity schemes. In case of Cr:Nd:GGG laser the optimal mirror reflectivity for out of cavity nonlinear conversion is equal to 47%, but for intracavity scheme the optimum is about 70%.

The dependences of pulse energy E_{out} , pulse duration τ and intracavity power P_{cav} as a function of distance L from the output mirror having the optimal reflectivity R_{opt} are shown in Fig.8. Changing the distance L , the power density at SA is changed due to variation of intracavity mode size in chosen hemispherical resonator. As one can see, the maximum output energy and shortest pulse duration for Cr,Nd:GGG and Nd:YAG lasers are realized at the shortest distance between passive Q-switch and output mirror, where laser mode have the smallest size. The optimal position of SA in Nd:YAP laser was equal to $\sim 30 \text{ mm}$ and differs from that for Cr,Nd:GGG and Nd:YAG lasers due to different thermal lensing of studied crystals.

To summarize data on passive Q-switching of Cr,Nd:GGG, Nd:YAP and Nd:YAG lasers with the $\text{Nd}^{2+}:\text{SrF}_2$ crystals, the dependences of pulse energy E_{out} , pulse duration τ , and intracavity power P_{cav} as function of initial

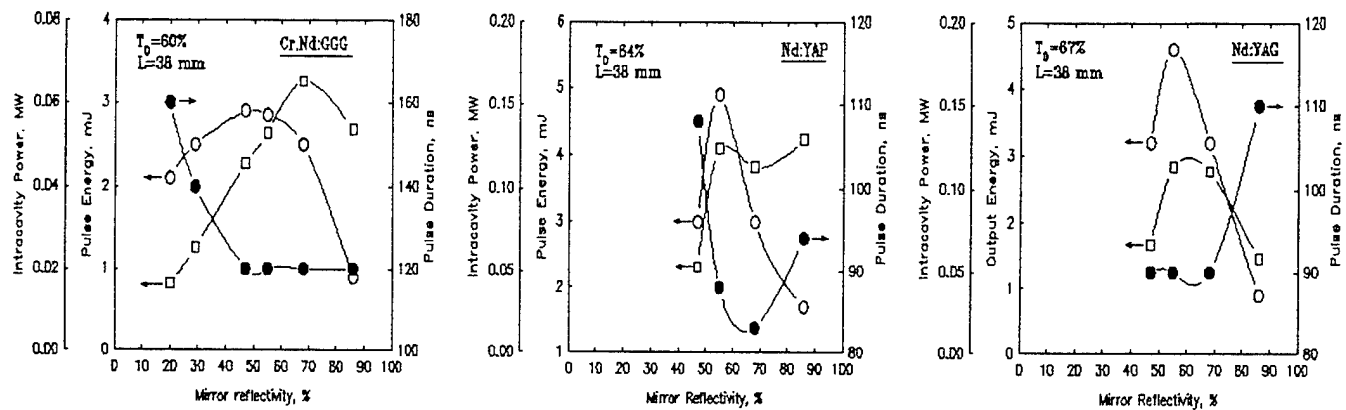


Fig. 7. Output pulse energy \circ , pulse duration \bullet and intracavity power \square versus reflectivity of output mirror for $1.3 \mu\text{m}$ Cr,Nd:GGG, Nd:YAP and Nd:YAG lasers with $\text{Nd}^{2+}:\text{SrF}_2$ passive Q-switch.

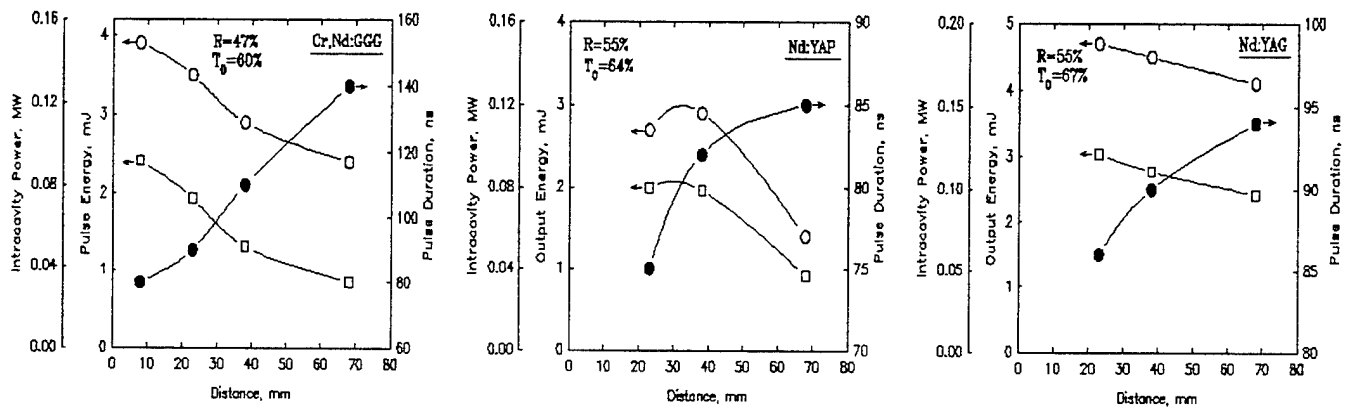


Fig. 8. Output pulse energy \circ , pulse duration \bullet and intracavity power \square versus distance L from output mirror of $1.3 \mu\text{m}$ Cr,Nd:GGG, Nd:YAP and Nd:YAG lasers with $\text{Nd}^{2+}:\text{SrF}_2$ passive Q-switch.

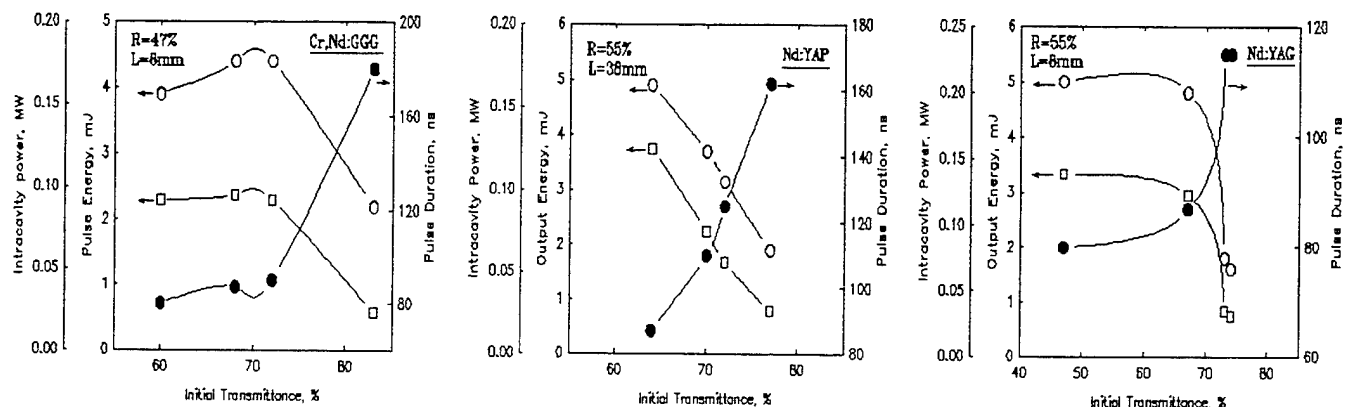


Fig. 9. Output pulse energy \circ , pulse duration \bullet and intracavity power \square of $1.3 \mu\text{m}$ Cr,Nd:GGG, Nd:YAP and Nd:YAG lasers versus the initial transmittance of $\text{Nd}^{2+}:\text{SrF}_2$ passive Q-switch.

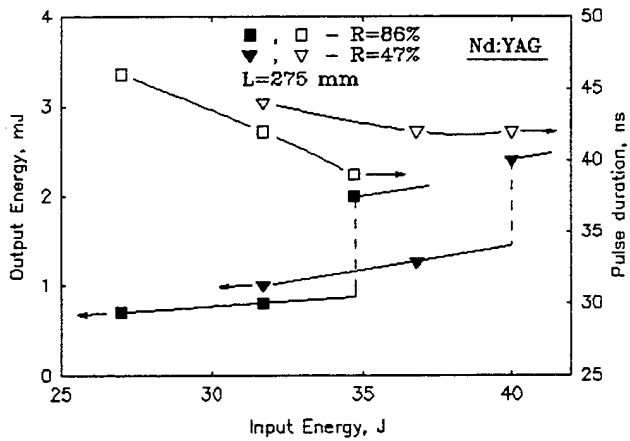


Fig. 10. Output energy (1,3), and duration (2,4) of V^{3+} :YAG passively Q-switched Nd:YAG laser.

transmittance T_0 of the saturable absorber for the optimal reflectivity of output mirror and optimal distance L are shown in Fig.9. The pulse energy and intracavity power increases and pulse duration decreases with decreasing of initial transmittance of Nd^{2+} :SrF₂ crystal. In case of Nd^{2+} :SrF₂ crystalline SA with the (64±4)% initial transmittance the (4-5) mJ single transverse mode energy per Q-switched pulse and the (80-90) ns pulse duration were obtained for all the studied laser active media. The maximum intracavity power density was in the range of 100-150 kW/cm².

It should be noted that in experiments with the Nd^{2+} :SrF₂ crystals having initial transmittance $T_0=47\%$ the minimum pulse duration as small as 45 ns was obtained when 10 mm long Nd^{2+} :SrF₂ crystal was placed at the minimal possible distance L from the output mirror of Nd:YAG laser utilizing the 3mmx60mm size rod (see Fig.12 curves 3 and 4).

2.4. Passive Q-switching of 1.3 μm Nd:YAG laser with the V^{3+} :YAG crystalline saturable absorber

Like in previous experiments with Nd^{2+} :SrF₂ crystals, the 490 mm hemispherical cavity was used. The active laser medium was Nd:YAG crystal with 6 mm diameter and 60 mm long. The V^{3+} :YAG with 55% initial transmittance at 1.34 μm wavelength and 3 mm thickness was used. The crystal was placed much farther from the output mirror of the hemispherical resonator than Nd^{2+} :SrF₂ crystal.

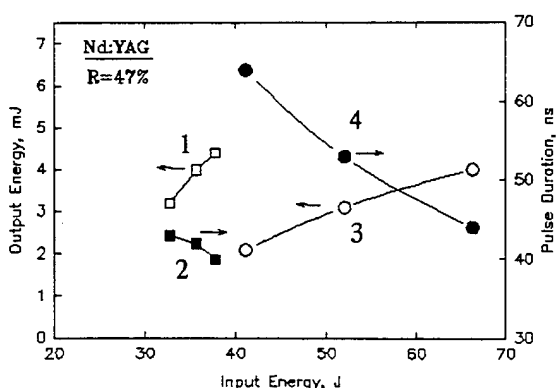


Fig. 12. Single pulse output energy (1,3), and pulse duration (2,4) of Nd:YAG laser with V^{3+} :YAG (1,2) passive Q-switch placed at $L=240$ mm and Nd^{2+} :SrF₂ (3,4) placed at $L=3$ mm.

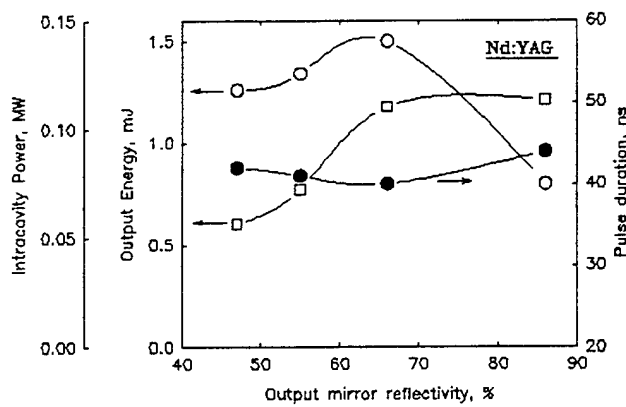


Fig. 11. Single pulse output energy O, pulse duration ● and intracavity power □ versus output mirror reflectivity of Nd:YAG laser with V^{3+} :YAG.

The dependences of energy E_{out} and duration τ of output pulse as function of input energy E_{in} for the Nd:YAG laser with V^{3+} :YAG Q-switch and different reflectivities of output mirror are shown in Fig.10. Variations of maximum single pulse energy E_{out} , duration of the pulse τ and intracavity power $P_{cav}=E_{out}/[\tau(1-R)]$ versus output mirror reflectivity R are shown in Fig.11. As one can see, the maximum energy of single giant pulse $E_{out}\sim 1.5$ mJ and shortest pulse duration $\tau\sim 40$ ns are realized for the output mirror with reflectivities in the range of (60-70) %. But the the maximum intracavity power $P_{cav}\sim 110$ kW is realized for higher reflectivities $R=68-86$ %. These data were obtained when V^{3+} :YAG crystal was placed at 275 mm distance from the output coupler.

In order to increase power density at SA (due to higher focusing if intracavity radiation) the distance L was reduced to the value of 240 mm. The V^{3+} :YAG crystal can operate only

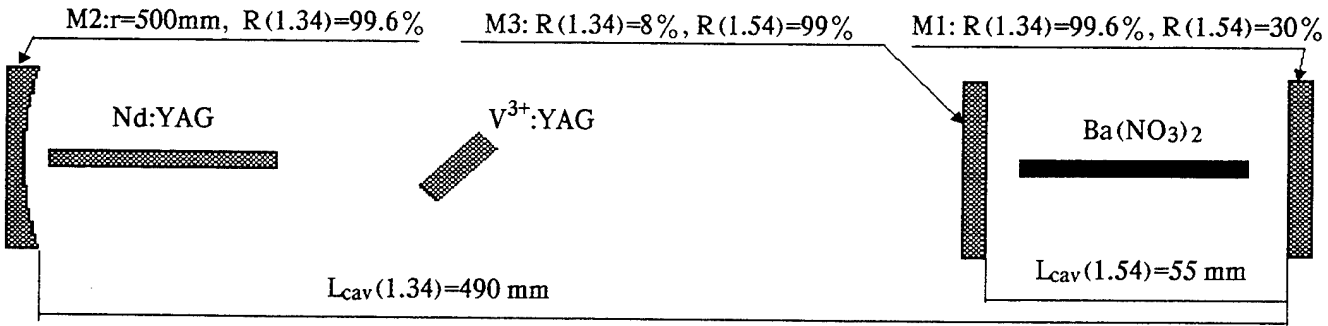


Fig. 13. Scheme of eye-safe $\text{Ba}(\text{NO}_3)_2$ crystal Raman laser out of cavity pumped by $1.3 \mu\text{m}$ Nd:YAG laser passively Q-switched with $\text{V}^{3+}\text{:YAG}$ crystal.

for reflectivities of output mirror less than 55%, since at higher reflectivities it was damaged by increased intracavity power density. The dependences of energy and duration of output laser pulse as function of pump power for 47% reflectivity of output mirror and reduced distance $L=240 \text{ mm}$ are shown in Fig. 12 by curves 1 and 2. A single Q-switched laser output pulse of 4.4 mJ energy and 40 ns duration was obtained for this Nd:YAG laser with $\text{V}^{3+}\text{:YAG}$ passive Q-switch. In Fig. 12 the energy and duration of output pulse as function of pump power for the Nd:YAG laser with $\text{Nd}^{2+}\text{:SrF}_2$ crystal are also shown for comparison.

2.5. Eye safe $\text{Ba}(\text{NO}_3)_2$ crystal Raman laser pumped by the Nd:YAG laser Q-switched with $\text{V}^{3+}\text{:YAG}$ saturable absorber

Stimulated Raman scattering (SRS) of the $1.3 \mu\text{m}$ radiation of Nd:YAG laser Q-switched with the help of $\text{V}^{3+}\text{:YAG}$ saturable absorber was realized in 50 mm long $\text{Ba}(\text{NO}_3)_2$ crystal. Intracavity pumping SRS scheme of Raman laser was used, as it is shown in Fig. 13. To achieve maximum pump power density the $\text{Ba}(\text{NO}_3)_2$ crystal was placed in the waist of the pump beam near the flat mirror. This mirror was totally reflecting at the $1.3 \mu\text{m}$ and served as output coupler of Raman laser. The third additional rear mirror of Raman laser had high transmittance at pump wavelength. For this configuration the Nd:YAG/ $\text{V}^{3+}\text{:YAG}$ pump laser can operate at $1.319 \mu\text{m}$ or/and $1.338 \mu\text{m}$ wavelengths. The Raman lasing was obtained at two wavelengths $1.530 \mu\text{m}$ or/and $1.556 \mu\text{m}$ too. These output wavelengths correspond to first Stokes Raman frequencies for $\text{Ba}(\text{NO}_3)_2$ crystal with the 1047 cm^{-1} Raman shift³. The shape of $1.556 \mu\text{m}$ laser pulse is shown in Fig. 14. Parameters of the eye-safe laser are summarized in Table 2, where lasing wavelength λ , output pulse energy E_{out} , pulse duration τ , energy conversion efficiency η and pulse repetition rate f are listed. The intracavity

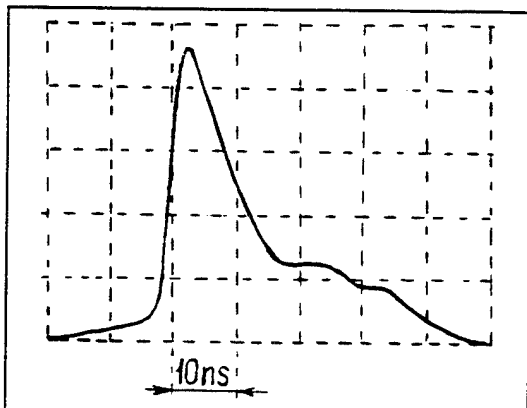


Fig. 14. Output pulse shape of intracavity pumped eye-safe $\text{Ba}(\text{NO}_3)_2$ crystal Raman laser

Table 2. Parameters of $\text{Ba}(\text{NO}_3)_2$ Raman lasers pumped with $1.34 \mu\text{m}$ passively Q-switched Nd:YAG/ $\text{V}^{3+}\text{:YAG}$ (intracavity) and Nd:YAG/ $\text{Nd}^{2+}\text{:SrF}_2$ (out of cavity) lasers.

Pump Scheme	$\lambda, \mu\text{m}$	$E_{\text{out}}, \text{mJ}$	τ, ns	$\eta, \%$	f, pps
Intracavity	1.556	1.5	10-12	90	10
Out of cavity	1.556	0.9	10-12	20	10

pumped $\text{Ba}(\text{NO}_3)_2$ crystal Raman laser emitted the 1.5 mJ energy per pulse having the 10-12 ns duration at half maximum. Obtained output pulse energy at eye-safe wavelength was about 90% of that generated at $1.3\ \mu\text{m}$ without $\text{Ba}(\text{NO}_3)_2$ crystal for optimal reflectivity of output mirror.

2.6. Eye safe $\text{Ba}(\text{NO}_3)_2$ crystal Raman laser pumped by the Nd:YAG laser Q-switched with $\text{Nd}^{2+}:\text{SrF}_2$ saturable absorber

Out of cavity scheme, shown in Fig. 15, was used to obtain SRS with passively Q-switched Nd:YAG/ $\text{Nd}^{2+}:\text{SrF}_2$ laser. The $\text{Nd}^{2+}:\text{SrF}_2$ crystal had 47% initial transmittance at $1.34\ \mu\text{m}$ wavelength. The output mirror of the pump laser had 47% reflectivity at $1.34\ \mu\text{m}$ and served as rear mirror of Raman laser. The spherical mirror with the 1500 mm curvature radius and the 80% reflectivity at $1.54\ \mu\text{m}$ had 20% reflectivity at $1.34\ \mu\text{m}$ and was used as output coupler of the Raman laser. The $\text{Ba}(\text{NO}_3)_2$ crystal was placed close to the output mirror of pump laser.

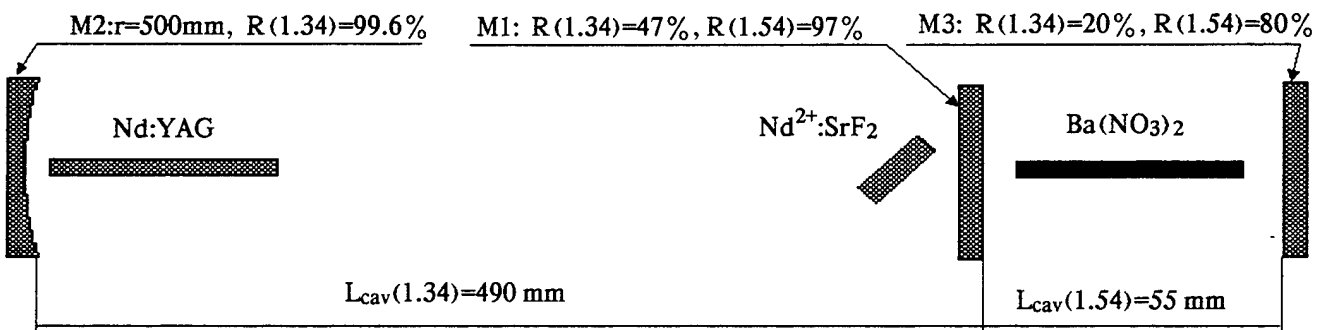


Fig. 15. Scheme of eye-safe $\text{Ba}(\text{NO}_3)_2$ crystal Raman laser out of cavity pumped by $1.3\ \mu\text{m}$ Nd:YAG laser passively

Parameters of eye safe radiation, obtained for the out of cavity pumping scheme are listed in Table 2. Without $\text{Ba}(\text{NO}_3)_2$ crystal the pump laser generated single pulses of 4.5 mJ energy and 72 ns duration at $1.338\ \mu\text{m}$ wavelength. In cavity scheme of this type Raman laser generated $1.556\ \mu\text{m}$ wavelength pulses with the energy of 0.9 mJ and duration of 10-12 ns at half-height level. The 20% energy conversion efficiency of the Raman laser was obtained, and considerable shortening of the output eye-safe laser pulse ensured conversion without loss in peak power of the pulse.

3. CONCLUSIONS

In conclusion, we have studied Q-switching properties of $\text{Nd}^{2+}:\text{SrF}_2$ and $\text{V}^{3+}:\text{YAG}$ crystalline saturable absorbers in $1.3\ \mu\text{m}$ Nd:YAG, Nd:YAP and Cr,Nd:GGG lasers. Giant pulses as short as 40 ns and energies per pulse up to 5 mJ were obtained for these $1.3\ \mu\text{m}$ passively Q-switched lasers. Simple intracavity and out of cavity pumped $\text{Ba}(\text{NO}_3)_2$ crystal Raman lasers were realized on the basis of Nd:YAG laser passively Q-switched with $\text{Nd}^{2+}:\text{SrF}_2$ and $\text{V}^{3+}:\text{YAG}$ crystals. The $1.55\ \mu\text{m}$ eye safe pulses of the Raman laser with the 10 ns duration and up to 1.5 mJ energy have been obtained.

4. ACKNOWLEDGMENT

This work was partially supported by DRET and THOMSON-TRT DEFENSE.

5. REFERENCES

1. T.T. Basiev, S.B. Mirov, and S.A. Sychev, "Passive Laser Q-switches Based on $\text{MeF}_2:\text{Nd}^{2+}$ (Me-Ca , Sr , Ba) crystals", in Solid State Lasers and New Materials, V.V. Osiko, ed.; Proc. SPIE, vol. 1839, pp. 182-197, 1992.
2. V.P. Mikhailov, N.I. Zhavoronkov, N.V. Kuleshov, V.A. Sandulenko, K.V. Yumashev, P.V. Prokoshin, in Conference on Lasers and Electro-Optics, vol. 8, 1994, OSA Technical Digest Series, pp. 390-391.

3. A.S. Eremenko, S.N. Karpukhin, and A.I. Stepanov, "SRS of the second harmonic of neodymium laser in nitrate crystals", Sov. J. Quantum Electron., vol. 10, p.113, 1980.

4. Yu.L. Crusco, S.I. Marennikov, and V.P. Chebotaev, "Tunable color center lasers", Bul. Acad. Sci. USSR, Phys. Ser., vol. 44, pp. 15-23, 1980.

5. T.T. Basiev, S.B. Mirov, "Room Temperature Tunable Color Center Lasers", in Laser Science and Technology book series, ed. V.S. Letokhov, C.V. Sank, Y.R. Shen, Harwood Academic Publishers, 1993.

Spectroscopic and laser properties of Nd³⁺ doped fluoride crystals in 1.3 μm region

T.T. Basiev, V.B. Sigachev, M.E. Doroshenko, A.G. Papashvili, V.V. Osiko
General Physics Institute, Russian Academy of Sciences, Vavilov Street 38, Moscow
Russian Federation, Telephone: (095) 135-02-67, Fax: (095) 135-02-70.

ABSTRACT

For a number of neodymium doped fluoride crystals both with regular and disordered structure the Judd-Ofelt analysis of absorption spectra have been performed, and fluorescence and lasing spectra were studied in order to reveal most promising materials for optical amplification in 1.3 μm telecommunication window. The most suitable crystalline media investigated was found to be cubic disordered fluorides based on (50-70)% SrF₂-(50-30)% CaF₂ solid solutions with Nd³⁺ optical centers having tetragonal local symmetry. These crystals have (a) low value of excited state absorption line strength, (b) high metastable level lifetime (1.2-1.3 ms), (c) high enough emission cross section for fluorescence ($\sim 4 \times 10^{-21} \text{ cm}^2$), and (d) proper fluorescence peak at about 1310 nm wavelength and comparatively wide fluorescence band with about 20 nm FWHM.

1. INTRODUCTION

The problem of optical signals amplification in 1.3 μm telecommunication window stimulates the search and study of active media suitable for this purpose. A gain medium has to possess the following properties: (a) high and isotropic gain in (1.28-1.32) μm range, and (b) high pumping efficiency at wavelengths of most suitable pump sources (for instance, diode lasers). The utilization of ${}^4\text{F}_{3/2}-{}^4\text{I}_{13/2}$ transition of Nd³⁺ ions in crystals and glasses is one of the ways to solve this problem. But two main difficulties have to be overcome for Nd³⁺ doped media. First of all, it is necessary to shift Nd³⁺ emission to the desired spectral position, since the fluorescence of Nd³⁺ ions is usually observed at wavelengths around 1.34 μm¹. The second obstacle is excited state absorption (ESA) at ${}^4\text{F}_{3/2}-{}^4\text{G}_{7/2}$ transition, that can reduce or suppress totally gain at ${}^4\text{F}_{3/2}-{}^4\text{I}_{13/2}$ transition²⁻⁴. Since the optical properties of Nd³⁺ ion (positions, widths and intensities of spectral lines) depend on crystal or glass host, the mentioned difficulties can be avoided by means of search of laser media providing short wavelength and broad band emission at ${}^4\text{F}_{3/2}-{}^4\text{I}_{13/2}$ transition and low ESA losses at competitive ${}^4\text{F}_{3/2}-{}^4\text{G}_{7/2}$ transition.

The goal of this work is to study absorption and fluorescence spectra and lasing properties of a number of Nd³⁺ doped fluoride crystals in order to estimate their applicability to 1.3 μm amplifiers.

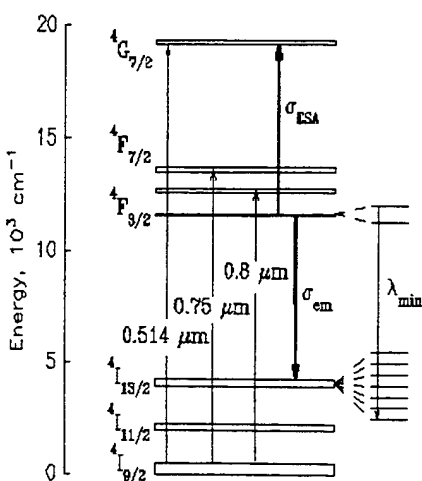


Fig.1. Energy level diagram of Nd³⁺ ion.

2. BACKGROUND

2.1. Influence of host material on wavelength of ${}^4\text{F}_{3/2}-{}^4\text{I}_{13/2}$ transition

The energy level diagram of Nd³⁺ ion is shown in Fig.1. Shortest wavelength emission λ_{\min} near 1.3 μm realizes for transition from upper Stark level of ${}^4\text{F}_{3/2}$ manifold to lower Stark level of ${}^4\text{I}_{13/2}$ manifold. The value of λ_{\min} depends on two following factors: (a) energy position of gravity center of ${}^4\text{F}_{3/2}$ and ${}^4\text{I}_{13/2}$ levels, and (b) their Stark splittings. The higher position of ${}^4\text{F}_{3/2}$ level and Stark splittings of ${}^4\text{F}_{3/2}$ and ${}^4\text{I}_{13/2}$ levels the shorter emission wavelength is. Let us analyze how the host material affects the λ_{\min} .

Energy position of ${}^4\text{I}_{13/2}$ and ${}^4\text{I}_{11/2}$ levels do not depend on type of host material and is determined only by the value of spin-orbit splitting of ${}^4\text{I}$ state of Nd³⁺ ion. Compared to free Nd³⁺ ion the energy position of high-lying energy levels (${}^4\text{F}_{3/2}$, ${}^4\text{F}_{5/2}$, ${}^4\text{S}_{3/2}$, ${}^4\text{F}_{7/2}$, ..., ${}^4\text{G}_{5/2}$, ${}^2\text{G}_{7/2}$, ${}^4\text{G}_{7/2}$) in a crystal is shifted to lower values. The reason of this shift is shielding of electrostatic Coulomb interaction between 4f electrons, that

is due to partial overlapping of 4f electron orbits of Nd³⁺ ion and orbits of surrounding anions of the crystal host (ligands). This phenomenon was called in literature as "nephelauxetic shift" and is observed as the long wavelength shift of all optical transitions of RE ion in the host materials with the increase of covalency of RE - ligand bond.

The literature data analysis⁵ shows that the value of nephelauxetic shift depends mainly on the type of host crystal anion (O²⁻, Br⁻, Cl⁻, F⁻) which is characterized by its charge and ion radius. So, oxide crystals and glasses, especially simple oxides, usually have the largest value of overlapping of RE ion and ligand wave functions and largest nephelauxetic shift. Chloride (LaCl₃) and bromide (LaBr₃) crystals display the reduction of nephelauxetic shift and the increase of the bond ionicity. For fluoride crystals and glasses (ionic radius of F⁻ is smaller than that for Cl⁻ and Br⁻) the high degree of ionic bond (i.e. small covalency) is typical. Therefore fluoride crystals and glasses have smaller value of overlapping of RE ion and ligand wave functions, and as a result they have smaller values of nephelauxetic shift, higher energy positions of levels and shorter wavelengths of optical transitions.

Requirement of maximum possible Stark splitting of considered energy levels is modified for the ⁴F_{3/2} level due to necessity of appreciable thermal population of its upper Stark level at room temperature (T=300K). Therefore Stark splitting of ⁴F_{3/2} level is limited by the value of thermal energy kT at room temperature (kT~210 cm⁻¹). The Stark splittings of ⁴F_{3/2} and ⁴I_{13/2} energy levels depend on the crystal field strength, that is characterized by the crystal field parameters B_n (n=2,4,6). The crystal field parameters are the functionals of electronic density in the crystal with parametric dependence on crystal structure⁶. The B₂ is low symmetry and B₄, B₆ are high symmetry parameters of crystal field. For our particular case it is important, that the Stark splittings of ⁴I_{13/2} and ⁴F_{3/2} manifolds have different dependences on crystal field symmetry. The Stark splitting of ⁴I_{13/2} level strongly depends on high symmetry parameters of the crystal field B₄ and B₆, and its degeneracy can be removed in crystal field of cubic symmetry. The ⁴F_{3/2} level is splitted only in the field with the symmetry lower than the cubic one and the splitting value depends on low symmetry parameter of crystal field B₂. Different response of Stark splittings of ⁴F_{3/2} and ⁴I_{13/2} levels to the different symmetry of crystal field allows to realize the moderate splitting value of ⁴F_{3/2} level and large splitting of ⁴I_{13/2} level. Therefore to shift optical transition to short wavelength region due to Stark splitting, it is necessary to choose host crystal with optical centers having large values of high symmetry parameters of crystal field and small values of low symmetry parameters.

2.2. Gain properties of Nd³⁺ ion near 1.3 μm

The gain coefficient G(λ) of an optical signal at wavelength λ is proportional to the product of active medium gain cross section σ_g(λ) and upper storage level lifetime τ. These parameters depend on spectral properties of active ion in gain medium.

The gain cross section σ_g(λ) of Nd³⁺ doped active medium in the 1.3 μm region is determined by the difference between the stimulated emission cross section σ_{em}(λ) for ⁴F_{3/2}-⁴I_{13/2} gain transition and excited state absorption cross section σ_{esa}(λ) for ⁴F_{3/2}-⁴G_{7/2} loss transition:

$$\sigma_g(\lambda) = \sigma_{em}(\lambda) - \sigma_{esa}(\lambda) = \sigma_{em}(\lambda) [1 - \sigma_{esa}(\lambda) / \sigma_{em}(\lambda)] \quad (1)$$

To provide positive gain the condition σ_{esa}(λ) / σ_{em}(λ) < 1 have to be fulfilled. This condition can be rewritten through line strengths (S_{em} and S_{esa}) and normalized line shapes (g_{em}(λ) and g_{esa}(λ)) of corresponding transitions:

$$\frac{\sigma_{esa}(\lambda)}{\sigma_{em}(\lambda)} = \frac{S_{esa} g_{esa}(\lambda)}{S_{em} g_{em}(\lambda)} = \eta(\lambda) \frac{S_{esa}}{S_{em}} < 1, \quad (2)$$

where η(λ)=g_{esa}(λ)/g_{em}(λ) is the line shapes ratio. The parameter η(λ)S_{esa}/S_{em} involved in (2) contains two parts, integral and spectral ones, which are determined respectively by the ratio of integral line strengths and the ratio of spectral line shapes of the transitions considered. In particular case of η(λ)=1 (the same fluorescence and ESA line shapes) the gain occurs for

$$S_{esa}/S_{em} < 1 \text{ or } S_{em}/S_{esa} > 1. \quad (3)$$

In our study the line strength ratio S_{em}/S_{esa} will be used to characterize potentialities of Nd³⁺ doped crystals as a gain media near 1.3 μm wavelength.

Judd-Ofelt theory can be used to express line strengths of electronic transitions through phenomenological parameters depending on host material. The line strength of an electric dipole J-J' transition can be presented as a sum

of products of six parameters^{7,8}:

$$S(J \rightarrow J') = \sum_{t=2,4,6} \Omega_t | \langle J || U^{(t)} || J' \rangle |^2 \quad (4)$$

Here $\langle J || U^{(t)} || J' \rangle$ are doubly reduced matrix elements of the unit tensor operators $U^{(t)}$ of rank $t=2,4,6$. Their values depend only on type of rare-earth ion and transition under consideration. Ω_2 , Ω_4 , and Ω_6 are the host material dependent intensity parameters that characterize the strength of rare-earth ion interaction with crystal field. To simplify notation, the $U^{(t)}$ symbol instead of $| \langle J || U^{(t)} || J' \rangle |^2$ will be further used.

Writing the ratio of line strengths for ${}^4F_{3/2} - {}^4I_{13/2}$ and ${}^4F_{3/2} - {}^4G_{7/2}$ transitions through specific values of matrix elements $U^{(t)}$ ⁹⁻¹¹, the condition of positive gain (3) can be expressed as follows:

$$\frac{S_{\text{esa}}}{S_{\text{em}}} = \frac{0.0983 \Omega_2 + 0.0584 \Omega_4}{0.212 \Omega_6} < 1 \quad (5)$$

From Eq. (5) follows, that, to provide positive gain at ${}^4F_{3/2} - {}^4I_{13/2}$ transition, it is necessary to find host material possessing small Ω_2 and Ω_4 intensity parameters and large Ω_6 intensity parameter, i.e. material with high symmetry optical centers is necessary.

Table 1. Properties of studied fluoride crystals.

Composition, mol %	ρ , g/cm ³	N, 10^{20} cm ⁻³	n
MeF₂-NdF₃ (fluorite type structure, space group O_h⁵)			
99.7% CaF ₂ :0.3% NdF ₃	3.18	0.69	1.43
71.5% CaF ₂ :28% SrF ₂ :0.5% NdF ₃	3.37	1.10	1.44
49.2% CaF ₂ :50% SrF ₂ :0.8% NdF ₃	3.71	1.73	1.44
29.2% CaF ₂ :70% SrF ₂ :0.8% NdF ₃	3.92	1.68	1.44
99.95% SrF ₂ :0.05% NdF ₃	4.24	0.11	1.44
99.7% SrF ₂ :0.3% NdF ₃	4.24	0.61	1.44
99.7% CdF ₂ :0.3% NdF ₃	6.64	0.88	1.58
99.7% BaF ₂ :0.3% NdF ₃	4.83	0.49	1.47
MeF₂-LnF₃-NdF₃ (yttrifluorite type structure, space group O_h⁵)			
96.1% CaF ₂ :2.3% YF ₃ :1.6% NdF ₃	3.21	3.76	1.43
88.5% SrF ₂ :10% LaF ₃ :1.5% NdF ₃	4.44	3.00	1.46
68.5% SrF ₂ :30% LaF ₃ :1.5% NdF ₃	4.78	2.92	1.49
58.5% SrF ₂ :40% LaF ₃ :1.5% NdF ₃	4.95	2.89	1.50
86.6% BaF ₂ :12.3% LaF ₃ :1.1% NdF ₃	4.97	1.85	1.48
LnF₃-MeF₂-NdF₃ (tysonite type structure, space group D_{3d}⁴)			
99% LaF ₃ :1% NdF ₃	5.94	1.79	1.60
96% LaF ₃ :3% SrF ₂ :1% NdF ₃	5.89	1.94	1.60
86.5% LaF ₃ :12% SrF ₂ :1.5% NdF ₃	5.75	2.80	1.58
50% LaF ₃ :48.5% SrF ₂ :1.5% NdF ₃	5.09	3.15	1.52
99% CeF ₃ :1% NdF ₃	6.16	1.88	1.62
91.7% CeF ₃ :6.6% SrF ₂ :1.65% NdF ₃	6.03	3.12	1.61
84.85% CeF ₃ :13.5% SrF ₂ :1.65% NdF ₃	5.90	3.13	1.59
Space group O_h⁵			
5NaF:9YF ₃ :1% NdF ₃	3.55	1.94	1.47

3. OBJECTS OF RESEARCH

According to previous analysis, to provide low nephelauxetic shift of Nd³⁺ energy levels the fluoride crystals with disordered structure were selected as the best ones for our study. The necessity of investigation of disordered crystals or crystalline solid solutions having wide inhomogeneously broadened spectral lines of Nd³⁺ ions is due to requirement of maximum width of gain band and the possibility to realize smooth variations of optical properties of Nd³⁺ ions in solid solutions. The following groups of Nd³⁺-doped disordered fluoride crystals were grown and studied:

a) cubic symmetry crystals of CaF₂, SrF₂, BaF₂, CdF₂ and solid solutions of SrF₂-CaF₂ with fluorite type structure;

b) cubic symmetry crystals of SrF₂-LaF₃, CaF₂-YF₃, BaF₂-LaF₃ with yttrifluorite type structure;

c) hexagonal symmetry solid solutions of LaF₃-SrF₂, CeF₃-SrF₂ with tysonite type structure;

d) cubic symmetry crystal of 5NaF-9YF₃.

All the crystals were grown by Bridgman-Stockbarger technique. Compositions of the crystals were measured by electron beam micro-probe technique.

The quantitative composition of the crystals investigated, their space group symmetry, specific weight ρ , Nd³⁺ ions concentration N, and refractive index n are given in Table 1.

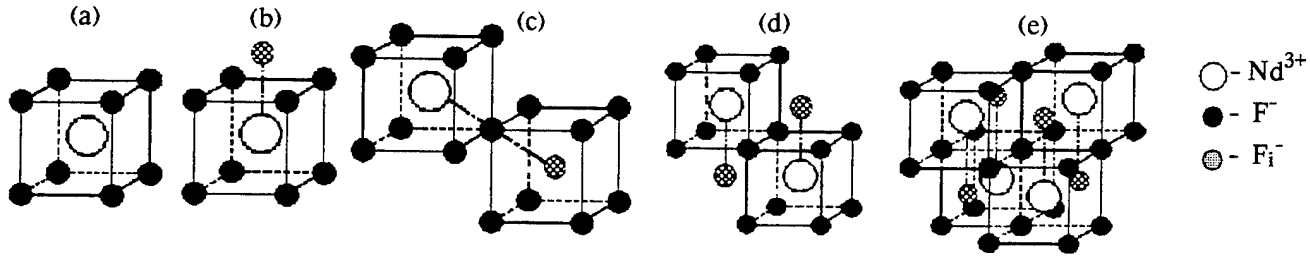


Fig. 2. Models of various Nd³⁺ centers in fluorite type structure crystals: O_h symmetry center (a), C_{4v} symmetry center or L center (b), C_{3v} symmetry center or L* center (c), C₈ symmetry center or M center (d), C₈ symmetry center or N center (e).

Heterovalent character of Nd³⁺ substitution in studied fluorides results in a variety of charge compensation centers. Different surrounding of Nd³⁺ ions gives rise to their different absorption and fluorescence properties. A lot of various Nd³⁺ optical centers has been observed in the alkaline earth fluorides and their solid solutions^{12,13}.

Alkaline earth fluoride crystals MeF₂ (Me²⁺ = Ca²⁺, Sr²⁺, Ba²⁺, Cd²⁺) have cubic-tetrahedral coordination (space group O_h⁵), where each Me²⁺ ion is cubically coordinated by eight F⁻ ions, and each F⁻ ion is coordinated by four Me²⁺ ions. The trivalent Nd³⁺ dopant ions are distributed in the sites of Me²⁺ sublattice. The 1/3 of the F⁻ ions from the hole number in NdF₃ admixture occupy the octahedral interstitial positions of crystal lattice. Due to Coulomb interaction of Nd³⁺ ion and interstitial fluorine F_i⁻ charge compensated Nd³⁺-F_i⁻ pairs and their clusters have to be formed in the crystal.

Possible structural models of impurity Nd³⁺ centers in the MeF₂:NdF₃ crystals are shown in Fig.2. These Nd³⁺ centers can be divided into single and clustered ones. The single Nd³⁺ ion centers can have cubic (O_h), tetragonal (C_{4v}) and trigonal (C_{3v}) symmetry. Cubic symmetry center is Nd³⁺ ion without local charge compensation (Fig.2,a). Tetragonal symmetry center, or so-called L center, is single Nd³⁺ ion compensated with F_i⁻ ion located in the nearest neighbor interstitial position in the <100> directions (Fig.2,b). Trigonal symmetry is due to F_i⁻ compensating ion located in the next nearest neighbor interstitial position in the <111> directions (Fig.2,c). The most simple clustered centers, having rhombic (C₈) symmetry, are shown in Fig.2, d and e. These clustered centers are referred respectively as M and N centers. M center is composed of two Nd³⁺-F_i⁻ pairs. The N-center is the cluster of four Nd³⁺-F_i⁻ pairs.

In CaF₂, SrF₂ crystals and their solid solutions the single Nd³⁺ ion centers preferably with tetragonal symmetry dominate for low enough Nd³⁺ concentrations. When the concentration of Nd³⁺ ions in the crystals is increased sharp rise of rhombic M centers and N centers concentration is observed.

In case of MeF₂-LnF₃:NdF₃ crystals with yttrifluorite structure there are two types of trivalent lanthanide Ln³⁺ ions. Therefore rhombic center composed of Nd³⁺-Ln³⁺-(F_i⁻)₂ cluster (so-called M' center), and rhombic center composed of Nd³⁺_n-(Ln³⁺)_{4-n}-(F_i⁻)₄ cluster (so-called N' center) can form. In crystals with yttrifluorite structure clustered rhombic symmetry M' and N' centers are predominating types of Nd³⁺ centers.

4. RESULTS AND DISCUSSION

4.1. Absorption spectra and Judd-Ofelt analysis

Absorption spectra of studied crystals in the range of 300-1000 nm were recorded at room temperature using double-ray spectrophotometer. The data acquisition was accomplished with the help of an IBM PC computer. Absorption spectra were transformed to absorption coefficient spectra k(λ), that were integrated over each of nine absorption bands in order to calculate line strengths of corresponding transitions S_{meas} according to the following relation¹⁰:

$$S_{\text{meas}}(J \rightarrow J') = \frac{3ch(2J+1)}{8\pi e N \bar{\lambda}} \left[\frac{9\bar{\pi}}{(\bar{\pi}^2 + 2)^2} \right] \int k(\lambda) d\lambda \quad (6)$$

Here N is the Nd³⁺ concentration, $\bar{\lambda}$ is the average wavelength for the J-J' transition, $\bar{\pi}$ is the medium refractive

index corresponding to average wavelength. In general case refractive index dispersion $n(\lambda)$ has to be known for calculation of line strengths. But in our calculations the refractive index dispersion was neglected and data, taken from literature and listed in Table 1, were used.

Nine measured line strengths S_{meas} were least-squares fitted to calculate the set of intensity parameters Ω_t ($t=2, 4, 6$) according to Eq.(4). The ratio of line strengths $S_{\text{em}}/S_{\text{esa}}$ for $^4F_{3/2}-^4I_{13/2}$ emission and $^4F_{3/2}-^4G_{7/2}$ excited state absorption, that characterize the quality of material for $1.3 \mu\text{m}$ amplifier, was calculated using formula (5).

The Ω_t intensity parameters were also calculated with the help of only three absorption bands corresponding to transitions from $^4I_{9/2}$ ground state to $^4F_{3/2}$ (band 1), $^4F_{7/2} + ^4S_{3/2}$ (band 3), and $^4G_{5/2} + ^4G_{7/2}$ (band 5) final states. These bands were selected for calculations of Ω_t parameters due to following reason. The line strengths of these bands depend mainly on one of three Ω_t ($t=2, 4, 6$) parameters, since the influence of other two residual parameters Ω_1 is minimized because of small values of corresponding matrix elements. So, line strength of band 1 is mainly determined by the $\Omega_4 U^{(4)}$ product, since $U^{(2)}=0$ and $U^{(6)}=U^{(4)}/4.08$. The line strength of band 3 is depended only on $\Omega_6 U^{(6)}$ product, since $U^{(2)}=U^{(6)}/658$, and $U^{(4)}=U^{(6)}/14.7$. The line strength of band 5 is determined mainly by the $\Omega_2 U^{(2)}$ product, since $U^{(4)}=U^{(2)}/1.65$, and $U^{(6)}=U^{(2)}/14.6$. The Ω_2 , Ω_4 , and Ω_6 intensity parameters were unambiguously found from the solution of the set of three equations (4) written for measured line strengths of these three absorption bands. The comparison of measured line strengths with line strengths calculated on the basis of analysis of three and nine absorption bands is presented in Table 2. The calculations appear to be good in both cases. If the nine bands fit gives smaller rms error for line strengths, the three bands calculation gives more precise results for five absorption bands corresponding to lower lying final states. Three bands calculation algorithm usually results in larger value of Ω_2 parameter, smaller value of Ω_4 parameter, about the same value of Ω_6 parameter, and about the same value of $S_{\text{em}}/S_{\text{esa}}$ ratio (see foot-note in Table 2). Below we will use data obtained for calculations on the basis of three measured line strengths.

Table 2. Comparison of measured and calculated line strengths of 99.5% SrF₂:0.5% NdF₃ crystal.

Band No	Final States of Transition	Average wavelength, nm	Line Strength, 10^{-20} cm^2		
			Meas.	Calculated	
				3 bands *	9 bands **
1	$^4F_{3/2}$	869	0.384	0.384	0.520
2	$^4F_{5/2}, ^2H_{9/2}$	795	1.470	1.411	1.526
3	$^4F_{7/2}, ^4S_{3/2}$	740	1.494	1.495	1.485
4	$^4F_{9/2}$	662	0.180	0.195	0.249
5	$^4G_{5/2}, ^2G_{7/2}$	576	1.457	1.457	1.473
6	$^4G_{7/2}, ^4G_{9/2}, ^2K_{13/2}$	515	0.917	0.576	0.680
7	$^4G_{9/2}, ^4G_{11/2}, ^2D_{3/2}, ^2K_{15/2}$	466	0.257	0.131	0.155
8	$^2P_{1/2}, ^2D_{5/2}$	426	0.056	0.047	0.069
9	$^4D_{1/2}, ^4D_{3/2}, ^4D_{5/2}, ^2I_{11/2}$	351	1.025	0.704	1.018

* $\Omega_2, \Omega_4, \Omega_6 = (0.66, 1.13, 2.19) \times 10^{-20} \text{ cm}^2$, RMS Err. = $1.997 \times 10^{-21} \text{ cm}^2$, $S_{\text{em}}/S_{\text{esa}} = 3.54$

** $\Omega_2, \Omega_4, \Omega_6 = (0.32, 1.74, 2.14) \times 10^{-20} \text{ cm}^2$, RMS Err. = $1.250 \times 10^{-21} \text{ cm}^2$, $S_{\text{em}}/S_{\text{esa}} = 3.42$

Calculated intensity parameters Ω_t and ratios $S_{\text{em}}/S_{\text{esa}}$ for all studied fluoride crystals are listed in Table 3. Concerning these data it should be noted, that each type of optical centers in the studied multisite crystals has its own set of spectroscopic parameters. In rigorous Judd-Ofelt analysis of absorption spectra of the crystals it is necessary to know absorption spectrum of each type of optical centers and their absolute concentration. Due to complicity of such kind of analysis we used integral absorption spectra and total Nd³⁺ concentration in our calculations. Therefore the intensity parameters we have determined belong to dominating type of centers or quasi-center. Also it is necessary to bear in mind, that unlike Ω_t parameters line strengths ratio $S_{\text{em}}/S_{\text{esa}}$ is independent on Nd³⁺ concentration.

In case of studied MeF₂-LnF₃:NdF₃, LnF₃-MeF₂:NdF₃ and 5NaF-9YF₃:NdF₃ solid solutions intensity parameters Ω_t and ratio $S_{\text{em}}/S_{\text{esa}}$ belong most probably to clustered low symmetry centers, which are the major type of centers in these crystals. It should be noted that in Judd-Ofelt

analysis we neglected the absorption anisotropy phenomena in the crystals with hexagonal structure.

Much more complicated situation realizes for alkaline earth fluoride crystals $\text{MeF}_2:\text{NdF}_3$, since the dominating type of Nd^{3+} optical centers strongly depends on concentration of NdF_3 . So, Judd-Ofelt parameters, and line strengths ratio $S_{\text{em}}/S_{\text{esa}}$ of single-ion centers can be derived for crystals with low enough concentration of NdF_3 . Our analysis of low temperature absorption spectra structure of as-grown $(1-x)\text{SrF}_2:x\text{NdF}_3$ crystals shown that noticeable clustering to the $(\text{Nd}^{3+}-\text{F}_i)^2$ centers starts when Nd^{3+} concentration reaches 0.2 atomic %. At lower concentrations the tetragonal symmetry L centers is the only type of optical centers revealed in absorption spectra. Therefore results of Judd-Ofelt analysis for $\text{SrF}_2:0.05\%$ NdF_3 crystal shown in Table 3 correspond to tetragonal symmetry centers of Nd^{3+} ion. This type of centers has about 3 times higher Ω_6 intensity parameter than Ω_2 and Ω_4 parameters, and as a result it has high line strengths ratio $S_{\text{em}}/S_{\text{esa}}$, which value reaches 4.4. Clustered centers concentration is increased with the rise of Nd^{3+} concentration, but the tetragonal symmetry L centers are still predominate in $\text{SrF}_2:\text{NdF}_3$ crystals up to 1 at. % of Nd^{3+} . Reduction of line strengths ratio $S_{\text{em}}/S_{\text{esa}}$ to about 3.5 in $\text{SrF}_2:0.5\%$ NdF_3 crystal is probably the display

Table 3. Calculated Judd-Ofelt parameters Ω_t ($t=2,4,6$) and predicted line strengths ratio $S_{\text{em}}/S_{\text{esa}}$, spontaneous probability A for $^4\text{F}_{3/2}-^4\text{I}_{13/2}$ transition, radiative τ_r and measured τ_{meas} lifetimes of $^4\text{F}_{3/2}$ level in Nd^{3+} doped fluoride crystals

Composition, mol %	Judd-Ofelt parameters, 10^{-20} cm^2			$\frac{S_{\text{em}}}{S_{\text{esa}}}$	A, s^{-1}	$\tau_r, \mu\text{s}$	$\tau_{\text{meas}}, \mu\text{s}$
	Ω_2	Ω_4	Ω_6				
MeF ₂ -NdF ₃ (fluorite type structure)							
99.7% CaF ₂ :0.3% NdF ₃	0.83	0.86	3.34	5.37	145	973	1160
71.5% CaF ₂ :28% SrF ₂ :0.5% NdF ₃	0.29	1.21	2.22	4.72	98	1190	1260
49.2% CaF ₂ :50% SrF ₂ :0.8% NdF ₃	0.32	1.36	1.89	3.64	84	1260	
29.2% CaF ₂ :70% SrF ₂ :0.8% NdF ₃	0.63	0.77	2.09	4.12	92	1410	1290
99.95% SrF ₂ :0.05% NdF ₃	0.58	0.71	2.05	4.40	91	1460	1350
99.5% SrF ₂ :0.5% NdF ₃	0.66	1.13	2.19	3.54	97	1220	1340
99.7% CdF ₂ :0.3% NdF ₃	1.26	1.34	4.93	5.16	292	477	
99.7% BaF ₂ :0.3% NdF ₃	0.64	0.23	0.65	1.79	30	4330	
MeF ₂ -LnF ₃ -NdF ₃ (yttrifluorite type structure)							
96.1% CaF ₂ :2.3% YF ₃ :1.6% NdF ₃	0.38	2.48	3.79	4.4	164	667	560
88.5% SrF ₂ :10% LaF ₃ :1.5% NdF ₃	0.56	2.51	3.82	4.0	176	620	490
68.5% SrF ₂ :30% LaF ₃ :1.5% NdF ₃	0.49	2.85	3.33	3.29	164	602	560
58.5% SrF ₂ :40% LaF ₃ :1.5% NdF ₃	0.31	2.77	3.87	4.27	194	545	570
86.6% BaF ₂ :12.3% LaF ₃ :1.1% NdF ₃	0.33	0.75	1.51	4.17	73	1650	540
LnF ₃ -MeF ₂ -NdF ₃ (tysonite type structure)							
99% LaF ₃ :1% NdF ₃	0.72	1.95	2.26	2.59	139	705	670
96% LaF ₃ :3% SrF ₂ :1% NdF ₃	1.04	1.87	2.57	2.58	158	665	610
86.5% LaF ₃ :12% SrF ₂ :1.5% NdF ₃	0.86	2.06	3.42	3.54	202	558	570
48.5% SrF ₂ :50% LaF ₃ :1.5% NdF ₃	0.96	1.76	3.41	3.68	179	665	550
99% CeF ₃ :1% NdF ₃	0.94	2.53	3.34	2.93	214	483	330
91.7% CeF ₃ :6.6% SrF ₂ :1.65% NdF ₃	1.76	2.23	4.18	2.93	263	447	280
84.85% CeF ₃ :13.5% SrF ₂ :1.65% NdF ₃	1.67	2.76	5.78	3.76	349	348	250
5NaF:9YF ₃ :1% NdF ₃	0.78	1.49	2.41	3.13	114	985	870
ZBLAN ^[16]	1.9	3.5	3.7	2.0		504	
ZBLAN ^[17]	2.2	2.82	3.94	2.0			

of the clusters influence on results of Judd-Ofelt calculations performed on the basis of integral absorption spectra. High line strengths ratio $S_{\text{em}}/S_{\text{esa}}=5.37$ was obtained for $\text{CaF}_2:0.3\% \text{NdF}_3$ crystal, in spite of the fact that the clustering in CaF_2 starts at considerably lower Nd^{3+} concentrations compared to SrF_2 . For the $\text{SrF}_2-\text{CaF}_2:\text{NdF}_3$ solid solutions the line strength ratios $S_{\text{em}}/S_{\text{esa}}$ are in the range of 3.6-5, i.e. between values characteristic to $\text{SrF}_2:0.5\% \text{NdF}_3$ and $\text{CaF}_2:0.3\% \text{NdF}_3$ crystals. High line strengths ratio $S_{\text{em}}/S_{\text{esa}}=5.16$ was also obtained for $\text{CdF}_2:0.3\% \text{NdF}_3$ crystal with low Nd^{3+} concentration. The $\text{BaF}_2:0.3\% \text{NdF}_3$ crystal is clearly distinguished among studied fluorite type structure crystals by low values of intensity parameters ($\Omega_1 < 0.65 \times 10^{-20} \text{ cm}^2$) and very low line strengths ratio $S_{\text{em}}/S_{\text{esa}}=1.79$. These data for $\text{BaF}_2:0.3\% \text{NdF}_3$ crystal correspond most probably to trigonal symmetry centers (Fig. 2, c), which predominate in BaF_2 , as it was identified earlier in other works^{14,15}.

Results of Judd-Ofelt analysis allow to compare studied groups of crystals in terms of ratio of line strengths for gain and loss transitions from ${}^4\text{F}_{3/2}$ level of Nd^{3+} ion near $1.3 \mu\text{m}$ wavelength. The highest values of $S_{\text{em}}/S_{\text{esa}}$ ratio in the range of the 4-5 is realized in alkaline earth fluoride crystals CaF_2 , SrF_2 , CdF_2 and solid solutions $\text{SrF}_2-\text{CaF}_2$ for low enough Nd^{3+} ion concentrations, where high symmetry single-ion Nd^{3+} optical centers predominate over clusters. Therefore these crystals have low Ω_2 and Ω_4 intensity parameters and high Ω_6 intensity parameter. Somewhat lower ratios $S_{\text{em}}/S_{\text{esa}}=3-4.4$ are realized in crystals $\text{MeF}_2-\text{LnF}_3:\text{NdF}_3$ with yttrifluorite type structure, where lower symmetry rhombic M', and N' optical centers and their complexes predominate. And at last the smallest $S_{\text{em}}/S_{\text{esa}}$ ratios varying in the range of the 2.6-3.7 have hexagonal solid solutions of $\text{LaF}_3-\text{SrF}_2:\text{NdF}_3$ and $\text{CeF}_3-\text{SrF}_2:\text{NdF}_3$ and cubic solid solution of $5\text{NaF}-9\text{YF}_3:\text{NdF}_3$. It should be noted that the ratio $S_{\text{em}}/S_{\text{esa}}$ for all the studied fluoride crystals except $\text{BaF}_2:\text{NdF}_3$ is higher than that ratio in well known ZBLAN: Nd^{3+} glass, which value does not exceed 2^{16,17}.

4.2. Fluorescence properties

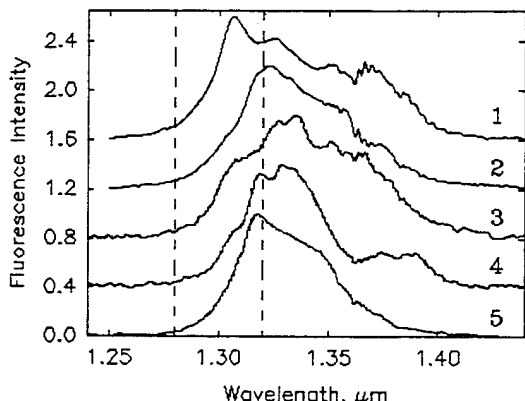
Room-temperature fluorescence was excited by the 514.5 nm line of Ar^+ -laser, dispersed by the 1-m double grating monochromator, and detected by liquid nitrogen cooled PbS photoresistor using the lock-in amplifier. Also fluorescence was excited by various wavelengths of tunable alexandrite laser. The data acquisition was performed by computer.

Fluorescence spectra of $\text{MeF}_2-\text{LnF}_3:\text{NdF}_3$ and $5\text{NaF}-9\text{YF}_3:\text{NdF}_3$ cubic crystals, $(1-x)\text{LaF}_3-x\text{SrF}_2:\text{NdF}_3$ and $(1-x)\text{CeF}_3-x\text{SrF}_2:\text{NdF}_3$ hexagonal crystals are shown in Figs. 3, 4, and 5, respectively. Fluorescence spectra of Nd^{3+} doped alkaline earth fluorides and $(1-x)\text{CaF}_2-x\text{SrF}_2$ solid solutions are shown in Figs. 6 and 7. Dashed vertical lines in Figs. 3-7 indicate boundaries of $1.28-1.32 \mu\text{m}$ spectral band which is interesting for $1.3 \mu\text{m}$ amplifiers. For comparison the fluorescence spectrum of Nd^{3+} doped ZBLAN glass is shown in Fig.3.

Substantial inhomogeneous broadening of fluorescence lines is one of the main feature of mixed crystals of fluorides. This broadening is illustrated in Fig.4, where unpolarized fluorescence spectra of $(1-x)\text{LaF}_3-x\text{SrF}_2:\text{NdF}_3$ solid solutions in comparison with spectrum of ordered $\text{LaF}_3:\text{NdF}_3$ crystal are shown. The fluorescence spectra of $\text{LaF}_3-\text{SrF}_2:\text{NdF}_3$ solid solutions are anisotropic like the spectrum of $\text{LaF}_3:\text{NdF}_3$ crystal, but they display high inhomogeneous line broadening. So, in case of $86.5\% \text{LaF}_3-12\% \text{SrF}_2:1.5\% \text{NdF}_3$ crystal the fluorescence line full width at half maximum (FWHM) is equal to $\Delta\nu \sim 390 \text{ cm}^{-1}$. This is more than one order of magnitude larger than the fluorescence lines width for $\text{LaF}_3:\text{NdF}_3$. It should be noted that the maximum of $\text{LaF}_3:\text{NdF}_3$ fluorescence spectrum shifts from the $\lambda_{\text{max}}=1.33 \mu\text{m}$ to the $\lambda_{\text{max}}=1.318 \mu\text{m}$ wavelength in case of $\text{LaF}_3-12\% \text{SrF}_2:\text{NdF}_3$ mixed crystals. Rise of SrF_2 concentration in solid solution up to 50 mol. % does not result in considerable changes of λ_{max} and $\Delta\nu$. The analogous behavior is observed for the $\text{CeF}_3-\text{SrF}_2:\text{NdF}_3$ solid solutions and $\text{CeF}_3:\text{NdF}_3$ crystal (Fig.5).

The highest degree of inhomogeneous line broadening among studied fluorides realizes for $\text{LaF}_3-\text{SrF}_2:\text{NdF}_3$, $\text{CeF}_3-\text{SrF}_2:\text{NdF}_3$,

Fig. 3. Room temperature fluorescence spectra of Nd^{3+} ions in $5\text{NaF}-9\text{YF}_3:1\% \text{NdF}_3$ (1), $68.5\% \text{SrF}_2:30\% \text{LaF}_3:1.5\% \text{NdF}_3$ (2), $96.1\% \text{CaF}_2:2.3\% \text{YF}_3:1.6\% \text{NdF}_3$ (3) and $86.6\% \text{BaF}_2:12.3\% \text{LaF}_3:1.1\% \text{NdF}_3$ (4) crystals and ZBLAN glass (5) at 514.5 nm excitation.



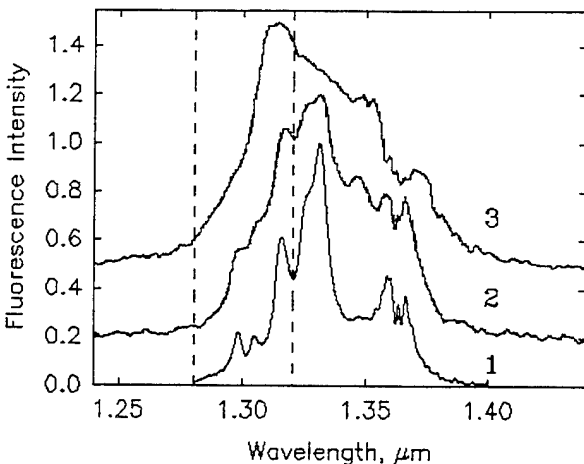


Fig. 4. Unpolarized room temperature fluorescence spectra of Nd^{3+} ions in 99% LaF_3 :1% NdF_3 (1), 96% LaF_3 :3% SrF_2 :1% NdF_3 (2) and 96.5% LaF_3 :12% SrF_2 :1.5% NdF_3 (3) at 514.5 nm excitation.

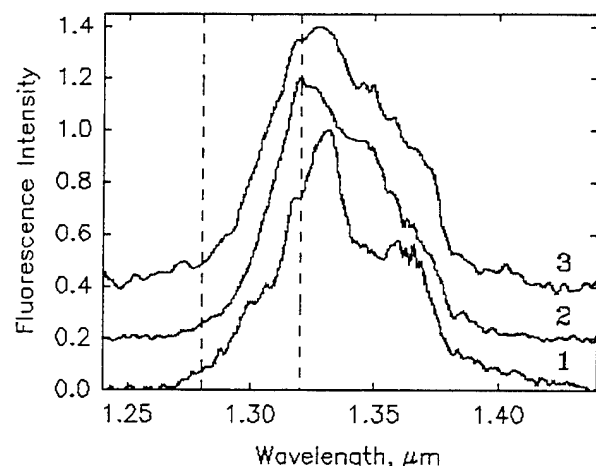


Fig. 5. Unpolarized room temperature fluorescence spectra of Nd^{3+} ions in 99% CeF_3 :1% NdF_3 (1), 91.7% CeF_3 :6.6% SrF_2 :1.65% NdF_3 (2) and 84.85% CeF_3 :13.5% SrF_2 :1.65% NdF_3 (3) at 514.5 nm excitation.

$\text{CaF}_2\text{-YF}_3\text{:NdF}_3$, $\text{BaF}_2\text{-LaF}_3\text{:NdF}_3$, and $5\text{NaF}\text{-9YF}_3\text{:NdF}_3$ solid solutions. The latter crystal is interesting due to shortest wavelength of maximum fluorescence intensity peak, as it is clearly seen in Fig.3. The fluorescence of $5\text{NaF}\text{-9YF}_3\text{:NdF}_3$ crystal have maximum at $1.307 \mu\text{m}$ and large width $\Delta\nu=460 \text{ cm}^{-1}$. For comparison in ZBLAN glass the value of λ_{\max} is equal to $1.318 \mu\text{m}$, and FWHM is about two times narrower ($\Delta\nu=260 \text{ cm}^{-1}$). The longest wavelength position of fluorescence peak is observed for the $\text{BaF}_2\text{-12\% LaF}_3\text{:NdF}_3$ ($\lambda_{\max}=1.328 \mu\text{m}$ and $\Delta\nu=220 \text{ cm}^{-1}$) and $\text{CaF}_2\text{-2.3\% YF}_3\text{:NdF}_3$ ($\lambda_{\max}=1.336 \mu\text{m}$ and $\Delta\nu=410 \text{ cm}^{-1}$) crystals. It should be noted that fluorescence spectra of $\text{MeF}_2\text{-LnF}_3\text{:NdF}_3$, $\text{LnF}_3\text{-MeF}_2\text{:NdF}_3$ and $5\text{NaF}\text{-9YF}_3\text{:NdF}_3$ solid solutions do not depend considerably on excitation wavelength and Nd^{3+} ions concentration.

Different situation realizes for CaF_2 and SrF_2 crystals and their solid solutions. Considerable dependence of fluorescence spectra on excitation wavelength λ_{ex} is the feature of alkaline earth fluoride crystals. For instance, two different fluorescence spectra corresponding to fluorescence of different optical centers of Nd^{3+} ions can be clearly identified for $\text{SrF}_2\text{:0.8\% NdF}_3$ crystal at two different excitation wavelengths as it shown in Fig.6 by the spectrum 4 ($\lambda_{\text{ex}}=752 \text{ nm}$) and in Fig.7 by the spectrum 1 ($\lambda_{\text{ex}}=514.5 \text{ nm}$). The same spectrum like at 514.5 nm excitation was obtained at 743 nm excitation wavelength. As one can see from the spectra, if 514.5 nm and 743 nm wavelengths excite preferably short wavelength fluorescence of tetragonal L centers in $\text{SrF}_2\text{:NdF}_3$, the 752 nm excitation gives rise long wavelength fluorescence of clustered Nd^{3+} centers.

Fluorescence properties of CaF_2 and SrF_2 crystals and their solid solutions strongly depend also on Nd^{3+} concentration. Examples of such dependence of fluorescence spectra for $\text{CaF}_2\text{:7\% NdF}_3$ and $\text{CaF}_2\text{:0.3\% NdF}_3$ crystals for the same excitation wavelength are shown in Figs. 6 (spectrum 1) and 7 (spectrum 6), respectively. It is clearly seen that the higher is the Nd^{3+} ions concentration the larger is the contribution of rhombic clustered centers fluorescence. Fluorescence of the rhombic centers is strongly quenched, and the quantum efficiency of the fluorescence is only 5% of that for tetragonal ones. Moreover the peak of fluorescence spectrum of rhombic centers is out of desired gain band near $1.3 \mu\text{m}$. It should be noted that the analogous spectrum is observed for clustered $\text{Nd}^{3+}\text{-Y}^{3+}\text{-(F}_i^-\text{)}_2$ and $\text{Nd}^{3+}\text{-Lu}^{3+}\text{-(F}_i^-\text{)}_2$ centers (M' centers) in $\text{CaF}_2\text{-YF}_3\text{:NdF}_3$ and $\text{CaF}_2\text{-LuF}_3\text{:NdF}_3$ crystals, but the fluorescence of M' centers is not quenched.

Quite different situation is realized for tetragonal symmetry L centers in $\text{CaF}_2\text{:NdF}_3$, $\text{SrF}_2\text{:NdF}_3$ crystals and their solid solutions. As seen from Fig. 7 the fluorescence spectra of L centers in $\text{CaF}_2\text{:NdF}_3$, $\text{SrF}_2\text{:NdF}_3$ crystals and $(1-x)\text{CaF}_2\text{-xSrF}_2\text{:NdF}_3$ solid solutions are well matched to desired gain band, since three most intensive short wavelength lines are in the $1.29\text{-}1.32 \mu\text{m}$ range. The addition of SrF_2 to $\text{CaF}_2\text{:NdF}_3$ results in inhomogeneous

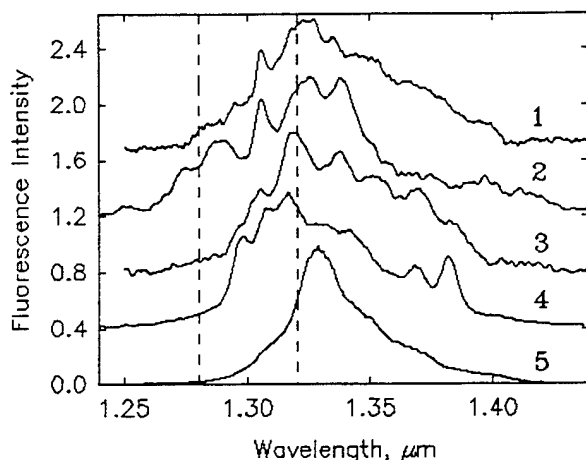


Fig. 6. Room temperature fluorescence spectra of 93% CaF₂:7% NdF₃ (1), 97.7% BaF₂:0.3% NdF₃ (2), 99.7% CdF₂:0.3% NdF₃ (3) at 514.5 nm excitation and 99.2% SrF₂:0.8% NdF₃ (4), 49% CaF₂:49% SrF₂:2% NdF₃ (5) at 752 nm excitation with predominating fluorescence of clustered Nd³⁺ centers.

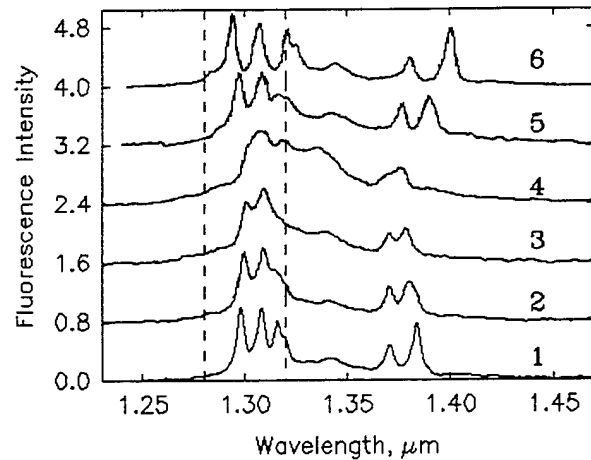


Fig. 7. Room temperature fluorescence spectra of 99.2% SrF₂:0.8% NdF₃ (1), 9.2% CaF₂:90% SrF₂:0.8% NdF₃ (2), 29.2% CaF₂:70% SrF₂:0.8% NdF₃ (3), 49.2% CaF₂:50% SrF₂:0.8% NdF₃ (4), 71.5% CaF₂:28% SrF₂:0.8% NdF₃ (5) and 99.7% CaF₂:0.3% NdF₃ (6) at 514.5 nm excitation with predominating fluorescence of tetragonal L-centers.

broadening of fluorescence lines, but not so dramatic as in the case of LaF₃-SrF₂:NdF₃, CaF₂-YF₃:NdF₃, BaF₂-LaF₃:NdF₃ crystals. Variation of the (1-x)CaF₂-xSrF₂:NdF₃ solid solution composition affects most considerably on the monotonic shift of all lines maxima due to variation of ⁴I_{13/2} level Stark splitting ΔE. So, the ⁴I_{13/2} level splitting value ΔE changes continuously from about 590 cm⁻¹ in CaF₂ to about 480 cm⁻¹ in SrF₂ passing through minimum value 380 cm⁻¹ in 50% CaF₂-50% SrF₂. These variations of Stark splitting correlate with the rise of crystal lattice unit from 0.5464 nm in CaF₂ to 0.578 nm in SrF₂. It should be noted also that rise of CaF₂ admixture in (1-x)CaF₂-xSrF₂:NdF₃ solid solution results in increase of clustered centers fluorescence intensity. Compositions with x=50-70 mol. % possess maximum inhomogeneous broadening of fluorescence lines of L centers and have comparatively high Nd³⁺ concentration, up to which L centers predominate.

Calculated Judd-Ofelt intensity parameters Ω_i were used to predict probabilities for spontaneous transitions from ⁴F_{3/2} level of Nd³⁺ ion and its radiative lifetime τ_r in studied fluoride crystals. The probability A(J'-J) for spontaneous electric dipole J'-J transition were calculated using the following relation:

$$A(J \rightarrow J') = \frac{64\pi^4 e^2}{3h(2J'+1)\lambda^3 n} \left[\frac{(n^2+2)^2}{9} \right] S(J \rightarrow J'). \quad (7)$$

Radiative lifetime τ_r of ⁴F_{3/2} level is the reciprocal of total spontaneous emission probability:

$$\tau_r = \left[\sum A(^4F_{3/2} \rightarrow ^4I_J) \right]^{-1}, \quad (8)$$

where summation is over all lower lying states with J=15/2, 13/2, 11/2, and 9/2.

Spontaneous emission probability for ⁴F_{3/2}-⁴I_{13/2} transition and radiative lifetime τ_r, that were calculated using relations (7) and (8), are summarized in Table 3. Calculated radiative lifetimes for studied crystals are in a good agreement with lifetimes τ_{meas} measured for the exponential part of decay curve at long time tail for the 790 nm excitation by the nanosecond pulsed Ti:Al₂O₃ crystal laser. It should be noted that the measured decay times in CaF₂ and SrF₂ crystals and their solid solutions correspond to lifetimes of tetragonal symmetry L centers. Therefore some discrepancy for CaF₂:0.3% NdF₃, SrF₂:0.5% NdF₃, and 71.5% CaF₂-28% SrF₂:0.5% NdF₃ crystals may be due to clustered centers influence on results of the Judd-Ofelt calculations.

Measured fluorescence spectra I(λ), that were preliminary corrected on monochromator-detector spectral response,

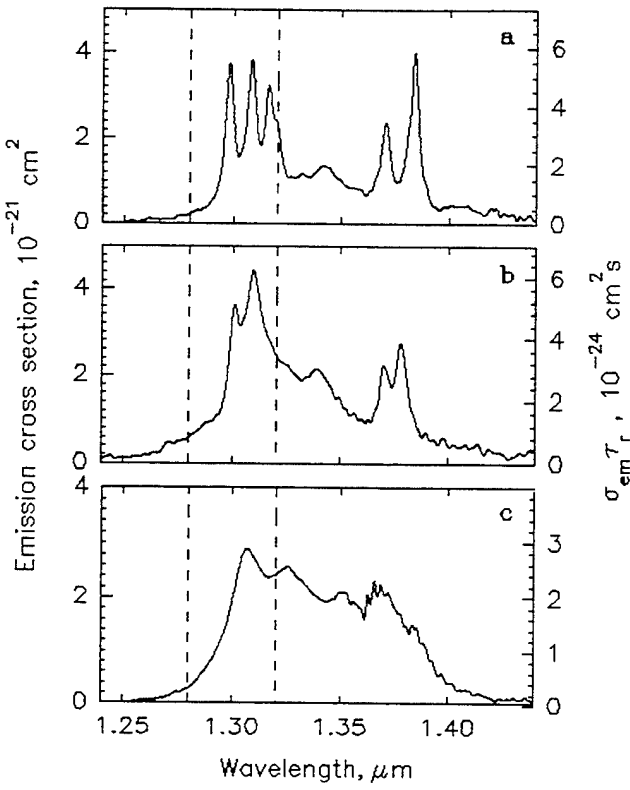


Fig. 8. Stimulated emission cross section spectra $\sigma_{\text{em}}(\lambda)$ and maximum possible gain $G_{\max}(\lambda) \sim \sigma_{\text{em}}(\lambda)\tau_r$ for $\text{SrF}_2:0.8\% \text{NdF}_3$ (L-centers) (a), $29.2\% \text{CaF}_2:70\% \text{SrF}_2:0.8\% \text{NdF}_3$ (L-centers) (b) and $5\text{NaF}-9\text{YF}_3:1\% \text{NdF}_3$ (c) crystals.

and results of Judd-Ofelt analysis were used to calculate cross section for fluorescence emission according to Fuchtbauer-Ladenburg equation:

$$\sigma_{\text{em}}(\lambda) = \frac{\lambda^5}{8\pi c n^2} \frac{I(\lambda)}{\int \lambda I(\lambda) d\lambda} A ({}^4F_{3/2} \rightarrow {}^4I_{13/2}) \quad (9)$$

Emission cross section spectra $\sigma_{\text{em}}(\lambda)$ for tetragonal symmetry L centers in $\text{SrF}_2:0.8\% \text{NdF}_3$ and $\text{CaF}_2:70\% \text{SrF}_2:0.8\% \text{NdF}_3$ crystals, and for $5\text{NaF}-9\text{YF}_3: \text{NdF}_3$ crystal, which fluorescence is well matched to desired gain band, are shown in Fig.8. For comparison the emission cross section spectra for $\text{BaF}_2:0.3\% \text{NdF}_3$ crystal and clustered Nd^{3+} centers in $68.5\% \text{SrF}_2:30\% \text{LaF}_3:1.5\% \text{NdF}_3$ and $96.1\% \text{CaF}_2:2.3\% \text{YF}_3:1.6\% \text{NdF}_3$ crystals are shown in Fig. 9. As one can see from the spectra in Figs.8 and 9 the peak emission cross sections for these crystals except $\text{BaF}_2:0.3\% \text{NdF}_3$ are in the range of $(3-5) \times 10^{-21} \text{ cm}^2$. Extremely small spontaneous emission probability in $\text{BaF}_2:0.3\% \text{NdF}_3$ crystal gives rise to low emission cross section, which peak value reaches only $0.8 \times 10^{-21} \text{ cm}^2$.

Emission cross section spectra $\sigma_{\text{em}}(\lambda)$ and calculated radiative lifetimes τ_r can be used to predict maximum possible gain G_{\max} for studied media. The maximum possible gain at ${}^4F_{3/2}-{}^4I_{13/2}$ transition is proportional to product of emission cross section $\sigma_{\text{em}}(\lambda)$ and radiative lifetime τ_r , since it realizes for vanishing ESA losses (i.e. $\sigma_{\text{esa}}=0$) and zero nonradiative relaxation from ${}^4F_{3/2}$ metastable level (i.e. $\tau_{\text{meas}}=\tau_r$). To compare the gain properties of some of the studied crystals the right axis of the spectra in Figs. 8 and 9 is rescaled in units of $\sigma_{\text{em}}(\lambda)\tau_r$ product. The $\sigma_{\text{em}}(\lambda)\tau_r$ data for 1.28-1.32 μm spectral band are summarized also in Table 4. The highest values of $\sigma_{\text{em}}(\lambda)\tau_r = (5-6) \times 10^{-24} \text{ cm}^2 \text{s}$ are realized for emission peaks of tetragonal symmetry Nd^{3+} centers in SrF_2 crystal and $\text{CaF}_2:70\% \text{SrF}_2$ solid solution. Due to long radiative lifetime in $\text{BaF}_2:0.3\% \text{NdF}_3$ crystal the $\sigma_{\text{em}}(\lambda)\tau_r$ product in 1.28-1.32 μm range is higher than in

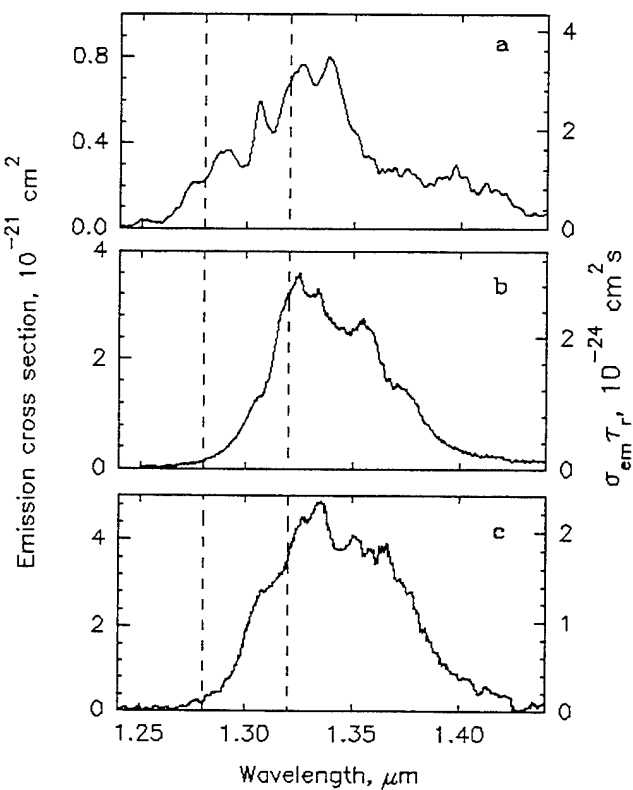


Fig. 9. Stimulated emission cross section spectra $\sigma_{\text{em}}(\lambda)$ and maximum possible gain $G_{\max}(\lambda) \sim \sigma_{\text{em}}(\lambda)\tau_r$ of $\text{BaF}_2:0.3\% \text{NdF}_3$ (a), $68.5\% \text{SrF}_2:30\% \text{LaF}_3:1.5\% \text{NdF}_3$ (b) and $96.1\% \text{CaF}_2:2.3\% \text{YF}_3:1.6\% \text{NdF}_3$ (c) crystals.

$5\text{NaF}-9\text{YF}_3:\text{NdF}_3$, $68.5\%\text{SrF}_2-30\%\text{LaF}_3:1.5\%\text{NdF}_3$ and $96.1\%\text{CaF}_2-2.3\%\text{YF}_3:1.6\%\text{NdF}_3$ crystals. But the problem for $\text{BaF}_2:0.3\%\text{NdF}_3$ crystal is low $S_{\text{em}}/S_{\text{esa}}$ ratio.

4.3. Laser oscillation spectra

Gain properties of studied fluoride crystals were established during the laser experiments. The pump source was free-running alexandrite laser with $100\ \mu\text{s}$ pulse duration and $30\ \text{mJ}/\text{pulse}$ output energy. Wavelength of alexandrite laser was tuned in the range of $740-755\ \text{nm}$ by means of intracavity birefringent filter. Laser oscillation of Nd^{3+} doped fluoride crystals was excited in the $50\ \text{mm}$ long hemispherical cavity, composed of dielectric mirrors with reflectivities as high as 99.3% in the $1.28-1.40\ \mu\text{m}$ band. Crystal rods with polished end faces were $5-10\ \text{mm}$ in diameter and $20-40\ \text{mm}$ long. The length of a crystal providing $70-80\%$ absorption of pump energy was used. The crystal was placed close to flat mirror through which focused pump beam was delivered. Transmittance of the flat mirror at pump wavelengths was 90% . The focusing of $4\ \text{mm}$ diameter pump beam was performed by the spherical lens with $120\ \text{mm}$ focal length placed at $120\ \text{mm}$ distance from the surface of flat mirror. Laser light transmitted through the concave mirror was focused on the slit of 0.5-m monochromator. The diffuse neutral filter was placed before the monochromator slit. The laser oscillation or fluorescence spectra were detected using Ge-photodiode and box-car integrator.

Laser oscillation at ${}^4\text{F}_{3/2}-{}^4\text{I}_{13/2}$ transition of Nd^{3+} ions was obtained for the $99.2\%\text{SrF}_2:0.8\%\text{NdF}_3$ crystal, and $68.5\%\text{SrF}_2-30\%\text{LaF}_3:1.5\%\text{NdF}_3$ and $49\%\text{SrF}_2-49\%\text{CaF}_2:2\%\text{NdF}_3$ solid solutions.

Laser oscillation spectrum of $68.5\%\text{SrF}_2-30\%\text{LaF}_3:1.5\%\text{NdF}_3$ crystal at $748\ \text{nm}$ pump wavelength is shown in Fig. 10. Corresponding emission cross section spectrum is presented in Fig. 9,b. Simultaneous laser oscillation was obtained at $1324\ \text{nm}$, $1332\ \text{nm}$ and $1356\ \text{nm}$ lines. The strongest $1324\ \text{nm}$ line corresponds to the wavelength of fluorescence peak. Laser oscillation spectrum of the $68.5\%\text{SrF}_2-30\%\text{LaF}_3:1.5\%\text{NdF}_3$ crystal was practically independent on pump wavelength.

Laser oscillation spectrum for the $49\%\text{SrF}_2-49\%\text{CaF}_2:2\%\text{NdF}_3$ crystal at $752\ \text{nm}$ pumping is shown in Fig. 11. Due to high content of NdF_3 the rhombic symmetry clustered centers predominate in this crystal. Therefore only long wavelength oscillation of clustered centers was obtained independently on pump wavelength. The $49\%\text{SrF}_2:49\%\text{CaF}_2:2\%\text{NdF}_3$ crystal laser oscillated in the $1330-1335\ \text{nm}$ band at the peak of fluorescence spectrum, that is shown in Fig. 6 (spectrum 5).

Lasing of both tetragonal single-ion and rhombic clustered Nd^{3+} optical centers was realized in the $99.2\%\text{SrF}_2:0.8\%\text{NdF}_3$ crystal for different pump wavelengths. Position of pump wavelengths relatively absorption band of $99.2\%\text{SrF}_2:0.8\%\text{NdF}_3$ crystal and two different laser oscillation spectra are shown in Fig. 12. Laser oscillation of L centers was obtained at $743\ \text{nm}$ pump wavelength (Fig. 12 b). Four laser lines at $1298\ \text{nm}$, $1308\ \text{nm}$, $1316\ \text{nm}$ and

Table 4. Values of product of stimulated emission cross section and radiative lifetime, $\sigma_{\text{em}}(\lambda)\tau_r$, in wavelength range $\lambda=1280-1320\ \text{nm}$ for a number of studied fluoride crystals.

Composition, mol. %	λ , nm	$\sigma_{\text{em}}\tau_r$, $10^{-24}\ \text{cm}^2\text{s}$
99.2% SrF ₂ :0.8% NdF ₃ (L-centers)	1280	0.35
	1298*	5.45
	1308*	5.59
	1316*	4.70
	1320	3.46
CaF ₂ -70% SrF ₂ :0.8% NdF ₃ (L-centers)	1280	0.81
	1301*	5.10
	1310*	6.24
	1320	3.48
5NaF-9YF ₃ :1% NdF ₃	1280	0.28
	1307*	2.85
	1320	2.37
99.7% BaF ₂ :0.3% NdF ₃	1280	0.99
	1320	2.96
SrF ₂ -30% LaF ₃ :1.5% NdF ₃	1280	0.13
	1320	1.87
CaF ₂ -2.3% YF ₃ :1.6% NdF ₃	1280	0.13
	1320	2.40

* values correspond to wavelengths of local peaks

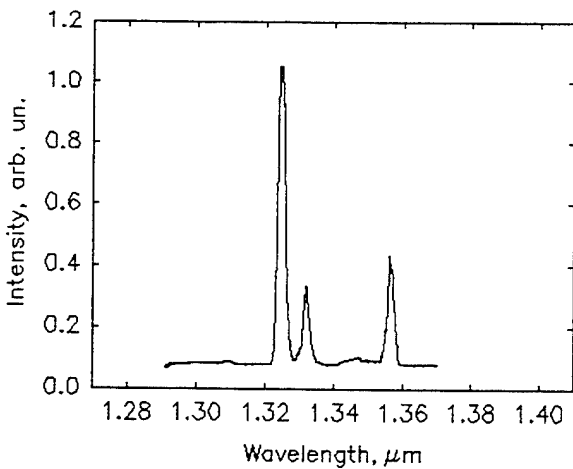


Fig. 10. Laser oscillation spectrum of 68.5%SrF₂-30%LaF₃:1.5%NdF₃ crystal.

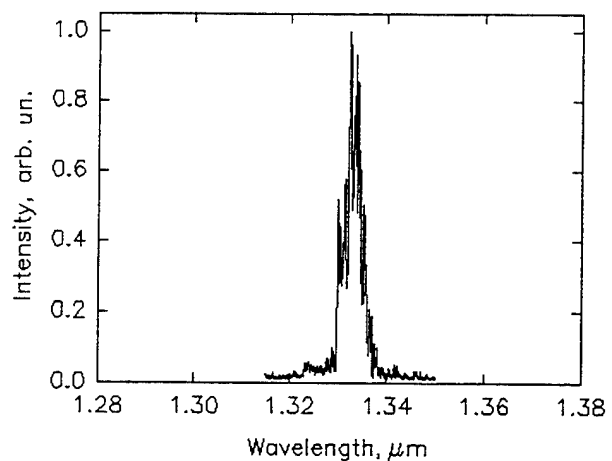


Fig. 11. Laser oscillation spectrum of 49%SrF₂-49%CaF₂:2%NdF₃ crystal.

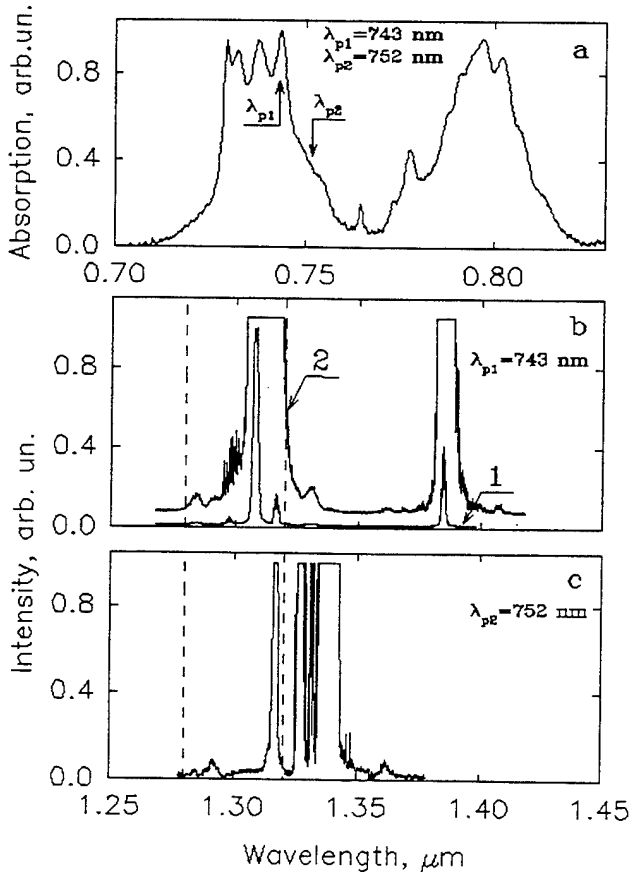


Fig. 12. Different pump wavelengths $\lambda_{p1}=743 \text{ nm}$ and $\lambda_{p2}=752 \text{ nm}$ relatively absorption band of 99.2%SrF₂:0.8%NdF₃ crystal (a) and laser oscillation spectra of L-centers at $\lambda_{p1}=743 \text{ nm}$ (spectrum 2 was recorded with 1.5 times wider slit compared to spectrum 1) (b) and clustered centers at $\lambda_{p2}=752 \text{ nm}$ (c).

1384 nm wavelengths oscillated simultaneously. These laser lines correspond to fluorescence line peaks of L centers, which stimulated emission cross section spectrum is shown in Fig.8,a. If the stimulated emission cross sections of short wavelength peaks is related as 0.97:1:0.84, the same relationship between intensities of laser lines is equal to 0.05:1:0.17. Low intensity of shortest wavelength laser line at 1298 nm may be due to increased ESA losses at this wavelength. In case of 752 nm pumping the long wavelength lasing of clustered centers occurred (Fig.12 c). Corresponding fluorescence spectrum of the crystal is shown in Fig.6 (spectrum 4). Oscillation of clustered centers was obtained at four lines simultaneously: 1317 nm, 1327 nm, 1332 nm, and 1338 nm wavelengths. The most intensive laser lines at 1327 nm and 1338 nm correspond to positions of fluorescence peaks of clustered centers.

CONCLUSIONS

A number of Nd³⁺ doped fluoride crystals with disordered structure have been studied by means of conventional optical spectroscopy and site selective spectroscopy in order to identify material that can serve as gain medium in 1.3 μm telecommunication window. The following families of disordered fluoride crystals doped with Nd³⁺ ions were grown and studied: a) fluorite type structure MeF₂ crystals (Me=Ca, Sr, Ba, Cd) and solid solution CaF₂-SrF₂, b) yttrifluorite type structure MeF₂-RF₃ solid solutions (Me=Ca, Sr, Ba, and R=Y, La), c) tysonite type structure RF₃-SrF₂ solid solutions (R=La,Ce), and d) cubic crystal of 5NaF-9YF₃.

To predict gain properties of the crystals the Judd-Ofelt analysis for intensities of Nd³⁺ ion optical transitions was carried out on the basis of measured absorption spectra.

The set of Ω_2 , Ω_4 , and Ω_6 intensity parameters have been found for all the studied crystals. Using these data line strength S_{em} of $^4F_{3/2}-^4I_{13/2}$ gain transition, and line strength S_{esa} of $^4F_{3/2}-^4G_{7/2}$ excited state absorption transition were calculated. The ratio of emission and ESA line strengths S_{em}/S_{esa} was found to be 3.6-5.3 in CaF_2 , SrF_2 , CdF_2 crystals and CaF_2-SrF_2 solid solutions, 3.3-4.4 in CaF_2-YF_3 , SrF_2-LaF_3 and BaF_2-LaF_3 solid solutions, 3.13 in $5NaF-9YF_3$ crystal, 2.6-3.7 in LaF_3-SrF_2 and CeF_3-SrF_2 solid solutions, and the least value of 1.79 in BaF_2 crystal.

Measured fluorescence spectra of studied crystals at $^4F_{3/2}-^4I_{13/2}$ transition have substantial inhomogeneously broadened shapes. The nature of the drastic inhomogeneous splitting and broadening of the spectra is the multisite character of Nd^{3+} optical centers that is due to the heterovalent substitution in the crystals. Shortest wavelength fluorescence with maxima in the $1.29-1.32\mu m$ band was observed for tetragonal symmetry Nd^{3+} centers in SrF_2 , CaF_2 and CaF_2-SrF_2 solid solutions, and for $5NaF-9YF_3$ crystal. For the clustered Nd^{3+} centers in alkaline earth fluorides and for other studied crystals the fluorescence peaks are at wavelengths grater than $1.32\mu m$, but all the crystals have substantial short wavelength fluorescence side bands in desired $1.28-1.32\mu m$ spectral range.

Judd-Ofelt calculation results and measured fluorescence spectra were used to predict product of stimulated emission cross section $\sigma_{em}(\lambda)$ and radiative lifetime τ_r , that is a characteristic of maximum attainable gain. The highest values of $\sigma_{em}(\lambda)\tau_r=(5-6)\times 10^{-24}\text{ cm}^2\text{s}$ in $1.3\mu m$ telecommunication window was found to realize for emission peaks of single-ion tetragonal symmetry Nd^{3+} centers in SrF_2 crystal and SrF_2-CaF_2 solid solutions. For other crystals the product $\sigma_{em}(\lambda)\tau_r$ is varying from about $0.2\times 10^{-24}\text{ cm}^2\text{s}$ to about $3\times 10^{-24}\text{ cm}^2\text{s}$ in the range of $1.28-1.32\mu m$.

Laser oscillation at $^4F_{3/2}-^4I_{13/2}$ transition have been realized for $SrF_2:0.8\%NdF_3$, $48\%CaF_2-48\%SrF_2:2\%NdF_3$, and $68.5\%SrF_2-30\%LaF_3:1.5\%NdF_3$ crystals. Obtained laser oscillation spectra confirm that positive gain occurs for these crystals at least at fluorescence maxima. The short wavelength lasing of tetragonal symmetry Nd^{3+} centers and long wavelength laser oscillation of rhombic clustered centers was realized in $SrF_2:0.8\%NdF_3$ crystal for different pump wavelengths. Laser oscillation of tetragonal symmetry centers occurred at 1298 nm, 1308 nm, and 1316 nm wavelengths.

Taking into account the requirements to gain medium of $1.3\mu m$ optical amplifier, we conclude that the most promising crystals investigated are cubic disordered fluorides based on $(50-70)\%SrF_2-(50-30)\%CaF_2$ solid solutions containing Nd^{3+} optical centers having local tetragonal symmetry. These crystals combine most of the necessary properties, since they possess (a) small value of ESA line strength ($S_{em}/S_{esa}\sim 4$), (b) high metastable level lifetime ($1.2-1.3\text{ ms}$), (c) high gain value ($\sigma_{em}(\lambda)\tau_r=(5-6)\times 10^{-24}\text{ cm}^2\text{s}$), and (d) proper fluorescence peak at about 1310 nm wavelength and comparatively wide fluorescence band with about 20 nm FWHM.

ACKNOWLEDGEMENTS

This work was supported in part by AT&T Bell Labs.

REFERENCES

1. A.A.Kaminskii, *Laser crystals*, Springer-Verlag, New-York, vol.14, 1981.
2. W.J.Miniscalco, L.J.Andrews, B.A.Thompson, R.S.Quimby, L.J.B.Vacha, and M.G.Drexhage, "1.3 μm fluoride fiber laser", *Electron. Lett.*, vol.24, pp.28-29, 1988.
3. Y.Miyajima, T.Komukai, and T.Sugawa, "1.31-1.36 μm optical amplification in Nd^{3+} -doped fluorzirconate fiber", *Electron. Lett.*, vol.26, pp.194-195, 1990.
4. M.L.Dakss, and W.J.Miniscalco, "Fundamental limits on Nd^{3+} doped fiber amplifier performance at 1.3 μm ", *IEEE Photon. Technol. Lett.*, vol.2, pp.650-652, 1990.
5. E.F.Kustov, G.A.Bondurkin, A.N.Murav'ev, and V.P.Orlovskii, "Electronic spectra of rare earth element compounds", Nauka, Moscow, 1981 (in Russian).
6. M.V.Eremin, A.A.Kornienko, "The Superposition Model in Crystal Field Theory", *Phys. Stat. Solidi B*, vol. 79, pp.775-785, 1977.
7. B.R.Judd, "Optical absorption intensities of rare earth ions", *Phys. Rev.*, vol.127, pp.750-761, 1962.
8. G.S.Ofelt, "Intensities of crystal spectra of rare-earth ions", *J. Chem. Phys.*, vol.37, pp.511-520, 1962.

9. W.T.Carnall, P.R.Fields, and K.Rajnak, "Electronic energy levels in the trivalent lanthanide aquo ions. I. Pr^{3+} , Nd^{3+} , Pm^{3+} , Sm^{3+} , Dy^{3+} , Ho^{3+} , Er^{3+} , and Tm^{3+} ", *J. Chem. Phys.*, vol.49, pp.4424-4442, 1968.
10. W.F.Krupke, "Induced-emission cross section in neodymium laser glasses", *IEEE J. Quant. Electron.*, vol. 10, pp.450-457, 1974.
11. A.A.Kaminskii, and B.M.Antipenko, "Multilevel operating schemes of crystalline lasers", Nauka, Moscow, 1989 (in Russian).
12. V.V.Osiko, Yu.K.Voron'ko, A.A.Sobol, "Spectroscopic investigation of defect structures and Structural transformations in ionic crystals", in *Crystals 10, Growth, Properties, and Applications*, ed. H.C.Freyherdt, Berlin, Springer-Verlag, pp.37-86, 1984.
13. O.A.Alimov, T.T.Basiev, S.B.Mirov, "Spectral and relaxation characteristics of local electron states of impurities in structurally disordered matrices", in *Selective Laser Spectroscopy of Activated Crystals and Glasses*, ed. V.V.Osiko, N.Y., Nova Science Publishers, Proceedings of the Institute of General Physics Academy of Sciences of the USSR, vol.9, pp.1-66.
14. C.G. Andeen, J.J. Fontanella, M.C. Wintersgill, P.J. Welcher, R.J. Kimble, Jr., and G.E. Matthews, Jr., "Clustering in rear-earth-doped alkaline earth fluorides", *J. Phys. C*, vol.14, pp.3557-3575, 1981.
15. J. Corish, C.R.A. Catlow, P.W.M.Jacobs, and S.H.Ong, "Defect aggregation in anion-excess fluorides. Dopant monomers and dimers", *Phys. Rev. B*, vol. 25, pp. 6425-6438, 1982.
16. A. Tesar, J. Campbell, M. Weber, C. Weinzapfel, "Optical properties and laser parameters of Nd^{3+} -doped fluoride glasses", *Optical Materials*, vol. 1, pp. 217-234, 1992.
17. J.L. Adam, N. Rigout, E. Denoue, F. Smektala, J. Lucas, "Optical properties of Ba-In-Ga-based fluoride glasses for amplification at $1.3 \mu\text{m}$ ", *Proc. SPIE*, vol. 1581, pp. 155-165, 1991.

The Cr⁴⁺: Y₃ Al₅ O₁₂ laser crystal in tunable sub-picosecond laser under strong aberration

U.U.Broslavez, A.A.Fomichov, V.D.Lokhnygin, O.O.Silichev.

Moscow Institute of Physics and Technology, Laser Center,
Institutsky per., 9, Moscow reg., Dolgoprudny, 141700,
Russia.

ABSTRACT

In this paper we report our investigation of mode-locked and Q-switched regime in Cr⁴⁺:Y₃Al₅O₁₂ laser with synchronous pumping by Nd:YAG laser. We have obtained mode-locked generation of tunable radiation in the range from 1,350 to 1,500 nm. In our investigation we have found position in stability area where the laser operates in mode-locked or Q-switch regime. In the edge of stability we observe Q-switch regime of laser operation with rectangular output pulses. We have analyzed the properties of main optical elements in our laser systems to find out to which extend these elements could be considered as temporal Gaussian systems, and simulated on a computer the ultra-short pulse evolution in the laser resonator for the investigation of the structure of the transformation phase space. The presence of aberration being a source of the ultra-short pulses distortion could drastically complicate a phenomenon.

1. EXPERIMENTAL PROCEDURE AND DISCUSSION

Recently, several new techniques for passive mode locking have been developed. By Kerr lens mode locking (KLM) femtosecond pulses from Ti:sapphire (Ti:Al₂O₃) lasers have been generated. These mode-locking techniques have been successfully applied to other new laser media. There has been a great interest in Cr⁴⁺ doped materials as sources for the near infrared spectral region.¹ These are such materials as Cr:Forsterite, Cr⁴⁺:YAG, Cr⁴⁺:Y₂SiO₅. Cr⁴⁺:YAG has been demonstrated as an active media for a cw laser at room temperature, with a Nd:YAG laser pumping.

In this paper we report our investigation of mode-locked and Q-switch regime in Cr⁴⁺:YAG laser with synchronous pumping. Our experiments have been performed using Nd:YAG laser "Argo" for synchronous pumping Cr⁴⁺:Y₃Al₅O₁₂ laser. We have obtained mode-locked generation of tunable radiation in the range from 1,350 to 1,500 nm under synchronous pumping this active element by YAG laser. There was a generation without Kerr nonlinear mechanism with pulse duration in ps range and repetition rate of 320 MHz. Such laser can generate radiation with a wavelength in the region where there is a small dispersion spreading in quartz, that allows to investigate a system in a simplified manner for obtaining short impulses.^{2,3}

The Cr⁴⁺:YAG - laser has consisted of Cr⁴⁺:YAG rod placed into the astigmatically compensated, four mirror cavity Fig.1. The Cr⁴⁺:YAG laser rod was cut at Brewster's angle with the length of the crystal 20 mm. The 'end' and 'output' mirrors are flat and the concave mirrors are of 10 cm curvature. All mirrors were high reflection for obtaining mode - locked generation, but when generation was

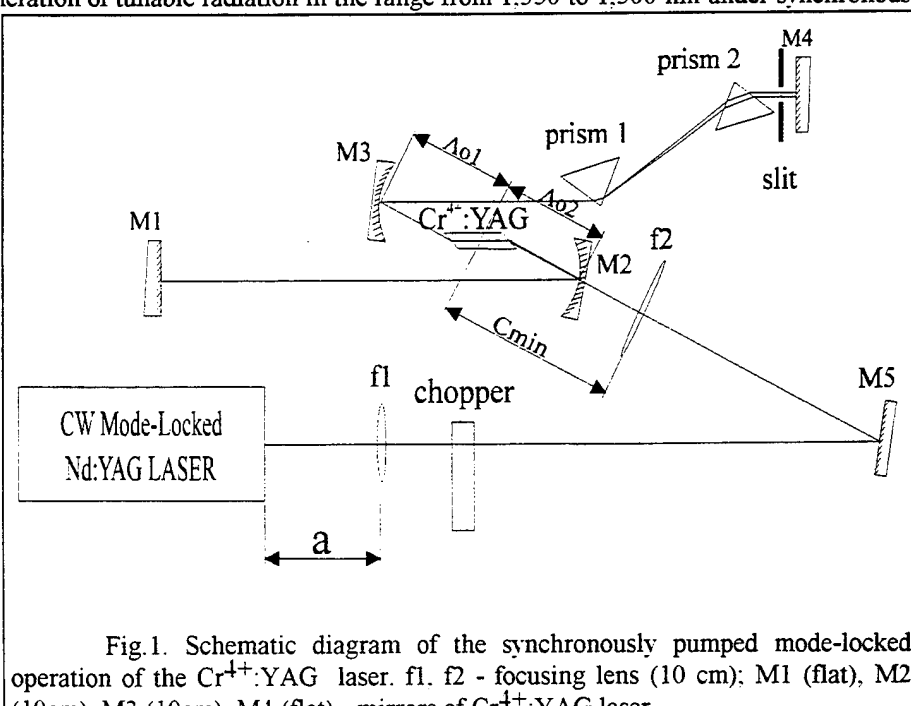


Fig.1. Schematic diagram of the synchronously pumped mode-locked operation of the Cr⁴⁺:YAG laser. f1, f2 - focusing lens (10 cm); M1 (flat), M2 (10cm), M3 (10cm), M4 (flat) - mirrors of Cr⁴⁺:YAG laser .

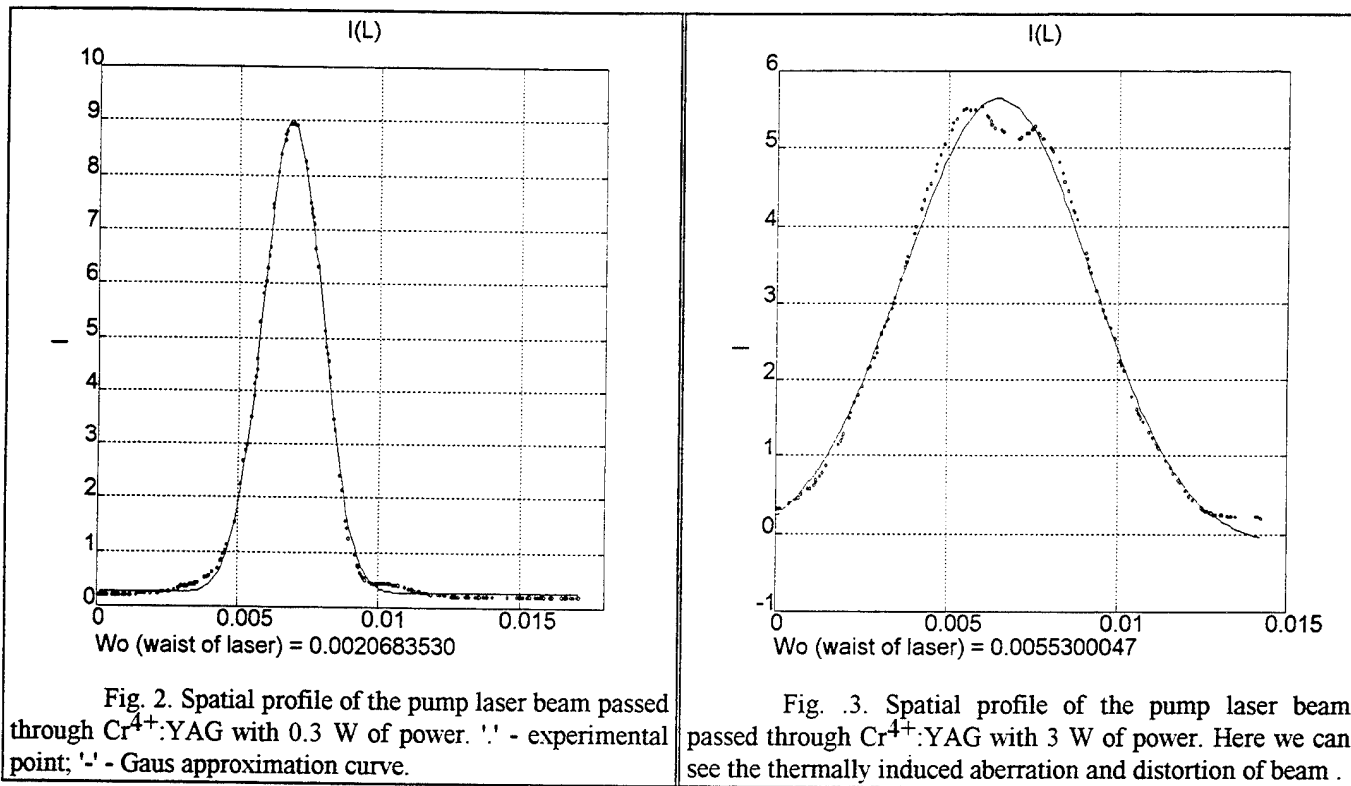


Fig. 2. Spatial profile of the pump laser beam passed through $\text{Cr}^{4+}\text{-YAG}$ with 0.3 W of power. '—' - experimental point; '---' - Gaus approximation curve.

Fig. 3. Spatial profile of the pump laser beam passed through $\text{Cr}^{4+}\text{-YAG}$ with 3 W of power. Here we can see the thermally induced aberration and distortion of beam .

achieved the output mirror was changed by 0.5% coupler. The pump beam was focused in 40 mkm waist. The repetition rate of pump laser pulses is 160 MHz. In our experiments, wavelength tuning has been accomplished by translating a variable aperture slit perpendicular to the cavity axis between prism 2 and mirror M4. The SiO_2 Brewster prisms allow a convenient control of the cavity dispersion.

For obtaining high efficiency of generation in CW regime the $\text{Cr}^{4+}\text{-YAG}$ rod is cooled down to 0 C. That give the increase in efficiency about 30%. The $\text{Cr}^{4+}\text{-YAG}$ also possess some disadvantages - strong thermal lens and radiation depolarization. Special efforts have to be made to investigate its influence on the mechanism of generation in this material and the possibility of obtaining stable generation. By computer simulation and measuring in laser active medium we have obtained that thermal lens in $\text{Cr}^{4+}\text{-YAG}$ has about 7 mm focus length and the characteristic rise time is about 4 ms.

We have calculated the mode size in relation to the thermal lens, mode size changes that are due to the Kerr lens, and the modulation of the round trip transmission by the thermal lens aberration aperture. As the pump power

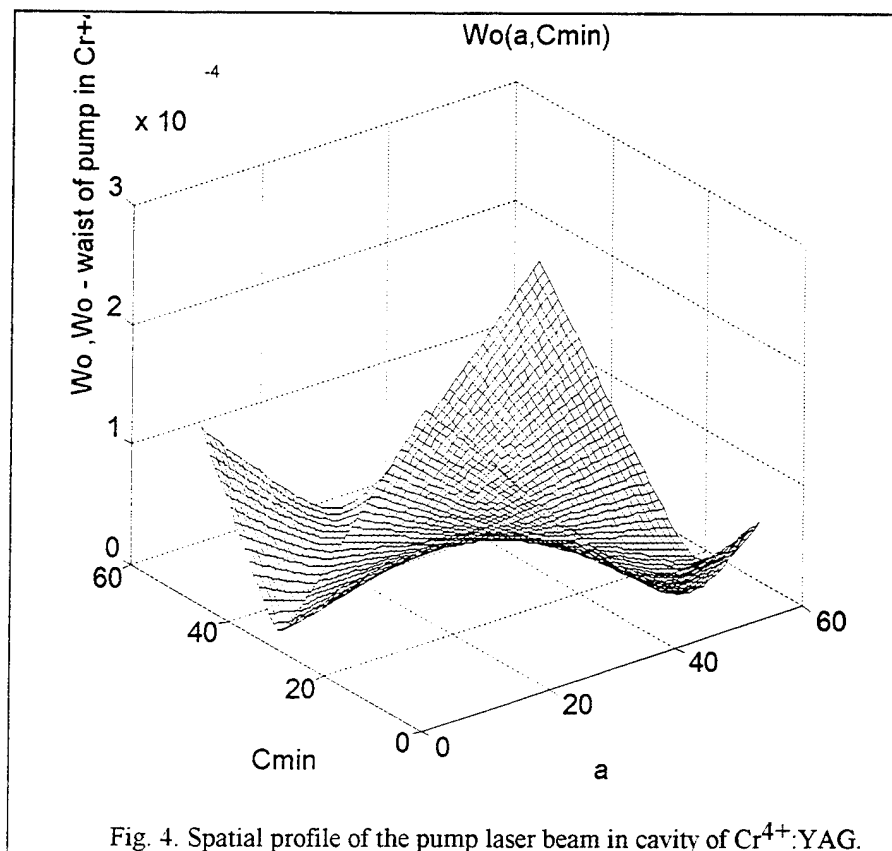


Fig. 4. Spatial profile of the pump laser beam in cavity of $\text{Cr}^{4+}\text{-YAG}$.

changes, the cavity must be adjusted to compensate for the changing thermal lens. Aberration thermal lens plays a significant aperturing role in our laser. It causes mode - size dependent diffractive losses. For adjusting the size of aberration aperture, we calculate the mode size of pump beam depending on distance between focusing lens and pump laser waist position.

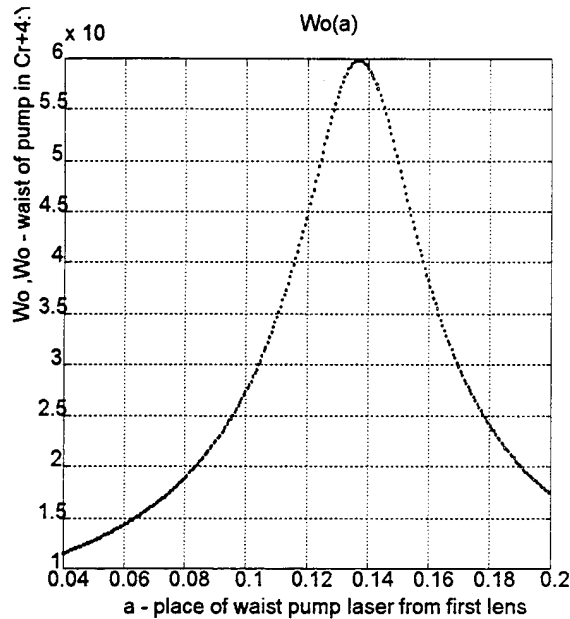


Fig. 5. Dependence of pump beam waist in Cr⁴⁺:YAG on length 'a'.

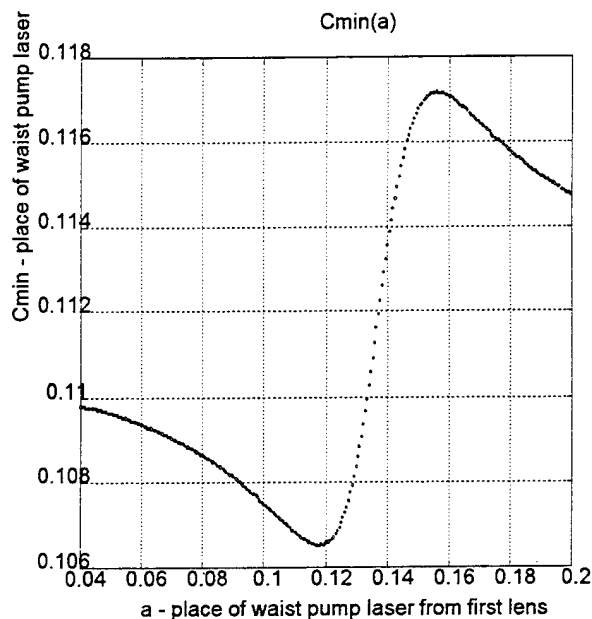


Fig. 6. Dependence of the location of the pump beam waist in Cr⁴⁺:YAG on length 'a'.

In our investigation we have found position in stability area where the laser operates in mode - locked or Q-switch regime. The laser has threshold for mode - locked regime near 7 W. Synchronous mode locking is obtained by matching the

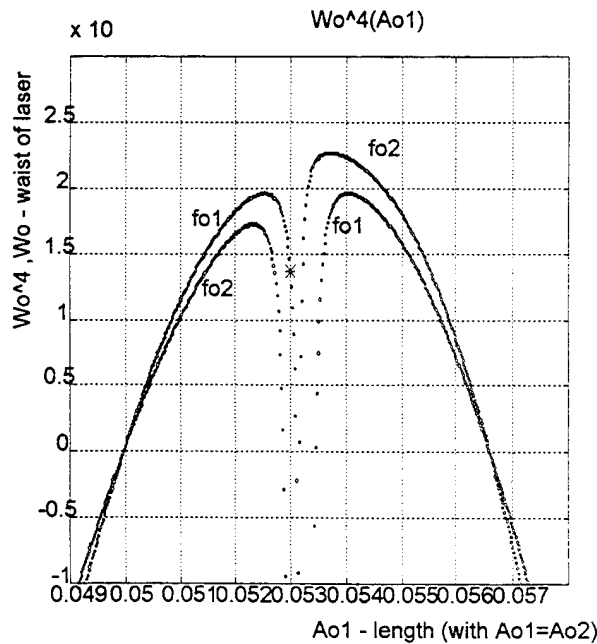


Fig. 7. Region of laser stable operation for lens with fo₁ = 10 m and with fo₂ = 0.02 m.

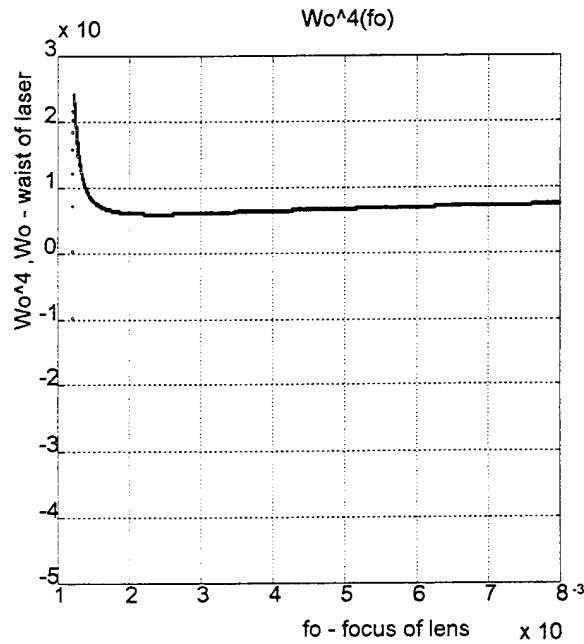


Fig. 8. Waist of laser versus lens focus in active media

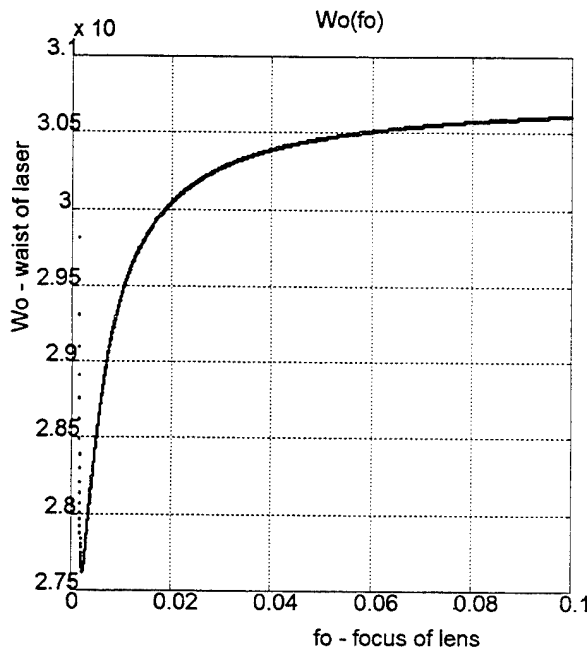


Fig. 9. Waist of laser versus lens focus in active media

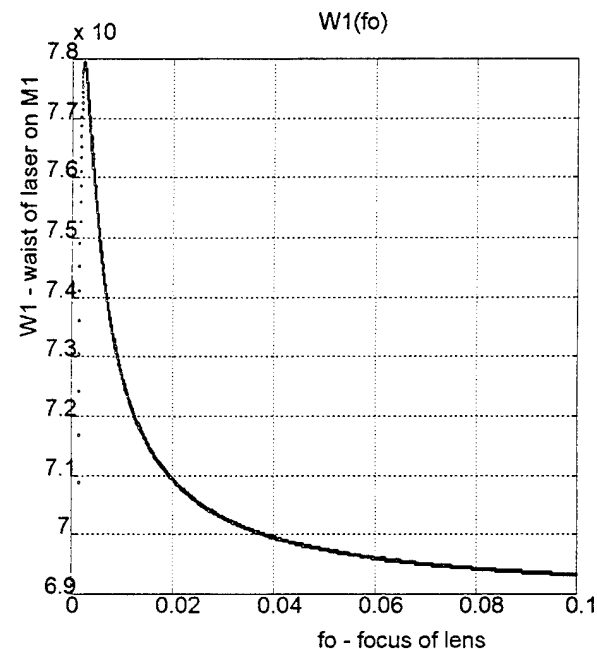


Fig. 10. Waist of laser on 'end' mirror versus lens focus in active media

cavity length to that of the pump laser. With cavity being properly adjusted and waist size matching with size of pump waist pulses at repetition rate 320 MHz were observed. The generation pulses are not very stable because of the pump power is not very stable (stability better than 1% in average pump power is required).

In the edge of stability we observe Q-switch regime operation of laser with rectangular output pulses. The pulse repetition rate is about 1000 Hz, with shape near meander. Such pulses generation may be explained by the delay in thermal lens formation, when the absorption pump power depends on the level of generated radiation power.

For obtaining optimal modulation, when the lens in active media changes, we calculate area where waist of laser depends on value of lens focus in the cavity. The optimal region of operation the laser for obtaining mode-locked is in the edge of stability. This curve shows that for obtaining KLM in this laser the pump power instability must be better than 1%, as the Kerr lens is more weaker than the thermal lens. The Kerr lens has been calculated under a parabolic approximation of the index variation and effective focal length about 10 cm has been obtained for 10 W average intracavity power and 1 ps pulse duration.

Our calculations of the mode size show that the Kerr lens induces no significant beam radius reduction when the cavity is close to the middle of its stability regime that required for minimized influence of strong thermal lens. That is why we introduce the Kerr-shift mode locking mechanism.⁶ By using a wavelength-dependent intracavity aperture, self-phase modulation (self-phase modulation is achieved through Kerr effect) in active medium produces a self-wavelength shift to reduce intracavity losses. We moved a knife edge (fig.11) into the laser beam, which shifted the center wavelength of the optical spectrum toward longer wavelength and changed the average output power. Power pulses enhance self-phase modulation and increase frequency shift; thus the laser can reduce its losses more effectively.

The Kerr-shift mode locking mechanism allowed us to reduce the influence of strong thermal lens in Cr⁴⁺:YAG and increase the index of modulation.

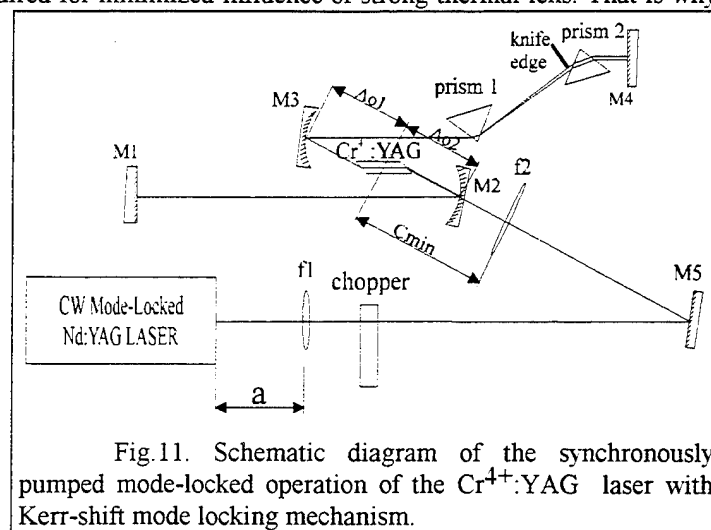


Fig.11. Schematic diagram of the synchronously pumped mode-locked operation of the Cr⁴⁺:YAG laser with Kerr-shift mode locking mechanism.

Carried out preliminary investigations of the Cr⁴⁺:YAG material have shown very good prospects for using it in the master oscillator to obtain Kerr mode-locked. For this reason we have investigated theoretically and by computer simulation the formation of ultra-short pulses in our laser system using the idea of the description of ultra-short coherent optical pulses as temporal Gaussian beams analogous to complex Ermit-Gaussian beams^{4,5} with displaced center which are well known in the spatial beam optics. We have analyzed the properties of main optical elements in our laser systems to find out to which extend these elements could be considered as temporal Gaussian systems and designed a program for a computer simulation of the ultra-short pulses evolution in the laser resonator for the investigation of the structure of the transformation phase space. The presence of aberration being a source of the ultra-short pulses distortion could drastically complicate a phenomenon. The transformation of temporal complex parameters for elements in our laser system is shown in of 1/(chirp) and 1/(duration pulse) axes and the transformation of spatial complex parameters is shown in of 1/(waist)² and 1/(R_{curvature}) axes. Energy of pulses depends of number cycles. On the fig.12-16 we have analyzed the laser system without Kerr lens feedback.

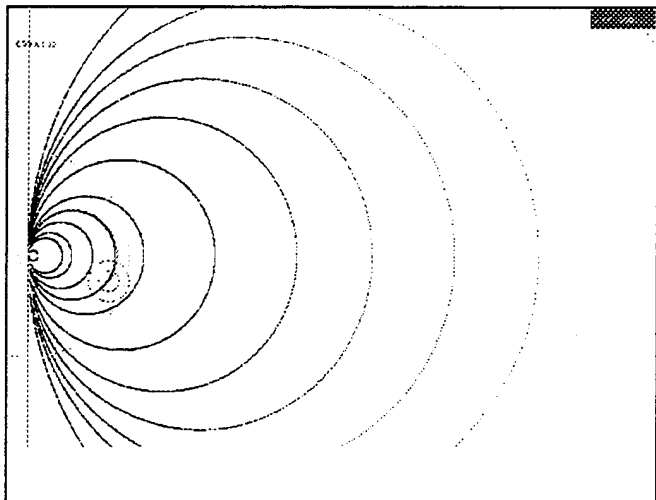


Fig. 12. The phase portrait of 'Chirp' and 'Duration' system with dispersion element.

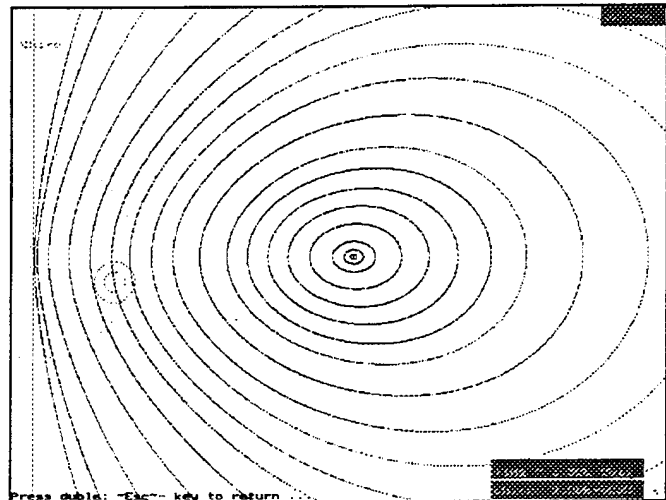


Fig. 13. The phase portrait of 'Chirp' and 'Duration' system with dispersion and Kerr modulation element.

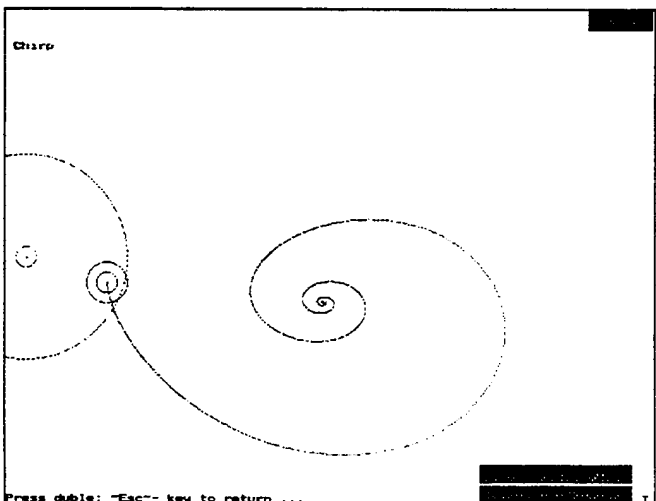


Fig. 14. The phase portrait of 'Chirp' and 'Duration' system with dispersion, Kerr modulation, and frequency filter element with small bandwidth.

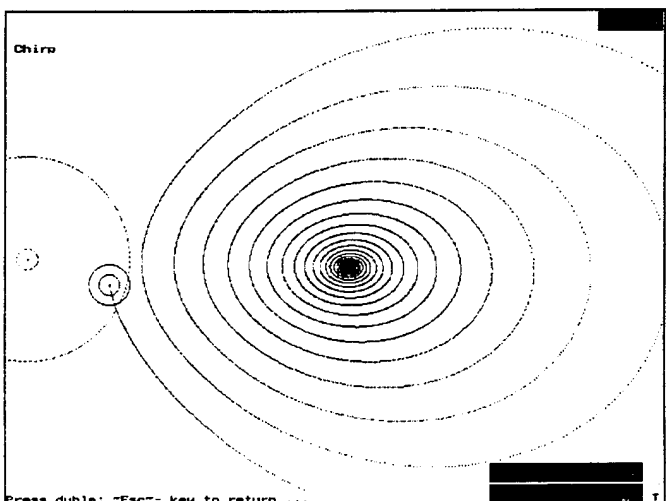


Fig. 15. The phase portrait of 'Chirp' and 'Duration' system with dispersion, Kerr modulation, and frequency filter element with large bandwidth.

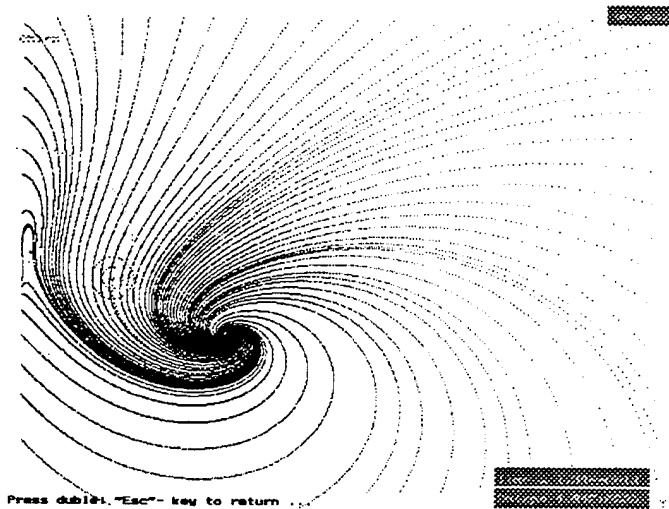


Fig.16. The phase portrait of 'Chirp' and 'Duration' system with dispersion, Kerr modulation, and frequency filter element with other parameters.

On the fig.17-21 we have analyzed the laser system with Kerr lens feedback in the phase trajectory of five-dimensional space. The investigation of the structure of the phase space transformation shows that the transformation possess an asymptotically stable stationary point and more complicated structure. Our calculations show that the sign of dispersion is very important for formation of phase portrait in our laser system

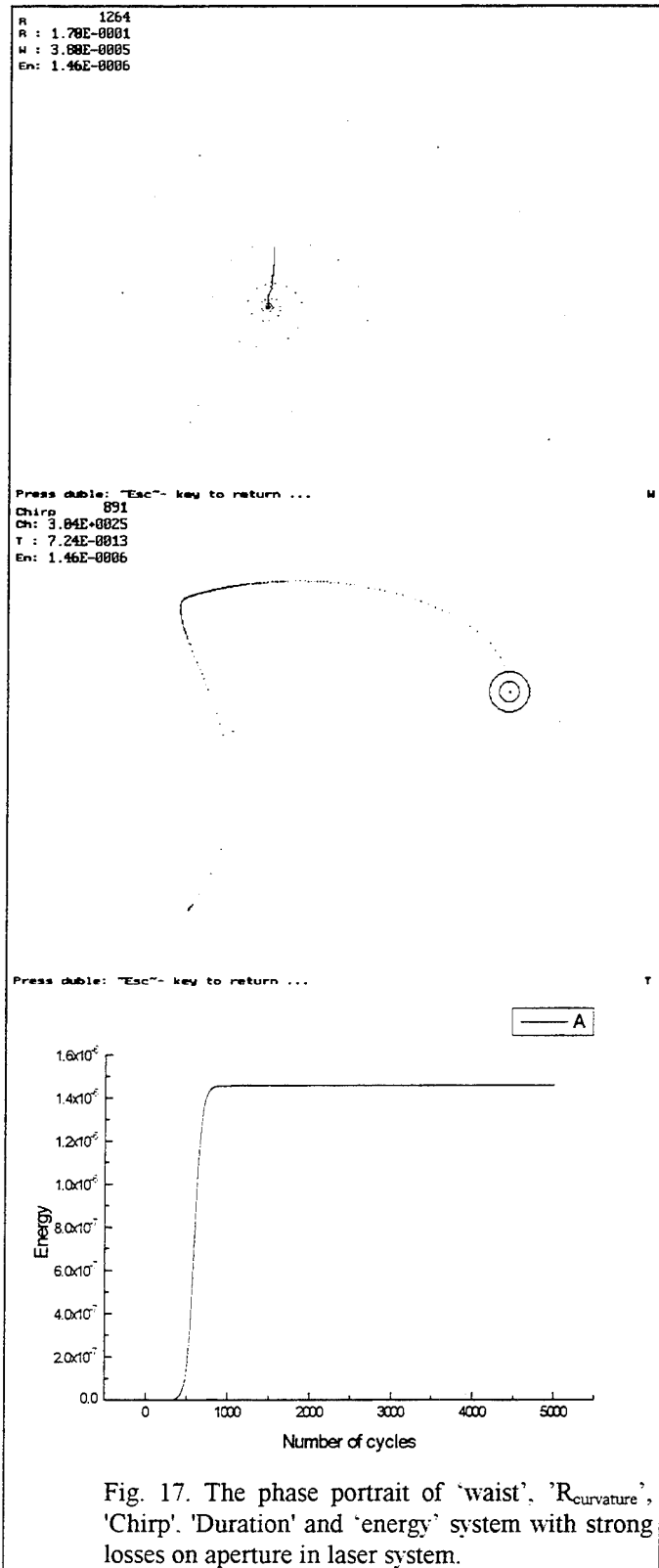


Fig. 17. The phase portrait of 'waist', ' $R_{\text{curvature}}$ ', 'Chirp', 'Duration' and 'energy' system with strong losses on aperture in laser system.

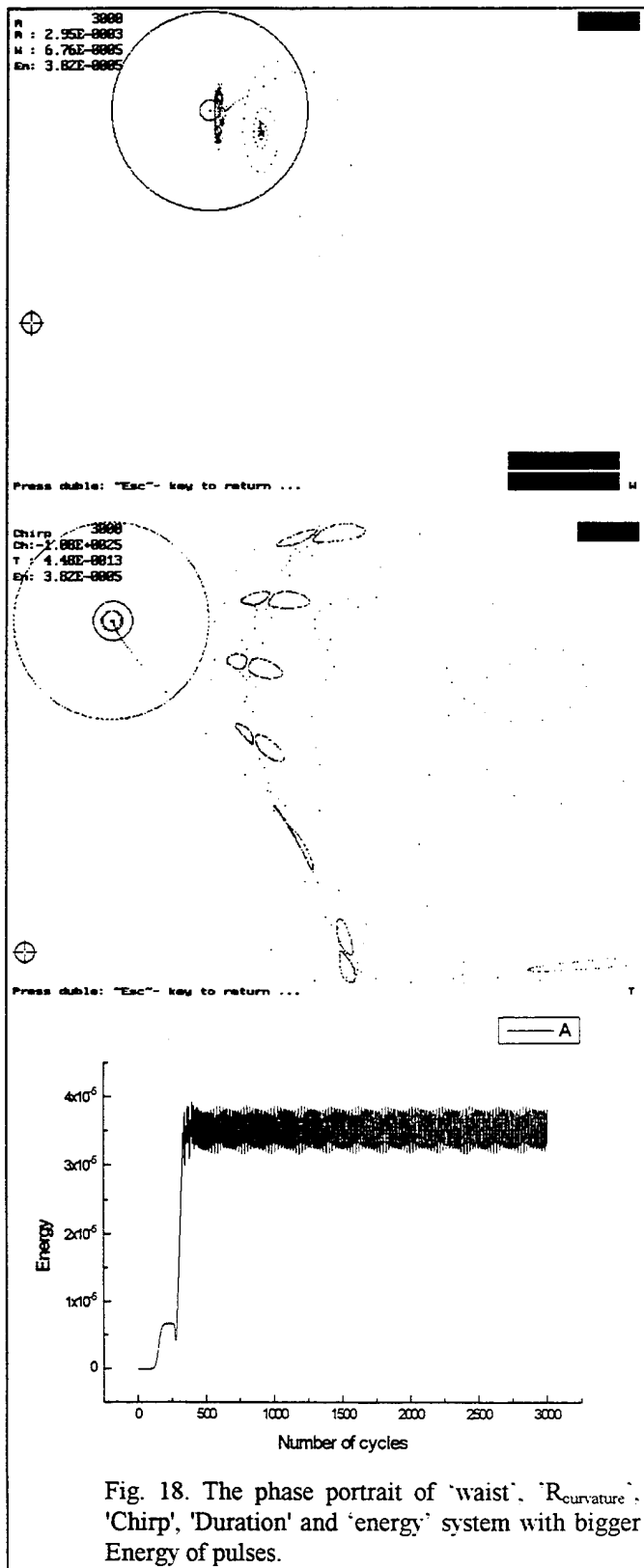


Fig. 18. The phase portrait of 'waist', ' $R_{\text{curvature}}$ ', 'Chirp', 'Duration' and 'energy' system with bigger Energy of pulses.

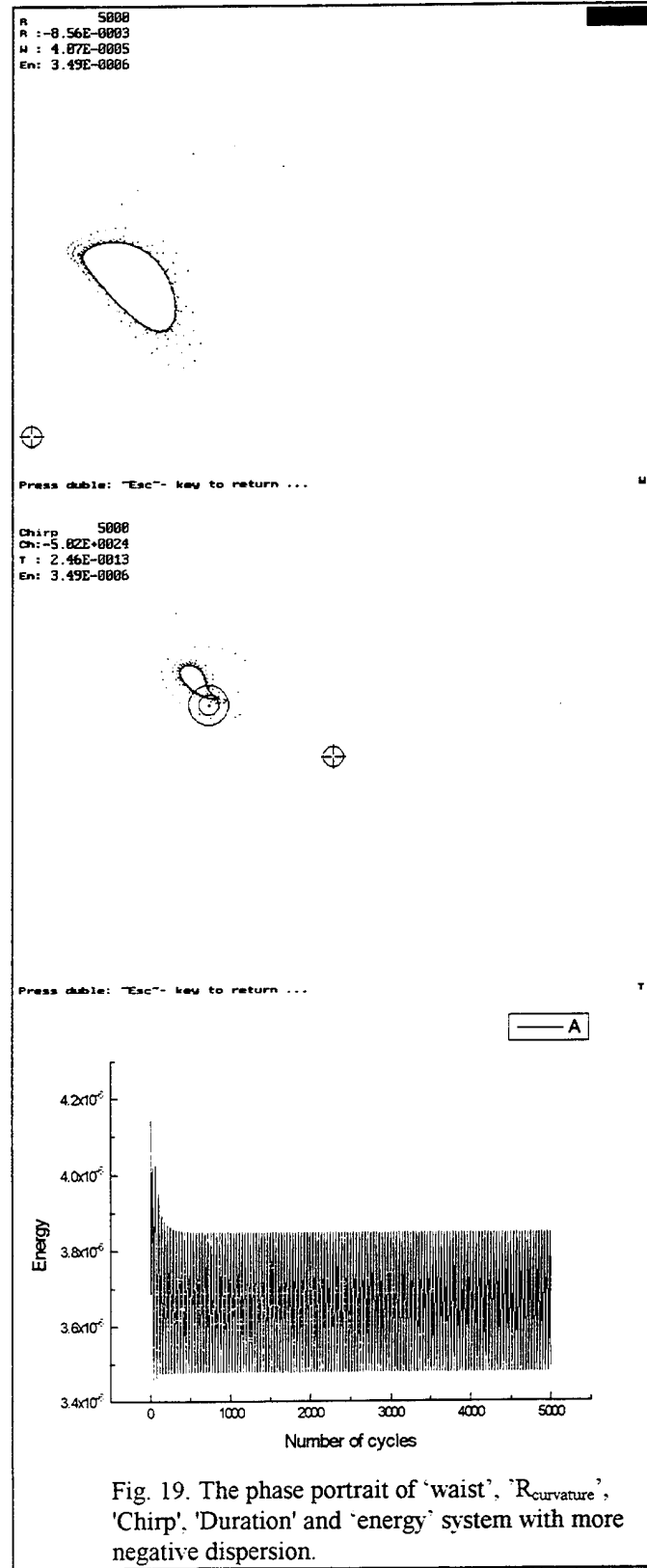


Fig. 19. The phase portrait of 'waist', ' $R_{\text{curvature}}$ ', 'Chirp', 'Duration' and 'energy' system with more negative dispersion.

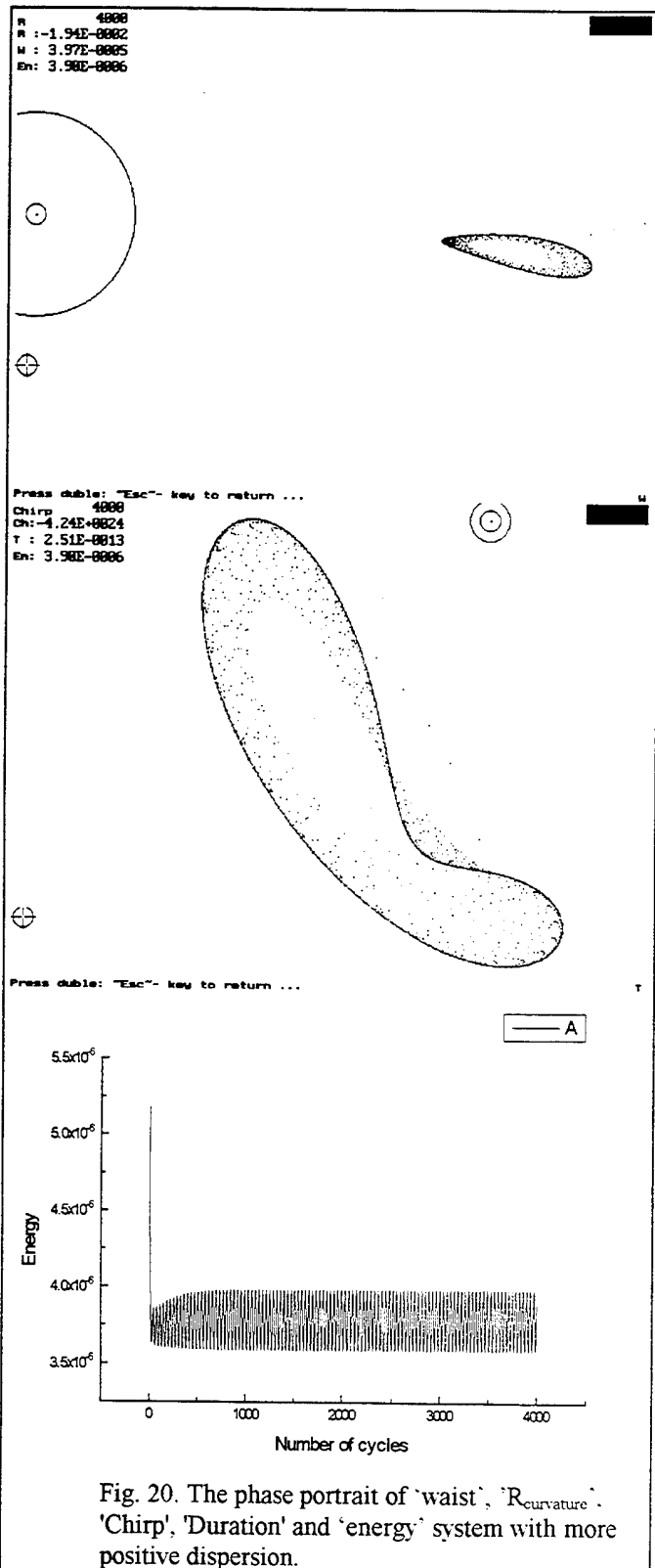


Fig. 20. The phase portrait of 'waist', ' $R_{\text{curvature}}$ ', 'Chirp', 'Duration' and 'energy' system with more positive dispersion.

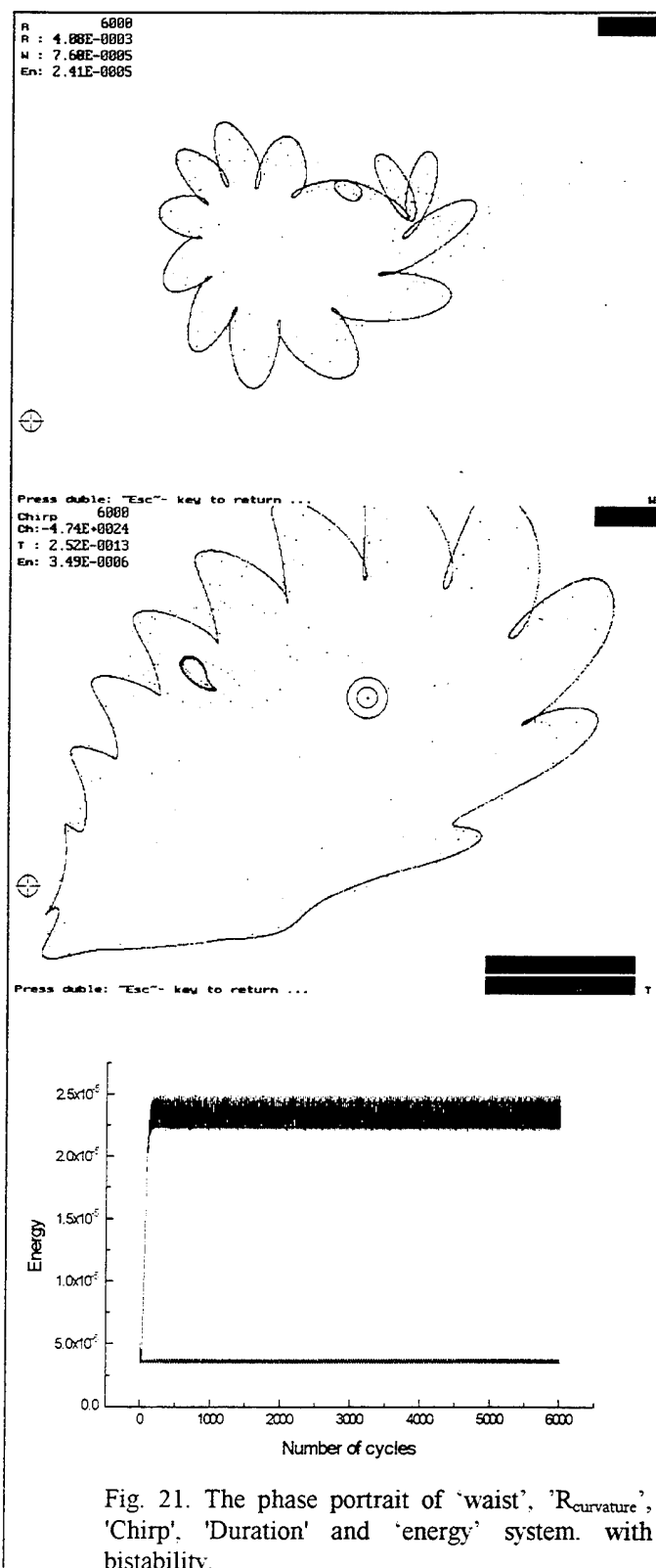


Fig. 21. The phase portrait of 'waist', ' $R_{\text{curvature}}$ ', 'Chirp', 'Duration' and 'energy' system. with bistability.

2. CONCLUSION

We have taken into account the self-action effects for ultra-short optical pulses propagation in intracavity second harmonic generation. The computer simulation have shown the presence of asymptotically stable stationary point in behavior of temporal Gaussian beam similar spatial mode structure in the resonators, when the temporal mode does not change passing through all dispersion element in laser.

In conclusion, we have demonstrated Cr⁴⁺:YAG laser operation in mode-locked and Q-switch regime on the edge of stability region.

3. REFERENCES

1. Howard Nathel, Alphan Sennaroglu, Clifford R. Pollock, Cornell Univ, "Mode-locked, Cr⁺⁴ solid-state lasers.", Lawrence Livermore National Laboratory.
2. S.A. Akhmanov, V.A. Visloukh, A.S. Chirkin "**OPTICS OF FEMTOSECOND LASER PULSES**", Moscow, (1988).
3. T. Brabec, P.F. Curley, S.M.J. Kelly, E. Wintner, ..., "Ultrashort Pulses from Ti:Sapphire Lasers", UPS'93, (1993).
4. Oscar E. Martinez and Juian L. A. Chilla "Self-mode-locking of Ti:sapphire lasers: matrix formalism", OPTICS LETTERS, Vol. 17, No. 17, (1992).
5. Silichev O.O, Fomichev A.A., "Matrix Method of Femto-Second Laser Pulses Propagation Calculation", UPS'93, (1993).
6. U.Keller, T.H.Chiu, J.F.Ferguson, "Femtosecond Kerr-shift-mode-locked Nd:glass laser that uses an A-FPSA as a continuous starting mechanism" At&T Bell Laboratories QELS'93.

Up-conversion: factors in absolute efficiency

W. A. Sibley

The University of Alabama at Birmingham, Birmingham, AL 35294

ABSTRACT

Infrared-to-visible up-conversion processes can be very important in device applications. Numerous investigators have evaluated various materials for device potential. The limiting factor is the efficiency of the process. The efficiency depends on many factors with the most important ones being energy transfer and multiphonon transitions.

Keywords: up-conversion process, multiphonon transition rates, multiphonon emission rate

1. INTRODUCTION

Infrared-to-visible up-conversion processes can be very important in device applications as noted by A. F. Milton in 1972.¹ Auzel² and Wright³ have provided excellent reviews of the process and numerous investigators have evaluated various materials for device potential. The limiting factor is the efficiency of the process. The efficiency depends on many factors with the most important ones being energy transfer and multiphonon transitions.

2. MULTIPHONON TRANSITION RATES

Weber⁴ developed a method of comparing the multiphonon transition rates in different materials that is very useful. Reisfeld and her collaborators⁵⁻⁷ as well as others⁸ have used this method to evaluate efficient host materials for the up-conversion process. Figure 1, in which the energy gap between adjacent energy levels for an active ion is plotted versus the multiphonon emission rate, illustrates the results from these experiments. Note that the fluoride glass ZBLA, a fluorozirconate glass containing Zirconium, Barium, Lanthanum, and Aluminum and a Bar-

ium/Thorium Fluoride glass appear to provide the best choice for low multiphonon losses. In fact, fluoride materials appear to be the best possible host for up-conversion device opportunities; although significant efficiencies have been observed in other materials as well. More information on the figure is provided in reference 8.

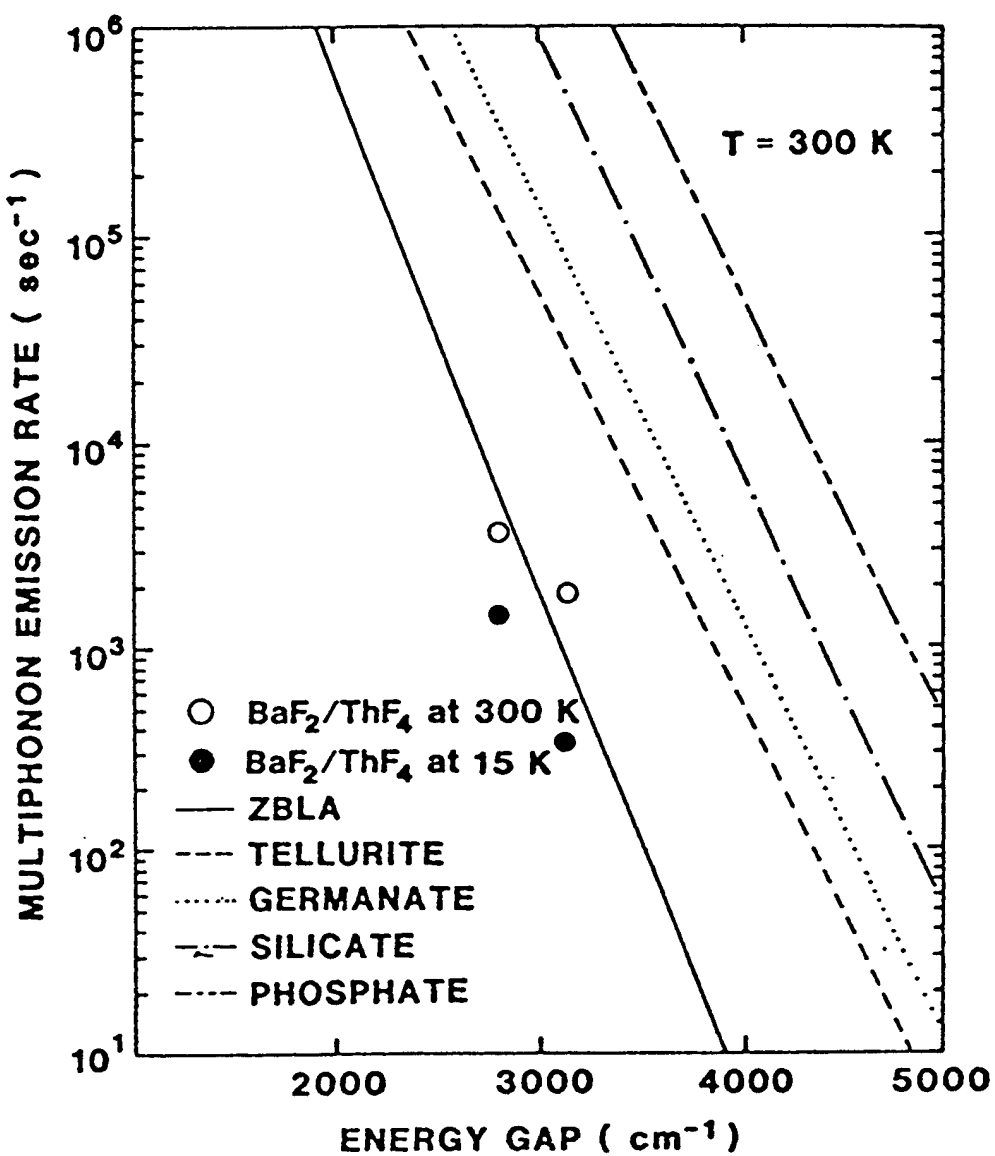


Fig. 1. Multiphonon emission rates of Er^{3+} in various materials at 300K as a function of the energy gap to the next lower level.⁸

3. ENERGY TRANSFER

Since energy transfer plays such a key role in up-conversion and laser processes, it is important to determine ways to estimate the effectiveness of the various transitions for system such as Erbium and Thulium. The relevant energy level diagrams of $Er - Er$ and $Er - Tm$ system are shown below with the appropriate rate equations. It should be noted that the transition rates between levels, W_{ij} , are very sensitive to the multiphonon processes mentioned earlier, and can dominate the process when effective phonon energies are high.

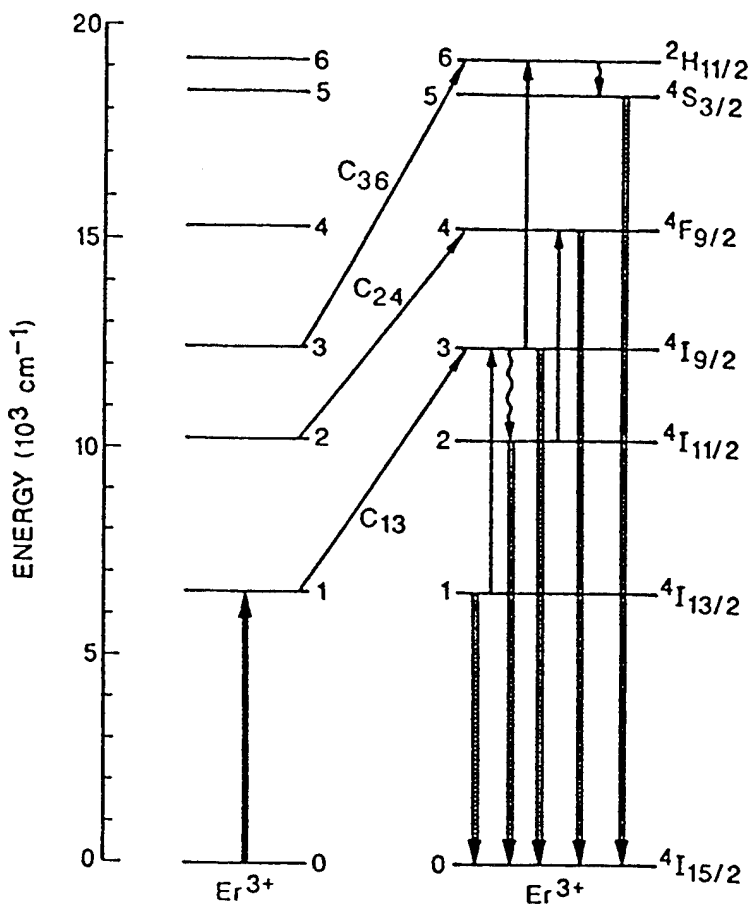


Fig. 2. Energy-level diagram of Er^{3+} ion and up-conversion excitation scheme.

$$\dot{n}_1 = \sigma_{01}\Phi N_E - \sigma_{13}\Phi n_1 - C_{13}n_1^2 + W_{21}n_2 - \tau_1^{-1}n_1 = 0, \quad (1)$$

$$\dot{n}_2 = W_{32}n_3 - W_{21}n_2 - \sigma_{24}\Phi n_2 - C_{24}n_2n_1 - \tau_2^{-1}n_2 = 0, \quad (2)$$

$$\dot{n}_3 = W_{43}n_4 - W_{32}n_3 + \sigma_{13}\Phi n_1 - \sigma_{36}\Phi n_3 + C_{13}n_1^2 - C_{36}n_3n_1 - \tau_3^{-1}n_3 = 0, \quad (3)$$

$$\dot{n}_4 = W_{54}n_5 - W_{43}n_4 + \sigma_{24}\Phi n_2 + C_{24}n_2n_1 - \tau_4^{-1}n_4 = 0, \quad (4)$$

$$\dot{n}_5 = W_{65}n_6 - W_{54}n_5 - \tau_5^{-1}n_5 = 0, \quad (5)$$

$$\dot{n}_6 = \sigma_{36}\Phi n_3 + C_{36}n_3n_1 - W_{65}n_6 = 0, \quad (6)$$

where n_i is the electron population in level i , W_{ij} represent the transition rates between levels i and j , τ_i terms are the radiative lifetimes, Φ is the incident flux, σ_{ij} are absorption cross sections between levels i and j , and N_E is the population of Er^{3+} ions in the ground state. The rate equations neglect stimulated emission as well as the relatively weak four-photon up-conversion to the $^2H_{9/2}$ level (producing the blue 410nm emission). Transitions from the $^4S_{3/2}$ and $^4F_{9/2}$ levels to the $^4I_{11/2}$ and $^4I_{13/2}$ levels are likewise neglected.

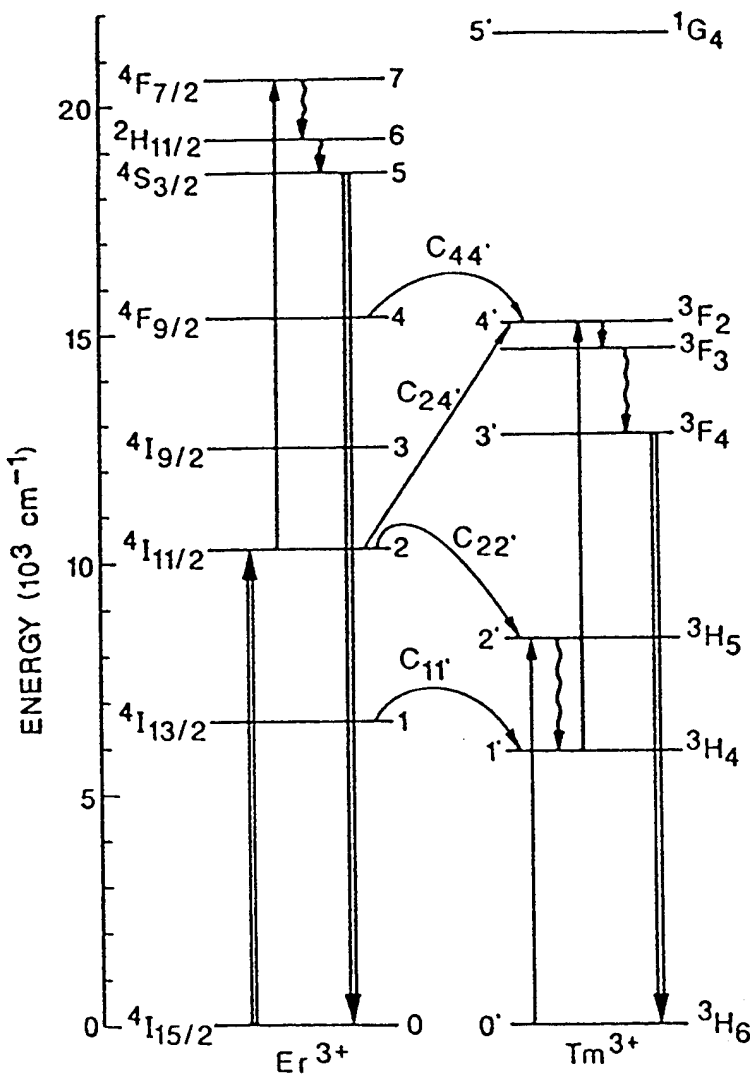


Fig. 3. Models for up-conversion in Er^{3+} - Tm^{3+} system.
Energy levels and transitions of the Er^{3+} - Tm^{3+} ions which are not considered important in the up-conversion process have been omitted.

$$\dot{n}_1 = W_{21}n_2 - C_{11'}n_1N_T + C_{1'1}n_{1'}N_E - \tau_1^{-1}n_1 = 0, \quad (7)$$

$$\dot{n}_2 = \sigma_{02}\Phi N_E - C_{22'}n_2N_T - \tau_2^{-1}n_2 - W_{21}n_2 = 0, \quad (8)$$

$$\dot{n}_{1'} = C_{11'}n_1N_T - C_{1'1}n_{1'}N_E + W_{2'1}n_{2'} - \tau_{1'}^{-1}n_1 = 0, \quad (9)$$

$$\dot{n}_{2'} = C_{22'}n_2N_T - W_{2'1}n_{2'} = 0. \quad (10)$$

The energy transfer products, $C_{ij}n_i n_j$, are related to the applicable Forster-Dexter model of dipole-dipole interactions portrayed below:

$$P_{da} = \frac{1}{\tau_d} \frac{3\hbar^4 c^4}{4\pi n^4} \frac{Q_a}{R_{da}^6} \int \frac{f_d(E)F_a(E)}{E^4} dE. \quad (11)$$

The energy transfer product $C_{ij}n_i$ is also related to R the critical interaction distant, such that when $R_{da} = R_0$, $P_{da}\tau_d = 1$, where P_{da} is the transition probability. In terms of R_0 , we can write

$$P_{da} = \frac{R_0^6}{\tau_d R_{da}^6}. \quad (12)$$

So that

$$R_0 = \frac{3\hbar^4 c^4 Q_a}{4\pi n^4} \int \frac{f_d(E)F_a(E)}{E^4} dE. \quad (13)$$

Moreover, since the transfer coefficients in the rate equations can be related to P , it is possible to use the relationships developed by Inokuti and Hirayama⁹ to find that

$$C_{ij}N_a = \frac{N_a R_0^6}{(N_a + N_d)\tau_d R_{da}^6}. \quad (14)$$

If a distance R_{NN} is chosen so there is a $1 \sim 1/e$ probability of finding a nearest neighbor, then for a random distribution

$$R_{NN} \approx \frac{0.62}{(N_a + N_d)^{1/3}}. \quad (15)$$

The combination of these last two equations leads to the expression

$$C_{ij}N_a \approx 17.6 N_a R_0^6 (N_a + N_d) / \tau_d, \quad (16)$$

from which a family of curves can be generated to provide an estimate for the magnitude of the energy transfer coefficients. This is depicted in Fig. 4 which is taken from the work of Yeh et al.¹⁰

From the information presented above and Fig. 4, it should be possible to "tailor make" glass or crystal combinations to provide the best chance of producing an effective up-conversion device. The work of Yeh et al^{8,10} and of Chen¹¹ provides an experimental check on this.

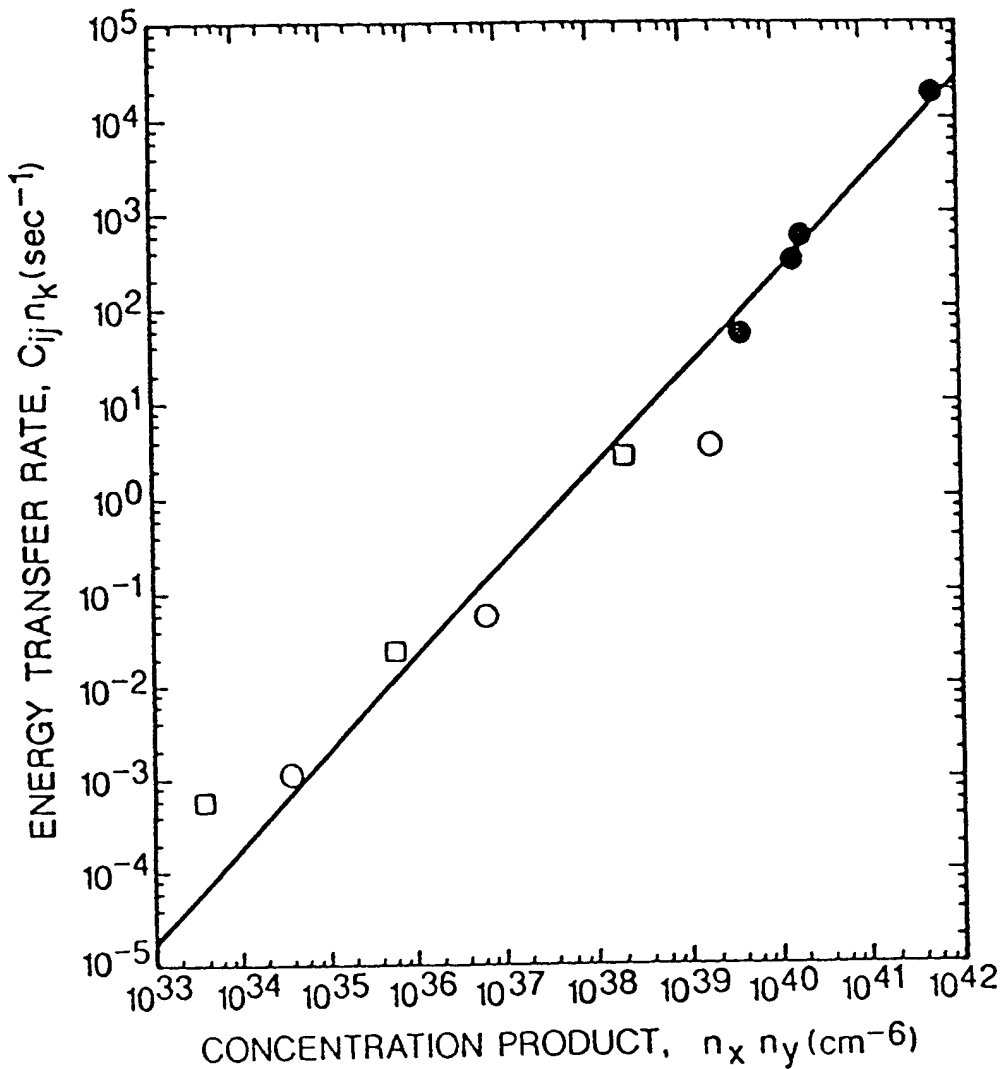


Fig. 4. Dependence of energy-transfer rate between the interacting levels on the concentration product.¹⁰

4. DISCUSSION

From the rate equations presented with Figs. 2 and 3 it is evident that a low phonon frequency host is the best material to promote up-conversion efficiency. The work of Yeh et al¹⁰ indicates that absolute efficiencies of around 10% can be obtained for the two photon up-conversion process in fluoride materials. The figures below are from Yeh's work and provide an idea of the overall efficiency that can be expected for two and three photon processes.

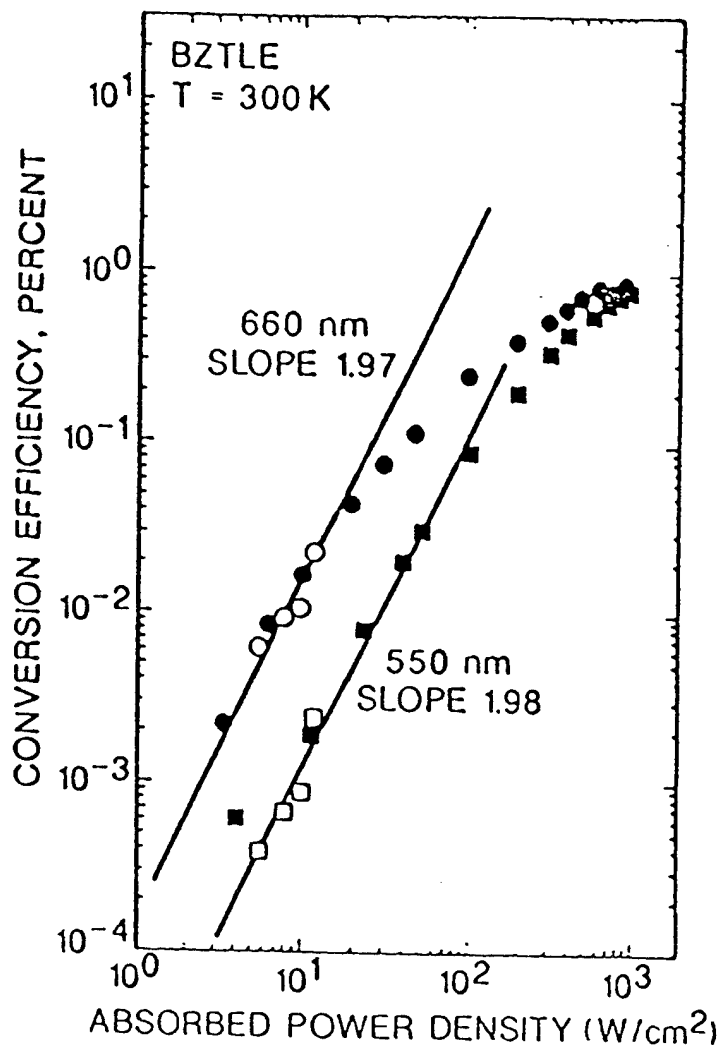


Fig. 5. Dependence of $Er^{3+} - 4S_{3/2}$ up-conversion efficiency(lower curve) and $4F_{9/2}$ up-conversion efficiency (upper curve) on the $1.5\mu m$ incident absorbed-light intensity. The closed-symbol data points were obtained by exciting the $1.5\mu m$ transition with the intense color-center laser, and the open data points, with the weaker diode laser.¹⁰

It is also clear that energy transfer plays a major role in most situations when the incident light intensity is less than about 200 Watts/cm². This implies that the distribution of the active ions in the host matrix and the overlap integral between the absorption and emission levels in the energy transfer equation are very important.

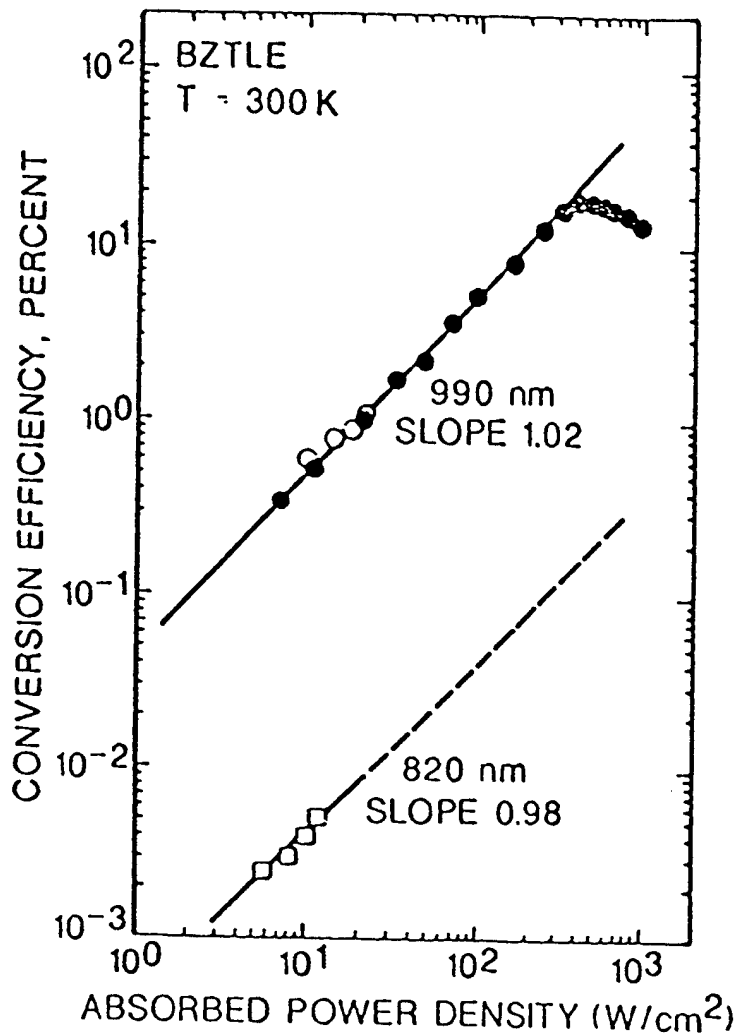


Fig. 6. Dependence of $Er^{3+} - ^4I_{11/2}$ up-conversion efficiency (upper curve) and $^4I_{9/2}$ up-conversion efficiency (lower curve) on the $1.5\mu m$ incident absorbed-light intensity. The closed-symbol data points were obtained by exciting the $1.5\mu m$ transition with the intense color-center laser, and the open data points, with the weaker diode laser.¹⁰

Since energy transfer has both a forward and backward reaction, as noted by Wright sometime ago,³ this overlap integral plays a special role. For like ions such as Erbium-Erbium transitions the overlap is large, but the backreaction is also high. When different ions are used, $Er - Tm$ for example, because the energy level for Tm^{3+} is below that of Er^{3+} , the backreaction is small, but so is the overlap integral. When the transitions are sharp this leads to less efficiency than when inhomogenous broadening of the levels is present as in the glass. This type behaviour can be seen from a comparison of energy transfer coefficients for $Er - Tm$ in glass and in $KCaF_3$. In $KCaF_3$, the Er^{3+} ions apparently enter easily so that large concentrations can be introduced, but there is evidently only one site symmetry which leads to very sharp line transitions. In the glass inhomogeneous broadening occurs which allows for a greater overlap integral and thus higher energy transfer coefficients. For example the $C_{11'}N_T$ term in the glass is $290s^{-1}$; whereas, for the crystal the same term is $16s^{-1}$. This suggests that crystals containing a number of site symmetries which perturb the various energy levels might be more efficient than crystals with only one impurity site symmetry. As noted the absolute efficiency for Er^{3+} ions in heavy metal fluoride glass has been measured by Yeh et al.¹⁰ Saturation of the efficiency, which is on the order of 1 – 10% for certain transitions, occurs around 300 Watts/cm². The work of Reiche et al¹² also shows blue-green up-conversion in fluoroindate glasses. As further work is done it will be interesting to compare the rate equations for high intensity excitation and for crystals versus glasses in these high intensity regions.

5. REFERENCES

1. A. F. Milton, Applied Optics, **11**, 2311, 1972.
2. F. E. Auzel, IEEE **61**, 758, 1973.
3. J. C. Wright, in Radiationless Processes in Molecules and Condensed Phases, Vol 15 of Topics in Applied Physics, edited by F. K. Fong, 239, Springer, N. Y. 1976.
4. M. J. Weber, Phys. Rev. **157**, 262, 1967; Phys. Rev. **B8**, 54, 1973.
5. R. Reisfeld, E. Greenberg, R. N. Brown, M. G. Drexhage and C. K. Jorgensen, Chem. Phys. Letters, **95**, 91, 1983.
6. R. Reisfeld, G. Katz, N. Spector, C. K. Jorgensen, C. Jacoboni, R. DePape, J. Solid State Chem. **41**, 253, 1982.
7. R. Reisfeld, G. Katz, C. Jacoboni, R. Depape, M. G. Drexhage, R. N. Brown and C. K. Jorgensen, J. Solid State Chem. **48**, 323, 1983.
8. D. C. Yeh, W. A. Sibley, M. Suscavage and M. G. Drexhage, J. Appl. Physics, **62**, 266, 1987.
9. M. Inokuti and F. Hirayama, J. Chem. Phys. **43**, 1978, 1965.
10. D. C. Yeh, W. A. Sibley, I. Schneider, R. S. Afzal and I. Affarwal. J. Appl. Phys. **69**, 1648, 1991.
11. C. Y. Chen, W. A. Sibley, D. C. Yeh and C. A. Hunt, J. Lum., **43**, 185, 1989.
12. R. Reiche, L. A. D. Nunes, C. C. Corvlko, Y. Messaddeg and M. A. Aegeerter, Solid State Commun., **85**, 773, 1993.

Optical properties of nonstoichiometric fluorite crystals doped with Nd³⁺ and Pr³⁺ in 1.3 μm spectral range.

M.Yu. Sharonov, B.K. Sevastyanov, Z.I.Zmurova, E.A. Krivandina, A.A. Bystrova, I.I. Buchinskaya, and B.P. Sobolev

Institute of Crystallography, Russian Academy of Science, Leninsky pr. 59, Moscow, Russia

ABSTRACT

Optical properties more than 120 multicomponent nonstoichiometric fluoride crystals $M^{+2}F_m^{-}R^{3+}F_n$ with CaF₂ structure doped with Nd³⁺ and Pr³⁺ were studied especially in 1.3 μm spectral range which is promising for operation in the second telecommunication window. The direct measurements of excited state absorption and single pass gain in 1.3 μm range have been carried out for Na_{0.4}Y_{0.6}F_{2.2} and Ca_{0.9}Y_{0.1}F_{2.1} crystals. The effective cross-sections and halfwidth of gain band have been determined ($\sigma_{max}=2.2\pm0.7 \cdot 10^{-21} \text{ cm}^2$, $\Delta=40 \text{ cm}^{-1}$ and $\sigma_{max}=4.5\pm0.9 \cdot 10^{-21} \text{ cm}^2$, $\Delta=60 \text{ cm}^{-1}$, respectively). The line's strengths in Ba_{1-x}Gd_xF_{2+x}:Pr crystals have been found to be raised in nonstoichiometric crystals in comparison with stoichiometric ones due to formation of another type of optical centers. The energy of destruction of these Pr³⁺ positions have been determined to be 280 cm⁻¹. The mean decay rate of Yb³⁺ is found to be proportional to multiplying of Yb³⁺ and Pr³⁺ concentrations in Yb³⁺ sensitized BaGdF:Yb,Pr and PbCdF:Yb,Pr crystals. The optimal concentrations of Yb and Pr and single pass gain coefficient have been calculated.

1. INTRODUCTION

Recently much attention was devoted to the investigation of active materials for amplification in the second telecommunication window (1.28 - 1.32 μm) used for the creation of optical amplifiers for fiber communication. The most promising ions are Nd³⁺ and Pr³⁺ ($^4F_{3/2}-^4I_{13/2}$ and $^1G_4-^3H_5$ transitions, respectively). The most promising matrices for the broadband amplification are the matrices with the great number of active centers with different crystal fields resulting in wide inhomogeneously broadened bands in the absorption and luminescence spectra. This inhomogeneity of the crystal field can be caused by partial disordering of structure.

Among the crystals with such feature of crystalline structure, there is the large family of nonstoichiometric phases with fluorite structure formed in double (and more complicated) MF_m-RF_n systems¹. They have a common formula $M_{1-x}R_xF_{m(1-x)+nx}$ and are characterized by a high concentrations of structural defects. The defects are caused by fluorine ions in interstitial sites, by the vacancies in the basic anion motive and by "sort" defects of cations disposed in equivalent cation positions. The concentration and the type of such defects are chosen in wide intervals, changing the ratio of crystal components and its elemental composition. The fluorite structure has high isomorphous capacity in respect to different cations, including rare earth elements.

Fluoride materials with CaF₂-type structure show low phonon energies and, consequently, low probability of nonradiative transitions between the closely situated energy levels. This fact is essential for the transitions from the 1G_4 level of Pr³⁺ ions (a quenching channel $^1G_4-^3F_3$).

In this paper were investigated the influence of the chemical composition with various structural defects on the spectroscopic properties and on the amplification bands in Nd-doped nonstoichiometric $M_{1-x}R_xF_{2+x}$ and $Na_{0.5-x}Y_{0.5+x}F_{2+2x}$ crystals with fluorite structure and the spectroscopic properties of Pr-doped (and sensitized by Yb³⁺) nonstoichiometric phases Ba_{1-x}R_xF_{2+x} (R = Ce, Gd), Ca_{1-x}La_xF_{2+x} and stoichiometric Pb_{0.67}Cd_{0.32}F₂ with fluorite structure characterized by the most low phonon energies and by different types of structural (anionic and cationic) defects.

2. MATERIALS

The nonstoichiometric fluorite crystals may be divided into two groups by the positions of interstitial F⁻ ions. In one of these groups F⁻ ions are displaced along a triple axis from the center of cubic void (1/2, 1/2, 1/2) to a 32-fold *f*-complex, in the other group they are displaced along a double axis to 48-fold *i*-complex of a space group Fm3m^{1,2}. These groups are essentially differed each other by the interatomic distances between the metal and implanted fluorine ion and by the symmetry of local environment of metal ion. The third type of structural defects is substitution of M²⁺ - ions by another divalent or trivalent cations. This substitution produces only "sort" - type defects in cationic sublattice and exists for all three groups of studied crystals.

The studied crystals were grown by Stockbarger-Bridgman technique using the crystal growth device constructed in the Institute of Crystallography. The graphite heaters and containers were used. A fluorizing atmosphere was created by pyrolysis of Teflon. The diameters of typical single crystals were ~10 mm, their lengths were up to 30 mm.

2.1 Nd³⁺ doped crystals.

Among the numerous of $M_{1-x}R_xF_{m(1-x)+nx}$ fluoride phases three series have been chosen, which are characterized by:

- variable type of M²⁺-cation in the row of increasing of ionic radius Na-Ca-Sr-Ba;
- variable R³⁺ -cation in the rare earth elements row with fixed M²⁺ cation;
- the substitution of M²⁺ for M' ²⁺ in fluorite structure.

The first and the second series have heterovalent isomorphous substitutions that are accompanied with disordering of anionic motive, and the third - with an isovalent substitution and with a conservation of fluoride matrix stoichiometry.

2.2 Pr³⁺ doped crystals.

In this study were selected the crystals with the most low phonon energies of matrices among studied crystals:

- Ca_{0.9}La_{0.1}F_{2.1}:Pr - with *f*-complex partial occupation by interstitial F⁻-ions;
- Ba_{1-x}Gd_xF_{2+x}:Pr (x = 0, 0.1, 0.2, 0.3) and Ba_{1-x}Ce_xF_{2+x}:Pr (x = 0.01, 0.1, 0.3) - with partial occupation of *i*-complex;
- Pb_{0.67}Cd_{0.33}F₂:Pr - with different types of cations in fluorite structure with undisturbed anionic sublattice.

The most promising Ba_{1-x}Gd_xF_{2+x} and Pb_{0.67}Cd_{0.33}F₂ crystals were sensitized by Yb³⁺.

3. OPTICAL PROPERTIES OF MATERIALS DOPED WITH Nd³⁺

The scheme of energy levels of Nd³⁺ ion is shown in Fig. 1. The luminescence in 1.3 μm range correspond to $^4F_{3/2}-^4I_{13/2}$ electronic transition. In this region there is an excited state absorption (ESA) $^4F_{3/2}-^4G_{7/2}, ^4G_{9/2}$ which can overlapped with emission band.

3.1 $^4F_{3/2}-^4I_{13/2}$ luminescence and probabilities of transitions.

In fluoride crystals the forming of the numerous types of active centers in fluoride crystals is possible³⁻⁵, resulting the variation of crystal field leading to different Stark splitting and, therefore, to formation of the different shape of absorption and luminescence bands. The luminescence spectra of $^4F_{3/2} - ^4I_{13/2}$ electronic transition are shown in Fig. 2. The luminescence spectra $^4F_{3/2} - ^4I_{13/2}$ transition in all investigated $M_{1-x}R_xF_{m(1-x)+nx}$ crystals show the wide bands with feeble noticed structure. The halfwidth of luminescence band is mainly determined by the sort of M²⁺ cation. The sort of R³⁺ cation in $M_{1-x}R_xF_{2+x}$ (M=Ca, Sr, Ba) crystals has really no influence on the halfwidth of luminescence band but results in the redistribution of the intensities of Stark components of $^4F_{3/2} - ^4I_{13/2}$ electronic transitions, indicating the change in ion local environment symmetry with the changes of R³⁺ cation sort. The position of luminescence bands gravity centers and their halfwidth are showed in Table 1.

The calculation of transition probabilities and the corresponding values of decay times was carried out on the basis of Judd-Ofelt theory^{6,7}. Intensity parameters Ω_i and the calculated decay time are given in Table 1. The decay times of metastable $^4F_{3/2}$ transition in the stoichiometric single-center CaF₂, SrF₂, BaF₂ crystals are equal to 1000, 1280, 4000 μs, respectively. The decay times of metastable state is significantly less than in single-center MF₂ crystals. The calculations based on Judd-Ofelt theory show that the calculated lifetimes are close to the experimental values. The formation of centers with high electron transitions probabilities in nonstoichiometric fluoride phases in comparison with stoichiometric phases may be used for increasing lasers and amplifiers efficiency, this effect was reported for the first time in^{8,9}. The strong dependence of probabilities of electronic transitions on concentration of R³⁺ ions was noticed also in¹⁰. Some difference between Judd-Ofelt calculations for our data and data published in¹⁰ for BaF₂:Nd can be explained by cluster formation at more high concentration of Nd in our crystals.

The most wide luminescence bands have Na_{0.5-x}R_{0.5+x}F_{2+2x} (R=Y, Lu) and Ca_{1-x}R_xF_{2+x} (R=La, Ce, Gd, Y) crystals.

Table 1.

Chemical formula	Gravity center of 1.3 μm lum. / halfwidth, nm	Max. of ESA $^4F_{3/2} - ^4G_{7/2}$	τ meas., μs	Judd-Ofelt param., 10^{-20} cm^2			τ calc. μs	
				Ω_2	Ω_4	Ω_6		
$\text{Na}_{0.4}(\text{Y}_{0.995}\text{Nd}_{0.005})_{0.6}\text{F}_{2.2}$	1332/83	1316	1100	0.8	2.0	2.5	936	
$\text{Na}_{0.4}(\text{Lu}_{0.995}\text{Nd}_{0.005})_{0.58}\text{F}_{2.16}$	1332/83	1316	1090	0.9	1.9	2.5	966	
$\text{Ca}_{0.9}\text{La}_{0.09}\text{Nd}_{0.01}\text{F}_{2.1}$	1340/70	1312	570	0.25	3.5	4.4	545	
$\text{Ca}_{0.9}\text{Ce}_{0.09}\text{Nd}_{0.01}\text{F}_{2.1}$	1338/70	1312	550	0.13	3.7	4.3	553	
$\text{Ca}_{0.94}\text{Gd}_{0.05}\text{Nd}_{0.01}\text{F}_{2.06}$	1338/70	1312	430	0.25	2.9	4.0	635	
$\text{Ca}_{0.89}\text{Y}_{0.1}\text{Nd}_{0.01}\text{F}_{2.1}$	1338/70	1312	550	0.04	3.3	4.5	560	
$\text{Ca}_{0.99}\text{Nd}_{0.01}\text{F}_{2.01}$	-a)	-a)	1000					
$\text{CaF}_2\text{:Nd}^b)$			1000					
$\text{Sr}_{0.95}\text{Sc}_{0.04}\text{Nd}_{0.01}\text{F}_{2.05}$	1335/40	-	600	0.1	3.5	4.6	534	
$\text{Sr}_{0.85}\text{Gd}_{0.14}\text{Nd}_{0.01}\text{F}_{2.15}$	1334/40	1315	420	0.01	5.3	5.8	405	
$\text{Sr}_{0.9}\text{Y}_{0.09}\text{Nd}_{0.01}\text{F}_{2.01}$	1334/40	1315	330	0.01	4.4	5.5	450	
$\text{SrF}_2\text{:Nd}^b)$			1280	0.24	1.24	1.72	1410	
$\text{Ba}_{0.69}\text{La}_{0.3}\text{Nd}_{0.01}\text{F}_{2.31}$	1333/40	1314	460	0	4.0	5.7	450	
$\text{Ba}_{0.9}\text{Gd}_{0.09}\text{Nd}_{0.01}\text{F}_{2.1}$	1333/40	1314	560	0.05	4.4	5.0	480	
	x=0.04	1335/40	1314	570	0.1	3.7	4.4	500
$\text{Ba}_{0.99-x}\text{Y}_x\text{Nd}_{0.01}\text{F}_{2.01+x}$	x=0.09	1335/40	1314	470	0.05	4.2	5.0	440
	x=0	-a)	-a)	4000	0.3	1.5	1.6	1330
$\text{BaF}_2\text{:Nd}^b)$			4500	0.25	0.41	0.43	4700	
$\text{Pb}_{0.665}\text{Cd}_{0.33}\text{Nd}_{0.005}\text{F}_{2.005}$	1336/50	1311	410	0.18	5.2	6.1	382	

a) the great number of sharp lines b) from¹⁰

3.3 Excited state absorption and amplification

The excited state absorption from $^4F_{3/2}$ level of the Nd³⁺ ion is a serious problem for creation of broadband amplifiers and lasers in 1.3 μm region, due to partial overlapping with $^4F_{3/2} - ^4I_{13/2}$ luminescence band. This absorption band is connected with $^4F_{3/2} - ^4G_{7/2}$ electronic transition. The position of the peak of this ESA band can be determined from absorption spectra as a difference between the positions of $^4G_{7/2}$ and $^4F_{3/2}$ gravity centers of absorption bands. Data obtained are exhibited in Table 1 in column 3. One can see, the peak of $^4F_{3/2} - ^4G_{7/2}$ band (that corresponds to ESA) for all nonstoichiometric fluoride phases, is located near 1312-1316 nm and, consequently overlaps with a luminescence band.

Taking into account, that the $^4F_{3/2}$ level is the initial level for $^4F_{3/2} - ^4G_{7/2}$ and $^4F_{3/2} - ^4I_{13/2}$ transitions, and the wavelengths of these transitions are close, one can write based on Judd-Ofelt theory the ratio of $^4F_{3/2} - ^4G_{7/2}$ and $^4F_{3/2} - ^4I_{13/2}$ electronic transition probabilities:

$$K = \frac{A_{^4F_{3/2}-^4G_{7/2}}}{A_{^4F_{3/2}-^4I_{13/2}}} = 0.48 \frac{\Omega_2}{\Omega_6} + 0.29 \frac{\Omega_4}{\Omega_6} \quad (1)$$

The parameter K is equal to 0.39 and 0.22-0.26 for $\text{Na}_{0.5-x}\text{R}_{0.5+x}\text{F}_{2+2x}$ (R=Y, Lu) and $\text{Ca}_{1-x}\text{R}_x\text{F}_{2+x}$ (R=La, Y, Ce, Gd) crystals, respectively. In $\text{Ca}_{1-x}\text{R}_x\text{F}_{2+x}$ (R=La, Y, Ce, Gd) crystals the halfwidth of $^4F_{3/2} - ^4G_{7/2}$ band is almost two times less than the halfwidth of $^4F_{3/2} - ^4I_{13/2}$ emission band and, consequently, one would expect, that the ratio of ESA and

emission cross-sections will be ~ 0.8 for $\text{Na}_{0.5-x}\text{R}_{0.5+x}\text{F}_{2+2x}$ ($\text{R}=\text{Y}, \text{Lu}$) crystals and ~ 0.5 for $\text{Ca}_{1-x}\text{R}_x\text{F}_{2+x}$ ($\text{R}=\text{La}, \text{Y}, \text{Ce}, \text{Gd}$) crystals.

We carried out the direct measurement of ESA and amplification in 1140-1440 nm range for $\text{Na}_{0.5-x}\text{Y}_{0.5+x}\text{F}_{2+2x}$ and $\text{Ca}_{1-x}\text{Y}_x\text{F}_{2+x}$ crystals. Among the great number of crystals studied by us, the above mentioned crystals have the broadest luminescence bands. Taking into account that in the studied wavelength region there is no ground state absorption, one can write the expression for changing of probe light passed through unpumped and pumped sample:

$$\ln(I_u/I_p) = (\sigma_{\text{ESA}} - \sigma_{\text{em}})N^*l \quad (2)$$

where I_u and I_p are the intensities of light passed through unpumped and pumped sample, σ_{ESA} and σ_{em} are the ESA and emission cross-sections, respectively, N^* is the population of ${}^4\text{F}_{3/2}$ level and l is the length of crystal.

The light amplification in the sample must lead to the increase of the signal I_p in comparison with I_u , and, consequently, to the negative values of $\ln(I_u/I_p)$. The absorption caused by optical pumping, leads to darkening of the sample and, consequently, to the positive values of $\ln(I_u/I_p)$.

The experimental setup for the ESA and gain measurements is shown in Fig. 3a. The spectrum of $\ln(I_u/I_p)$ value is shown in Fig. 3b. In the Fig. 3b the left scale corresponds to the cross-sections units, and right scale - to $\ln(I_u/I_p)$ units. The emission cross-section spectra calculated with the use of transition probabilities obtained from Judd-Ofelt analysis are shown in the same figure.

The ESA band with maximum at 1230 nm corresponds to ${}^4\text{F}_{3/2} - {}^4\text{G}_{9/2}$ electron transition. The maximum of amplification band is ~ 1365 nm, the halfwidth of amplification band is 40 nm for $\text{Na}_{0.5-x}\text{Y}_{0.5+x}\text{F}_{2+2x}$ crystal and 60 nm for $\text{Ca}_{1-x}\text{Y}_x\text{F}_{2+x}$ crystal. The difference between the emission spectrum and the amplification spectrum is explained by the overlapping of ESA and luminescence bands. This ESA band corresponds to ${}^4\text{F}_{3/2} - {}^4\text{G}_{7/2}$ electron transition and has a maximum at 1315 nm. The maximum values of the ESA cross-section and emission cross-section are approximately equal for $\text{Na}_{0.5-x}\text{Y}_{0.5+x}\text{F}_{2+2x}$ crystals (the ratio is 1:1) and their ratio is about 1:2 for $\text{Ca}_{1-x}\text{R}_x\text{F}_{2+x}$ crystals. The experimental positions of maximum of the ESA ${}^4\text{F}_{3/2} - {}^4\text{G}_{7/2}$ bands and of the ESA and emission cross-sections agree well with the above calculated values.

Though luminescence band halfwidth for $\text{Na}_{0.5-x}\text{Y}_{0.5+x}\text{F}_{2+2x}$ crystals is 10 nm more than that for $\text{Ca}_{1-x}\text{R}_x\text{F}_{2+x}$ crystals, the amplification spectrum halfwidth of $\text{Ca}_{1-x}\text{R}_x\text{F}_{2+x}$ crystals is 20 nm more. The reason is that in the former crystal the ESA cross-section of (${}^4\text{F}_{3/2} - {}^4\text{G}_{7/2}$) band is less than in the latter one. Among the crystals investigated by us the $\text{Ca}_{1-x}\text{R}_x\text{F}_{2+x}$ crystals have the widest amplification bandwidth. The measured effective emission cross-section $\sigma_{\text{eff}} = \sigma_{\text{em}} - \sigma_{\text{ESA}}$ is $4.5 \pm 0.9 \cdot 10^{-21} \text{ cm}^2$ for $\text{Ca}_{1-x}\text{R}_x\text{F}_{2+x}$ crystal, and $2.2 \pm 0.7 \cdot 10^{-21} \text{ cm}^2$ for $\text{Na}_{0.5-x}\text{Y}_{0.5+x}\text{F}_{2+2x}$ crystal in the peak of amplification band.

4. OPTICAL PROPERTIES OF MATERIALS DOPED WITH Pr^{3+}

The scheme of energy levels of Pr^{3+} ion is shown in Fig. 4. The luminescence in 1.3 μm range correspond to ${}^1\text{G}_4 - {}^3\text{H}_5$ electronic transition. The main problems for creating the active media doped with Pr^{3+} in this region are nonradiative decay through ${}^1\text{G}_4 - {}^3\text{F}_3$ channel and strong concentration quenching.

4.1 Absorption spectra and decay times

Fig. 5 shows the dependencies of the decay rate (determined as $1/\tau$, where τ is the decay time) of ${}^3\text{P}_0$ and ${}^1\text{G}_4$ levels on concentration of Pr^{3+} ions. The best fit approximations by linear dependencies calculated by the least square method are summarized in Table 2.

Table 2.

Chemical formula	Decay rate, sec ⁻¹	
	³ P ₀ level	¹ G ₄ level
Ba _{0.9-x} Gd _{0.1} Pr _x F _{2.1+x}	5650*(100x)+21500	6105*(100x)+2940
Ba _{0.8-x} Gd _{0.2} Pr _x F _{2.1+x}	6530*(100x)+22320	6733*(100x)+3540
Ba _{0.7-x} Gd _{0.3} Pr _x F _{2.1+x}	7600*(100x)+23500	7190*(100x)+3980
Ca _{0.9-x} La _{0.1} Pr _x F _{2.1+x}	8030*(100x)+16860	20320*(100x)+4910
(Pb _{0.67} Cd _{0.33}) _{1-x} Pr _x F _x	3680*(100x)+30050	1340*(100x)+5083

In Fig. 6 the room temperature absorption spectra of the crystals BaF₂ and Ba_{0.7}Gd_{0.3}F_{2.3} are given in the region 400 - 700 nm. One can see that a large number of sharp lines in BaF₂ crystal are united in structureless bands as the fraction of trifluoride CeF₃ and GdF₃ increases, the integral absorption coefficient $\int k(\lambda)d\lambda$ strongly increasing for all absorption bands.

Fig. 7 shows the dependence of the integral absorption coefficient of ¹D₂ band from the fraction of CeF₃ and GdF₃ in the crystals at the fixed concentration of Pr³⁺ (0.2 at %). The dependence on concentration of Ce and Gd is close to square root dependence.

The decay rate of ³P₀ level is practically independent on temperature (42 μs at 80 K and 36 μs at 500 K). This fact gives an evidence that the decay of ³P₀ levels is mainly radiative and, therefore, the decay rate at a low concentration of Pr³⁺ characterizes the probabilities of electronic transitions from ³P₀ level. The probabilities are determined by a local environment of Pr³⁺. The decay rate of ³P₀ level changes not more than on 10 % at the increasing of GdF₃ from 10 to 30 mole % in Ba_{1-x}Gd_xF_{2+x} crystals, while the integral absorption coefficients show approximately 1.5-fold changes for all bands. That is why the increasing of integral absorption coefficient upon the fraction of GdF₃ in the crystals cannot be connected with essential change of the local environment of Pr³⁺ ions which gives the main part of observed luminescence and absorption bands in Ba_{1-x}Gd_xF_{2+x} crystals. Such behavior of integral absorption coefficient can be explained by formation of Pr³⁺ centers with another symmetry.

The structural studies shows two variants of location of an interstitial fluorine ion in M_{1-x}R_xF_{2+x} crystals: 32-fold *f*-complex and 48-fold *i*-complex². The *f*-complexes dominate in Ca_{1-x}La_xF_{2+x}, the *i*-complexes dominate in Ba_{1-x}R_xF_{2+x} crystals. No data about the type of complexes in (Pb_{0.67}Cd_{0.33})_{1-x}R_xF_{2+x} are now available.

The probabilities of electronic transitions in Ca_{1-x}La_xF_{2+x}:Pr (x = 0 - 0.2) and Pb_{0.67}Cd_{0.33}F₂:Pr crystals are in approximately 10 times more than in BaF₂:Pr crystals. This fact shows that in Ca_{1-x}La_xF_{2+x}:Pr and Pb_{0.67}Cd_{0.33}F₂:Pr crystals the symmetry of local environment of Pr³⁺ ions is lower than in BaF₂:Pr crystals.

The experimental data discussed above show that the increasing of the CeF₃ and GdF₃ concentration in the Ba_{1-y}(Ce, Gd)_yPr_xF_{2+y+x} crystals leads to formation of new centers with more high probabilities of electronic transitions than that in pure BaF₂ crystals and, consequently, with more low symmetry of local environment of Pr³⁺ ions. The number of such centers rises on the increasing of CeF₃ and GdF₃ concentration, leading to the increasing of the integral absorption coefficients. The weak increase of the probability of transitions (and hence the decay rate of ³P₀ level) upon the increasing of the fraction of GdF₃ in the Ba_{1-x}Gd_xF_{2+x}:Pr crystals may be due to an increasing of crystal field on Pr³⁺ ions, which correlates with the decrease of the parameter of the lattice in Ba_{1-x}Gd_xF_{2+x} upon the increasing of the fraction of trifluoride GdF₃ ($a = 6.200 - 0.623x$, where a is the lattice parameter and x is the concentration of GdF₃¹¹).

The temperature dependence of the integral absorption coefficient of ³P₂-³P₀ group of lines in crystals Ba_{1-y}Gd_yF_{2+y} (y = 0.1; 0.3) is shown in Fig. 8. We explain the observed character of the temperature dependence by redistribution of Pr³⁺ ions from the low symmetrical positions of Pr³⁺ ions to the high symmetrical ones (with parity forbidden transitions). The process results in the reduce of the integral absorption coefficients. Such changing of Pr³⁺ ions positions is attributed to the shift of the interstitial F⁻ ions. The best fit approximation of the experimental data gives the energy gap of activation equal to 280 cm⁻¹ for the both crystals. In Fig. 8 this approximation is shown by a solid line.

4.2 Calculation of line's strengths

The strengths of lines and the probabilities of electronic transitions in 4*f*-ions are usually described by the Judd-Ofelt theory^{6,7}. In the case of Pr³⁺ ions this scheme of calculation meets some problems. First, the number of the transitions

which may be found from the absorption spectra are small, second, the calculated values of the line strength for 3P_0 - 3P_2 lines are essentially smaller than the experimental ones. In some cases the value of the parameter Ω_2 is negative, being in the contradiction with the Judd-Ofelt theory.

Kornienko at all. have modified the Judd-Ofelt theory taking into account the dependence of the Judd-Ofelt approximation on the energy of manifolds¹². Neglecting the electron correlation effects for the electric dipole transitions the expression was obtained:

$$S_{JJ'}^{ed} = \sum_{t=2,4,6} \Omega_t [1 + 2\alpha(E_J + E_{J'} - 2E_c)] \langle 4fLSJ \| U_t \| 4f'L'S'J' \rangle^2 \quad (3)$$

where Ω_t - are the modified parameters of Judd-Ofelt theory, α is the additional parameter. E_J and $E_{J'}$ are the energies of the J and J' manifolds, E_c is the energy of the center of gravity of the 4f configuration of Pr³⁺ ions, equal to 9940 cm⁻¹.

In order to increase a number of the experimental line's strengths we have used the date obtained from the luminescence spectra and the measured lifetime of 3P_0 -level.

The Judd-Ofelt and Kornienko at all. calculations are summarized in Table 3. For these calculations we used the experimental line's strengths of 3P_0 - 3H_4 ; 3H_5 ; 3H_6 ; 3F_3 ; 3F_4 transitions obtained from emission spectra and 3H_4 - 3P_2 ; (3P_1 , 1I_6), 3P_0 , 1D_2 , 3F_4 , 3F_3 obtained from absorption spectra. The root mean square deviations (R.M.S) between the experimental and calculated values for all these transitions are given in Table 3 (columns 5 and 10).

Table 3.

Chemical formula	Judd-Ofelt parameters, 10^{-20}			R.M.S deviat. 10^{-20}	Kornienko at all. parameters 10^{-20} 10^{-5}				R.M.S deviat. 10^{-20}
	Ω_2	Ω_4	Ω_6		Ω_2	Ω_4	Ω_6	α	
Ba _{0.7} Gd _{0.3} F _{2.3}	-0.04	3.3	6.1	1.1	0.467	4.1	26.4	2.6	0.25
Ca _{0.9} La _{0.1} F _{2.1}	0.08	2.7	5.1	0.63	1.5	2.6	20.6	2.3	0.27
Pb _{0.67} Cd _{0.33} F ₂	0.37	2.6	8.4	1.01	0.91	1.6	32.3	2.3	0.58

The mean root square deviations are in to 2-4 times smaller in Kornienko at all. calculations and the better agreement between calculated and experimental line's strengths for 3P_2 - 3P_0 is obtained in the case of this theory.

4.3 Yb³⁺ sensitized crystals

It is difficult to pump directly 1G_4 level of Pr³⁺ ion due to very small absorption cross-section of 3H_4 - 1G_4 electronic transition. This problem may be solved by Yb³⁺ sensitization, as the absorption spectrum of $^2F_{5/2}$ - $^2F_{7/2}$ electronic transition of Yb³⁺ ions has a good overlapping with spectrum of laser diode pumping and a large value of cross-section. We studied Ba_{0.932-x-y}Gd_{0.068}Yb_xPr_yF_{2.068+x+y} and (Pb_{0.67}Cd_{0.33})_{1-x-y}Yb_xPr_yF_{2+x+y} ($x=0-0.03$; $y=0-0.02$) crystals, which have the lowest concentration quenching among the studied crystals. The IR absorption and emission spectra of Pr-doped and Yb sensitized crystals are shown in Fig. 9.

The curve of decay of donor ions (Yb³⁺) is described by the following equation in all studied range of concentrations of Yb and Pr ions:^{13,14}

$$I = I * \exp\left(-\frac{t}{\tau_0} - W*t - \gamma*\sqrt{t}\right) \quad (4)$$

W is proportional to $x*y$ (where x is a concentration of acceptors and y is a concentration of donors); for random distribution of donors and acceptors γ is proportional to acceptors concentration. In studied crystals γ -coefficient is depended both donors both acceptors concentrations. Such behavior can be explained by clusters formation, which was also observed in structural investigations.

The mean decay rate in $\text{Ba}_{0.932-x-y}\text{Gd}_{0.068}\text{Yb}_x\text{Pr}_y\text{F}_{2.068+x+y}$ and $(\text{Pb}_{0.67}\text{Cd}_{0.33})_{1-x-y}\text{Yb}_x\text{Pr}_y\text{F}_{2+x+y}$ crystals is proportional to $x+y$. The best fits are $W=(1.49 \cdot 10^7 \cdot x+y+340) \text{ sec}^{-1}$ and $W=(1.45 \cdot 10^7 \cdot x+y+780) \text{ sec}^{-1}$ for $\text{Ba}_{0.932-x-y}\text{Gd}_{0.068}\text{Yb}_x\text{Pr}_y\text{F}_{2.068+x+y}$ and $(\text{Pb}_{0.67}\text{Cd}_{0.33})_{1-x-y}\text{Yb}_x\text{Pr}_y\text{F}_{2+x+y}$ crystals, respectively.

Considering the system with donors and acceptors 1 and 2, where the excitation is transferred from donors to acceptors 1 and the acceptors 1 have a probability to emit light or to disappear without radiation after the interaction with the acceptors 2 one can write for CW pumping:¹⁵

$$N_{a1} = N_{a1}^0 * \eta_{a1} + N_d^0 * (1 - \eta_d) * \eta_{a1} \quad (5)$$

where N_{a1} is the population of the donor excited state, N_d^0 and N_{a1}^0 are the quantities of donors and acceptors 1 excited directly per temporal unit, η_{a1} and η_d are the quantum efficiency of the luminescence of the donors and acceptors 1. Then:¹⁵

$$\eta_{a1} = \tau_{a1}^{-1} * \int \exp(-t/\tau_{a1}) \Pi_{a1}(t) dt \quad (6)$$

$$\eta_d = \tau_d^{-1} * \int \exp(-t/\tau_d) \Pi_d(t) dt \quad (7)$$

where τ_{a1} and τ_d are lifetimes in the absence of ion-ion interactions, $\Pi_{a1}(t)$ and $\Pi_d(t)$ are the functions describing the energy transfer between donors and acceptors 1.

At CW pumping when N_{Yb}^0 is determined by the equality of the pumping rate and decay rate we can write for the amplification coefficient (neglecting the influence of saturation effects):

$$K = [\sigma_{em} * \tau_{Yb} * P_0 / (\hbar v_p * A)] * [1 - \exp(-\alpha * l)] * [1 - \eta_d] * \eta_{a1}, \quad (8)$$

where $\hbar v_p$ is the photon energy of the pumping light, σ_{em} is the cross-section of ${}^1\text{G}_4 - {}^3\text{H}_5$ transition, τ_{Yb} is Yb^{3+} ion decay time, α is absorption coefficient at the pumping wavelength, A is the cross section of the pumping and amplification beams at the suggestion of 100% spatial overlapping of the beams, l is the length of sample, P_0 is the pump power. The η_{a1} and η_d were determined from decay of Yb^{3+} ions discussed above and dependence on concentration of decay rate of ${}^1\text{G}_4$ level of Pr^{3+} ions given in Table 2.

The results of the calculations of gain coefficient depending on Pr^{3+} and Yb^{3+} concentrations are shown in Fig. 10. At the calculation we suggest that the crystal length is 1.5 cm, diameter of pumping beam is 100 μm (it is of the same order of magnitude as the diameter of caustic of the TEM_{00} mode in the resonator with the 5 cm - length). The $\text{Ba}_{0.911}\text{Gd}_{0.068}\text{Yb}_{0.02}\text{Pr}_{0.001}\text{F}_{2.089}$ crystals with optimal Yb and Pr concentrations were grown with good optical quality.

5. CONCLUSIONS

The great number of variations of physical properties and formation of many types of optical centers in nonstoichiometric fluoride crystals with CaF_2 type of structure in dependence on chemical composition make this materials very promising for constructing of active optical media. The spectroscopy and gain measurements shows that $\text{Ca}_{0.9}\text{Y}_{0.1}\text{F}_{2.1}:\text{Nd}^{3+}$ crystals are promising for broadband operation in 1.3 μm region with maximal cross-section $4.5 \pm 0.9 \cdot 10^{-21} \text{ cm}^2$. It have been found that among the large number of nonstoichiometric fluoride crystals doped with Pr^{3+} ion the most perspective crystals for broadband operation in 1.3 μm region are sensitized by Yb^{3+} ions $\text{Ba}_{0.911}\text{Gd}_{0.068}\text{Yb}_{0.02}\text{Pr}_{0.001}\text{F}_{2.089}$ crystals with gain coefficient up to 0.6 dB per one Wt of pumping energy.

6. ACKNOWLEDGMENTS

This research was financial supported in part by AT&T Bell Laboratories.

7. REFERENCES

1. B.P.Sobolev, "Non-stoichiometry in inorganic fluorides and phases with fluorite structure", *Butll. Soc. Cat. Cien.*, Vol. 12, N 2, pp. 275-332, 1991.

2. V.B.Alexandrov, "X-ray and neutron diffraction studies of non-stoichiometric fluorite phases $M_{1-x}R_xF_{2+x}$ ($M=Ca, Sr, Ba; R=Ln, Y$)", *Butll. Soc. Cat. Cien.*, Vol. 12, N 2, pp. 333-347, 1991.
3. Ya.E.Kariss, M.N.Tolstoi, and P.P.Feofilov, "On the luminescence and absorption of trivalent neodymium in crystals of the fluorite type", *Opt. Spectrosc. (USSR)*, Vol. 18, pp. 247-250, 1965.
4. V.V.Osiko, "Termodinamic of optical centers in CaF_2 - TR^{3+} crystals", *Soviet Physcs-Solid State*, Vol. 7, pp. 1047-1056, 1965.
5. Yu.K.Voron'ko, A.A.Kaminskii, and V.V.Osiko, "Analysis of the optical spectra of $CaF_2:Nd^{3+}$ (type 1) crystals", *Soviet Phys. JETP*, Vol. 22, pp. 295-300, 1966.
6. B.R.Judd, "Optical absorption intensities of rare-earth ions", *Phys. Rev.*, Vol. 127, pp. 750-761, 1962.
7. G.S.Ofelt, "Intensities of crystal spectra of rare-earth ions", *J.Chem.Phys.*, Vol. 37, pp. 511-520, 1962.
8. A.A.Kaminskii, V.V.Osiko, V.T.Udovenchik, "Stimulated emission of SrF_2 - LaF_3 crystals doped with Nd at room temperature", *Jurnal Prikladnoi Spectroscopii (USSR)*, Vol. 6, N 1, pp. 40-44, 1967.
9. Kh.S.Bagdasarov, Yu.K.Voron'ko, A.A.Kaminskii, V.V.Osiko, "Systems based on fluorides as an active materials for quantum electronic", *Izvestia AN SSSR Neorganicheskie materialy (USSR)*, Vol.1, N 12, pp.2088-2092, 1965.
10. S.A.Payne, J.A.Caird, L.L.Chase, L.K.Smith, N.D.Nielsen, and W.F.Krupke, "Spectroscopy and gain measurements of Nd^{3+} in SrF_2 and other fluorite-structure hosts", *J.Opt.Soc.Am.B*, Vol. 8, N 4, pp. 726-740, 1991
11. P.P.Fedorov, B.P.Sobolev, "Dependence on concentration of lattice parameters of $M_{1-x}R_xF_{2+x}$ phases with fluorite structure", *Kristallographia (USSR)*, N 4, pp.92-95, 1992.
12. A.A.Kornienko, A.A.Kaminskii, E.B.Dunina, "The reason of nonadequate of Judd-Ofelt approximation at considering of optical spectrum of Pr^{3+} ion in crystals", *Phys.status Solidi*, Vol. 157, pp.267-273, 1990.
13. Yu.K.Voron'ko, T.T.Mamedov, V.V.Osiko, V.P.Sakun, I.A.Shcherbakov, "Investigation of the nature of nonradiative excitation energy relaxation in condensed media with a high activator concentration", *Jurnal experimentalnoi i teoreticheskoi phiziki (USSR)*, Vol. 71, N 2, pp. 478-496, 1976.
14. I.A.Bondar, A.I.Burstein,A.V.Krutikov,L.P.Mezentseva,V.V.Osiko,V.P.Sakun,V.A.Smirnov,I.A.Shcherbakov, *Jurnal experimentalnoi i teoreticheskoi phiziki (USSR)*, Vol. 81, N 1, pp. 96-114, 1981.
15. V.A.Smirnov, I.A.Shcherbakov, "Kinetic of energy transfer and potential of chromium ions as active particles of solid state lasers", *Spectroscopy of Crystals*, ed. Kaplyanskii, pp. 21-42, Nauka, Leningrad, 1985.

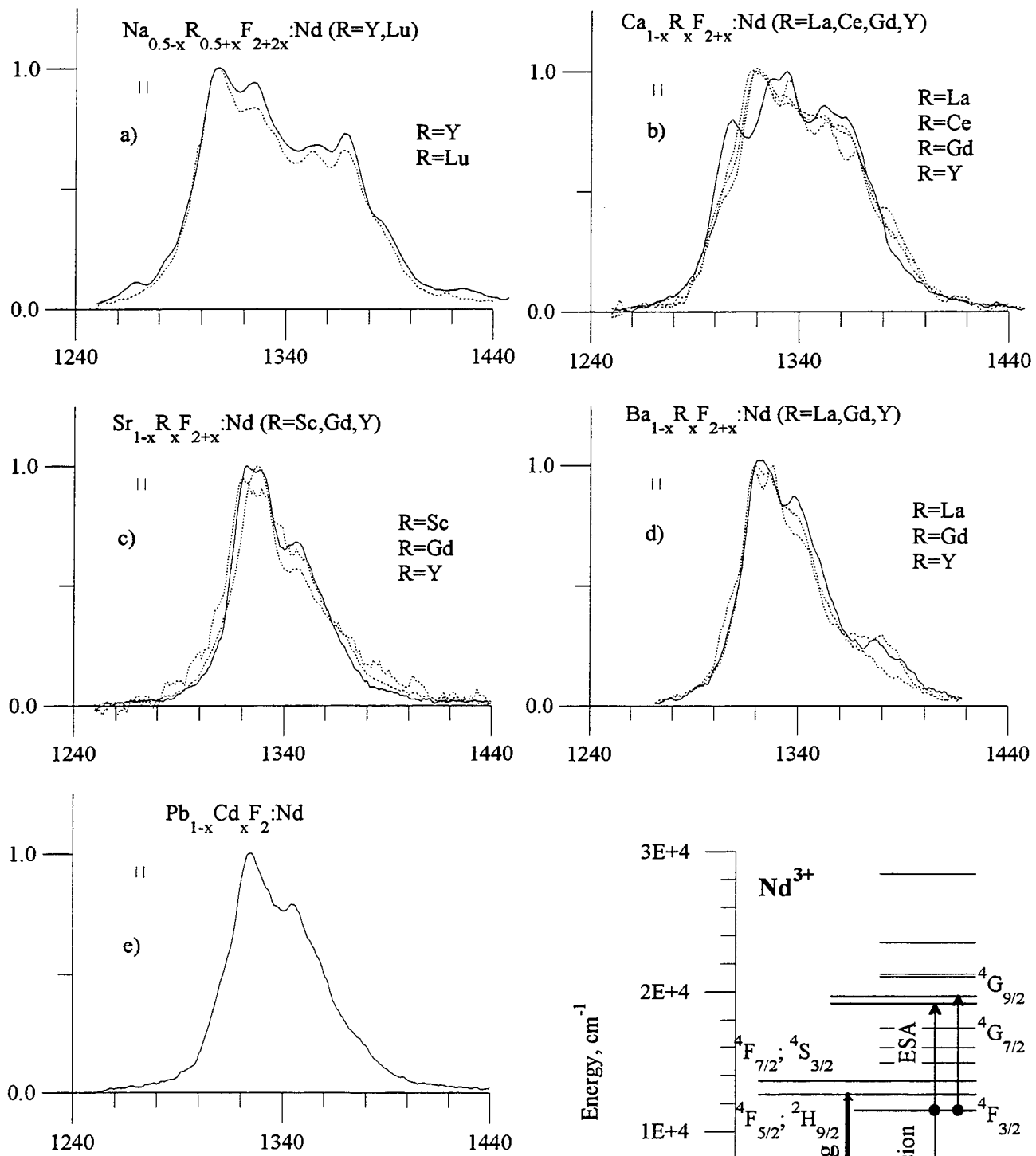


Fig. 2 (a-e). Luminescence spectra of ${}^4F_{3/2}$ - ${}^4I_{13/2}$ transition in nonstoichiometric crystals with CaF_2 -type structure

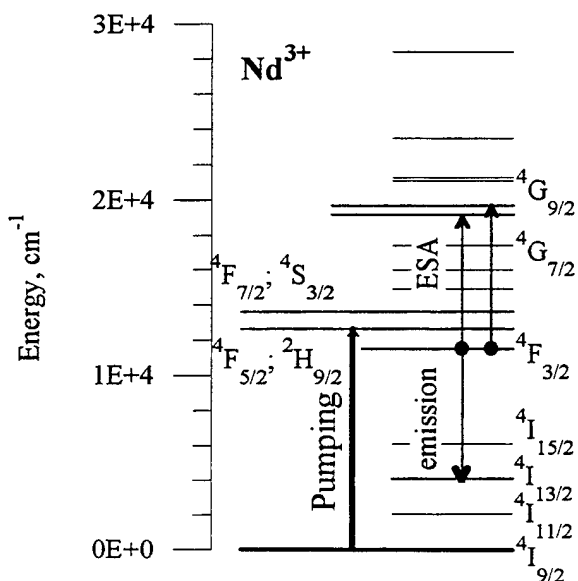


Fig. 1. Scheme of energy levels of Nd^{3+} ions.

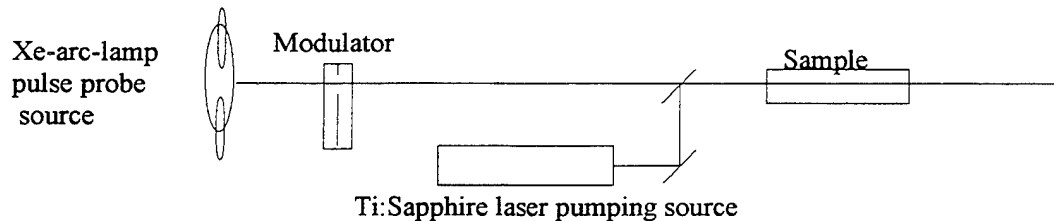


Fig. 3a. Experimental setup of ESA/Gain measurements

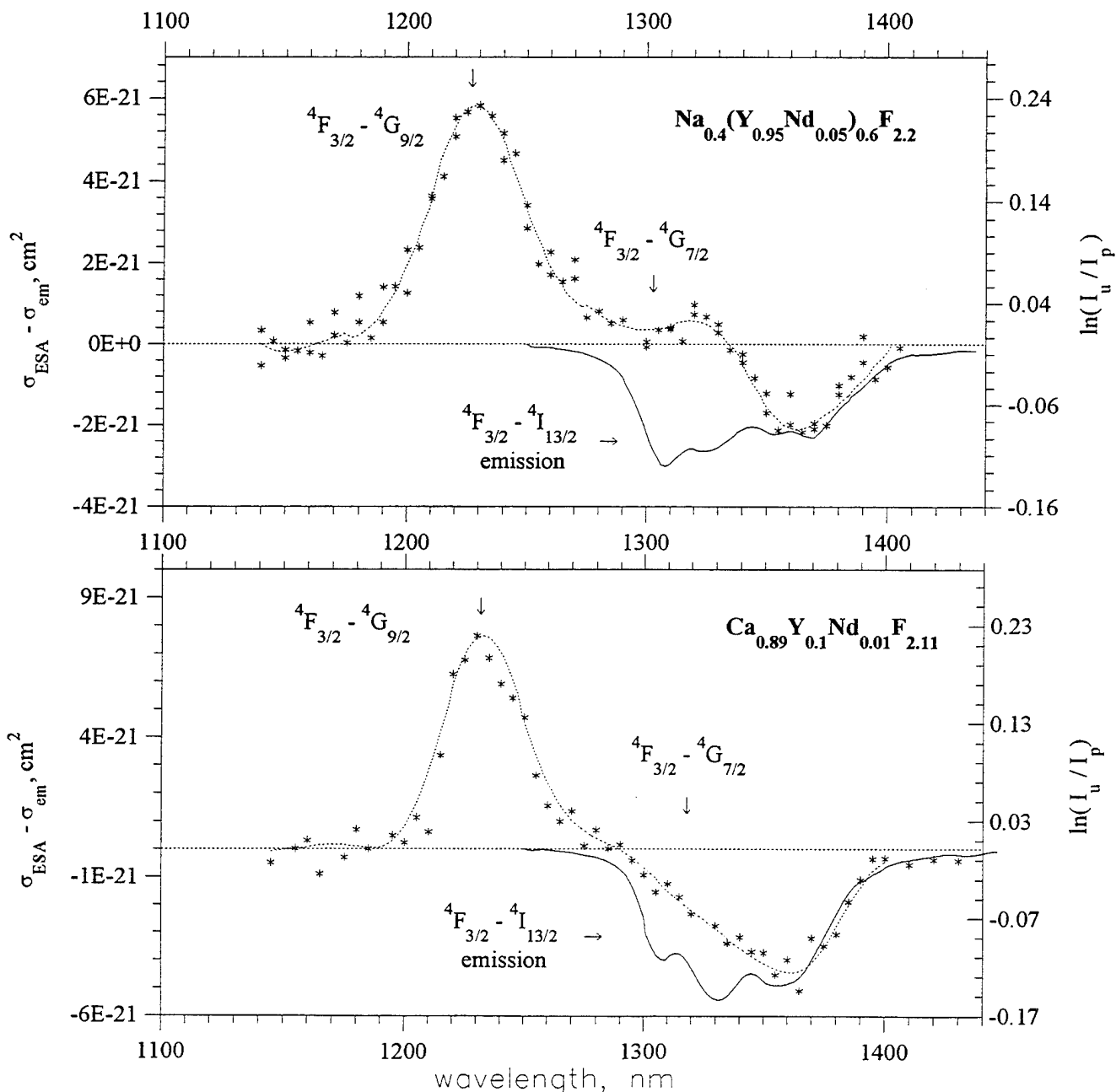


Fig. 3b. Excited state absorption and gain in 1.3μ range in Nd doped $\text{Na}_{0.4}\text{Y}_{0.6}\text{F}_{2.2}$ and $\text{Ca}_{0.9}\text{Y}_{0.1}\text{F}_{2.1}$ crystals

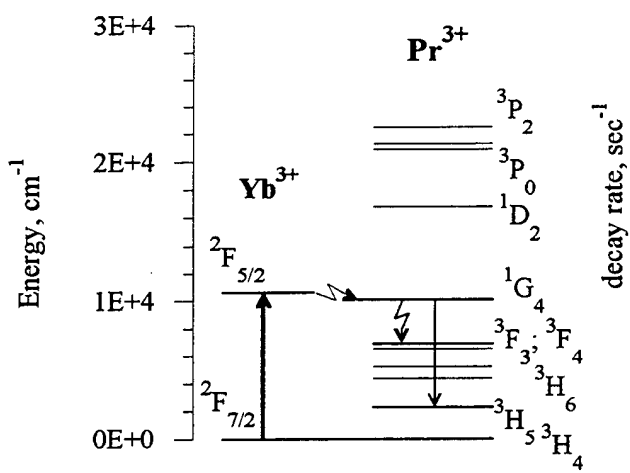


Fig. 4. Energy scheme of Pr^{3+} and Yb^{3+} ions

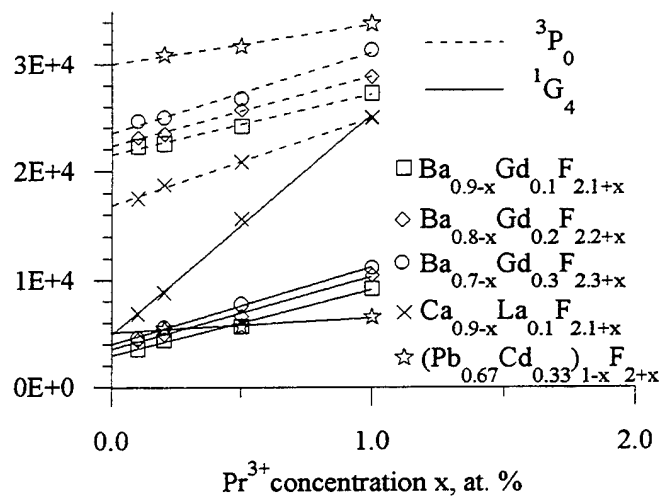


Fig. 5. Decay rate versus Pr^{3+} concentration

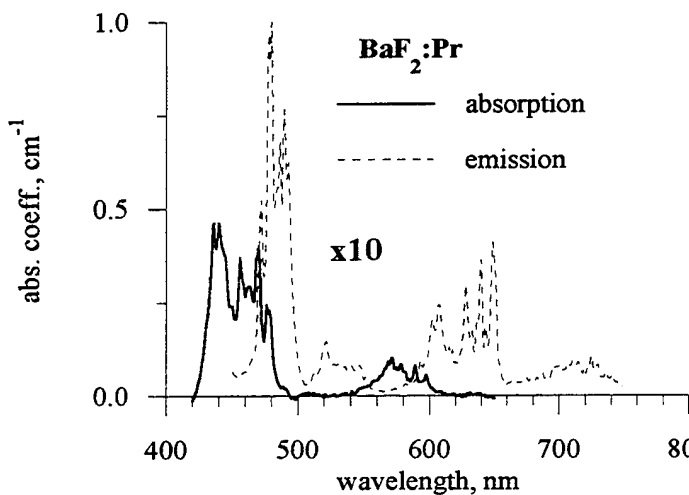


Fig. 6. Absorption and luminescence spectra of $\text{Ba}_{1-x}\text{Gd}_x\text{F}_{2+2x}:\text{Pr}$ crystals

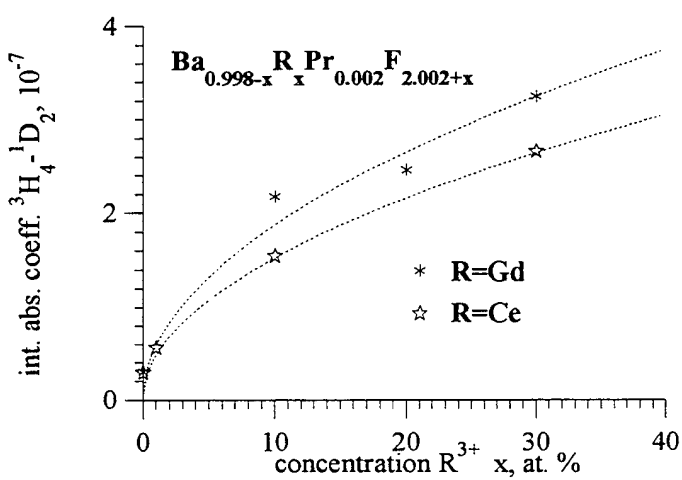
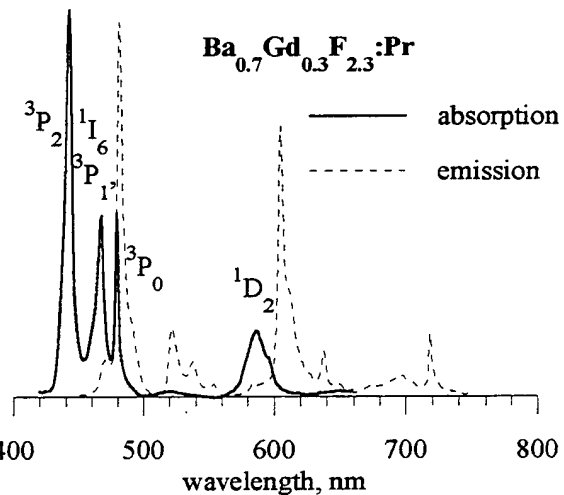


Fig. 7. Integral absorption coefficient of 1D_2 bands versus R^{3+} concentration

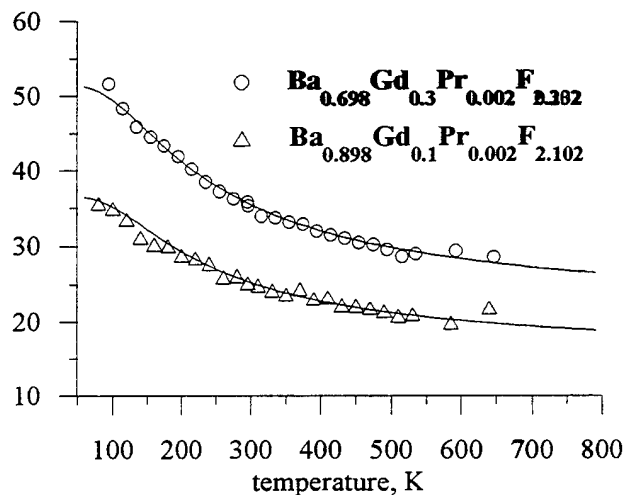


Fig. 8. Temperature dependence of integral abs. coefficient of $^3P_2 - ^3P_0$ group of lines

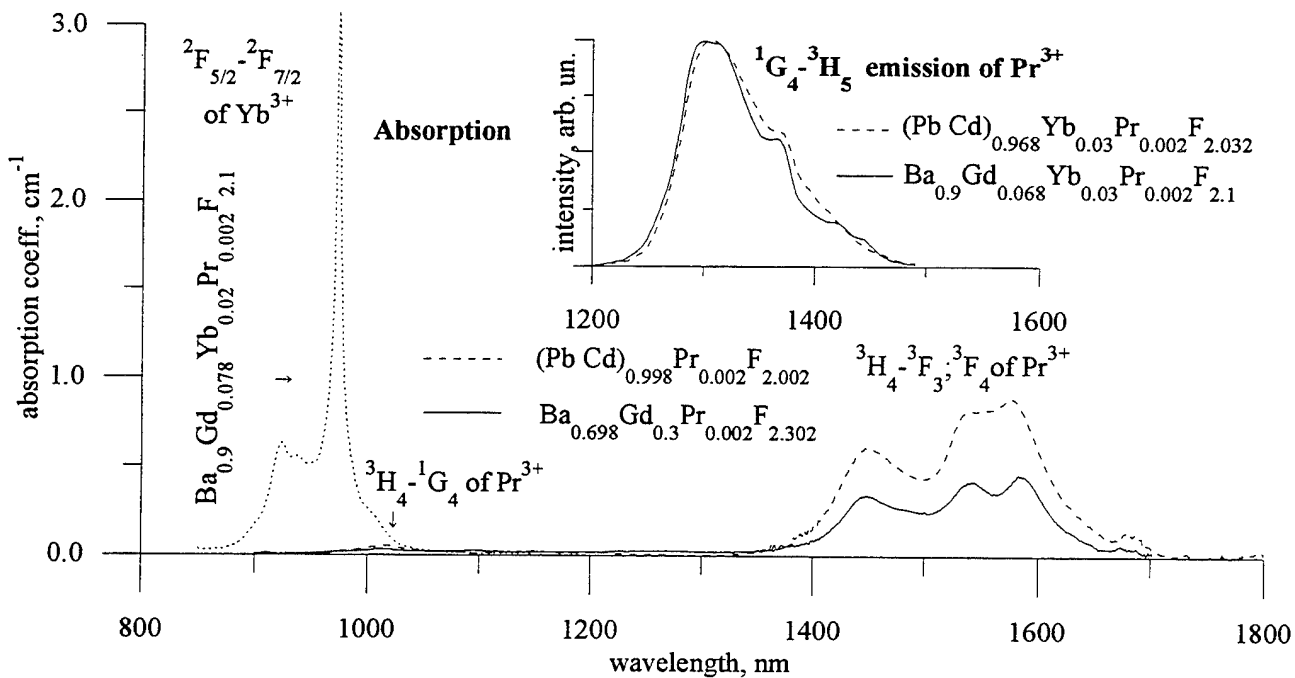


Fig. 9. Luminescence and absorption spectra in the near IR region of Pr doped and Yb sensitized crystals with low concentration quenching

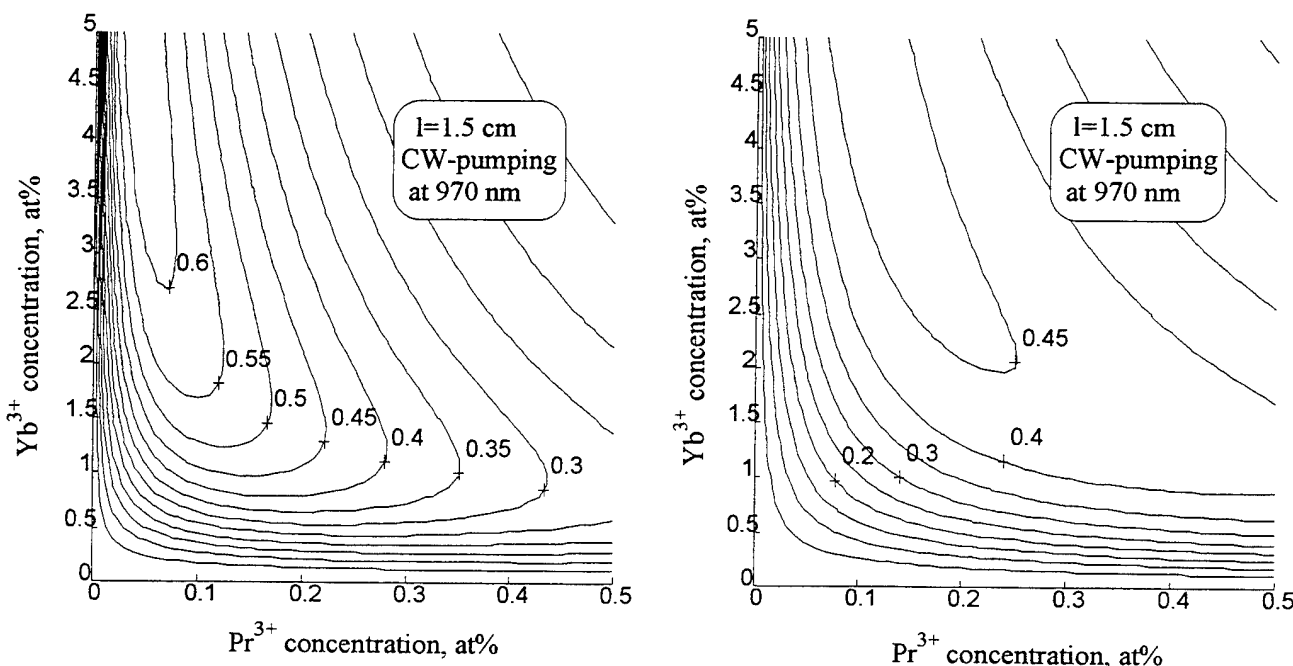


Fig 10a. Calculated gain coefficient (dB/Wt) versus Yb^{3+} and Pr^{3+} concentrations in $\text{Ba}_{0.932-x-y}\text{Gd}_{0.068}\text{Yb}_x\text{Pr}_y\text{F}_{2.068+x+y}$ crystals

Fig 10b. Calculated gain coefficient [dB/Wt] versus Yb^{3+} and Pr^{3+} concentrations in $(\text{Pb}_{0.67}\text{Cd}_{0.33})_{1-x-y}\text{Yb}_x\text{Pr}_y\text{F}_{2+x+y}$ crystals

ESA spectroscopy measurement of Charge Transfer bands in doped ionic crystals.

B.K.Sevastyanov

Institute of Crystallography of Russian Academy of Sciences, Leninsky prospect. 59, Moscow, Russia, 117333

ABSTRACT

Possibilities of the Excited State Absorption (ESA) spectroscopy as the method of investigation of Charge Transfer (ChT) process in doped ionic crystals are discussed. Temperature dependence of ChT bands of the Cr^{3+} ions doped crystals suggests that ChT process is mainly donor nature e.g. [(3d \rightarrow 4s or 3d \rightarrow (ligand orbital)].

ChT bands positions of $\text{Ti}^{3+}\text{:Al}_2\text{O}_3$ and $\text{Cr}^{3+}\text{:Li}_2\text{Ge}_7\text{O}_{15}$ crystals measured by ESA spectroscopy and two-step photoionization method are approximately the same for each crystal.

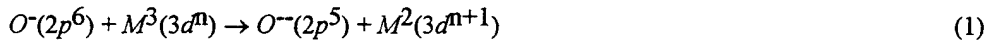
Wide-band gain of $\text{Cr}^{3+}\text{:LGO}$ crystal is overlaped by strong ESA band prevents laser effect in the whole luminescence range.

1. INTRODUCTION

1.1 Charge Transfer bands studies.

The problems of ChT transitions of electrons between dopant metal ions and nearest ligands in ionic crystals is the object of searching interest. Theoretical foundation of ChT transitions in the crystals was given by McClure¹. Deep earlier experimental study of ChT spectra have been fulfilled by Tippins² on the row of iron group ions in Al_2O_3 . Experimental observation of ChT bands and their temperature dependence of iron group ions in fluoride crystals is given in the paper of Sabatini, Salwin, and McClure³. During last several years the ideas of ChT transitions are used for explanation of some laser properties of the crystals^{4,5}.

The most considerably experimental study of ChT spectra have been fulfilled by Tippins² who investigate the spectra of V^{3+} , Ti^{3+} , Cr^{3+} , Mn^{3+} , Fe^{3+} , Ni^{3+} ions in Al_2O_3 crystal by the GSA (Ground State Absorption) method. Tippins proposed acceptor model of charge transfer, which can be described by the formula:



In other words this model assumes transitions of electrons from orbital of oxygen ligand to metal dopant ion. Threshold energy of the transitions may be described by the equation:

$$hv_{\text{thresh.}} = C - I(M^{3+}) + \Delta E_d \quad (2)$$

here C - is the constant depending on Madelung energy, $I(M^{3+})$ - the third ionization potential of the metal ion; ΔE_d - the difference of energy of initial and final state of the dopant metal ion.

Tippins fulfilled detail measurements of the positions of ChT band in the spectra, but he didn't measure temperature dependence of the ChT band and could not completely prove an acceptor model of the process. But mainly temperature dependence of the ChT bands provides us necessary information for determination of transition character³.

In both cases^{2,3} ChT band is founded on strong background of the edge of fundamental absorption of the crystal host. Naturally, it makes difficulties in measuring correctly parameters of the band in this conditions and the more its temperature dependence. These parameters may be characterized only qualitatively. Authors of the paper³, measuring temperature dependence of ChT bands, went to conclusion that not acceptor but donor process of the charge transfer [(3d \rightarrow 4s or 3d \rightarrow (ligand orbital)] is preferable for 3d ions. In the temperature dependence measurement it is possible to observe two phenomena:

- decreasing of oscillator strength when temperature reduces;
- shifting of the band maxima to blue side of the spectra.

Authors of paper³ observed these two features of the ChT spectra qualitatively.

The development of this research still not intensive and systematic. Difficulties of the investigation are of two types. The first is an imperfection of the theory of the process. The second is very difficult spectroscopic experiment. The

measurement is necessary to carry out in deep vacuum UV range, to have very thin and heavy concentrated specimens. There are also specific difficulties caused by spectroscopy itself. The ChT bands have very high intensity, approximately two order of value larger than the bands belonging to intra-ion transitions (IT) of the dopant ion. And practically impossible to measure ChT and IT bands in the same experiment by using one specimen. But namely such measurement is necessary for correct information.

In this paper we would like to pay attention on possibilities which gives the method of ESA spectroscopy for searching ChT band in ESA spectra.

1.2 Principles of ESA spectroscopy.

The method of ESA spectroscopy was developed by Gires and Mayer⁶. They observed in UV region ChT bands caused by transition $^2E \rightarrow \text{ChT}$ Zone in Ruby. Kushida also observed this band⁷. But there was no any investigations of parameters of the band. At that period we searched several crystals doped with Cr³⁺ ions: Al₂O₃, MgAl₂O₃, Y₃Al₅O₁₂, BeAl₂O₄, and others⁸⁻¹³. And every crystal showed very strong ChT band in ESA spectra.

The ESA spectroscopy method deals with measuring of optical transmission unpumped and pumped investigated media. Optical density of the specimen can be written in these two cases:

$$I_u = I_0 \exp\{-n_0 \sigma_1(\lambda) - \rho(\lambda)L\} \quad (3)$$

$$I_p = I_0 \exp\{-n_1 \sigma_1(\lambda) - n_2 \sigma_2(\lambda) - \rho(\lambda)L\}, \quad (4)$$

here I_u , I_p , I_0 - intensity of probe light passing through unpumped, pumped specimen and without specimen; n_1 , n_2 - populations of the ground and excited states, n_0 - dopant concentration; σ_1 , σ_2 - absorption cross-sections of ground and excited states; ρ - nonresonance absorption and scattering of 1 cm length of the media; L - optical length.

Suppose $n_0 \approx n_1 + n_2$ the variation of optical density Δk is:

$$\Delta k = (1/L) \cdot \ln(I_u/I_p) = n_2 [\sigma_2(\lambda) - \sigma_1(\lambda)] \quad (5)$$

There are two essential conclusions:

- the ESA method makes it possible to exclude background caused by the edge of fundamental absorption of the crystal host.
- in the region of ChT band usually $\sigma_2 \gg \sigma_1$ and

$$\Delta k \approx n_2 \sigma_2(\lambda) \quad (6)$$

this equation shows possibilities of measuring the spectrum of IT and ChT transitions with the same specimen. Indeed, varying intensity of the pump we change n_2 to obtain Δk in measurable diapason of optical density. The measurement of GSA does not allow this.

In the case of absence of metastable level among the energetical levels of dopant ion the ESA measurement can be carried out nevertheless. Indeed laser methods of pumping make it possible to populate even short life-time level. And large value of cross-section σ promotes to the measurement.

2. RESULTS AND DISCUSSION

2.1 Cr³⁺: Al₂O₃, Cr³⁺:MgAl₂O₄ crystals

The results of our measurements of Cr³⁺:Al₂O₃ crystal by ESA method at 300 and 77 K are given in Fig. 1. Table 1 shows parameters of these bands comparing with IT band transitions: Y-band ($^4A_2 \rightarrow ^4T_2$) and the band $^2E \rightarrow ^2A_2(t_{2g}^2)$. Intensity of these both bands are approximately equal, as they are both belong to IT transitions. As temperature decreases the intensity of these bands in any case does not diminish. Oscillator strength f (OS) of ChT band approximately 50 times larger than OS of another bands. It decreases of 10-15% as the temperature fall down from 300 to 77 K.

This effect of decreasing of OS ChT band more significant in Cr³⁺:MgAl₂O₄ crystal (Fig. 2, Table 2). The ratio (f₃₀₀/f₇₇)=2 in this case. It is possible to suppose that larger value of the ratio in the case of Cr³⁺:MgAl₂O₄ than Cr³⁺:Al₂O₃ can be explained by the fact that the symmetry of Cr³⁺ sites in magnesium spinel is higher than in ruby. Analogous situation was described by Ferguson et al¹⁴.

Comparing the results of ESA measurement of ChT bands with the results of GSA^{2,3} it can be seen that accuracy of the former method is higher than GSA method because of elimination of strong background of the fundamental absorption edge.

Table 1. Ground and Excited State Absorption bands in Ruby

Polarization	T(K)	GSA-band ${}^4A_2 \rightarrow {}^4T_2(t_2^2, e)$		ESA-band ${}^2E \rightarrow {}^2A_2(t_2^2, e)$		Charge Transfer band (ESA)	
		Position (eV)	Oscillator strength	Position (eV)	Oscillator strength	Position (eV)	Oscillator strength
$E \perp c$	300					6.86	$9.6 \cdot 10^{-2}$
	77					6.91	$8.6 \cdot 10^{-2}$
$E \parallel c$	300		$2.3 \cdot 10^{-3}$		$1.8 \cdot 10^{-3}$	6.86	$8.8 \cdot 10^{-2}$
	77				$2.2 \cdot 10^{-3}$	6.91	$7.5 \cdot 10^{-2}$

Table 2. ESA bands of Magnesium Spinel (MgAl₂O₄:Cr³⁺)

T(K)	ESA-band ${}^2E \rightarrow {}^2T_2(t_2^2, e)$		Charge Transfer band ${}^2E \rightarrow (\text{ChT})$	
	Position (eV)	Oscillator strength	Position (eV)	Oscillator strength
300	3.84	$4.2 \cdot 10^{-4}$	6.75	$3.4 \cdot 10^{-2}$
77	4.0	$6.8 \cdot 10^{-4}$	6.75	$1.6 \cdot 10^{-2}$

2.2 Ti³⁺:Al₂O₃ crystal

Next point of our interest is ChT band of Ti³⁺:Al₂O₃ crystal. In the GSA spectra it appears at 220 nm (5.64 eV) and at 3.04 eV in ESA spectra (Fig. 3). Observation of the ChT band in Ti³⁺:Al₂O₃ and its position in the spectra allows us to combine the energetical levels diagram of Ti³⁺ ion with transfer zone of the crystal (Fig. 5). The experimental results of Basun et al⁴ on two-step photoionization of titanium sapphire coincide with our ESA data. Indeed as can be seen from Fig. 5 when the Ti³⁺:Al₂O₃ crystal is pumped by N₂- and Cu-lasers simultaneously ($\lambda_{\text{Cu}}=2.43$ eV, $\lambda_{\text{N}2}=3.7$ eV) electrons first populate the lower excited level and than ChT band. The photocurrent appears under action of N₂ and Cu - lasers trough the specimen⁴.

2.3 Cr³⁺:Li₂Ge₇O₁₅ (Cr³⁺:LGO) crystal

In Cr³⁺:LGO crystals the "classic" high crystal field spectra of Cr³⁺ ions in octahedral symmetry sites take place. There are two broad absorption bands at 600 nm (${}^4A_2 \rightarrow {}^4T_2$) and 420 nm (${}^4A_2 \rightarrow {}^4T_1$), sharp R-lines (${}^4A_2 \rightarrow {}^2E$) at 695 nm. Through the region of 650-800 nm the Cr³⁺:LGO shows strong wide -band luminescence. At 10°C the LGO crystal undergoes the ferroelectric transition D_{2h} → C_{2v}.

The edge of fundamental absorption pure LGO crystal was found at 250 nm (4.96 eV). For Cr³⁺:LGO crystals very strong absorption band arises at 320 nm (3.9 eV) (GSA method). Measurement of ESA-spectra of the Cr³⁺:LGO shows very strong absorption trough the whole spectral region (Fig. 4). On the smooth curve of ESA spectra it can be seen slight maxima at 420, 470 and 530 nm. We suppose that these maxima correspond to transitions to doublet excited states c ${}^2T_2(t_2^2, e)$, c 2T_1 , b 2T_1 , c 2T_2 .

Excitation Cr³⁺:LGO by Ar- and He-Ne lasers simultaneously induce photocurrent (I) which is quadratic to pumping light intensity P (I~P²)¹⁵. It is known, that Powell¹⁶ fulfilled the experiment for obtaining lasing of Cr³⁺:LGO crystals

in R-lines. There was not any laser effect. Analogous attempt was undertaken by us. We investigated possibility of obtaining laser effect in diapason of wide-band luminescence of Cr³⁺:LGO. It is known that forecast of laser properties of media convenient to carry out with the help of McCumber's¹⁷ equations. But in these equations ESA spectrum does not take into account. If modify McCumber's equations and include in the term describing excited absorption, the formula for gain of the media is in the form:

$$G_\lambda(w) = g_\lambda(w) - A_\lambda^{ESA}(w) \quad (7)$$

here

$$g_\lambda(w) = \left[\frac{2\pi c}{wn_\lambda(w)} \right]^2 f_\lambda(w) N_0 \left[p^+ \left(1 + e^{-\frac{\hbar(w-w_0)}{kT}} \right) - e^{-\frac{\hbar(w-w_0)}{kT}} \right] \quad (8)$$

$$A_\lambda^{ESA}(w) = \left[\frac{2\pi c}{wn_\lambda(w)} \right]^2 f_\lambda(w) N_0 \left[p^+ \frac{\sigma_{e\lambda}^{ESA}(w)}{\sigma_{e\lambda}(w)} \right] \quad (9)$$

Here $g_\lambda(w)$ is the McCumber's expression for gain of the media without taking into account of ESA spectra, $A_\lambda^{ESA}(w)$ - term caused by ESA absorption; $\sigma_{\lambda}^{ESA}(w) = a_\lambda^{ESA}(w)/N_+$, $a_\lambda^{ESA}(w)$ - absorption coefficient of ESA, N_+ - population of excited state. McCumber's analysis of Cr³⁺:LGO without ESA absorption gives for gain $g_\lambda(w)$ maximum value $5 \cdot 10^{-21} \text{ cm}^2$. But ESA exceeds about 10^{-18} cm^2 approximately constant throw the whole diapason of luminescence. Than Cr³⁺:LGO can not be a pretender as laser material neither three level nor wide band scheme.

3. ACKNOWLEDGMENTS

The author is thankful to colleges V.P.Orekhova, M.Yu.Sharonov and O.V.Kravchuk for help in experiment, discussions and preparing this paper.

4. REFERENCES

1. D.S. McClure, "Electronic spectra of Molecules and Crystals", *Solid State Phys.*, Vol. 8, pp.1-47, pp.399-525, 1959.
2. H.H.Tippins, "Charge transfer Spectra of Transition-Metal Ions in Corundum", *Phys.Rev.*, B.1., N1, pp.126-135, 1970.
3. J.F.Sabatini, A.E.Salwin, and D.S. McClure, "High-energy optical absorption bands in transition-metal ions in fluoride host crystals", *Phys.Rev.*, B.11, pp.3832-3841, 1975.
4. S.A.Basun, S.P.Feofilov, A.A.Kaplyanskii, B.K.Sevastyanov, M.Yu.Sharonov, and L.S.Starostina, "Photoelectric studies of two-step photoionization of Ti³⁺ ions", *Journal of Luminescence*, Vol. 53, pp.28-31, 1992.
5. K.Petermann, "The role of excited-state absorption in tunable solid-state laser", *Optical and Quantum Electronics*, Vol.22, pp.199-218, 1990.
6. P.F.Gires and G.Mayer, "Proprietes optiques du rubis fortement exite", *Ann. de Radioelectricite*, Vol. 18, N 72, pp.112-122, 1963.
7. T.Kushida, "Absorption Spectrum of Optically Pumped Ruby. I Experimental Studies of Spectrum in Excited States", *J. Phys Soc. Jap.*, Vol. 21, N7, pp.1331-1341, 1966.
8. B.K.Sevastyanov, V.P.Orekhova, "Optical spectra of excited Cr³⁺ ions in magnesium spinel MgAl₂O₄", *Quantum Electronic* (Soviet), Vol. 1, pp.125-134, 1971 (Russian).
9. D.T.Sviridov, B.K.Sevastyanov, V.P.Orekhova, R.K.Sviridova, T.F.Veremeichik, "Optical absorption Spectra of Excited Cr³⁺ ions in MgAl₂O₄ at 300 and 77 K", *Optica and Spectroscopy*, Vol. 35, pp. 102-107, 1975.
10. B.K.Sevastyanov, D.T.Sviridov, V.P.Orekhova, L.B.Pasternak, R.K.Sviridova, T.F.Veremeichik, "Optical absorption spectra of excited Cr³⁺ ions in Y₃Al₅O₁₂", *Quantum Electronics* (Soviet), Vol.4(10), pp. 55-62, 1972, (Russian).
11. B.K.Sevastyanov, Yu.L.Remigailo, T.F.Veremeichik, V.P.Orekhova, "Excited State Absorption of Alexandrite", *Reports of Academy of Science of the USSR* (Russian), Vol.285, N 5, pp.1119-1124, 1985.

12. B.K.Sevastyanov, "ESA-spectroscopy of crystals doped with Cr³⁺ ions", (Rewiew), in "Spectroscopy of the Crystals", "Nauka" (Science), Leningrad,pp. 122-154, 1975,(Russian).
13. B.K.Sevastyanov, "Excited State spectroscopy of laser crystals and tunable lasers", in "Proc. of the Indo-USSR workshop on Growth and Charakterization of laser and no-linear crystals", ed. by G.P.Kothiyal and B.Ghosh.,Bhaba Atomic Research Center, Bombay ,pp.1-42, 1988.
14. J. Ferguson, D.L.Wood, and K.Knox, "Crystal-Field spectra of d³, d⁷ ions. II. KCoF₂, CoCl₂, CoBr₂ and CoWO₄", *J. Chem. Phys.*, Vol. 39, N4, p.881-889 ,1963.
15. S.A.Basun, S.P.Feofilov, A.A.Kaplyanskii, A.B.Bykov, B.K.Sevastyanov, and M.Yu.Sharonov, "Dynamical electron and phonon processes in the excited state of Cr³⁺ : LGO crystals",*Journal of Luminescence*, Vol. 53, pp. 24-27,1992.
16. R.C.Powell, "Energy Transfer between Chromium Ions in Nonequivalent Sites in Li₂Ge₇O₁₅", *Phys. Rev.*, Vol. 173, N 2, pp. 358-373, 1968.
17. D.E. Mc Cumber, "Theory of Phonon-Terminated Optical Masers", *Phys. Rev.*, Vol. 134, pp.A 299 - A306, 1964.

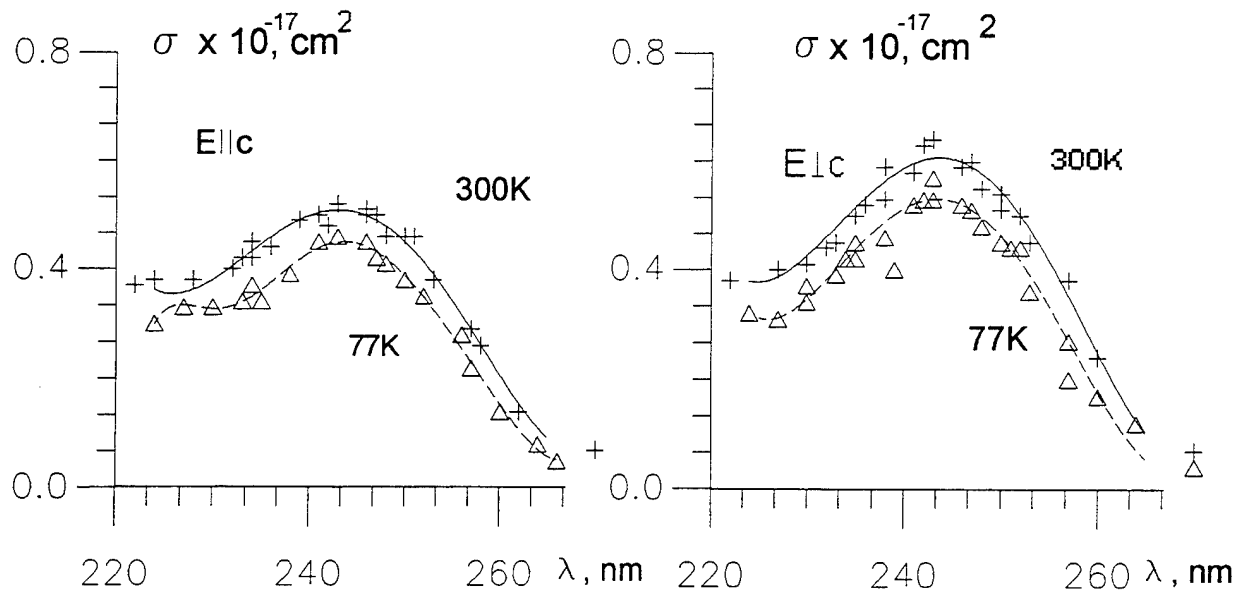


Fig.1 Charge Transfer Band in ESA Spectra of Cr^{3+} : Al_2O_3

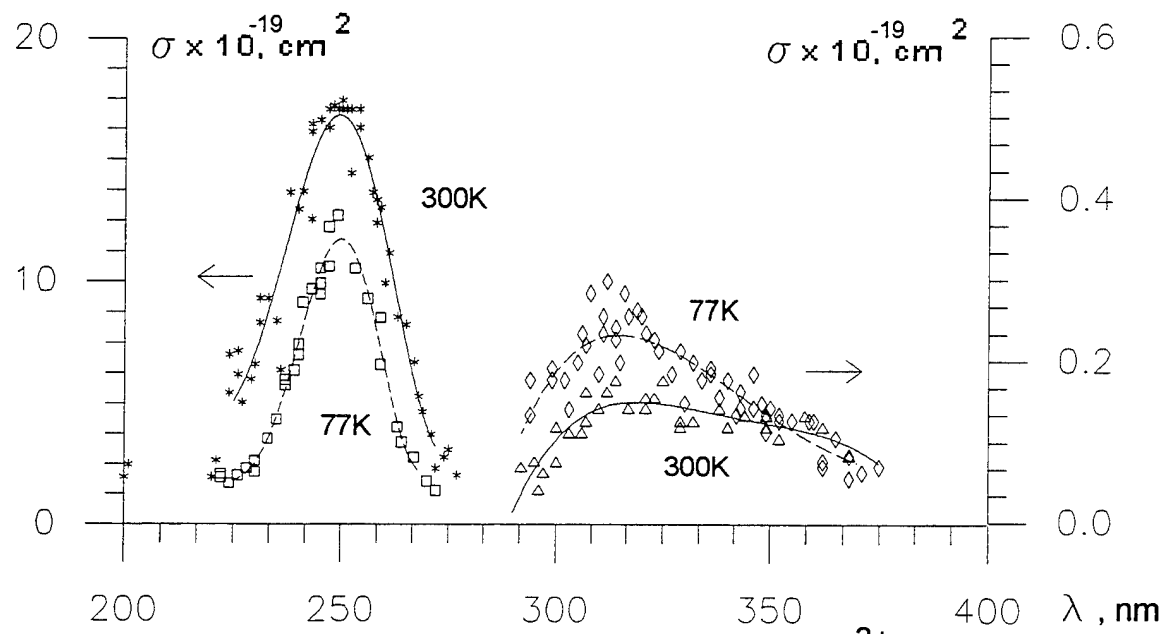


Fig.2 Excited State Absorption Spectra of Cr^{3+} : MgAl_2O_4

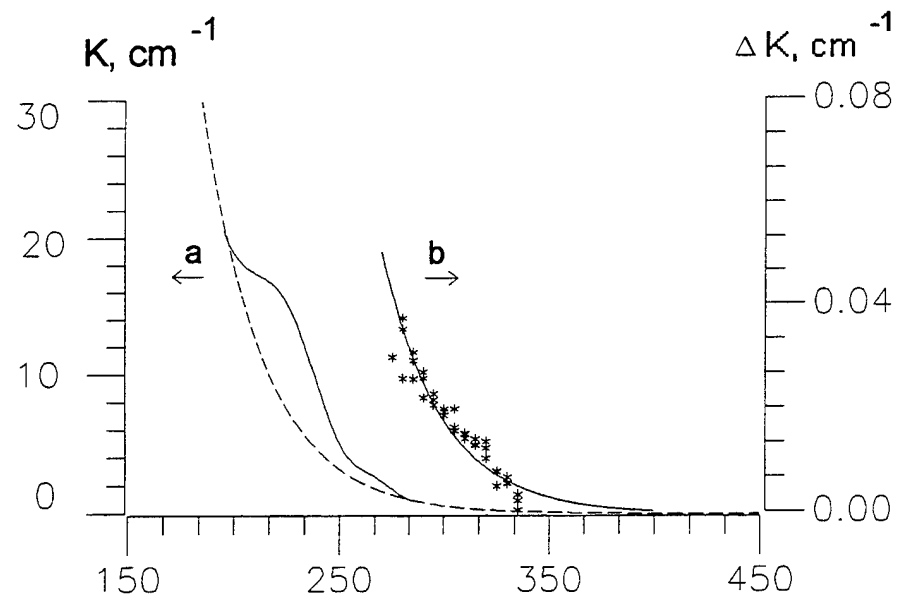


Fig.3 Charge Transfer Bands in GSA (a) end ESA (b)
Spectra of $Ti^{3+}:Al_2O_3$

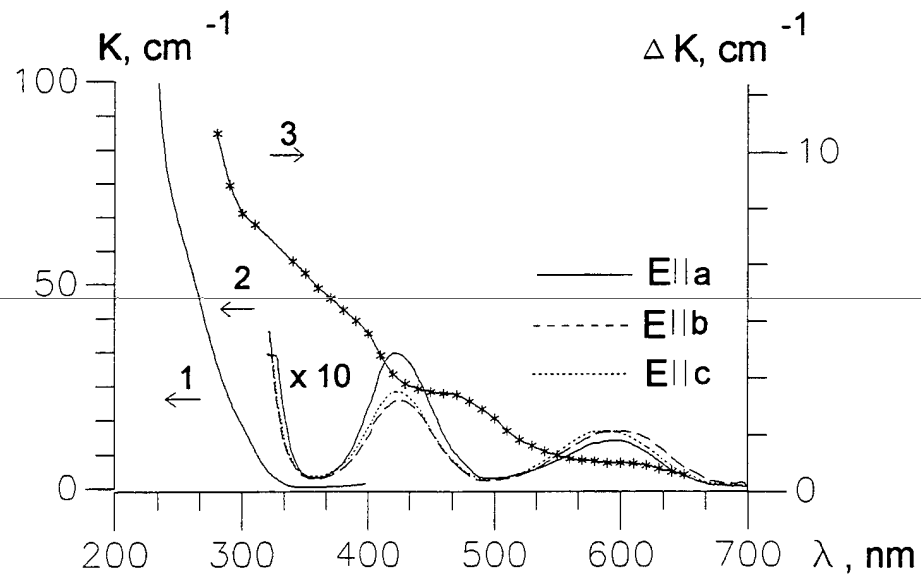


Fig.4 GSA (1,2) and ESA (3) Spectra of $Cr^{3+}:LGO$

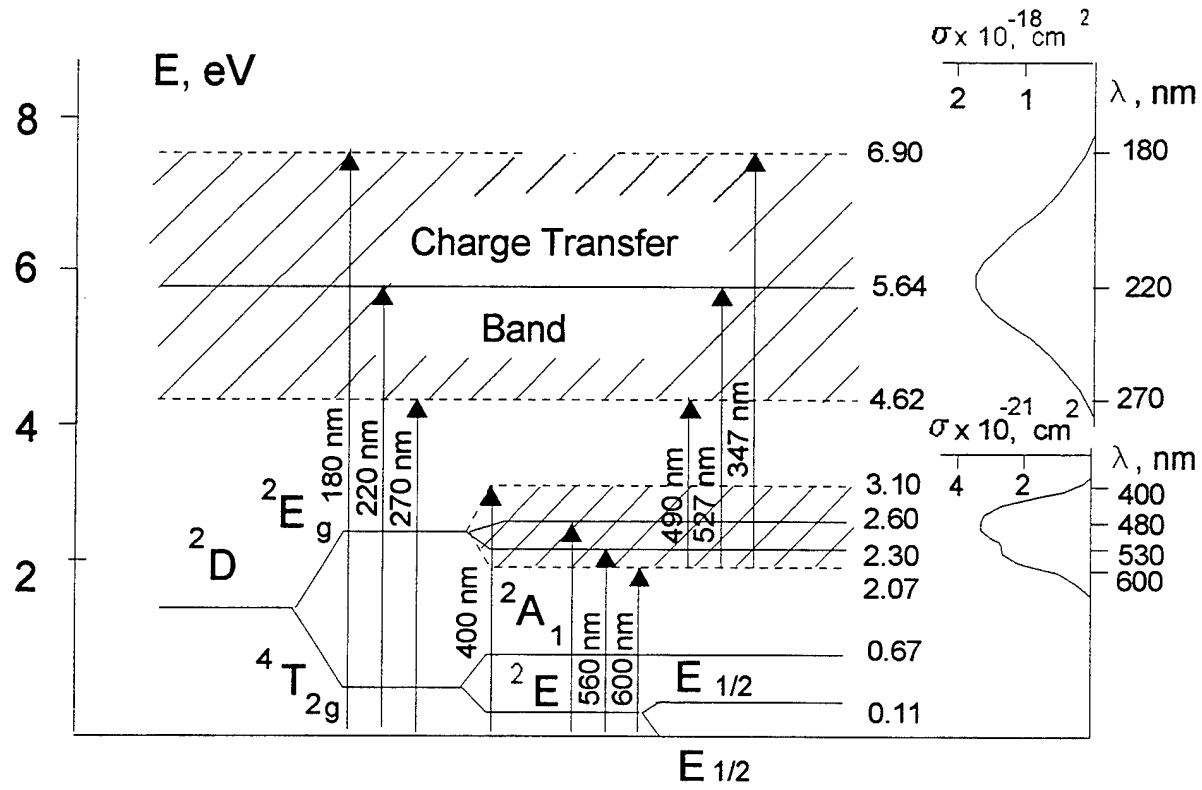


Fig.5 Energy levels diagram of Ti^{3+} : Al_2O_3 crystal

EXCITED STATE ABSORPTION SPECTRA OF RE-DOPED LASER GLASSES

A.K.Przhevuskii and M.Yu.Kirshin

Research and Technological Institute of Optical Materials
36/1, Babushkina St., 193171, St. Petersburg, Russia

ABSTRACT

Recent data on the excited state absorption (ESA) in the glasses doped with Nd^{3+} , Er^{3+} , Pr^{3+} is reviewed. In particular, the data on Russian commercial laser glasses are presented. The different techniques applied to obtain ESA data are analyzed and classified into two groups: 1) the methods using indirect measurements and based on the results of approximate theories, 2) the methods using direct spectral measurements of the pumped samples. The possibilities of predictions of glass composition effect on the ESA are considered.

1. INTRODUCTION

Recent development of RE-doped glasses for lasers and amplifiers put in the forefront the investigation of the excited state absorption (ESA) corresponding to optical transitions from states excited with pumping. ESA exerts influence on operation of optical amplifiers in a variety of fashions. If frequency of ESA coincides with signal frequency, the gain is determined by the difference of stimulated emission cross-section $\sigma_{\text{em}}(\nu)$ and excited state absorption cross-section $\sigma_{\text{ESA}}(\nu)$. As a result, ESA decreases gain and may transfer gain into loss if $\sigma_{\text{ESA}} > \sigma_{\text{em}}$. Such case is for glasses with neodymium¹⁻³ and praseodymium^{4,5}, which are promising candidates for fiber amplifier in the $1.3\mu\text{m}$ region. Another negative influence of ESA on amplifier parameters takes place if ESA bands overlap with ground state absorption bands. This overlap decreases the efficiency of pumping in relevant spectral regions. This is the situation for erbium doped glasses⁶.

ESA can manifest itself not only as negative factor. It can provide stepwise up-conversion pumping. The pumping of this type was realized in Tm^7 , Ho^8 , Pr^9 , and Er^{10} fibre lasers. Positive ESA influence on laser operation may consist also in depopulation of the final level of stimulated transition as in case of $2.7\mu\text{m}$ CW erbium fiber laser¹¹.

The above-mentioned ESA effects are necessary elements of fiber amplifier models. The modeling of amplifiers on Pr-, Nd-, and Er-doped fibers has shown that ESA governs gain characteristics, quantum conversion efficiency and other important parameters of these devices¹²⁻¹⁶.

Although the attempts to measure ESA in RE-doped glasses had been making since 60th, obtained results were few in number until recent time because experimental difficulties¹⁷⁻²⁰. The development of RE-doped fiber n offered new experimental technique for these measurements. Samples in fiber form allow to reach more efficient pumping than bulk samples with less powerful sources. As a consequence, a lot of information on ESA in RE-doped glasses was obtained and new techniques for this purpose were proposed in last few years. In this paper we review the data on ESA in RE-doped glasses and the methods used to obtain them. In particular, the data on Russian commercial neodymium laser glasses are presented.

2. METHODS FOR DETERMINATION OF ESA IN RE-DOPED GLASSES

In describing the methods used for determination of the ESA parameters, we classify them into two groups. In the first group we place "indirect" methods, in which ESA does not occur. These methods are based on results of some theories connecting ESA parameters with other ones. In the second group we place methods, where in the course of measurement ESA process occurs really. First we consider the indirect methods.

2.1. Application of the Judd theory.

According to this theory the line strength s corresponding to the optical transitions in 4f electron shell between manifolds SLJ and $S'L'J'$ may be represent in the form²¹

$$S = \sum_{\lambda=2,4,6} |\langle u^\lambda \rangle|^2 \Omega_\lambda , \quad (1)$$

where $|\langle u^\lambda \rangle|$ are double reduced matrix elements, which exhibit negligible variations with host, and Ω_λ are Judd parameters embodied host effects. Thus line strengths of all optical transitions RE ion in a particular host are completely determined by three parameters Ω_λ . Having found the values of these parameters from measurements of usual ground state absorption spectrum, one can calculate from (1) line strength of any other optical transition - for instance, ESA transitions. The line strength value allows to determine the other integral intensity parameters - oscillator strength and integral cross section²².

Such procedure was first used by Krupke^{22,23} in his study of ESA parameters for neodymium laser glasses. At a later time this method was applied many times^{15,24-27,35}. The matrix elements for ESA transitions are tabulated in ²⁴ (Nd) and in ²⁸ (all RE ions). When the possibility was to compare results of application of relation (1) with experimental data the disagreement was usually no more than 20%. It is something of a mystery because Judd theory is based on assumptions that fail badly for RE ions. The Judd analysis gives parameters defining integral intensities of ESA bands. In order to find the spectral shapes of these bands one of the following methods can be used.

2.2. Application of the thermodynamic relation between absorption and fluorescence spectra³⁰.

If lifetime of final state L'S'J' of ESA transition LSJ->L'S'J' is large enough to observe the reverse radiation transition L'S'J'->LSJ, than the shape of relevant fluorescence band can be used to find the shape of ESA band from the following relation²⁹:

$$\sigma_a(v) = \sigma_e(v) \exp[(hv - \mu)/kT] , \quad (2)$$

where σ_a , σ_e , are absorption and emission cross-sections respectively, μ is an effective energy gap between the states, and kT is Boltzmann's factor.

This method was first applied to Pr³⁺ ions in fluorozirconate glass ZBLAN³⁰, and then to Pr³⁺ in cadmium halide and sulphide glasses³¹. The merit of the method is that it can be used in cases when the initial state of ESA transitions has short life time and poor population. The necessary condition for the method is possibility to observe the fluorescence from final ESA state.

Relation (1) implies that thermodynamically equilibrium distribution exists over the energy levels of initial and final manifolds. In case of inhomogeneous spectral contour the equilibrium must be established in ensemble of inhomogeneous optical centres³². This means that the rate of energy migration between rare earth centres must be higher than the rate of decay of excited state. The last condition may be difficult attained in some cases since the increase of activator content results in growing not only migration rate but decay rate as well because of cross relaxation.

2.3. Measurement of excitation spectrum of upconversion fluorescence.

This method and the following one can be named as "direct" because they are performed under conditions where ESA really occurs. In measurement of excitation spectrum the intensity of upconversion fluorescence is monitored when wavelength of exciting laser light is scanned. The excitation consists of two steps, at the first step, GSA occurs, and at the second one, ESA takes place. The pump wavelength dependence of fluorescence intensity $J(\lambda)$ is³³

$$J(\lambda) \sim I^2(\lambda) \lambda^2 \sigma_{GSA}(\lambda) \sigma_{ESA}(\lambda) , \quad (3)$$

where $I(\lambda)$ is intensity of exciting beam, and σ_{GSA} and σ_{ESA} are cross sections of GSA and ESA respectively. Having measured $\sigma_{GSA}(\lambda)$ in separate experiment, one can obtain $\sigma_{ESA}(\lambda)$ dependence from (3). It should be

pointed that relation (3) does not take into account the excitation distribution over the Stark sublevels after the first step. In this way the ESA spectra of erbium-doped glasses were measured in $1\mu\text{m}$ region³³ and $1.5\mu\text{m}$ region³⁴. It should be noted that fluorescence is measured in spectral region different from ESA region. This allows to avoid spurious signals and to use the detector of high sensitivity.

2.4. Pump-probe technique.

In this subsection several methods are combined whose specificity is measurement of transmission of tunable probe beam while the sample is pumped. This technique was the first one used to determine ESA spectra in RE-doped glasses. In the early experiments the samples in the form of laser rod were maintained in cavity reflector and were pumped with flash lamp. Only for Er³⁺- and Sm²⁺-doped glasses such conditions could provide the pumping that permitted to measure ESA certainty. Parasitic signals from pumping light and luminescence of sample hampered measurements.

As noted above, the development of RE-doped fiber brought into existence the new modifications of probe-pump method. The fiber form of sample gives possibility to obtain high density of pumping light with CW laser of moderate power. It allows to use modulation technique providing the sensitivity of comparing probe beam intensities with and without pumping.

Several investigations with pump-probe method were carried out on single mode fibers³⁶⁻³⁸. The pumping power about several mW was large enough to detect ESA in these fibers. However, the production of such samples is too complicated in order to use them for investigation of glass composition effects. That is why the modification of method came into use that permitted to study the hand-drawn, unclad fibers with diameter about $100\mu\text{m}$ ³⁹. Apparatus of this type we used in study of ESA spectra of Nd-doped glasses. It is described below. Completing this section we shall point out two specific variants of probe-pump technique.

The first one was used by Vance in study of ESA in neodymium laser glasses in $1.06\mu\text{m}$ region. The sample heated to populate $^4\text{I}_{11/2}$ level was irradiated with intense $1.06\mu\text{m}$ laser beam that played two roles, namely, pumping source and probe light. Under such conditions $^4\text{I}_{11/2} \rightarrow ^4\text{F}_{3/2}$ transition was saturated. From analysis of saturation curves Vance determined that ESA cross section at $1.06\mu\text{m}$ equal one-third the stimulated emission cross section. The further investigations have shown that this estimation is too high.

The other specific variant of probe-pump method described in paper⁴⁰ is based on measurement and analysis of amplified spontaneous emission (ASE) spectra. In this method the neodymium glass rod in cavity reflector was pumped by flash lamp and ASE spectra were measured for two cases of apparatus arrangement. In one case a mirror was situated behind the sample so that the feedback light passed through sample and was detected. In other case the mirror and feedback light were lacking. Comparing ASE spectra for these two cases, the authors⁴⁰ determined spectra of ESA and stimulated emission. The advantage of this approach is that fluorescence light is used as the probe one whereas in other variant of pump-probe technique it is source of parasite signals. However this approach permits to determine ESA only in spectral regions of fluorescence.

3. EXPERIMENT

Scheme of our apparatus realizing pump-probe technique is shown in Fig.1. In principal features it follows works³⁹. The tungsten lamp is used as source of probe light and krypton laser is used for pumping. The principle of measurement of small variations of sample transmission consists in the application of two modulations and two lock-in amplifiers. The modulation of laser beam (10Hz) is applied in order to increase accuracy of comparing the probe light intensities with and without pumping. The modulation of probe light (1000Hz) is used to avoid fluorescence signal. The first lock-in amplifier is tuned to frequency of probe light. The time constant of this amplifier is chosen so small that output signal contains the frequency of laser modulation. The second lock-in amplifier is tuned to frequency of 10Hz and detects signal in usual way with large time constant. After passing sample, a probe light is analyzed with double monochromator and is detected with germanium photodiode. In spectral regions where ESA overlaps with fluorescence, the 10Hz signal on photodiode may be very high. To eliminate from it, the frequency filters serve in the first lock-in and in circuit

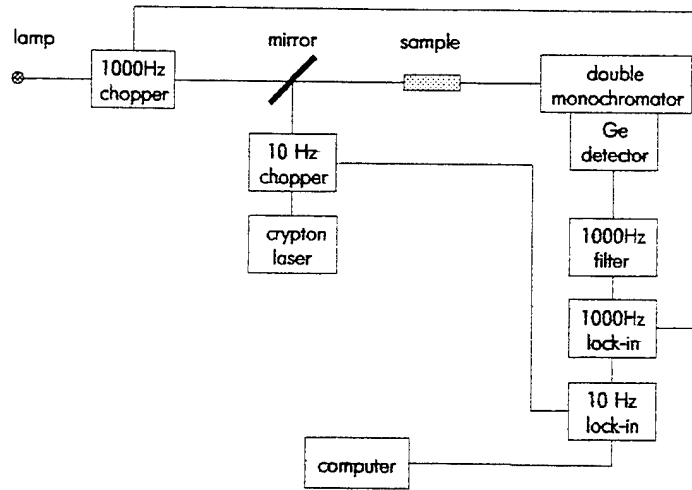


Fig.1. Scheme of apparatus used to measure ESA spectra

after photodiode. For increasing a signal/noise ratio, a signal was transformed in digital form and was processed with PC IBM-386.

The two commercial Russian laser glasses were investigated - silicate GLS-2 and phosphate GLS-22 with neodymium density $\sim 2 \cdot 10^{20} \text{ cm}^{-3}$ in both. The samples had fiber form $\sim 5\text{cm}$ in length and $\sim 100\mu\text{m}$ in diameter. In measurement they absorbed $\sim 0.5\text{W}$ of krypton laser radiation at 531nm .

In accordance with diagram of Nd^{3+} energy levels, the two ESA bands locate in the spectral region $1.2\text{-}1.4\mu\text{m}$. They correspond to the following transitions: $^4F_{3/2} \rightarrow ^4G_{9/2}$ ($1.24\mu\text{m}$) and $^4F_{3/2} \rightarrow ^4G_{7/2}, ^2K_{13/2}$ ($1.3\mu\text{m}$). On the basis of Judd theory, we determined the integral values of cross section $\int \sigma(v)dv$ for these bands using Ω_λ parameters obtained from GSA spectra⁴¹. These data as well as data for emission transition $^4F_{3/2} \rightarrow ^4I_{13/2}$ are presented in table 1.

Table 1.
Integral cross section $\int \sigma(v)dv, 10^{18}\text{cm}$

Transition	GLS-2	GLS-22
$^4F_{3/2} \rightarrow ^4G_{9/2}$	1.4	2.4
$^4F_{3/2} \rightarrow ^4G_{7/2}, ^2K_{13/2}$	1.3	1.9
$^4F_{3/2} \rightarrow ^4I_{13/2}$	1.5	2.7

The ESA band in region $1.24\mu\text{m}$ is higher in intensity than $1.31\mu\text{m}$ band and which is more it does not overlap with luminescence band. The difficulties of its measurement are limited to the improving of signal/noise ratio. The obtained spectra are presented in Fig. 2,3. They are normalized by square under spectral shape in accordance with data table 1.

For both glasses in spectral region $1.27\text{-}1.40\mu\text{m}$ where ESA overlapped with fluorescence, our apparatus recorded a sum of useful signal and masking one. We found that masking signal is caused by nonlinear

properties of our apparatus. The amplitude of masking signal was proportional to intensity of probe light and intensity of fluorescence as well. By virtue of the fact that the spectral dependence of masking signal reproduced the contour of fluorescence band $^4F_{3/2} \rightarrow ^4I_{13/2}$, the useful signal was found as difference between experimental spectral shape measured with our apparatus and fluorescence shape. The needed normalization of spectral shapes was performed so that values of integral cross sections for ESA $^4F_{3/2} \rightarrow ^4G_{7/2}, ^2K_{13/2}$ and for stimulated radiation $^4F_{3/2} \rightarrow ^4I_{13/2}$ were consistent with data of table 1.

Fig.2 and 3 show obtained spectra. They exhibit the same features as neodymium ESA spectra published in paper¹⁵. The spectra possess region where ESA exceeds gain and region where gain exceeds ESA.

4. DISCUSSION

To give an insight into the state of investigations of ESA spectra in RE-doped glasses we present in table 2 the list of all works in this field that we are familiar with. Addressing to this table we discuss below the state of experimental technique, some effects of glass composition and the problem of prediction of ESA spectrum's variation with composition.

4.1. The state of experimental technique.

Table 2 shows that presently every particular method of ESA spectrum measurement is applied to definite class of cases. This is because the cases essentially differ in life times of states between which ESA transitions occur. Different methods are based on these differences and complement each other. The cases when different methods can be applied are few in number. Up till now we have no possibility to compare the ESA spectra obtained with several methods for one glass.

The measurement of ESA spectra with pump-probe method in spectral range where ESA overlaps with fluorescence is of particular difficult. Important example is ESA spectrum of neodymium glasses in region $1.3\mu\text{m}$. The cause lies in the fact that ESA signal is measured on the background of intense fluorescence signal. Arising difficulties were noted in describing our experiments. It seems likely that the significant noise on spectra of paper and essential difference between data³⁶ and are resulted from the same cause. Improvement of experimental technique for this case is desirable.

4.2. Effect of glass composition.

As expected, the variations of ESA spectra with glass composition are similar to variations of GSA spectra. We set off two groups of compositions from data of table 2. In the first group we place nonoxide glasses (fluorine and sulphite ones). It is known that the probabilities of nonradiative transitions for number of states RE ions in these glasses are essentially smaller than similar probabilities in oxide glasses because of the fact that the border frequency of vibronic spectrum is smaller. As a result the possible ESA transitions in nonoxide glasses are more numerous than in oxide ones and ESA can be studied with use of methods inapplicable to oxide glasses. As the examples ESA transitions from $^4I_{11/2}, ^4F_{9/2}$ states in Er^{3+} and from $^{11}G_4$ state in Pr^{3+} (table 2) are. Another features of ESA spectra of nonoxide glasses consist in shift of all bands in highfrequency side for reason of variation of covalence of chemical bonds RE with ligands.

Silica glasses doped with Al, P, Ge, F comprise the second group of compositions that should be pointed. These compositions were studied for purpose of fiber communication. Tightly coordinated structure of silica glass makes the introduction of RE ion difficult, which leads to arrangement of RE ion near doping ions, clustering RE ions, and to the fact that spectra of RE ions in silica differ from spectra of RE ions in all other oxide glasses. Such specificity manifests itself in ESA spectra of Er^{3+} ³⁹ and Nd^{3+} ³⁶. Clustering Er^{3+} ions was shown to exert influence on the pumping dependence of ESA⁴³. All properties of silica glasses are very sensitive to variations of doping addition. For instance the addition of Al_2O_3 results in disappearance of Er ion clustering.

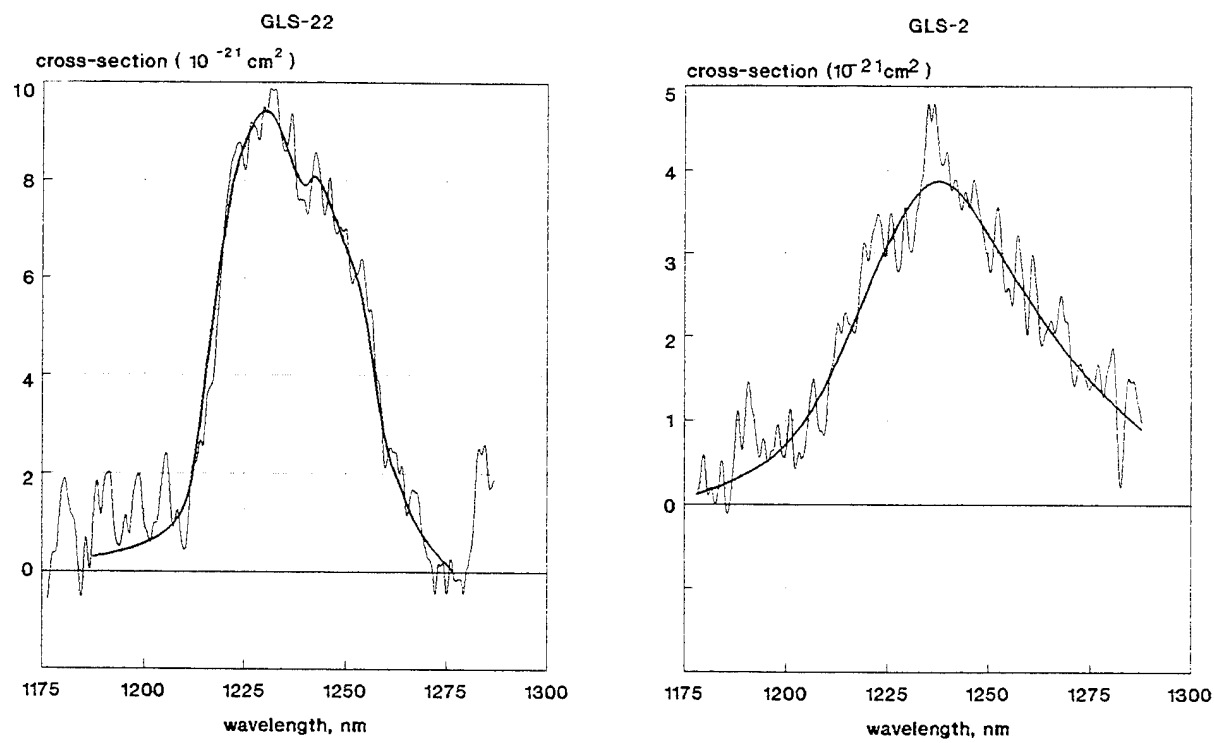


Fig.2. ESA spectra of phosphate glass GLS-22 and silicate glass GLS-2

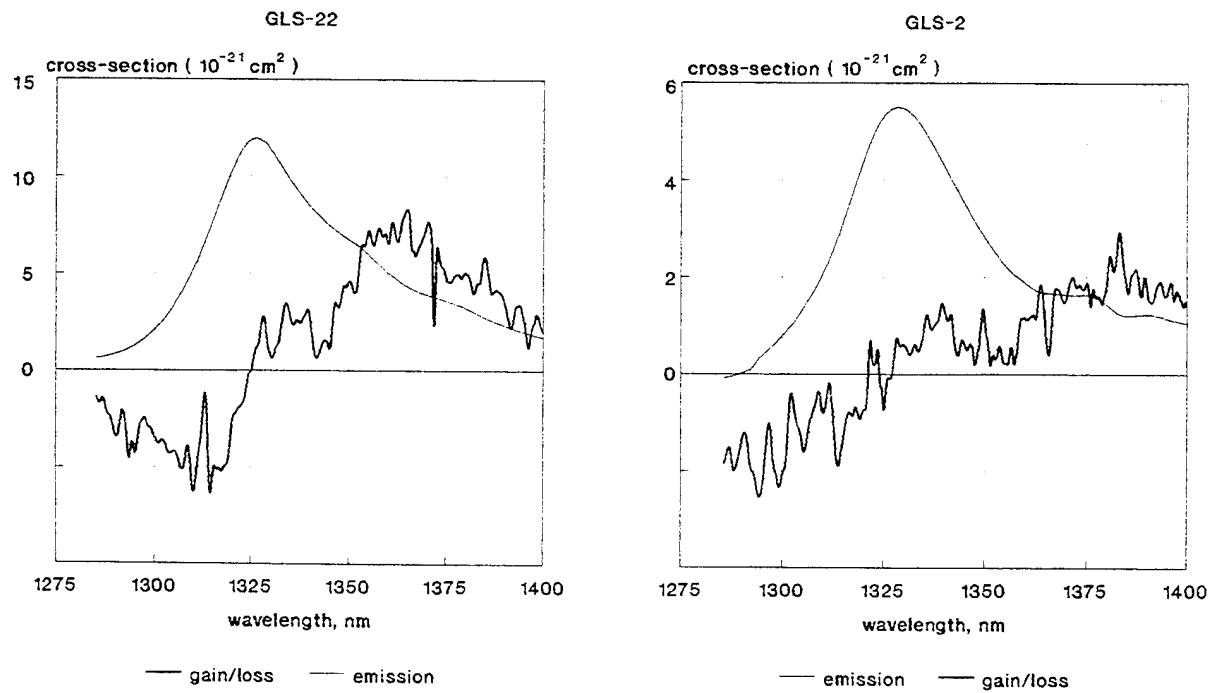


Fig.3. Gain/loss and emission cross-section spectra of phosphate glass GLS-22 and silicate glass GLS-2.

Data on ESA spectra of RE-doped glasses

Table 2.

RE ion	Glass	Spectral region of measurement Initial state of ESA transitions	Method*	Refer.
Er ³⁺	Li-Mg-Al silicate; Na-Al phosphate	460-1700nm; $^4I_{13/2}$	PP	18
Er ³⁺	K-Na-Ba silicate	460-700nm; $^4I_{13/2}$	PP	17
Er ³⁺	silicate (Yb); phosphate (Yb)	1050-1150nm; $^4I_{13/2}$	PP	42
Er ³⁺	silica (Ge, P, Al, F); fluorozirconate ZBLAN	420-850nm, detailed results for 650nm and 800nm; $^4I_{13/2}$	PP	38
Er ³⁺	silica (Ge, B, P, Al)	470-850nm; $^4I_{13/2}$	PP	37
Er ³⁺	silicate, fluorozirconate, phosphate, fluorophosphate	760-900nm; $^4I_{13/2}$ (all hosts), $^4I_{11/2}$, $^4F_{9/2}$ (fluorozirconate)	PP	39
Er ³⁺	fluorophosphate, fluorozirconate	940-1000nm; $^4I_{11/2}$	FES	33
Er ³⁺	silica (Al, P)	1460-1640nm; $^4I_{13/2}$	FES	34
Nd ³⁺	silica (Ge, Al)	900-1400nm; $^4F_{3/2}$	PP	36
Nd ³⁺	fluorozirconate ZBLAN	1260-1380nm; $^4F_{3/2}$	PP	3
Nd ³⁺	silicate LG680, phosphate LG760	regions of emission bands $^4F_{3/2} \rightarrow$ $^4I_{9/2}$, $^4I_{11/2}$, $^4I_{13/2}$; $^4F_{3/2}$	PP	40
Nd ³⁺	silicate ED2, phosphate LHG8, fluorophosphate (high F, low F), fluoroberyllate, fluorozirconate	1160-1400nm; $^4F_{3/2}$	PP	15
Nd ³⁺	silicate GLS-2, phosphate GLS-22	1160-1400nm; $^4F_{3/2}$	PP	present paper
Pr ³⁺	fluorozirconate ZBLAN	700-1000nm, 1200-1600nm; 1G_4	AFR	30
Pr ³⁺	Cd-halide, Ga-sulphite	1200-1600nm; 1G_4	AFR	31
Sm ²⁺	silica (Al)	1200-1700nm; 5D_0	PP	19

* PP - pump probe ; AFR - absorption fluorescence relation ; FES - fluorescence excitation spectrum

4.3. Prediction of variation of ESA with composition.

In principle, the prediction problem for ESA spectra does not differ from similar problem for GSA spectra. As to integral intensities, their values can be evaluated from (1) applying the numerous published data on Judd parameters for glasses of diverse compositions. Empirical dependencies of Judd parameters on glass composition

can serve for prediction of the integral intensities of ESA spectral bands. An example of such analysis was performed in paper²⁶. In order to estimate Nd-doped glass as possible material for amplifier at 1.3μm the authors introduced the following Figure of Merit (FM)

$$FM = \tau(f_{se} - f_{ESA}) \quad (4)$$

where: f_{se} and f_{ESA} are oscillator strengths for stimulated emission and ESA correspondingly; τ is lifetime of excited state. The calculation with the use of relation (1) and published data on Judd parameters exhibited that FM values were greatest for fluoroberyllate glasses and were smallest for silicate ones (even negative for some compositions).

The prediction of position and spectral shape is more difficult. In paper⁴⁴ the spectral positions of neodymium ESA bands for alkaline fluorozirconate glasses were estimated as difference of positions of corresponding bands in GSA spectra. The measurement showed that the whole range of variation of ESA band position was only about 4nm with exchange alkaline type from Li to Cs. As this value is only ~0.1 of ESA bandwidth, the variations in shape may be more important for quantum electronics applications.

As far as we know the prediction of ESA band shape was not attempted although this property is very important for lasers and optical amplifiers, especially when their performance is controlled by difference between ESA and GSA spectra, or ESA and stimulated emission spectra. Such difference is very sensitive to glass composition as was shown for Nd-doped glasses in 1.3μm spectral region^{15,36}. We suppose that the prediction of spectral shapes can be based on spectrum classification described in paper⁴⁵. Investigation of Nd-doped glasses presented in this paper has shown that there are a number of cases when the same spectrum was obtained for glasses of different glass formers. It was proved that all the multiformity of neodymium spectra in oxide glasses could be described by small number (less than 10) of "basis" spectra so that any new spectrum could be considered as "intermediate" one between two basis spectra. Certainly, the extending such classification on ESA spectra calls for further investigations.

5. CONCLUSION

At present time, ESA in RE-doped glasses is considered as property that determines the choice of glass composition for use in fiber lasers and amplifiers. The determination of ESA parameters is urgent task of glass spectroscopy. In order to perform it, the several experimental methods have been developed. In present state of ESA investigations, every particular method is applied to definite class of cases. Investigations were concentrated on Pr-, Nd-, and Er-doped glasses. Silica glasses and fluorine ones are two groups of compositions, whose ESA properties possess specific features. Empirical dependencies of Judd parameters on glass composition can serve for prediction the integral intensities of bands in ESA spectra. For prediction of spectral contours, it is proposed to spread the classification of GSA spectra on ESA spectra.

6. ACKNOWLEDGMENT

The experimental part of this work was carried out in frame of joint program with Corning Corporation. The authors would like to thank C.Lerminiaux, S.G.Lunter, and L.B.Glebov for their encouragement and helpful dissension. They wish to thank M.V.Kharchenko for manufacturing the glass fibers.

7. REFERENCES

1. W.J.Miniscalco, L.J.Andrews, B.A.Thompson, R.S.Quimbi, L.I.B.Vacha, and M.G.Drexhage, "1.3μm fluoride fibre laser", *Electron.Lett.*, Vol.24, No1, pp.28-29, 1988.
2. M.C.Brierley and C.A.Millar, "Amplification and lasing at 1350nm in a neodymium doped fluorozirconate fibre", *Electron.Lett.*, Vol.24, No7, pp.438-439, 1988.
3. M.Brierley, S.Carter, P.France, and I.E.Pedersen, "Amplification in the 1300nm telecommunications window in a Nd-doped fluoride fibre", *Electron.Lett.*, Vol.26, No5, pp.329-330, 1990.
4. Y.Durteste, M.Monerie, J.Y.Allain, and H.Poignant, "Amplification and lasing at 1.3μm in praseodymium-doped fluorozirconate fibres", *Electron.Lett.*, Vol.27, No8, pp.626-628, 1991.

5. S.F.Carter, D.Szebesta, S.T.Davey, R.Wyatt, M.C.Brierley, and P.W.France, "Amplification at $1.3\mu\text{m}$ in a Pr^{3+} -doped single-mode fluorozirconate fibre", *Electron.Lett.*, Vol.27, No8, pp.628-629, 1991.
6. R.J.Mears and S.R.Baker, "Erbium fibre amplifiers and lasers", *Opt.Quantum Electron.*, Vol.24, pp.517-538, 1992.
7. J.Y.Allain, M.Monerie, and H.Poignant, "Blue upconversion fluorozirconate fibre laser", *Electron.Lett.*, Vol.26, No3, pp.166-167, 1990.
8. J.Y.Allain, M.Monerie, and H.Poignant, "Room temperature cw tunable green upconversion holmium fibre laser", *Electron.Lett.*, Vol.26, No4, pp.261-262, 1990.
9. R.G.Smart, D.C.Hanna, A.C.Tropper, S.T.Davey, S.F.Carter, and D.Szebesta, "CW room temperature upconversion lasing at blue, green and red wavelength in infrared-pumped Pr^{3+} -doped fluoride fibre", *Electron.Lett.*, Vol.27, No14, pp.1307-1309, 1991.
10. C.A.Miller, M.C.Brierley, M.H.Hunt, and S.F.Carter, "Efficient upconversion pumping at 801nm of an erbium-doped fluoride fibre operating at 850nm ", *Electron.Lett.*, Vol.26, No , pp.1871-1872, 1990.
11. M.C.Brierley and P.W.France, "Contineous wave lasing at $2.7\mu\text{m}$ in a erbium-doped fluorozirconate fibre", *Electron.Lett.*, Vol.24, No15, pp.935-937, 1988.
12. P.R.Morkel and R.I.Laming, "Theoretical modeling of erbium-doped fiber amplifiers with excited-state absorption", *Opt.Lett.*, Vol.14, No19, pp.1062-1064, 1989.
13. M.L.Dakss and W.J.Miniscalco, "Fundamental limits on Nd^{3+} -doped fiber amplifier performance at $1.3\mu\text{m}$ ", *IEEE Photon.Technol.Lett.*, Vol.2, No9, pp.650-652, 1990.
14. S.Zemon, B.Pedersen, G.Lambert, W.J.Miniscalco, B.T.Hall, R.C.Folweiler, B.A.Thompson, and L.J.Andrews, "Excited-state-absorption cross sections and amplifier modeling in the 1300nm region for Nd-doped glasses", *IEEE Photon.Technol.Lett.*, Vol.4, No3, pp.244-247, 1992.
15. S.Zemon, W.J.Miniscalco, G.Lambert, B.A.Thompson, M.A.Newhouse, P.A.Tick, L.J.Button, and D.W.Hall, "Comparison of Nd $^{3+}$ -doped glasses for amplification in the 1300nm region", in *Fiber Laser Sources and Amplifiers IV*, M.J.F.Digonnet, E.Snitzer, Editors, *Proc.SPIE* 1789, pp.58-65, 1993.
16. B.Pedersen, W.J.Miniscalco, S.Zemon, and R.S.Qrimby, "Analysis of Pr^{3+} - and Nd^{3+} -doped fiber amplifiers at 1300nm ", *Ibid.*, pp.191-200.
17. C.Robinson, "Excited-state absorption in fluorescent uranium, erbium, and copper-tin glasses", *J.Opt.Soc.Amer.*, Vol.57, No1, pp.4-7, 1967.
18. V.P.Kolobkov, P.I.Kudryashov, Yu.A.Rubinov, N.M.Bokin, and V.K.Zakharov, "Photo-induced absorption of Er^{3+} ions in glass", *Zh.Prikl.Spektrosk.(Russ.)*, Vol.77, No1, pp.161-163, 1972.
19. V.P.Kolobkov, P.I.Kudryashov, G.A.Starostina, and V.I.Shirokov, "Photoluminescence and photo-induced absorption of Sm^{2+} in vitreous silica", *Sov.J.Glass.Phys.Chem.(USA)*, Vol.5, No4, pp.403-407, 1979.
20. M.E.Vance, "Saturation and excited-state absorption in neodymium laser glass", *IEEE J.Quantum Electronics*, QE-6, No5, pp.249-253, 1970.
21. B.R.Judd, "Optical absorption intensities of rare earth ions", *Phys.Rev.*, Vol.127, No3, pp.750-761, 1962.
22. W.F.Krupke, "Radiative transition probabilities within the $4f^3$ ground configuration of Nd:YAG", *IEEE J.Quantum Electronics*, QE-7, No4, pp.153-159, 1971.
23. W.F.Krupke, "Induced-emission cross section in neodymium laser glasses", *IEEE J.Quantum Electronics*, QE-10, No4, pp.450-457, 1974.
24. N.B.Brachkovskaya and A.K.Przhevuskii, "Excited state absorption of neodymium glasses", *Dep.VINITI* No7476-B, *Zh.Prikl.Spektrosk.(Russ.)*, Vol.50, No2, p.89, 1989.
25. L.J.Andrews, W.J.Miniscalco, and T.Wei, "Excited state absorption of rare earth in fiber amplifiers", in *Proc.1st Int.Shcool on Excited States of Transition Elements*, ed.B.Jezowska-Trzebiatowska, pp.9-30, 1989.
26. W.J.Miniscalco, B.A.Thompson, M.L.Dakss, S.A.Zemon, and L.J.Andrews, "The measurement and analysis of cross section for rare-earth-doped glasses", in *Fiber Laser Sources and Amplifiers III*, M.J.Digonnet, E.Snitzer, Ed., *Proc.SPIE* 1581, pp.80-90, 1992.
27. J.L.Adam, N.Rigout, E.Denoue, F.Smektala, and J.Lucas, "Optical properties of Ba-In-Ga-based fluoride glasses for amplification at $1.3\mu\text{m}$ ", *Ibid.*, pp.155-165.
28. A.A.Kaminskii and B.M.Antipenko, "Multilevel Functional Schemes of Crystal Lasers", Nauka, Moskow, 1989.
29. D.E.McCumber, "Einstein relations connecting broadband emission and absorption spectra", *Phys.Rev.*, Vol.136, No4A, pp.954-957, 1964.

30. R.S.Quimby and B.Zheng, "New excited-state absorption measurement technique and application to Pr³⁺-doped fluorozirconate glass", *Appl.Phys.Lett.*, Vol.60, No9, pp.1055-1057, 1992.

31. D.W.Hewak, B.Samson, J.A.Medeiros Neto et.al., "Application of low phonon energy glasses for optical amplification at 1.3 microns", in *Fiber Laser Sources and Amplifiers V*, M.J.F.Digonnet, Ed., *Proc.SPIE* 2073, pp.127-137.

32. A.K.Przhevuskii, E.D.Trifonov, and A.S.Troshin, "Relation between the absorption and equilibrium luminescence spectra of glasses activated by rare earth ions", *Opt.Spectrosc.(USA)*, Vol.42, No3, pp.284-286, 1977.

33. R.S.Quimby, W.J.Miniscalco, and B.Thompson, "Excited state absorption at 980nm in erbium doped glass", in *Fiber Laser Sources and Amplifiers III*, M.J.Digonnet, E.Snitzer, Ed., *Proc.SPIE* 1581, pp.72-79, 1991.

34. R.Wyatt, "Spectroscopy of Rare Earth Doped Fibres", in *Fiber Laser Sources and Amplifiers I*, *Proc.SPIE* 1171, pp.54-64, 1989.

35. R.S.Quimby, W.J.Miniscalco, "Modified Judd-Offelt technique and application to optical transitions in Pr³⁺-doped glasses", *J.Appl.Phys.*, Vol.75, No1, pp.613-615, 1994.

36. P.R.Morkel, M.C.Farries, and S.B.Pool, "Spectral variation of excited state absorption in neodymium doped fibre lasers", *Optics Comm.*, Vol.65, No5, pp.349-352, 1988.

37. R.I.Laming, S.B.Pool, and E.J.Tarbox, "Pump excited-state absorption in erbium-doped fibers", *Optics Lett.*, Vol.13, No12, pp.1084-1086.

38. C.G.Atkins, J.R.Armitage, R.Wyatt, B.J.Ainslie, and S.P.Craig-Ryan, "Pump excited state absorption in Er³⁺-doped optical fibres", *Optics Comm.*, Vol.73, No3, pp.217-222, 1989.

39. S.Zemon, G.Lambert, W.J.Miniscalco, R.W.Davies, B.T.Hall, R.C.Folweiler, T.Wei, L.J.Andrews, and M.P.Singh, "Excited state cross sections for Er-doped glasses", in *Fiber Laser Sources and Amplifiers II*, M.J.Digonnet, Ed., *Proc.SPIE* 1373, pp.21-32, 1990.

40. J.Furthner, A.Penzkofer, "Emission spectra and cross-section spectra of neodymium laser glasses", *Opt. Quantum Electron.*, Vol.24, pp.591-601, 1992.

41. N.B.Brachkovskaya, A.A.Grubin, S.G.Lunter, A.K.Przhevuskii, E.L.Raab, and M.N.Tolstoi, "Intensities of optical transitions in absorption and luminescence spectra of neodymium in glasses", *Sov.J.Quantum Elektron.*, Vol.6, No5, pp.534-537, 1976.

42. E.I.Galant, V.N.Kalinin, A.A.Mak, D.S.Prilezhaev, A.K.Przhevuskii, M.N.Tolstoi, and V.A.Fromzel, "Stimulated emission from laser pumped ytterbium and erbium activated glasses", *Sov.J.Quantum Elektron.*, Vol.6, No10, pp.1190-1195, 1976.

43. R.S.Quimby, W.J.Miniscalco, and B.Thompson, "Quantitative characterization of clustering in erbium-doped silica glass fiber", in *Fiber Laser Sources and Amplifiers V*, M.J.Digonnet, Ed., *Proc.SPIE* 2073, pp.2-12, 1994.

44. T.Kogo, M.Onishi, S.Hirao, Y.Chigusa, K.Nakazato, M.Shigematsu, S.Suzuki, and M.Watanabe, "A study of the control of Nd³⁺ energy levels in fluorozirconate glasses", *J.Non.Cryst.Solids*, Vol.140, No1-3, pp.233-237, 1992.

45. A.A.Dymnikov and A.K.Przhevuskii, "The classification of the spectra of rare-earth ions in glass. Neodymium-doped glasses", *Proc.XV Intern.Congress on Glass*, Vol.4, pp.145-150, Leningrad, 1990.

Characterization of Nd:GdVO₄ crystals for high efficiency diode pumped lasers

I.A.Shcherbakov and A.I.Zagumennyi

General Physics Institute, Academy of Sciences, Vavilov St. 39
117942 Moscow, Russia, Fax:(095)135-11-24

1. INTRODUCTION

For small and efficient diode pumped solid state laser systems it is desirable to decrease the apparatus effort in temperature control of the laser diode pump and to increase the tolerance in the wavelength selection. Therefore it is necessary that the laser material features high absorption coefficients and large absorption linewidths. The promising crystal for diode pumped solid-state lasers is Nd:YVO₄, in which it are both, broad homogeneous absorption lines and homogeneous emission lines have high peak crosssections. However, the crystals grown of Nd:YVO₄ of high optical quality meets a lot of difficulties, which prevent wide use of this material. In this paper we report about the growing and laser operation of Nd:GdVO₄. From technological point of view this material has a number of advantages, which open the possibility the growth his large size crystal for mass production.

In the last few years a handful of neodimium-doped vanadium-based crystals have been identified as potential successors to Nd:YAG. These crystals include yttrium orthovanadate (YVO₄), gadolinium orthovanadate (GdVO₄) and strontium fluorovanadate (SVAP or Sr₅(VO₄)₃F) are promising substitutes for Nd:YAG in diode-pumped laser products. The laser cross section for the vanadate crystals range from 1.8 to 5.6 times greater than Nd:YAG. They also maintain a strong singline emission with nearly the same peak wavelength as Nd:YAG.

The vanadate crystals are uniaxial, producing only polarized laser output, thus undesirable thermally induced birefringence. In addition, the peak pump wavelength for all crystals is 808 nm, the standard wavelength of currently manufactured high power diodes for laser pumping. Broad pump bandwidths of Nd³⁺ ions in vanadate laser materials mean more efficient pumping operation at a wider range of temperatures and a range of diode specifications, resulting in a less-expensive product.

For the first time in work at Moscow General Physics Institute (GPI) and Institute of Laser Physics (Hamburg, Germany) examined Nd:GdVO₄ in a diode-pumped laser [1,2,3].

2. Nd:GdVO₄ Crystal Growth.

Nd:GdVO₄ crystals were grown by the Czochralski technique in a radio-frequency-heated iridium crucible. The orientation of growth was <100>, <001> or <101>. The Nd³⁺ concentration varied from 0.9 at.% up to 6 at.%. The temperature of melting for Nd concentration of 2 at.% in melt was 1795° C and it decreases at higher concentration of neodymium ions.

For laser application a 100 mm long Nd-doped crystal of 25x25 mm section was grown a long the C- axis and a crystals of 16x22 mm section a long <101> by using a iridium crucible 80 mm in diameter. Growth conditions were characterized by pulling rate of 1.5 and 1.8 h⁻¹, rotation rate of 15-20 r.p.m. and atmosphere of nitrogen containing 2% by volume of oxygen. The crystals was fired at 1200° C for 10 h in air. Because the crystal is needed to subject to post growth annealing in air to oxidize V³⁺ back to V⁵⁺.

3. SPECTROSCOPY

3.1. The absorption of Nd:GdVO₄ in the region of 800-815 nm.

The uniaxial crystal Nd:GdVO₄ shows strong polarization dependent absorption transition due to the anisotropic crystal field. At 808.4 nm the peak absorption coefficient for Epump//C-axis is 74 cm⁻¹ for 1.2at.% neodymium doping level, resulting in an effective absorption cross section of 3.1*10⁻¹⁹ cm². For Epump \perp C-axis the absorption coefficient is only 10 cm⁻¹. High absorption coefficient (74 cm⁻¹) was measured correct in [1] at 120 μ m thick 1.2at.%Nd:GdVO₄ (Fig.1). But for real application are used Nd:GdVO₄ samples of 1 mm or 2.5 mm thick and inexpensive diode with broad emission spectrum. Therefore real "effectively" absorption of diode pump light is lower in Nd:GdVO₄. In [4] it demonstrated that the absorption band of Nd:GdVO₄ in the area of 808 nm for two polarizations by tuning the wavelength of a SDL-2462 array output radiation. The effectively absorption coefficient was obtained to be 20cm⁻¹ for Epump//C-axis and 12 cm⁻¹ for Epump \perp c-axis.

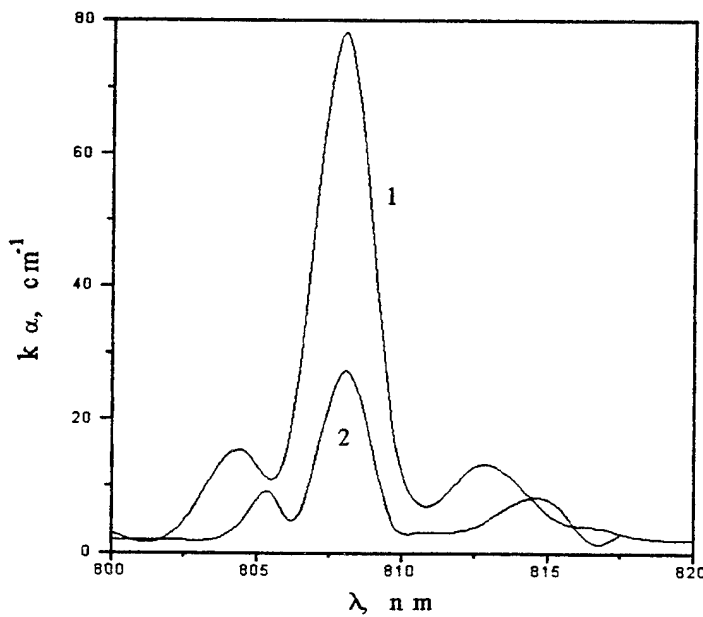


Fig.1. Absorption spectra of Nd:GdVO₄ crystal at 300K.

3.2.. Fluorescence

The polarization dependent fluorescence spectrum was measured with a fourier transform spectrometer using a 808 nm CW excitation from a laser diode with polarization parallel to the c-axis [3]. To examine if there is an overlap of transition lines, it has been investigated the absorption and fluorescence spectra at 77 K. It was not possible to resolve the Stark-splitting of the ⁴F_{3/2} level in Nd:GdV0₄, although there is a ΔE of 18 cm⁻¹ published for Nd:YVO₄. But in [12] the absorption and emission of Nd ions were measured at 2K and it found that ⁴F_{3/2} Stark-splitting in GdVO₄ is about 2 cm⁻¹. The Nd:GdVO₄ lines are much broader than Nd:YVO₄.

4.LASING PERFORMANCE.

4.1. High power lasing of Nd:GdVO₄ crystals at 1.06 mm.

Laser experiments were performed with a 2mm thick 1.2at.%Nd:GdVO₄ crystal samples [3]. The crystal has been oriented with the C-axis parallel to the polarization direction of the laser diode. The crystal mounted on a copper plate near a plane HR-mirror. The output coupler had a 50 mm radius curvature and 3% transmission at 1.06 μm . The laser cavity was nearly hemispherical. The pump source was a SDL-2482 diode with an emitting area of 500x1 μm and a CW-power of 2.3 W at 808.4 nm. The pump beam was first collimated in one direction using a collimating optic with 5 mm focal length. A cylindrical lens behind the collimator corrected the astigmatism. Focusing of the pump beam (120x20 μm) was achieved by a 4 cm focal lens. The losses of the uncoated optical pump system were about 33%. The crystal absorbed about 97% of the diode pump light. With the 3% output coupler it has been obtained 825 mW output power at an incident diode power of 1540 mW behind the plane mirror. This corresponded to a slope efficiency of 57 % with respect to the absorbed pump power during laser action, in order to avoid bleaching of the neodimium groundstate. Crystal reflections have not been taken into account. Fig.2. shows an input-output of Nd:GdVO₄ and for comparison a measurement with an identical Nd:YAG setup (slope efficiency 53%).

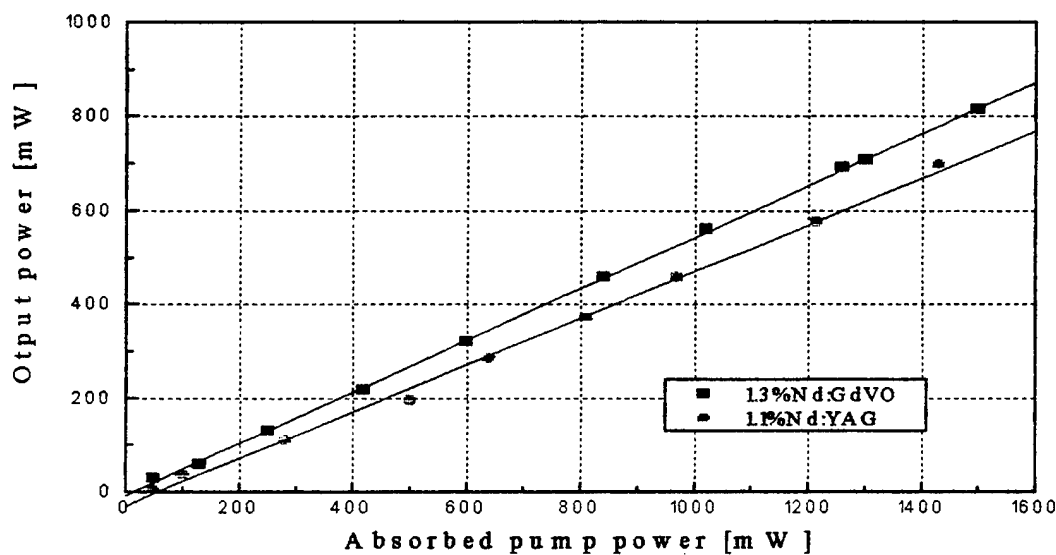


Fig 2. Diod pumped lasing at 1.06 μm of Nd:GdVO₄ and Nd:YAG under identical conditions

4.2. Lasing at 1.34 mm.

Laser experiments at 1.34 μm with a 500 mW diode laser pump yielded 58 mW output power, while the crystal absorbed 280 mW. The slope efficiency was 26% when using a 5% output coupler in the experimental setup described in [3].

4.3. Pump Nd:GdVO₄ crystal without the precise control of the output wavelength a laser diode-source

Laser experiments were carried out with a 250 mW laser diode source and 1.3at.%Nd:GdVO₄ samples of 1mm and 2.5 mm length. The output power of Nd:GdVO₄ laser as a function of the diode temperature is shown in Fig.3. It is easy to see from these measurements Nd:GdVO₄ crystal of chosen thickness to demonstrate broad-band independence on the diode temperature and can be pumped by the laser diode without fine thermal control [5].

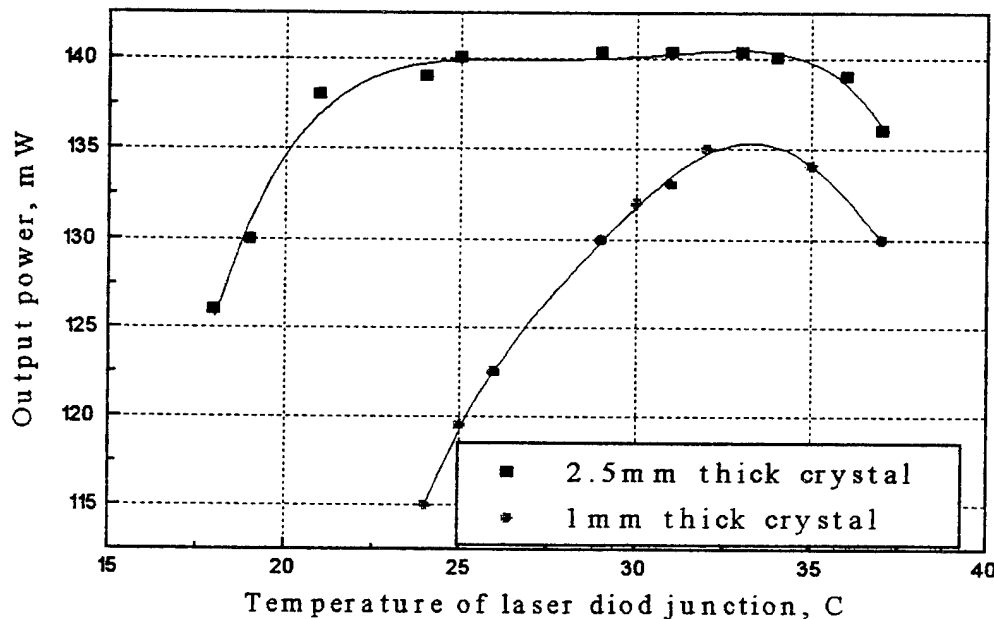


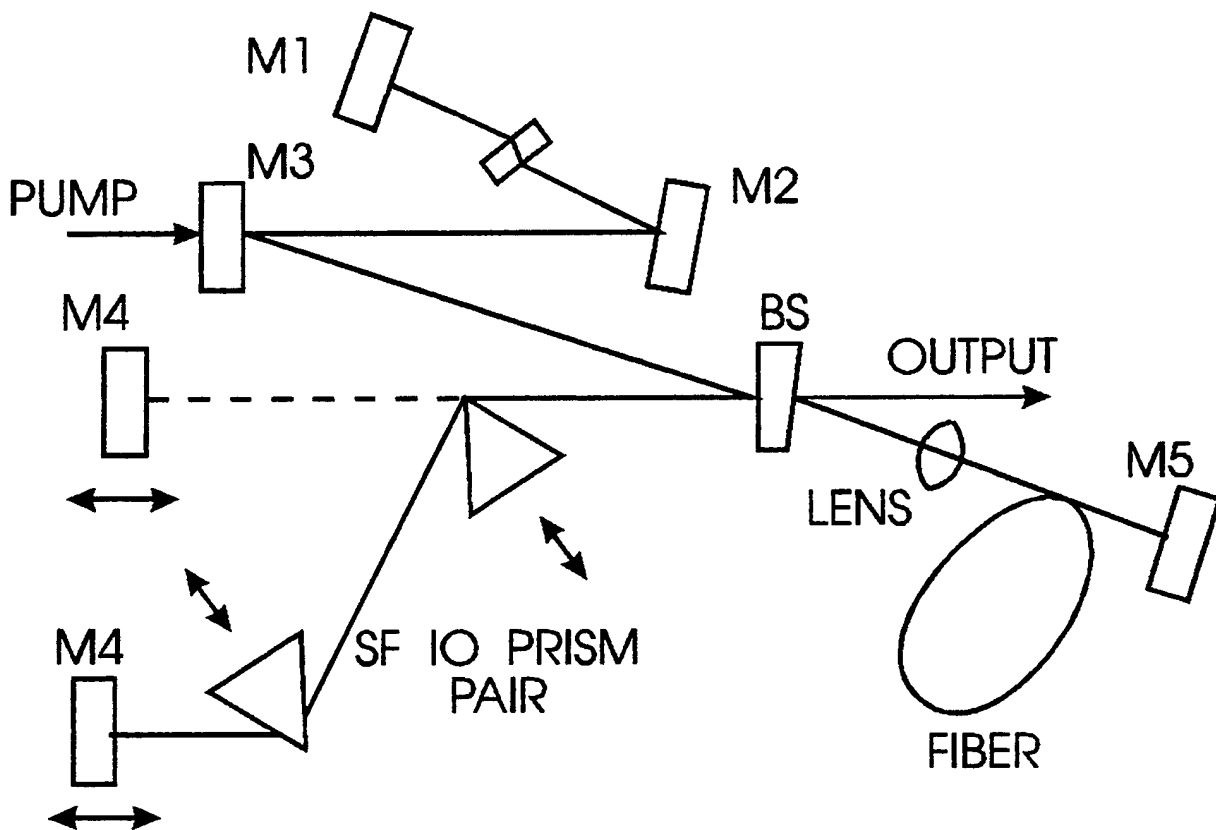
Fig.3 Nd:GdVO₄
Dependence of optical efficiency

4.4. CW passive mode-locking Nd:GdVO₄ laser

The best result a diode-pumped Nd:YAG laser demonstrated by using self-starting additive-pulse mode (APM) locking with a nonlinear external cavity [6] and the pulse duration of 1.7 psec are generated at an average output power of 25 mW without the need for active amplitude or phase modulation. Pulse duration of 1.5 psec are generated Nd:YLF [7]. In the APM system are the pulses much shorter than for active mode locking. Even shorter pulse duration can be anticipated in Nd:glass or Nd:crystals, in which the gain bandwidth is broader. Widely used nearly homogeneously broadened hosts like YAG and YLF have narrow emission and absorption lines.

New laser material Nd:GdVO₄ is a Gd analog to an YVO₄ crystal and possesses a unique combination of broad 10 nm intensive absorption band at 808 nm combined with relatively broad 1.2 nm emission line at 1062.9 nm, it are suitable for ultrashort-pulse generation as well. In [9] reported the first demonstration of a thin-plate Nd:GdVO₄ passively mode-locked a laser, pumped by a Kr⁺-laser ($\lambda=799$ and 752 nm) to simulate diode-pumping. Self-starting APM was achieved for a range of

externally cavity parameters in passive mode-locking a laser using a dispersively balanced nonlinear Michelson interferometer.



The shortest pulses were obtained by using a beam splitter (BS) of 90% and a fiber length 30-76 cm. The prism pair comprised 60° prisms made from SF10 glass with the light incident close to Brewster's angle. The cavity design is shown schematically in [8]. The spectrum of the laser output pulse and second-harmonic-generation (SHG) autocorrelation trace of pulse of LBO crystal (0.3 mm in length) was measured with a spectrometer and an optical multichannel analyzer. The active medium was a 1-mm-thick plate of 1.3 at.% Nd:GdVO₄ crystals, cooled through its side surfaces. The waist diameters inside the crystal were 15 μm for resonator beam and 23 μm for pump beam. To characterize TEM₀₀-mode CW laser performance, a short cavity, consisting of mirrors M1, M2, M3 and an output coupler at the place of beam splitter BS was used. The lasing data are summarized in Table 1.

At maximum available pump power of 2.15 W (1.6 W absorbed), output power of 690 mW was obtained without beam profile or efficiency degrading. For mode-locking experiments a full version of the cavity was used. To stabilize interferometrically two arms of a nonlinear interferometer mirror M4 was mounted on a piezoelectrically translator (PZT), controlled by a servo loop. At 1.75 W of pump power (1.3 W absorbed) the laser produced stable train of pulses with $\tau=2.4$ ps with output power of 300 mW. The spectral width of the mode-locked laser output was 0.6 nm, yielding time-bandwidth product $\Delta\tau\Delta\nu=0.36$. This value is close to that of a transform-limited pulse, indicating that the pulse is almost free of frequency chirp. This can be also seen from an interferometric autocorrelation trace. These data are obtained without optimization of the fiber length in the nonlinear arm of the resonator, which

gives us hope to produce pulses of even shorter duration, utilizing full 1.2-nm-wide linewidth of the material.

Table 1

Output coupling (%)	Pout (mW)	Slope efficiency (%)
3.5	565	41
5	615	45
10	645	48
16	660	51

4.6. Stability of optical quality of Nd:GdVO₄.

Optical quality of the vanadate crystal which was checked by measuring the laser output power from different points of the crystal aperture [4]. The crystal was moved across the optical axis of the cavity in two perpendicular directions with 250 μm step. The decrease of the output power in any point of the crystal aperture (ring with 4 mm diameter) was found to be not more than 10%.

5. DISCUSSION.

5.1. Technological point of view of vanadate laser hosts.

In [12] the Center for Research and Education in Optics and Lasers (CREOL) of University of Central Florida reported the comparison of physical properties, spectroscopy, lasing performance and crystal growth of Nd:YVO₄, Nd:GdVO₄, Nd:Sr₅(PO₄)₃F, Nd:Ca₅(PO₄)₃F, Nd:Sr₅(VO₄)₃F and it concluded that Nd:Sr₅(PO₄)₃F (Nd:SFAP) at present time have significantly less problems in terms of growth and one has the best chance to performance and availability for miniature Nd laser. Of course, each individual crystal has its own problems. But looking all the criteria's this comparison and experience of GPI group [11] in growing Nd:YVO₄, Nd:YAG, Nd:Cr:YSGG, Nd:Cr:GSGG, GdVO₄, Nd:GdVO₄, Yb:GdVO₄, Tm:GdVO₄, Ho,Tm:GdVO₄, Er:GdVO₄ we conclude that, from technological point of view and properties of Nd:GdVO₄ crystal has a number of advantages than the above indicated crystals for small and efficient diode pumped solid state laser systems.

5.1.1. Nd ions distribution coefficient

A crystal of uniform composition throughout its length can only be grown from a melt that has the so-called congruent melting composition. When this composition is used in the melt, the composition at the melt/crystal interface remains stable even when the growth rate fluctuates because of fluctuations in melt flow or temperature. This minimized growth striations and the tendency toward constitutional supercooling, and results better crystal quality. For example, The melt point of pure YVO₄ is 1810°C and it of Nd_{0.045}Y_{0.955}VO₄ (composition for growth 1.5at.%Nd:YVO₄ crystal) Nd:YVO₄ is 1785°C. This means that the congruent melting composition of Nd:YVO₄ is not situated.

It is obvious that the constitutional super-cooling in this case is caused by both the influence of Nd-dopant on the melt point and the difference from unity of the distribution coefficients Nd³⁺ ions. The fact that CZ growth of Nd:YVO₄ is from a polycomponent solution, constitutional supercooling presents a serious problem (scattering centers or smoke) and therefore the fact that this is a solution growth also seriously limits growth rate (0.8-1.5 mm per hour).

GPI group [11] determined the distribution coefficients of Nd ions in GdVO₄ and YVO₄ using standard free-electron microprobe analyze (Table 2). For guarantee laser parameter in Nd-doped

commercial laser rod it use for theirs production a laser crystal boule containing of Nd³⁺ions with the accuracy 0.1at.% . Using this fact, together with Nd distribution coefficients, it is very easy to make a direct comparison for commercially available new potential laser host. The closeness of the Nd³⁺ dopant distribution coefficeints to unity gives the opportunity of pulling Nd-laser crystal up to the crystallized melt fraction g = 10% -56% without significant variation of the Nd³⁺ions along the boule of laser crystals (Table 2). The combination of the growth rate, large size of crystal boule, value of crystallized melt fraction g(%) and easy to fabricate of laser samples will determine the cost and the suitable for mass production new Nd-doped laser crystals.

The crystallized melt fraction g(%) we calculated using the well-known Pfann equation suitable for the CZ method:

$$C_s = C_o K(1-g)^{K-1}$$

where C_s is the dopant concentration in the crystal and C_o is the dopant concentration in the melt, K is distribution coefficient of Nd³⁺ions

Table 2.

The crystallized melt fraction g(%) with variation 0.1at.% of the Nd concentration along the boule

1.1at.% Nd-doped crystal	Distribution coefficients of Nd ions	Ref.	Nd ions concentration (at.%)			Growth rate (mm/hr)	g (%)
			Melt	Top	Bottom		
Nd:YAG	0.18	[10]	5.56	1.0	1.1	0.7	11%
Nd:YVO ₄	0.35	[11]	3.14	1.1	1.2	1.5	13%
Nd:GdVO ₄	0.9	[11]	1.22	1.1	1.2	1.8	56%
Nd:Sr ₅ (PO ₄) ₃ F	0.36	[12]	3.14	1.1	1.2	1.0	13%
Nd:Ca ₅ (PO ₄) ₃ F	0.52	[12]	2.12	1.1	1.2	1.0	16%
Nd:Sr ₅ (VO ₄) ₃ F	0.24	[12]	4,58	1.1	1.2	1.5	11%

5.1.2. Czochralski growth of vanadate crystals.

Yttrium vanadate has been grown from the flux and by the Czochralski method. The largest single Nd:YVO₄ crystals have been obtained from Czochralski growths. However, serious problems such as inclusions, color center, cleavage and diameter control still persist in the growth of really high-quality crystals. It has been reported in the literature, that the melt of Nd:YVO₄ is not stable. At the melting point of YVO₄ 1810°C, it loses oxygen very rapidly $YVO_4 \rightleftharpoons YVO_{4-x} + 0.5x O_2$. The decomposition of YVO₄ melt also causes, instead of a monocomponent system, it is a polycomponent system, a solution of two or more YVO_{4-x} compounds with different x values.

From GPI group work [11] we indicated that the growth of (1-3)at.%Nd:GdVO₄, Yb:GdVO₄, GdVO₄, is much easier than of (1-3)at.%Nd:YVO₄ or 5at.%Tm:GdVO₄ because the boules last two crystals occasionally grew in a spiral or corkscrew from rather than the desired cylindrical form. Usually the spiral would be preceded by an azimuthal asymmetry, which has the appearance of a "foot". In [12] CREOL group tried to grow of Nd:GdVO₄ and "found that the growth is equally difficult with the same problem of green tint and smoke". In first GPI experiment with Nd:YVO₄ and Nd:GdVO₄ we have indentified several problems in crystal growth: spiral boule growth, boule cracking, fine scattering ("smoke"), optical homogeneity, color centres of V³⁺. Resembiancy problems we investigated last ten

years for such laser hosts as gadolinium-scandium-gallium garnet (Nd:Cr:GSGG) and yttrium-scandium-gallium garnet (Nd:Cr:YSSG, Er:Cr:YSGG) or in the work of LLNL for Nd:Cr:GSGG crystal [13].

Now GPI group have made substantial progress toward obtaining large, high-quality Nd:GdVO₄ crystals for use in diode pump laser. In growing Nd:GdVO₄, we based our work on a sizable body of information and experience in growing GGG (Gd₃Ga₅O₁₂), which is grown commercially in 10 cm diameter x 23 cm boules, and Nd,Cr:GSGG crystal boules up to 13 cm in diameter and 20 cm long [13]. We believe that the growth of Nd:GdVO₄ is close to a growth of gallium garnet and we do not foresee any difficulty to grow large size crystal for mass production. The growth rate Nd:GdVO₄ is about 3 times than of Nd:YAG and this makes cost comparable to Nd:YAG.

6.CONCLUSIONS

In conclusion we would like to point, that it has been achieved high slope efficiencies under diode pumping with a new material: Nd:GdV04. The material offers large effective absorption and emission cross-sections coupled with a relative broad absorption line. The laser performance is expected to be much tolerant to diode wavelength variation than Nd:YAG, and is therefore an interesting candidate for future application. Besides, the growing of high-quality Nd:GdVO₄, in principle, is easier realized from the point of view of impurity segregation than Nd:YVO₄. That is connected with distribution coefficients Nd³⁺ much nearer to the unity. It has been obtained efficient mode-locked operation of the new Nd:GdVO₄ laser material, yielding stable 5 nJ pulses with 2.4 ps duration, which is comparable to that of YAG and YLF. Spectral properties favorable for diode pumping and good CW lasing performance make this new material highly attractive for all-solid-state ultrashort-pulse laser system.

REFERENCE.

- [1] A.I.Zagumennyi, V.G.Ostroumov, I.A.Shcherbakov, T.Jensen , J.P.Meyn and .G.Huber. "Nd:GdVO₄ crystals - a new material for diode-pumped solid state lasers". Sov.J.Quantum Electron. 22, p.1071, 1992; OSA Proceedings.of ASSL'93. Topical meeting (New Orleans, USA, p.52-54, 1993.)
- [2]. T.Jensen, J.-P.Meyn, G.Huber, V.G.Ostroumov, I.A.Shcherbakov and A.I.Zagumennyi: Conference on Lasers and Electro-Optics, CFE4, p.590, 1993.
- [3] T.Jensen,V.G.Ostroumov, J.-P.Meyn, G.Huber, I.A.Shcherbakov and A.I.Zagumennyi. "Spectroscopic characterization and laser performance of diode pumped Nd:GdVO₄". Appl. Phys. vol.B 58, N5, p.373 - 379, 1994.
- [4] Klimov I.V., Mikhailov V.A., Shcherbakov I.A., Zagumennui A.I., K.-J.Boller, J.Bartschke, R.Knappe, and R.Wallenstein "Nd:GdVO₄-Laser with Nonlinear Transformation of Frequency". Conference on lasers and electro-optics/Europe * European quantum electronics conference (CLEO/EUROPE '94 and EQEC'94) Amsterdam, The Netherlands,
- [5] A.I.Zagumennyi, N.V.Kravtsov, O.E.Nanii, M.Yu.Nikolskii, A.M.Prokhorov, V.V.Firsov, I.A.Shcherbakov. "GdVO₄:Nd laser pumped by a semiconductor laser". Sov.J.Quantum Electron 20, N 12 (Russia),1993.
- [6] Goodberlet J., Jacobson J.,Fujimoto J.G.,Schulz P.A., Fan T.Y. "Self-starting additive-pulse mode -locked diode-pumped Nd:YAG laser". Opt.Lett., 1990, v.15, p.504
- [7] Malcom G.P.A., Curley P.F., Ferguson A.I. "Additive-pulse mode-locking of a diode-pumped Nd:YLF laser." Opt.Lett.,1990, v.15, p.1303.
- [8] Spielmann Ch., Krausz F., Brobec T.,Winter E.,Schmidt A.J. "Femtosecond passive mode-locking of

a solid-state laser using a dispersively balanced nonlinear Michelson interferometer".
Appl.Phys.Lett., 1990, v.58, p.2470.

[9] E.Sorokin, I.Sorokina, E. Wintner, A.I.Zagumennyi, I.A. Shcherbakov: "CW pasive mode-locking of a new Nd:GdVO₄ laser" OSA Proceedings of ASSL'1993, p.203

[10] Brandle C.D., Vanderleeden J.C. "Growth, Optical properties and CW laser action of Neodimium doped gadolinium -scandium-aluminum garnet" IEEE journal of Quantume Electronics, (1974)v.10, No 1, p.67-71.

[11] Zagumennyi A.I., Zavartsev Yu.D., Studenikin P.A., Shcherbakov I.A. to be published results.

[12] Bruce H.T.Chai "Recent development of high efficiency Nd miniature laser host materials". To be published in SPIE-Proceedings: Novel Laser Sources and Aplications (1994)

[13] S.E.Stokowski, M.H.Randles, and R.C.Morris " Growth and Characterization of Large Nd,Cr:GSGG crystals for High-average-power slab lasers" IEEE journal of Quantume Electronics, (1988)v.24, No 6, p.934 - 945.

Author Index

Andrianov, D. G., 115
Astapenko, Valerie A., 58, 61
Balykin, V. I., 19
Basiev, Tasoltan T., 164, 171, 179
Bilger, G., 51
Bonch-Bruevich, Aleksei M., 11
Breteau, Jean-Marc, 154
Broslavez, U. U., 107, 193
Buchinskaya, I. I., 211
Bystrova, A. A., 211
Chastookhin, E. M., 126
Denisov, Yu. V., 95
Dodel, G., 51
Doroshenko, M. E., 171, 179
Dostálová, Tat'jana, 72
Ermakov, Igor V., 164
Fomichov, Alexey A., 193
Fomitchev, A. A., 107
Fotakis, Costas, 72
Gordienko, Vyacheslav M., 126
Grigoropoulos, Costas P., 22, 32, 41
Himmlová, L., 72
Jastrabík, Lubomír, 72, 79
Jelínek, Miroslav, 72, 79, 84
Kadlec, J., 72
Kamychenko, V. V., 138
Kantor, Zoltan, 45
Kartuzov, Valery V., 134, 138
Khromov, V. V., 11
Kirshin, M. Yu., 231
Klimonskii, S. O., 115
Krasíkov, Igor V., 134
Krasilov, Yu. I., 95
Krivandina, E. A., 211
Kurochkin, Nikolay N., 126
Lebedev, V. F., 65
Leiderer, Paul, 32, 41
Lokhnygin, Vladimir D., 193
Lubnin, E. N., 115
Macháč, P., 88
Madii, V. A., 95
Maksimov, V. V., 143
Marchenko, V. M., 65
Metal, Martin, 84
Mikhailova, G. N., 115
Myslík, Vladimír, 84, 88
Olšan, V., 72
Orlov, A. N., 143
Osiko, Vyacheslav V., 171, 179
Panchenko, Vladislav Ya., 126
Papashvili, Alexander G., 171, 179
Park, Hee K., 22, 32, 41
Piglmayer, K., 45
Poon, Chie C., 32, 41
Pospíchal, M., 72
Prokhorov, Alexander M., 115, 143, 164
Przhevuskii, Alexander K., 231
Przhibelskii, S. G., 11
Rotmistrovsky, Cyril E., 134
Rybaltovskii, A. O., 65
Schmauder, R., 51
Seferov, A. S., 115
Sevastyanov, B. K., 211, 223
Sharonov, M. Yu., 211
Shcherbakov, Ivan A., 241
Sibley, William A., 202
Sidoryuk, Oleg E., 58, 61
Sigachev, Valery B., 171, 179
Silichev, Oleg O., 193
Šimečková, M., 72
Sobolev, B. P., 211
Takai, Mikio, 2
Tam, Andrew C., 22, 32, 41
Tikhomirov, V. A., 65
Toth, Zsolt, 45
Troitskii, A. V., 115
Trtík, V., 79
Ushanova, Elena, 58
Vaks, V. G., 138
Vartanyan, T. A., 11
Vrňata, M., 88
Yakshin, M. A., 107
Yavaş, Oğuz, 32, 41
Zagumennyi, A. I., 241
Zmurova, Z. I., 211
Zubovich, A., 95
Zverev, Peter G., 164, 171